The Multiscale Wavelet Finite Element Method for Structural Dynamics

A thesis submitted for the degree of

Doctor of Philosophy

by

MUTINDA MUSUVA

Supervisor

Dr. Cristinel Mares

Department of Mechanical, Aerospace and Civil Engineering

College of Engineering, Design and Physical Sciences

Brunel University London

January 2015

Abstract

The Wavelet Finite Element Method (WFEM) involves combining the versatile wavelet analysis with the classical Finite Element Method (FEM) by utilizing the wavelet scaling functions as interpolating functions; providing an alternative to the conventional polynomial interpolation functions used in classical FEM. Wavelet analysis as a tool applied in WFEM has grown in popularity over the past decade and a half and the WFEM has demonstrated potential prowess to overcome some difficulties and limitations of FEM. This is particular for problems with regions of the solution domain where the gradient of the field variables are expected to vary fast or suddenly, leading to higher computational costs and/or inaccurate results. The properties of some of the various wavelet families such as compact support, multiresolution analysis (MRA), vanishing moments and the "two-scale" relations, make the use of wavelets in WFEM advantageous, particularly in the analysis of problems with strong nonlinearities, singularities and material property variations present.

The wavelet based finite elements (WFEs) presented in this study, conceptually based on previous works, are constructed using the Daubechies and B-spline wavelet on the interval (BSWI) wavelet families. These two wavelet families possess the desired properties of multiresolution, compact support, the "two scale" relations and vanishing moments. The rod, beam and planar bar WFEs are used to study structural static and dynamic problems (moving load) via numerical examples. The dynamic analysis of functionally graded materials (FGMs) is further carried out through a new modified wavelet based finite element formulation using the Daubechies and BSWI wavelets, tailored for such classes of composite materials that have their properties varying spatially. Consequently, a modified algorithm of the multiscale Daubechies connection coefficients used in the formulation of the FGM elemental matrices and load vectors in wavelet space is presented and implemented in the formulation of the WFEs. The approach allows for the computation of the integral of the products of the Daubechies functions, and/or their derivatives, for different Daubechies function orders. The effects of varying the material distribution of a functionally graded (FG) beam on the natural frequency and dynamic response when subjected to a moving load for different velocity profiles are analysed. The dynamic responses of a FG beam resting on a viscoelastic foundation are also analysed for different material distributions, velocity and viscous damping profiles.

The approximate solutions of the WFEM converge to the exact solution when the order and/or multiresolution scale of the WFE are increased. The results demonstrate that the Daubechies and B-spline based WFE solutions are highly accurate and require less number of elements than FEM due to the multiresolution property of WFEM. Furthermore, the applied moving load velocities and viscous damping influence the effects of varying the material distribution of FG beams on the dynamic response. Additional aspects of WFEM such as, the effect of altering the layout of the WFE and selection of the order of wavelet families to analyse static problems, are also presented in this study.

Acknowledgements

First and foremost, I would like to thank God for the opportunity to perform this study and the countless blessings He has bestowed upon me. I am thankful for the strength and encouragement provided through others.

I would like to thank my supervisor Dr. Cristinel Mares, who has been extremely helpful during my PhD program. Thank you for the help, guidance and advice you continually offered. You are very much appreciated.

I would like to acknowledge and thank my parents Prof. and Mrs. J. K. Musuva, for the constant prayers, sacrifices, support and guidance they have continually given. Words alone cannot express the gratitude I have. May God continue to keep you and bless you.

I am forever grateful to my family for their assistance, sacrifices and encouragement during my studies. I would particularly like to recognise my sisters, Mwende and Munini, my brother Muoka and my brothers-in-law, Patrick and Mark.

Special thanks to Lorna for being very loving, supportive, understanding and encouraging during my studies. I know it was not easy and I really appreciate the assistance, motivation and care you have offered during this time.

I would like to also mention and thank Victor, Joan, Tharaka, Jean, Chris, Tony, Timothy, Janerose, Jack, Tomi and the many others who have offered their help, support and encouragement during my research.

Finally, I would like to acknowledge and thank Brunel University and its staff.

Authors Declaration

I, Mutinda Musuva declare that, except where explicit reference is made to the contribution of others, that this PhD Thesis is the result of my own work under the supervision and assistance of Dr. C. Mares and to the best of my knowledge has not been submitted for any other degree at Brunel University London or any other institution.

Signature: _____

Printed name: _____

Date: _____

Publications

Musuva, M. and Mares, C. (2012), "The Wavelet Finite Element Analysis of a Beam Subjected to a Moving Load." *Proceedings of the First International Conference on Railway Technology: Research, Development and Maintenance* (p. Paper 120). Stirlingshire: Civil-Comp Press Ltd. – Railways 2012 - 18-20 April 2012, Las Palmas de Gran Canaria, Spain.

Musuva, M. and Mares, C. (2012), "Vibration of Frame and Structures Using Wavelet Finite Elements." *Journal of Physics: Conference series 382.* Bristol: IOP Publishing Ltd. – Modern Practice in Stress and Vibration Analysis (MPSVA) 2012 - 29-31 August 2012, Glasgow, Scotland.

Musuva, M., Koziol, P., Mares, C. and Neves, M. M. (2014), "The Analysis of Beam Subject to Moving Load Using: Coiflets, the Wavelet Finite Element Method and the Finite Element Method." *Proceedings of the Second International Conference on Railway Technology: Research, Development and Maintenance*. (p. Paper 222) Stirlingshire: Civil-Comp Press Ltd. – Railways 2014 - 8-11 April 2014, Ajaccio, Corsica, France.

Musuva, M. and Mares, C. (2014), "The Dynamic Analysis of Functionally Graded Materials (FGM) using the Wavelet Finite Element Method (WFEM)." *Proceedings of the 26th International Conference on Noise and Vibration Engineering* – ISMA 2014 - 15-17 September 2014, Leuven, Belgium.

Table of Contents

List of Figures

List of Tables

Abbreviations

WFEM(s)	Wavelet Finite Element Method(s)
FEM(s)	Finite Element Method(s)
MRA	Multiresolution Analysis
WFE(s)	Wavelet Finite Element(s)
BSWI	B-Spline Wavelet on the Interval
FGM(s)	Functionally Graded Material(s)
FG	Functionally Graded
DOF(s)	Degree(s) of Freedom
PDE(s)	Partial Differential Equations
B-Wavelet	B-spline Wavelet
BEM	Boundary Element Method
ODE(s)	Ordinary Differential Equation(s)
LPG	Liquefied Petroleum Gas
HCSWI	Hermite Cubic Spline Wavelet on the Interval
LMS	Linear Multistep Method

Nomenclature

$f(x)$	Arbitrary function of x	j	Multiresolution scale
V_j	Scaling function subspace at scale j	W_j	Wavelet function subspace at scale j
Q_j	Projection on subspace W_j	P_j	Projection on subspace V_j
ϕ	Scaling function	ψ	Wavelet function
$\phi_k^j(x)$	Orthonormal basis of subspace V_j	$\psi_k^j(x)$	Orthonormal basis of subspace W_j
$L^2(\mathbb{R})$	Hilbert Space	$\mathbb{Z}$	Set of integers
$\mathbb{R}$	Set of real numbers	$\mathbb{N}$	Set of natural numbers
a_k^j	Coefficients in subspace V_j	b_k^j	Coefficients in subspace W_j
$h(k)$	Scaling function filter coefficients	$g(k)$	Wavelet function filter coefficients
DL	Daubechies wavelet family order L	DL_j	Daubechies wavelet family order L at scale j
$\phi_L(x)$	Daubechies scaling function order L scale at $j = 0$	$\psi_L(x)$	Daubechies wavelet function order L at scale $j = 0$
$p_L(k)$	Daubechies scaling function normalised filter coefficients order L	$q_L(k)$	Daubechies wavelet function filter normalised coefficients order L
$\phi_{L,k}^j(x)$	Daubechies scaling function translates k of order L at scale j	$\psi_{L,k}^j(x)$	Daubechies wavelet function translates k of order L at scale j
$\phi_{L,k}^{j,(m)}(x)$	Daubechies m^{th} derivative scaling function order L at scale j	$\psi_{L,k}^{j,(m)}(x)$	Daubechies m^{th} derivative wavelet function order L at scale j
$[\boldsymbol{I}]$	Identity Matrix	$\mathcal{X}_{[0,1]}(x)$	Characteristic function
$M_k^{j,m}$	Daubechies m^{th} Moments at scale j	${}_{a,b}\Gamma_{k,l}^{j,d_1,d_2}$	Daubechies 2-term connection coefficients at scale j for scaling functions order a and b
DL_j	Daubechies WFE of order L at multiresolution scale j	$\Upsilon_k^{j,m}$	Daubechies distributed load vector connection coefficient at scale j
BSWIm_j	BSWI wavelet family order m at scale j	$B_{m,k}^j(x)$	m^{th} order B-spline at scale j
V_j^m	m^{th} order cardinal B-spline subspace at scale j	W_j^m	m^{th} order B-wavelet subspace at scale j
$p_m(k)$	m^{th} order cardinal B-spline filter coefficients	$q_m(k)$	m^{th} order B-wavelet filter coefficients
$\widehat{N}_m(\omega)$	m^{th} order cardinal B-spline Fourier transform	$\hat{\psi}_m(\omega)$	m^{th} order B-wavelet Fourier transform
$L_m(x)$	m^{th} order fundamental cardinal spline	$\hat{L}_m(\omega)$	m^{th} order fundamental cardinal spline Fourier transform

t_k	B-spline knot sequence at scale $j = 0$	t_k^j	B-spline knot sequence at scale j
$\phi_{m,k}^j(x)$	m^{th} order BSWI scaling function at scale j	$\psi_{m,k}^j(x)$	m^{th} order BSWI wavelet function at scale j
$\phi_{m,k}^{j,(n)}$	m^{th} order BSWI n^{th} derivative of scaling function at scale j	$N_m(x)$	m^{th} order cardinal B-spline
$\Lambda_{i,k,l}^{j,d_1,d_2,d_3}$	Daubechies 3-term connection coefficients at scale j	n_s	Number of elemental segments within each WFE
x_i	Elemental node coordinate value	r	Number of elemental nodes within each WFE
ξ	Natural coordinate	n	Total number of DOFs within each WFE
ξ_i	Elemental node natural coordinate	$a_{z,k}^j$	Wavelet coefficients corresponding to axial DOFs in wavelet space
u_i	Local axial displacement at elemental node i in physical space	$b_{z,k}^j$	Wavelet coefficients corresponding to beam elemental DOFs in wavelet space
f_{xi}	Local axial force component at elemental node i	$\phi_{z,k}^j(\xi)$	Wavelet scaling function order z at scale j
f_{yi}	Local transverse force component at elemental node i	U_i	Global nodal axial displacement
$f_d(\xi)$	Distributed load function	V_i	Global nodal transverse displacement
Π^a	Potential energy with respect to axial deformation	F_{Xi}	Global nodal axial force component
Ω^a	Work potential via externally applied axial loads	F_{Yi}	Global nodal transverse force component
U^a	Axial strain energy	σ	Stress
A	Element cross-sectional area	ε	Strain
E	Young's Modulus	$\acute{m}_i$	Local bending moment at elemental node i
L_e	Length of element	v_i	Local transverse displacement at elemental node i in physical space
ρ	Material density	θ_i	Local rotation at elemental node i in physical space
Π^b	Potential energy with respect to transverse deformation	I	Moment of inertia
Ω^b	Work potential via externally applied transverse and bending loads	ρ	Material density
U^b	Beam bending strain energy	$\delta(x)$	Dirac Delta function
$V(x)$	Shear force function	$H(x)$	Heaviside function
$\frac{1}{R}$	Curvature	c	Speed of moving load

$\acute{\lambda}$	Eigenvalues corresponding to the inverse of the buckling loads	t	time
Q	Magnitude of moving Load	x_0	Location of moving load in local coordinates
ω	System natural frequencies	ξ_0	Location of moving load in natural coordinates
α_d	Rayleigh damping coefficient (stiffness)	P	Magnitude of transverse point load
β_d	Rayleigh damping coefficient (mass)	q_0	Magnitude of the varying load function
EI	Beam bending stiffness	$M(x)$	Bending Moment function
f_i	i^{th} mode natural frequency in Hz	Ω	Angular frequency of harmonic force
Δt	Time integration time step	c	Speed of moving load
$\acute{\delta}$	Newmark time integration parameter	ζ_i	i^{th} mode damping ratio
α_s	Non-dimensional velocity parameter	ω_i	i^{th} mode natural frequency in rad·s^{-1}
$\acute{\gamma}$	Newmark time integration parameter	c_{cr}	Moving load critical velocity
V_u	Upper surface volume fraction	T_n	Period corresponding to the n^{th} mode of vibration
V_l	Lower surface volume fraction	b	Beam width
n	Power law exponent	λ_i	Non-dimensional frequency
υ	Poisson's ratio	h	Beam height
G	Shear modulus	γ	Decrement of discontinuity intensity
K	Bulk modulus	$q(x)$	Varying load function
E_u	Upper surface Young's Modulus	ρ_l	Lower surface material density
E_l	Lower surface Young's modulus	ρ_u	Upper surface material density
$\{\boldsymbol{u_e}\}$	Local axial rod DOFs vector in physical space	$\{\boldsymbol{f_{r,e}^{n,w}}\}$	Rod element nodal concentrated force vector in wavelet space
$\{\boldsymbol{a_e}\}$	Vector containing wavelet coefficients $a_{z,k}^{j}$	$\{\boldsymbol{f_{r,e}^{n,p}}\}$	Rod element nodal concentrated force vector in physical space
$\{\boldsymbol{\Phi_z^j}(\xi)\}$	Vector containing scaling functions $\phi_{z,k}^{j}(\xi)$	$\{\boldsymbol{f_{r,e}^{d,w}}\}$	Rod element distributed force vector in wavelet space
$\{\boldsymbol{\Phi'^j_z}(\xi)\}$	Vector containing 1$^{\text{st}}$ derivative of scaling functions $\phi'^{j}_{z,k}(\xi)$	$\{\boldsymbol{f_{r,e}^{d,p}}\}$	Rod element distributed force vector in physical space
$\{\boldsymbol{N_{r,e}}(\xi)\}$	Wavelet based axial rod element shape function vector	$\{\boldsymbol{f_{r,e}^{p}}\}$	Total rod element force vector in physical space
$\{\boldsymbol{b_e}\}$	Vector containing wavelet coefficients $b_{z,k}^{j}$	$\{\boldsymbol{U_e}\}$	Global axial rod DOFs vector in physical space

$\{\boldsymbol{\Phi'^{j}_{z}}(\xi)\}$	Vector containing 1st derivative of scaling functions $\phi'^{j}_{z,k}(\xi)$	$\{\varepsilon_e^a\}$	Vector containing axial strains at elemental nodes within each WFE
$\{\boldsymbol{N_{b,e}}(\xi)\}$	Wavelet based beam element shape function vector	$\{\sigma_e^a\}$	Vector containing axial stresses at elemental nodes within each WFE
$\{\boldsymbol{\Phi''^{j}_{z}}(\xi)\}$	Vector containing 2nd derivative of scaling functions $\phi''^{j}_{z,k}(\xi)$	$\{\boldsymbol{v_e}\}$	Local beam DOFs vector in physical space
$\{\acute{V}\}$	Vector containing system mode shapes	$\{\boldsymbol{f^{n,w}_{b,e}}\}$	Beam element nodal concentrated force vector in wavelet space
$\{\boldsymbol{N'_{r,e}}(\xi)\}$	First derivative of rod WFE shape function vector	$\{\boldsymbol{f^{n,p}_{b,e}}\}$	Beam element nodal concentrated force vector in physical space
$\{\boldsymbol{f^{d,w}_{b,e}}\}$	Beam element distributed force vector in wavelet space	$\{\boldsymbol{f^{m,w}_{b,e}}\}$	Beam element bending moment vector in wavelet space
$\{\boldsymbol{f^{d,p}_{b,e}}\}$	Beam element distributed force vector in physical space	$\{\boldsymbol{f^{m,p}_{b,e}}\}$	Beam element bending moment vector in physical space
$\{\boldsymbol{f^{p}_{b,e}}\}$	Total beam element load vector in physical space	$\{\boldsymbol{f^{p,w}_{b,e}}(t)\}$	Moving load element vector in wavelet space
$\{\boldsymbol{f^{p,p}_{b,e}}(t)\}$	Moving load element vector in physical space	$\{\boldsymbol{\Upsilon^{j,m}}\}$	Daubechies connection coefficient vector for distributed loads at scale *j*
$\{\acute{H}\}$	Vector containing mode shapes for plane bar	${}^{A}E_e$	Axial stiffness of FGM beam WFE
$\{\ddot{\boldsymbol{H}}_{\boldsymbol{p}}(t)\}$	Acceleration vector for frame structure	${}^{B}E_e$	Axial-bending coupling stiffness of FGM beam WFE
$\{\boldsymbol{H_p}(t)\}$	System DOFs vector for frame structure	${}^{C}E_e$	Bending stiffness of FGM beam WFE
$\{\boldsymbol{F_p}(t)\}$	Time dependent moving load vector for frame structure.	$[\boldsymbol{m^{w}_{b,e}}]$	Beam element mass matrix in wavelet space
$[\boldsymbol{k^{p}_{r,e}}]$	Rod element stiffness matrix in physical space	$[\boldsymbol{m^{p}_{b,e}}]$	Beam element mass matrix in physical space
$[\boldsymbol{m^{w}_{r,e}}]$	Rod element mass matrix in wavelet space	$[\boldsymbol{M_p}]$	System mass matrix for plane bar
$[\boldsymbol{m^{p}_{r,e}}]$	Rod element mass matrix in physical space	$[\boldsymbol{K_p}]$	System stiffness matrix for plane bar
${}^{A}[\boldsymbol{k^{w}_{e}}]$	Axial stiffness matrix of FGM beam WFE in wavelet space	$[\boldsymbol{c^{p}_{b,e}}]$	Beam element damping matrix in physical space
${}^{B}[\boldsymbol{k^{w}_{e}}]$ ${}^{C}[\boldsymbol{k^{w}_{e}}]$	Axial-bending coupling stiffness matrices of FGM beam WFE in wavelet space	$[\boldsymbol{\Gamma}^{j,d_1,d_2}]$	Matrix containing the two-term connection coefficients at scale *j*
${}^{D}[\boldsymbol{k^{w}_{e}}]$	Bending stiffness matrix of FGM beam WFE in wavelet space	$[K_E]$	System elastic stiffness matrix
${}^{A}[\boldsymbol{m^{p}_{e}}]$	Axial mass matrix of FGM beam WFE in physical space	$[K_G]$	System geometric stiffness

$^{B}[\boldsymbol{m}_{e}^{p}]$ $^{C}[\boldsymbol{m}_{e}^{p}]$	Axial-bending coupling mass matrices of FGM beam WFE in physical space	*p*-FEM-*m*	*p* FEM element of order *m*
$^{D}[\boldsymbol{m}_{e}^{p}]$	Bending mass matrix of FGM beam WFE in physical space	FEM-n_e	Classical FEM element with n_e elements
$[\boldsymbol{T}_{r}^{G}]$	Rod element rotation matrix	$[\boldsymbol{k}_{b,e}^{w}]$	Beam element stiffness matrix in wavelet space
$[\boldsymbol{T}_{b}^{w}]$	Beam wavelet transformation matrix	$[\boldsymbol{k}_{b,e}^{p}]$	Beam element stiffness matrix in physical space

1. Introduction

1.1. Background

It is generally very difficult to formulate and apply exact closed form solutions in the analysis of complex engineering problems, particularly in structural analysis; due to the general realistic nature of such problems which may exhibit varying complexities, high gradients and strong irregularities within the systems e.g., suddenly varying loading conditions, contrasting material composition or geometric variations. The existing mathematical tools may require the system model to be simplified via certain assumptions and generalizations for these complex structural problems. This may lead to inaccuracies, inefficiencies of the method or even the inability to correctly describe the properties and behaviour of the system under certain conditions. The preferred approach, instead of significantly simplifying the structural systems, is to try and retain these complexities and find an approximate numerical solution for the system. This is carried out to better predict the behaviour of such systems and has given rise to numerical methods such as the classical Finite Element Method (FEM).

FEM is a numerical analysis technique used to solve various engineering problems by obtaining their approximate solutions. The method involves breaking down a system into many small interconnected sub-regions called finite elements and each element has an assumed approximate solution. Thus, the conditions for overall equilibrium of the structure are derived, yielding an approximate solution for the displacements and stresses [1]. The classical and adaptive FEMs where for example, the number of elements or the order of the polynomial basis in areas with high local gradients are increased to accurately approximate the solutions, may encounter significant difficulties in obtaining sufficient accuracy, efficiency and/or rapid convergence to the exact solution. This has led to the formulation of other numerical approximation techniques such as the wavelet based finite element method [2,3].

The concept of wavelet analysis stems from a blend of ideas by researchers, from a wide variety of disciplines, over the past few decades. However, the term as we now generally know it was introduced three decades ago by Grossman and Morlet [4]. Furthermore, given the evolution of this mathematical analysis tool, its definition is consistently being modified to cater for the new ideas and applications it is used for. The term wavelet can be generally defined as a class of basis functions that meet certain mathematical requirements to represent

functions locally, both in space (frequency) and time [5]. Moreover, wavelets allow for analysis of functions or data to be carried out at different resolutions (scales).

They have some similar attributes to classical Fourier functions. Though wavelets are not deemed to be replacements for classical Fourier approaches, they provide an alternative due to the fact that the Fourier functions are localised in space but not in time (they are global). Therefore, time localised functions can be analysed both conveniently and accurately with wavelets. The use of wavelets is vastly growing due to their ideal general properties such as multiresolution, compact support and the "two scale relation". They offer a considerable number of opportunities for design manipulation so as to be handcrafted to meet the desired requirements for specific applications. Therefore, new wavelet formulations are continually being developed for these applications and some of the common wavelets include: Haar wavelet, B-spline wavelet, Coiflets, Daubechies wavelet, and trigonometric wavelet families.

The Wavelet Finite Element Method (WFEM) involves combining wavelet analysis with the classical FEM by utilizing the wavelet and scaling functions as interpolating functions, thus providing an alternative to the conventional polynomial interpolating functions used in FEM. The method offers vast potential for the accurate and efficient analysis of fast varying and complex problems through the implementation of the essential wavelet multiresolution property. Through multiresolution analysis, it is possible to alter the scale of a local Wavelet Finite Element (WFE) without changing the initial model mesh [6,7]. This is an advantageous property in the analysis of structures with high gradients and singularities present.

To date, research has been carried out with regards to the formulation of different wavelet based finite elements using various wavelet families. Although these fundamental formulations have been described in literature, for instance, the Daubechies wavelet based FEM [6,8-10], the B-Spline Wavelet on the Interval (BSWI) [7,11,12] and the trigonometric wavelet based FEMs [13,14], a comparative study of the performance and implementation of the different WFEMs has not been conducted to date. Moreover, there are domains of structural analysis currently being developed where the use, understanding and scope of implementing WFEM remain partially or entirely unexplored.

One such area is the formulation of a wavelet based finite element method for the static and dynamic structural analysis of functionally graded materials (FGM). Functionally graded materials are a relatively new class of composites which consists of two or more materials

(often metals and ceramics), that comprise of different material and physical properties, varying continuously with spatial coordinates.

Therefore, this study describes and verifies not only the fundamental principles of the WFEM from previous work, but also the implementation of the method constructed using different wavelet families. Furthermore, the WFEMs are used in the static and dynamic analysis of structural systems under quick varying loading conditions, with an emphasis on moving load problems. Moreover, the research extends to the analysis and verification of this numerical approach to solve structures varying in composition, material properties and/or geometric properties. A new modified wavelet based finite element approach is proposed in the analysis of dynamic structural problems for FGMs. The wavelet based FGM finite elements are formulated using the Daubechies and BSWI wavelet families. This is a novel application of the method and there is no evidence suggesting it has been carried out or published, to the best of the author's knowledge.

1.2. Research objectives

The aim of this study is to analyse and verify the multiscale wavelet based finite element method applied to complex problems with strong singularities and/or variations in composition, loading conditions, geometry and material properties. This is achieved via the following objectives:

- Review fundamental principles of the WFEM from past work for 2 wavelet families (Daubechies and BSWI wavelet families) based on their properties of multiresolution, compact support, "two-scale" relation and vanishing moments.
- Develop algorithms to analyse and verify the implementation of WFEM with respect to the general rod, beam and plane bar elements using the different wavelet families for structural static and dynamic problems.
- Compare the different WFEM formulations and solutions to ascertain the strengths and limitations for the different wavelet families while verifying, identifying discrepancies and clarifying aspects of WFEM with respect to past work.
- Implement the WFEM formulations for the dynamic analysis of moving load problems due to fast or sudden variations of the loading conditions.
- Develop and present a new modified multiscale wavelet based finite element approach for the analysis of functionally graded beams using the Daubechies and BSWI wavelet families. These WFE formulations are applied in free vibration and

dynamic response analysis of functionally graded beams, where regions of the solution domain are expected to vary fast or suddenly.

- Develop a modified algorithm to evaluate the Daubechies integral of the products of scaling functions, and/or their derivatives (connection coefficients), for different orders of the wavelet family at any multiresolution scale. These connection coefficients are used to formulate the wavelet space elemental matrices and load vectors of not only a functionally graded beam, but also homogeneous rod, beam and plane bar elements.
- Present guidelines with respect to the application of WFEM for problems where the variation of stiffness or loading conditions require a dense mesh in the h-method and compare the WFEM formulations with the classical FEM approach (h or p method).
- Investigate the effects of varying the material distribution of a functionally graded material on the dynamic response of a functionally graded (FG) beam resting on a viscoelastic foundation for different velocity and damping profiles.

1.3. Thesis outline

This thesis contains a detailed analysis on the implementation of wavelets with the classical finite element method to formulate a wavelet based finite element method. The derivation of the element formulations as well as the strengths and weaknesses of the method are discussed. Its implementation to moving load problems and application in the analysis of functionally graded materials is outlined. The structure of the thesis is as follows:

Chapter 1 contains a brief introduction and overview of the study presented in this thesis. The wavelet finite element method is introduced and described, citing unexplored areas in which the method can be potentially implemented. The main aims and objectives of this study are defined; followed by an overview of the presented study. The main contributions of the study are also highlighted in this chapter.

Chapter 2 includes a literature review focusing on the advancements made with respect to the wavelet based finite element method. Relevant related works that have contributed to the current state of research are discussed. The different wavelet families that have been employed to create various wavelet based finite elements are also presented. Their applications, limitations and strengths, as investigated by other researchers, are further highlighted. An overview of functionally graded beams and the current advancements made with respect to their analysis is also presented in this chapter.

The definition and key concepts of wavelets and the multiresolution analysis are discussed in Chapter 3. Key properties and requirements of multiresolution for general wavelet analysis are presented. Furthermore, a mathematical approach is outlined and discussed with respect to the derivation and formulation of the BSWI and Daubechies scaling functions, wavelet functions and corresponding derivatives of the scaling functions; based on previous works. The general properties of these wavelet families are also discussed and linked with the formulation of the WFEM. A new modified formulation of the Daubechies connection coefficients used in the evaluation of the elemental matrices and load vectors is also presented in this chapter.

Chapter 4 highlights the key theories and aspects of the finite element method that are related to the formulation and implementation of the WFEM. The classical and *p*-*h* adaptive FEMs, which are to be compared with the WFEM solutions, are also briefly discussed. Fundamental theories and formulations relating to the dynamic analysis of structural problems are highlighted.

Consequently, the derivation and detailed discussion of the wavelet based finite elements implemented for both BSWI and Daubechies wavelet families are presented in Chapter 5. The axial rod, Euler Bernoulli beam and plane bar wavelet based elements are formulated; with common loading conditions highlighted. The representation of a beam resting on a foundation is also illustrated and derived based on the wavelet finite element approach.

Some numerical examples are outlined in Chapter 6 to validate and compare the wavelet based finite element method's ability to analyse static structural problems with various analytical and FEM approaches. The examples include problems that possess varying loading and boundary conditions as well as geometric and material properties. A thorough comparison of results is carried out with those presented in previous studies. A comprehensive study based on wavelet order selection of the Daubechies and BSWI WFEM, specific to static problems, is also presented.

In Chapter 7, the WFEM is used to solve moving load problems with the aim of validating, comparing and highlighting the ability of the method (in comparison to existing analytical, semi-analytical and classical FEM approaches). Numerical examples are presented, varying from a simply supported beam subjected to a moving point load to a beam on a viscoelastic foundation subjected to subcritical, critical and supercritical moving loads. The BSWI and

Daubechies based WFEM solutions are compared with each other to identify their strengths and/or limitations in the analysis of moving load problems.

Chapter 8 focuses on the new modified wavelet based finite element approach used to analyse functionally graded materials. Key theoretical aspects, based on the gradation of the FG beam and the formulation of the proposed method, are presented in this chapter. The free vibration analysis of a steel-alumina functionally graded beam is carried out using the WFEM and the solutions are compared with the classical FEM and results obtained previously from similar studies. The effects of varying the material distribution on the dynamic response of the FG beam and moving load critical velocities are analysed. Different damping and moving load velocity profiles are implemented in the analysis when the FG beam is resting on a viscoelastic foundation.

The concluding Chapter 9 contains an overview of the study and key findings of this research. Suggestions for further work are stated based on the current advancements of WFEM.

1.4. Main contributions

The main contributions and aspects of novelty resulting from the work carried out in this thesis include the following, and to the best of the author's knowledge, are presented for the first time:

i. A comparative study of the Daubechies WFEM, BSWI WFEM and the classical finite element method is carried out for a variation of static and dynamic problems based on a generalized framework implemented.
ii. Comparisons and the effects of altering the order and/or multiresolution of the wavelet based finite elements on the accuracy of approximation of the natural frequencies and dynamic responses for homogenous and FG beam systems.
iii. The formulation and implementation of the Euler Bernoulli wavelet based functionally graded beam element. Furthermore, a modified algorithm that allows for the computation of Daubechies multiscale connection coefficients which have the products of different order scaling functions and/or their derivatives. These connection coefficients are used in the formulation of the Daubechies based functionally graded beam WFEs and are also implemented for homogeneous rod, beam and plane bar elements.

iv. Analysis of the moving load critical velocity and variation of the dynamic response with respect to different material distributions of a functionally graded beam on a viscoelastic foundation subjected to a moving point load. The analysis is carried out for different moving load velocity and system damping profiles using the Daubechies and BSWI based WFEMs.

The analysis of moving load problems is of practical importance and relevance in the field of railway design and maintenance, while the use and analysis of functionally graded materials for many engineering applications is ever growing. The results and findings presented in this study verify the practical potential, relevance and importance of the wavelet finite element method as an analysis tool with respect to these fields of study. The diversity of the method, with respect to its application and formulation in the analysis of structural problems, is still limited. Therefore, there are opportunities for further investigation of the method.

2. Literature Review

Summary

In this chapter, a literature review is presented focusing on previous relevant research carried out on the wavelet finite element method and its current advancements. The applications of the method and outcomes of research carried out are discussed. The Daubechies and BSWI wavelet based finite element methods and their applications will be taken into consideration specifically. However, WFEMs that employ other wavelet families will also be mentioned in this chapter. A brief introduction into wavelet analysis and the finite element method is presented, which will be expounded further in Chapter 3 and Chapter 4 respectively. Furthermore, the current developments in the research of functionally graded beams are discussed.

2.1. Brief introduction of wavelet analysis

Wavelets provide a tool for time-frequency localization and its transform is dependent on scale and location of a signal evolving in time [15]. In other words, functions can be represented simultaneously in frequency (space) and time; at different resolutions. The wavelet functions are therefore distinct to the space-localised Fourier functions; which are not localised in time [16]. The concept itself can be viewed as a unification of ideas in the various fields originating over the decades. The fundamental concepts and ideologies behind the wavelet transform have been around for many years and there has been some controversy about the origin of wavelet theory. Some of the recent "discoveries" by the researchers, who were at the core of establishing the wavelet theory as we now know it, came up with relatively similar work that had already been done a few decades back by others [17]. The development of the wavelet analysis came from separate efforts that were not part of a consistent theory and it was only recently realised that the work done was actually the foundation of modern wavelet theory. Grossman and Morlet [4] are credited with the introduction of the term and methodology of wavelets by means of wavelet analysis as a tool for signal analysis of seismic data. Further advances in the theory were later made in 1985 by Stephane Mallat [18] who presented a study on the theory and formulation of wavelet orthonormal bases, and related their properties to those of multiresolution approximations of $L^2(\mathbb{R})$. Furthermore, the quadrature mirror filters and pyramid algorithms were related to these wavelet bases. He was able to present a more efficient and effective approach for the

wavelet orthonormal bases with respect to multiresolution analysis. This later on motivated Y. Meyer, a harmonic analyst at the time, to recognise numerous classical results in the theory and point out that there was indeed a connection between the powerful existing techniques in mathematical study of singular integral operators with signal analysis methods [19]. From this point on the concept caught the attention of other physicists and mathematicians which included Ingrid Daubechies. After taking keen interest in the work that was already done in the field by those before (particularly Mallat and Mayer's work), Daubechies [20] made a major breakthrough in the field of wavelets towards the end of the 1980s by constructing a family of orthonormal wavelets with compact support. Daubechies [15,20] was able to formulate the Daubechies family of wavelets which led to their success; proving to be the basis of wavelet analysis as we know it today.

Daubechies [15] monitored the trend in publications with respect to modern wavelet analysis in the early 1980s and it was discovered that its implementation was limited, with only very few scientific papers being published. It was mainly used by mathematicians as a tool to decompose data, functions or operators into different components. From the 1990s, the interest in the use of the wavelet transform had seen an exponential increase and the growth in popularity was among researchers in various fields of study, particularly those in science and engineering.

To date, wavelet analysis has diversified in application and this is evident from the research of its implementation in medicine [21,22], finance [23], signal processing and geophysics [24], astronomy [25] and chemistry [26], just to name a few. Subsequently, the subject is now vast and the wavelets are applied to handcrafted applications in various disciplines to cater for their specific requirements. This is attributed to the key desirable general properties of wavelets which offer numerous avenues for design manipulation to meet the necessary desired requirements. In other words, wavelets in general are versatile and can be easily manipulated, with new families being developed and tailored for specific applications. Furthermore, properties such as multiresolution, compact support and vanishing moments make various families of wavelets desirable. This demonstrates the importance and relevance of wavelet analysis, with many possible avenues for its application.

2.2. The finite element method

It is common practice in the structural engineering field to analyse and predict the behaviour of various systems. A practical approach can be applied by carrying out experimental testing

under certain conditions and assumptions to obtain valid and realistic results. However, this can be a very complex and costly approach, especially if the analysis on the limitations of systems is carried out. Therefore, various theoretically and mathematically based approaches have been investigated to carry out the analysis of systems. In structural analysis, analytical and semi-analytical approaches are continually being developed to represent the physical systems. Nevertheless, it is generally very difficult to apply exact closed form solutions in the analysis of the engineering problems due to existing mathematical tools not being sufficient enough. Furthermore, it may be very difficult to mathematically represent the varying complexities and irregularities (e.g. geometry or material composition) which may be present [1].

Therefore, a number of numerical approaches have been developed to approximately describe the behaviour of engineering systems. One such approach is the finite element method (FEM), which has become the foundation for solving complex engineering problems, particularly in structural analysis due to its diversity as well as versatility. FEM uses trial functions, which are a combination of a class of functions, to obtain the approximate solutions over the system's domain [27]. Discretization of a system into elements leads to the solution domain being broken down into sub-domains and the elements are regions of space where the displacement field exists. The nodes connect these elements and are therefore the locations in space where the displacement and its derivatives are evaluated. From a mathematical point of view, the finite element mesh is considered to be a spatial subdivision. Over the solution domain, continuous functions are expressed in terms of the field variable nodal values, or their derivatives, and are used to approximate the behaviour of the unknown field variables [28].

The behaviour of the field variables is described by interpolating or approximating functions, defined over each finite element. A collection of these functions over the entire domain provide piecewise approximations to the field variables. The classical finite element methods use polynomials to represent these functions as they are convenient to apply mathematically and easy to manipulate. It is important that the selection of right interpolating functions is carried out to ensure convergence of the approximate solution to the exact solution [29].

The method is popular in various engineering fields and this is evident from the fact that the method is not only restricted to structural analysis, but can also be applied to analyse heat transfer [27-29], fluid flow [30,31], distribution of electric or electromagnetic potential [32] problems; giving rise to its vast growing popularity over the decades. The digital computer

age has also advanced the use of the method as larger and more complex engineering problems can be solved with increased accuracy, while simultaneously reducing the computational costs. Furthermore, it has enhanced the manner of attaining the approximate solutions efficient and practically viable.

However, it is important to note that there is a trade-off between computational costs and improving the approximate solution accuracy. Thus, for one to achieve higher levels of accuracy of the solution, more computational power is required to achieve this; which can be a costly drawback. This is particularly the case where the gradient of the field variables are expected to vary suddenly or quickly. Difficulties emerge when analysing such systems and sometimes lead to slow convergence, inaccurate results and/or higher computational costs, since finer meshes are required [7,28].

2.3. The wavelet finite element method

Different approaches have been developed to overcome some of the short comings of the finite element method such as the Boundary Element Method (BEM), adaptive Finite element methods, meshless methods, just to name a few [33]. Given that at the time computational power was not as high as it is currently, the need for efficiency in the method of analysis was necessary. One other approach that has been developed in recent years is the Wavelet Finite Element Method (WFEM). The method combines the attractive wavelets with the conventional finite element method. The desirable properties of wavelets allows for their utilisation in solving the Partial Differential Equations (PDEs).

Multiresolution is one of the most outstanding features of wavelet theory and it is the backbone of WFEM [6,7]. Specific wavelet based finite elements can be selected and analysed at finer scales, without modifying the initial system model, via the multiresolution property. This is advantageous since the accuracy of the solution, particularly in areas with high gradients and singularities present, can be greatly improved. Furthermore, computational costs are reduced since fewer elements are required to achieve acceptable levels of accuracy due to rapid convergence of the method [6,7]. Multiresolution arises from the "two-scale" relation, which is another key property of wavelets [20]. It allows for the convenient and free transformation of scaling and wavelet functions between different resolutions, thus improving the analysis precision. Another key feature of majority of wavelets is compact support which is also achievable via the two scale relation. The scaling and wavelet functions are finitely bound (non-zero over a finite range) and this is attractive for WFEM formulations since the

elements generated have less degrees of freedom. This is an ideal feature, in terms of computational efficiency, accuracy and convenience, for analysing problems of areas with high local gradients [10].

These are just but a few of the most common properties of wavelets. However, it is important to identify the requirements to be satisfied when choosing a particular wavelet basis for the WFEM. FEM requires that the compatibility and completeness requirements be satisfied, with the addition of convergence of the approximate solution, for accurate results. The wavelet basis should be able to ensure these requirements are met and furthermore, it should have good numerical performance to allow easy implementation and treatment of boundary conditions when used. Computational efficiency is another key factor and motivation for the development of WFEM. It is ideal to have low order polynomials generated by the wavelet basis as well as good decomposition and reconstruction of the field variable for multiresolution to be effective and improve on the efficiency of the method.

For these reasons, the WFEM has become a potentially powerful tool in the analysis of problems with irregularities; which offer the classical FEM difficulties in their analysis. Due to the adaptability of the wavelets, different wavelet families are being developed and customised for specific problems. They are implemented in WFEM based on their properties, and advancements for their applications have been continually researched.

2.3.1. The Daubechies wavelet finite element method

The Daubechies wavelet is one of the families that have been used in the formulation of the WFEs. The scaling functions are used as interpolating functions due to the key desirable properties of the wavelet family. It is also one of the primary wavelet families initially used in solution of PDEs, and subsequently implemented in WFEM. The properties of the Daubechies wavelet include multiresolution, orthogonality, vanishing moments, compact support and the "two scale" relation [20]. However, the Daubechies scaling functions (and their derivatives) have no explicit expression; therefore requiring the evaluation of what is commonly referred to as connection coefficients, to solve PDEs [34-36]. The term connection coefficients, as described by Latto et al. [36], are the integral of the products of the wavelet scaling functions and/or their derivatives (including translates). A more detailed discussion into the formulation and theory of connection coefficients is presented in Chapter 3.

Ko et al. [2,9] are credited with the conceptualization and development of the Daubechies wavelet based finite element method. They implement the Daubechies wavelet basis

functions to formulate a tensor product finite element, which is used solve a 1D and 2D second order Neumann problem. The rate of convergence of the results achieved by the wavelet based approach is found to be good, with the exception of the Daubechies order $L = 12$, which is attributed to shortening the connection coefficients to a fixed number of accurate digits. Ko et al. [37] also use the Daubechies wavelets to develop a class of triangular finite elements. The tensor-product wavelet elements in the geometry of the triangular elemental domain are characterized using a multivalued scaling equation.

The wavelet Galerkin finite element method is implemented by Zhou et al. [38] to analyse the bending of plates and beams. The Daubechies wavelet is used to carry out this analysis, and the results obtained are of good accuracy. The accuracy of the results is improved by increasing the order of the wavelet scaling functions.

Ma et al. [10] enhance the work carried out in Ko et al. [2,9] by developing a wavelet based beam finite element using the Daubechies D*12* (order $L = 12$) wavelet for static analysis. The beam element is formulated in wavelet space and the corresponding elemental degrees of freedom are represented by wavelet coefficients. In their work, they present a layout of the beam element such that, for compatibility at the borders of adjacent elements to be ensured, the transverse displacement and rotation DOFs must be present at each elemental end node. In their formulation, the stiffness matrix in wavelet space is obtained via the connection coefficients bound on the interval $[0,1]$, as described by Ko et al. [9], and is then transformed into physical space by the use of a wavelet based transformation matrix. Two static problems are used to verify the correctness of the element and the results are compared with the classical FEM solutions. The results indicate the WFEM achieves high levels of accuracy with fewer elements. However, there is no clear indication or formulation of the wavelet based load vectors and multiresolution is not taken into consideration in their study. Moreover, there are no suggestions on whether the layout of the element presented can be altered or what the effects of this are on the accuracy of the results. Ma et al. [10] state that other orders of the Daubechies wavelet can be implemented in the formulation of the beam WFE and indicate that higher orders lead to more accurate results; but subsequently higher computational costs. However, there is no comparison of results with respect to the order of the Daubechies WFE implemented.

Chen et al. [8] formulate a two dimensional Daubechies wavelet finite element which is used to analyse the bending of a thin plate. Furthermore, a new formulation to evaluate the load vector on the interval $[0,1]$ in wavelet space is presented and found to be more efficient than

the approach presented by Chen et al. [39]. The algorithms presented for the evaluation of the stiffness matrices and load vectors are carried out at multiresolution scale $j = 0$. The results presented show that the approach leads to highly accurate results and could be improved by increasing the order or multiresolution of the WFE. Moreover, the numerical examples selected include [8]; the analysis of Cook's plane stress problem, stress analysis of an L-shaped plate and thermal analysis of a paper steady-state. Through these examples, the capability of the Daubechies WFEM to accurately solve problems with singularities present in higher dimensional elements is illustrated.

Chen et al. [6] present a novel algorithm to evaluate the connection coefficients at different multiresolution scales; bound on the interval $[0,1]$. The algorithm presented takes into consideration the Daubechies scaling functions of the same order L. The multiscale connection coefficients are then used to analyse a static plate problem, where the accuracy results are improved via a multiscale lifting scheme. The results show that increasing the multiresolution of the WFEs improves the accuracy of the results.

Diaz et al. [40] implement the Daubechies WFEM based on the formulations described by Ma et al. [10] and Chen et al. [8] to analysis static beam and plate problems. The formulation of the plate is based on Mindlin-Reissner plate theory, where shear deformation is taken into consideration through the thickness of the plate. In their analysis, they conclude that in the application of beam problems, the convergence of the solutions for Daubechies wavelet family of order $L < 12$ is obtained by increasing the number of elements. Furthermore, it is stated that the orders of the scaling functions used must be $L = 2^k + 4$ for $k \in z$ and $k > 0$, where L is the order of the Daubechies scaling function. Moreover, the results for $L \geq 20$ are inaccurate due to numerical deterioration when evaluating the connection coefficients. It is therefore unclear, based on these results and conclusions, which orders of the Daubechies WFEM can be implemented in the analysis of beam structures, considering the numerical examples carried out are for a Daubechies D*12* wavelet beam, similar to Ma et al. [10]. Furthermore, their analysis does not include multiresolution and therefore, if their findings are valid, it is not clear what the effect of implementing multiresolution on the accuracy of results is.

Diaz et al. [41] compare the Daubechies wavelet and B-spline wavelet formulated plate WFEM solutions. The plates are formulated based on Mindlin-Reissner and Kirchhoff plate theories for static analysis, under uniform loading. The D*10* WFEM results are also compared with classic finite element method solutions, and it is stated that the wavelet based solutions

take a third of the time it takes for classical FEM solutions to achieve similar levels of accuracy.

Zhang et al. [42] use the two dimensional Daubechies scaling functions to formulate the WFEM and apply it to analyse the fluid-saturated porous media elastic wave equation. The results are compared with the classical FEM and they are highly accurate, possessing a good convergence rate.

The Daubechies wavelet is used to formulate Rayleigh-Euler and Rayleigh Timoshenko beam wavelet finite elements by Wang et al. [43]. These wavelet based beam elements are used with the genetic algorithm for crack detection and are validated with experimental data. The results are found to be accurate, and the method efficient.

Zhao and Wang [44] use the Daubechies WFEM to analyse a tank and investigate the thermal stress distribution along the vertical direction of the tank wall. The results obtained for the high gradient problems analysed are accurate and performed better than the classical FEM; giving better accuracy and requiring fewer elements for the analysis. Zhao [45] uses the Daubechies WFEM to analyse a Liquefied Petroleum Gas (LPG) tank under fire based on the gas-liquid coupled theory. From his analysis, the WFEM is compared with experimental data and the classical FEM to obtain the variation of temperature and pressure of the gas/liquid in the tank. The results obtained via WFEM are in very good agreement with experimental results. Furthermore, the WFEM solutions are better in accuracy and computational efficiency than the classical FEM. Zhao [46] carries out a further analysis of a gate rotor shaft with multiple cracks based on the Daubechies WFEM. Zhao implements an identification procedure and evaluates the changing rate of the natural frequencies via free vibration analysis. According to the analysis, the WFEM approach is in very good agreement with the actual solutions obtained; thus illustrating that the method can be successfully implemented in identifying multi-cracks on the rotor shaft.

Zhou Y. and Zhou J. [47] use independent wavelet coefficients to represent the boundary DOFs for beams and thin plates via a modified wavelet approximation. This enables the homogeneous and non-homogeneous boundary conditions to be treated in a similar manner as conventional FEM. They implement their approach to analyse the bending and dynamic response of thin plates using the Daubechies wavelet order D*6* at multiresolution scale *3*. The results presented are in good agreement with the compared FEM and analytical solutions, and the approach offers an avenue for handling general boundary conditions.

Mitra and Gopalakrishnan [48] propose a novel wavelet based spectral finite element to study elastic wave propagation in 1-D connected waveguides using Daubechies scaling functions for approximation in time. This approach reduces the PDEs to ODEs (Ordinary Differential Equations) in spatial dimensions, which are decoupled via an eigenvalue analysis; hence decreasing the computational costs. They indicate that the proposed method would work well with other compact supported wavelet bases such as B-splines. Mitra and Gopalakrishnan [49] then extract the wave characteristics via the Daubechies based spectrally formulated wavelet finite element. Numerical experiments are performed to study frequency-dependent wave characteristics in elementary rod, Euler-Bernoulli and Timoshenko beams. Furthermore, they formulate higher order composite beams to study wave propagation [50]. Numerical experiments are performed to investigate the wave propagation due to broad band impulse load and modulated sinusoidal pulse. In their analyses, they conclude the use of the Daubechies wavelets improves the accuracy and efficiency of the solutions.

There are two key limitations of implementing the Daubechies wavelet for the formulation of WFEMs. The first of these is the lack of symmetry (symmetry of the wavelet or scaling function curve with respect to the *y* axis) and an explicit expression for the wavelet and scaling functions. This makes the evaluation of numerical integrals problematic due to the unusual smoothness characteristics. Therefore, in order to formulate the element matrices and load vectors, the connection coefficients must be evaluated. The second is with respect to the accuracy of the method. The results presented demonstrate that the solutions are highly accurate, but for certain orders of the Daubechies WFEs. However, it is not clear which orders the Daubechies WFE are restricted to; with respect to the type of element and problem being analysed. Moreover, the effects of altering the element layout are not clearly stated. Majority of the problems analysed are of a static nature and the implementation of the method for the analysis of dynamic problems is limited. Furthermore, the implementation and the performance analysis of the method in the dynamic response of structural problems, with fast varying loading conditions and material properties, are also limited. This offers an opportunity for further research, which is to be investigated in this study.

2.3.2. The BSWI wavelet finite element method

It was necessary to carry out further research to identify other wavelet families, which had explicit expressions and could be implemented in the WFEM, to overcome the limitations of the Daubechies WFEM. The spline wavelets were identified as a potential family of wavelets

that could be implemented in WFEM. The spline wavelets have uniform translation of the bases, explicit expressions, compact support and sufficient smoothness of low order polynomials [3].

Chen et al. [3] combine the conventional finite element method with the accuracy of the spline functions as shape functions for free vibration analysis of frame structures. Based on the properties of the spline wavelets, they are sufficient for the variational method to solve differential equations in a multi-level approach. They implement this proposed method on a Euler Bernoulli beam, with cubic splines used to approximate the variable function in the elements. The analysis of a Vierendeel frame and triangular structures are carried out via numerical examples. The results show that the accuracy of the solutions would increase with an increase in refinement.

Pengcheng and Peixiang [51] present a multivariable spline element method and use the interpolation functions of cubic B-splines of duality in product form to construct the entire independent field functions for plates and flat spherical shells with a square base. Pengcheng and Peixiang [52] later extend their work in [51], to analyse moderately thick plates (the effects of transverse shear and rotary inertia are taken into account). They derive the spline finite elements based on the potential energy principle. In both cases they are able to satisfy the natural boundary conditions using the variational principle and their results show good convergence and high accuracy. The interpolations of the bicubic splines have few unknowns while still maintaining strong continuity and high precision of approximation. Therefore, Pengcheng and Peixiang [53] use bicubic splines in the product form to construct multi-field functions for static analysis of a plate on elastic foundations. This is carried out via the multivariable spline element method.

Chui and Quak [54] construct the semi-orthogonal B-spline Wavelet on the Interval (BSWI) which has the desirable properties of multiresolution, compact support, explicit expressions, smoothness and symmetry. This implies that the scaling and wavelet functions can be evaluated with ease and used in the formulation of the WFEM.

Xiang et al. [11] implement the BSWI to construct a wavelet based C^0 type plane elastomechanics element and Mindlin plate based on 2-D tensor product of the BSWI wavelet family. They carry out a static analysis for moderately thick and thick square plates, under uniform and concentrated static loading. The BSWI plate WFEM solutions for order 2 and scale 3 (BSWI2_3) are compared with that of order 4 and multiresolution scale 3 (BSWI4_3). The results indicate that the BSWI4_3 WFEM solution give more accurate results, however the

computational costs are significantly higher due to the subsequent increase in the number of knots of each element. The BSWI2_3 WFEM results are inaccurate, except when the thickness-span ratio is high. For the analysis of moderately thick and thick plates, the BSWI4_3 element is suitable for the analysis. They further conclude that the layout of the elemental nodes can be modified, provided that the wavelet transformation matrix is not singular.

Thin and moderately thick truncated conical shell wavelet finite elements with independent slope-deformation are constructed by Xiang et al. [55] using the BSWI wavelet family. The static analysis is carried out for a thin truncated conical shell and the results obtained via 8 BSWI2_3-4_3 (123 DOFs) WFEs are of significantly better accuracy when compared with the traditional finite element (723 DOFs) solutions. This demonstrates the efficiency and effectiveness of the BSWI WFEM in the analysis of thin and moderately thick shells.

Xiang et al. [7] proceed to construct a range of BSWI based WFEs, which include the axial rod, beam (Timoshenko and Euler Bernoulli), plane bar, spatial bar and plane truss WFEs. A lifting scheme for the corresponding elements is also presented. Numerical examples are carried out to validate the constructed WFEs and compared with classical finite elements. The Euler Bernoulli and Timoshenko BSWI2_3 and BSWI4_3 beam wavelet finite elements are analysed for static problems under a distributed and uniform load respectively. The results show that the BSWI4_3 WFEM results are highly accurate with significantly less DOFs than the classical FEM solution. Furthermore, provided the wavelet transformation matrix is non-singular, the BSWI WFEs can freely be constructed.

A new BSWI thin C^1 plate element based on Kirchhoff plate theory is formulated and analysed by Xiang et al. [12,56] for static and dynamic problems. A square plate formulated using BSWI4_3 WFEs is subjected to a static load and subsequently, a free vibration analysis is carried. The free vibration of the skew plate is also analysed for different boundary conditions and the results compared with those obtained from literature. The BSWI4_3 WFEM solutions are highly accurate for the thin plate but it is highlighted that when the lifting scheme is implemented to improve the accuracy, the process becomes complex.

Rotor-bearing systems are analysed using a new BSWI rotating Rayleigh-Timoshenko shaft wavelet based finite element formulated by Xiang et al. [57]. The analysis demonstrates that the shear-locking phenomenon is significantly eliminated when using the BSWI based WFEs due to the attractive properties of the BSWI wavelet family.

The static and forced vibration analysis of a thin plate and a thin plate on an elastic foundation, using a multivariable BSWI thin plate WFEs formulation, are carried out by Zhang et al. [58]. It is concluded that increasing the number of kinds of variables not only increases the accuracy of the solution, but also the computational costs. The results show that the static and forced vibration results of both cases analysed are highly accurate. The BSWI based WFEM has also been recently used in the analysis of elastic wave propagation for a cracked arch. Yang et al. [59], formulate the arch based on Castigliano's theorem and Paris equation to accurately describe the wave motion behaviour for curved structures. Yang et al. [60] progress their research and analyse curved beams using the BSWI based WFEM. In their numerical examples, they analyse the static behaviour of a pinched ring and cantilever curved beam. Furthermore, the carry out the free vibration analysis of a hinged arch, a thin circular ring, a three-span clamped arch and a 90° arch with different boundary conditions. Their findings indicate that the BSWI based WFEM is suitable to carry out the static and free vibration analysis of curved beams, attaining satisfactory levels of accuracy due to the BSWI wavelet properties.

2.3.3. Other wavelet finite element methods

There are other wavelet families that have been implemented to formulate the wavelet based finite element method for the analysis of various engineering problems. One such wavelet family that has been applied recently is the explicitly expressed trigonometric Hermite wavelet. He and Ren [13] present the formulation and theory of the trigonometric wavelet beam finite element. In their analysis they compare the solutions of the classical FEM and trigonometric based WFEM via numerical examples. They carry out a static, free vibration and stability (buckling) analysis of beams structures. They conclude that high levels of accuracy are achieved with fewer elements, particularly for free vibration analysis, due to the multiresolution property. Furthermore, the trigonometric wavelet family has good approximation characteristics, and the approach overcomes the limitations of the Daubechies and BSWI based WFEMs with respect to the application of boundary conditions. Moreover, adjacent WFEs can be connected conveniently without the use of a wavelet transformation matrix and this allows for the trigonometric WFEs to be implemented simultaneously with classical FEs within the same system. He and Ren [14] formulate thin plate trigonometric based WFEs using a two dimensional tensor product trigonometric Hermite wavelet. The results obtained from the static analysis of a thin plate subjected to a uniformly distributed load, free vibration analysis and buckling analysis for different boundary conditions, are

compared with the classical FEM solutions. The results obtained are highly accurate, with fewer WFEs implemented in comparison to the classical FEM solutions.

The Hermite Cubic Spline Wavelet on the Interval (HCSWI) based WFEM [61-63], polynomial WFEM [64,65] and the second generation WFEM [66,67], are other wavelet based finite element approaches that have been very recently introduced and researched on. Li and Chen [68] have very recently presented a synthesis and summary critical review, of not only the wavelet based finite element methods, but also other wavelet based numerical methods for engineering problems. It must be noted that the study presented in this thesis had already been initiated and significantly advanced when some of the relatively new WFEMs were emerging. Furthermore, the current developments of the BSWI based WFEM demonstrate the potential and how exceptional the approach is for the analysis of different structural problems. The high levels of accuracy and efficiency of the method have thus attracted the attention of researchers. This is attributed to the desirable properties of the BSWI wavelet family, which include: compact support, symmetry, explicit expressions, multiresolution and semi-orthogonality. However, majority of the problems analysed using the method are static and free vibration problems.

2.4. Functionally graded materials

Over the past decades, the evolution of composite materials in various engineering applications, particularly in the defence, aerospace and automotive industries, has been keenly observed. The need for light weight materials that possess high strength to weight and stiffness to weight ratios has led to the fabrication and application of composite materials that combine two or more materials varying in properties [69]. However, there are several limitations of conventional composite material applications in highly intense conditions, particularly high temperature environments, where the desirable properties of these composites would diminish. Furthermore, complications arising from the interface such as; material debonding or increased stress concentration that would lead to weakening of the composite material or crack propagation at the interface, have led to further research being carried out to mitigate these inadequacies [70].

Functionally graded materials (FGM) are a relatively new class of composite materials which consists of two or more materials (often metals and ceramics), with the continuous and gradual variation of material composition with respect to space. The individual constituent materials possess different properties, for example: chemical, physical, thermal, mechanical

and electrical properties [71]. Therefore, the effective properties of functionally graded materials vary according to the material distribution of the constituent materials. The term and concept was introduced in the mid 80s by a faction of Japanese material scientists [72] with an aim to develop thermal barrier materials capable of withstanding high temperature gradients between the surfaces whilst withstanding significant mechanical loading. In a bid to decrease some limitations of conventional composites, research into FGM is rapidly growing so as to have a better understanding and improve on these advanced materials.

Research has been, and continues to be carried out on the analysis of FGMs to better understand their behaviour under certain conditions. Majority of the research presented in literature is in relation to plates and shells. The critical review provided by Jha et al. [73], on the recent developments and studies of functionally graded plates, is recommended by the author. The research carried out on functionally graded beams is not as widespread as functionally graded plates and shells, which have a wider range of applications. Nonetheless, the need to analyse the behaviour of functionally graded beams is rapidly growing for both practical and theoretical purposes. Furthermore, majority of the research presented with respect to functionally graded beams involves static and free vibration analysis.

The research based on the effects of shear deformation and rotary inertia on the free vibration of functionally graded beams is carried out using different analytical and numerical approaches. The thermoelastic behaviour of FG beams is investigated by Chakraborty et al. [69], who implement a new exact shear deformable FG beam finite element formulation based on the Timoshenko beam theory. They carry out a static, free vibration and wave propagation analysis based on the exponential and power laws of gradation. According to their results, the FG beams have the stress jumps smoothened and the natural frequencies differ significantly with respect to the material distribution of the FGM. The free vibration of short functionally graded beams is compared by Aydogdu and Taskin [74] for different beam theories. The analysis is carried out by implementing the Euler Bernoulli, parabolic shear deformation and exponential shear deformation beam theories based on Hamilton's principle. The free vibration analysis of the FG beam, which is formulated using the power law and exponential law, is carried out and the results obtained via the different beam theories are compared. The Euler Bernoulli FG beam natural frequencies are found to be higher than the other higher order beam theory solutions when the value of the slenderness ratio is small (< 20); for different material distributions. This is because the Euler Bernoulli beam theory does not take into consideration shear deformation and rotational inertia, unlike the higher order

shear deformation theories. Therefore, the Euler Bernoulli beam is stiffer, leading to higher values of natural frequencies when the slenderness ratio is small. Furthermore, the difference in the natural frequencies increases with the modes of vibrations.

Kadoli et al. [75] applied the classical finite element method to analyse the static deflection and stresses of a transversely varying functionally graded beam, based on higher-order shear deformation theory and power law of gradation. Through their analysis of static FG beams, it is found that the material distribution significantly influences the deflection, stresses and location of the neutral surface. Sina et al. [76] and Thai and Vo [77] implement analytical approaches to obtain the natural frequencies of transverse varying FG beams using different higher-order shear deformation theories. Their solutions are found to be consistent with other previously presented FG beam analysis approaches.

Pradhan and Chakraverty [78] compare the natural frequencies of a Euler Bernoulli functionally graded beam with those of a Timoshenko FG beam using the Rayleigh-Ritz method. The beam material distribution variation is based on the power law and occurs in the transverse direction. In their analysis, they investigate the effect of varying the slenderness ratio on the natural frequencies and compare the results obtained via the classical and first order Timoshenko beam theories. Their results are consistent with the findings in [74,77]; where the Euler Bernoulli FG beam solution overestimates the natural frequencies for low values of the slenderness ratio. However, it is stated that when the value of the slenderness ratio is increased, the natural frequencies at each mode of vibration, based on the two beam theories, gradually converge. Therefore, the Euler Bernoulli beam theory can be used to accurately analyse the free and forced vibration of slender FG beams for different material distributions.

A significant quantity of the research conducted on functionally graded materials, particularly beams, is based on transverse gradation of the material distribution. A limited number of studies have been carried out with respect to axially varying functionally graded beams. This is attributed to the fact that the practical use of axially varying functionally graded beams is, at present, very limited. However, the classical finite element method is implemented by Alshorbagy et al. [79] to analyse the free vibration of a Euler Bernoulli FG beam. The results presented illustrate that the axial material distribution variation influences the natural frequencies of the FG beam. Haung and Li [80] obtain the natural frequencies of an axially varying tapered functionally graded beam by transforming the problem in to Fredholm integral equations. Their approach is verified for the analysis of axially varying FG beams via

numerical examples and the results are in good agreement with the classical FEM and Rayleigh method solutions. Shahba and Rajasekaran [81] use a differential transform element method to carry out a free vibration and buckling analysis of a tapered Euler Bernoulli FG beam.

Although majority of the research conducted on functionally graded beams has been focused on free vibration analysis, there has been some research carried out on the dynamic response of FG beams subjected to a moving load. The free vibration and dynamic response of a Euler Bernoulli FG beam with open cracks, simultaneously subjected to a transverse moving load and axial compressive force, is investigated by Yang et al. [82]. The analysis is carried out using an analytical approach, and the transverse material gradation of the FG beam is approximated using the exponential law. In their findings, they conclude that the location of the edge cracks has a significant effect on the natural frequencies.

Simsek and Kocaturk [83] analyse the free vibration and dynamic response of a Euler Bernoulli FG beam subjected to a concentrated moving harmonic load. The transverse variation of the material properties are based on the power law and exponential law. The Lagrange's equations are used to derive the governing system of equations of motion. In their work, the effects of varying the material distributions, via the power law exponent, on the natural frequencies and dynamic response of the FG beam are investigated. Furthermore, the effects of the velocity and the excitation frequency of the moving harmonic load on the dynamic response of the FG beam are also analysed. The dynamic responses of the FG beam, based on classical, first order shear deformation and third order shear deformation beam theories, both subjected to a moving mass, are subsequently carried out by Simsek [84]. Simsek [85] later extends this work to analyse the non-linear dynamic behaviour of a transversely varying Timoshenko FG beam subjected to a moving harmonic load.

Khalili et al. [86] investigate the dynamic response of a simply supported FG beam subjected to a moving load by combining the Rayleigh-Ritz method and the Differential Quadrature Method (DQM). The FG beam is formulated based on the Euler Bernoulli beam theory and the dynamic response of the FG beam is analysed for different material distributions. The beam is subjected to a moving point load, and subsequently a moving mass, where the inertia effects of the load are taken into consideration. From their results, they conclude that the inertia effects of the load influence the dynamic behaviour of the FGM beam. Furthermore, the variation of the material distribution also influences the dynamic response of the functionally graded beam.

2.5. Conclusion

A critical review of the wavelet finite element method and functionally graded materials has been presented in this Chapter. The advancements that have led to the current state of research of the WFEM were discussed. The finite element method and wavelet theory were also introduced. There are avenues that exist for the implementation of the wavelet finite element method, which are yet to be explored. Based on the popularity and desirable properties of the Daubechies and BSWI based WFEMs, the two approaches are selected for implementation in this study. Furthermore, given the limited research that has been carried out up to this point, there is an opportunity to investigate the application of the two wavelet based finite element methods with respect to dynamic problems, particularly moving load problems. Furthermore, additional clarity of their application with regards to selection, performance and implementation of the wavelet family orders and multiresolution scales in the analysis of beams, is an area that needs to be addressed and further investigated.

Following a critical review of the research carried out on the analysis of functionally graded materials, particularly FG beams, it was ascertained that there are still opportunities for contribution in the subject area. The dynamic response of FG beams on a viscoelastic foundation subjected to fast variations in loading conditions, such as moving loads, is one such avenue that can be further explored. Areas that can possibly be investigated include: the effects of damping and applied moving load for different velocity profiles on the dynamic response of functionally graded beams of varying material distributions. To the best of the author's knowledge, no work has been presented or published with respect to the dynamic response of functionally graded beams on a viscoelastic foundation, subjected to fast moving loads, using WFEM. The efficiency and effectiveness of the WFEM allows for such an analysis to be carried out, given that the method accurately approximates field variables with fewer DOFs.

3. Wavelet Analysis and Multiresolution Analysis

Summary

The general theories and main principles of wavelet analysis are described in the first part of this chapter through the definition of key concepts of multiresolution analysis (MRA). The properties and conditions necessary for multiresolution to occur, as well as the resultant scaling and wavelet functions that satisfy these conditions, are discussed based on previous works. The reconstruction and decomposition aspects relating to multiresolution for wavelet analysis are presented in Appendix A.1 The two wavelet families used in the formulation of WFEs in this study; the Daubechies wavelet and B-Spline Wavelet on the Interval (BSWI), are introduced and presented in this chapter.

The Daubechies wavelet family is defined with the key properties of the scaling and wavelet functions highlighted. The filter coefficients, scaling and wavelet functions and their derivatives are mathematically presented and discussed in this chapter. Solving partial differential equations (PDEs) using the Daubechies wavelets requires the evaluation of moments and connection coefficients. These coefficients are introduced and formulated in this chapter. A modified approach used to evaluate the multiscale connection coefficients implemented in the formulation of the wavelet based element matrices and general distributed load vectors are presented. The integral of the product of the multiscale Daubechies scaling functions and/or their derivatives of different orders can be computed using this approach. The detailed mathematical formulations used to evaluate the filter coefficients and moments are presented in Appendix A.2.

The general and Cardinal B-spline families of wavelets are introduced and their properties presented. The evaluation of the scaling and wavelet functions of the general B-splines are carried out using knot sequences, which are also derived. The general splines are then used to formulate the BSWI scaling and wavelet functions. The properties of the BSWI scaling and wavelet functions and their derivatives are introduced and expressed mathematically. The cardinal B-splines are formulated and discussed in Appendix A.3.1.

3.1. Concepts of multiresolution and wavelet theory

Wavelets are described a class of basis functions that represent functions locally; both in space (frequency) and time. Furthermore, wavelets allow for analysis of functions or data to

be carried out at different resolutions (scales). There are certain mandatory requirements that a function must satisfy so as to be classified as a wavelet function [5]. However, different wavelet families will exhibit different properties based on their formulation. There are similarities between wavelet functions and classical Fourier functions. However, the Fourier functions are localised only in space. This implies that the represented Fourier functions do not have a particular frequency (or location) associated over a particular time interval. This is a welcoming advantage of wavelets over classical Fourier representations as they can be used to represent time varying functions locally or analyse time-dependent data.

The wavelet basis emanates from a set of wavelet coefficients associated at a particular location in time and exist in different multiresolution scales. In relation to data and frequency, the coefficients at coarse resolution scales are associated with low frequency features. As the resolution scales become finer, more information (detail) is added from the higher resolution coefficients. Therefore, the coefficients at very fine resolution scales are associated with high frequency details that are highly localized [68]. There are some functions associated with wavelets which include the scaling and wavelet functions emanating from multiresolution analysis (MRA). It is therefore important to begin by defining MRA and the properties of MRA that govern wavelet theory. The discussions and mathematical formulations presented in this section are based on general wavelet and MRA theory; similar to those presented in [15,16,19,20,87].

Let f be a function of the complete function space $L^2(\mathbb{R})$, i.e., $f \in L^2(\mathbb{R})$. There exists a nested sequence of closed approximation subspaces V_j $(j \in \mathbb{Z})$ associated with the decomposition of $L^2(\mathbb{R})$. There also exists an orthogonal complement subspace W_j $(j \in \mathbb{Z})$ of corresponding subspace V_j. Multiresolution analysis refers to the simultaneous appearance of multiple scales in function decompositions in the Hilbert space $L^2(\mathbb{R})$ (infinite vector space with natural inner product norm providing a distance function) using the sequence of closed subspaces V_j. Therefore in principle, in order for multiresolution to occur, the subspaces V_j satisfy the following properties [19]:

$$\cdots V_{-2} \subset V_{-1} \subset V_0 \subset V_1 \subset V_2 \subset \cdots \quad \textbf{(3.1)}$$

$$V_{j+1} = V_j \oplus W_j \quad \textbf{(3.2)}$$

$$\overline{\bigcup_{j \in \mathbb{Z}} V_j} = L^2(\mathbb{R}) \quad \textbf{(3.3)}$$

$$\bigcap_{j \in \mathbb{Z}} V_j = \{0\} \tag{3.4}$$

$$f_2(x) = f(2x) \; \forall \; x$$
$$f \in V_j \Leftrightarrow f_2 \in V_{j+1} \qquad j \in \mathbb{Z} \tag{3.5}$$

$$f_n(x) = f(x - n)$$
$$f \in V_0 \Leftrightarrow f_n \in V_0 \qquad n \in \mathbb{Z} \tag{3.6}$$

The first property from equation (3.1) implies that the closed subspace V_j is included within the next subspace V_{j+1} and subsequently all other higher subspaces as illustrated in Figure 3-1. Therefore, any function f within subspace V_j belongs in all higher spaces. The second condition from equation (3.2) states that the sum of the subspaces W_j and V_j produces the subspace at the next scale V_{j+1}.

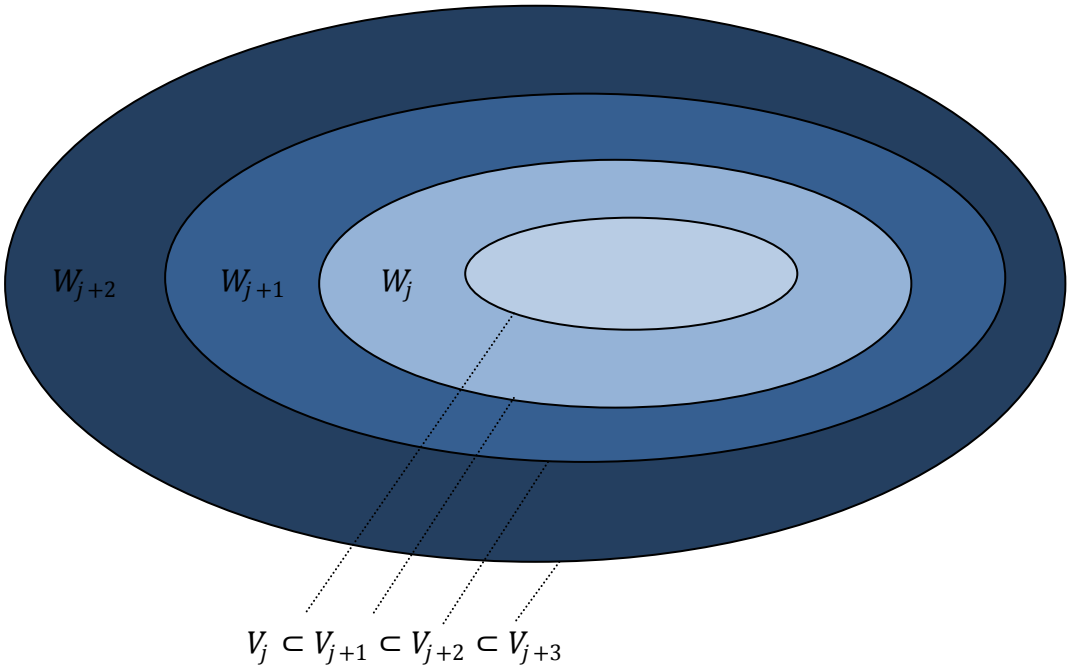

Figure 3-1: Illustration of multiresolution subspaces V_j and W_j.

In other words, the complement subspace W_j contains the additional "detail" for V_{j+1} and can be described as the differences of subspaces V_{j+1} and V_j. It is easy to deduce from equation (3.2) and Figure 3-1 that [16]

$$V_{j+1} = V_0 \oplus W_0 \oplus W_1 \oplus W_2 \cdots \oplus W_j \tag{3.7}$$

The union of the subspaces V_j leads to the space $L^2(\mathbb{R})$ from the condition in (3.3) [87]. Consider the orthogonal projection $P_j f$ of f onto the corresponding subspace V_j. The completeness property in equation (3.3) implies that [20]:

$$\lim_{j \to \infty} P_j f = f \quad \text{for all} \quad f \in L^2(\mathbb{R}) \tag{3.8}$$

Furthermore, from equation (3.4) the intersection of the subspaces V_j is a null space. However, the crucial condition for multiresolution is expressed in equation (3.5) to which the subspaces V_j are scale invariant. Therefore, at scale j, the finer resolution of a function f in subspace V_0 is $f(2^j \cdot)$ in V_j. Equation (3.6) represents the shift invariance condition, meaning that the translates of any function in subspace V_j remain in the same subspace [15]. Let the scaling function of the multiresolution analysis $\phi \in L^2(\mathbb{R})$. Thus, the orthonormal basis of V_j is defined as:

$$\phi_k^j(x) = 2^{\frac{j}{2}} \phi(2^j x - k) \qquad k \in \mathbb{Z} \tag{3.9}$$

Given that the above properties, including equation (3.9) are satisfied, there exists a wavelet function $\psi \in L^2(\mathbb{R})$ to which the wavelet orthonormal basis for subspace W_j is defined as:

$$\psi_k^j(x) = 2^{\frac{j}{2}} \psi(2^j x - k) \qquad k \in \mathbb{Z} \tag{3.10}$$

The scaling and wavelet functions correspond to the subspaces V_j and W_j respectively. One can therefore identify the key properties of the wavelet and the corresponding subspace W_j from the conditions expressed in equations (3.1)-(3.6) and (3.9) as follows [20]:

$$\bigoplus_{j \in \mathbb{Z}} W_j = L^2(\mathbb{R}) \tag{3.11}$$

$$f \in W_j \Leftrightarrow f_2 \in W_{j+1} \qquad j \in \mathbb{Z} \tag{3.12}$$

$$f \in W_j \Leftrightarrow f_n \in W_j \qquad n \in \mathbb{Z} \tag{3.13}$$

$$W_j \perp W_{j'} \quad if \quad j \neq j' \tag{3.14}$$

Equation (3.11) implies that the orthogonal subspaces W_j result from the decomposition of $L^2(\mathbb{R})$. The wavelet subspaces W_j, and subsequently the functions within these subspaces, inherit the scale and shift invariance properties from the scaling function subspaces V_j; as expressed in equations (3.12) and (3.13). The wavelet subspaces are orthonormal from the condition expressed in (3.14). Thus, if all the conditions described above are met, then the scaling and wavelet functions satisfy [20]:

$$\int_{-\infty}^{\infty} \phi(x)dx \neq 0 \quad \textbf{(3.15)}$$

$$\int_{-\infty}^{\infty} \psi(x)dx = 0 \quad \textbf{(3.16)}$$

The decomposition and reconstruction of the wavelet functions and coefficients are presented in Appendix A.1 for a better understanding of how multiresolution in wavelets is achieved.

3.2. Daubechies wavelet

The Daubechies wavelet, as earlier mentioned, is one of the popular wavelet families used as a mathematical analysis tool. This family of wavelets, developed by Ingrid Daubechies [20], have the properties of compact supported orthonormal wavelets. The presented formulations and discussions are based on her work published in [20,15].

In this study, the Daubechies wavelet family order is denoted by D*L*, where the order *L* is an even integer greater than 0 and corresponds to the number of filter coefficients $p_L(k)$ for $k = 0,1,\dots,L-1$. These coefficients govern the corresponding orders of the wavelet family through the two scale relation

$$\phi_L(x) = \sqrt{2}\sum_{k=0}^{L-1} h_L(k)\phi_L(2x-k) \quad \textbf{(3.17)}$$

$$\phi_L(x) = \sum_{k=0}^{L-1} p_L(k)\phi_L(2x-k) \quad \textbf{(3.18)}$$

and the wavelet equation

$$\psi_L(x) = \sqrt{2}\sum_{k} g_L(k)\phi_L(2x-k) \quad \textbf{(3.19)}$$

$$\psi_L(x) = \sum_{k} q_L(k)\phi_L(2x-k) \quad \textbf{(3.20)}$$

The normalized wavelet function filter coefficients $q_L(k)$ and scaling function filter coefficients $p_L(k)$ have the relation $q_L(k) = (-1)^k p_L(1-k)$. The scaling functions $\phi_L(x)$ and wavelet functions $\psi_L(x)$ of Daubechies family of order *L* are bound in the interval $[0, L-1]$ and $[1-\frac{L}{2}, \frac{L}{2}]$ respectively. This is an attractive feature of compact support that the Daubechies family of wavelets possess. The scaling and wavelet functions defined in equations (3.18) and (3.20) satisfy the following properties:

$$\int_{-\infty}^{\infty} \phi_L(x)dx = 1 \tag{3.21}$$

$$\int_{-\infty}^{\infty} \phi_L(x-k)\phi_L(x-l)dx = \delta_{k,l} \tag{3.22}$$

$$\int_{-\infty}^{\infty} \phi_L(x)\psi_L(x-k)dx = 0 \tag{3.23}$$

$$\int_{-\infty}^{\infty} x^m \psi_L(x)dx \ = 0 \qquad m = 0,1,\dots,\frac{L}{2}-1 \tag{3.24}$$

The multiresolution scaling and wavelet basis corresponding to the subspaces V_j and W_j for the Daubechies wavelet family of order L are defined as:

$$\phi_{L,k}^j(x) = 2^{\frac{j}{2}}\phi_L(2^j x - k) \tag{3.25}$$

$$\psi_{L,k}^j(x) = 2^{\frac{j}{2}}\psi_L(2^j x - k) \tag{3.26}$$

Furthermore, the Daubechies family of wavelets satisfy the following orthogonal properties at a scale j:

$$\int_{-\infty}^{\infty} \phi_{L,k}^j(x)\phi_{L,l}^j(x)dx = \delta_{k,l} \tag{3.27}$$

$$\int_{-\infty}^{\infty} \psi_{L,k}^j(x)\psi_{L,l}^j(x)dx = \delta_{k,l} \tag{3.28}$$

$$\int_{-\infty}^{\infty} \phi_{L,k}^j(x)\psi_{L,l}^j(x)dx = 0 \tag{3.29}$$

3.2.1. The Daubechies filter coefficients $p_L(k)$

Daubechies [20] in her monograph outlined and proved the properties and conditions satisfied by the Daubechies filter coefficients from the conditions of the scaling and wavelet functions in (3.21)-(3.24). The properties of these filter coefficients include:

$$\sum_k h_L(k) = \sqrt{2} \tag{3.30}$$

$$\sum_k g_L(k) = 0 \tag{3.31}$$

$$\sum_k h_L(k)h_L(k-2l) = \delta_{0,l} \tag{3.32}$$

$$\sum_k g_L(k)h_L(k-2m) = 0 \tag{3.33}$$

The property in equation (3.30) is commonly referred to as the normalization condition. It is as a result of the scaling function integral having the non vanishing property in equation (3.21). Equation (3.32) highlights the orthogonality property of the filter coefficients which ensures that the orthonormality condition of the scaling functions, as expressed in equation (3.22), is met. In order for the orthogonality property between the scaling and wavelet functions in equation (3.23) to be met, the filter coefficients used to construct these functions must themselves possess the orthogonality requirement expressed in equation (3.32). The Daubechies filter coefficient formulations, as described by Daubechies [20], Strang and Nguyen [16] and Hong et al. [88], are derived in greater detail in Appendix A.2.1. Table A-2 contains the normalized filter coefficients $\sum_k p_L(k) = 2$ for D*4* to D*16* as computed by the author using the Mathematica version 7 program.

3.2.2. Evaluation of the Daubechies scaling and wavelet functions

The Daubechies wavelet scaling functions are calculated by solving the refinement equation (3.18). The initial step is to obtain the values of $\phi_L(x)$ at integer points. We can express the refinement equation in matrix form as:

$$\begin{Bmatrix} \phi_L(0) \\ \phi_L(1) \\ \vdots \\ \phi_L(L-2) \\ \phi_L(L-1) \end{Bmatrix} = \begin{bmatrix} p(0) & 0 & \cdots & 0 & 0 \\ p(2) & p(1) & \cdots & 0 & 0 \\ \vdots & \vdots & \ddots & \vdots & \vdots \\ 0 & 0 & \cdots & p(L-2) & p(L-3) \\ 0 & 0 & \cdots & 0 & p(L-1) \end{bmatrix} \begin{Bmatrix} \phi_L(0) \\ \phi_L(1) \\ \vdots \\ \phi_L(L-2) \\ \phi_L(L-1) \end{Bmatrix} \qquad \textbf{(3.34)}$$

$$_{(L \text{ x } 1)}\{\boldsymbol{\Phi_L}\} = {}_{(L \text{ x } L)}[\mathbf{P_L}]_{(L \text{ x } 1)}\{\boldsymbol{\Phi_L}\}$$

where the $(L \text{ x } 1)$ column vector $\boldsymbol{\Phi_L}$ contains the scaling functions at integer points with the support $[0, L-1]$ and the $(L \text{ x } L)$ matrix $[\mathbf{P_L}]$ contains the filter coefficients for order D*L*. Equation (3.34) represents the eigenvalue problem for the matrix $[\mathbf{P_L}]$, to which the eigenvector corresponding to the eigenvalue 1 contains the scaling functions at integer points $\phi_L(x)$ for $0 \leq x \leq L-1$. The normalisation condition (3.21) is obtained through the eigenvector normalisation

$$\sum_x \phi_L(x) = 1 \qquad \textbf{(3.35)}$$

Though the scaling functions have been obtained at integer points, it is necessary to evaluate the scaling functions $\phi_L(x)$ for $x \in \mathbb{R}$. Therefore, from the two scale equation, the scaling functions are computed at half integer points and these values are used to evaluate $\phi_L(x)$ at quarter integer points and so on. This is achieved recursively at dyadic points $x = \frac{k}{2^i}$ for

$k, i \in \mathbb{Z}$ and $i \geq 0$. Thus, $\phi_L(x)$ for $x \in \mathbb{R}$, can be approximated by the dyadic points to various degrees of accuracy as illustrated in Figure 3-2.

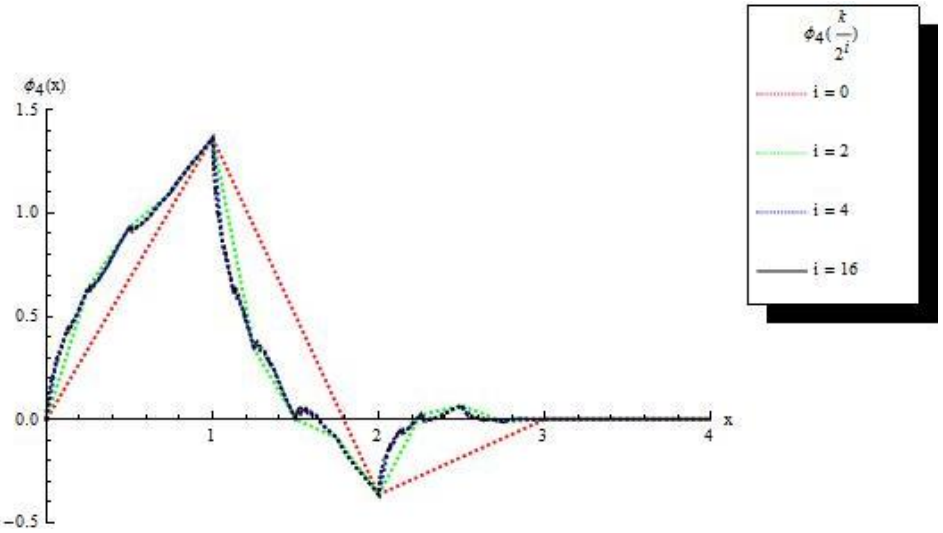

Figure 3-2: Daubechies D*4* scaling functions $\phi_4\left(\frac{k}{2^i}\right)$ for different values of *i*.

The computational cost increases with an increase of the level of accuracy required through the increasing number of dyadic points. From Figure 3-2, it is observed that the values for $\phi_4\left(\frac{k}{2^i}\right)$ at $i = 4$ are almost as accurate as those obtained when $i = 16$.

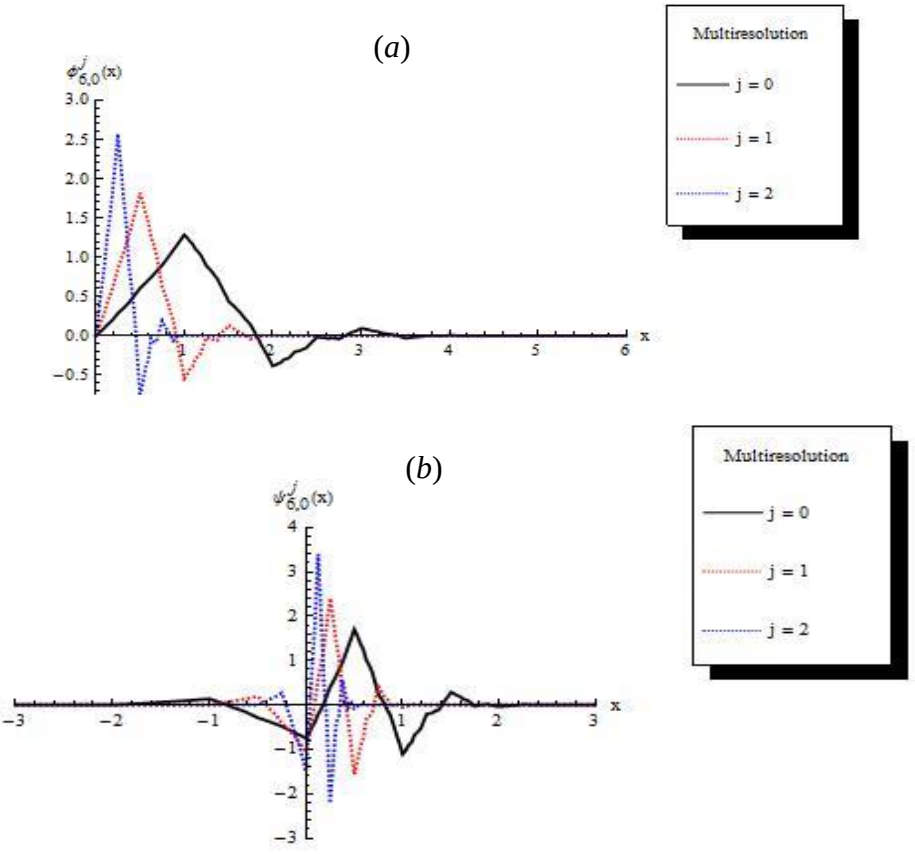

Figure 3-3: Daubechies D*6* scaling $\phi^j_{6,0}(x)$ and wavelet $\psi^j_{6,0}(x)$ function at different multiresolution levels *j*.

Therefore, in practice one can select a lower value of i that gives an acceptable level of accuracy, and then carry out an interpolation for the approximate values of $\phi_L(x)\ for\ x \in \mathbb{R}$ within these dyadic points to reduce the computational time. The wavelet functions are then computed from equation (3.20) once the scaling functions are evaluated. Subsequently, the scaling and wavelet functions at different multiresolution j can be calculated from the relations in equations (3.25) and (3.26) respectively. Figure 3-3 shows the comparison of the scaling and wavelet functions for D*6* at different scales *j*.

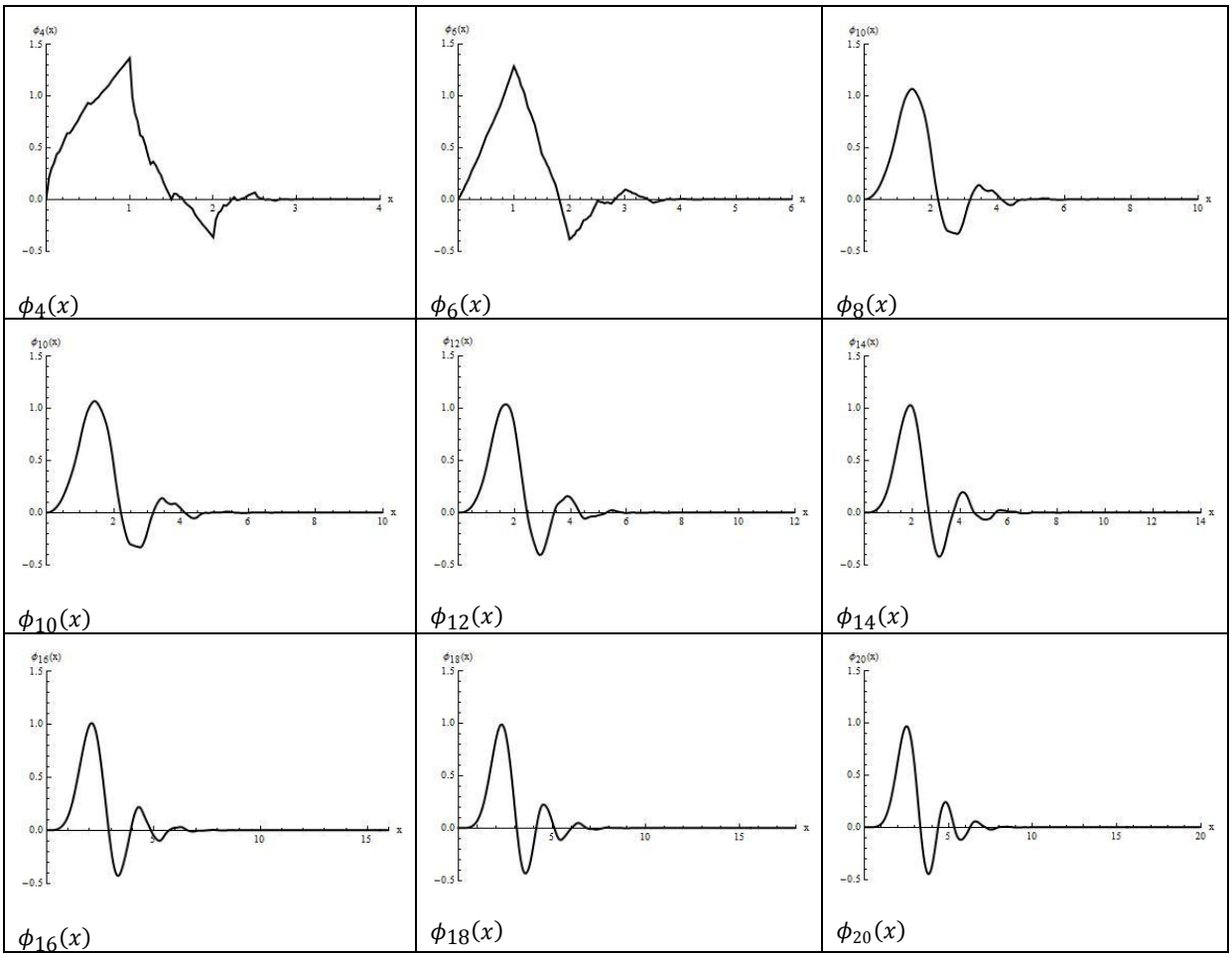

Figure 3-4: The Daubechies scaling functions $\phi_L(x)$ plots for order D*4* – D*20*.

Figure 3-4 and Figure 3-5 include graphic plots of the Daubechies scaling and wavelet functions respectively for order D*4* – D*20*. The number of vanishing moments increases with an increase in the order D*L* and moreover, the support of both scaling and wavelet functions also increases. Therefore, if a function is approximated by a set of polynomials, the accuracy of $\phi_{L,k}(x)$ to approximate the function increases with order D*L*. It is evident from the graphs in Figure 3-4 and Figure 3-5 that both $\phi_L(x)$ and $\psi_L(x)$ become smoother with an increase of the number of vanishing moments. This means that increasing the order of the wavelet

increases the order of the polynomials x^m, where $0 \leq m \leq \frac{L}{2} - 1$, that can be represented exactly via the scaling function and its translates.

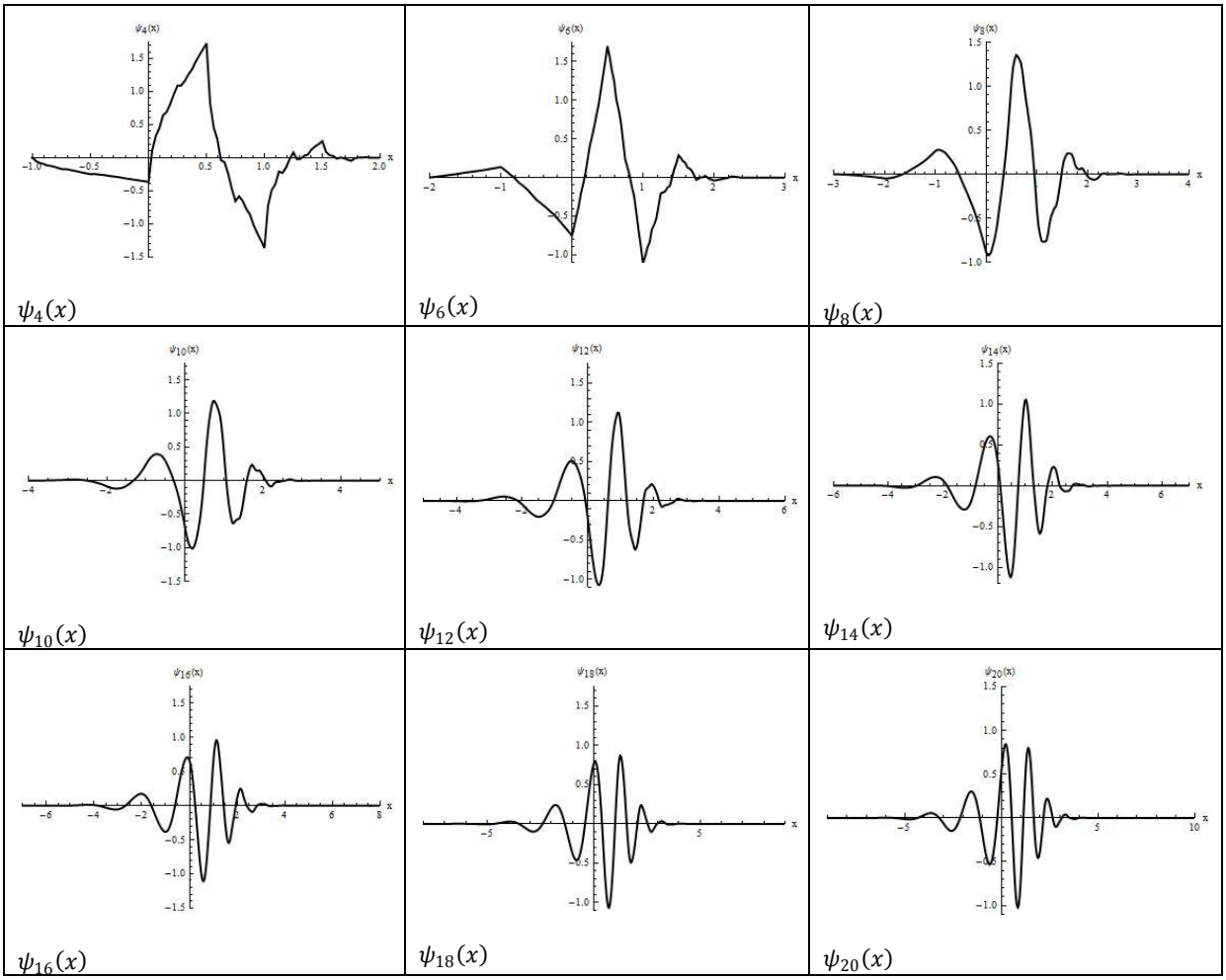

Figure 3-5: The Daubechies wavelet functions $\psi_L(x)$ plots for order D*4* – D*20*.

3.2.3. The Daubechies scaling function derivatives $\boldsymbol{\phi_L^{(m)}(x)}$

The derivatives of the Daubechies wavelet scaling functions are essential in the formulation and implementation of the Daubechies based wavelet finite elements. It is therefore necessary to highlight some key aspects related to the evaluation of these functions. Similar to the scaling functions, the derivatives have no explicit expression, thus the derivatives are calculated recursively by evaluating a system of equations. The approach highlighted in this section is similar to that provided by Zhou et al. [38]. Let the derivative of the scaling function of Daubechies family D*L* be denoted by

$$\phi_L^{(m)}(x) = \frac{d^m \phi_L(x)}{dx^m} \tag{3.36}$$

By differentiating the refinement equation (3.18) m times, the derivative of the scaling function from equation (3.36) becomes

$$\phi_L^{(m)}(x) = 2^m \sum_{k=0}^{L-1} p(k)\, \phi_L^{(m)}(2x-k) \tag{3.37}$$

The support for the scaling function is $[0, L-1]$ and therefore the support of the m^{th} derivative of the scaling function is also $\phi_L^{(m)}(x) \subseteq [0, L-1]$. Similar to the evaluation of the scaling functions, it is necessary to evaluate the derivatives first at integer points; within the support limits. This gives rise to a system of equations at all integer points within the corresponding support as shown below.

$$\begin{gathered}
\phi_L^{(m)}(0) = 2^m p(0)\phi_L^{(m)}(0) \\
\phi_L^{(m)}(1) = 2^m \left[p(0)\phi_L^{(m)}(2) + p(1)\phi_L^{(m)}(1) + p(2)\phi_L^{(m)}(0)\right] \\
\vdots \\
\phi_L^{(m)}(L-2) = 2^m \left[p(L-3)\phi_L^{(m)}(L-1) + p(L-2)\phi_L^{(m)}(L-2) + p(L-1)\phi_L^{(m)}(L-3)\right] \\
\phi_L^{(m)}(L-1) = 2^m p(L-1)\phi_L^{(m)}(L-1)
\end{gathered} \tag{3.38}$$

This can be represented in matrix form as:

$$\begin{Bmatrix} \phi_L^{(m)}(0) \\ \phi_L^{(m)}(1) \\ \vdots \\ \phi_L^{(m)}(L-2) \\ \phi_L^{(m)}(L-1) \end{Bmatrix} = 2^m \begin{bmatrix} p(0) & 0 & \cdots & 0 & 0 \\ p(2) & p(1) & \cdots & 0 & 0 \\ \vdots & \vdots & \ddots & \vdots & \vdots \\ 0 & 0 & \cdots & p(L-2) & p(L-3) \\ 0 & 0 & \cdots & 0 & p(L-1) \end{bmatrix} \begin{Bmatrix} \phi_L^{(m)}(0) \\ \phi_L^{(m)}(1) \\ \vdots \\ \phi_L^{(m)}(L-2) \\ \phi_L^{(m)}(L-1) \end{Bmatrix} \tag{3.39}$$

$$_{(L \text{ x } 1)}\left\{\boldsymbol{\Phi}_L^{(m)}\right\} = 2^m \, _{(L \text{ x } L)}[\mathbf{P}_{\boldsymbol{L}}] \, _{(L \text{ x } 1)}\left\{\boldsymbol{\Phi}_L^{(m)}\right\}$$

This is rewritten as:

$$(2^m \, _{(L \text{ x } L)}[\mathbf{P}_{\boldsymbol{L}}] - \, _{(L \text{ x } L)}[\boldsymbol{I}]) \, _{(L \text{ x } 1)}\left\{\boldsymbol{\Phi}_L^{(m)}\right\} = \, _{(L \text{ x } 1)}\{\mathbf{0}\} \tag{3.40}$$

where $\left\{\boldsymbol{\Phi}_L^{(m)}\right\} = \left\{\phi^{(m)}(0), \phi^{(m)}(1), \cdots, \phi^{(m)}(N-2), \phi^{(m)}(N-1)\right\}^{\mathrm{T}}$ is the column matrix containing the derivatives at integer points, $[\boldsymbol{I}]$ is an $(L \text{ x } L)$ identity matrix, and $[\boldsymbol{P_L}]$ is the filter coefficient matrix with entries $\boldsymbol{P_L}_{k,l} = p_L(2k-l)$. The matrix $[\boldsymbol{P_L}]$ matrix is singular, and in order to determine a unique solution, a normalizing condition is necessary. The moment condition expressed in equation (3.24) (which is discussed further in the next section) gives rise to the equation presented by Beylkin [34]

$$\sum_{k=-\infty}^{k=\infty} k^m \phi(x-k) = x^m + \sum_{k=1}^{k=m} (-1)^k \binom{m}{k} x^{m-k} \int_{-\infty}^{\infty} \phi(z) z^k \, dz \tag{3.41}$$

$\int_{-\infty}^{\infty} \phi_L(x) x^m dx$ is defined as the moment of the scaling functions. Differentiating equation (3.41) m times we obtain

$$\sum_{k=-\infty}^{k=\infty} k^m \phi^{(m)}(x-k) = m! \qquad \textbf{(3.42)}$$

Therefore, adding the normalizing condition (3.42) to the set of equations in (3.40) allows the evaluation of $\phi_L^{(m)}(x)$ at integer points. Through recursion, the values at dyadic points can be solved via equation (3.37) in an approach similar to that used to obtain the scaling functions.

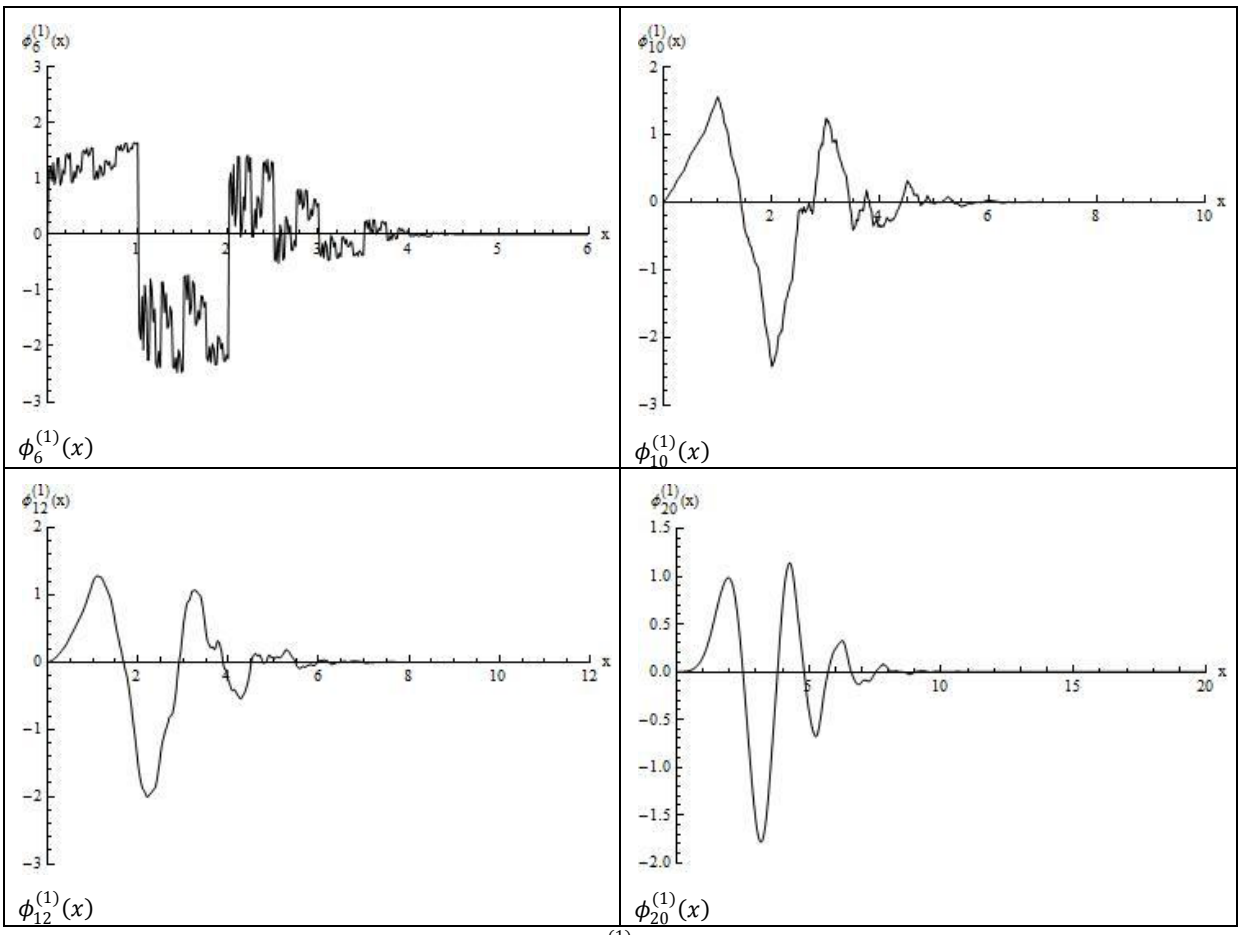

Figure 3-6: The Daubechies scaling function 1st derivative $\phi_L^{(1)}(x)$ plots for order D*4*, D*10*, D*12* and D*20*.

Figure 3-6 above contains the plot of the first derivative of the scaling functions for Daubechies D*4*, D*10*, D*12* and D*20* wavelets. It is observed that as the order of the wavelet increases, the first derivative of the scaling function becomes smoother. Furthermore, as the order of the derivative $m \to \frac{L}{2} - 1$, the more irregular the curves of $\phi_L^{(m)}(x)$ become. The m^{th} derivative of the scaling functions at different multiresolution scales can also be computed by differentiating equation (3.25) m times. Thus,

$$\phi_{L,k}^{j,(m)}(x) = 2^{j\left(m+\frac{1}{2}\right)} \phi_L^{(m)}(2^j x - k) \qquad \textbf{(3.43)}$$

Equation (3.43) can be evaluated from the values obtained from equation (3.37).

3.2.4. The Daubechies moments

A vital property of the Daubechies wavelet family is the vanishing moment condition which is expressed in equation (3.24). The ability of the Daubechies wavelet to accurately represent a function is dependent on the number of vanishing moments. Daubechies wavelets of order L have $\frac{L}{2}-1$ vanishing moments [20] and this property ensures that a polynomial x^m, where $0 \leq m \leq \frac{L}{2}-1$, is in the multiresolution spaces V_j. Furthermore, the vanishing moments describe the number of times the Daubechies wavelet DL is continuously differentiable. Therefore, the Daubechies wavelet DL belongs to $C^{\frac{L}{2}-1}$. This vanishing moment property implies that the translates of the Daubechies scaling functions, $\phi_L(x-k)$ of order L, can directly represent a polynomial of order x^m where $0 \leq m \leq \frac{L}{2}-1$ [36]. Mathematically, this is expressed as [36]:

$$x^m = \sum_k M_k^m \, \phi_L(x-k) \tag{3.44}$$

The coefficients M_k^m denote the moments of the scaling function and its translates at V_0. Thus, the moments are evaluated from the expression

$$M_k^m = M_{0,k}^m = \langle x^m, \phi_L(x-k) \rangle = \int_{-\infty}^{\infty} x^m \phi_L(x-k) dx \tag{3.45}$$

$$M_k^m = \sum_{l=0}^{m} \binom{m}{l} i^{m-l} \, M_0^l \tag{3.46}$$

where M_0^m is the m^{th} moment of the scaling function and is evaluated as:

$$M_0^m = M_0^{0,m} = \langle x^m, \phi_L(x) \rangle = \int_{-\infty}^{\infty} x^m \phi_L(x) dx \tag{3.47}$$

$$M_0^m = \frac{1}{2(2^m-1)} \sum_{l=0}^{m-1} \binom{m}{l} M_0^l \sum_{i=0}^{L-1} p_L(i) \, i^{m-l} \tag{3.48}$$

The moments $M_k^{j,m}$ of the scaling function translates, can also be evaluated in the multiresolution space V_j; where

$$M_k^{j,m} = \langle x^m, \phi_{L,k}^j(x) \rangle = \int_{-\infty}^{\infty} x^m \phi_{L,k}^j(x) dx \tag{3.49}$$

$$M_k^{j,m} = \frac{1}{2^{j\,(m+\frac{1}{2})}} \sum_{l=0}^{m} \binom{m}{l} k^{m-l}\, M_0^{0,l} \tag{3.50}$$

The function x^m can be represented in terms of the moments and scaling functions at multiresolution scale *j* as:

$$x^m = \sum_k M_k^{j,m}\, \phi_{L,k}^{j}(x) \tag{3.51}$$

The moments described above are derived in more detail in Appendix A.2.2 using a similar approach as outlined by Latto et al. [36] for moments at scale $j \geq 0$.

3.2.5. The Daubechies connection coefficients

The Wavelet-Galerkin approximation is formulated via the integrals of the scaling and/or wavelet functions. However, the integrals can be expressed in terms of the scaling functions since the wavelet function is evaluated from the scaling function as shown in equation (3.26). In the case of some wavelet families such as the Daubechies wavelet, the scaling and wavelet functions have no explicit expression. Furthermore, the derivatives of the scaling functions are highly oscillatory, particularly for the low order wavelet families and/or the high order derivatives. This implies that the integrals cannot be evaluated directly in closed form and require the computation of what is commonly referred to as connection coefficients. There are different forms of connection coefficients described in the literature, however in this study, the term connection coefficients will refer to the integral of products of the scaling functions and/or derivatives of the scaling functions [36]. The general connection coefficients are defined as follows:

1. The 2-term scaling function connection coefficients:

$$\Gamma_{k,l}^{d_1,d_2} = \int_a^b \phi_L^{(d_1)}(x-k)\phi_L^{(d_2)}(x-l)dx \tag{3.52}$$

2. The connection coefficients of the form

$$\Upsilon_k^m = \int_0^1 \chi_{[0,1]}(x)x^m \phi_L(x-k)dx \tag{3.53}$$

Beylkin [34] computed the 2-term scaling function connection coefficients with the integral limits $-\infty$ to ∞, denoted as:

$${}^1\Gamma_k^{0,d_2} = \int_{-\infty}^{\infty} \phi_L(x-k)\phi_L^{(d_2)}(x)dx \tag{3.54}$$

He applied the same algorithm to obtain the integral of products of the scaling and/or wavelet functions and the corresponding derivative operators. These functions were then applied to compute the nonstandard form of the Hilbert transform and functional derivatives. Dahmen and Micchelli [35] also used these connection coefficients to solve PDEs using the Wavelet-Galerkin method.

Latto et al. [36] presented an algorithm to evaluate the general *n*-term connection coefficients, with integral limits $-\infty$ to ∞, by implementing the two-scale relation of the scaling functions and the moment equations to generate a set of homogeneous equations and normalizing equations respectively. They presented algorithms for the 2-term and 3-term connection coefficients which are expressed as:

$$ {}^{1}\Gamma_{k,l}^{d_1,d_2} = \int_{-\infty}^{\infty} \phi_L^{(d_1)}(x-k)\phi_L^{(d_2)}(x-l)dx \tag{3.55} $$

$$ {}^{1}\Lambda_{i,k,l}^{d_1,d_2,d_3} = \int_{-\infty}^{\infty} \phi_L^{(d_1)}(x-i)\phi_L^{(d_2)}(x-k)\phi_L^{(d_3)}(x-l)dx \tag{3.56} $$

Chen et al. in [39] and [89] furthered Beylkin's [34] work by presenting finite bound connection coefficients of the form

$$ {}^{2}\Gamma_{k}^{d_1,0} = \int_{0}^{y} \phi_L^{(d_1)}(x-k)\phi_L(x)dx \tag{3.57} $$

Discussing key errors found in [39], Zhang et al. [90] corrected them giving a clearer conceptualization of these connection coefficients. The connection coefficients presented by Beylkin [34], Latto et al. [36] and Dahmen and Micchelli [35], with unbound integral limits, were classified by Romine and Peyton [91] as "improper" connection coefficients. In their technical report, they presented "proper" 2-term and 3-term connection coefficients to which the integral limits are on a finite bound domain 0 to *y*.

$$ {}^{3}\Gamma_{k,l}^{d_1,d_2} = \int_{0}^{y} \phi_L^{(d_1)}(x-k)\phi_L^{(d_2)}(x-l)dx \tag{3.58} $$

$$ {}^{2}\Lambda_{i,k,l}^{d_1,d_2,d_3} = \int_{0}^{y} \phi_L^{(d_1)}(x-i)\phi_L^{(d_2)}(x-k)\phi_L^{(d_3)}(x-l)dx \tag{3.59} $$

They identified that the improper connection coefficients presented by Latto et al. [36] experienced inadequacies when implementing boundary conditions since they did not accurately solve the inner product near the limits of a finitely bound interval. Furthermore, the standard numerical quadrature of the integrals near the boundary using the improper

connection coefficients, were unfeasible due to the highly oscillatory basis functions of the Daubechies wavelets. The proper connection coefficients were employed to solve a one dimensional Poisson problem with Dirichlet boundary conditions. Lin and Zhou [92] presented "proper" 2-term and 3-term connection coefficients for the Daubechies and Coiflets family of wavelets with the integral limits between 0 and 2^j of the form

$$ {}^{4}\Gamma_{k,l}^{d_1,d_2} = \int_0^{2^j} \phi_L^{(d_1)}(x-k)\phi_L^{(d_2)}(x-l)dx \tag{3.60} $$

$$ {}^{3}\Lambda_{i,k,l}^{d_1,d_2,d_3} = \int_0^{2^j} \phi_L^{(d_1)}(x-i)\phi_L^{(d_2)}(x-k)\phi_L^{(d_3)}(x-l)dx \tag{3.61} $$

to solve Burgers equation.

With regards to the formulation of the Daubechies based WFEs, the integrals in the formulation of the elemental matrices and load vectors are in the bounded domain [0,1]. Ko et al. [9] used a similar approach to Latto et al. [36] to derive connection coefficients bound on the unit interval by solving an eigenvalue problem formed from a set of homogenous equations.

$$ {}^{5}\Gamma_{k,l}^{d_1,d_2} = \int_0^{1} \phi_L^{(d_1)}(x-k)\phi_L^{(d_2)}(x-l)dx \tag{3.62} $$

However, to uniquely solve for these connection coefficients, additional normalization conditions are generated from the moment condition of the Daubechies wavelets highlighted in equation (3.51). Ko et al. [9] applied these connection coefficients to solve a one dimensional, second order Neumann problem. Ma et al. [10] constructed a wavelet based beam element, Chen et al. [8] constructed a wavelet based thin plate and Diaz et al. [40] also constructed beam and plate WFEs using the connection coefficients (3.62); to formulate the elemental matrices. The formulation of the load vectors for distributed loading also requires the evaluation of the connection coefficients as expressed in equation (3.53) bound in the domain [0,1]. Ma et al. [10] outlined an algorithm to evaluate these connection coefficients, which were also employed by Chen et al. [8]. However, the connection coefficients expressed in equations (3.53) and (3.62) are formulated at multiresolution scale $j = 0$. In order to take advantage of the multiresolution properties, Chen et al. [6] presented connection coefficients computed at different multiresolution scale *j*, following a similar approach outlined by Ma et al. [10] and Ko et al. [9].

$$ {}^{6}_{L}\Gamma^{j,d_1,d_2}_{k,l} = \int_0^1 \phi_L^{(d_1)}(2^j x - k)\phi_L^{(d_2)}(2^j x - l)dx \quad \textbf{(3.63)} $$

However this algorithm is for the evaluation of the connection coefficients of the same order *L*. In this study, it is necessary to evaluate the connection coefficients of different order scaling functions in order to obtain the wavelet space WFE matrices for beam elements with axial deformation taken into account as well as the Daubechies based functionally graded beam element presented in Chapter 8.

Multiscale two-term connection coefficients of the form $_{a,b}\Gamma^{j,m,n}_{k,l}$

A modified connection coefficient algorithm which takes into account different orders of the scaling functions, at different multiresolution scale *j*, is presented. These connection coefficients, formulated following a similar algorithm presented by Chen et al. [6], are later implemented in the analysis of FG beams. To the best of the author's knowledge this algorithm, and the consequent implementation in the formulation of FG beams, is presented for the first time. These connection coefficients allow for the evaluation of Daubechies based wavelet finite element matrices where integral of the products of the approximating scaling functions, with respect to the axial and transverse displacement functions, are of different wavelet order. We define the following two-term connection coefficient

$$ {}_{a,b}\Gamma^{j,d_1,d_2}_{k,l} = \int_0^1 \phi^{j,(d_1)}_{a,k}(\xi)\phi^{j,(d_2)}_{b,l}(\xi)d\xi \quad \textbf{(3.64)} $$

where a and b are the orders of the scaling function of the Daubechies wavelets at multiresolution j. The values d_1 and d_2 denote the order of the derivative of the scaling functions. Equation (3.64) can be rewritten as

$$ {}_{a,b}\Gamma^{j,d_1,d_2}_{k,l} = 2^j \int_{-\infty}^{\infty} \mathcal{X}_{[0,1]}(\xi)\phi_a^{(d_1)}(2^j\xi - k)\phi_b^{(d_2)}(2^j\xi - l)d\xi \quad \textbf{(3.65)} $$

We define the characteristic function $\mathcal{X}_{[0,1]}(x)$:

$$ \mathcal{X}_{[0,1]}(x) = \begin{cases} 1 & 0 \le x \le 1 \\ 0 & \text{otherwise} \end{cases} \quad \textbf{(3.66)} $$

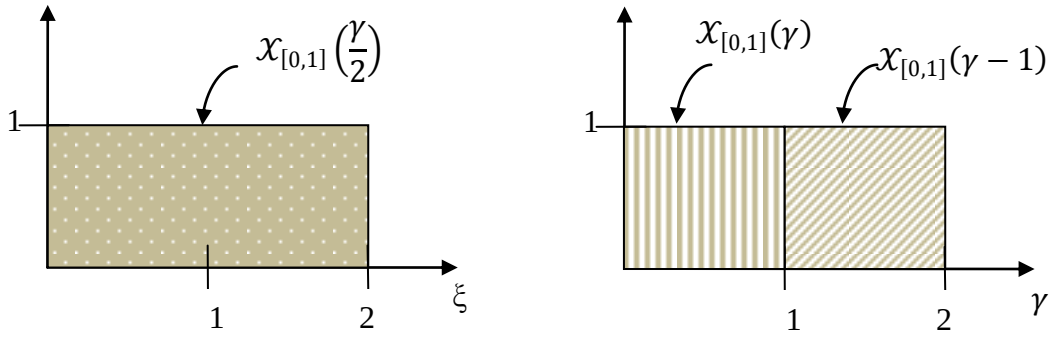

Figure 3-7: The characteristic function $\mathcal{X}_{[0,1]}\left(\frac{\gamma}{2}\right)$.

The characteristic function also satisfies a two-scale relation

$$\mathcal{X}_{[0,1]}\left(\frac{\gamma}{2}\right) = \begin{cases} 1 & 0 \le \gamma \le 2 \\ 0 & \text{otherwise} \end{cases}$$

$$\mathcal{X}_{[0,1]}\left(\frac{\gamma}{2}\right) = \mathcal{X}_{[0,1]}(\gamma) + \mathcal{X}_{[1,2]}(\gamma) = \mathcal{X}_{[0,1]}(\gamma) + \mathcal{X}_{[0,1]}(\gamma-1) \tag{3.67}$$

According to the two scale relation of the scaling function in equation (3.25),

$$\phi_L(2^j\xi - k) = \sum_r p(r)\phi_L\left(2^{j+1}\xi - 2k - r\right) \tag{3.68}$$

Furthermore, differentiating equation (3.68) *m* times,

$$2^{jm}\,\phi_L^{(m)}(2^j\xi - k) = 2^{(j+1)m}\sum_r p(r)\phi_L^{(m)}\left(2^{j+1}\xi - 2k - r\right) \tag{3.69}$$

Substituting (3.69) into equation (3.65) for derivatives of order d_1 and d_2 respectively,

$$\begin{aligned} {}_{a,b}\Gamma_{k,l}^{j,d_1,d_2} = 2^j \int_{-\infty}^{\infty} \mathcal{X}_{[0,1]}(\xi) 2^{d_1} \sum_r p(r)\phi_a^{(d_1)}\left(2^{j+1}\xi - 2k\right. \\ \left. - r\right) 2^{d_2} \sum_s p(s)\phi_b^{(d_2)}(2^{j+1}\xi - 2l - s)\, d\xi \end{aligned} \tag{3.70}$$

Let $2\xi = \gamma$ thus $dx = \frac{d\gamma}{2}$. Substituting into (3.70)

$$\begin{aligned} &{}_{a,b}\Gamma_{k,l}^{j,d_1,d_2} = \\ &2^{j+d_1+d_2}\sum_{r,s} p(r)p(s)\int_{-\infty}^{\infty} \mathcal{X}_{[0,1]}\left(\frac{\gamma}{2}\right)\phi_a^{(d_1)}(2^j\gamma - 2k - r)\phi_b^{(d_2)}(2^j\gamma - 2l - s)\frac{d\gamma}{2} \end{aligned} \tag{3.71}$$

Substituting the characteristic function in equation (3.67) into equation (3.71)

$$
\begin{aligned}
{}_{a,b}\Gamma_{k,l}^{j,d_1,d_2} &= 2^{j+d_1+d_2-1}\sum_{r,s} p(r)p(s)\int_{-\infty}^{\infty}\left[\chi_{[0,1]}(\gamma)+\chi_{[0,1]}(\gamma-1)\right]\phi_a^{(d_1)}(2^j\gamma-2k \\
&\quad -r)\phi_b^{(d_2)}(2^j\gamma-2l-s)d\gamma \\
{}_{a,b}\Gamma_{k,l}^{j,d_1,d_2} &= 2^{j+d_1+d_2-1}\sum_{r,s} p(r)p(s)\int_{-\infty}^{\infty}\chi_{[0,1]}(\gamma)\phi_a^{(d_1)}(2^j\gamma-2k-r)\phi_b^{(d_2)}(2^j\gamma-2l \\
&\quad -s)d\gamma+\int_{-\infty}^{\infty}\left[\chi_{[0,1]}(\gamma-1)\phi_a^{(d_1)}(2^j\gamma-2k-r)\phi_b^{(d_2)}(2^j\gamma-2l-s)\right]d\gamma
\end{aligned}
\tag{3.72}
$$

However, from equation (3.65)

$$
{}_{a,b}\Gamma_{2k+r,2l+s}^{j,d_1,d_2} = 2^j\int_{-\infty}^{\infty}\left[\chi_{[0,1]}(\gamma)\phi_a^{(d_1)}(2^j\gamma-2k-r)\phi_b^{(d_2)}(2^j\gamma-2l-s)\right]d\gamma \tag{3.73}
$$

$$
{}_{a,b}\Gamma_{2k+r-2^j,2l+s-2^j}^{j,d_1,d_2} = 2^j\int_{-\infty}^{\infty}\left[\chi_{[0,1]}(\gamma-1)\phi_a^{(d_1)}(2^j\gamma-2k-r)\phi_b^{(d_2)}(2^j\gamma-2l-s)\right]d\gamma \tag{3.74}
$$

We can therefore substitute equations (3.73) and (3.74) into (3.72).

$$
{}_{a,b}\Gamma_{k,l}^{j,d_1,d_2} = 2^{d_1+d_2-1}\sum_{r,s} p_a(r)p_b(s)\left[{}_{a,b}\Gamma_{2k+r,2l+s}^{j,d_1,d_2}+{}_{a,b}\Gamma_{2k+r-2^j,2l+s-2^j}^{j,d_1,d_2}\right] \tag{3.75}
$$

Equation (3.75) can be rewritten as

$$
\begin{aligned}
{}_{a,b}\Gamma_{k,l}^{j,d_1,d_2} &= 2^{d_1+d_2-1}\sum_{r,s}[p_a(r-2k)p_b(s-2l) \\
&\quad +p_a\left(r-2k+2^j\right)p_b\left(s-2l+2^j\right)]\,\Gamma_{r,s}^{j,d_1,d_2}
\end{aligned}
\tag{3.76}
$$

where $2-a\le k,r\le 2^j-1$ and $2-b\le l,s\le 2^j-1$. Equation (3.76) can be expressed in matrix form as follows:

$$
\begin{aligned}
&\left((a+2^j-2)(b+2^j-2)\times 1\right)\left\{{}_{a,b}\Gamma^j\right\} = \\
&2^{d_1+d_2-1}\left((a+2^j-2)(b+2^j-2)\times(a+2^j-2)(b+2^j-2)\right)\left[\boldsymbol{{}_{a,b}P}\right]\left((a+2^j-2)(b+2^j-2)\times 1\right)\left\{{}_{a,b}\Gamma^j\right\}
\end{aligned}
\tag{3.77}
$$

where ${}_{a,b}\Gamma^j$ is a vector of length $\left(\left(a+2^j-2\right)\left(b+2^j-2\right)\text{ x }1\right)$ containing the connection coefficients, while the square matrix $\left[\boldsymbol{{}_{a,b}P}\right]$ contains the filter coefficients as expressed in equation (3.76) with the dimensions $\left(\left(a+2^j-2\right)\left(b+2^j-2\right)\times\left(a+2^j-2\right)\left(b+2^j-2\right)\right)$. Equation (3.77) can be rewritten as:

$$\left(2^{d_1+d_2-1}{}_{\left((a+2^j-2)(b+2^j-2)\times(a+2^j-2)(b+2^j-2)\right)}\left[{}_{a,b}\boldsymbol{P}\right]-\right.$$
$$a+2j-2b+2j-2\times a+2j-2b+2j-2\boldsymbol{I}a+2j-2b+2j-2\times 1a,b\Gamma j=a+2j-2b+2j-2\times 10 \quad \textbf{(3.78)}$$

$\boldsymbol{I}$ is the $\left(\left(a+2^j-2\right)\left(b+2^j-2\right)\times\left(a+2^j-2\right)\left(b+2^j-2\right)\right)$ identity matrix. However, equation (3.78) cannot uniquely define the generalized connection coefficients since the matrix $(2^{d_1+d_2-1}\left[{}_{a,b}\boldsymbol{P}\right]-\boldsymbol{I})$ is singular. Therefore, it is necessary to employ the moment condition to formulate the normalizing conditions required to generate a sufficient number of inhomogeneous equations so as to uniquely determine the connection coefficients. These additional normalizing equations are formulated from the fact the Daubechies scaling functions of order *a* can exactly represent any polynomial of order *m* with $0 \le m \le \frac{a}{2}-1$.

$$\xi^m = 2^{\frac{j}{2}}\sum_k M_{j,k}^m \phi_L\left(2^j\xi-k\right) \quad \textbf{(3.79)}$$

$M_k^{j,m}$ are the moments described in equation (3.49). For the sake of uniformity of the formulation presented, let the moments associated with the scaling function of order *a* and *b* be denoted as ${}_aM_k^{j,m}$ and ${}_bM_l^{j,n}$ respectively. Differentiating equation (3.79) d_1 times with $L=a$:

$$\begin{aligned}
m\,\xi^{m-1} &= 2^{\frac{j}{2}}2^j\sum_k {}_aM_k^{j,m}\phi_a'(2^j\xi-k)\\
m(m-1)\,\xi^{m-2} &= 2^{\frac{j}{2}}2^{2j}\sum_k {}_aM_k^{j,m}\phi_a''(2^j\xi-k)\\
&\vdots\\
m(m-1)\cdots m-(d_1-2)\,\xi^{m-d_1+1} &= 2^{\frac{j}{2}}2^{(d_1-1)j}\sum_k {}_aM_k^{j,m}\phi_a''(2^j\xi-k)\\
m(m-1)\cdots\left(m-(d_1-2)\right)\left(m-(d_1-1)\right)\xi^{m-d_1} &= 2^{j\left(d_1+\frac{1}{2}\right)}\sum_k {}_aM_k^{j,m}\phi_a^{(d_1)}(2^j\xi-k)
\end{aligned} \quad \textbf{(3.80)}$$

Similarly, for a polynomial of order *n* with $0 \le n \le \frac{b}{2}-1$,

$$\xi^n = 2^{\frac{j}{2}}\sum_k M_{j,k}^n \phi_b\left(2^j\xi-k\right) \quad \textbf{(3.81)}$$

Differentiating equation (3.81) d_2 times

$$n(n-1)\cdots\big(n-(d_2-2)\big)\big(n-(d_2-1)\big)\,\xi^{n-d_2} = 2^{j(d_2+\frac{1}{2})}\sum_{l} {}_bM_l^{j,n}\,\phi_b^{(d_2)}(2^j\xi-l) \tag{3.82}$$

Multiplying equation (3.80) by equation (3.82) and integrating the products:

$$\begin{aligned}\int_0^1 n(n-1)\cdots\big(n-(d_2-2)\big)\big(n-(d_2-1)\big)\,\xi^{n-d_2} m(m-1)\cdots\big(m-(d_1-2)\big)\big(m\\ -(d_1-1)\big)\,\xi^{m-d_1}\,d\xi\\ = 2^j\,2^{j\,d_1}\,2^{j\,d_2}\int_0^1\sum_{k,l} {}_aM_k^{j,m}\,\phi_a^{(d_1)}(2^j\,\xi-k)\;{}_bM_l^{j,n}\,\phi_b^{(d_2)}(2^j\,\xi-l)\,d\xi\end{aligned}$$

$$\begin{aligned}\int_0^1 m(m-1)\cdots\big(m-(d_1-2)\big)\big(m-(d_1-1)\big)n(n-1)\cdots\big(n-(d_2-2)\big)\big(n\\ -(d_2-1)\big)\;\xi^{m+n-d_1-d_2}\,d\xi\\ = 2^{j(d_1+d_2+1)}\sum_{k,l} {}_aM_k^{j,m}\;{}_bM_l^{j,n}\int_0^1\phi_a^{(d_1)}\left(2^j\xi-k\right)\phi_b^{(d_2)}\left(2^j\xi-l\right)d\xi\end{aligned} \tag{3.83}$$

However,

$$\int_0^1 \xi^{m+n-d_1-d_2}\,d\xi = \frac{1}{m+n-d_1-d_2+1} \tag{3.84}$$

Thus, substituting equations (3.65) and (3.84) into equation into equation (3.83)

$$\begin{aligned}\frac{m(m-1)\cdots\big(m-(d_1-2)\big)\big(m-(d_1-1)\big)n(n-1)\cdots\big(n-(d_2-2)\big)\big(n-(d_2-1)\big)}{m+n-d_1-d_2+1}\\ = 2^{j\,(d_1+d_2)}\sum_{k,l} {}_aM_k^{j,m}\;{}_bM_l^{j,n}\;{}_{a,b}\Gamma_{k,l}^{j,d_1,d_2}\\ \frac{m!\,n!}{(m-d_1-1)!\,(n-d_2-1)!\,(m+n-d_1-d_2+1)}\\ = 2^{j\,(d_1+d_2)}\sum_{k,l} {}_aM_k^{j,m}\;{}_bM_l^{j,n}\;{}_{a,b}\Gamma_{k,l}^{j,d_1,d_2}\end{aligned} \tag{3.85}$$

For a Daubechies wavelet family at any scale j, there are $\left(\frac{ab}{4}\right)$ number of normalizing equations that can be generated from equation (3.85). This can be expressed as:

$$\left(\left(\tfrac{ab}{4}\right)\times\left(a+2^j-2\right)\left(b+2^j-2\right)\right)\left[{}_{a,b}\boldsymbol{M^j}\right]_{\left(\left(a+2^j-2\right)\left(b+2^j-2\right)\times 1\right)}\left\{{}_{a,b}\Gamma^j\right\} = \left(\left(\tfrac{ab}{4}\right)\times 1\right)\{\boldsymbol{n_c}\} \tag{3.86}$$

where matrix $\left[{}_{a,b}\boldsymbol{M^j}\right]$ contains the corresponding moments as expressed in equation (3.86), $\left\{{}_{a,b}\Gamma^j\right\}$ is the vector containing the connection coefficients and the vector $\{\boldsymbol{n_c}\}$ contains the

left hand side entries corresponding values of equation (3.86). The normalizing system of equations in (3.86) can now be employed to uniquely determine the connection coefficients as expressed in equation (3.78). In order to reduce on computational costs, the connection coefficients are evaluated once and then stored. If the order of the Daubechies scaling functions is $L = a = b$, the connection coefficients are identical to those expressed in equation (3.62) as formulated by Chen et al. [6].

The multiscale connection coefficients of the form $\Upsilon_k^{j,m}$

Chen et al. [6] also presented an algorithm to evaluate the multiscale connection coefficients of the form

$$\Upsilon_k^{j,m} = 2^{\frac{j}{2}} \int_0^1 x^m \phi_L(2^j \xi - k) d\xi = 2^{\frac{j}{2}} \int_{-\infty}^{\infty} \mathcal{X}_{[0,1]}(\xi) \xi^m \phi_L(2^j \xi - k) d\xi \qquad \textbf{(3.87)}$$

These connection coefficients are implemented to evaluate the wavelet space distributed load vector. Chen et al. [6] presented an algorithm to calculate these connection coefficients at different multiresolution scale j. However in this study, a simpler and more efficient approach is presented. The connection coefficient of the form $\Upsilon_k^{j,m}$ is formulated from a correlation of the 2-term connection coefficients ${}_{a,b}\Gamma_{k,l}^{j,d_1,d_2}$ and moments $M_l^{j,m}$ at multiresolution scale j. Substituting equation (3.79) into (3.87),

$$\Upsilon_k^{j,m} = 2^j \int_{-\infty}^{\infty} \mathcal{X}_{[0,1]}(x) \sum_l M_{j,l}^m \phi_L\left(2^j x - l\right) \phi_L(2^j x - k) dx$$

$$\Upsilon_k^{j,m} = 2^j \sum_l M_l^{j,m} \int_{-\infty}^{\infty} \mathcal{X}_{[0,1]}(x) \phi_L\left(2^j x - l\right) \phi_L(2^j x - k) dx \qquad \textbf{(3.88)}$$

However, from equation (3.65)

$$2^j \int_{-\infty}^{\infty} \mathcal{X}_{[0,1]}(x) \phi_L\left(2^j x - l\right) \phi_L(2^j x - k) dx = {}_{L,L}\Gamma_{k,l}^{j,0,0} \qquad \textbf{(3.89)}$$

Thus, substituting equation (3.89) into equation (3.88)

$$\Upsilon_k^{j,m} = \sum_l M_l^{j,m} \, {}_{L,L}\Gamma_{k,l}^{j,0,0} \qquad \textbf{(3.90)}$$

This can be expressed in matrix form as:

$$\begin{Bmatrix} \Upsilon_{2-L}^{j,0} \\ \Upsilon_{3-L}^{j,0} \\ \vdots \\ \Upsilon_{2^j-2}^{j,0} \\ \Upsilon_{2^j-1}^{j,0} \end{Bmatrix} =$$

$$\begin{bmatrix} {}_{L,L}\Gamma_{2-L,2-L}^{j,0,0} & {}_{L,L}\Gamma_{2-L,3-L}^{j,0,0} & \cdots & {}_{L,L}\Gamma_{2-L,l}^{j,0,0} & \cdots & {}_{L,L}\Gamma_{2-L,2^j-2}^{j,0,0} & {}_{L,L}\Gamma_{2-L,2^j-1}^{j,0,0} \\ {}_{L,L}\Gamma_{3-L,2-L}^{j,0,0} & {}_{L,L}\Gamma_{3-L,3-L}^{j,0,0} & \cdots & {}_{L,L}\Gamma_{3-L,l}^{j,0,0} & \cdots & {}_{L,L}\Gamma_{3-L,2^j-2}^{j,0,0} & {}_{L,L}\Gamma_{3-L,2^j-1}^{j,0,0} \\ \vdots & \vdots & \ddots & \vdots & \ddots & \vdots & \vdots \\ {}_{L,L}\Gamma_{k,2-L}^{j,0,0} & {}_{L,L}\Gamma_{k,3-L}^{j,0,0} & \cdots & {}_{L,L}\Gamma_{k,l}^{j,0,0} & \cdots & {}_{L,L}\Gamma_{k,2^j-2}^{j,0,0} & {}_{L,L}\Gamma_{k,2^j-1}^{j,0,0} \\ \vdots & \vdots & \ddots & \vdots & \ddots & \vdots & \vdots \\ {}_{L,L}\Gamma_{2^j-2,2-L}^{j,0,0} & {}_{L,L}\Gamma_{2^j-2,3-L}^{j,0,0} & \cdots & {}_{L,L}\Gamma_{2^j-2,l}^{j,0,0} & \cdots & {}_{L,L}\Gamma_{2^j-2,2^j-2}^{j,0,0} & {}_{L,L}\Gamma_{2^j-2,2^j-1}^{j,0,0} \\ {}_{L,L}\Gamma_{2^j-1,2-L}^{j,0,0} & {}_{L,L}\Gamma_{2^j-1,3-L}^{j,0,0} & \cdots & {}_{L,L}\Gamma_{2^j-1,l}^{j,0,0} & \cdots & {}_{L,L}\Gamma_{2^j-1,2^j-2}^{j,0,0} & {}_{L,L}\Gamma_{2^j-1,2^j-1}^{j,0,0} \end{bmatrix} \begin{Bmatrix} M_{2-L}^{j,m} \\ M_{3-L}^{j,m} \\ \vdots \\ M_{l}^{j,m} \\ \vdots \\ M_{2^j-2}^{j,m} \\ M_{2^j-1}^{m} \end{Bmatrix}$$

$$\left((L+2^j-2)\times 1\right)\{\boldsymbol{\Upsilon^{j,m}}\} = \left((L+2^j-2)\times(L+2^j-2)\right)[\boldsymbol{\Gamma^{j,0,0}}]\left((L+2^j-2)\times 1\right)\{\boldsymbol{M^{j,m}}\} \qquad \textbf{(3.91)}$$

Once the 2-term multiscale connection coefficients ${}_{L,L}\Gamma_{k,l}^{j,0,0}$, corresponding to the mass matrix in wavelet space (discussed further in Chapter 5), and moments $M_l^{j,m}$ have been evaluated and stored, it is more convenient and less computationally costly to use this approach to calculate the load vector connection coefficients in wavelet space. However, if the connection coefficients ${}_{L,L}\Gamma_{k,l}^{j,0,0}$ are not already evaluated or required e.g., in the static analysis of the wavelet based rod or beam element, it is more convenient to compute $\Upsilon_k^{j,m}$ using the approach presented by Chen et al. [6].

3.3. B-splines and B-spline wavelet on the interval (BSWI)

Basis splines, commonly referred to as B-splines, for a given knot sequence can be constructed by taking the piecewise polynomials between the knots. The knots are joined in such a way that the B-splines obtain a certain order of overall smoothness. In this section, the formulation and discussion of the BSWI is presented. However, the inner scaling and wavelet functions of the BSWI wavelet family are obtained from general B-Splines and the B-wavelet. Therefore, the formulation and properties of the cardinal B-splines, general B-splines and the B-wavelet are presented in Appendix A.3.The mathematical representation is conceptually based on the general theory of B-splines as presented by [19,93,94].

In order to derive the BSWI scaling and wavelet functions it is important to define and formulate the B-splines at multiresolution scale *j*. The B-splines formulated in Appendix

A.3.2, are at scale $j = 0$. Therefore, the basis functions in subspace V_j for B-splines of order m and scale $j > 0$ are expressed as [54]:

$$B_{m,k}^{j}(x) = \left(t_{k+m}^{j} - t_{k}^{j}\right)\left[t_{k}^{j}, \ldots, t_{k+m}^{j}\right]_{f}(t - x)_{+}^{m-1} \tag{3.92}$$

with the knot sequence

$$\begin{gathered}\left\{t_{k}^{j}\right\}_{k=-m+1}^{2^{j}+m-1} \\ t_{k}^{j} \leq t_{k+1}^{j}\end{gathered} \tag{3.93}$$

Following the procedure for general B-splines in Appendix A.3, equation (3.92) can be expressed explicitly as:

$$B_{m,k}^{j}(x) = \frac{x - t_{k}^{j}}{t_{k+m-1}^{j} - t_{k}^{j}} B_{m-1,k}^{j}(x) + \frac{t_{k+m}^{j} - x}{t_{k+m}^{j} - t_{k+1}^{j}} B_{m-1,k+1}^{j}(x) \tag{3.94}$$

$$B_{1,k}^{j}(x) = \begin{cases} 1 & k \leq x \leq k+1 \\ 0 & otherwise \end{cases} \tag{3.95}$$

The support of the basis functions in equation (3.94) is

$$_{supp}\, B_{m,k}^{j}(x) = \left[t_{k}^{j}, t_{k+m}^{j}\right] \tag{3.96}$$

B-splines with multiple *y* knots at a point within the knot sequence are defined as *y*-tuple knots. The B-spline basis of the knot sequence expressed in equation (3.93) has *m*-tuple knots at 0 and 1 and simple knots inside the unit interval. Therefore, for the knot sequence on interval [0,1], t_k^j is given as [95]:

$$t_{k}^{j} = \begin{cases} 0 & -m+1 \leq k < 1 \\ 2^{-j}k & 1 \leq k < 2^{j} \\ 1 & 2^{j} \leq k \leq 2^{j} + m - 1 \end{cases} \tag{3.97}$$

At the boundary points 0 and 1, the knots coalesce and form multiple knots for the BSWI. Inside the interval though, the knots are simple and hence smoothness is unaffected. At any scale *j*, the discretization step is $\frac{1}{2^j}$ for $j > 0$; thus, there are 2^j segments in [0,1]. Given the limits $k \in [-m+1, 2^j + m - 1]$, the number of knots at an end is $m - 1$ ($m - 1$-tuple knots, $2m - 2$ for both ends). The total number of knots is given by the difference of the maximum and minimum limits i.e., $2^j + m - 1 - (-m + 1) = 2^j + 2m - 2$. We can therefore find the number of inner knots as $2^j + 2m - 2 - (2m - 2) = 2^j$. This gives rise to a condition for the minimum value of scale *j* that must be satisfied to ensure that there is at least one inner scaling function in the formulation of the BSWI scaling functions. Given that the number of end knots is $2m - 2$, and total knots is $2^j + m - 2$, then

$$2^j \geq 2m - 1 \quad \textbf{(3.98)}$$

Table 3-1 below gives the knot sequence $\{t_k^j\}$ for B-splines of order $m = 3$ for different multiresolution scale *j*. The knots sequences at each multiresolution scale have 3-tuple knots at each boundary 0 and 1. The knots are increasing through the sequence and obey the property $t_k^j \leq t_{k+1}^j$. Furthermore, as the scale j increases, the number of inner knots increases; while the end multiple knots are not affected.

$\boldsymbol{j}$	$t_{\boldsymbol{m}}^{\boldsymbol{j}} = \{\boldsymbol{t}_{\boldsymbol{m},-\boldsymbol{m}+\boldsymbol{1}}^{\boldsymbol{j}}, \ldots, \boldsymbol{t}_{\boldsymbol{m},\boldsymbol{k}}^{\boldsymbol{j}}, \ldots, \boldsymbol{t}_{\boldsymbol{m},2^{\boldsymbol{j}}+\boldsymbol{m}-\boldsymbol{1}}^{\boldsymbol{j}}\}$
0	$\{0,0,0,1,1,1\}$
1	$\{0,0,0,\frac{1}{2},1,1,1\}$
2	$\{0,0,0,\frac{1}{4},\frac{1}{2},\frac{3}{4},1,1,1\}$
3	$\{0,0,0,\frac{1}{8},\frac{1}{4},\frac{3}{8},\frac{1}{2},\frac{5}{8},\frac{3}{4},\frac{7}{8},1,1,1\}$
4	$\{0,0,0,\frac{1}{16},\frac{1}{8},\frac{3}{16},\frac{1}{4},\frac{5}{16},\frac{3}{8},\frac{7}{16},\frac{1}{2},\frac{9}{16},\frac{5}{8},\frac{11}{16},\frac{3}{4},\frac{13}{16},\frac{7}{8},\frac{15}{16},1,1,1\}$

Table 3-1: Knot sequence values for B-spline $m = 3$ at multiresolution $0 \leq j \leq 4$.

In general, $B_{m,k}^j(x)$ contains multiple knots at 0 for k = -m+1, ..., 1, and similarly at 1 for k = 2^j –m+1, ..., 2^j-1. The basis $B_{m,k}^j(x)$ from the inner knots corresponds to the m^{th} cardinal B-splines at multiresolution *j*:

$$N_m(x) = m[0, 1, \ldots, m](t - x)_+^{m-1} \quad \textbf{(3.99)}$$

$$B_{m,k}^j(x) = N_m\left(2^j x - k\right) \qquad 0 \leq k < 2^j - m + 1 \quad \textbf{(3.100)}$$

The normalising factor $2^{\frac{j}{2}}$ is omitted for convenience and computation purposes. Let the scaling function of the BSWI be defined as:

$$\phi_{m,k}^j(x) = B_{m,k}^j(x) \qquad 0 \leq k < 2^j - m + 1 \quad \textbf{(3.101)}$$

Given that the B-splines of order m are in C^{m-2}, (for example cubic splines are in C^1), the function $f(x)$ bound by limits $[a, b]$ can be transferred to [0,1]. This transformation is carried out via the transformation formula $t = \frac{x-a}{b-a}$. Thus, only the m^{th} order B-spline space within the limits [0,1] is necessary [96]. The scaling function $\phi_{m,k}^j(x)$ can be differentiated $m - 1$ times. As earlier mentioned, the support of the B-splines without the multiple nodes are within m segments while the corresponding semi-orthogonal wavelet are within $2m - 1$

segments at scale j = 0. Thus, the requirement $2^j \geq 2m-1$ must be met so as to have at least one inner wavelet at the interval [0,1] and multiresolution j [96]. We define the spline spaces [95]:

$$\begin{aligned} S_{m,t_m^{(j)}} &\coloneqq s_m^j = \{s \in C^{m-2}[0,1]: s_{|t_k^{(j)},t_{k+1}^{(j)}} \in \Pi_{m-1}(k = 0,\dots,2^j-1)\} \\ \tilde{S}_{2m,t_m^{(j+1)}} &\coloneqq \langle B_{m,k}^{j+1}: k = -m+1,\dots,2^{j+1}-m-1\rangle \\ \tilde{S}^0{}_{2m,t_m^{(j+1)}} &\coloneqq \{s \in \tilde{S}_{2m,t_m^{(j+1)}}: s\left(t_k^{(j)}\right) = 0 \quad (k = 0,\dots,2^j)\} \end{aligned} \tag{3.102}$$

Therefore, it is most convenient to use the B-wavelets as described in Appendix A.3.3 to formulate the inner BSWI wavelet functions from the relation

$$\psi_{m,k}^j(x) = \psi_m(2^j x - k) \tag{3.103}$$

$$\psi_{m,k}^j(x) = \frac{1}{2^{m-1}} \sum_{l=0}^{2m-2} (-1)^l N_{2m}(l+1) B_{2m,2i+l}^{j+1,(m)}(x) \tag{3.104}$$

where $B_{2m,k}^{j+1,(m)}(x)$ is the m^{th} derivative for the B-spline of order 2m and scale $j+1$; which can be computed explicitly given the values of $B_{m,k}^j(x)$ have been computed from equation (3.94). If j_0 is the multiresolution scale for this requirement to have at least one inner B-wavelet, the scaling and wavelet functions of the BSWI are obtained as [96]:

$$\phi_{m,k}^j(x) = \begin{cases} B_{m,k}^{j_0}(2^{j-j_0}x) & -m+1 \leq k \leq -1 \\ B_{m,0}^{j_0}(2^{j-j_0}x - 2^{-j_0}k) & 0 \leq k \leq 2^j - m \\ B_{m,2^j-k-m}^{j_0}(1-2^{j-j_0}x) & 2^j - m + 1 \leq k \leq 2^j - 1 \end{cases} \tag{3.105}$$

$$\psi_{m,k}^j(x) = \begin{cases} \psi_{m,k}^{j_0}(2^{j-j_0}x) & -m+1 \leq k \leq -1 \\ \psi_{m,0}^{j_0}(2^{j-j_0}x - 2^{-j_0}k) & 0 \leq k \leq 2^j - 2m + 1 \\ \psi_{m,2^j-k-2m+1}^{j_0}(1-2^{j-j_0}x) & 2^j - 2m + 2 \leq k \leq 2^j - m \end{cases} \tag{3.106}$$

Since BSWI scaling functions are expressed explicitly, the derivatives of the scaling functions can be obtained by directly differentiating equation (3.105).

$$\phi_{m,k}^{j,(n)}(x) = \frac{d^n \phi_{m,k}^j(x)}{dx^n} \tag{3.107}$$

In this study, the BSWI of order m at scale j will be referred to as BSWIm_j for convenience. As an example, the formulation of the BSWI3_3 is presented. The knot sequence from equation (3.93) for m = 3, j = 3 is:

$$t_k^3 = \begin{cases} 0 & -2 \le k < 1 \\ \frac{1}{8}k & 1 \le k < 8 \\ 1 & 8 \le k \le 10 \end{cases}$$

$$t_k^3 = \{\, 0,0,0,\frac{1}{8},\frac{1}{4},\frac{3}{8},\frac{1}{2},\frac{5}{8},\frac{3}{4},\frac{7}{8},1,1,1\}$$

Applying equations (3.94) and (3.105), we find the functions of the B-splines as:

$$\phi_{3,-1}^3(x) = \begin{cases} (1-8x)^2 & 0 \le x < \frac{1}{8} \\ 0 & \text{Otherwise} \end{cases} \qquad \phi_{3,-1}^3(x) = \begin{cases} -16x(-1+6x) & 0 \le x < \frac{1}{8} \\ 2(1-4x)^2 & \frac{1}{8} \le x < \frac{1}{4} \\ 0 & \text{Otherwise} \end{cases}$$

$$\phi_{3,0}^3(x) = \begin{cases} 32x^2 & 0 \le x < \frac{1}{8} \\ -\frac{3}{2} + 24x - 64x^2 & \frac{1}{8} \le x < \frac{1}{4} \\ \frac{1}{2}(3-8x)^2 & \frac{1}{4} \le x < \frac{3}{8} \\ 0 & \text{Otherwise} \end{cases} \qquad \phi_{3,1}^3(x) = \begin{cases} \frac{1}{2}(1-8x)^2 & \frac{1}{8} \le x < \frac{1}{4} \\ -\frac{11}{2} + 40x - 64x^2 & \frac{1}{4} \le x < \frac{3}{8} \\ 8(1-2x)^2 & \frac{3}{8} \le x < \frac{1}{2} \\ 0 & \text{Otherwise} \end{cases}$$

$$\phi_{3,2}^3(x) = \begin{cases} 2(1-4x)^2 & \frac{1}{4} \le x < \frac{3}{8} \\ -\frac{23}{2} + 56x - 64x^2 & \frac{3}{8} \le x < \frac{1}{2} \\ \frac{1}{2}(5-8x)^2 & \frac{1}{2} \le x < \frac{5}{8} \\ 0 & \text{Otherwise} \end{cases} \qquad \phi_{3,3}^3(x) = \begin{cases} \frac{1}{2}(3-8x)^2 & \frac{3}{8} \le x < \frac{1}{2} \\ -\frac{39}{2} + 72x - 64x^2 & \frac{1}{2} \le x < \frac{5}{8} \\ 2(3-4x)^2 & \frac{5}{8} \le x < \frac{3}{4} \\ 0 & \text{Otherwise} \end{cases}$$

$$\phi_{3,4}^3(x) = \begin{cases} 8(1-2x)^2 & \frac{1}{2} \le x < \frac{5}{8} \\ -\frac{59}{2} + 88x - 64x^2 & \frac{5}{8} \le x < \frac{3}{4} \\ \frac{1}{2}(7-8x)^2 & \frac{3}{4} \le x < \frac{7}{8} \\ 0 & \text{Otherwise} \end{cases} \qquad \phi_{3,5}^3(x) = \begin{cases} \frac{1}{2}(5-8x)^2 & \frac{5}{8} \le x < \frac{3}{4} \\ -\frac{83}{2} + 104x - 64x^2 & \frac{3}{4} \le x < \frac{7}{8} \\ 32(-1+x)^2 & \frac{7}{8} \le x < 1 \\ 0 & \text{Otherwise} \end{cases}$$

$$\phi_{3,6}^3(x) = \begin{cases} 2(3-4x)^2 & \frac{3}{4} < x \le \frac{7}{8} \\ -16(5-11x+6x^2) & \frac{7}{8} < x \le 1 \\ 0 & \text{Otherwise} \end{cases} \qquad \phi_{3,7}^3(x) = \begin{cases} (7-8x)^2 & \frac{7}{8} < x \le 1 \\ 0 & \text{Otherwise} \end{cases}$$

The scaling functions of BSWI3_3 and its 1st & 2nd derivatives are presented in Figure 3-8. For order $m = 3$ at scale $j = 3$, the corresponding requirement scale j_0 is 3 (for at least one inner wavelet function to exist). Therefore, it can be observed that there are 2 (i.e. $m-1$) boundary scaling functions at 0 and 1, with a further 6 (i.e.,$2^j - m + 1$) inner scaling functions.

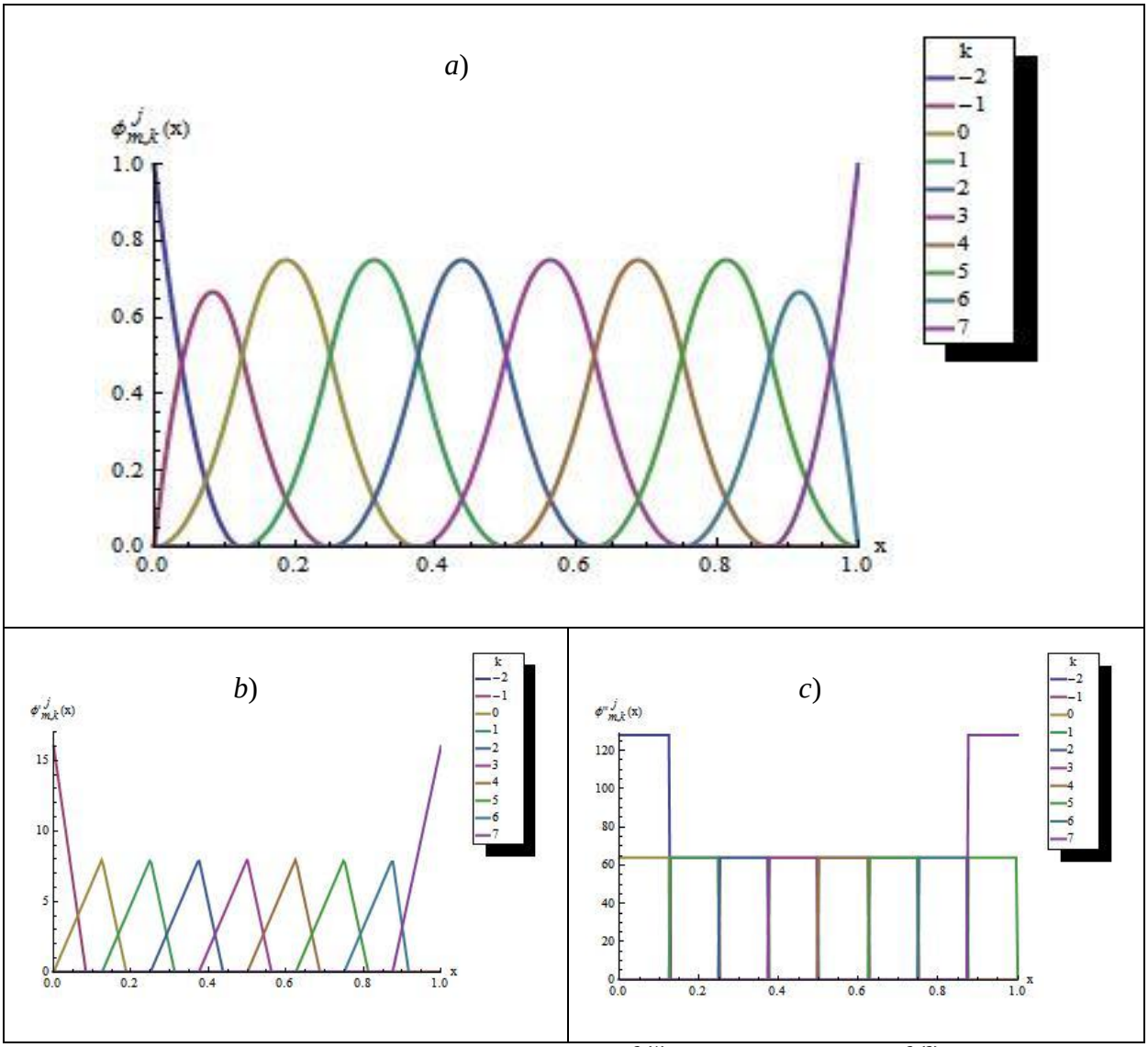

Figure 3-8: BSWI3$_3$ *a*) scaling functions $\phi_{3,k}^{3}(x)$ *b*) 1st derivative $\phi_{3,k}^{3,(1)}(x)$ and *c*) 2nd derivative $\phi_{3,k}^{3,(2)}(x)$.

3.4. Conclusion

The key aspects of general wavelet theory and multiresolution analysis were introduced and discussed in this chapter. The Daubechies and BSWI wavelets both possess the key properties of multiresolution, compact support and the "two-scale" relation. They can therefore be used to accurately represent polynomial functions. Thus, based on these attractive properties, the two wavelet families are selected for the formulation of the wavelet based finite element method.

The Daubechies scaling and wavelet functions, as well as their derivatives, are not expressed explicitly. It is therefore necessary to evaluate the connection coefficients to solve partial differential equations (PDEs) using the Daubechies wavelets. A modified formulation to evaluate the multiscale connection coefficients was presented, to the best of the author's

knowledge, for the first time in this chapter. The integral of the product of the multiscale Daubechies scaling functions and/or their derivatives that differ in wavelet order L, can be computed using this approach. Furthermore, a simplified algorithm to evaluate the connection coefficients employed to evaluate the distributed load vector in wavelet space was also presented. The connection coefficients are necessary to evaluate Daubechies wavelet based finite element matrices and load vectors in wavelet space. The theoretical and mathematical representation of the BSWI scaling functions and wavelet functions were also described and discussed in this chapter.

4. The Finite Element Method and Adaptive Finite Element Methods

Summary

The WFEM is based on the implementation of key properties of wavelet analysis and the finite element method. In this chapter, the significant aspects of FEM are discussed, with some of the common approaches used in the generation of the system matrices and equations highlighted. This chapter is based on general finite element theory and contains concepts and discussions as presented in [27,29-31,97,98]. The general static and dynamic FEM analysis theory is briefly presented. A brief overview of adaptive refinement finite element methods, used to improve the accuracy of results in FEM, is also discussed. Finally, aspects such as, the damping and direct time integration methods for dynamic analysis, are briefly described. The formulations and discussions presented in this chapter are necessary to give a preliminary introduction and understanding of the concepts behind the WFEM; including key requirements necessary to ensure convergence of the approximation solutions. Furthermore, the examples and discussions presented in later chapters will also entail a comparison of WFEM and FEM formulations and solutions. In this study, the problems analysed and discussed are of a structural nature and therefore, emphasis will be given to the method's implementation to structural static and dynamic problems. The finite element matrices and load vectors, associated with this chapter and numerical examples to be carried out in later chapters, are highlighted in Appendix B.

4.1. Finite element approximation functions

The classical finite element method employs polynomials as interpolating/approximation functions. The field variable $u(x)$ is approximated by a polynomial of order *n* [30]:

$$u(x) = \sum_{i=0}^{n} \acute{\alpha}_i x^i$$
$$u(x) = \{\acute{\mathbf{p}}\}^T \{\acute{\alpha}\} \tag{4.1}$$

The vector $\{\acute{\mathbf{p}}\}^T = \{1, x, x^2, \dots x^n\}$ contains the basis functions x^i and the vector $\{\acute{\alpha}\}$ contains the unknown coefficients $\acute{\alpha}_i$ corresponding to the degrees of freedom within the element. There are certain conditions these functions must satisfy in order to ensure correct

approximation of the field variable and convergence to the exact solution. These include [27,30,31]:

1. The approximation functions must be represented by the complete order of the polynomial to ensure convergence to the exact solution without omitting any lower order terms.
2. The approximation functions representing the field variable should vary smoothly and be continuous for all DOFs within the finite element; thus preventing discontinuities.
3. The approximation functions should be continuous between adjacent elements for all DOFs at boundary nodes and/or surfaces; thus preventing discontinuities between elements.

The above fundamental requirements of the approximation functions can be summed up as the completeness condition 1 and continuity conditions 2 and 3. The continuity of a piecewise function is described by C^m for the m^{th} order derivative of the function. In a case where the field variable in itself is continuous within both the element and across adjacent elements, the element is said to be C^0 continuous e.g., one dimensional rod element. However, if the field variable and its first derivative are continuous between adjacent elements, then this is a C^1 element e.g., beam or plate elements where the continuity of the rotation is ensured [31].

4.2. Formulation of element matrices

There are different approaches that are used in the evaluation and analysis of different engineering problems using FEM. The type of approach selected mainly depends on the nature of the problem to be analysed, to ensure that the modelling and formulation of the system(s) representation is fundamentally carried out correctly and efficiently. Some of these approaches include the direct equilibrium method, work and energy methods and weight residual methods [27]. The direct equilibrium method is a convenient and simplified approach to analyse one dimensional static elements, where the force equilibrium conditions of the elements are used to obtain the element nodal force-displacement equations via the stiffness matrix [31]. This method is limited to simple elements and problems, therefore in this study, attention will be focused on the multifaceted and commonly used work/energy methods and weight residual methods.

In accordance to the work and formulations of FEM and WFEM presented in this thesis, the principle of minimum potential energy and the Hamilton principle are introduced and briefly discussed. These two approaches are used to describe the governing equations of the basic

axial rod elements, Euler-Bernoulli beam elements and planar bar elements for both FEM and WFEM; for static and dynamic problems respectively.

4.2.1. Principle of minimum potential energy

For generally linear elastic elements, the principle of minimum potential energy approach is applicable to obtain the static system equations. The principle states that [31]:

> "Of all admissible displacements that a body can assume, the true one, corresponding to the satisfaction of stable equilibrium of the body, is identified by a minimum value of the total potential energy."

The term admissible requires that the displacement doesn't contravene the compatibility properties and boundary conditions. In general, the total potential energy Π_p is the sum of the internal strain energy U_s within the system and the work done by external forces Ω_f. Mathematically this is expressed as [29]:

$$\Pi_p = U_s + \Omega_f \tag{4.2}$$

The strain energy is the internal energy stored due to deformation of the linearly elastic material from external work done by external loads acting on the material. In this formulation, the strain energy is taken to be positive and the work done by external loads is negative. Therefore, the strain energy for an elastic structure is described mathematically as [29]:

$$U_s = \frac{1}{2}\iiint_{vol} \varepsilon^T \sigma \, d\bar{V} \tag{4.3}$$

where σ is the stress, ε the strain and $\bar{V}$ is the volume of the element. The work done by external forces is dependent on the external forces acting on the system. For example, a system subjected to surface loading (f_s), body loading (f_b) and nodal point loads (f_i), the total work done by the external forces is given by:

$$\Omega_f = -\left(\sum_i u_i f_i + \iint_S u^T f_s \, dS + \iiint_{Vol} u^T f_b \, d\bar{V}\right) \tag{4.4}$$

where u is the displacement. Then at equilibrium, according to the principle of minimum potential energy

$$\delta\Pi_p = \delta U_s + \delta\Omega_f = 0 \tag{4.5}$$

4.2.2. Hamilton's principle

Hamilton's principle is an approach used to obtain the system equations for dynamic analysis. In the case of the principle of minimum potential energy, the equilibrium equations of the system are not time variant. However, when the state of the system changes with respect to time, the Hamilton's principle is applied. The principle states that [1]:

> "Of all the admissible time histories of displacement, the history corresponding to the actual solution makes the Lagrangian functional a minimum."

The term admissible requires that the displacement doesn't contravene the compatibility properties, the boundary conditions and conditions of the system at initial and final times, t_i and t_f, respectively. Mathematically the principle is expressed as [1]:

$$\delta \int_{t_i}^{t_f} \mathcal{L}\, dt = 0 \tag{4.6}$$

where $\mathcal{L}$ is the Langranian functional given by

$$\mathcal{L} = \Lambda_k - U_s + \Omega_f \tag{4.7}$$

U_s, Λ_k, and Ω_f denote entire system's strain energy, kinetic energy and work done by external forces respectively. The strain energy and work by external forces are as described in the Section 4.2.1. The kinetic energy is represented mathematically as

$$\Lambda_k = \frac{1}{2} \iiint_{vol} \rho \dot{u}^T \dot{u} d\bar{V} \tag{4.8}$$

where $\dot{u} = \frac{du}{dt}$ is the velocity.

4.2.3. Weighted residual methods

The finite element method can be applied using a different approach known as the weighted residual method, to obtain the finite element equations for a system. In general, the basic principle of weighted residual methods involves obtaining an approximate solution of the independent variable (displacement, temperature etc.), via governing differential equations describing the system behaviour, using trial functions [31]. Consider a function p that is produced from the function u via the differential operator D

$$D\,[u] = p \tag{4.9}$$

Let the function $\tilde{u}$, made up of the linear combination of basis functions ϕ_i, be the approximate of u [1]:

$$u \cong \tilde{u} = \sum_{i=1}^{n} a_i \phi_i \tag{4.10}$$

where a_i are unknown constants. It follows that when $\tilde{u}$ is substituted into equation (4.9), the result is not exactly p and the difference, what is referred to the error or residual, *R*. Mathematically, this can be expressed as [29]:

$$D\,[\tilde{u}] \neq p$$
$$R = D\,[\tilde{u}] - p \neq 0 \tag{4.11}$$

The idea of weighted residual methods is to ensure that the error or residual R from $D\,[\tilde{u}]$ is reduced to a minimum by averaging it over the entire domain [31]. Thus, in order to obtain the exact solution, then *R* must be zero [27]

$$\iiint_{vol} R d\bar{V} = 0 \tag{4.12}$$

This is achieved by applying a weight function W_i to equation (4.12) [29]

$$\iiint_{vol} W_i R d\bar{V} = 0 \quad \text{for} \quad i = 1,2,\dots,n \tag{4.13}$$

where the number of weight functions W_i correspond exactly to the number of coefficients a_i. This leads to *n* number of equations. Equation (4.13) describes the general fundamentals of the weighted function method. The weight functions may be applied differently and this leads to different weight residual numerical approximation methods. The most common of these methods in FEM include: sub-domain method, collocation method, least squares method and Galerkin method.

The collocation method or point collocation method, applies the Dirac delta function δ_i as the weight function [1].

$$\iiint_{vol} \delta_i R dV = 0 \quad \text{for} \quad i = 1,2,\dots,n \tag{4.14}$$

where

$$\delta_i = \delta(x - x_i) = \begin{cases} 1 & x = x_i \\ 0 & \text{otherwise} \end{cases} \quad \textbf{(4.15)}$$

The residuals are forced to zero at a number of specified discrete points *i* corresponding to the unknown coefficients a_i. Although the method is computationally inexpensive, the method does not lead to the formulation of symmetric element matrices nor positive definite matrices. Furthermore, the residual isn't guaranteed to be zero at the specified points unless the more and more points are employed in the approximation function [27].

The sub-domain method involves dividing the domain *V* into smaller sub-domains V_i and subsequently setting the integral of the residual within these sub-domains to zero [31]. This is mathematically expressed as:

$$\sum_i \iiint_{V_i} W_i R d\bar{V}_i = 0 \quad \text{for} \quad i = 1,2,\dots,n \quad \textbf{(4.16)}$$

where the weight function

$$W_i = \begin{cases} 1 & x \in V_i \\ 0 & x \notin V_i \end{cases} \quad \textbf{(4.17)}$$

The sub-domains correspond to the number of unknown coefficients.

The least squares approach in contrast requires that the integral of the squared residuals, with respect to the *n* number of unknown coefficients a_i, is minimized over the entire domain. Therefore, the weight function is [27]:

$$W_i = \frac{\partial R}{\partial a_i} \quad \textbf{(4.18)}$$

and thus,

$$\frac{\partial}{\partial a_i} \iiint_{vol} R^2 d\bar{V} = 0 \quad \text{for} \quad i = 1,2,\dots,n \quad \textbf{(4.19)}$$

Although the FEM element matrices are positive definite and symmetric when formulated using the least squares approach, the method is computationally involving and tedious as it is difficult to control the weight functions.

The Galerkin method

The Galerkin method applies the shape functions N_i as the weight functions. This implies that [27]:

$$\iiint_{vol} N_i R dV = 0 \quad \text{for} \quad i = 1,2,\dots,n \tag{4.20}$$

where n corresponds to the total number of unknown coefficients a_i linked to the DOFs within the element. Thus, the residual R^e of all DOFs within each element is evaluated as [30]:

$$\{R^e\} = \iiint_{vol} [N]^T f(\phi_i) dV \tag{4.21}$$

where $f(\phi_i)$ is a function describing the governing differential equations. The residuals are obtained for all elements within the system and assembled. The system equations are then obtained by forcing the system residual to zero. If the same approximating function in equation (4.10) is used in the Galerkin method as in the energy methods, provided a functional is obtained to describe the governing differential equations of the system, then both methods yield the same results [29].

Given that the shape functions are used as the weighted functions, then the levels of accuracy necessary for the solution of the problem will dictate the number of terms of the shape functions used; i.e., the order of the interpolating functions used to approximate the function in equation (4.10).

4.3. The adaptive refinement finite element techniques

The primary and/or secondary field variables evaluated from the finite element procedures are an approximation of the exact solution for the given mesh generated; specific to the problem being evaluated. In general engineering practice, the level of accuracy for most engineering problems allows for a 5% error deviation of the approximation solution [29]; although this may vary. Therefore, if the desired level of accuracy is not achieved from FEM solutions, there are techniques applicable to improve the accuracy of the solutions. These procedures in general require that after the initial analysis is carried out, the error of the existing solution is evaluated and compared with the predetermined acceptable level of accuracy. If the solution has not met the permissible accuracy levels, these procedures are implemented and another comparison of the improved solution is carried out again. This is achieved until the desired accuracy levels are met. These procedures are what shall be referred to as adaptive refinement finite element techniques in this thesis. The most common of these procedures are highlighted below.

h-refinement

The *h*-refinement procedure involves changing the size of existing elements in the FEM mesh, by either increasing or decreasing the size of the elements, leading to an increase or decrease in the number of elements respectively within the system [31]. It is important to note that the element types and order of the approximating functions remain the same. There are a number of ways to which this can be achieved. Firstly, one can subdivide already existing elements into smaller elements to ensure that the original element boundaries remain throughout refinement. However, in the case of an element that is subdivided adjacent to one that is not, particularly for 2D or 3D models, there are hanging points that exist and must have local constraints implemented, which can be computationally expensive. Secondly, the entire original mesh can be regenerated by changing the size of the elements.

p-refinement

The *p*-refinement approach involves changing the degree of the approximation functions, while still ensuring the conditions highlighted in Section 4.1 are met. However, the element sizes remain the same, and therefore the original mesh remains unchanged. This can be achieved by either increasing the order of the approximation function uniformly through the domain or locally via hierarchical refinement [1]. The method is desirable due to the higher rate of convergence, yet it is computationally more demanding than the *h*-refinement approach. Given that the rate of convergence is better, this means that the number of refinements, and re-evaluated solutions corresponding to these refinements, are less in number than *h*-refinement.

The *h*-refinement and *p*-refinement methods can be combined by simultaneously altering the mesh size and order of the approximation functions. This is commonly referred to as the *hp*-refinement method.

It must be noted that though the discussed adaptive procedures are mainly carried out to improve the accuracy of the results, there may be instances where the acceptable levels of accuracy are met, yet the mesh is coarsened over the entire problem domain, or locally, so as to reduce the computational cost and increase efficiency.

4.4. The finite element shape functions

The FEM shape functions, specific to the axial rod, Euler-Bernoulli beam and planar bar element, have been defined in Appendix B. However, the conditions set for the approximation function polynomials in Section 4.1 lead to the general properties of shape functions in FEM.

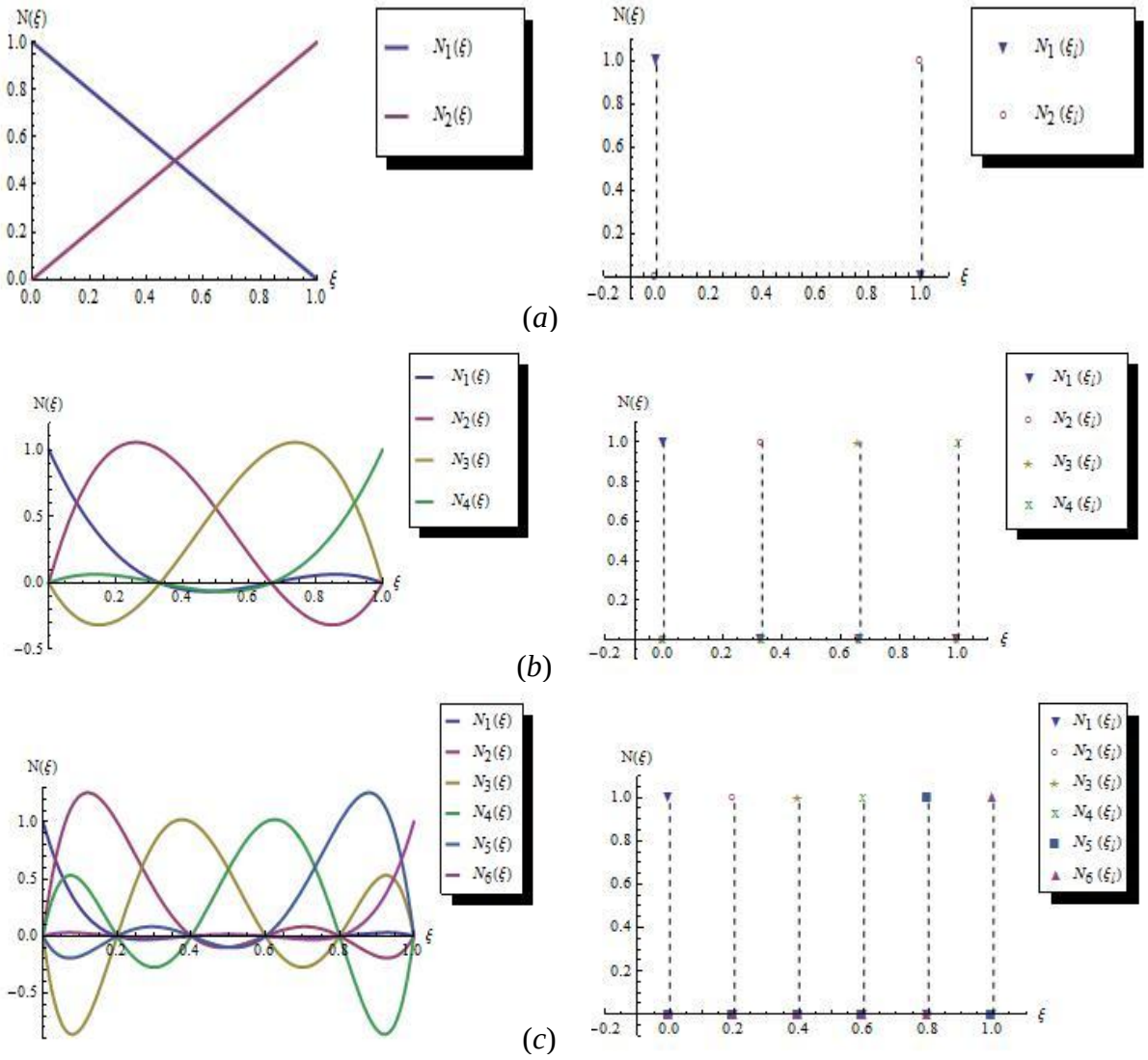

Figure 4-1 : Axial rod element a) 1st degree b) 3rd degree c) 5th degree polynomial based shape functions $N_k(\xi)$ and $N_k(\xi_i)$.

4.4.1. Delta function property

The delta function property of the shape function is expressed mathematically as [30]:

$$N_k(\xi_i) = \delta_{k,k} = \begin{cases} 1 & k = i \\ 0 & k \neq i \end{cases} \tag{4.22}$$

where $\delta_{k,i}$ is the Kronecker delta function, $N_k(\xi)$ is the shape function corresponding to DOF $1 \leq k \leq n$ within element e and ξ_i is the natural coordinate corresponding to nodes $1 \leq i \leq r$

within the element. The total number of DOFs within the element is *n* and the total number of nodes is *r*. The property means that the value of $N_k(\xi)$ is 1 at the node at which its corresponding DOF is located and 0 at all other nodes.

In the case of the axial rod formulated via *m* degree polynomials, the shape functions for *m* = *a*) 1, *b*) 3 and *c*) 5 are presented on the left hand side of Figure 4-1. The plots illustrating the delta function property for the corresponding shape functions are on the right hand side.

Figure 4-2 illustrates the beam finite element shape functions $N_k(\xi)$ and $N_k(\xi_i)$ (left hand side and right hand respectively) of polynomial order *m* = *a*) 3, *b*) 5 and *c*) 7. The shape functions corresponding to the vertical displacement DOFs all meet the delta function property as shown in the plots on the right hand side.

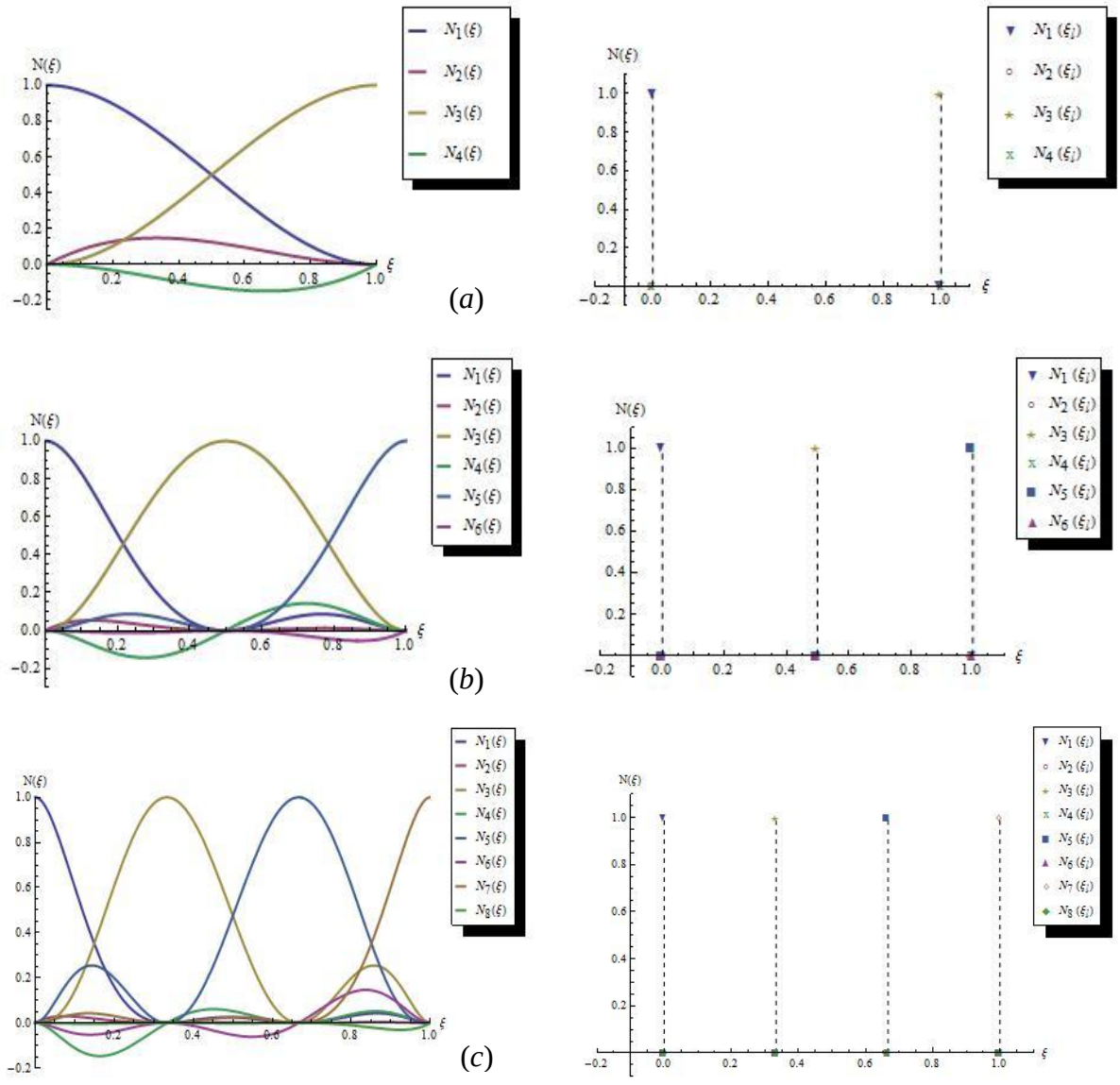

Figure 4-2 : Beam element a)3rd degree b) 5th degree c) 7th degree polynomial based shape functions $N_k(\xi)$ and $N_k(\xi_i)$.

4.4.2. Completeness

The completeness property of the shape functions is exemplified by two conditions. The first of these is referred to as the partition of unity condition, which requires that at any point ξ along the element (one dimensional element in this case), the sum of all the shape functions corresponding to the DOFs within the element equals 1 [30]. Mathematically this is expressed as:

$$\sum_{i=0}^{n} N_k(\xi) = 1 \tag{4.23}$$

This implies that the field variable approximation function selected should ensure that for any displacements resulting from the rigid body motion, there isn't any straining within the element [31]. It must be mentioned that although the sum of the shape functions equals 1 from equation (4.23), the shape functions do not have to be bound by $0 \leq N_k(\xi) \leq 1$ within the element.

The second condition is called the linear field reproduction and is expressed mathematically as [30]:

$$\sum_{i=0}^{n} N_k(\xi)\, \xi_k = \xi \tag{4.24}$$

This effectively implies that the approximation function of the field variable should allow the shape functions to reproduce the linear field. This in turn allows for constant strain through the element to be obtained, provided the nodal field variables are compatible with a constant strain condition [30].

4.4.3. Compatibility

The compatibility property is ensured when the field variable approximation function is continuous between adjacent element boundaries [29]. The shape functions emanating from these approximation functions must also ensure this condition is satisfied.

Combining all these properties leads to the convergence of the approximate field variables to the exact solution; with increase of elements or order of the polynomial functions.

4.5. Dynamic vibration

The analysis of static structural problems does not take into account the variation of the field variables with time [31]. However, there are many structural engineering problems that

require the analysis of the variable fields with respect to time. This is commonly referred to as dynamic analysis and it involves analysing the behaviour of a system within a given time frame; while subjected to certain conditions. It is important to carry out such an analysis since the mass within a structural system accelerates over time, contributing inertial effects within the system that may cause an increase or decrease of the statically analysed field variables [27]. Furthermore, the frequencies and mode shapes associated with a system, enable structural analysts to predict the behaviour of the system when subjected to various time-dependent loading conditions [1]. Application of such external loading that corresponds to the natural frequencies of the system leads to resonance, where the system begins to oscillate significantly with high displacements; which can lead to local failure or even entire failure of the system. Thus, it is important to ensure that the external loading frequencies are remote to the natural frequencies of the structure. In this section key dynamic analysis theories related to FEM and WFEM are discussed.

4.5.1. Eigenvalue analysis of free undamped vibration

The natural frequencies and modes shapes of a system are evaluated by carrying out an eigenvalue analysis of the system matrices. An undamped system made up of a total of *n* DOFs, with the global stiffness matrix $[K]$, mass matrix $[M]$ and load vector $\{F_t\}$, is governed by the dynamic global system equation [27]:

$$[M]\{\ddot{U}_t\} + [K]\{U_t\} = \{F_t\} \tag{4.25}$$

where $\{\ddot{U}_t\}$ and $\{U_t\}$ are the system nodal acceleration and displacement vectors respectively. The free undamped vibration analysis of the system is carried out when no external load is applied on the system, thus $\{F_t\} = \{0\}$ and equation (4.25) becomes:

$$[M]\{\ddot{U}_t\} + [K]\{U_t\} = \{0\} \tag{4.26}$$

The displacements at time *t* can be expressed with respect to vibration as [29]:

$$\{U_t\} = \{\acute{U}\} \sin \omega t \tag{4.27}$$

where $\{\acute{U}\}$ contains the normal modes corresponding to the natural angular frequency ω. Differentiating equation (4.27) with respect to *t*

$$\{\dot{U}_t\} = \omega\{\acute{U}\} \cos \omega t \tag{4.28}$$

$$\{\ddot{U}_t\} = -\omega^2\{\acute{U}\} \sin \omega t \tag{4.29}$$

Substituting equations (4.27) and (4.29) into equation (4.26)

$$[K]\{\acute{U}\} - \omega^2[M]\{\acute{U}\} = \{0\}$$
$$\left[[K] - \omega^2[M]\right]\{\acute{U}\} = \{0\} \quad \textbf{(4.30)}$$

Equation (4.30) is the eigenvalue equation. For the vector $\{\acute{U}\}$ to be none-zero, $\left[[K] - \omega^2[M]\right] = \{0\}$. Thus, the determinant of $\left[[K] - \omega^2[M]\right]$ is zero [97].

$$\text{Det}\ ([K] - \omega^2[M]) = 0 \quad \textbf{(4.31)}$$

From the eigenvalue equation, the eigenvalues are the squared natural frequencies ω^2 and the eigenvectors contain the vibration normal modes $\{\acute{U}\}$. The total number of eigenvalues and corresponding eigenvectors obtained from the eigenvalue equation is n. Thus, for the i^{th} mode of vibration [99],

$$[K]\{\acute{U}\}_i = {\omega_i}^2[M]\{\acute{U}\}_i \quad \textbf{(4.32)}$$

The eigenvector of another j^{th} mode of vibration is denoted by $\{\acute{U}\}_j$. Premultiplying equation (4.32) by the transpose of $\{\acute{U}\}_j$, we obtain

$$\{\acute{U}\}_j{}^T[K]\{\acute{U}\}_i = {\omega_i}^2\{\acute{U}\}_j{}^T[M]\{\acute{U}\}_i \quad \textbf{(4.33)}$$

Similarly,

$$\{\acute{U}\}_i{}^T[K]\{\acute{U}\}_j = {\omega_j}^2\{\acute{U}\}_i{}^T[M]\{\acute{U}\}_j \quad \textbf{(4.34)}$$

Given that the mass and stiffness matrices are symmetric,

$$\{\acute{U}\}_j{}^T[K]\{\acute{U}\}_i = \{\acute{U}\}_i{}^T[K]\{\acute{U}\}_j \quad \textbf{(4.35)}$$

and

$$\{\acute{U}\}_j{}^T[M]\{\acute{U}\}_i = \{\acute{U}\}_i{}^T[M]\{\acute{U}\}_j \quad \textbf{(4.36)}$$

If equation (4.34) is subtracted from equation (4.33) with equations (4.35) and (4.36) implied, then [99]:

$$\left({\omega_i}^2 - {\omega_j}^2\right)\{\acute{U}\}_j{}^T[M]\{\acute{U}\}_i = 0 \quad \textbf{(4.37)}$$

From equation (4.37) it is apparent that if ${\omega_i}^2 \neq {\omega_j}^2$, then

$$\{\acute{U}\}_j{}^T[M]\{\acute{U}\}_i = 0 \quad \textbf{(4.38)}$$

and from the relation in equation (4.33)

$$\{\acute{U}\}_j^T [K]\{\acute{U}\}_i = 0 \quad \textbf{(4.39)}$$

The orthogonality properties of the eigenvectors with respect to the system's mass and stiffness matrices are evident from equations (4.38) and (4.39) respectively [99]. When $i = j$;

$$\{\acute{U}\}_j^T [M]\{\acute{U}\}_i = m_i \quad \textbf{(4.40)}$$

$$\{\acute{U}\}_j^T [K]\{\acute{U}\}_i = k_i \quad \textbf{(4.41)}$$

where m_j and k_j are defined as the modal mass and modal stiffness scalar values corresponding to the i^{th} mode of vibration for an undamped system. Therefore, equation (4.33) becomes:

$$k_i = \omega_i{}^2 m_i \quad \textbf{(4.42)}$$

4.5.2. Damping and finite elements

The amplitude of vibration in dynamic system analysis may decay with time due to the dissipation of the energy within the system. This is commonly referred to as damping and may be caused intentionally, so as to limit excessive and/or peak vibrations, or may originate from within the dynamic system. The cause and type of damping in a physical problem is a contributing factor as to how the influence of damping within the system is represented in the mathematical model. There are different classes of damping, and the most common include [29]:

Viscous damping: This is the most common form of damping found in structural dynamics problems. It is the cyclic dissipation of energy proportional to the frequency and square of the amplitude of vibration. The damping originates from viscous dampers and/or fluids adjacent to the system.

Hysteresis damping: This is also commonly referred to as material or solid damping which originates from within the element material and is independent of the frequency. Furthermore, the cyclic energy dissipation is proportional to the square of the amplitude of vibration.

Coulomb damping: This is damping that is caused due to dry friction and can be represented in terms of the viscous damping coefficient by drawing a comparison between the energy lost in the system due to viscous effects and to that lost due to the dry friction.

The viscous damping is of greater significance to the dynamic analysis carried out in this study, and for this reason shall be described in greater detail than the other forms of damping.

Proportional viscous damping

Proportional viscous damping is a common form of damping that is used in structural analysis; the damping matrix is proportional to the stiffness and mass matrices of the element. This is expressed mathematically as [27]:

$$[C] = \beta_d[\mathrm{K}] + \alpha_d\,[M] \tag{4.43}$$

where β_d and α_d are the proportional viscous damping coefficients. The orthogonality of the damping matrix gives:

$$\{\acute{U}\}_i^{\,T}[C]\{\acute{U}\}_i = 2\omega_i\zeta_i \tag{4.44}$$

From the orthogonality properties of the stiffness and mass matrices in equation (4.34), multiply equation (4.43) by $\{\acute{U}\}_i^{\,T}\{\acute{U}\}_i$:

$$\{\acute{U}\}_i^{\,T}[C]\{\acute{U}\}_i = \beta_d\{\acute{U}\}_i^{\,T}[K]\{\acute{U}\}_i + \alpha_d\{\acute{U}\}_i^{\,T}[M]\{\acute{U}\}_i$$

$$2\omega_i\zeta_i = \beta_d{\omega_i}^2 + \alpha_d$$

$$\zeta_i = \frac{\alpha_d}{2\omega_i} + \frac{\beta_d\omega_i}{2} \tag{4.45}$$

ζ_i and ω_i are the damping ratios and angular frequencies corresponding to the i^{th} mode of vibration. In general [100]:

$$\zeta\ = \alpha_d\ \frac{1}{2\omega} + \beta_d\,\frac{\omega}{2} \tag{4.46}$$

The damping ratio ζ is the damping value d_d relative to critical damping d_{cr}.

$$\zeta\ = \frac{d_d}{d_{cr}} \tag{4.47}$$

In order to obtain the damping coefficients multiple DOF system, a system of *n* equations corresponding to the first *n* modes is evaluated [100].

$$\begin{aligned}
\zeta_1\ &= \alpha_d\ \frac{1}{2\ \omega_1} + \beta_d\,\frac{{\omega_1}^2}{2}\\
\zeta_2\ &= \alpha_d\ \frac{1}{2\ \omega_2} + \beta_d\,\frac{{\omega_2}^2}{2}\\
&\vdots\\
\zeta_n\ &= \alpha_d\ \frac{1}{2\ \omega_n} + \beta_d\,\frac{{\omega_n}^2}{2}
\end{aligned} \tag{4.48}$$

Damping of a dynamic system is categorized as either under-damped, critically damped or over damped. An under-damped system is one that has damping significantly less than the value of the critical damping; thus the damping ratio is $\zeta < 1$ and the system vibration is expected to decay while oscillating. A critically damped system is one that has the damping equal to the critical damping value i.e., $\zeta = 1$. Finally an over-damped system is a system whose damping is significantly larger than the critical damping, therefore $\zeta > 1$, and it is expected that the decay of vibration will occur without oscillation.

4.6. Direct time integration

Various engineering structural problems may require a system to be analysed over a given period of time to investigate the system's behaviour as various conditions of the system vary with time e.g., time dependent external loading conditions. This is often referred to as the response history of the system. The general finite element equation of equilibrium governing the dynamic behaviour of a structural system is defined as [27]:

$$[M]\{\ddot{U}_t\} + [C]\{\dot{U}_t\} + [K]\{U_t\} = \{F_t\} \quad \textbf{(4.49)}$$

where $[M]$, $[C]$ and $[K]$ are the global system mass, damping and stiffness matrices respectively, and the vector $\{F_t\}$ denotes the applied external loads at time *t*. The vectors $\{\ddot{U}_t\}$, $\{\dot{U}_t\}$ and $\{U_t\}$ are the acceleration, velocity and displacement vectors of the finite element system at nodal points at time *t*.

The direct time integration method is one of the most popular and applied approaches used to evaluate the vectors $\{\ddot{U}_t\}$, $\{\dot{U}_t\}$ and $\{U_t\}$ at time intervals Δt. The term direct refers to the fact that the method is used to evaluate equation (4.49) directly without any transformation of the governing equation. This is an advantage of the method over other approaches, such as the modal method, where the governing system equations are transformed into modal displacements [27]. In general, the initial vectors $\{\ddot{U}_t\}$, $\{\dot{U}_t\}$ and $\{U_t\}$ at time $t = 0$ are known, and the direct time integration method is applied to solve equation (4.49) at the next time step $t + \Delta t$ by using the solutions from the previous time steps. The direct time integration methods are generally classified into two main categories: explicit and implicit methods. The explicit time integration methods require a critical time step Δt_{cr}, which if exceeded, the solution becomes unstable [29]. Explicit time integration schemes, such as the central difference method, are commonly used. The method is therefore referred to as conditionally stable and the time step Δt_{cr} is significantly small; consequently computationally intensive.

In contrast, the implicit time integration schemes do not have a requirement on the size of the time step Δt to ensure the stability of the solution. The approach is therefore unconditionally stable and the time step applied only affects the accuracy of the solution [27]. The Houbolt method, Newmark method and Wilson θ method are common implicit time integration schemes.

The implicit time integration methods are computationally more costly than the explicit methods at each time step. However, given that implicit methods are unconditionally stable, the time intervals are significantly larger and thus require less number of iterations than explicit methods. Furthermore, implicit time integration approaches are preferred in the analysis of structural dynamic problems; where the time dependent variations are relatively slow over a longer time span. In contrast, explicit methods are preferred to analyse short time span problems; where the variation of conditions within the system is relatively fast e.g., impact problems.

Majority of the numerical examples involving dynamic analysis in this study will involve moving load problems. The implicit time integration approach is therefore preferred to the explicit approach. The Newmark time integration method (Linear Multistep Method (LMS)), which is the most commonly applied approach, is defined and discussed in this section. It will be used as a time integration scheme in the analysis of the dynamic system numerical examples in this thesis.

4.6.1. The Newmark (Linear Multistep) Method

The Newmark time integration method is outlined in this section in a similar approach as described by Bathe [27]. The following initial assumptions are made with regards to the velocity $\dot{U}$ and lateral displacement U at time $t + \Delta t$, where Δt is the time interval between time steps.

$$\dot{U}_{t+\Delta t} = \dot{U}_t + \left[(1 - \acute{\delta})\ddot{U}_t + \acute{\delta}\ddot{U}_{t+\Delta t}\right]\Delta t \tag{4.50}$$

$$U_{t+\Delta t} = U_t + \dot{U}_t \Delta t + \left[\left(\frac{1}{2} - \acute{\gamma}\right)\ddot{U}_t + \acute{\gamma}\ddot{U}_{t+\Delta t}\right]\Delta t^2 \tag{4.51}$$

where the Newmark time integration parameters $\acute{\delta}$ and $\acute{\gamma}$ are selected to ensure accuracy and stability. The general outline to obtain the parameters is given as $\acute{\delta} \geq 0.5$ and $\acute{\gamma} \geq 0.25(0.5 + \acute{\delta})^2$. The acceleration $\ddot{U}_{t+\Delta t}$ can be expressed from equation (4.51) as:

$$U_{t+\Delta t} = U_t + \dot{U}_t \Delta t + \left(\frac{\Delta t^2}{2} - \gamma \Delta t^2\right)\ddot{U}_t + \gamma \ddot{U}_{t+\Delta t}\Delta t^2$$

$$\ddot{U}_{t+\Delta t} = \frac{1}{\gamma \Delta t^2}\left(U_{t+\Delta t} - U_t - \dot{U}_t \Delta t - \frac{\Delta t^2}{2}\ddot{U}_t + \gamma \ddot{U}_t \Delta t^2\right)$$

$$\ddot{U}_{t+\Delta t} = \frac{1}{\gamma \Delta t^2} U_{t+\Delta t} - \frac{1}{\gamma \Delta t^2} U_t - \frac{1}{\gamma \Delta t}\dot{U}_t - \frac{1}{2\gamma}\ddot{U}_t + \ddot{U}_t$$

$$\ddot{U}_{t+\Delta t} = \frac{1}{\gamma \Delta t^2} U_{t+\Delta t} - \frac{1}{\gamma \Delta t^2} U_t - \frac{1}{\gamma \Delta t}\dot{U}_t - \left(\frac{1}{2\gamma} - 1\right)\ddot{U}_t \quad \textbf{(4.52)}$$

Substituting equation (4.52) into (4.49)

$$\dot{U}_{t+\Delta t} = \dot{U}_t + \left[(1-\delta)\ddot{U}_t + \delta\left(\frac{1}{\gamma \Delta t^2} U_{t+\Delta t} - \frac{1}{\gamma \Delta t^2} U_t - \frac{1}{\gamma \Delta t}\dot{U}_t + \left(1 - \frac{1}{2\gamma}\right)\ddot{U}_t\right)\right]\Delta t$$

$$\dot{U}_{t+\Delta t} = \dot{U}_t + (1-\delta)\ddot{U}_t \Delta t + \frac{\delta}{\gamma \Delta t} U_{t+\Delta t} - \frac{\delta}{\gamma \Delta t} U_t - \frac{\delta}{\gamma}\dot{U}_t + \left(1 - \frac{1}{2\gamma}\right)\delta \Delta t \ddot{U}_t$$

$$\dot{U}_{t+\Delta t} = \left(1 - \frac{\delta}{\gamma}\right)\dot{U}_t - \frac{\delta}{\gamma \Delta t} U_t + \left[(1-\delta)\Delta t + \left(1 - \frac{1}{2\gamma}\right)\delta \Delta t\right]\ddot{U}_t + \frac{\delta}{\gamma \Delta t} U_{t+\Delta t}$$

$$\dot{U}_{t+\Delta t} = \left(1 - \frac{\delta}{\gamma}\right)\dot{U}_t - \frac{\delta}{\gamma \Delta t} U_t + \left(1 - \frac{\delta}{2\gamma}\right)\Delta t \ddot{U}_t + \frac{\delta}{\gamma \Delta t} U_{t+\Delta t} \quad \textbf{(4.53)}$$

The equilibrium equation in (4.49) at time $t + \Delta t$ is

$$M\ddot{U}_{t+\Delta t} + C\dot{U}_{t+\Delta t} + KU_{t+\Delta t} = F_{t+\Delta t} \quad \textbf{(4.54)}$$

Thus, substituting the acceleration $\ddot{U}_{t+\Delta t}$ and velocity $\dot{U}_{t+\Delta t}$ from equations (4.52) and (4.53) respectively into the equilibrium equation (4.54)

$$M\left[\frac{1}{\gamma \Delta t^2} U_{t+\Delta t} - \frac{1}{\gamma \Delta t^2} U_t - \frac{1}{\gamma \Delta t}\dot{U}_t + \left(1 - \frac{1}{2\gamma}\right)\ddot{U}_t\right]$$
$$+ C\left[\left(1 - \frac{\delta}{\gamma}\right)\dot{U}_t - \frac{\delta}{\gamma \Delta t} U_t + \left(1 - \frac{\delta}{2\gamma}\right)\Delta t \ddot{U}_t + \frac{\delta}{\gamma \Delta t} U_{t+\Delta t}\right] + KU_{t+\Delta t} = F_{t+\Delta t}$$

$$\left(\frac{1}{\gamma \Delta t^2} M + \frac{\delta}{\gamma \Delta t} C + K\right) U_{t+\Delta t} - M\left[\frac{1}{\gamma \Delta t^2} U_t + \frac{1}{\gamma \Delta t}\dot{U}_t + \left(\frac{1}{2\gamma} - 1\right)\ddot{U}_t\right]$$
$$- C\left[\left(\frac{\delta}{\gamma} - 1\right)\dot{U}_t + \frac{\delta}{\gamma \Delta t} U_t + \left(\frac{\delta}{2\gamma} - 1\right)\Delta t \ddot{U}_t\right] = F_{t+\Delta t} \quad \textbf{(4.55)}$$

The effective load vector $\acute{F}_{t+\Delta t}$ at time $t + \Delta t$ is

$$\left(\frac{1}{\gamma \Delta t^2} M + \frac{\delta}{\gamma \Delta t} C + K\right) U_{t+\Delta t} = \acute{F}_{t+\Delta t} \quad \textbf{(4.56)}$$

and the corresponding effective stiffness matrix $\acute{K}$

$$\frac{1}{\gamma \Delta t^2} M + \frac{\delta}{\gamma \Delta t} C + K = \acute{K} \quad \textbf{(4.57)}$$

Therefore, substituting equation (4.56) into (4.55), the effective load vector can be expressed as:

$$\acute{F}_{t+\Delta t} - M\left[\frac{1}{\gamma \Delta t^2} U_t + \frac{1}{\gamma \Delta t}\dot{U}_t + \left(\frac{1}{2\gamma} - 1\right)\ddot{U}_t\right] - C\left[\left(\frac{\delta}{\gamma} - 1\right)\dot{U}_t + \frac{\delta}{\gamma \Delta t} U_t + \left(\frac{\delta}{2\gamma} - 1\right)\Delta t \ddot{U}_t\right] = F_{t+\Delta t}$$

$$\acute{F}_{t+\Delta t} = F_{t+\Delta t} + M\left[\frac{1}{\gamma \Delta t^2} U_t + \frac{1}{\gamma \Delta t}\dot{U}_t + \left(\frac{1}{2\gamma} - 1\right)\ddot{U}_t\right] + C\left[\left(\frac{\delta}{\gamma} - 1\right)\dot{U}_t + \frac{\delta}{\gamma \Delta t} U_t + \left(\frac{\delta}{2\gamma} - 1\right)\Delta t \ddot{U}_t\right] \quad \textbf{(4.58)}$$

We define the integration constants

$$a_0 = \frac{1}{\gamma \Delta t^2},\ a_1 = \frac{\delta}{\gamma \Delta t},\ a_2 = \frac{1}{\gamma \Delta t},\ a_3 = \left(\frac{1}{2\gamma} - 1\right)$$
$$a_4 = \left(\frac{\delta}{\gamma} - 1\right),\ a_5 = \left(\frac{\delta}{2\gamma} - 1\right)\Delta t,\ a_6 = (1 - \delta)\Delta t\ ,a_7 = \delta \Delta t \quad \textbf{(4.59)}$$

Hence, substituting the integration constants from equation (4.59) into equations (4.50) and (4.52), we obtain the acceleration and velocity at time $t + \Delta t$ as:

$$\ddot{U}_{t+\Delta t} = a_0(U_{t+\Delta t} - U_t) - a_2\dot{U}_t - a_3\ddot{U}_t \quad \textbf{(4.60)}$$

$$\dot{U}_{t+\Delta t} = \dot{U}_t + a_6\ddot{U}_t + a_7\ddot{U}_{t+\Delta t} \quad \textbf{(4.61)}$$

Similarly, substituting the constants into equations (4.57) and (4.56), the effective stiffness matrix and load vector can be expressed as:

$$a_0 M + a_1 C + K = \acute{K} \quad \textbf{(4.62)}$$

$$(a_0 M + a_1 C + K)U_{t+\Delta t} = \acute{F}_{t+\Delta t} \quad \textbf{(4.63)}$$

Furthermore, substituting equation (4.59) into equation (4.58)

$$\acute{F}_{t+\Delta t} = F_{t+\Delta t} + M\left[a_0 U_t + a_2\dot{U}_t + a_3\ddot{U}_t\right] + C\left[a_1 U_t + a_4\dot{U}_t + a_5\ddot{U}_t\right] \quad \textbf{(4.64)}$$

A summary of the step by step solution of the dynamic analysis of systems using the Newmark time integration method is highlighted in the flowchart in Figure 4-3.

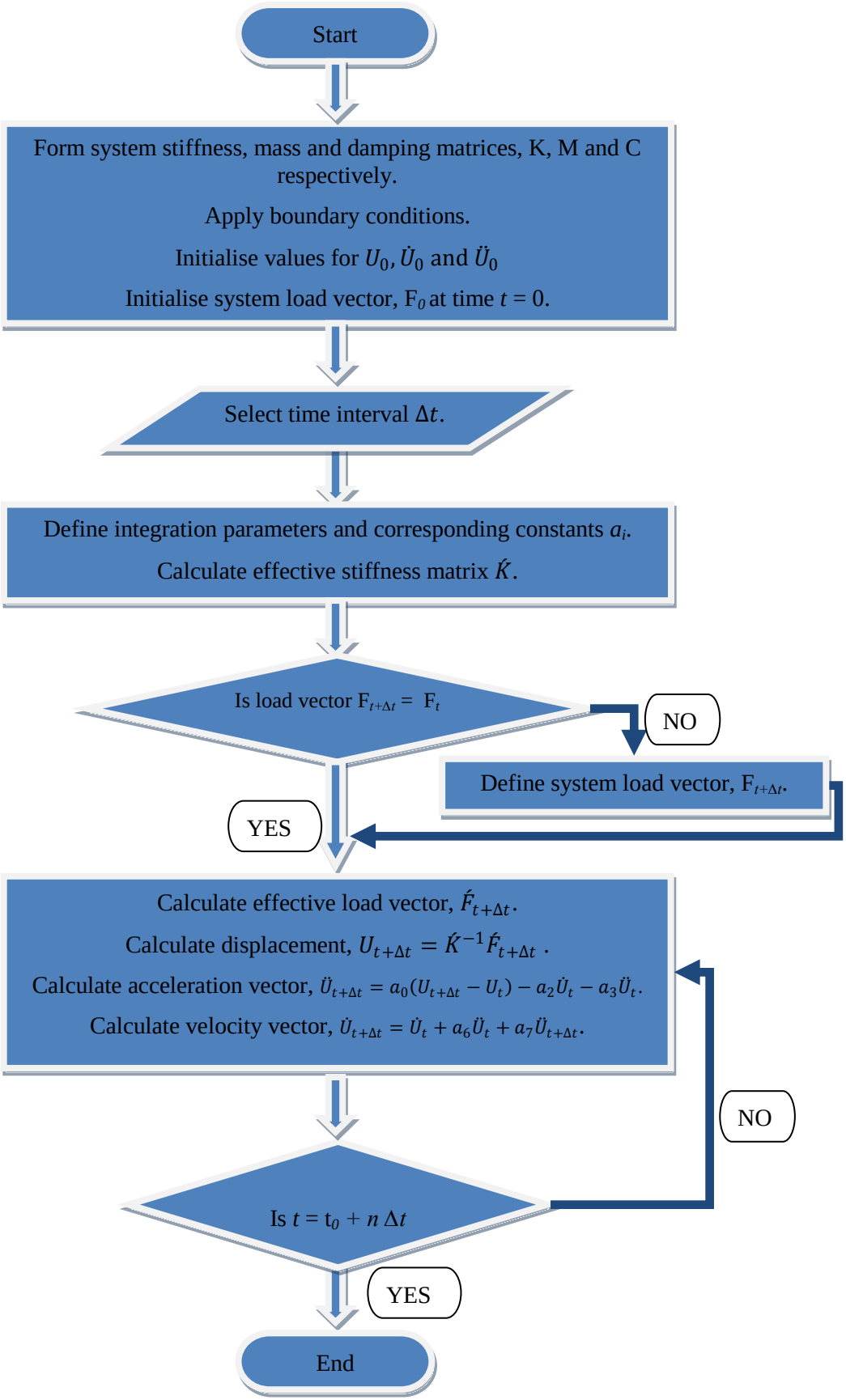

Figure 4-3: Newmark time integrating method flowchart

4.7. Conclusion

Key aspects of the classical finite element method were presented in this chapter. Brief discussions on the approximation functions and the different theories/methods used to evaluate engineering problems using FEM were included. Furthermore, different refinement techniques implemented in FEM to improve on the accuracy of the approximated solutions were outlined. The classical FEM will in this study be compared with the WFEM and it was therefore necessary to discuss the various properties and requirements associated with the method. The static and dynamic analyses of different structural problems are later presented in this thesis. Thus, key aspects dealing with vibration analysis, damping of systems and time integration methods, used to solve for the dynamic response of systems, are outlined. The key areas that were focused on included: free undamped vibration, proportional viscous damping and the Newmark time integration method (Linear Multistep Method).

The content in this chapter was not only presented to aid in understanding future discussions carried out in this study when comparing the FEM to WFEM. The aspects outlined form a basis for the formulation of the wavelet based finite element method for different structural problems. The formulations for the mass matrix, stiffness matrix and load vectors associated with rod, beam and plane bar finite elements are derived in Appendix B.

5. The Wavelet Based Finite Element Method

Summary

In this chapter, the formulation of the wavelet based finite elements is carried out and discussed. The formulations presented are unified and can be implemented for both BSWI and Daubechies WFEM based on the general wavelet and finite element theory discussed in Chapter 3 and Chapter 4 respectively. Furthermore, the formulations described at length in this chapter are conceptually based on Daubechies [6,8,10] and BSWI [7] WFEMs described in literature. The rod element, Euler Bernoulli beam element and plane bar element, for frame structure analysis, are formulated using the Daubechies and BSWI wavelet families for static and dynamic analysis. Moreover, the general formulations of the moving load wavelet based vector and foundation matrices are presented in this chapter. Key aspects and properties of the wavelet based finite elements with respect to wavelet families, shape functions, layout of the elements and order selection, are also discussed.

5.1. Axial rod wavelet finite element

The general formulation of a multiscale one dimensional axial rod WFE is carried out in this section. The layout of the rod wavelet based element of length L_e is described in Figure 5-1.

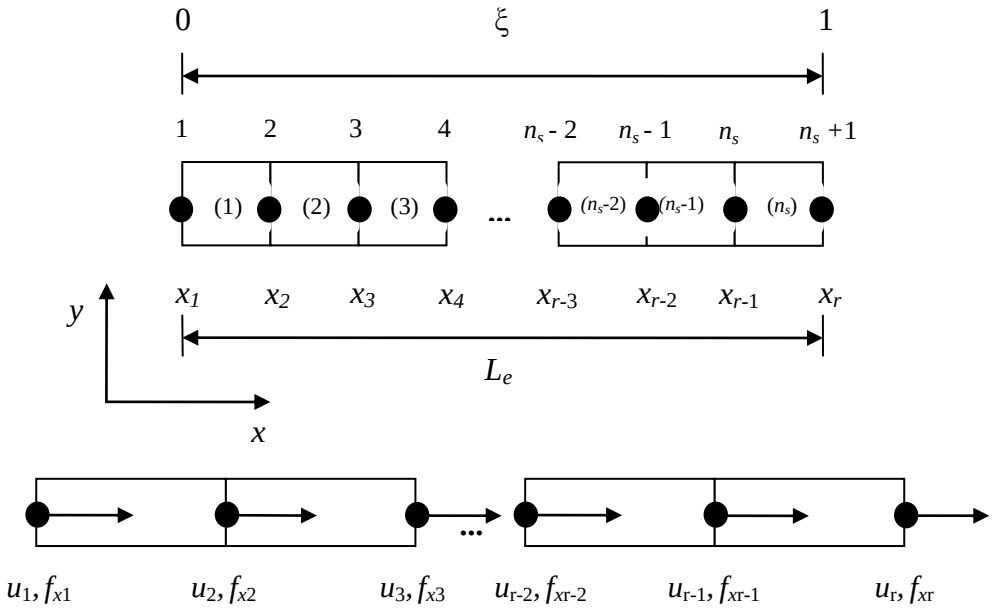

Figure 5-1 : Axial rod wavelet finite element layout.

Each WFE is divided into n_s equal elemental segments (indicated with brackets) and $r = n_s + 1$ elemental nodes, formulated in the local *x-y* coordinate. Each elemental node within

the rod element only has one degree of freedom (DOF) corresponding to the axial deformation u_i. The axial nodal point force in local coordinates is denoted by f_{xi}. The total number of DOFs within each WFE is denoted by *n*, which in this case corresponds to the total number of elemental nodes i.e., $n = r$ for $n, r \in \mathbb{N}$. The vector containing all the axial DOFs in physical space within the rod WFE is denoted by $\{\boldsymbol{u_e}\}$:

$$\{\boldsymbol{u_e}\} = \{u_1\ u_2\ \cdots\ u_{r-1}\ u_r\}^T \tag{5.1}$$

where $u_i = u(x_i)$ represents the elemental node axial deformation DOF at node *i* corresponding to coordinate position x_i. Therefore, at node *i*

$$x_i \in [x_1, x_r] \quad i \in \mathbb{N} \text{ and } (1 \leq i \leq r) \tag{5.2}$$

One can therefore describe the general and nodal natural coordinates as:

$$\xi = \frac{x - x_1}{x_r - x_1} = \frac{x - x_1}{L_e} \qquad (0 \leq \xi \leq 1) \tag{5.3}$$

$$\xi_i = \frac{x_i - x_1}{L_e} \qquad (0 \leq \xi_i \leq 1,\ 1 \leq i \leq r) \tag{5.4}$$

In classical FEM formulations, polynomial functions are used as interpolating functions to approximate the corresponding DOFs. However, for the BSWI and Daubechies WFEMs, the respective wavelet scaling functions of the wavelet families are used instead [7,9,10]. Given that a wavelet family scaling function of order *z* at multiresolution scale *j* is employed, the unknown axial deformations in physical space at natural coordinate ξ, for $(0 \leq \xi \leq 1)$, can be defined as:

$$u(\xi) = \sum_{k=h}^{2^j - 1} a_{z,k}^j\ \phi_{z,k}^j(\xi)$$

$$u(\xi) = \begin{Bmatrix} \phi_{z,h}^j(\xi) & \phi_{z,h+1}^j(\xi) & \cdots & \phi_{z,2^j-2}^j(\xi) & \phi_{z,2^j-1}^j(\xi) \end{Bmatrix} \begin{Bmatrix} a_{z,h}^j \\ a_{z,h+1}^j \\ \vdots \\ a_{z,2^j-2}^j \\ a_{z,2^j-1}^j \end{Bmatrix}$$

$$u(\xi) = {}_{(1\ \mathrm{x}\ n)}\{\boldsymbol{\Phi_z^j}(\xi)\}\ {}_{(n\ \mathrm{x}\ 1)}\{\boldsymbol{a_e}\} \tag{5.5}$$

where $\{\boldsymbol{\Phi_z^j}(\xi)\}$ is a vector containing the scaling functions of order *z* and at multiresolution scale *j*. The vector $\{\boldsymbol{a_e}\}$ contains wavelet coefficients $a_{z,k}^j$, which represent the elemental DOFs in wavelet space. The dimensions of the vectors in equation (5.5), the wavelet elemental matrices and load vectors are dependent on the wavelet family, the order *z* of the

wavelet family and the multiresolution scale j implemented. The physical space axial deformation at a particular elemental node i can be obtained from the relation in equation (5.5) as:

$$u_i = u(\xi_i) = \sum_{k=h}^{2^j-1} a_{z,k}^j \, \phi_{z,k}^j(\xi_i) = {}_{(1\,\mathrm{x}\,n)}\{\boldsymbol{\Phi}_{\boldsymbol{z}}^{\boldsymbol{j}}(\xi_i)\}\ {}_{(n\,\mathrm{x}\,1)}\{\boldsymbol{a_e}\} \tag{5.6}$$

Therefore, the axial deformation in physical space for all elemental nodes as described in equation (5.1) can be represented in form of equation (5.6) as follows:

$$\begin{Bmatrix} u_1 \\ u_2 \\ \vdots \\ u_{r-1} \\ u_r \end{Bmatrix} = \begin{bmatrix} \phi_{z,h}^j(\xi_1) & \phi_{z,h+1}^j(\xi_1) & \cdots & \phi_{z,2^j-2}^j(\xi_1) & \phi_{z,2^j-1}^j(\xi_1) \\ \phi_{z,h}^j(\xi_2) & \phi_{z,h+1}^j(\xi_2) & \cdots & \phi_{z,2^j-2}^j(\xi_2) & \phi_{z,2^j-1}^j(\xi_2) \\ \vdots & \vdots & \ddots & \vdots & \vdots \\ \phi_{z,h}^j(\xi_{r-1}) & \phi_{z,h+1}^j(\xi_{r-1}) & \cdots & \phi_{z,2^j-2}^j(\xi_{r-1}) & \phi_{z,2^j-1}^j(\xi_{r-1}) \\ \phi_{z,h}^j(\xi_r) & \phi_{z,h+1}^j(\xi_r) & \cdots & \phi_{z,2^j-2}^j(\xi_r) & \phi_{z,2^j-1}^j(\xi_r) \end{bmatrix} \begin{Bmatrix} a_{z,h}^j \\ a_{z,h+1}^j \\ \vdots \\ a_{z,2^j-2}^j \\ a_{z,2^j-1}^j \end{Bmatrix}$$

$$\{\boldsymbol{u_e}\} = \begin{bmatrix} \{\boldsymbol{\Phi}_{\boldsymbol{z}}^{\boldsymbol{j}}(\xi_1)\} \\ \{\boldsymbol{\Phi}_{\boldsymbol{z}}^{\boldsymbol{j}}(\xi_2)\} \\ \vdots \\ \{\boldsymbol{\Phi}_{\boldsymbol{z}}^{\boldsymbol{j}}(\xi_{r-1})\} \\ \{\boldsymbol{\Phi}_{\boldsymbol{z}}^{\boldsymbol{j}}(\xi_r)\} \end{bmatrix} \begin{Bmatrix} a_{z,h}^j \\ a_{z,h+1}^j \\ \vdots \\ a_{z,2^j-2}^j \\ a_{z,2^j-1}^j \end{Bmatrix}$$

$${}_{(n\,\mathrm{x}\,1)}\{\boldsymbol{u_e}\} = {}_{(n\,\mathrm{x}\,n)}[\boldsymbol{R_r^w}]_{(n\,\mathrm{x}\,1)}\{\boldsymbol{a_e}\} \tag{5.7}$$

The matrix $[\boldsymbol{R_r^w}]$ contains the scaling function vectors $\{\boldsymbol{\Phi}_{\boldsymbol{z}}^{\boldsymbol{j}}(\xi_i)\}$ approximating the axial deformation at the corresponding elemental nodes. The wavelet coefficients $a_{z,k}^j$ can then be obtained from equation (5.7).

$${}_{(n\,\mathrm{x}\,1)}\{\boldsymbol{a_e}\} = {}_{(n\,\mathrm{x}\,n)}[\boldsymbol{R_r^w}]^{-1}{}_{(n\,\mathrm{x}\,1)}\{\boldsymbol{u_e}\} \tag{5.8}$$

Therefore, by substituting equation (5.8) into (5.6), the axial deformation at node i can be expressed as

$$u_i = \begin{Bmatrix} \phi_{z,h}^j(\xi_i) & \phi_{z,h+1}^j(\xi_i) & \cdots & \phi_{z,2^j-2}^j(\xi_i) & \phi_{z,2^j-1}^j(\xi_i) \end{Bmatrix} \times$$

$$\times \begin{bmatrix} \phi_{z,h}^j(\xi_1) & \phi_{z,h+1}^j(\xi_1) & \cdots & \phi_{z,2^j-2}^j(\xi_1) & \phi_{z,2^j-1}^j(\xi_1) \\ \phi_{z,h}^j(\xi_2) & \phi_{z,h+1}^j(\xi_2) & \cdots & \phi_{z,2^j-2}^j(\xi_2) & \phi_{z,2^j-1}^j(\xi_2) \\ \vdots & \vdots & \ddots & \vdots & \vdots \\ \phi_{z,h}^j(\xi_{r-1}) & \phi_{z,h+1}^j(\xi_{r-1}) & \cdots & \phi_{z,2^j-2}^j(\xi_{r-1}) & \phi_{z,2^j-1}^j(\xi_{r-1}) \\ \phi_{z,h}^j(\xi_r) & \phi_{z,h+1}^j(\xi_r) & \cdots & \phi_{z,2^j-2}^j(\xi_r) & \phi_{z,2^j-1}^j(\xi_r) \end{bmatrix}^{-1} \begin{Bmatrix} u_1 \\ u_2 \\ \vdots \\ u_{r-1} \\ u_r \end{Bmatrix}$$

$$u_i = {}_{(1\,\mathrm{x}\,n)}\{\boldsymbol{\Phi}_{\boldsymbol{z}}^{\boldsymbol{j}}(\xi_i)\}\ {}_{(n\,\mathrm{x}\,n)}[\boldsymbol{T_r^w}]\ {}_{(n\,\mathrm{x}\,1)}\{\boldsymbol{u_e}\} = \{\boldsymbol{N_{r,e}}(\xi_i)\}\{\boldsymbol{u_e}\} \tag{5.9}$$

The general axial deformation at any point along the rod element can be generalised as

$$u(\xi) = {}_{(1\text{ x }n)}\left\{\boldsymbol{\Phi}_{\boldsymbol{z}}^{\boldsymbol{j}}(\xi)\right\}_{(n\text{ x }n)}[\boldsymbol{T}_{\boldsymbol{r}}^{\boldsymbol{w}}]_{(n\text{ x }1)}\{\boldsymbol{u}_{\boldsymbol{e}}\} \tag{5.10}$$

The matrix $[\boldsymbol{T}_{\boldsymbol{r}}^{\boldsymbol{w}}] = [\boldsymbol{R}_{\boldsymbol{r}}^{\boldsymbol{w}}]^{-1}$ is the axial rod wavelet transformation matrix with the scripts *r* and *w* denoting rod and wavelet respectively. The vector containing the wavelet based axial rod shape functions is denoted by $\left\{\boldsymbol{N}_{\boldsymbol{r},\boldsymbol{e}}(\xi)\right\}$, where

$${}_{(1\text{ x }n)}\left\{\boldsymbol{N}_{\boldsymbol{r},\boldsymbol{e}}(\xi)\right\} = {}_{(1\text{ x }n)}\left\{\boldsymbol{\Phi}_{\boldsymbol{z}}^{\boldsymbol{j}}(\xi)\right\}_{(n\text{ x }n)}[\boldsymbol{T}_{\boldsymbol{r}}^{\boldsymbol{w}}] \tag{5.11}$$

5.1.1. Stiffness matrix formulation

In general, the total potential energy within an axial rod Π^a, is described as [31]:

$$\Pi^a = U^a + \Omega^a \tag{5.12}$$

where U^a is the axial strain energy and Ω^a is the work potential via externally applied axial loads. Suppose the axial rod is subjected to nodal point loads f_{xi} and distributed loading $f_d(x)$, then the potential energy within the axial rod can be generally expressed as [27,31]:

$$\Pi^a = \int_0^l \frac{EA}{2}\left(\frac{du(x)}{dx}\right)^2 dx - \sum_i u(x_i)f_{xi} - \int_0^l f_d(x)u(x)\,dx \tag{5.13}$$

where *E* is the Young's modulus, *A* is the cross-sectional area and *l* is the length of the rod. Therefore, according to the principle of minimum potential energy,

$$\delta\,\Pi^a = \delta\,U^a + \delta\,\Omega^a = 0 \tag{5.14}$$

Following the discretization of the rod into elements, the axial stain energy within each WFE of length L_e is expressed in natural coordinate system as:

$$U_e^a = \frac{1}{2}\frac{EA}{L_e}\int_0^1 \left(\frac{du(\xi)}{d\xi}\right)^T \left(\frac{du(\xi)}{d\xi}\right) d\xi \tag{5.15}$$

Substituting equation (5.10) into equation (5.15):

$$U_e^a = \frac{1}{2}\frac{EA}{L_e}\{\boldsymbol{u}_{\boldsymbol{e}}\}^T \int_0^1 [\boldsymbol{T}_{\boldsymbol{r}}^{\boldsymbol{w}}]^T \left\{\frac{d\boldsymbol{\Phi}_{\boldsymbol{z}}^{\boldsymbol{j}}(\xi)}{d\xi}\right\}^T \left\{\frac{d\boldsymbol{\Phi}_{\boldsymbol{z}}^{\boldsymbol{j}}(\xi)}{d\xi}\right\} [\boldsymbol{T}_{\boldsymbol{r}}^{\boldsymbol{w}}]\, d\xi \;\; \{\boldsymbol{u}_{\boldsymbol{e}}\} \tag{5.16}$$

One can now obtain the stiffness matrix of the rod element in wavelet space, $\left[\boldsymbol{k}_{\boldsymbol{r},\boldsymbol{e}}^{\boldsymbol{w}}\right]$, as:

$$[\boldsymbol{k}_{r,e}^{w}] = \int_0^1 \left\{\frac{d\boldsymbol{\Phi}_{z}^{j}(\xi)}{d\xi}\right\}^T \left\{\frac{d\boldsymbol{\Phi}_{z}^{j}(\xi)}{d\xi}\right\} d\xi$$

$$_{(n\ \mathrm{x}\ n)}[\boldsymbol{k}_{r,e}^{w}] = \int_0^1 \{\boldsymbol{\Phi}'^{j}_{z}(\xi)\}^T \{\boldsymbol{\Phi}'^{j}_{z}(\xi)\} d\xi \qquad \textbf{(5.17)}$$

The wavelet space stiffness matrix of the rod WFE formulated using a wavelet family of order *z* at multiresolution scale *j* is symmetric and has the general form

$$[\boldsymbol{k}_{r,e}^{w}] = \begin{bmatrix} k_{h,h}^{z,j}{}_{\boldsymbol{r}} & k_{h,h+1}^{z,j}{}_{\boldsymbol{r}} & \cdots & k_{h,2^j-2}^{z,j}{}_{\boldsymbol{r}} & k_{h,2^j-1}^{z,j}{}_{\boldsymbol{r}} \\ k_{h+1,h}^{z,j}{}_{\boldsymbol{r}} & k_{h+1,h+1}^{z,j}{}_{\boldsymbol{r}} & \cdots & k_{h+1,2^j-2}^{z,j}{}_{\boldsymbol{r}} & k_{h+1,2^j-1}^{z,j}{}_{\boldsymbol{r}} \\ \vdots & \vdots & \ddots & \vdots & \vdots \\ k_{2^j-2,h}^{z,j}{}_{\boldsymbol{r}} & k_{2^j-2,h+1}^{z,j}{}_{\boldsymbol{r}} & \cdots & k_{2^j-2,2^j-2}^{z,j}{}_{\boldsymbol{r}} & k_{2^j-2,2^j-1}^{z,j}{}_{\boldsymbol{r}} \\ k_{2^j-1,h}^{z,j}{}_{\boldsymbol{r}} & k_{2^j-1,h+1}^{z,j}{}_{\boldsymbol{r}} & \cdots & k_{2^j-1,2^j-2}^{z,j}{}_{\boldsymbol{r}} & k_{2^j-1,2^j-1}^{z,j}{}_{\boldsymbol{r}} \end{bmatrix} \qquad \textbf{(5.18)}$$

where

$$k_{k,l}^{z,j}{}_{\boldsymbol{r}} = \int_0^1 \phi'^{j}{}_{z,k}(\xi)\phi'^{j}{}_{z,l}(\xi) d\xi \qquad \textbf{(5.19)}$$

Given that the stiffness matrix described in equation (5.18) is in wavelet space, it is important to transform the matrix into physical space via the wavelet transformation matrix $[\boldsymbol{T}_{\boldsymbol{r}}^{\boldsymbol{w}}]$ and apply the relevant material properties of the rod. Therefore, the rod WFE stiffness matrix in physical space (denoted by superscript *p*) for an element *e* is given by:

$$[\boldsymbol{k}_{r,e}^{p}] = \frac{EA}{L_e}[\boldsymbol{T}_{\boldsymbol{r}}^{\boldsymbol{w}}]^T \int_0^1 \{\boldsymbol{\Phi}'^{j}_{z}(\xi)\}^T \{\boldsymbol{\Phi}'^{j}_{z}(\xi)\}\ d\xi\ [\boldsymbol{T}_{\boldsymbol{r}}^{\boldsymbol{w}}]$$

$$_{(n\ \mathrm{x}\ n)}[\boldsymbol{k}_{r,e}^{p}] = \frac{EA}{L_e}{}_{(n\ \mathrm{x}\ n)}[\boldsymbol{T}_{\boldsymbol{r}}^{\boldsymbol{w}}]^T{}_{(n\ \mathrm{x}\ n)}[\boldsymbol{k}_{r,e}^{w}]_{(n\ \mathrm{x}\ n)}[\boldsymbol{T}_{\boldsymbol{r}}^{\boldsymbol{w}}] \qquad \textbf{(5.20)}$$

5.1.2. Load vector formulation

Assuming the rod element is subjected to nodal axial point forces f_{xi} and a distributed force $f_d(\xi)$, the total work potential within each axial rod WFE, expressed in natural coordinates, is

$$\Omega_e^a = -\left(\sum_{i=1}^{r} u(\xi_i) f_{xi} + L_e \int_0^1 f_d(\xi) u(\xi) d\xi\right) \qquad \textbf{(5.21)}$$

Substituting equation (5.10) into (5.21)

$$\Omega_e^a = -\left(\{\boldsymbol{u}_e\}^T \sum_{i=1}^{r} [\boldsymbol{T}_{\boldsymbol{r}}^{\boldsymbol{w}}]^T \left\{\boldsymbol{\Phi}_{z}^{j}(\xi_i)\right\}^T f_{xi} + \{\boldsymbol{u}_e\}^T L_e \int_0^1 f_d(\xi) [\boldsymbol{T}_{\boldsymbol{r}}^{\boldsymbol{w}}]^T \left\{\boldsymbol{\Phi}_{z}^{j}(\xi)\right\}^T d\xi\right) \qquad \textbf{(5.22)}$$

From equation (5.22), the load vector containing the element axial point loads in wavelet space is obtained as:

$$_{(n\text{ x }1)}\{\boldsymbol{f}_{\boldsymbol{r,e}}^{\boldsymbol{n,w}}\} = \sum_{i=1}^{r}\{\boldsymbol{\Phi}_{\boldsymbol{z}}^{\boldsymbol{j}}(\xi_i)\}^T \tag{5.23}$$

and subsequently in physical space, after applying the wavelet transformation matrix,

$$_{(n\text{ x }1)}\{\boldsymbol{f}_{\boldsymbol{r,e}}^{\boldsymbol{n,p}}\} = \sum_{i} {}_{(n\text{ x }n)}[\boldsymbol{T}_{\boldsymbol{r}}^{\boldsymbol{w}}]^T \, {}_{(n\text{ x }1)}\{\boldsymbol{\Phi}_{\boldsymbol{z}}^{\boldsymbol{j}}(\xi_i)\}^T f_{xi} \tag{5.24}$$

Similarly, the equivalent nodal load vector for the distributed load in wavelet space is

$$_{(n\text{ x }1)}\{\boldsymbol{f}_{\boldsymbol{r,e}}^{\boldsymbol{d,w}}\} = \int_0^1 f_d(\xi)\{\boldsymbol{\Phi}_{\boldsymbol{z}}^{\boldsymbol{j}}(\xi)\}^T d\xi \tag{5.25}$$

and in physical space

$$_{(n\text{ x }1)}\{\boldsymbol{f}_{\boldsymbol{r,e}}^{\boldsymbol{d,p}}\} = L_e \, {}_{(n\text{ x }n)}[\boldsymbol{T}_{\boldsymbol{r}}^{\boldsymbol{w}}]^T \, {}_{(n\text{ x }1)}\{\boldsymbol{f}_{\boldsymbol{r,e}}^{\boldsymbol{d,p}}\} \tag{5.26}$$

The total force vector of the external forces acting on the rod element in physical space $\{\boldsymbol{f}_{\boldsymbol{r,e}}^{\boldsymbol{p}}\}$, is sum of the axial nodal point forces and the distributed nodal equivalents given in equations (5.24) and (5.26) respectively. Thus,

$$_{(n\text{ x }1)}\{\boldsymbol{f}_{\boldsymbol{r,e}}^{\boldsymbol{p}}\} = {}_{(n\text{ x }1)}\{\boldsymbol{f}_{\boldsymbol{r,e}}^{\boldsymbol{n,p}}\} + {}_{(n\text{ x }1)}\{\boldsymbol{f}_{\boldsymbol{r,e}}^{\boldsymbol{d,p}}\} \tag{5.27}$$

5.1.3. Mass matrix formulation

The axial kinetic energy, Λ_e^a, within the rod element is defined as [27]:

$$\Lambda_e^a = \frac{1}{2}\rho A L_e \int_0^1 \dot{u}(\xi)^T \, \dot{u}(\xi) d\xi \tag{5.28}$$

where $\dot{u}(\xi) = \frac{\partial u(\xi)}{\partial t}$ is the axial velocity. The wavelet based approximation for the axial deformation from equation (5.10) is substituted into equation (5.28).

$$\Lambda_e^a = \{\dot{\boldsymbol{u}}_{\boldsymbol{e}}\}^T \frac{1}{2}\rho A L_e \int_0^1 [\boldsymbol{T}_{\boldsymbol{r}}^{\boldsymbol{w}}]^T \left\{\boldsymbol{\Phi}_{\boldsymbol{z}}^{\boldsymbol{j}}(\boldsymbol{\xi})\right\}^T \left\{\boldsymbol{\Phi}_{\boldsymbol{z}}^{\boldsymbol{j}}(\boldsymbol{\xi})\right\} [\boldsymbol{T}_{\boldsymbol{r}}^{\boldsymbol{w}}] \, d\xi \; \{\dot{\boldsymbol{u}}_{\boldsymbol{e}}\} \tag{5.29}$$

It is therefore possible to acquire the mass matrix for the rod element in wavelet space from equation (5.29) as:

$$_{(n\ \mathrm{x}\ n)}[\boldsymbol{m}^{\boldsymbol{w}}_{\boldsymbol{r},\boldsymbol{e}}] = \int_0^1 \left\{\boldsymbol{\Phi}^{\boldsymbol{j}}_{\boldsymbol{z}}(\boldsymbol{\xi})\right\}^T \left\{\boldsymbol{\Phi}^{\boldsymbol{j}}_{\boldsymbol{z}}(\boldsymbol{\xi})\right\} d\xi \tag{5.30}$$

The mass matrix of the axial rod WFE of order *z* and multiresolution scale *j* is also symmetric and takes the form

$$[\boldsymbol{m}^{\boldsymbol{w}}_{\boldsymbol{r},\boldsymbol{e}}] = \begin{bmatrix} m^{z,j}_{h,h}{}_{\boldsymbol{r}} & m^{z,j}_{h,h+1}{}_{\boldsymbol{r}} & \cdots & m^{z,j}_{h,2^j-2}{}_{\boldsymbol{r}} & m^{z,j}_{h,2^j-1}{}_{\boldsymbol{r}} \\ m^{z,j}_{h+1,h}{}_{\boldsymbol{r}} & m^{z,j}_{h+1,h+1}{}_{\boldsymbol{r}} & \cdots & m^{z,j}_{h+1,2^j-2}{}_{\boldsymbol{r}} & m^{z,j}_{h+1,2^j-1}{}_{\boldsymbol{r}} \\ \vdots & \vdots & \ddots & \vdots & \vdots \\ m^{z,j}_{2^j-2,h}{}_{\boldsymbol{r}} & m^{z,j}_{2^j-2,h+1}{}_{\boldsymbol{r}} & \cdots & m^{z,j}_{2^j-2,2^j-2}{}_{\boldsymbol{r}} & m^{z,j}_{2^j-2,2^j-1}{}_{\boldsymbol{r}} \\ m^{z,j}_{2^j-1,h}{}_{\boldsymbol{r}} & m^{z,j}_{2^j-1,h+1}{}_{\boldsymbol{r}} & \cdots & m^{z,j}_{2^j-1,2^j-2}{}_{\boldsymbol{r}} & m^{z,j}_{2^j-1,2^j-1}{}_{\boldsymbol{r}} \end{bmatrix} \tag{5.31}$$

where

$$m^{z,j}_{k,l}{}_{\boldsymbol{r}} = \int_0^1 \phi^j_{z,k}(\xi)\phi^j_{z,l}(\xi) d\xi \tag{5.32}$$

Carrying out a similar procedure as outlined in equation (5.20), one can formulate the mass matrix in physical space via the transformation of equation (5.30) using the wavelet transform matrix for the rod element.

$$[\boldsymbol{m}^{\boldsymbol{p}}_{\boldsymbol{r},\boldsymbol{e}}] = \rho A L_e [\boldsymbol{T}^{\boldsymbol{w}}_{\boldsymbol{r}}]^T \int_0^1 \left\{\boldsymbol{\Phi}^{\boldsymbol{j}}_{\boldsymbol{z}}(\xi)\right\}^T \left\{\boldsymbol{\Phi}^{\boldsymbol{j}}_{\boldsymbol{z}}(\xi)\right\} d\xi\, [\boldsymbol{T}^{\boldsymbol{w}}_{\boldsymbol{r}}]$$

$$_{(n\ \mathrm{x}\ n)}[\boldsymbol{m}^{\boldsymbol{p}}_{\boldsymbol{r},\boldsymbol{e}}] = \rho A L_e\ {}_{(n\ \mathrm{x}\ n)}[\boldsymbol{T}^{\boldsymbol{w}}_{\boldsymbol{r}}]^T\ {}_{(n\ \mathrm{x}\ n)}[\boldsymbol{m}^{\boldsymbol{w}}_{\boldsymbol{r},\boldsymbol{e}}]_{(n\ \mathrm{x}\ n)}\, [\boldsymbol{T}^{\boldsymbol{w}}_{\boldsymbol{r}}] \tag{5.33}$$

It is therefore possible to express the kinetic energy of the rod element in terms of the mass matrix evaluated in equation (5.33) as:

$$\Lambda^a_e = \frac{1}{2}\,{}_{(1\ \mathrm{x}\ n)}\{\dot{\boldsymbol{u}}_{\boldsymbol{e}}\}^T\,{}_{(n\ \mathrm{x}\ n)}[\boldsymbol{m}^{\boldsymbol{p}}_{\boldsymbol{r},\boldsymbol{e}}]_{(n\ \mathrm{x}\ 1)}\{\dot{\boldsymbol{u}}_{\boldsymbol{e}}\} \tag{5.34}$$

5.1.4. Two dimensional global transformation

In the WFEM, each element is formulated in its own arbitrary local coordinate system, which is relative to the system's global coordinate system. When an axial rod has all the elements sharing the same local and global axes, the system is analysed using the element matrices and force vectors directly. However, if the local coordinate system of an element or group of elements within the system does not coincide with the global coordinate system as illustrated in Figure 5-2, the element matrices and load vectors need to be expressed in relation to the overall global coordinate system. The axial deformation at an elemental node *i* with respect to the local coordinate is denoted by u_i and the corresponding equivalent global coordinate

DOFs are U_i (longitudinal) and V_i (transverse) respectively. The axial force component acting along the element in the local x axis at node i is f_{xi}, while F_{Xi} and F_{Yi} denote the force components acting in the global X and Y axes respectively.

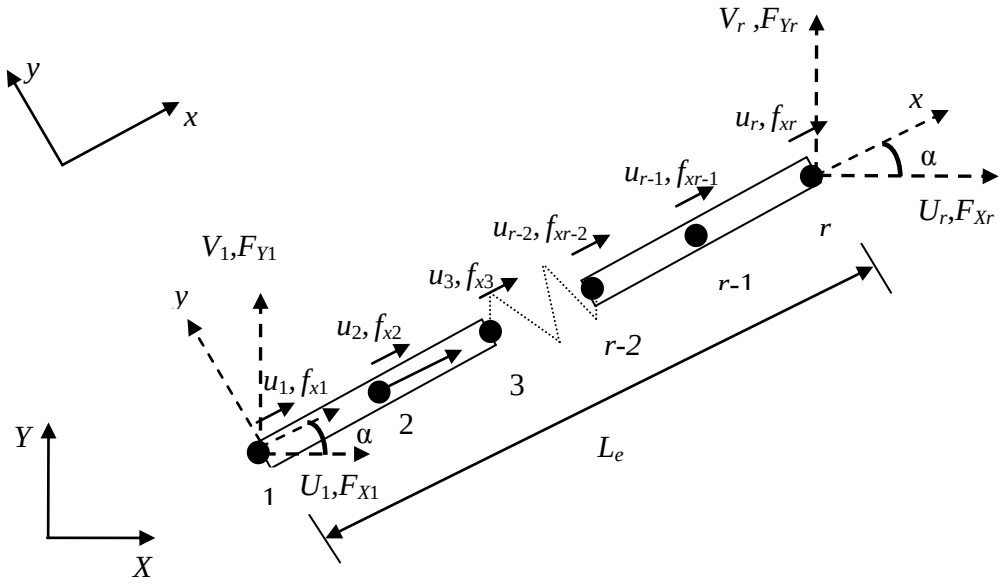

Figure 5-2 : Local and global nodal displacements of axial rod wavelet finite element.

The arbitrary angle of orientation between the local coordinate and global coordinate system is denoted by α and is assumed to remain unchanged for each elemental node within the same WFE. This is because the axial deformation and elemental nodal forces are assumed to act along the same local axial axis through all elemental nodes within the same WFE. The relationship between the local and global displacements for any elemental node i is:

$$u_i = U_i \cos\alpha + V_i \sin\alpha$$
$$u_i = \{\cos\alpha \quad \sin\alpha\}\begin{Bmatrix} U_i \\ V_i \end{Bmatrix} \tag{5.35}$$

where

$$\cos\alpha = \frac{X_r - X_1}{L_e}$$
$$\sin\alpha = \frac{Y_r - Y_1}{L_e} \tag{5.36}$$

X_i and Y_i are the global coordinate values corresponding to the local coordinate value x_i at node i. The length L_e of the element can be evaluated from the two element end node global coordinate values.

$$L_e = \sqrt{(X_r - X_1)^2 + (Y_r - Y_1)^2} \tag{5.37}$$

Let the vector containing the WFE DOFs in the global coordinate system be expressed as:

$$\{\boldsymbol{U_e}\} = \begin{Bmatrix} U_1 \\ V_1 \\ U_2 \\ V_2 \\ \vdots \\ U_{r-1} \\ V_{r-1} \\ U_r \\ V_r \end{Bmatrix} \tag{5.38}$$

From the relation of the local and global coordinate systems highlighted in equation (5.35), the relationship between the local and global coordinate displacement vectors for the two dimensional axial rod WFE is

$$\begin{Bmatrix} u_1 \\ u_2 \\ \vdots \\ u_{r-1} \\ u_r \end{Bmatrix} = \begin{bmatrix} \cos\alpha & \sin\alpha & 0 & 0 & \cdots & 0 & 0 & 0 & 0 \\ 0 & 0 & \cos\alpha & \sin\alpha & \cdots & 0 & 0 & 0 & 0 \\ \vdots & \vdots & \vdots & \vdots & \ddots & \vdots & \vdots & \vdots & \vdots \\ 0 & 0 & 0 & 0 & \cdots & \cos\alpha & \sin\alpha & 0 & 0 \\ 0 & 0 & 0 & 0 & \cdots & 0 & 0 & \cos\alpha & \sin\alpha \end{bmatrix} \begin{Bmatrix} U_1 \\ V_1 \\ U_2 \\ V_2 \\ \vdots \\ U_{r-1} \\ V_{r-1} \\ U_r \\ V_r \end{Bmatrix}$$

$$_{(n \text{ x } 1)}\{\boldsymbol{u_e}\} = {}_{(n \text{ x } 2n)}[\boldsymbol{T_r^G}]_{(2n \text{ x } 1)}\{\boldsymbol{U_e}\} \tag{5.39}$$

$[\boldsymbol{T_r^G}]$ is the rotation matrix or global transformation matrix for the rod WFE. Therefore, the element physical stiffness matrix $[\boldsymbol{K_{r,e}^p}]$, mass matrix $[\boldsymbol{M_{r,e}^p}]$ and load vector $\{\boldsymbol{F_{r,e}^p}\}$ of the WFE rod element in global coordinates are evaluated by applying the rotation matrix $[\boldsymbol{T_r^G}]$.

$$_{(2n \text{ x } 2n)}[\boldsymbol{K_{r,e}^p}] = {}_{(2n \text{ x } n)}[\boldsymbol{T_r^G}]^T {}_{(n \text{ x } n)}[\boldsymbol{k_{r,e}^p}]_{(n \text{ x } 2n)}[\boldsymbol{T_r^G}] \tag{5.40}$$

$$_{(2n \text{ x } 2n)}[\boldsymbol{M_{r,e}^p}] = {}_{(2n \text{ x } n)}[\boldsymbol{T_r^G}]^T {}_{(n \text{ x } n)}[\boldsymbol{m_{r,e}^p}]_{(n \text{ x } 2n)}[\boldsymbol{T_r^G}] \tag{5.41}$$

$$_{(2n \text{ x } 1)}\{\boldsymbol{F_{r,e}^p}\} = {}_{(2n \text{ x } n)}[\boldsymbol{T_r^G}]^T {}_{(n \text{ x } 1)}\{\boldsymbol{f_{r,e}^p}\} \tag{5.42}$$

5.1.5. Assembly and application of boundary conditions

In general, the assembly of the wavelet based finite elements is carried out in a similar manner to the classical finite element method. For an axial rod with a total of n_e WFEs, the total global stiffness and mass matrices and load vector in physical space are given by:

$$[\boldsymbol{K_r}] = \sum_{e=1}^{n_e} [\boldsymbol{K_{r,e}^p}] \tag{5.43}$$

$$[\boldsymbol{M_r}] = \sum_{e=1}^{n_e} [\boldsymbol{M_{r,e}^p}] \tag{5.44}$$

$$\{\boldsymbol{F_r}\} = \sum_{e=1}^{n_e} \{\boldsymbol{F_{r,e}^p}\} \tag{5.45}$$

The boundary conditions are applied similar to classical FEM by omitting the corresponding affected rows and columns, thus reducing the size of the overall system matrices and load vectors. Therefore, the governing equation describing the static behaviour of the system is expressed as:

$$[\boldsymbol{K_r}]\{\boldsymbol{U_r}\} = \{\boldsymbol{F_r}\} \tag{5.46}$$

5.1.6. Axial stresses and strains

The axial strains and stresses at the nodal points, for a static case, can be evaluated from the solved axial deformations obtained in equation (5.46). From the strain-displacement relationship $\varepsilon = \left(\frac{du(x)}{dx}\right)$, the axial strain $\varepsilon_e^a(\xi)$ and stress $\sigma_e^a(\xi)$ at a point ξ within a given element *e*, is obtained as [30]:

$$\varepsilon_e^a(\xi) = \left(\frac{du(\xi)}{dx}\right) = \frac{1}{L_e}\frac{du(\xi)}{d\xi} = \frac{1}{L_e}\frac{d}{d\xi}\{\boldsymbol{N_{r,e}}(\xi)\}\{\boldsymbol{u_e}\}$$

$$\varepsilon_e^a(\xi) = \frac{1}{L_e}\{\boldsymbol{N'_{r,e}}(\xi)\}\{\boldsymbol{u_e}\} \tag{5.47}$$

$$\sigma_e^a(\xi) = E\,\varepsilon_e^a(\xi) = E\,\frac{1}{L_e}\{\boldsymbol{N'_{r,e}}(\xi)\}\{\boldsymbol{u_e}\} \tag{5.48}$$

where $\{\boldsymbol{N'_{r,e}}(\xi)\}$ is first derivative of the rod WFE shape function vector obtained in equation (5.11) and thus

$$_{(1\text{ x }n)}\{\boldsymbol{N'_{r,e}}(\xi)\} = _{(1\text{ x }n)}\left\{\frac{d\boldsymbol{\Phi_z^j}(\xi)}{d\xi}\right\}\ _{(n\text{ x }n)}[\boldsymbol{T_r^w}] \tag{5.49}$$

The vector $\left\{\frac{d\boldsymbol{\Phi_z^j}(\xi)}{d\xi}\right\}$ is the derivative of the scaling functions used to approximate the axial deformation. Therefore, the element vectors containing the axial strains $\{\varepsilon_e^a\}$ and stresses $\{\sigma_e^a\}$ at the elemental nodes within a wavelet based rod element are evaluated as follows:

$$\{\varepsilon_e^a\} = \frac{1}{L_e}\begin{bmatrix} \{\boldsymbol{N'_{r,e}}(\xi_1)\} \\ \{\boldsymbol{N'_{r,e}}(\xi_2)\} \\ \vdots \\ \{\boldsymbol{N'_{r,e}}(\xi_{r-1})\} \\ \{\boldsymbol{N'_{r,e}}(\xi_r)\} \end{bmatrix}\{\boldsymbol{u_e}\} \tag{5.50}$$

$$\{\sigma_e^a\} = E\,\{\varepsilon_e^a\} = \frac{E}{L_e}\begin{bmatrix} \{\boldsymbol{N'_{r,e}}(\xi_1)\} \\ \{\boldsymbol{N'_{r,e}}(\xi_2)\} \\ \vdots \\ \{\boldsymbol{N'_{r,e}}(\xi_{r-1})\} \\ \{\boldsymbol{N'_{r,e}}(\xi_r)\} \end{bmatrix}\{\boldsymbol{u_e}\} \tag{5.51}$$

5.1.7. Daubechies axial rod wavelet finite element

A Daubechies wavelet family of order *L* can represent any polynomial whose order is up to but not greater than $\frac{L}{2} - 1$ [10,36]. Hence for a static case, the lowest Daubechies family that is theoretically applicable in the formulation of a one dimensional axial rod WFE is D*4*. For a general axial rod with *n* DOFs formulated using the Daubechies wavelet D*L* at multiresolution scale *j*, the axial displacement field is given by:

$$u(\xi) = \sum_{k=2-L}^{2^j-1} a_{L,k}^j\, \phi_{L,k}^j(\xi) \tag{5.52}$$

Thus, in the formulation of the axial rod, the Daubechies WFE has a total of $n = 2^j + L - 2$ DOFs. The shape functions of the Daubechies based axial rod WFE are obtained from equation (5.11) as

$$\underset{(1\,\mathrm{x}\,n)}{^{D}}\{\boldsymbol{N_{r,e}}(\xi)\} = \underset{(1\,\mathrm{x}\,n)}{^{D}}\{\boldsymbol{\Phi_L^j}(\xi)\}\;\underset{(n\,\mathrm{x}\,n)}{^{D}}[\boldsymbol{T_r^w}] \tag{5.53}$$

where ${}^{D}[\boldsymbol{T_r^w}]$ is the Daubechies wavelet transformation matrix for the axial rod WFE. The number of shape functions within a given rod element correspond to the number of DOFs i.e., $n = 2^j + L - 2$. Figure 5-3 illustrates the (*a*) D6_0 and (*b*) D6_1 Daubechies wavelet based axial rod element shape functions in physical space; $N_k(\xi)$ and $N_k(\xi_i)$ for $1 \leq i, k \leq n$. The Daubechies wavelet based axial rod elements of order $DL \geq D4$ at multiresolution *j*, possess the delta function, completeness and compatibility properties as highlighted in Section 4.4. This implies that increasing the order of the Daubechies wavelet, multiresolution scale and/or number of elements within the system ensures the approximate solution converges to the exact solution.

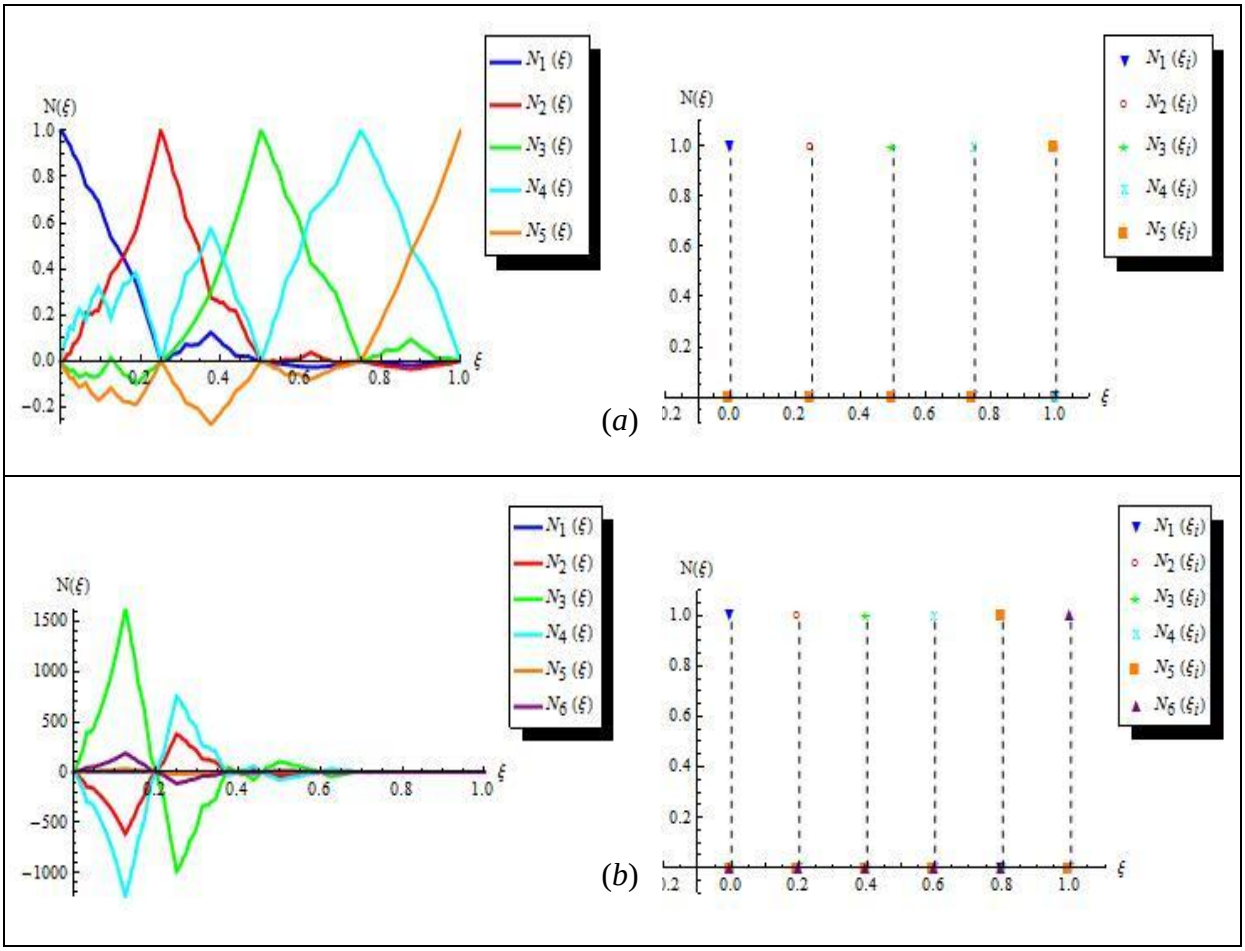

Figure 5-3 : Axial rod Daubechies based wavelet element shape functions $N_k(\xi)$ and $N_k(\xi_i)$ for (a) D6_0 (b) D6_1.

The Daubechies scaling functions and derivatives of the scaling functions cannot be expressed explicitly. Therefore, the computation of the element matrices and load vectors cannot be calculated directly. This requires the evaluation of the Daubechies connection coefficients so as to carry out the calculation of the integral of the products of the scaling functions and/or their derivatives [36]. Defining the two term connection coefficients necessary to evaluate the element matrices as

$$ {}_{L,L}\Gamma_{k,l}^{j,d_1,d_2} = \int_0^1 \phi_L^{(d_1)}(2^j\xi - k)\phi_L^{(d_2)}(2^j\xi - l)d\xi \qquad \textbf{(5.54)} $$

The connections coefficients $\Gamma_{k,l}^{j,d_1,d_2} = {}_{L,L}\Gamma_{k,l}^{j,d_1,d_2}$ are the entries of the element matrices in wavelet space for the limits $2 - L \le k, l \le 2^j - 1$.

$$ \left((2^j+L-2)\,\mathrm{x}\,(2^j+L-2)\right)[\boldsymbol{\Gamma}^{j,d_1,d_2}] = \begin{bmatrix} \Gamma_{2-L,2-L}^{j,d_1,d_2} & \Gamma_{3-L,2-L}^{j,d_1,d_2} & \cdots & \Gamma_{2^j-2,2-L}^{j,d_1,d_2} & \Gamma_{2^j-1,2-L}^{j,d_1,d_2} \\ \Gamma_{2-L,3-L}^{j,d_1,d_2} & \Gamma_{3-L,3-L}^{j,d_1,d_2} & \cdots & \Gamma_{2^j-2,3-L}^{j,d_1,d_2} & \Gamma_{2^j-1,3-L}^{j,d_1,d_2} \\ \vdots & \vdots & \ddots & \vdots & \vdots \\ \Gamma_{2-L,2^j-2}^{j,d_1,d_2} & \Gamma_{3-L,2^j-2}^{j,d_1,d_2} & \cdots & \Gamma_{2^j-2,2^j-2}^{j,d_1,d_2} & \Gamma_{2^j-1,2^j-2}^{j,d_1,d_2} \\ \Gamma_{2-L,2^j-1}^{j,d_1,d_2} & \Gamma_{3-L,2^j-1}^{j,d_1,d_2} & \cdots & \Gamma_{2^j-2,2^j-1,}^{j,d_1,d_2} & \Gamma_{2^j-1,2^j-1}^{j,d_1,d_2} \end{bmatrix} \qquad \textbf{(5.55)} $$

Therefore, the Daubechies wavelet space stiffness and mass matrices, from equations (5.17) and (5.30) respectively, are expressed as:

$$\left((2^j+L-2)\text{ x }(2^j+L-2)\right)^{D}[\boldsymbol{k}_{\boldsymbol{r,e}}^{\boldsymbol{w}}] = 2^{2j}\left[\boldsymbol{\Gamma}^{j,1,1}\right] \tag{5.56}$$

$$\left((2^j+L-2)\text{ x }(2^j+L-2)\right)^{D}[\boldsymbol{m}_{\boldsymbol{r,e}}^{\boldsymbol{w}}] = \left[\boldsymbol{\Gamma}^{j,0,0}\right] \tag{5.57}$$

When carrying out the evaluation of the connection coefficients, as presented in Section 3.2.5, the normalizing factor 2^{jm} of the m^{th} derivative of the Daubechies scaling function present on the left hand side of equation (5.58) was omitted from the calculations for convenience.

$$2^{jm}\,\phi_L^{(m)}(2^j\xi - k) = 2^{(j+1)m}\sum_r p(r)\phi_L^{(m)}\left(2^{j+1}\xi - 2k - r\right) \tag{5.58}$$

It is for this reason that a normalizing factor $\left(2^{2j}\right)$ is introduced in the wavelet based stiffness matrix formulation. The Daubechies wavelet transformation matrix ${}^{D}[\boldsymbol{T}_{\boldsymbol{r}}^{\boldsymbol{w}}]$ is then applied to transform the stiffness and mass matrices from wavelet space into physical space.

Similarly, the distributed forces acting on the element require another form of connection coefficients to be evaluated; depending on the function of the forces. In the case of a uniformly distributed load, the function representing the force is a constant. Therefore, given an axial uniformly distributed load $f_d(\xi) = P$ N·m^{-1}, the Daubechies force vector in wavelet space is

$${}^{D}\left\{\boldsymbol{f}_{\boldsymbol{r,e}}^{\boldsymbol{d,w}}\right\} = \int_0^1 \left\{\boldsymbol{\Phi}_{\boldsymbol{L}}^{\boldsymbol{j}}(\xi)\right\}^T d\xi = \int_0^1 \xi^0{}_{\left(1\text{ x }(2^j+L-2)\right)}\left\{\boldsymbol{\Phi}_{\boldsymbol{L}}^{\boldsymbol{j}}(\xi)\right\}^T d\xi \tag{5.59}$$

The values within the force vector are obtained from the connection coefficients of the form $\Upsilon_k^{j,0}$, $2-L \le k, l \le 2^j - 1$ as described in Section 3.2.5, for $m = 0$.

$$\Upsilon_k^{j,0} = \int_0^1 \xi^0 \phi_L(2^j\xi - k)d\xi \tag{5.60}$$

Thus, the uniformly distributed load equivalent column vector in wavelet space is

$$\left((2^j+L-2)\text{ x }1\right)^{D}\left\{\boldsymbol{f}_{\boldsymbol{r,e}}^{\boldsymbol{d,w}}\right\} = \{\boldsymbol{\Upsilon}^{\boldsymbol{j,0}}\} = \begin{Bmatrix} \Upsilon_{2-L}^{j,0} \\ \Upsilon_{3-L}^{j,0} \\ \vdots \\ \Upsilon_{2^j-2}^{j,0} \\ \Upsilon_{2^j-1}^{j,0} \end{Bmatrix} \tag{5.61}$$

Likewise, for a linearly varying load given by the function $f_d(\xi) = P\,\xi$ N·m^{-1}, the force vector in wavelet space is obtained from the same connection coefficients but with $m = 1$, i.e.,

$$\Upsilon_k^{j,1} = \int_0^1 \xi^1 \phi_L(2^j \xi - k) d\xi$$

$$\left((2^j + L - 2)\text{ x }1\right)^{D}\{\boldsymbol{f}_{\boldsymbol{r,e}}^{\boldsymbol{d,w}}\} = \{\boldsymbol{\Upsilon}^{\mathbf{j,1}}\} = \begin{Bmatrix} \Upsilon_{2-L}^{j,1} \\ \Upsilon_{3-L}^{j,1} \\ \vdots \\ \Upsilon_{2^j-2}^{j,1} \\ \Upsilon_{2^j-1}^{j,1} \end{Bmatrix} \quad \textbf{(5.62)}$$

In general, if a distributed load is represented by a function $f_d(\xi) = P\,\xi^m$ N·m^{-1} for example, one must evaluate the connection coefficients $\Upsilon_k^{j,m}$ so as to obtain the Daubechies wavelet space nodal force vector equivalent. This vector can be transformed into physical space via the Daubechies wavelet transformation matrix and subsequently transformed into global coordinates by applying the rotation matrix, if necessary.

5.1.8. BSWI axial rod wavelet finite element

In the case where the axial rod WFE is formulated using the BSWI family of order *m* and scale *j*, the unknown physical space axial deformation in natural coordinates ξ may be represented as [7]:

$$u(\xi) = \sum_{k=-m+1}^{2^j-1} a_{m,k}^j\, \phi_{m,k}^j(\xi) \quad \textbf{(5.63)}$$

Hence, the total number of elemental nodes in relation to the order and scale of the BSWI is $n = 2^j + m - 1$ and the total number of elemental segments is $n_s = 2^j + m - 2$. Figure 5-4 illustrates the (*a*) BSWI2_1 and (*b*) BSWI2_2 WFEs axial rod shape functions $N_k(\xi)$ and $N_k(\xi_i)$. Figure 5-4 (*a*) exemplifies the impact of a BSWI wavelet that does not meet the requirement $j \geq j_0$ as discussed in Section 3.3. To have at least one inner scaling function, BSWI of order $m = 2$ must have $j_0 \geq 2$. In a case where $j < j_0$, as illustrated in Figure 5-4 (*a*), the completeness requirement within the element is not met. Therefore, in the formulation of BSWI based WFEs in general, the condition $j \geq j_0$ must be satisfied [7] as shown in Figure 5-4 (*b*). Furthermore, taking into consideration that the BSWI wavelet of order *m* is in C^{m-2}, for an axial rod element which is in C^0, the orders that can be implemented in the formulation of the WFEs must be $m \geq 2$.

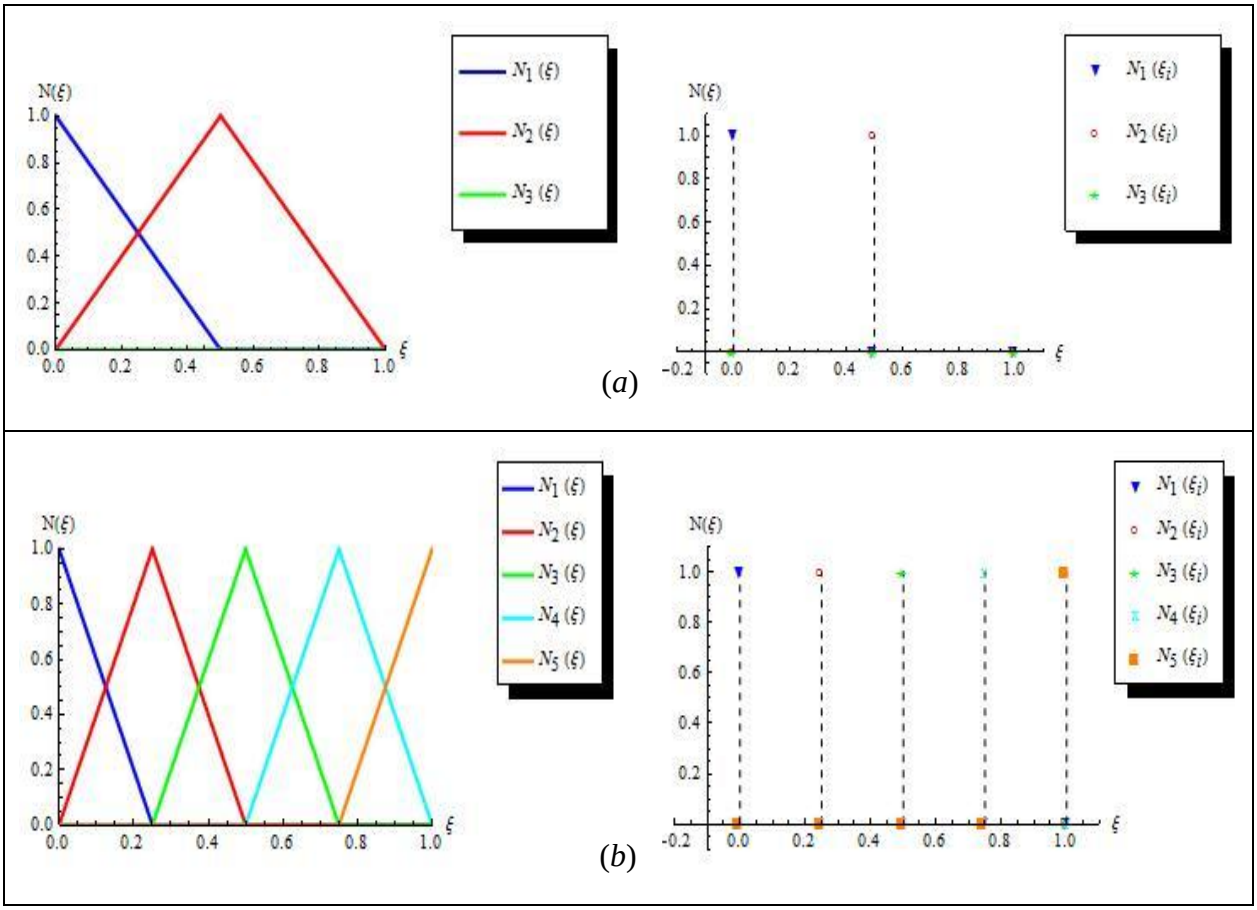

Figure 5-4 : Axial rod BSWI based wavelet element shape functions $N_k(\xi)$ and $N_k(\xi_i)$: (*a*) BSWI2_1 (*b*) BSWI2_2.

Figure 5-5 illustrates the shape functions (*a*) $N_k(\xi)$ and (*b*) $N_k(\xi_i)$ for the BSWI3_3 axial rod WFE. Provided the conditions $j \geq j_0$ and $m \geq 2$ are satisfied, the BSWI wavelet based rod element satisfies the delta function, completeness and compatibility properties highlighted in Section 4.4. The BSWI scaling functions and their derivatives are expressed explicitly, unlike the Daubechies wavelet family. Therefore, the integrals of the products of the BSWI scaling functions and/or their derivatives, used in the formulation of the element matrices and load vectors, can be evaluated directly without having to calculate the connection coefficients [7]. This is one of the advantages that BSWI based WFEs have over their Daubechies based counterparts.

Therefore in wavelet space, the mass and stiffness matrices of the BSWI axial rod element are obtained as:

$$\left((2^j+m-1)\ \text{x}\ (2^j+m-1)\right)^{BS}[\boldsymbol{m}^{\boldsymbol{w}}_{\boldsymbol{r,e}}] = \int_0^1 \{\boldsymbol{\Phi}^{\boldsymbol{j}}_{\boldsymbol{m}}(\xi)\}^T \{\boldsymbol{\Phi}^{\boldsymbol{j}}_{\boldsymbol{m}}(\xi)\} d\xi \qquad \textbf{(5.64)}$$

$$\left((2^j+m-1)\ \text{x}\ (2^j+m-1)\right)^{BS}[\boldsymbol{k}^{\boldsymbol{w}}_{\boldsymbol{r,e}}] = \int_0^1 \{\boldsymbol{\Phi}'^{\boldsymbol{j}}_{\boldsymbol{m}}(\xi)\}^T \{\boldsymbol{\Phi}'^{\boldsymbol{j}}_{\boldsymbol{m}}(\xi)\} d\xi \qquad \textbf{(5.65)}$$

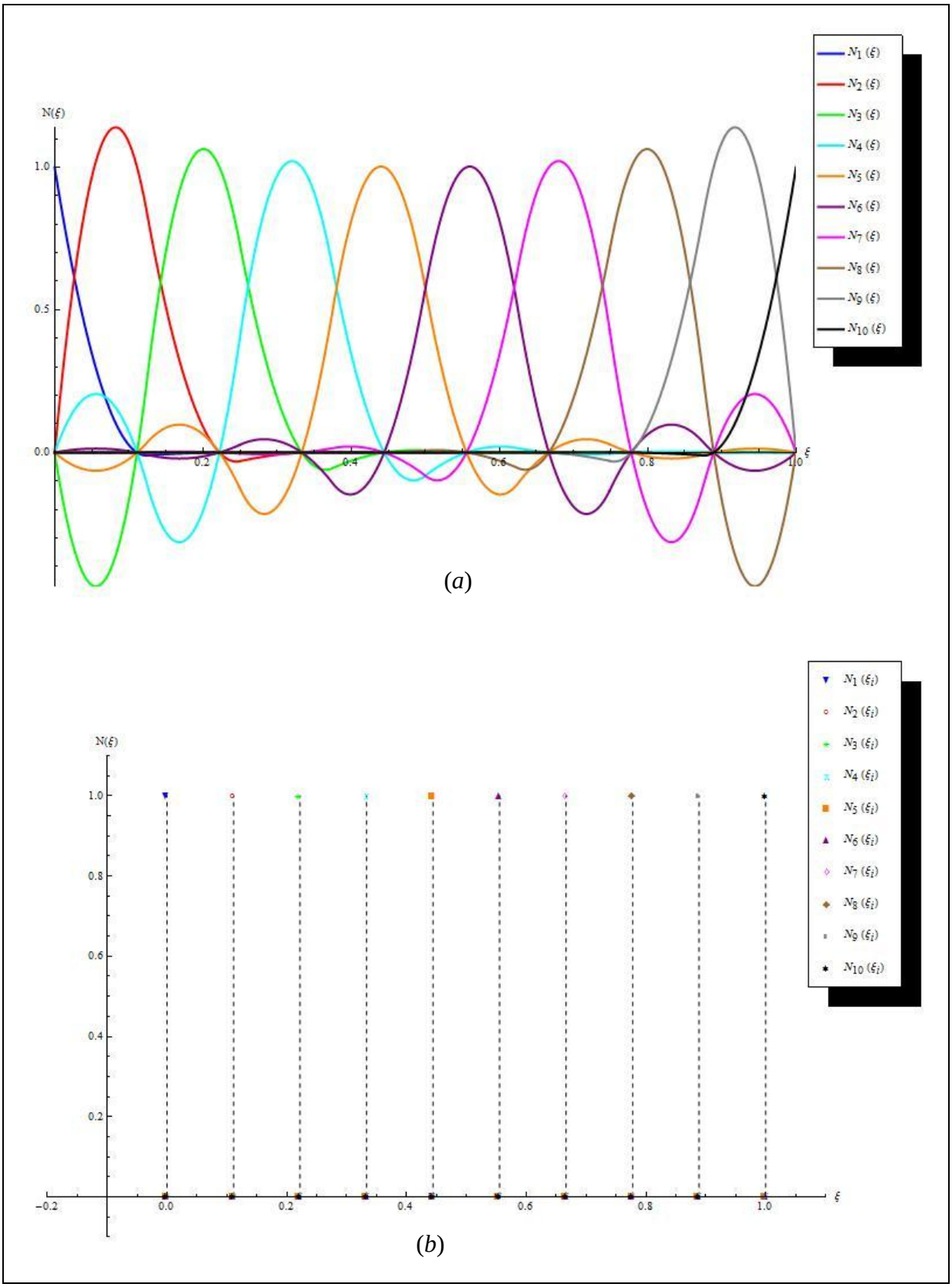

Figure 5-5 : Axial rod BSWI3_3 based wavelet element shape functions (*a*) $N_k(\xi)$ and (*b*) $N_k(\xi_i)$.

The BSWI equivalent wavelet force vectors are also simpler to obtain than the Daubechies based element since they can be evaluated directly in wavelet space without the need to obtain connection coefficients. Therefore, it is possible to conveniently evaluate more complicated loading expressions. Thus, for a uniformly distributed load, for example $f_d(\xi) = P$ N·m^{-1} acting along the length of the rod, the force vector in wavelet space of the BSWI element is

$$^{BS}\left\{\boldsymbol{f}_{\boldsymbol{r,e}}^{\boldsymbol{d,w}}\right\} = \int_0^{1}{}_{\left(1\ \mathrm{x}\ \left(2^j+m-1\right)\right)}\left\{\boldsymbol{\Phi}_{\boldsymbol{m}}^{\boldsymbol{j}}(\boldsymbol{\xi})\right\}^T d\xi \qquad \textbf{(5.66)}$$

while for a linearly varying load $f_d(\xi) = P\,\xi$ N·m^{-1}, the BSWI load vector is given as

$$^{BS}\left\{\boldsymbol{f}_{\boldsymbol{r,e}}^{\boldsymbol{d,w}}\right\} = \int_0^{1}\xi^1{}_{\left(1\ \mathrm{x}\ \left(2^j+m-1\right)\right)}\left\{\boldsymbol{\Phi}_{\boldsymbol{m}}^{\boldsymbol{j}}(\boldsymbol{\xi})\right\}^T d\xi \qquad \textbf{(5.67)}$$

The BSWI based WFE matrices and the total load vectors are then transformed into physical space via the use of the BSWI wavelet transformation matrix $^{BS}[\boldsymbol{T}_{\boldsymbol{r}}^{\boldsymbol{w}}]$.

5.2. Euler Bernoulli beam wavelet finite element

In this section, the wavelet based beam finite element is derived according to Euler Bernoulli beam theory. It is assumed that before and after bending occurs, the plane cross-sections remain plane and perpendicular to the axial centroidal axis of the beam. Therefore, the shear deformation effects are neglected. This assumption is valid for long or thin beams, which will be used in the analysis of different numerical examples within this study. The beam WFE of length L_e, is divided into n_s equally spaced elemental segments, connected by r elemental nodes at coordinate values $x_i \in [x_1, x_r]$ and $i \in \mathbb{N}$, in the local *x-y* coordinate as illustrated in Figure 5-6 below. The total number of DOFs within each beam element is n. The beam WFE has the transverse displacement v and rotation θ taken into account, with corresponding transverse forces f_y and moments $\acute{m}$ respectively. It is not mandatory for the rotation DOF to be present at each elemental node but the transverse displacement and rotation must be present at each elemental end node to ensure inter-element compatibility [6,7,10]. The inter-element compatibility is ensured when the transverse displacement and rotation fields are continuous and satisfy boundary conditions [27]. It is therefore necessary for the wavelet family implemented to satisfy the not only inter-element compatibility, but also internal compatibility. It is also important to mention that the number of elemental segments and nodes within each WFE depends on the number of DOFs at each elemental node.

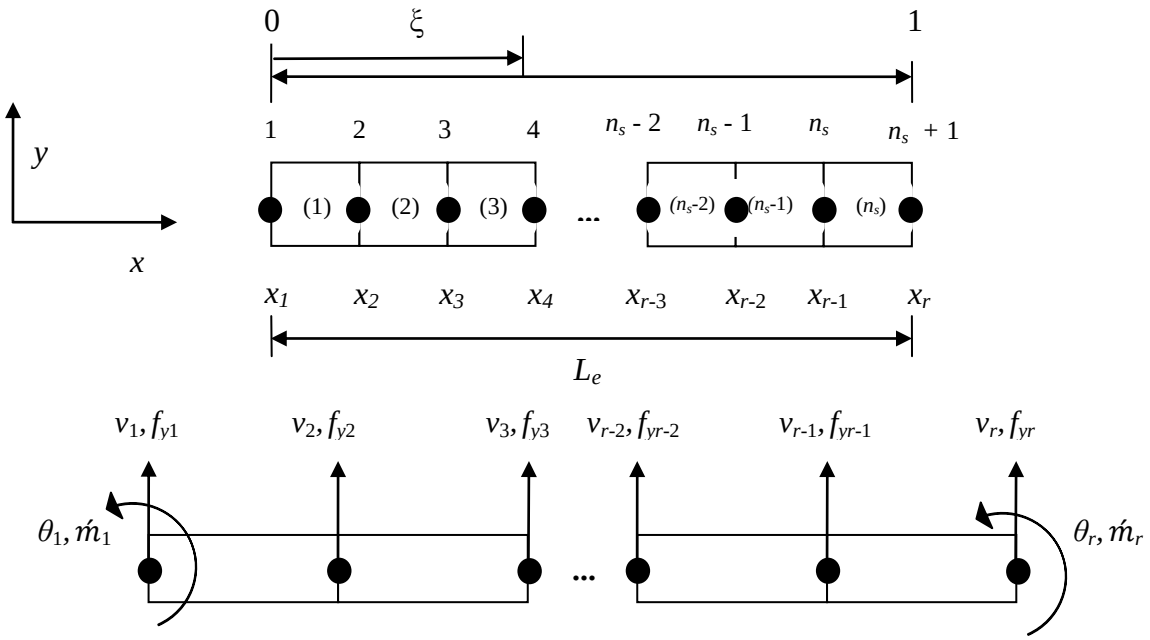

Figure 5-6 : Euler Bernoulli beam wavelet finite element layout.

In this case, the WFE beam has a transverse displacement DOF at each elemental node and a rotation DOF at each elemental end node i.e., $n-2$ displacement DOFs and 2 rotation DOFs in total for each WFE. Therefore, there are $r = n-2$ elemental nodes and $n_s = n-3$ elemental segments. Let the vector $\{\boldsymbol{v_e}\}$ denote all the physical DOFs within the beam element.

$$\{\boldsymbol{v_e}\} = \{v_1 \quad \theta_1 \quad v_2 \quad v_3 \quad \cdots \quad v_{r-2} \quad v_{r-1} \quad v_r \quad \theta_r \}^T \tag{5.68}$$

where $v_i = v(x_i)$ and $\theta_i = \theta(x_i)$ denote the nodal transverse displacement and rotation DOFs in local coordinates at elemental node *i*, corresponding to coordinate position x_i. The elemental node position coordinates within each WFE are expressed as:

$$x_i \in [x_1, x_r] \quad i \in \mathbb{N} \text{ and } (1 \leq i \leq r) \tag{5.69}$$

The general and nodal natural coordinates for the beam element are defined as:

$$\xi = \frac{x - x_1}{x_r - x_1} = \frac{x - x_1}{L_e} \qquad (0 \leq \xi \leq 1) \tag{5.70}$$

$$\xi_i = \frac{x_i - x_1}{L_e} \qquad (0 \leq \xi_i \leq 1, 1 \leq i \leq r) \tag{5.71}$$

By applying the wavelet family scaling functions of order *z* and at multiresolution scale *j* as interpolating functions, the deflection at any point of the WFE beam element can be approximated as:

$$v(\xi) = \sum_{k=h}^{2^j-1} b_{z,k}^j \, \phi_{z,k}^j(\xi)$$

$$v(\xi) = \begin{Bmatrix} \phi_{z,h}^j(\xi) & \phi_{z,h+1}^j(\xi) & \cdots & \phi_{z,2^j-2}^j(\xi) & \phi_{z,2^j-1}^j(\xi) \end{Bmatrix} \begin{Bmatrix} b_{z,h}^j \\ b_{z,h+1}^j \\ \vdots \\ b_{z,2^j-2}^j \\ b_{z,2^j-1}^j \end{Bmatrix}$$

$$v(\xi) = {}_{(1\,\mathrm{x}\,n)}\left\{\boldsymbol{\Phi}_{\boldsymbol{z}}^{\boldsymbol{j}}(\xi)\right\}_{(n\,\mathrm{x}\,1)}\{\boldsymbol{b_e}\} \qquad \textbf{(5.72)}$$

The rotation at any point of the beam WFE is also approximated as:

$$\theta(\xi) = \frac{\partial v(\xi)}{\partial x} = \frac{1}{L_e}\frac{\partial v(\xi)}{\partial \xi} = \frac{1}{L_e}\sum_{k=h}^{2^j-1} b_{z,k}^j \, \frac{\partial \phi_{z,k}^j(\xi)}{\partial \xi}$$

$$\theta(\xi) = \frac{1}{L_e}\begin{Bmatrix} \phi'^j_{z,h}(\xi) & \phi'^j_{z,h+1}(\xi) & \cdots & \phi'^j_{z,2^j-2}(\xi) & \phi'^j_{z,2^j-1}(\xi) \end{Bmatrix} \begin{Bmatrix} b_{z,h}^j \\ b_{z,h+1}^j \\ \vdots \\ b_{z,2^j-2}^j \\ b_{z,2^j-1}^j \end{Bmatrix}$$

$$\theta(\xi) = \frac{1}{L_e}\,{}_{(1\,\mathrm{x}\,n)}\left\{\boldsymbol{\Phi}'^{\boldsymbol{j}}_{\boldsymbol{z}}(\xi)\right\}_{(n\,\mathrm{x}\,1)}\{\boldsymbol{b_e}\} \qquad \textbf{(5.73)}$$

The vectors $\left\{\boldsymbol{\Phi}_{\boldsymbol{z}}^{\boldsymbol{j}}(\xi)\right\}$ and $\left\{\boldsymbol{\Phi}'^{\boldsymbol{j}}_{\boldsymbol{z}}(\xi)\right\}$ contain the scaling functions and first derivatives of the scaling functions respectively, while the vector $\{\boldsymbol{b_e}\}$ contains the unknown wavelet coefficients $b_{z,k}^j$ representing the beam DOFs in wavelet space. The transverse displacement and rotation DOFs for elemental node *i*, at coordinate position x_i, can therefore be expressed as:

$$v_i = {}_{(1\,\mathrm{x}\,n)}\left\{\boldsymbol{\Phi}_{\boldsymbol{z}}^{\boldsymbol{j}}(\xi_i)\right\}_{(n\,\mathrm{x}\,1)}\{\boldsymbol{b_e}\} \qquad \textbf{(5.74)}$$

$$\theta_i = \frac{1}{L_e}\,{}_{(1\,\mathrm{x}\,n)}\left\{\boldsymbol{\Phi}'^{\boldsymbol{j}}_{\boldsymbol{z}}(\xi_i)\right\}_{(n\,\mathrm{x}\,1)}\{\boldsymbol{b_e}\} \qquad \textbf{(5.75)}$$

The DOFs for the entire beam WFE in equation (5.68) can be represented in terms of equations (5.74) and (5.75). Therefore,

$$\begin{Bmatrix} u_1 \\ \theta_1 \\ u_2 \\ \vdots \\ u_{r-1} \\ u_r \\ \theta_r \end{Bmatrix} = \begin{bmatrix} \phi_{z,h}^j(\xi_1) & \phi_{z,h+1}^j(\xi_1) & \cdots & \phi_{z,2^j-2}^j(\xi_1) & \phi_{z,2^j-1}^j(\xi_1) \\ \frac{1}{L_e}\phi'^j_{z,h}(\xi_1) & \frac{1}{L_e}\phi'^j_{z,h+1}(\xi_1) & \cdots & \frac{1}{L_e}\phi'^j_{z,2^j-2}(\xi_1) & \frac{1}{L_e}\phi'^j_{z,2^j-1}(\xi_1) \\ \phi_{z,h}^j(\xi_2) & \phi_{z,h+1}^j(\xi_2) & \cdots & \phi_{z,2^j-2}^j(\xi_2) & \phi_{z,2^j-1}^j(\xi_2) \\ \vdots & \vdots & \ddots & \vdots & \vdots \\ \phi_{z,h}^j(\xi_{r-1}) & \phi_{z,h+1}^j(\xi_{r-1}) & \cdots & \phi_{z,2^j-2}^j(\xi_{r-1}) & \phi_{z,2^j-1}^j(\xi_{r-1}) \\ \phi_{z,h}^j(\xi_r) & \phi_{z,h+1}^j(\xi_r) & \cdots & \phi_{z,2^j-2}^j(\xi_r) & \phi_{z,2^j-1}^j(\xi_r) \\ \frac{1}{L_e}\phi'^j_{z,h}(\xi_r) & \frac{1}{L_e}\phi'^j_{z,h+1}(\xi_r) & \cdots & \frac{1}{L_e}\phi'^j_{z,2^j-2}(\xi_r) & \frac{1}{L_e}\phi'^j_{z,2^j-1}(\xi_r) \end{bmatrix} \begin{Bmatrix} b_{z,h}^j \\ b_{z,h+1}^j \\ \vdots \\ b_{z,2^j-2}^j \\ b_{z,2^j-1}^j \end{Bmatrix}$$

$$_{(n\ \mathrm{x}\ 1)}\{\boldsymbol{v_e}\} = \begin{bmatrix} \boldsymbol{\Phi_z^j}(\xi_1) \\ \frac{1}{L_e}\boldsymbol{\Phi'^j_z}(\xi_1) \\ \boldsymbol{\Phi_z^j}(\xi_2) \\ \vdots \\ \boldsymbol{\Phi_z^j}(\xi_{r-1}) \\ \boldsymbol{\Phi_z^j}(\xi_r) \\ \frac{1}{L_e}\boldsymbol{\Phi'^j_z}(\xi_r) \end{bmatrix} \begin{Bmatrix} b^j_{z,h} \\ b^j_{z,h+1} \\ \vdots \\ b^j_{z,2^j-2} \\ b^j_{z,2^j-1} \end{Bmatrix} = {}_{(n\ \mathrm{x}\ n)}[\boldsymbol{R_b^w}]_{(n\ \mathrm{x}\ 1)}\{\boldsymbol{b_e}\} \tag{5.76}$$

The wavelet coefficients $b^j_{z,i}$, representing the DOFs in wavelet space, can be obtained from equation (5.76).

$$_{(n\ \mathrm{x}\ 1)}\{\boldsymbol{b_e}\} = {}_{(n\ \mathrm{x}\ n)}[\boldsymbol{R_b^w}]^{-1}{}_{(n\ \mathrm{x}\ 1)}\{\boldsymbol{v_e}\} \tag{5.77}$$

Substituting equation (5.77) into equation (5.74)

$$v_i = \left\{\phi^j_{z,h}(\xi_i) \quad \phi^j_{z,h+1}(\xi_i) \quad \cdots \quad \phi^j_{z,2^j-2}(\xi_i) \quad \phi^j_{z,2^j-1}(\xi_i)\right\} \times$$

$$\times \begin{bmatrix} \phi^j_{z,h}(\xi_1) & \phi^j_{z,h+1}(\xi_1) & \cdots & \phi^j_{z,2^j-2}(\xi_1) & \phi^j_{z,2^j-1}(\xi_1) \\ \frac{1}{L_e}\phi'^j_{z,h}(\xi_1) & \frac{1}{L_e}\phi'^j_{z,h+1}(\xi_1) & \cdots & \frac{1}{L_e}\phi'^j_{z,2^j-2}(\xi_1) & \frac{1}{L_e}\phi'^j_{z,2^j-1}(\xi_1) \\ \phi^j_{z,h}(\xi_2) & \phi^j_{z,h+1}(\xi_2) & \cdots & \phi^j_{z,2^j-2}(\xi_2) & \phi^j_{z,2^j-1}(\xi_2) \\ \vdots & \vdots & \ddots & \vdots & \vdots \\ \phi^j_{z,h}(\xi_{r-1}) & \phi^j_{z,h+1}(\xi_{r-1}) & \cdots & \phi^j_{z,2^j-2}(\xi_{r-1}) & \phi^j_{z,2^j-1}(\xi_{r-1}) \\ \phi^j_{z,h}(\xi_r) & \phi^j_{z,h+1}(\xi_r) & \cdots & \phi^j_{z,2^j-2}(\xi_r) & \phi^j_{z,2^j-1}(\xi_r) \\ \frac{1}{L_e}\phi'^j_{z,h}(\xi_r) & \frac{1}{L_e}\phi'^j_{z,h+1}(\xi_r) & \cdots & \frac{1}{L_e}\phi'^j_{z,2^j-2}(\xi_r) & \frac{1}{L_e}\phi'^j_{z,2^j-1}(\xi_r) \end{bmatrix}^{-1} \begin{Bmatrix} u_1 \\ \theta_1 \\ u_2 \\ \vdots \\ u_{r-1} \\ u_r \\ \theta_r \end{Bmatrix}$$

$$v_i = {}_{(1\ \mathrm{x}\ n)}\left\{\boldsymbol{\Phi_z^j}(\xi_i)\right\}_{(n\ \mathrm{x}\ n)}[\boldsymbol{T_b^w}]_{(n\ \mathrm{x}\ 1)}\{\boldsymbol{v_e}\} \tag{5.78}$$

and (5.75)

$$\theta_i = \frac{1}{L_e}{}_{(1\ \mathrm{x}\ n)}\left\{\boldsymbol{\Phi'^j_z}(\xi_i)\right\}_{(n\ \mathrm{x}\ n)}[\boldsymbol{T_b^w}]_{(n\ \mathrm{x}\ 1)}\{\boldsymbol{v_e}\} \tag{5.79}$$

where $[\boldsymbol{T_b^w}] = [\boldsymbol{R_b^w}]^{-1}$ is the beam wavelet transformation matrix with the scripts *b* and *w* denoting beam and wavelet respectively. The wavelet based shape functions vector for the beam WFE in natural coordinates, is given as:

$$_{(1\ \mathrm{x}\ n)}\{\boldsymbol{N_{b,e}}(\xi)\} = {}_{(1\ \mathrm{x}\ n)}\left\{\boldsymbol{\Phi_z^j}(\xi)\right\}_{(n\ \mathrm{x}\ n)}[\boldsymbol{T_b^w}] \tag{5.80}$$

5.2.1. Stiffness matrix formulation

The potential energy within the Euler Bernoulli beam Π^b is [31]:

$$\Pi^b = U^b + \Omega^b \tag{5.81}$$

where U^b is the strain energy and Ω^b is the work potential of the beam. For a beam subjected to concentrated forces f_{yi}, distributed force $f_d(x)$, and bending moments $\acute{m}_i$, the potential energy within the Euler Bernoulli beam can be generally expressed as [27,31]:

$$\Pi^b = \int_0^l \frac{EI}{2}\left(\frac{d^2v}{dx^2}\right)^2 dx - \sum_i f_{yi}\, v(x_i) - \int_0^l f_d(x) v dx - \sum_k \acute{m}_k \frac{dv(x_k)}{dx} \qquad \textbf{(5.82)}$$

where E is the Young's modulus, I is the moment of inertia and l is the length of the beam. According to the principle of minimum potential energy,

$$\delta\, \Pi^b = \delta\, U^b + \delta\, \Omega^b = 0 \qquad \textbf{(5.83)}$$

and following the discretization of the beam into elements, the stain energy within each WFE of length L_e is expressed in natural coordinates as:

$$U_e^b = \frac{1}{2}\frac{E\, I}{{L_e}^3}\int_0^1 \left(\frac{d^2v(\xi)}{d\xi^2}\right)^T \left(\frac{d^2v(\xi)}{d\xi^2}\right) d\xi \qquad \textbf{(5.84)}$$

Expressing the strain energy equation in terms of the approximation of the transverse displacement via wavelet scaling functions, then

$$U_e^b = \frac{1}{2}\frac{E\, I}{{L_e}^3}\{\boldsymbol{v_e}\}^T \int_0^1 [\boldsymbol{T_b^w}]^T \left\{\frac{d^2\boldsymbol{\Phi_z^j}(\xi)}{d\xi^2}\right\}^T \left\{\frac{d^2\boldsymbol{\Phi_z^j}(\xi)}{d\xi^2}\right\} [\boldsymbol{T_b^w}]\, d\xi \{\boldsymbol{v_e}\} \qquad \textbf{(5.85)}$$

The stiffness matrix of the beam WFE in wavelet space, $\left[\boldsymbol{k_{b,e}^w}\right]$, is derived from equation (5.85) as:

$$[\boldsymbol{k_{b,e}^w}] = \int_0^1 \left\{\frac{\partial^2\boldsymbol{\Phi_z^j}(\xi)}{\partial\xi^2}\right\}^T \left\{\frac{\partial^2\boldsymbol{\Phi_z^j}(\xi)}{\partial\xi^2}\right\} d\xi$$

$$_{(n\,\mathrm{x}\,n)}[\boldsymbol{k_{b,e}^w}] = \int_0^1 \{\boldsymbol{\Phi''^j_z}(\xi)\}^T \{\boldsymbol{\Phi''^j_z}(\xi)\} d\xi \qquad \textbf{(5.86)}$$

where the vector $\left\{\boldsymbol{\Phi}''^{\boldsymbol{j}}_{\boldsymbol{z}}(\xi)\right\} = \left\{\phi''^j_{z,h}(\xi) \quad \phi''^j_{z,h+1}(\xi) \quad \cdots \quad \phi''^j_{z,2^j-2}(\xi) \quad \phi''^j_{z,2^j-1}(\xi)\right\}$ contains the second derivative of the scaling functions. Therefore, the stiffness matrix of the beam element formulated using a wavelet family of order z, at multiresolution scale j, is

$$[\boldsymbol{k_{b,e}^w}] = \begin{bmatrix} k^{z,j}_{h,h}{}_{\boldsymbol{b}} & k^{z,j}_{h,h+1}{}_{\boldsymbol{b}} & \cdots & k^{z,j}_{h,2^j-2}{}_{\boldsymbol{b}} & k^{z,j}_{h,2^j-1}{}_{\boldsymbol{b}} \\ k^{z,j}_{h+1,h}{}_{\boldsymbol{b}} & k^{z,j}_{h+1,h+1}{}_{\boldsymbol{b}} & \cdots & k^{z,j}_{h+1,2^j-2}{}_{\boldsymbol{b}} & k^{z,j}_{h+1,2^j-1}{}_{\boldsymbol{b}} \\ \vdots & \vdots & \ddots & \vdots & \vdots \\ k^{z,j}_{2^j-2,h}{}_{\boldsymbol{b}} & k^{z,j}_{2^j-2,h+1}{}_{\boldsymbol{b}} & \cdots & k^{z,j}_{2^j-2,2^j-2}{}_{\boldsymbol{b}} & k^{z,j}_{2^j-2,2^j-1}{}_{\boldsymbol{b}} \\ k^{z,j}_{2^j-1,h}{}_{\boldsymbol{b}} & k^{z,j}_{2^j-1,h+1}{}_{\boldsymbol{b}} & \cdots & k^{z,j}_{2^j-1,2^j-2}{}_{\boldsymbol{b}} & k^{z,j}_{2^j-1,2^j-1}{}_{\boldsymbol{b}} \end{bmatrix} \qquad \textbf{(5.87)}$$

where

$$k_{k,l\ \boldsymbol{b}}^{z,j} = \int_0^1 \phi''^{j}_{z,k}(\xi)\phi''^{j}_{z,l}(\xi)d\xi \tag{5.88}$$

The wavelet space stiffness matrix is transformed into physical space via the wavelet transformation matrix for the beam WFE. Therefore, taking into account the material properties of the element, the stiffness matrix of the element in physical space is

$$[\boldsymbol{k}_{\boldsymbol{b},\boldsymbol{e}}^{\boldsymbol{p}}] = \frac{E\ I}{{L_e}^3}[\boldsymbol{T}_{\boldsymbol{b}}^{\boldsymbol{w}}]^T \int_0^1 \{\boldsymbol{\Phi}''^{\boldsymbol{j}}_{\boldsymbol{z}}(\xi)\}^T \{\boldsymbol{\Phi}''^{\boldsymbol{j}}_{\boldsymbol{z}}(\xi)\}\, d\xi\, [\boldsymbol{T}_{\boldsymbol{b}}^{\boldsymbol{w}}]$$

$$_{(n\ \mathrm{x}\ n)}[\boldsymbol{k}_{\boldsymbol{b},\boldsymbol{e}}^{\boldsymbol{p}}] = \frac{E\ I}{{L_e}^3}\,_{(n\ \mathrm{x}\ n)}[\boldsymbol{T}_{\boldsymbol{b}}^{\boldsymbol{w}}]^T\,_{(n\ \mathrm{x}\ n)}[\boldsymbol{k}_{\boldsymbol{b},\boldsymbol{e}}^{\boldsymbol{w}}]_{(n\ \mathrm{x}\ n)}\,[\boldsymbol{T}_{\boldsymbol{b}}^{\boldsymbol{w}}] \tag{5.89}$$

Therefore, the strain energy within the beam element is obtained by substituting equation (5.89) into (5.85).

$$U_e^b = \frac{1}{2}\{\boldsymbol{v}_{\boldsymbol{e}}\}^T[\boldsymbol{k}_{\boldsymbol{b},\boldsymbol{e}}^{\boldsymbol{p}}]\,\{\boldsymbol{v}_{\boldsymbol{e}}\} \tag{5.90}$$

5.2.2. Load vector formulation

Similarly, the total work potential, Ω_e^b, within each beam WFE in the natural coordinate system, for a beam subjected to nodal moments, concentrated transverse forces and a distributed load, is expressed as:

$$\Omega_e^b = -\left(\sum_{i=1}^{r} v(\xi_i)f_{yi} + L_e\int_0^1 f_d(\xi)v(\xi)d\xi + \sum_k \acute{m}_k\frac{dv(\xi_k)}{dx}\right) \tag{5.91}$$

Substituting equation (5.72) into (5.91)

$$\begin{aligned}\Omega_e^b = -\Bigg(&\{\boldsymbol{v}_{\boldsymbol{e}}\}^T\sum_{i=1}^{r}[\boldsymbol{T}_{\boldsymbol{b}}^{\boldsymbol{w}}]^T\left\{\boldsymbol{\Phi}_{\boldsymbol{z}}^{\boldsymbol{j}}(\xi_i)\right\}^T f_{yi} + L_e\{\boldsymbol{v}_{\boldsymbol{e}}\}^T\int_0^1 f_d(\xi)[\boldsymbol{T}_{\boldsymbol{b}}^{\boldsymbol{w}}]^T\left\{\boldsymbol{\Phi}_{\boldsymbol{z}}^{\boldsymbol{j}}(\xi)\right\}^T d\xi \\ &+\frac{1}{L_e}\{\boldsymbol{v}_{\boldsymbol{e}}\}^T\sum_k[\boldsymbol{T}_{\boldsymbol{b}}^{\boldsymbol{w}}]^T\left\{\boldsymbol{\Phi}'^{\boldsymbol{j}}_{\boldsymbol{z}}(\xi_k)\right\}^T\acute{m}_k\Bigg)\end{aligned} \tag{5.92}$$

Thus, from equation (5.92), the vector containing the element concentrated point loads in wavelet space is obtained as:

$$_{(n\ \mathrm{x}\ 1)}\left\{\boldsymbol{f}_{\boldsymbol{b},\boldsymbol{e}}^{\boldsymbol{n},\boldsymbol{w}}\right\} = \sum_{i=1}^{r}\left\{\boldsymbol{\Phi}_{\boldsymbol{z}}^{\boldsymbol{j}}(\xi_i)\right\}^T \tag{5.93}$$

By applying the WFE beam wavelet transformation matrix, the vector containing the concentrated point loads, in physical space is

$$_{(n\text{ x }1)}\{\boldsymbol{f}_{\boldsymbol{b,e}}^{\boldsymbol{n,p}}\} = \sum_{i=1}^{r} {}_{(n\text{ x }n)}[\boldsymbol{T}_{\boldsymbol{b}}^{\boldsymbol{w}}]^{T}\ {}_{(n\text{ x }1)}\{\boldsymbol{\Phi}_{\boldsymbol{z}}^{\boldsymbol{j}}(\xi_i)\}^{T} f_{yi} \tag{5.94}$$

Similarly, the elemental bending moment vector in physical space, from equation (5.92), is given as:

$$_{(n\text{ x }1)}\{\boldsymbol{f}_{\boldsymbol{b,e}}^{\boldsymbol{m,p}}\} = \sum_{k} {}_{(n\text{ x }n)}[\boldsymbol{T}_{\boldsymbol{b}}^{\boldsymbol{w}}]^{T}\ {}_{(n\text{ x }1)}\{\boldsymbol{\Phi}'^{\boldsymbol{j}}_{\boldsymbol{z}}(\xi_k)\}^{T} \acute{m}_k \tag{5.95}$$

The equivalent elemental load vector with respect to the distributed load in wavelet space is

$$_{(n\text{ x }1)}\{\boldsymbol{f}_{\boldsymbol{b,e}}^{\boldsymbol{d,w}}\} = \int_{0}^{1} f_d(\xi)\{\boldsymbol{\Phi}_{\boldsymbol{z}}^{\boldsymbol{j}}(\xi)\}^{T} d\xi \tag{5.96}$$

In this case the equivalent concentrated loads are a combination of elemental node forces and moments at each elemental end node. It must be therefore noted that the equivalent concentrated loads are dependent on the representation of the beam element DOFs and layout initially selected. By applying the beam wavelet transformation matrix $[\boldsymbol{T}_{\boldsymbol{b}}^{\boldsymbol{w}}]$, the load vector in equation (5.96) is transformed into physical space and is expressed as:

$$_{(n\text{ x }1)}\{\boldsymbol{f}_{\boldsymbol{b,e}}^{\boldsymbol{d,p}}\} = L_e\,{}_{(n\text{ x }n)}[\boldsymbol{T}_{\boldsymbol{b}}^{\boldsymbol{w}}]^{T}\ {}_{(n\text{ x }1)}\{\boldsymbol{f}_{\boldsymbol{b,e}}^{\boldsymbol{d,p}}\} \tag{5.97}$$

The total force vector of the external loads in physical space acting on the beam element, $\{\boldsymbol{f}_{\boldsymbol{b,e}}^{\boldsymbol{p}}\}$, is sum of the nodal concentrated forces, nodal bending moments and the distributed force nodal equivalents given in equations(5.94), (5.95) and (5.97) respectively.

$$_{(n\text{ x }1)}\{\boldsymbol{f}_{\boldsymbol{b,e}}^{\boldsymbol{p}}\} = {}_{(n\text{ x }1)}\{\boldsymbol{f}_{\boldsymbol{b,e}}^{\boldsymbol{n,p}}\} + {}_{(n\text{ x }1)}\{\boldsymbol{f}_{\boldsymbol{b,e}}^{\boldsymbol{m,p}}\} + {}_{(n\text{ x }1)}\{\boldsymbol{f}_{\boldsymbol{b,e}}^{\boldsymbol{d,p}}\} \tag{5.98}$$

5.2.3. Mass matrix formulation

The transverse kinetic energy, Λ_e^b, of the beam element is

$$\Lambda_e^b = \frac{1}{2}\rho A L_e \int_0^1 \dot{v}(\xi)^T\ \dot{v}(\xi) d\xi \tag{5.99}$$

where $\dot{v}(\xi) = \frac{\partial v(\xi)}{\partial t}$, ρ is the density of the beam and A is the cross-sectional area of the beam. The wavelet based approximations of the displacements, via the scaling functions, are substituted into equation (5.99). Thus, the kinetic energy becomes

$$\Lambda_e^b = \{\dot{\boldsymbol{v}}_e\}^T \frac{1}{2} \rho A L_e \int_0^1 [\boldsymbol{T}_b^w]^T \left\{\boldsymbol{\Phi}_z^j(\xi)\right\}^T \left\{\boldsymbol{\Phi}_z^j(\xi)\right\} [\boldsymbol{T}_b^w] \, d\xi \, \{\dot{\boldsymbol{v}}_e\} \tag{5.100}$$

The mass matrix for the beam element in wavelet space from equation (5.100) is

$$_{(n \text{ x } n)}[\boldsymbol{m}_{b,e}^w] = \int_0^1 \left\{\boldsymbol{\Phi}_z^j(\xi)\right\}^T \left\{\boldsymbol{\Phi}_z^j(\xi)\right\} d\xi \tag{5.101}$$

Therefore, the mass matrix of the Euler Bernoulli beam WFE, formulated using a wavelet family of order *z* and multiresolution scale *j*, is given as:

$$[\boldsymbol{m}_{b,e}^w] = \begin{bmatrix} m_{h,h}^{z,j}{}_{\boldsymbol{b}} & m_{h,h+1}^{z,j}{}_{\boldsymbol{b}} & \cdots & m_{h,2^j-2}^{z,j}{}_{\boldsymbol{b}} & m_{h,2^j-1}^{z,j}{}_{\boldsymbol{b}} \\ m_{h+1,h}^{z,j}{}_{\boldsymbol{b}} & m_{h+1,h+1}^{z,j}{}_{\boldsymbol{b}} & \cdots & m_{h+1,2^j-2}^{z,j}{}_{\boldsymbol{b}} & m_{h+1,2^j-1}^{z,j}{}_{\boldsymbol{b}} \\ \vdots & \vdots & \ddots & \vdots & \vdots \\ m_{2^j-2,h}^{z,j}{}_{\boldsymbol{b}} & m_{2^j-2,h+1}^{z,j}{}_{\boldsymbol{b}} & \cdots & m_{2^j-2,2^j-2}^{z,j}{}_{\boldsymbol{b}} & m_{2^j-2,2^j-1}^{z,j}{}_{\boldsymbol{b}} \\ m_{2^j-1,h}^{z,j}{}_{\boldsymbol{b}} & m_{2^j-1,h+1}^{z,j}{}_{\boldsymbol{b}} & \cdots & m_{2^j-1,2^j-2}^{z,j}{}_{\boldsymbol{b}} & m_{2^j-1,2^j-1}^{z,j}{}_{\boldsymbol{b}} \end{bmatrix} \tag{5.102}$$

where

$$m_{k,l}^{z,j}{}_{\boldsymbol{b}} = \int_0^1 \phi_{z,k}^j(\xi) \phi_{z,l}^j(\xi) d\xi \tag{5.103}$$

The mass matrix in physical space is therefore,

$$[\boldsymbol{m}_{b,e}^p] = \rho A L_e [\boldsymbol{T}_b^w]^T \int_0^1 \left\{\boldsymbol{\Phi}_z^j(\xi)\right\}^T \left\{\boldsymbol{\Phi}_z^j(\xi)\right\} d\xi \, [\boldsymbol{T}_b^w]$$

$$_{(n \text{ x } n)}[\boldsymbol{m}_{b,e}^p] = \rho A L_e \;\; _{(n \text{ x } n)}[\boldsymbol{T}_b^w]^T \; _{(n \text{ x } n)}[\boldsymbol{m}_{b,e}^w]_{(n \text{ x } n)} [\boldsymbol{T}_b^w] \tag{5.104}$$

and subsequently the kinetic energy of the beam WFE becomes

$$\Lambda_e^b = \frac{1}{2} \, _{(1 \text{ x } n)}\{\dot{\boldsymbol{v}}_e\}^T \, _{(n \text{ x } n)}[\boldsymbol{m}_{b,e}^p]_{(n \text{ x } 1)}\{\dot{\boldsymbol{v}}_e\} \tag{5.105}$$

It is worth mentioning that the stiffness and mass matrices, both in wavelet and physical space, are symmetric.

5.2.4. Assembly and application of boundary conditions

The global system wavelet based beam stiffness matrix, mass matrix and load vector in physical space, for a beam made up of n_e elements, are given by:

$$[\boldsymbol{K}_b] = \sum_{e=1}^{n_e} [\boldsymbol{K}_{b,e}^p] \tag{5.106}$$

$$[\boldsymbol{M_b}] = \sum_{e=1}^{n_e} [\boldsymbol{M_{b,e}^p}] \tag{5.107}$$

$$\{\boldsymbol{F_b}\} = \sum_{e=1}^{n_e} \{\boldsymbol{F_{b,e}^p}\} \tag{5.108}$$

The boundary conditions can then be applied by omitting the corresponding rows and columns, thus reducing the size of the overall system matrices and load vectors. The deflection and rotation DOFs at corresponding nodal points are obtained by solving the system equations describing the Euler-Bernoulli beam static behaviour, which is expressed as:

$$[\boldsymbol{K_b}]\{\boldsymbol{V_b}\} = \{\boldsymbol{F_b}\} \tag{5.109}$$

where the vector $\{\boldsymbol{V_b}\}$ contains the system DOFs. The dynamic response of an undamped beam system is obtained by evaluating the global system governing equation described by:

$$[\boldsymbol{M_b}]\{\ddot{\boldsymbol{V}}_{\boldsymbol{b}}\} + [\boldsymbol{K_b}]\{\boldsymbol{V_b}\} = \{\boldsymbol{F_b}\} \tag{5.110}$$

where $\{\ddot{\boldsymbol{V}}_{\boldsymbol{b}}\}$ is the vector containing the accelerations at the nodal points of the beam.

5.2.5. Beam stresses and strains

According to the Euler-Bernoulli beam theory, the relation of the axial and transverse displacement within the wavelet based beam elements is expressed as $u(x) = -y\frac{\partial v(x)}{\partial x}$ [31]. The strain, at a point ξ within the beam WFE *e*, for a static case, is given as:

$$\varepsilon_e^b(\xi) = \frac{\partial u(x)}{\partial x} = -\frac{y}{{L_e}^2}\frac{\partial^2 v(\xi)}{\partial \xi^2} = -\frac{y}{{L_e}^2}\frac{\partial^2}{\partial \xi^2}\{\boldsymbol{N_{b,e}}(\xi)\}\{\boldsymbol{v_e}\}$$

$$\varepsilon_e^b(\xi) = -\frac{y}{{L_e}^2}\{\boldsymbol{N''_{b,e}}(\xi)\}\{\boldsymbol{v_e}\} \tag{5.111}$$

The normal bending stress is evaluated from the strain as follows:

$$\sigma_e^b(\xi) = E\varepsilon_e^b(\xi) = -\frac{yE}{{L_e}^2}\{\boldsymbol{N''_{b,e}}(\xi)\}\{\boldsymbol{v_e}\} \tag{5.112}$$

where $\{\boldsymbol{N''_{b,e}}(\xi)\}$ is the second derivative of the WFE shape function vector obtained in equation (5.80). Thus,

$$_{(1\ x\ n)}\{\boldsymbol{N''_{b,e}}(\xi)\} = {}_{(1\ x\ n)}\{\boldsymbol{\Phi''^{j}_{z}}(\xi)\}\ {}_{(n\ x\ n)}[\boldsymbol{T_b^w}] \tag{5.113}$$

The strain and stress vectors for the beam WFE, containing the strains and stresses at each elemental node, can be evaluated as follows:

$$\{\varepsilon_e^b\} = -\frac{y}{{L_e}^2}\begin{bmatrix} \{\boldsymbol{N''_{b,e}}(\xi_1)\} \\ \{\boldsymbol{N''_{b,e}}(\xi_2)\} \\ \vdots \\ \{\boldsymbol{N''_{b,e}}(\xi_{r-1})\} \\ \{\boldsymbol{N''_{b,e}}(\xi_r)\} \end{bmatrix}\{\boldsymbol{v_e}\} \tag{5.114}$$

$$\{\sigma_e^b\} = E\,\{\varepsilon_e^b\} = -\frac{yE}{{L_e}^2}\begin{bmatrix} \{\boldsymbol{N''_{b,e}}(\xi_1)\} \\ \{\boldsymbol{N''_{b,e}}(\xi_2)\} \\ \vdots \\ \{\boldsymbol{N''_{b,e}}(\xi_{r-1})\} \\ \{\boldsymbol{N''_{b,e}}(\xi_r)\} \end{bmatrix}\{\boldsymbol{v_e}\} \tag{5.115}$$

The curvature of the WFE beam is evaluated from the relation $\kappa_e^b(\xi) = \frac{1}{{L_e}^2}\frac{\partial^2 v(\xi)}{\partial \xi^2}$. Therefore,

$$\kappa_e^b(\xi) = \frac{1}{{L_e}^2}\{\boldsymbol{N''_{b,e}}(\xi)\}\{\boldsymbol{v_e}\} \tag{5.116}$$

The bending moment at natural coordinate ξ within the beam WFE is expressed as:

$$\acute{M}_e^b(\xi) = -\frac{EI}{{L_e}^2}\{\boldsymbol{N''_{b,e}}(\xi)\}\{\boldsymbol{v_e}\} \tag{5.117}$$

Furthermore, the shear force within the Euler Bernoulli beam wavelet based finite element is given as:

$$Q_e^b(\xi) = -\frac{EI}{{L_e}^3}\{\boldsymbol{N'''_{b,e}}(\xi)\}\{\boldsymbol{v_e}\} \tag{5.118}$$

where

$$_{(1\,\mathrm{x}\,n)}\{\boldsymbol{N'''^{e}_{b}}\} = _{(1\,\mathrm{x}\,n)}\left\{\frac{\partial^3 \boldsymbol{\Phi_z^j}(\xi_i)}{\partial \xi^3}\right\}\,_{(n\,\mathrm{x}\,n)}[\boldsymbol{T_b^w}] \tag{5.119}$$

The vectors containing the curvature, bending moments and shear forces within the beam WFE, at elemental nodes, can be evaluated by implementing the matrix containing the corresponding derivatives of shape functions.

5.2.6. Wavelet based moving load vector

Moving load problems are often characterised by the loading conditions varying in location and/or magnitude with respect to time. Consider a simply supported beam subjected to a moving load, represented by the function $q(x,t) = P\delta(x - x_0)$, where *P* is the magnitude of the moving point load, $\delta(x)$ is the Dirac Delta function and x_0 is the distance travelled by the moving load at time *t* from the left edge of the beam. The strain and kinetic energy of the

beam WFE are evaluated as presented in Sections 5.2.1 and 5.2.3 respectively. In order to demonstrate the evaluation of the wavelet based moving load vectors, consider a moving point load travelling across a beam wavelet finite element as illustrated in Figure 5-7.

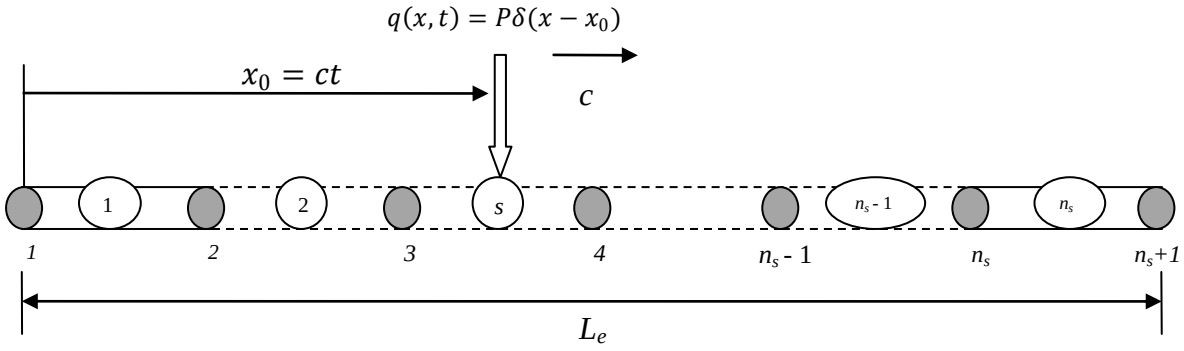

Figure 5-7: Layout of a beam WFE subjected to a moving point load.

Assuming the beam is modelled using one wavelet based finite element, the moving load travelling at a constant speed of c m·s^{-1} is expressed as:

$$q(x,t) = P\delta(x - x_0) \tag{5.120}$$

where $x_0 = ct$ is the distance travelled by the load at time t. The position of the moving load in natural coordinates, within the WFE at time t s is

$$\xi_0 = \frac{x_0}{L_e} \tag{5.121}$$

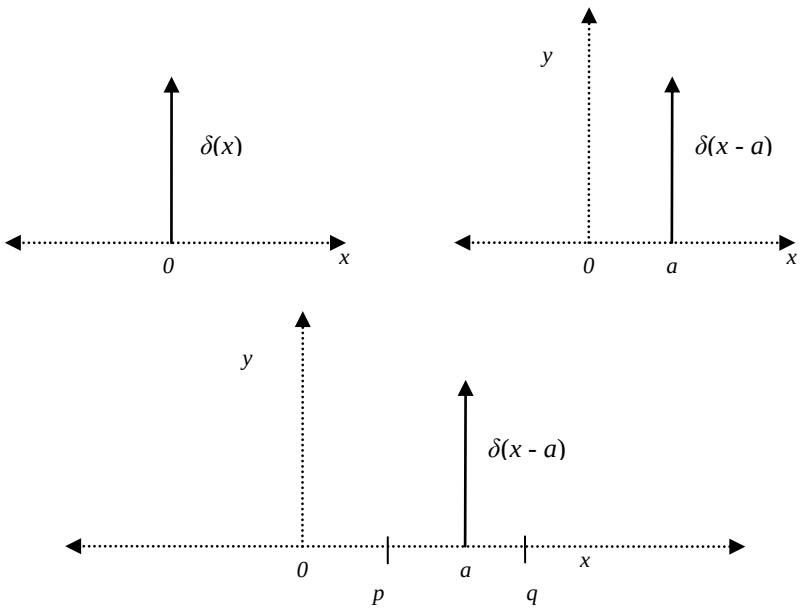

Figure 5-8: The Dirac Delta function.

The Dirac Delta function $\delta(x)$, or otherwise known as the unit impulse function, is defined by the following properties [101]:

$$\delta(x) = \begin{cases} 0 & x \neq 0 \\ \infty & x = 0 \end{cases} \tag{5.122}$$

$$\delta(x-a) = \begin{cases} 0 & x \neq a \\ \infty & x = a \end{cases} \tag{5.123}$$

$$\int_{-\infty}^{\infty} \delta(x)dx = \int_{-\infty}^{\infty} \delta(x-a)dx = 1 \tag{5.124}$$

$$\int_{-\infty}^{\infty} f(x)\,\delta(x)dx = f(x) \tag{5.125}$$

Alternatively, the Dirac function may be defined as the derivative of the unit step Heaviside function, $H(x)$, as follows [102]:

$$\delta(x) = \frac{dH(x)}{dx} \tag{5.126}$$

From equation (5.124), the Dirac function has a unit area. Therefore, as illustrated in Figure 5-8, given that $p < a < q$ [102],

$$\int_{-\infty}^{\infty} f(x)\,\delta(x-a)dx = f(a)$$

$$\int_{p}^{q} f(x)\,\delta(x-a)dx = \begin{cases} 0 & a < p < q \\ f(a) & p < a < q \\ 0 & p < q < a \end{cases} \tag{5.127}$$

The n^{th} derivative of the Dirac function is expressed as:

$$\int_{p}^{q} f(x)\,\delta^n(x-a)dx = \begin{cases} 0 & a < p < q \\ (-1)^n f^{(n)}(a) & p < a < q \\ 0 & p < q < a \end{cases} \tag{5.128}$$

Furthermore,

$$\delta(ax) = \frac{1}{a}\delta(x) \tag{5.129}$$

At a given time t, the moving load is at position ξ_0 and the potential work of the load at that instant is therefore expressed as:

$$\Omega_e^b(\xi_0) = \int_0^1 P\delta(\xi-\xi_0)v(\xi)d\xi = P\{\boldsymbol{v_e}\}^T \int_0^1 {}_{(1\,x\,n)}\{\boldsymbol{N_{b,e}}(\xi)\}^T \delta(\xi-\xi_0)d\xi$$

$$\Omega_e^b(\xi_0) = P_{(1\,x\,n)}\{\boldsymbol{v_e}\}^T\{\boldsymbol{N_{b,e}}(\xi_0)\}^T = P\,\{\boldsymbol{v_e}\}^T[\boldsymbol{T_b^w}]^T\{\boldsymbol{\Phi_z^j}(\xi_0)\}^T \tag{5.130}$$

Thus, the element load vector in wavelet space is obtained from equation (5.130) as

$$_{(n \text{ x } 1)}\left\{\boldsymbol{f}_{\boldsymbol{b,e}}^{\boldsymbol{p,w}}(t)\right\} = \left\{\boldsymbol{\Phi}_{\boldsymbol{z}}^{\boldsymbol{j}}(\xi_0)\right\}^T \tag{5.131}$$

and subsequently in physical space as:

$$_{(n \text{ x } 1)}\left\{\boldsymbol{f}_{\boldsymbol{b,e}}^{\boldsymbol{p,p}}(t)\right\} = \begin{Bmatrix} f_{y1} \\ \acute{m}_1 \\ f_{y2} \\ f_{y3} \\ \vdots \\ f_{yr-1} \\ f_{yr} \\ \acute{m}_r \end{Bmatrix} = P\,[\boldsymbol{T}_{\boldsymbol{b}}^{\boldsymbol{w}}]^T\left\{\boldsymbol{\Phi}_{\boldsymbol{z}}^{\boldsymbol{j}}(\xi_0)\right\}^T \tag{5.132}$$

The vector $\left\{\boldsymbol{f}_{\boldsymbol{b,e}}^{\boldsymbol{p,p}}(\boldsymbol{t})\right\}$ contains the equivalent WFE nodal forces and moments of the moving load, acting on element *e* in physical space, corresponding to the moving load position ξ_0 at time *t*, as illustrated in Figure 5-7. Given that the location and/or magnitude of the load varies with time and assuming at a new time the moving load is still acting within the same WFE, the new load vector is obtained via the scaling functions in equation (5.131) with respect to the new location of the moving load in natural coordinates i.e., the new value of position ξ_0. The numerical values of the shape functions, and consequently the load vector in wavelet space, will change according to this new external force location. Subsequently, the load vector in physical space corresponding to the new location with respect to time is evaluated by implementing the wavelet transformation matrix to the new wavelet space load vector. The other WFEs within the system that have no action of an external load at a particular time *t* have zero entries within the load vectors. When the moving load is acting on a new WFE, the scaling functions corresponding to the WFE subjected to the moving load are used to obtain the load vector for that particular element. Hence, it is evident that as the moving load travels from one WFE to the next, there is a shift in position of the equivalent WFE load vector with nonzero entries.

It is important to note that the forces and moments within the WFE load vector are dependent on the layout of the element selected, which in this case has the rotation DOFs only at the elemental end nodes and thus, the moments are only present at these corresponding nodes. Therefore, if the layout is altered and a rotation DOF is present within an inner elemental node, then a moment DOF will be present at the corresponding nodal position within the wavelet based element.

5.2.7. Beam on elastic foundation subjected to a moving load

Figure 5-9 is a diagram illustrating a simply supported beam resting on an elastic foundation. A beam of length *l*, is assumed to have a uniform cross-sectional area *A*, Young's modulus *E*, moment of inertia *I* and mass per unit length μ. k_f is the stiffness of the elastic foundation. The beam is subjected to a moving point load of magnitude *P* travelling at *c* m·s^{-1}.

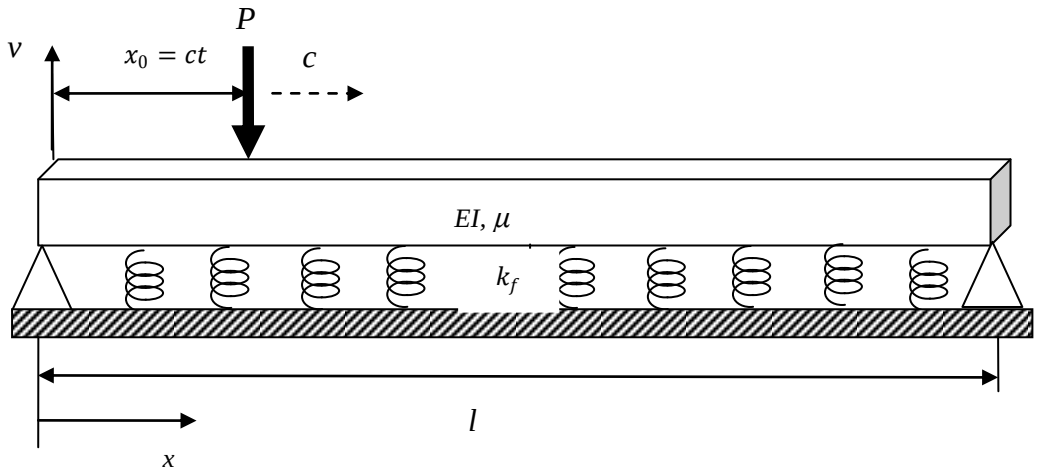

Figure 5-9: Simply supported uniform beam on an elastic foundation subjected to a moving point load.

The foundation is assumed to be a Winker foundation where force-deflection relationship is linear. Therefore, the beam wavelet finite element, as described in Figure 5-6, is resting on a series of closely spaced linear elastic springs representing the stiffness of the elastic foundation [103]. The total potential energy of the system is generalised as [104]:

$$\Pi^b = \int_0^l \frac{EI}{2}\left(\frac{d^2v}{dx^2}\right)^2 dx - \int_0^l P\delta(x - x_0)v dx + \int_0^l \frac{k_f}{2}v^2\, dx \qquad \textbf{(5.133)}$$

while the kinetic energy within each WFE of length L_e is given as

$$\Lambda_e^b = \frac{1}{2}\rho A \int_0^{L_e} \dot{v}^2\, dx \qquad \textbf{(5.134)}$$

and the strain energy due to bending of the beam WFE is

$$U_e^b = \int_0^{L_e} \frac{EI}{2}\left(\frac{d^2v}{dx^2}\right)^2 dx \qquad \textbf{(5.135)}$$

The work potential of the moving load travelling on the WFE is expressed as

$$\Omega_e^b = \int_0^{L_e} P\delta(x - x_0)v dx \qquad \textbf{(5.136)}$$

The strain energy, kinetic energy and work potential of the moving load for the WFE can be evaluated as described in Sections 5.2.1, 5.2.3 and 5.2.6 respectively. The potential energy of the elastic foundation on which the beam WFE is resting on is expressed as [104]:

$$U_e^f = \frac{k_f L_e}{2} \int_0^1 v(\xi)^T \, v(\xi) d\xi \tag{5.137}$$

The displacement field variable is expressed in terms of the wavelet scaling functions and therefore equation (5.137) becomes:

$$U_e^f = \frac{k_f L_e}{2} \{\boldsymbol{v_e}\}^T \int_0^1 [\boldsymbol{T_b^w}]^T \left\{\boldsymbol{\Phi_z^j}(\xi)\right\}^T \left\{\boldsymbol{\Phi_z^j}(\xi)\right\} [\boldsymbol{T_b^w}] d\xi \, \{\boldsymbol{v_e}\} \tag{5.138}$$

Therefore, the foundation stiffness matrix in wavelet space is evaluated as:

$$[\boldsymbol{k_{f,e}^w}] = \int_0^1 \left\{\boldsymbol{\Phi_z^j}(\xi)\right\}^T \left\{\boldsymbol{\Phi_z^j}(\xi)\right\} d\xi \tag{5.139}$$

Hence, the stiffness matrix of the foundation formulated using a wavelet family of order *z* and at multiresolution scale *j* is given as:

$$[\boldsymbol{k_{f,e}^w}] = \begin{bmatrix} k_{h,h}^{z,j}{}_{\boldsymbol{f}} & k_{h,h+1}^{z,j}{}_{\boldsymbol{f}} & \cdots & k_{h,2^j-2}^{z,j}{}_{\boldsymbol{f}} & k_{h,2^j-1}^{z,j}{}_{\boldsymbol{f}} \\ k_{h+1,h}^{z,j}{}_{\boldsymbol{f}} & k_{h+1,h+1}^{z,j}{}_{\boldsymbol{f}} & \cdots & k_{h+1,2^j-2}^{z,j}{}_{\boldsymbol{f}} & k_{h+1,2^j-1}^{z,j}{}_{\boldsymbol{f}} \\ \vdots & \vdots & \ddots & \vdots & \vdots \\ k_{2^j-2,h}^{z,j}{}_{\boldsymbol{f}} & k_{2^j-2,h+1}^{z,j}{}_{\boldsymbol{f}} & \cdots & k_{2^j-2,2^j-2}^{z,j}{}_{\boldsymbol{f}} & k_{2^j-2,2^j-1}^{z,j}{}_{\boldsymbol{f}} \\ k_{2^j-1,h}^{z,j}{}_{\boldsymbol{f}} & k_{2^j-1,h+1}^{z,j}{}_{\boldsymbol{f}} & \cdots & k_{2^j-1,2^j-2}^{z,j}{}_{\boldsymbol{f}} & k_{2^j-1,2^j-1}^{z,j}{}_{\boldsymbol{f}} \end{bmatrix} \tag{5.140}$$

where

$$k_{k,l}^{z,j}{}_{\boldsymbol{f}} = \int_0^1 \phi_{z,k}^j(\xi) \phi_{z,l}^j(\xi) d\xi \tag{5.141}$$

The matrix in equation (5.140) is equivalent to the wavelet space mass matrix of the beam as described in equation (5.102). Therefore, once the wavelet space mass matrices of the beam are evaluated for different wavelet orders and multiresolution scales, the matrices can be stored and used in the evaluation of the stiffness matrix for the elastic foundation so as to reduce the computational costs. The wavelet space foundation stiffness matrix is also transformed into physical space via the wavelet transformation matrix and is obtained as:

$$[\boldsymbol{k_{f,e}^p}] = k_f L_e \int_0^1 [\boldsymbol{T_b^w}]^T \left\{\boldsymbol{\Phi_z^j}(\xi)\right\}^T \left\{\boldsymbol{\Phi_z^j}(\xi)\right\} [\boldsymbol{T_b^w}] d\xi$$

$$_{(n\,x\,n)}[\boldsymbol{k}_{\boldsymbol{f,e}}^{\boldsymbol{p}}] = k_f L_{e\,(n\,x\,n)}[\boldsymbol{T}_{\boldsymbol{b}}^{\boldsymbol{w}}]^T{}_{(n\,x\,n)}[\boldsymbol{k}_{\boldsymbol{f,e}}^{\boldsymbol{w}}]_{(n\,x\,n)}[\boldsymbol{T}_{\boldsymbol{b}}^{\boldsymbol{w}}] \quad \textbf{(5.142)}$$

Therefore, the strain energy within the section of the foundation on which the wavelet based beam element is resting on is obtained by substituting equation (5.142) into (5.138).

$$U_e^f = \frac{1}{2}\{\boldsymbol{v_e}\}^T[\boldsymbol{k}_{\boldsymbol{f,e}}^{\boldsymbol{p}}]\ \{\boldsymbol{v_e}\} \quad \textbf{(5.143)}$$

When a system is damped, energy is dissipated from the system. Therefore, the dissipated energy of a viscoelastic foundation section, which has viscous damping effects taken into consideration with a WFE resting on it, is given as:

$$D_e^f = \frac{d_f}{2}\int_0^{L_e} v(x)^T\, v(x)dx = \frac{d_f L_e}{2}\int_0^1 v(\xi)^T\, v(\xi)d\xi \quad \textbf{(5.144)}$$

where d_f is the viscous damping of the foundation. Substituting equation (5.72) into (5.144)

$$D_e^f = \frac{d_f L_e}{2}\{\boldsymbol{v_e}\}^T\int_0^1 [\boldsymbol{T}_{\boldsymbol{b}}^{\boldsymbol{w}}]^T\left\{\boldsymbol{\Phi}_{\boldsymbol{z}}^{\boldsymbol{j}}(\xi)\right\}^T\left\{\boldsymbol{\Phi}_{\boldsymbol{z}}^{\boldsymbol{j}}(\xi)\right\}[\boldsymbol{T}_{\boldsymbol{b}}^{\boldsymbol{w}}]d\xi\,\{\boldsymbol{v_e}\} \quad \textbf{(5.145)}$$

The foundation viscous damping matrix in wavelet space is evaluated as:

$$[\boldsymbol{c}_{\boldsymbol{f,e}}^{\boldsymbol{w}}] = \int_0^1 \left\{\boldsymbol{\Phi}_{\boldsymbol{z}}^{\boldsymbol{j}}(\xi)\right\}^T\left\{\boldsymbol{\Phi}_{\boldsymbol{z}}^{\boldsymbol{j}}(\xi)\right\}d\xi \quad \textbf{(5.146)}$$

The damping matrix in equation (5.146) can also be evaluated from the already stored wavelet space mass matrix of the beam as described in equation (5.102). The physical space foundation damping matrix is obtained via the transformation of the wavelet space damping matrix using the wavelet transformation matrix.

$$[\boldsymbol{c}_{\boldsymbol{f,e}}^{\boldsymbol{p}}] = d_f L_e\int_0^1 [\boldsymbol{T}_{\boldsymbol{b}}^{\boldsymbol{w}}]^T\left\{\boldsymbol{\Phi}_{\boldsymbol{z}}^{\boldsymbol{j}}(\xi)\right\}^T\left\{\boldsymbol{\Phi}_{\boldsymbol{z}}^{\boldsymbol{j}}(\xi)\right\}[\boldsymbol{T}_{\boldsymbol{b}}^{\boldsymbol{w}}]d\xi$$

$$_{(n\,x\,n)}[\boldsymbol{c}_{\boldsymbol{f,e}}^{\boldsymbol{p}}] = d_f L_{e\,(n\,x\,n)}[\boldsymbol{T}_{\boldsymbol{b}}^{\boldsymbol{w}}]^T{}_{(n\,x\,n)}[\boldsymbol{c}_{\boldsymbol{f,e}}^{\boldsymbol{w}}]_{(n\,x\,n)}[\boldsymbol{T}_{\boldsymbol{b}}^{\boldsymbol{w}}] \quad \textbf{(5.147)}$$

5.2.8. Daubechies Euler Bernoulli beam wavelet finite element

For a Daubechies wavelet of order *L* and multiresolution scale *j*, the lowest order that can be theoretically implemented to formulate the Euler Bernoulli C^1 WFE is D*6*; since a Daubechies wavelet of order *L* can represent a polynomial of order equal to but not greater than $\frac{L}{2} - 1$ [10,36]. The vertical displacement and rotation within the WFE, with respect to the natural coordinates, are given as [6,10]:

$$v(\xi) = \sum_{k=2-L}^{2^j-1} b_{L,k}^j \, \phi_{L,k}^j(\xi) \tag{5.148}$$

$$\theta(\xi) = \frac{1}{L_e} \sum_{k=2-L}^{2^j-1} b_{L,k}^j \, \frac{\partial \phi_{L,k}^j(\xi)}{\partial \xi} \tag{5.149}$$

The total DOFs within a single Daubechies based element is $n = 2^j + L - 2$. Therefore, specific to this case with the rotation DOFs present only at the elemental end nodes, the total number of elemental nodes is $r = 2^j + L - 4$ and corresponding elemental segments $n_s = 2^j + L - 5$. The Daubechies based beam WFE shape functions are obtained from equation (5.80) as

$$\underset{(1 \text{ x } n)}{^D}\{\boldsymbol{N_{b,e}}(\xi)\} = \underset{(1 \text{ x } n)}{^D}\{\boldsymbol{\Phi_L^j}(\xi)\} \; \underset{(n \text{ x } n)}{^D}[\boldsymbol{T_b^w}] \tag{5.150}$$

where $^D[\boldsymbol{T_b^w}]$ is the Daubechies wavelet transformation matrix for the beam WFE. Figure 5-10 includes the plots of the shape functions $N_k(\xi)$ and $N_k(\xi_i)$, where $1 \leq k \leq n$ and $1 \leq i \leq r$, for the D10_0 beam WFE. It is observed that although the shape functions are not bound by $0 \leq N_k(\xi) \leq 1$, the completeness, compatibility and delta function properties are satisfied. This is the case for the Daubechies based beam WFE of order $L \geq 6$; at any multiresolution scale $j \geq 0$. This implies that convergence of the approximate field variables to the exact solution is ensured.

As earlier mentioned, the Daubechies WFE formulation requires the evaluation of the connection coefficients to obtain the wavelet based element matrices and distributed load vectors. The stiffness matrix in wavelet space is obtained from the two-term connection coefficients of the form:

$${}_{L,L}\Gamma_{k,l}^{j,2,2} = \int_0^1 \phi_L^{(2)}(2^j\xi - k)\phi_L^{(2)}(2^j\xi - l)d\xi \tag{5.151}$$

for the limits $2 - L \leq k, l \leq 2^j - 1$. The mass matrix is obtained from the two-term connection coefficients

$${}_{L,L}\Gamma_{k,l}^{j,0,0} = \int_0^1 \phi_L^{(0)}(2^j\xi - k)\phi_L^{(0)}(2^j\xi - l)d\xi \tag{5.152}$$

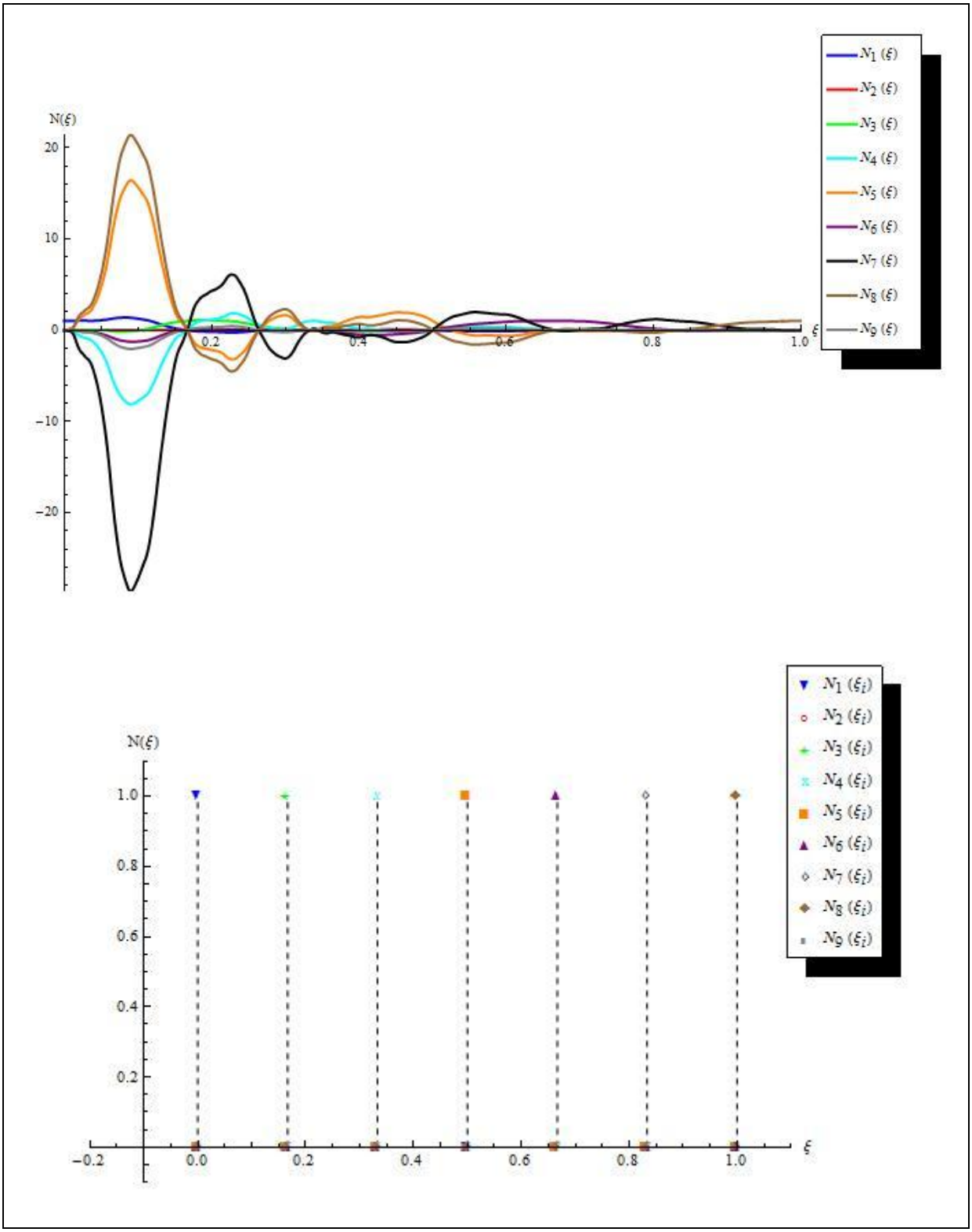

Figure 5-10 : Daubechies wavelet based beam element shape functions $N_k(\xi)$ and $N_k(\xi_i)$ for D10_0 WFE.

Therefore, the wavelet space stiffness and mass matrices of the Euler Bernoulli beam WFE from equations (5.86) and (5.101) can be expressed as:

$$\left((2^j+L-2)\text{ x }(2^j+L-2)\right)^{D}[\boldsymbol{k}^{\boldsymbol{w}}_{\boldsymbol{b,e}}] = 2^{4j}\left[\boldsymbol{\Gamma}^{j,2,2}\right] \qquad \textbf{(5.153)}$$

$$\left((2^j+L-2)\text{ x }(2^j+L-2)\right)^{D}[\boldsymbol{m}^{\boldsymbol{w}}_{\boldsymbol{b},\boldsymbol{e}}] = \left[\boldsymbol{\Gamma}^{j,0,0}\right] \tag{5.154}$$

In physical space, the Daubechies Euler Bernoulli beam WFE stiffness and mass matrices are evaluated as:

$$\begin{aligned}&\left((2^j+L-2)\text{ x }(2^j+L-2)\right)^{D}[\boldsymbol{k}^{\boldsymbol{p}}_{\boldsymbol{b},\boldsymbol{e}}]\\&= \frac{E\,I}{{L_e}^3}\left((2^j+L-2)\text{ x }(2^j+L-2)\right)^{D}[\boldsymbol{T}^{\boldsymbol{w}}_{\boldsymbol{b}}]^T\left((2^j+L-2)\text{ x }(2^j+L-2)\right)^{D}[\boldsymbol{k}^{\boldsymbol{w}}_{\boldsymbol{b},\boldsymbol{e}}]\left((2^j+L-2)\text{ x }(2^j+L-2)\right)^{D}[\boldsymbol{T}^{\boldsymbol{w}}_{\boldsymbol{b}}]\end{aligned} \tag{5.155}$$

$$\begin{aligned}&\left((2^j+L-2)\text{ x }(2^j+L-2)\right)^{D}[\boldsymbol{m}^{\boldsymbol{p}}_{\boldsymbol{b},\boldsymbol{e}}]\\&= \rho A L_e\left((2^j+L-2)\text{ x }(2^j+L-2)\right)^{D}[\boldsymbol{T}^{\boldsymbol{w}}_{\boldsymbol{b}}]^T\left((2^j+L-2)\text{ x }(2^j+L-2)\right)^{D}[\boldsymbol{m}^{\boldsymbol{w}}_{\boldsymbol{b},\boldsymbol{e}}]\left((2^j+L-2)\text{ x }(2^j+L-2)\right)^{D}[\boldsymbol{T}^{\boldsymbol{w}}_{\boldsymbol{b}}]\end{aligned} \tag{5.156}$$

For a distributed load, the equivalent nodal load vector in wavelet space is obtained via the connection coefficients of the form $\Upsilon_k^{j,m}$, for $2-L \le k \le 2^j-1$. The function representing the distribution of the load may vary. However, if the load $f_d(\xi) = P$ N·m^{-1} is uniformly distributed along the element, then the load vector in wavelet space is given as:

$$\Upsilon_k^{j,0} = \int_0^1 \xi^0 \phi_L(2^j\xi - k)dx$$

$$\left((2^j+L-2)\text{ x }1\right)^{D}\left\{\boldsymbol{f}^{\boldsymbol{d},\boldsymbol{w}}_{\boldsymbol{b},\boldsymbol{e}}\right\} = \{\boldsymbol{\Upsilon}^{\mathbf{j,0}}\} = \begin{Bmatrix}\Upsilon^{j,0}_{2-L}\\ \Upsilon^{j,0}_{3-L}\\ \vdots\\ \Upsilon^{j,0}_{2^j-2}\\ \Upsilon^{j,0}_{2^j-1}\end{Bmatrix} \tag{5.157}$$

Similarly, for a linearly varying distributed load given by the function $f_d(\xi) = P\,\xi$ N·m^{-1}, the force vector in wavelet space is obtained from the connection coefficients

$$\Upsilon_k^{j,1} = \int_0^1 \xi^1 \phi_L(2^j\xi - k)dx$$

$$\left((2^j+L-2)\text{ x }1\right)^{D}\left\{\boldsymbol{f}^{\boldsymbol{d},\boldsymbol{w}}_{\boldsymbol{b},\boldsymbol{e}}\right\} = \{\boldsymbol{\Upsilon}^{\mathbf{j,1}}\} = \begin{Bmatrix}\Upsilon^{j,1}_{2-L}\\ \Upsilon^{j,1}_{3-L}\\ \vdots\\ \Upsilon^{j,1}_{2^j-2}\\ \Upsilon^{j,1}_{2^j-1}\end{Bmatrix} \tag{5.158}$$

Thus, for a general distributed load function $f_d(\xi) = P\,\xi^m$ N·m^{-1}, the connection coefficients $\Upsilon_k^{j,m}$ are employed to determine the Daubechies wavelet space load vectors for the beam WFE. The Daubechies wavelet transformation matrix $^{D}[\boldsymbol{T}^{\boldsymbol{w}}_{\boldsymbol{b}}]$ is then applied to evaluate the

element load vectors in physical space. Furthermore, the stiffness and damping matrices for a viscoelastic foundation in wavelet space are obtained from the two term connection coefficients described in equation (5.152). The Daubechies wavelet transformation matrix and corresponding foundation coefficients are then applied to the matrices so as to obtain the physical foundation matrices.

5.2.9. BSWI Euler Bernoulli beam wavelet finite element

The unknown transverse displacement and rotation, with respect to the natural coordinate of the Euler Bernoulli beam element, can be expressed using the BSWI family of order *m* and at scale *j* in the formulation of the WFE as [7]:

$$v(\xi) = \sum_{k=-m+1}^{2^j-1} b_{m,k}^{j}\, \phi_{m,k}^{j}(\xi) \tag{5.159}$$

$$\theta(\xi) = \frac{1}{L_e} \sum_{k=-m+1}^{2^j-1} b_{m,k}^{j}\, \frac{\partial \phi_{m,k}^{j}(\xi)}{\partial \xi} \tag{5.160}$$

The total DOFs within the BSWI beam WFE is $n = 2^j + m - 1$, while the total number of elemental nodes is $r = 2^j + m - 3$ and the total number of elemental segments is $n_s = 2^j + m - 4$.

Figure 5-11 contains the Euler-Bernoulli beam shape functions $N_k(\xi)$ and $N_k(\xi_i)$, where $1 \le k \le n$ and $1 \le i \le r$, for the BSWI3_3 WFE. For a C^1 beam element, the order of the BSWI scaling function that can be implemented in the formulation of the WFEs must be $m \ge 3$.

Moreover, the multiresolution scale must be such that the requirement $j \ge j_0$ is satisfied. The BSWI beam WFEs possess the delta function, completeness and compatibility properties of the shape functions as illustrated in Figure 5-11. This ensures the convergence of the approximation field variables to the exact solution. The stiffness and mass matrices in wavelet space can be evaluated directly without calculating connection coefficients and are obtained as:

$$\left((2^j+m-1)\ \mathrm{x}\ (2^j+m-1)\right)^{BS}[\boldsymbol{k}_{b,e}^{w}] = \int_0^1 \{\boldsymbol{\Phi}''^{\boldsymbol{j}}_{\boldsymbol{m}}(\boldsymbol{\xi})\}^T \{\boldsymbol{\Phi}''^{\boldsymbol{j}}_{\boldsymbol{m}}(\boldsymbol{\xi})\} d\xi \tag{5.161}$$

$$\left((2^j+m-1)\ \mathrm{x}\ (2^j+m-1)\right)^{BS}[\boldsymbol{m}_{b,e}^{w}] = \int_0^1 \{\boldsymbol{\Phi}^{\boldsymbol{j}}_{\boldsymbol{m}}(\boldsymbol{\xi})\}^T \{\boldsymbol{\Phi}^{\boldsymbol{j}}_{\boldsymbol{m}}(\boldsymbol{\xi})\} d\xi \tag{5.162}$$

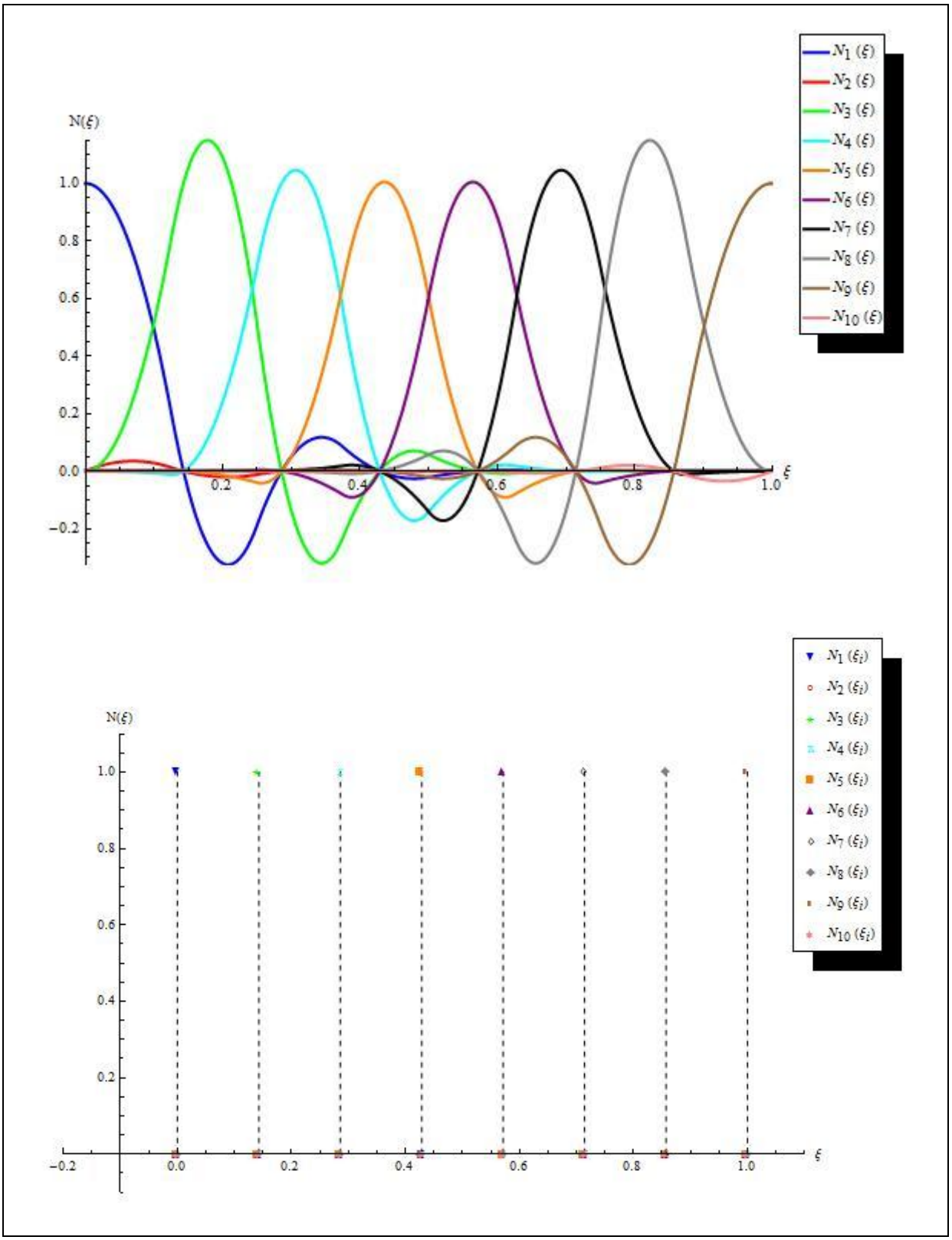

Figure 5-11 : BSWI wavelet based beam element shape functions $N_i(\xi)$ and $N_i(\xi_k)$ for BSWI3_3 WFE.

In physical space, the BSWI Euler Bernoulli beam WFE stiffness and mass matrices are expressed as:

$$\left(\left(2^j+m-1\right)\text{ x }\left(2^j+m-1\right)\right)^{BS}[\boldsymbol{k}_{b,e}^{\boldsymbol{p}}] = \frac{E\,I}{{L_e}^3}\left(\left(2^j+m-1\right)\text{ x }\left(2^j+m-1\right)\right)^{BS}[\boldsymbol{T}_{\boldsymbol{b}}^{\boldsymbol{w}}]^T\left(\left(2^j+m-1\right)\text{ x }\left(2^j+m-1\right)\right)^{BS}[\boldsymbol{k}_{b,e}^{\boldsymbol{w}}]\left(\left(2^j+m-1\right)\text{ x }\left(2^j+m-1\right)\right)^{BS}[\boldsymbol{T}_{\boldsymbol{b}}^{\boldsymbol{w}}] \quad \textbf{(5.163)}$$

$$\left(\left(2^j+m-1\right)\text{ x }\left(2^j+m-1\right)\right)^{BS}[\boldsymbol{m}_{b,e}^{\boldsymbol{p}}] = \rho A L_e\left(\left(2^j+m-1\right)\text{ x }\left(2^j+m-1\right)\right)^{BS}[\boldsymbol{T}_{\boldsymbol{b}}^{\boldsymbol{w}}]^T\left(\left(2^j+m-1\right)\text{ x }\left(2^j+m-1\right)\right)^{BS}[\boldsymbol{m}_{b,e}^{\boldsymbol{w}}]\left(\left(2^j+m-1\right)\text{ x }\left(2^j+m-1\right)\right)^{BS}[\boldsymbol{T}_{\boldsymbol{b}}^{\boldsymbol{w}}] \quad \textbf{(5.164)}$$

Furthermore, for a uniformly distributed load for example $f_d(\xi) = P$ N·m^{-1} acting along the length of the beam, the equivalent load vector in wavelet space of the BSWI element is

$$^{BS}\left\{\boldsymbol{f}_{\boldsymbol{b,e}}^{\boldsymbol{d,w}}\right\} = \int_0^1 \xi^0{}_{\left(1\text{ x }\left(2^j+m-1\right)\right)}\left\{\boldsymbol{\Phi}_{\boldsymbol{m}}^{\boldsymbol{j}}(\boldsymbol{\xi})\right\}^T d\xi \quad \textbf{(5.165)}$$

while for a linearly varying load $f_s(\xi) = P\,\xi$ N·m^{-1}, the equivalent load vector is given as:

$$^{BS}\left\{\boldsymbol{f}_{\boldsymbol{b,e}}^{\boldsymbol{d,w}}\right\} = \int_0^1 \xi^1{}_{\left(1\text{ x }\left(2^j+m-1\right)\right)}\left\{\boldsymbol{\Phi}_{\boldsymbol{m}}^{\boldsymbol{j}}(\boldsymbol{\xi})\right\}^T d\xi \quad \textbf{(5.166)}$$

The BSWI wavelet space foundation stiffness and damping matrices are computed from equation (5.162). The BSWI based WFE matrices and the total load vectors, are then transformed into physical space via the use of the BSWI wavelet beam transformation matrix $^{BS}[\boldsymbol{T}_{\boldsymbol{b}}^{\boldsymbol{w}}]$.

5.3. Two dimensional plane bar wavelet finite element

The two dimensional plane bar element takes into account the axial deformation, transverse deflection and rotation DOFs; it can therefore be subjected to axial and transverse loading as well as bending moments. The plane bar analysed and formulated in this section is assumed to be linearly elastic. Therefore, the two dimensional plane bar WFE is a superposition of the rod and Euler Bernoulli beam WFEs as described in Sections 5.1 and 5.2 respectively. Consider a two dimensional bar WFE, of length L_e, partitioned into n_s equally spaced elemental segments with r number of elemental nodes, at coordinate values x_i in the local x-y coordinate as illustrated in Figure 5-12.

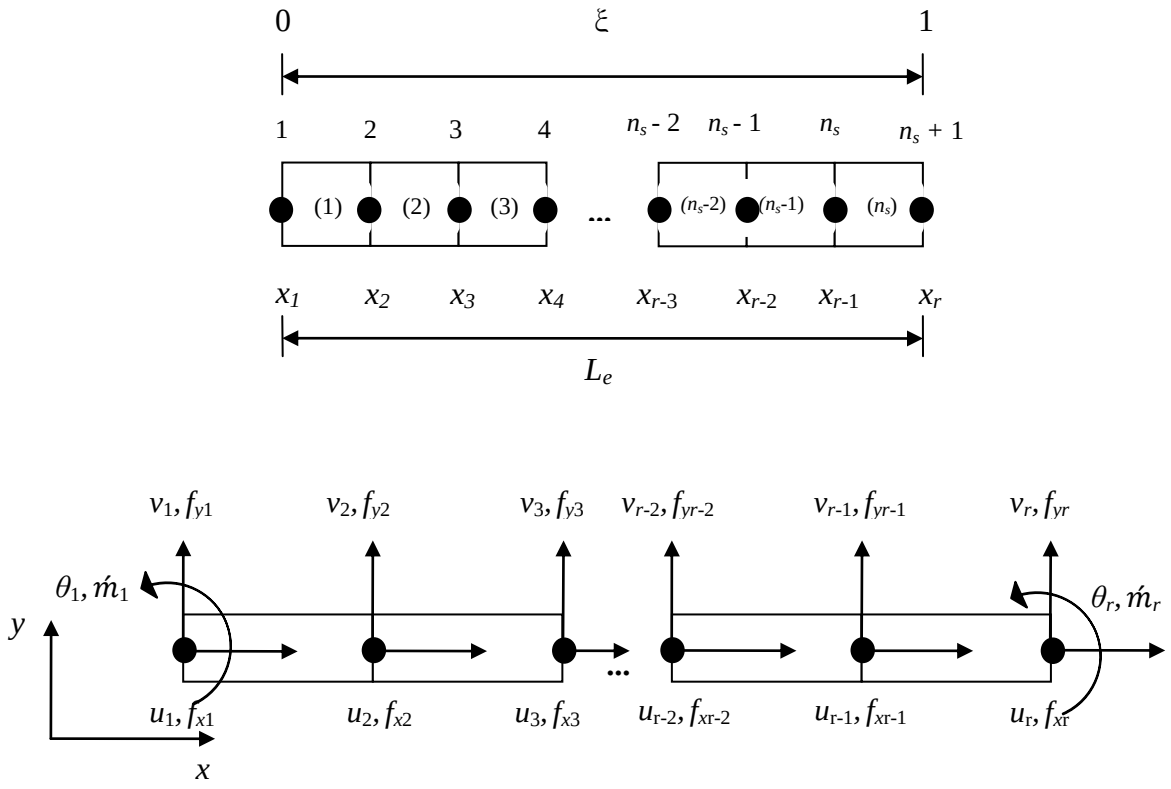

Figure 5-12 : Two dimensional plane bar wavelet finite element layout.

Each elemental node has an axial deformation in the *x* axis, u_i, and transverse displacement in the *y* axis, v_i. Furthermore, only the two end elemental nodes have the rotation about the *z* axis, θ_i. The vector $\{\boldsymbol{h_e}\}$ is defined as the vector containing all the physical DOFs within the plane bar WFE in the local coordinate system.

$$\{\boldsymbol{h_e}\} = \{u_1 \quad v_1 \quad \theta_1 \quad u_2 \quad v_2 \quad u_3 \quad v_3 \quad \cdots \quad u_{r-2} \quad v_{r-2} \quad u_{r-1} \quad v_{r-1} \quad u_r \quad v_r \quad \theta_r\}^T \qquad \textbf{(5.167)}$$

The transverse deflection and rotation of the WFE is approximated using scaling functions as described in equations (5.72) and (5.73) for a wavelet family of order *z* and at multiresolution scale *j*. However, in order to ensure that the axial DOFs correspond to each elemental node, at multiresolution scale *j*, the order of wavelet family used in (5.5) is $z - 2$. The total number of DOFs within the WFE is given by *n*. Therefore, the element DOFs in equation (5.167) can be expressed in terms of the wavelet scaling functions as:

$$\begin{Bmatrix} u_1 \\ v_1 \\ \theta_1 \\ u_2 \\ v_2 \\ u_3 \\ \vdots \\ v_{r-2} \\ u_{r-1} \\ v_{r-1} \\ u_r \\ v_r \\ \theta_r \end{Bmatrix} = \begin{bmatrix} \phi^j_{z-2,h}(\xi_1) & 0 & 0 & \phi^j_{z-2,h+1}(\xi_1) & 0 & \phi^j_{z-2,h+2}(\xi_1) & \cdots & 0 & \phi^j_{z-2,2^j-2}(\xi_1) & 0 & \phi^j_{z-2,2^j-1}(\xi_1) & 0 & 0 \\ 0 & \phi^j_{z,h}(\xi_1) & \phi^j_{z,h+1}(\xi_1) & 0 & \phi^j_{z,h+2}(\xi_1) & 0 & \cdots & \phi^j_{z,2^j-4}(\xi_1) & 0 & \phi^j_{z,2^j-3}(\xi_1) & 0 & \phi^j_{z,2^j-2}(\xi_1) & \phi^j_{z,2^j-1}(\xi_1) \\ 0 & \frac{1}{L_e}\phi'^j_{z,h}(\xi_1) & \frac{1}{L_e}\phi'^j_{z,h+1}(\xi_1) & 0 & \frac{1}{L_e}\phi'^j_{z,h+2}(\xi_1) & 0 & \cdots & \frac{1}{L_e}\phi'^j_{z,2^j-4}(\xi_1) & 0 & \frac{1}{L_e}\phi'^j_{z,2^j-3}(\xi_1) & 0 & \frac{1}{L_e}\phi'^j_{z,2^j-2}(\xi_1) & \frac{1}{L_e}\phi'^j_{z,2^j-1}(\xi_1) \\ \phi^j_{z-2,h}(\xi_2) & 0 & 0 & \phi^j_{z-2,h+1}(\xi_2) & 0 & \phi^j_{z-2,h+2}(\xi_2) & \cdots & 0 & \phi^j_{z-2,2^j-2}(\xi_2) & 0 & \phi^j_{z-2,2^j-1}(\xi_2) & 0 & 0 \\ 0 & \phi^j_{z,h}(\xi_2) & \phi^j_{z,h+1}(\xi_2) & 0 & \phi^j_{z,h+2}(\xi_2) & 0 & \cdots & \phi^j_{z,2^j-4}(\xi_2) & 0 & \phi^j_{z,2^j-3}(\xi_2) & 0 & \phi^j_{z,2^j-2}(\xi_2) & \phi^j_{z,2^j-1}(\xi_2) \\ \phi^j_{z-2,h}(\xi_3) & 0 & 0 & \phi^j_{z-2,h+1}(\xi_3) & 0 & \phi^j_{z-2,h+2}(\xi_3) & \cdots & 0 & \phi^j_{z-2,2^j-2}(\xi_3) & 0 & \phi^j_{z-2,2^j-1}(\xi_3) & 0 & 0 \\ \vdots & \vdots & \vdots & \vdots & \vdots & \vdots & \ddots & \vdots & \vdots & \vdots & \vdots & \vdots & \vdots \\ 0 & \phi^j_{z,h}(\xi_{r-2}) & \phi^j_{z,h+1}(\xi_{r-2}) & 0 & \phi^j_{z,h+2}(\xi_{r-2}) & 0 & \cdots & \phi^j_{z,2^j-4}(\xi_{r-2}) & 0 & \phi^j_{z,2^j-3}(\xi_{r-2}) & 0 & \phi^j_{z,2^j-2}(\xi_{r-2}) & \phi^j_{z,2^j-1}(\xi_{r-2}) \\ \phi^j_{z-2,h}(\xi_{r-1}) & 0 & 0 & \phi^j_{z-2,h+1}(\xi_{r-1}) & 0 & \phi^j_{z-2,h+2}(\xi_{r-1}) & \cdots & 0 & \phi^j_{z-2,2^j-2}(\xi_{r-1}) & 0 & \phi^j_{z-2,2^j-1}(\xi_{r-1}) & 0 & 0 \\ 0 & \phi^j_{z,h}(\xi_{r-1}) & \phi^j_{z,h+1}(\xi_{r-1}) & 0 & \phi^j_{z,h+2}(\xi_{r-1}) & 0 & \cdots & \phi^j_{z,2^j-4}(\xi_{r-1}) & 0 & \phi^j_{z,2^j-3}(\xi_{r-1}) & 0 & \phi^j_{z,2^j-2}(\xi_{r-1}) & \phi^j_{z,2^j-1}(\xi_{r-1}) \\ \phi^j_{z-2,h}(\xi_r) & 0 & 0 & \phi^j_{z-2,h+1}(\xi_r) & 0 & \phi^j_{z-2,h+2}(\xi_r) & \cdots & 0 & \phi^j_{z-2,2^j-2}(\xi_r) & 0 & \phi^j_{z-2,2^j-1}(\xi_r) & 0 & 0 \\ 0 & \phi^j_{z,h}(\xi_r) & \phi^j_{z,h+1}(\xi_r) & 0 & \phi^j_{z,h+2}(\xi_r) & 0 & \cdots & \phi^j_{z,2^j-4}(\xi_r) & 0 & \phi^j_{z,2^j-3}(\xi_r) & 0 & \phi^j_{z,2^j-2}(\xi_r) & \phi^j_{z,2^j-1}(\xi_r) \\ 0 & \frac{1}{L_e}\phi'^j_{z,h}(\xi_r) & \frac{1}{L_e}\phi'^j_{z,h+1}(\xi_r) & 0 & \frac{1}{L_e}\phi'^j_{z,h+2}(\xi_r) & 0 & \cdots & \frac{1}{L_e}\phi'^j_{z,2^j-4}(\xi_r) & 0 & \frac{1}{L_e}\phi'^j_{z,2^j-3}(\xi_r) & 0 & \frac{1}{L_e}\phi'^j_{z,2^j-2}(\xi_r) & \frac{1}{L_e}\phi'^j_{z,2^j-1}(\xi_r) \end{bmatrix} \begin{Bmatrix} a^j_{z-2,h} \\ b^j_{z,h} \\ b^j_{z,h+1} \\ a^j_{z-2,h+1} \\ b^j_{z,h+2} \\ a^j_{z-2,h+2} \\ \vdots \\ b^j_{z,2^j-4} \\ a^j_{z-2,2^j-2} \\ b^j_{z,2^j-3} \\ a^j_{z-2,2^j-1} \\ b^j_{z,2^j-2} \\ b^j_{z,2^j-1} \end{Bmatrix} \quad \textbf{(5.168)}$$

which can be expressed in matrix form as:

$$_{(n \text{ x } 1)}\{\boldsymbol{h_e}\} = {}_{(n \text{ x } n)}\left[\boldsymbol{R_p^w}\right]_{(n \text{ x } 1)}\{\boldsymbol{c_e}\} \tag{5.169}$$

The wavelet transformation matrix for the two dimensional plane bar is obtained from equation (5.169) as:

$$\left[\boldsymbol{T_p^w}\right] = \left[\boldsymbol{R_p^w}\right]^{-1} \tag{5.170}$$

5.3.1. Mass matrix formulation

The plane bar mass matrix is obtain via a superposition of the axial rod and Euler Bernoulli beam mass matrices in wavelet space from equations (5.31) and (5.102) respectively.

$$\left[\boldsymbol{m_{p,e}^w}\right] = \begin{bmatrix}
m_{h,h}^{z-2,j}{}_{r} & 0 & 0 & m_{h,h+1}^{z-2,j}{}_{r} & 0 & m_{h,h+2}^{z-2,j}{}_{r} & \cdots & m_{h,2^j-2}^{z-2,j}{}_{r} & 0 & m_{h,2^j-1}^{z-2,j}{}_{r} & 0 & 0 \\
0 & m_{h,h}^{z,j}{}_{b} & m_{h,h+1}^{z,j}{}_{b} & 0 & m_{h,h+2}^{z,j}{}_{b} & 0 & \cdots & 0 & m_{h,2^j-3}^{z,j}{}_{b} & 0 & m_{h,2^j-2}^{z,j}{}_{b} & m_{h,2^j-1}^{z,j}{}_{b} \\
0 & m_{h+1,h}^{z,j}{}_{b} & m_{h+1,h+1}^{z,j}{}_{b} & 0 & m_{h+1,h+2}^{z,j}{}_{b} & 0 & \cdots & 0 & m_{h+1,2^j-3}^{z,j}{}_{b} & 0 & m_{h+1,2^j-2}^{z,j}{}_{b} & m_{h+1,2^j-1}^{z,j}{}_{b} \\
m_{h+1,h}^{z-2,j}{}_{r} & 0 & 0 & m_{h+1,h+1}^{z-2,j}{}_{r} & 0 & m_{h+1,h+2}^{z-2,j}{}_{r} & \cdots & m_{h+1,2^j-2}^{z-2,j}{}_{r} & 0 & m_{h+1,2^j-1}^{z-2,j}{}_{r} & 0 & 0 \\
0 & m_{h+2,h}^{z,j}{}_{b} & m_{h+2,h+1}^{z,j}{}_{b} & 0 & m_{h+2,h+2}^{z,j}{}_{b} & 0 & \cdots & 0 & m_{h+2,2^j-3}^{z,j}{}_{b} & 0 & m_{h+2,2^j-2}^{z,j}{}_{b} & m_{h+2,2^j-1}^{z,j}{}_{b} \\
m_{h+2,h}^{z-2,j}{}_{r} & 0 & 0 & m_{h+2,h+1}^{z-2,j}{}_{r} & 0 & m_{h+2,h+2}^{z-2,j}{}_{r} & \cdots & m_{h+2,2^j-2}^{z-2,j}{}_{r} & 0 & m_{h+2,2^j-1}^{z-2,j}{}_{r} & 0 & 0 \\
\vdots & \vdots & \vdots & \vdots & \vdots & \vdots & \ddots & \vdots & \vdots & \vdots & \vdots & \vdots \\
m_{2^j-2,h}^{z-2,j}{}_{r} & 0 & 0 & m_{2^j-2,h+1}^{z-2,j}{}_{r} & 0 & m_{2^j-2,h+2}^{z-2,j}{}_{r} & \cdots & m_{2^j-2,2^j-2}^{z-2,j}{}_{r} & 0 & m_{2^j-2,2^j-1}^{z-2,j}{}_{r} & 0 & 0 \\
0 & m_{2^j-3,h}^{z,j}{}_{b} & m_{2^j-3,h+1}^{z,j}{}_{b} & 0 & m_{2^j-3,h+2}^{z,j}{}_{b} & 0 & \cdots & 0 & m_{2^j-3,2^j-3}^{z,j}{}_{b} & 0 & m_{2^j-3,2^j-2}^{z,j}{}_{b} & m_{2^j-3,2^j-1}^{z,j}{}_{b} \\
m_{2^j-1,h}^{z-2,j}{}_{r} & 0 & 0 & m_{2^j-1,h+1}^{z-2,j}{}_{r} & 0 & m_{2^j-1,h+2}^{z-2,j}{}_{r} & \cdots & m_{2^j-1,2^j-2}^{z-2,j}{}_{r} & 0 & m_{2^j-1,2^j-1}^{z-2,j}{}_{r} & 0 & 0 \\
0 & m_{2^j-2,h}^{z,j}{}_{b} & m_{2^j-2,h+1}^{z,j}{}_{b} & 0 & m_{2^j-2,h+2}^{z,j}{}_{b} & 0 & \cdots & 0 & m_{2^j-2,2^j-3}^{z,j}{}_{b} & 0 & m_{2^j-2,2^j-2}^{z,j}{}_{b} & m_{2^j-2,2^j-1}^{z,j}{}_{b} \\
0 & m_{2^j-1,h}^{z,j}{}_{b} & m_{2^j-1,h+1}^{z,j}{}_{b} & 0 & m_{2^j-1,h+2}^{z,j}{}_{b} & 0 & \cdots & 0 & m_{2^j-1,2^j-3}^{z,j}{}_{b} & 0 & m_{2^j-1,2^j-2}^{z,j}{}_{b} & m_{2^j-1,2^j-1}^{z,j}{}_{b}
\end{bmatrix} \tag{5.171}$$

The mass matrix is then transformed into physical space by implementing the wavelet transformation matrix for the plane bar.

$$_{(n \text{ x } n)}[\boldsymbol{m_{p,e}^p}] = \rho A L_e {}_{(n \text{ x } n)}\left[\boldsymbol{T_p^w}\right]^T {}_{(n \text{ x } n)}[\boldsymbol{m_{p,e}^w}]_{(n \text{ x } n)}\left[\boldsymbol{T_p^w}\right] \tag{5.172}$$

Alternatively, the elemental matrices of the plane bar element can be computed by the superposition of the axial rod and Euler Bernoulli beam respective elemental matrices directly in physical space in order to reduce the computation time of the higher order wavelet family WFE, at larger scales, during transformation from wavelet space.

5.3.2. Stiffness matrix formulation

The stiffness matrix is also obtained as a superposition of the axial rod stiffness matrix in equation (5.18) and Euler Bernoulli beam stiffness matrix in equation (5.87).

$$\left[\boldsymbol{k}_{\boldsymbol{p},\boldsymbol{e}}^{\boldsymbol{w}}\right] =$$

$$\begin{bmatrix}
k_{h,h}^{z-2,j}{}_{r} & 0 & 0 & k_{h,h+1}^{z-2,j}{}_{r} & 0 & k_{h,h+2}^{z-2,j}{}_{r} & \cdots & k_{h,2^j-2}^{z-2,j}{}_{r} & 0 & k_{h,2^j-1}^{z-2,j}{}_{r} & 0 & 0 \\
0 & k_{h,h}^{z,j}{}_{b} & k_{h,h+1}^{z,j}{}_{b} & 0 & k_{h,h+2}^{z,j}{}_{b} & 0 & \cdots & 0 & k_{h,2^j-3}^{z,j}{}_{b} & 0 & k_{h,2^j-2}^{z,j}{}_{b} & k_{h,2^j-1}^{z,j}{}_{b} \\
0 & k_{h+1,h}^{z,j}{}_{b} & k_{h+1,h+1}^{z,j}{}_{b} & 0 & k_{h+1,h+2}^{z,j}{}_{b} & 0 & \cdots & 0 & k_{h+1,2^j-3}^{z,j}{}_{b} & 0 & k_{h+1,2^j-2}^{z,j}{}_{b} & k_{h+1,2^j-1}^{z,j}{}_{b} \\
k_{h+1,h}^{z-2,j}{}_{r} & 0 & 0 & k_{h+1,h+1}^{z-2,j}{}_{r} & 0 & k_{h+1,h+2}^{z-2,j}{}_{r} & \cdots & k_{h+1,2^j-2}^{z-2,j}{}_{r} & 0 & k_{h+1,2^j-1}^{z-2,j}{}_{r} & 0 & 0 \\
0 & k_{h+2,h}^{z,j}{}_{b} & k_{h+2,h+1}^{z,j}{}_{b} & 0 & k_{h+2,h+2}^{z,j}{}_{b} & 0 & \cdots & 0 & k_{h+2,2^j-3}^{z,j}{}_{b} & 0 & k_{h+2,2^j-2}^{z,j}{}_{b} & k_{h+2,2^j-1}^{z,j}{}_{b} \\
k_{h+2,h}^{z-2,j}{}_{r} & 0 & 0 & k_{h+2,h+1}^{z-2,j}{}_{r} & 0 & k_{h+2,h+2}^{z-2,j}{}_{r} & \cdots & k_{h+2,2^j-2}^{z-2,j}{}_{r} & 0 & k_{h+2,2^j-1}^{z-2,j}{}_{r} & 0 & 0 \\
\vdots & \vdots & \vdots & \vdots & \vdots & \vdots & \ddots & \vdots & \vdots & \vdots & \vdots & \vdots \\
k_{2^j-2,h}^{z-2,j}{}_{r} & 0 & 0 & k_{2^j-2,h+1}^{z-2,j}{}_{r} & 0 & k_{2^j-2,h+2}^{z-2,j}{}_{r} & \cdots & k_{2^j-2,2^j-2}^{z-2,j}{}_{r} & 0 & k_{2^j-2,2^j-1}^{z-2,j}{}_{r} & 0 & 0 \\
0 & k_{2^j-3,h}^{z,j}{}_{b} & k_{2^j-3,h+1}^{z,j}{}_{b} & 0 & k_{2^j-3,h+2}^{z,j}{}_{b} & 0 & \cdots & 0 & k_{2^j-3,2^j-3}^{z,j}{}_{b} & 0 & k_{2^j-3,2^j-2}^{z,j}{}_{b} & k_{2^j-3,2^j-1}^{z,j}{}_{b} \\
k_{2^j-1,h}^{z-2,j}{}_{r} & 0 & 0 & k_{2^j-1,h+1}^{z-2,j}{}_{r} & 0 & k_{2^j-1,h+2}^{z-2,j}{}_{r} & \cdots & k_{2^j-1,2^j-2}^{z-2,j}{}_{r} & 0 & k_{2^j-1,2^j-1}^{z-2,j}{}_{r} & 0 & 0 \\
0 & k_{2^j-2,h}^{z,j}{}_{b} & k_{2^j-2,h+1}^{z,j}{}_{b} & 0 & k_{2^j-2,h+2}^{z,j}{}_{b} & 0 & \cdots & 0 & k_{2^j-2,2^j-3}^{z,j}{}_{b} & 0 & k_{2^j-2,2^j-2}^{z,j}{}_{b} & k_{2^j-2,2^j-1}^{z,j}{}_{b} \\
0 & k_{2^j-1,h}^{z,j}{}_{b} & k_{2^j-1,h+1}^{z,j}{}_{b} & 0 & k_{2^j-1,h+2}^{z,j}{}_{b} & 0 & \cdots & 0 & k_{2^j-1,2^j-3}^{z,j}{}_{b} & 0 & k_{2^j-1,2^j-2}^{z,j}{}_{b} & k_{2^j-1,2^j-1}^{z,j}{}_{b}
\end{bmatrix} \quad \textbf{(5.173)}$$

The stiffness matrix in wavelet space, from equation (5.173), is transformed into physical space via the plane bar wavelet transformation matrix $\left[\boldsymbol{T}_{\boldsymbol{p}}^{\boldsymbol{w}}\right]$.

$$_{(n \text{ x } n)}[\boldsymbol{k}_{\boldsymbol{p},\boldsymbol{e}}^{\boldsymbol{p}}] = {}_{(n \text{ x } n)}\left[\boldsymbol{B}_{\boldsymbol{p},\boldsymbol{e}}^{\boldsymbol{p}}\right]_{(n \text{ x } n)}\left[\boldsymbol{T}_{\boldsymbol{p}}^{\boldsymbol{w}}\right]^{T}{}_{(n \text{ x } n)}[\boldsymbol{k}_{\boldsymbol{p},\boldsymbol{e}}^{\boldsymbol{w}}]_{(n \text{ x } n)}\left[\boldsymbol{T}_{\boldsymbol{p}}^{\boldsymbol{w}}\right] \quad \textbf{(5.174)}$$

where the diagonal matrix $\left[\boldsymbol{B}_{\boldsymbol{p},\boldsymbol{e}}^{\boldsymbol{p}}\right]$ contains the element material values and is given by

$$_{(n \text{ x } n)}\left[\boldsymbol{B}_{\boldsymbol{p},\boldsymbol{e}}^{\boldsymbol{p}}\right] = \begin{bmatrix}
\frac{EA}{L_e} & 0 & 0 & 0 & 0 & 0 & 0 & 0 & 0 & 0 & 0 & 0 \\
0 & \frac{EI}{L_e{}^3} & 0 & 0 & 0 & 0 & 0 & 0 & 0 & 0 & 0 & 0 \\
0 & 0 & \frac{EI}{L_e{}^3} & 0 & 0 & 0 & 0 & 0 & 0 & 0 & 0 & 0 \\
0 & 0 & 0 & \frac{EA}{L_e} & 0 & 0 & 0 & 0 & 0 & 0 & 0 & 0 \\
0 & 0 & 0 & 0 & \frac{EI}{L_e{}^3} & 0 & 0 & 0 & 0 & 0 & 0 & 0 \\
0 & 0 & 0 & 0 & 0 & \frac{EA}{L_e} & 0 & 0 & 0 & 0 & 0 & 0 \\
0 & 0 & 0 & 0 & 0 & 0 & \ddots & 0 & 0 & 0 & 0 & 0 \\
0 & 0 & 0 & 0 & 0 & 0 & 0 & \frac{EA}{L_e} & 0 & 0 & 0 & 0 \\
0 & 0 & 0 & 0 & 0 & 0 & 0 & 0 & \frac{EI}{L_e{}^3} & 0 & 0 & 0 \\
0 & 0 & 0 & 0 & 0 & 0 & 0 & 0 & 0 & \frac{EA}{L_e} & 0 & 0 \\
0 & 0 & 0 & 0 & 0 & 0 & 0 & 0 & 0 & 0 & \frac{EI}{L_e{}^3} & 0 \\
0 & 0 & 0 & 0 & 0 & 0 & 0 & 0 & 0 & 0 & 0 & \frac{EI}{L_e{}^3}
\end{bmatrix} \quad \textbf{(5.175)}$$

5.3.3. Force vector formulation

The axial and bending loads described in Sections 5.1.2 and 5.2.2 respectively, are combined to obtain the equivalent load vectors for the plane bar WFE. The equivalent load vectors are superimposed once they have been transformed in to physical space for each element.

Therefore, the total load vector of the plane bar WFE in physical space is given as the sum of the total axial and bending loads, i.e.,

$$_{(n \text{ x } 1)}\{\boldsymbol{f}^{\boldsymbol{p}}_{\boldsymbol{p},\boldsymbol{e}}\} = {}_{(n \text{ x } 1)}\{\boldsymbol{f}^{\boldsymbol{p}}_{\boldsymbol{r},\boldsymbol{e}}\} + {}_{(n \text{ x } 1)}\{\boldsymbol{f}^{\boldsymbol{p}}_{\boldsymbol{b},\boldsymbol{e}}\} \qquad \textbf{(5.176)}$$

5.3.4. Two dimensional global transformation

Given that each plane bar WFE is formulated in its own arbitrary local coordinate system, it is important to transform each element into the system's global coordinates, if the two systems do not coincide. The relation of the local coordinate system to the two dimensional global coordinate system is shown in Figure 5-13.

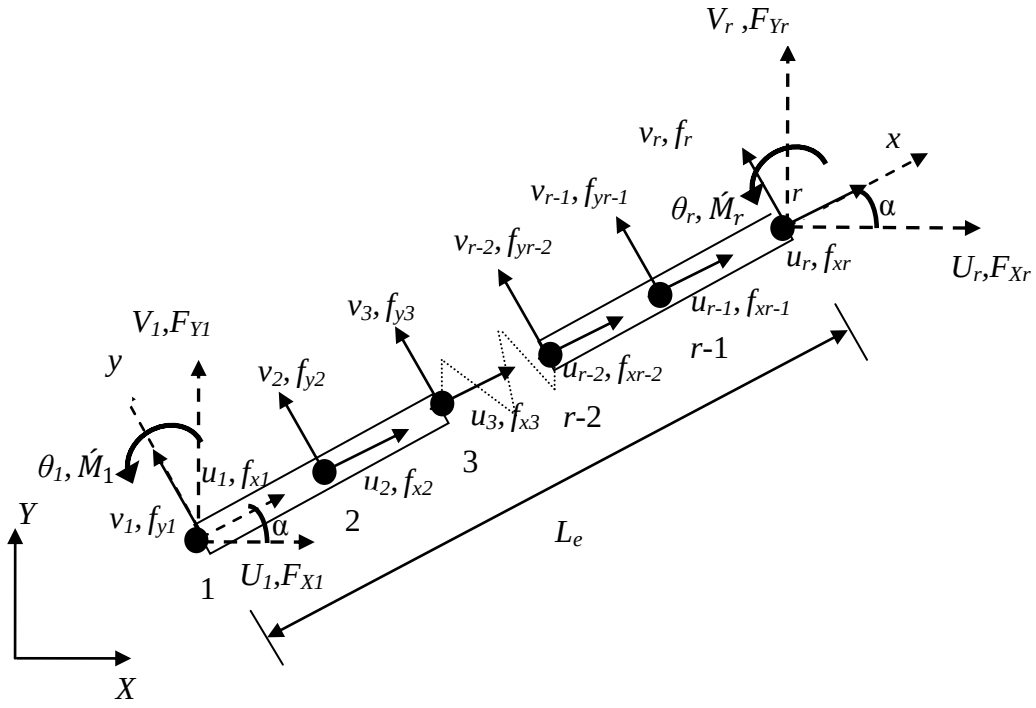

Figure 5-13 : Local and global coordinate system of a plane bar wavelet finite element.

The axial deformation, transverse displacement and rotation at an elemental node *i*, with respect to local coordinates, are denoted by u_i, v_i and θ_i respectively. The corresponding axial and transverse nodal forces and bending moments at node *i* are denoted by f_{xi}, f_{yi} and $\acute{m}_i$. The arbitrary angle of orientation between the local coordinate and global coordinate system is denoted by α and is assumed to remain unchanged for each elemental node within the same plane bar WFE. This is because all the elemental nodes are assumed to be along the same local axial axis. The component displacements in the global *X* and *Y* axes at node *i* are denoted by U_i and V_i respectively, while the force components are denoted by F_{Xi} and F_{Yi}. The rotation and corresponding moments in the global coordinates are denoted as θ_i and $\acute{M}_i$

respectively. From the figure above, the relationship between the local and global displacements at any elemental node *i* is

$$u_i = U_i \cos\alpha + V_i \sin\alpha$$
$$v_i = -U_i \sin\alpha + V_i \cos\alpha$$
$$\theta_i = \Theta_i$$
$$\begin{Bmatrix} u_i \\ v_i \\ \theta_i \end{Bmatrix} = \begin{bmatrix} \cos\alpha & \sin\alpha & 0 \\ -\sin\alpha & \cos\alpha & 0 \\ 0 & 0 & 1 \end{bmatrix} \begin{Bmatrix} U_i \\ V_i \\ \Theta_i \end{Bmatrix} \quad \textbf{(5.177)}$$

where

$$\cos\alpha = \frac{X_r - X_1}{L_e}$$
$$\sin\alpha = \frac{Y_r - Y_1}{L_e} \quad \textbf{(5.178)}$$

X_i and Y_i are the global coordinate values at node *i*. The length L_e of the element can be evaluated from the two extreme elemental node global coordinate values.

$$L_e = \sqrt{(X_r - X_1)^2 + (Y_r - Y_1)^2} \quad \textbf{(5.179)}$$

Therefore, the relation of the elemental nodes between the local and global coordinate system can be expressed as:

$$\begin{Bmatrix} u_1 \\ v_1 \\ \theta_1 \\ u_2 \\ v_2 \\ u_3 \\ v_3 \\ \vdots \\ u_{n-1} \\ v_{n-1} \\ u_n \\ v_n \\ u_{n+1} \\ v_{n+1} \\ \theta_{n+1} \end{Bmatrix} = \begin{bmatrix} \cos\alpha & \sin\alpha & 0 & 0 & 0 & 0 & 0 & \cdots & 0 & 0 & 0 & 0 & 0 & 0 & 0 \\ -\sin\alpha & \cos\alpha & 0 & 0 & 0 & 0 & 0 & \cdots & 0 & 0 & 0 & 0 & 0 & 0 & 0 \\ 0 & 0 & 1 & 0 & 0 & 0 & 0 & \cdots & 0 & 0 & 0 & 0 & 0 & 0 & 0 \\ 0 & 0 & 0 & \cos\alpha & \sin\alpha & 0 & 0 & \cdots & 0 & 0 & 0 & 0 & 0 & 0 & 0 \\ 0 & 0 & 0 & -\sin\alpha & \cos\alpha & 0 & 0 & \cdots & 0 & 0 & 0 & 0 & 0 & 0 & 0 \\ 0 & 0 & 0 & 0 & 0 & \cos\alpha & \sin\alpha & \cdots & 0 & 0 & 0 & 0 & 0 & 0 & 0 \\ 0 & 0 & 0 & 0 & 0 & -\sin\alpha & \cos\alpha & \cdots & 0 & 0 & 0 & 0 & 0 & 0 & 0 \\ \vdots & \vdots & \vdots & \vdots & \vdots & \vdots & \vdots & \ddots & \vdots & \vdots & \vdots & \vdots & \vdots & \vdots & \vdots \\ 0 & 0 & 0 & 0 & 0 & 0 & 0 & \cdots & \cos\alpha & \sin\alpha & 0 & 0 & 0 & 0 & 0 \\ 0 & 0 & 0 & 0 & 0 & 0 & 0 & \cdots & -\sin\alpha & \cos\alpha & 0 & 0 & 0 & 0 & 0 \\ 0 & 0 & 0 & 0 & 0 & 0 & 0 & \cdots & 0 & 0 & \cos\alpha & \sin\alpha & 0 & 0 & 0 \\ 0 & 0 & 0 & 0 & 0 & 0 & 0 & \cdots & 0 & 0 & -\sin\alpha & \cos\alpha & 0 & 0 & 0 \\ 0 & 0 & 0 & 0 & 0 & 0 & 0 & \cdots & 0 & 0 & 0 & 0 & \cos\alpha & \sin\alpha & 0 \\ 0 & 0 & 0 & 0 & 0 & 0 & 0 & \cdots & 0 & 0 & 0 & 0 & -\sin\alpha & \cos\alpha & 0 \\ 0 & 0 & 0 & 0 & 0 & 0 & 0 & \cdots & 0 & 0 & 0 & 0 & 0 & 0 & 1 \end{bmatrix} \begin{Bmatrix} U_1 \\ V_1 \\ \Theta_1 \\ U_2 \\ V_2 \\ U_3 \\ V_3 \\ \vdots \\ U_{n-1} \\ V_{n-1} \\ U_n \\ V_n \\ U_{n+1} \\ V_{n+1} \\ \Theta_{n+1} \end{Bmatrix}$$

$$_{(n\times 1)}\{\boldsymbol{h_e}\} = {}_{(n\times n)}\left[\boldsymbol{T_p^G}\right]_{(n\times 1)}\{\boldsymbol{H_e}\} \quad \textbf{(5.180)}$$

$$\{\boldsymbol{H_e}\} = \begin{Bmatrix} U_1 \\ V_1 \\ \theta_1 \\ U_2 \\ V_2 \\ U_3 \\ \vdots \\ V_{r-2} \\ U_{r-1} \\ V_{r-1} \\ U_r \\ V_r \\ \theta_r \end{Bmatrix} \quad \textbf{(5.181)}$$

$\left[\boldsymbol{T_p^G}\right]$ is the plane bar WFE rotation matrix or global transformation matrix. Transforming the elemental mass matrix, stiffness matrix and load vectors in equations (5.171), (5.174), and (5.176) from local to global coordinates, we have

$$_{(n\ \mathrm{x}\ n)}[\boldsymbol{K_{p,e}^p}] = {}_{(n\ \mathrm{x}\ n)}\left[\boldsymbol{T_p^G}\right]^T {}_{(n\ \mathrm{x}\ n)}[\boldsymbol{k_{p,e}^p}]_{(n\ \mathrm{x}\ n)}\left[\boldsymbol{T_p^G}\right] \quad \textbf{(5.182)}$$

$$_{(n\ \mathrm{x}\ n)}[\boldsymbol{M_{p,e}^p}] = {}_{(n\ \mathrm{x}\ n)}\left[\boldsymbol{T_p^G}\right]^T {}_{(n\ \mathrm{x}\ n)}[\boldsymbol{m_{p,e}^p}]_{(n\ \mathrm{x}\ n)}\left[\boldsymbol{T_p^G}\right] \quad \textbf{(5.183)}$$

$$_{(n\ \mathrm{x}\ 1)}\{\boldsymbol{F_{p,e}^p}\} = {}_{(n\ \mathrm{x}\ n)}\left[\boldsymbol{T_p^G}\right]^T {}_{(n\ \mathrm{x}\ 1)}\{\boldsymbol{f_{p,e}^p}\} \quad \textbf{(5.184)}$$

5.3.5. Assembly and application of boundary conditions

Once the element matrices and load vectors have been transformed in to physical space and further transformed into global coordinates, assembly of the system is carried out. For a plane bar with a total of n_e WFEs, the total global system stiffness matrix, mass matrix and load vector in physical space are given by:

$$[\boldsymbol{K_p}] = \sum_{e=1}^{n_e} [\boldsymbol{K_{p,e}^p}] \quad \textbf{(5.185)}$$

$$[\boldsymbol{M_p}] = \sum_{e=1}^{n_e} [\boldsymbol{M_{p,e}^p}] \quad \textbf{(5.186)}$$

$$\{\boldsymbol{F_p}\} = \sum_{e=1}^{n_e} \{\boldsymbol{F_{p,e}^p}\} \quad \textbf{(5.187)}$$

Assembly of the matrices and load vectors is carried out via the superposition approach, where the element matrices are expanded to the size of the system DOFs once transformation into the global coordinate system is carried out. The DOFs to which an element is not associated within the expanded matrix are replaced by zeros. The summations expressed in equations (5.185) - (5.187) are then applied to the expanded matrices. The boundary conditions are also applied by omitting the corresponding constrained rows and columns, thus reducing the size of the overall system matrices and load vectors.

5.3.6. Daubechies plane bar wavelet finite element

As earlier discussed in Sections 5.1.7 and 5.2.8, the Daubechies wavelet family of order L can represent any polynomial whose order is up to, but not greater than $\frac{L}{2} - 1$ [10,36]. Therefore, the axial deformation and the bending of the Daubechies plane bar WFE may only be

approximated theoretically by the Daubechies scaling functions of order not less than D*4* and D*6* respectively. Furthermore, if the order of the wavelet family chosen to approximate the transverse deflection and rotation is D*L*, then the axial deformation is approximated by the Daubechies wavelet D*L*-2 at scale j. This is specific to this formulation taking into consideration that the bending of the plane bar WFE, based on the Euler Bernoulli beam theory, has only rotations at the elemental end nodes. Therefore in general, the order of the Daubechies scaling function that is used to approximate the axial deformation is dependent on the DOFs at each elemental node with respect to the bending of the plane bar. Thus, the order should be selected to ensure that the axial deformation is present at each elemental node.

Specific to this formulation, the total number of elemental nodes is $r = 2^j + L - 4$ and the number of elemental segments is $n_s = 2^j + L - 5$. The total number of DOFs corresponding to the transverse deflection and rotation within the Daubechies planar bar WFE is $2^j + L - 2$, while the axial deformation total DOFs is $2^j + (L - 2) - 2$. Hence, the total number of DOFs within each plane bar WFE at scale j is $n = 2^{j+1} + 2L - 6$, where L is the order of the Daubechies wavelet family used to approximate the transverse deflection and rotation.

The elemental matrices are obtained via the evaluation of the connection coefficients for the axial rod and corresponding Euler Bernoulli beam WFE in wavelet space. They are then superimposed and transformed in to physical space via the wavelet transformation matrix for the bar WFE.

5.3.7. BSWI plane bar wavelet finite element

The BSWI based plane bar wavelet finite element via this approach requires that the least order of the BSWI wavelet family that can be used to approximate the axial and bending DOFs is BSWI2_j and BSWI4_j respectively. Furthermore, similar to the Daubechies formulation, if the order BSWIm_j is used to approximate the transverse deflection and rotation DOFs, then the BSWI wavelet of order $(m - 2)$ and at multiresolution scale j is used to approximate the axial deformation of the plane bar element. In accordance to this approach, where each elemental node has the axial and transverse deformation DOFs present and the rotation DOFs only present at each elemental end node, the total number of elemental nodes is $r = 2^j + m - 3$ and corresponding number of elemental segments is $n_s = 2^j + m - 4$. The total number of DOFs corresponding to the transverse deflection and rotation within the BSWI plane bar WFE is $2^j + m - 1$ and axial deformation is $2^j + (m - 2) - 1$.

Thus, for the BSWI of order m and at scale j, the total number of DOFs for each plane bar WFE is $n = 2^{j+1} + 2m - 4$.

5.4. Conclusion

The general unified formulations of the wavelet based axial rod, Euler Bernoulli beam and plane bar finite elements were presented in this chapter. The wavelet based elements were described in detail with the elemental matrices and load vectors presented; conceptually based on wavelet theory, finite element theory and previous works. The shape functions of the mentioned wavelet based elements were illustrated and discussed in this chapter, highlighting the conditions necessary for the implementation of the wavelet families with respect to the order selection. Furthermore, the formulations of the wavelet based moving load vectors, elastic foundation stiffness matrix and the foundation damping matrix were also discussed. The formulations presented can be implemented using the Daubechies and BSWI wavelet families. The scaling functions of the wavelet families were used to approximate the displacement field variables.

Due to the attractive properties of the wavelet families, which include; compact support, the "two-scale" relation and multiresolution, the WFEs presented possess the delta function, compatibility and completeness requirements necessary to ensure convergence of the approximate solution to the exact solution. Moreover, it was observed that in order to formulate the Daubechies wavelet based elements, the evaluation of the connection coefficients was necessary since the scaling functions and their derivatives cannot be expressed explicitly. However, this was not the case for the BSWI wavelet elements as the matrices and load vectors can be computed directly. This was consistent with the findings of Chen et al. [6], Xiang et al. [7] and Ma et al. [10].

The layout of the wavelet based elements, particularly for the beam and plane bar, can be altered for a wide variety of problems. Furthermore, the multiresolution aspect of the formulations makes the use of WFEM attractive in the analysis of structural static and dynamic problems.

6. The Wavelet Finite Element Method for Static Analysis

Summary

In this chapter, a number of simulated numerical examples are presented in order to highlight key features in implementing WFEM with respect to structural static analysis. Some of the numerical examples presented have been used in previous research as benchmarks in the analysis of some wavelet finite element methods. The algorithms of the different approaches, for all the simulated examples, are carried out using the Mathematica version 7 program. The examples in this chapter are analysed using the BSWI and Daubechies based wavelet finite element formulations and include the following:

Example 1: An axial rod subjected to a varying distributed load is analysed to illustrate the implementation of the WFEM with respect to static axial loading.

Example 2 [10,40]: A fixed-fixed uniform beam subjected to a linear varying load on the right half of the beam is analysed to investigate the WFEMs ability to analyse problems with fast variations in transverse loading. Furthermore, different layouts of the beam wavelet based element are implemented, compared and discussed.

Example 3 [10,40]: A simply supported stepped beam subjected to a uniformly distributed load is presented. The WFEMs are used to analyse a beam that has a flexural singularity present due to an abrupt change in flexural stiffness.

Example 4: The buckling of a two-stepped and three-stepped plane bar element is carried out to investigate the WFEM's ability to analyse linear buckling and attain the critical buckling loads when different boundary conditions are imposed.

The Daubechies and BSWI WFEs, for the various element formulations, are analysed and compared with *h* and *p* adaptive FE formulations, and in some cases, exact analytical solutions. A detailed analysis and discussion of the results is carried out for each case, with emphasis being drawn on the strengths, limitations and key features of the two wavelet based finite element methods. Some aspects of the method are clarified based on the findings from previous research.

6.1. Axial rod subjected to varying distributed Load

A uniform axial cantilever rod subjected to linear varying load $q(x)$, as illustrated in Figure 6-1, is analysed. The rod has a uniform cross sectional area $A = A_0$, Young's Modulus $E = E_0$ and length l. The varying load $q(x) = -q_0\, x$ is subjected along the free-fixed axial rod. One element is used to represent the rod using Daubechies and BSWI WFEM approaches. The results are compared with the classical FEM and an exact analytical approach.

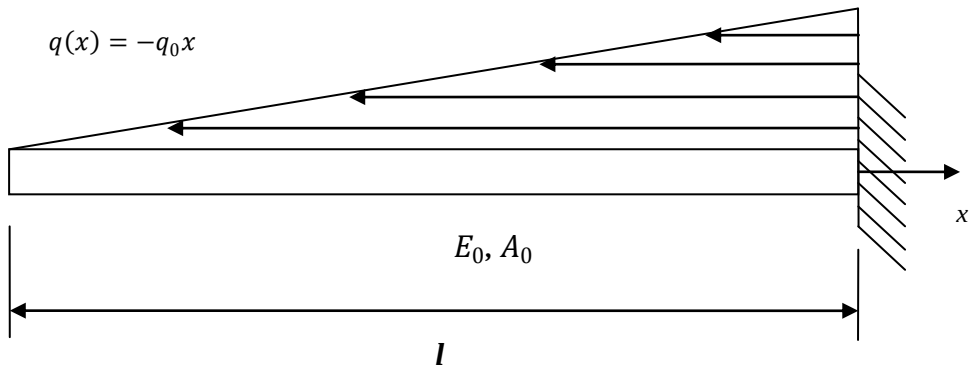

Figure 6-1: A uniform cantilever axial rod subjected to a varying load $q(x)$.

The exact solution for displacement at a particular point x can be obtained by solving [31]

$$u(x) = \frac{1}{EA}\int_{o}^{x} P\,(x)dx \tag{6.1}$$

where $P\,(x) = q(x)\frac{x}{2}$. Therefore, substituting the force function $q(x)$ into (6.1),

$$u(x) = \frac{1}{E_0 A_0}\int q_0 \frac{x^2}{2}\, dx = \frac{q_0}{6E_0 A_0}x^3 + C_1 \tag{6.2}$$

The constant C_1 is obtained from the boundary conditions. Therefore, for this particular cantilever example, the displacement on the right hand end is zero. Thus, C_1 is given as $\frac{-q_0}{6EA}l^3$. Substituting into equation (6.2), the axial deformation across the bar is:

$$u(x) = \frac{q_0}{6E_0 A_0}(x^3 - l^3) \tag{6.3}$$

The exact solution for axial stress and strain, at a point x on the rod, are obtained as:

$$\sigma(x) = \frac{P(x)}{A} = q_0 \frac{x^2}{2A_0} \tag{6.4}$$

$$\epsilon(x) = \frac{\sigma(x)}{E} = q_0 \frac{x^2}{2E_0A_0} \tag{6.5}$$

The number of elements, n_e, implemented in the FE model will be denoted by FEM-n_e. The rod finite element matrices and load vectors are described in Appendix B.1. The *p*-FEM rod is made up of only one element in this example. The potential energy of the axial rod is given by [31]:

$$\Pi^a = \int_0^l \frac{EA}{2}\left(\frac{du(x)}{dx}\right)^2 dx - \int_0^l q(x)u(x)dx \tag{6.6}$$

Following a similar procedure as highlighted in Section 5.1, the wavelet based stiffness matrix and load vector for the axial rod can be evaluated and then used to solve the governing equation of the system:

$$[\boldsymbol{K_r}]\{\boldsymbol{U_r}\} = \{\boldsymbol{F_r}\} \tag{6.7}$$

where $[\boldsymbol{K_r}]$ is the global system stiffness matrix in physical space, $\{\boldsymbol{U_r}\}$ is the global system vector containing the DOFs and $\{\boldsymbol{F_r}\}$ is the global loading vector containing the equivalent nodal loads of the system.

The deformation of the axial rod evaluated using one Daubechies WFE is plotted in Figure 6-2 for (*a*) different multiresolution scales *j* and (*b*) different orders D*L*, which is denoted as DL_j. The results of the axial deformation for the D6_j ($0 \leq j \leq 2$) WFE solution are in good agreement with the analytical solution, as presented in Figure 6-2 (*a*). Furthermore, increasing the scale increases the accuracy of the solution as the D6_2 WFE solution gives a better approximation than both D6_0 and D6_1. The DL_0 WFE axial deformation is plotted in Figure 6-2 (*b*), for the different wavelet orders $6 \leq L \leq 18$ (with the exception of D*10* and D*14*) at scale $j = 0$. The results are also in good agreement with the exact solution and increasing the order of the WFEs improves the accuracy of the solution. It is also observed from Figure 6-2 (*c*) that the solutions of the axial deformation at arbitrary point $0.1\,l$ for wavelet based elements D6_j, D8_j, D10_j, D12_j and D16_j, at scale $0 \leq j \leq 2$, have an absolute error below 1.5%. This shows that the Daubechies wavelet based element solution gives a very good approximation of the axial deformation for the range of Daubechies orders $6 \leq L \leq 18$. Furthermore, convergence of the Daubechies WFEM solution to the exact solution is observed when the order and/or multiresolution scale are increased.

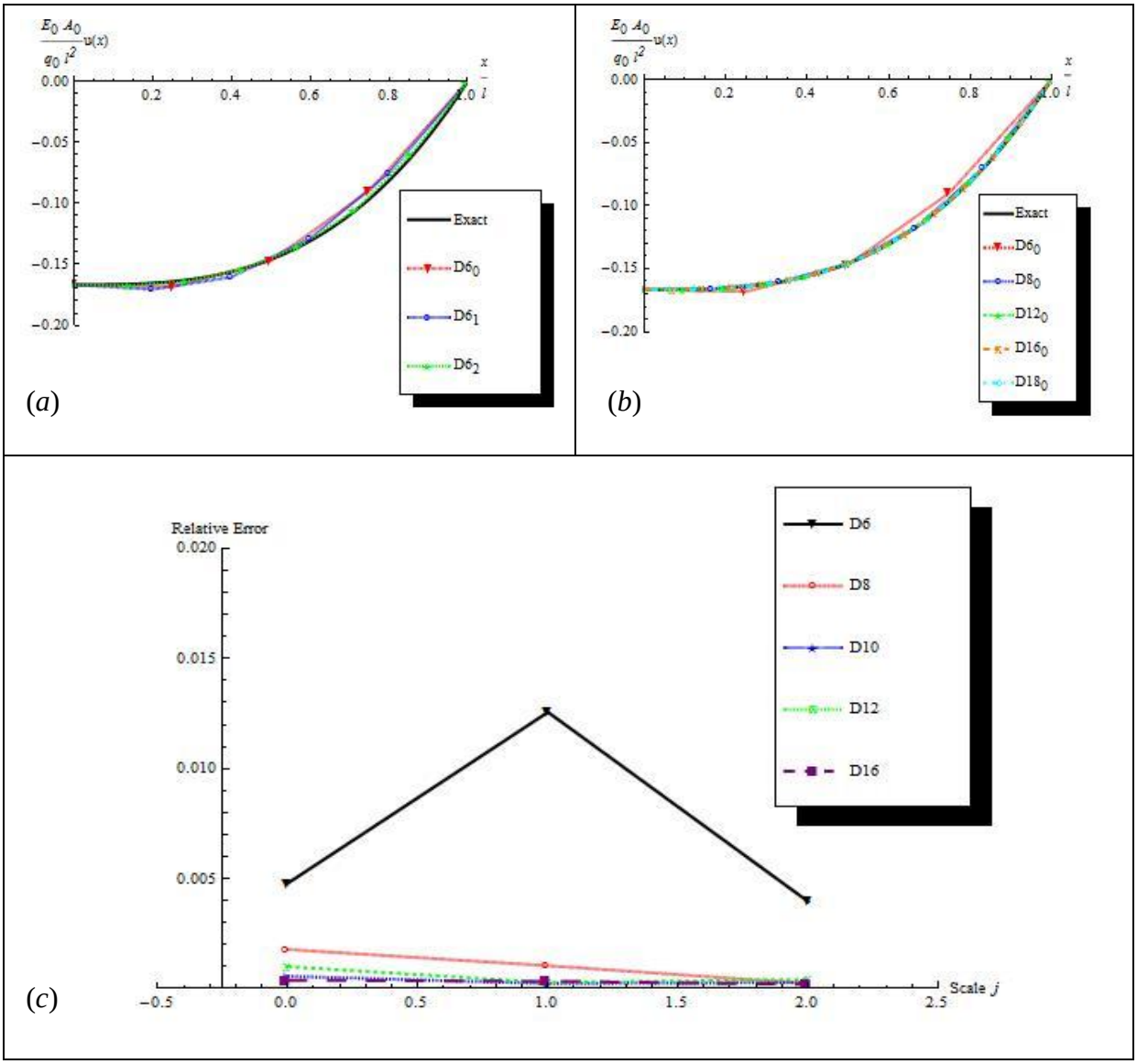

Figure 6-2: Axial deformation of a uniform cantilever rod subjected to a linear varying load $q(x)$ for Daubechies WFEM. (*a*) D6$_j$, (*b*) DL_0 and (*c*) Absolute relative error at $x = 0.1l$ for Daubechies WFEM.

Figure 6-3 (*a*) shows the axial deformation across the rod using the BSWI2$_j$ WFE. The results are also in good agreement with the exact analytical solution and increasing the multiresolution scale j increases the levels of accuracy. Furthermore, increasing the order of the BSWI wavelet subsequently results in a better approximation of the solution as observed in Figure 6-3 (*b*). Thus, with an increase in the order and/or scale of the WFE solution, the results converge to the exact solution as observed in Figure 6-3 (*c*). In general, the BSWI WFEM performs particularly well due to the fact that the scaling functions and their derivatives are expressed explicitly. There is therefore no need to evaluate connection coefficients and consequently the element matrices can be obtained directly, at high levels of accuracy.

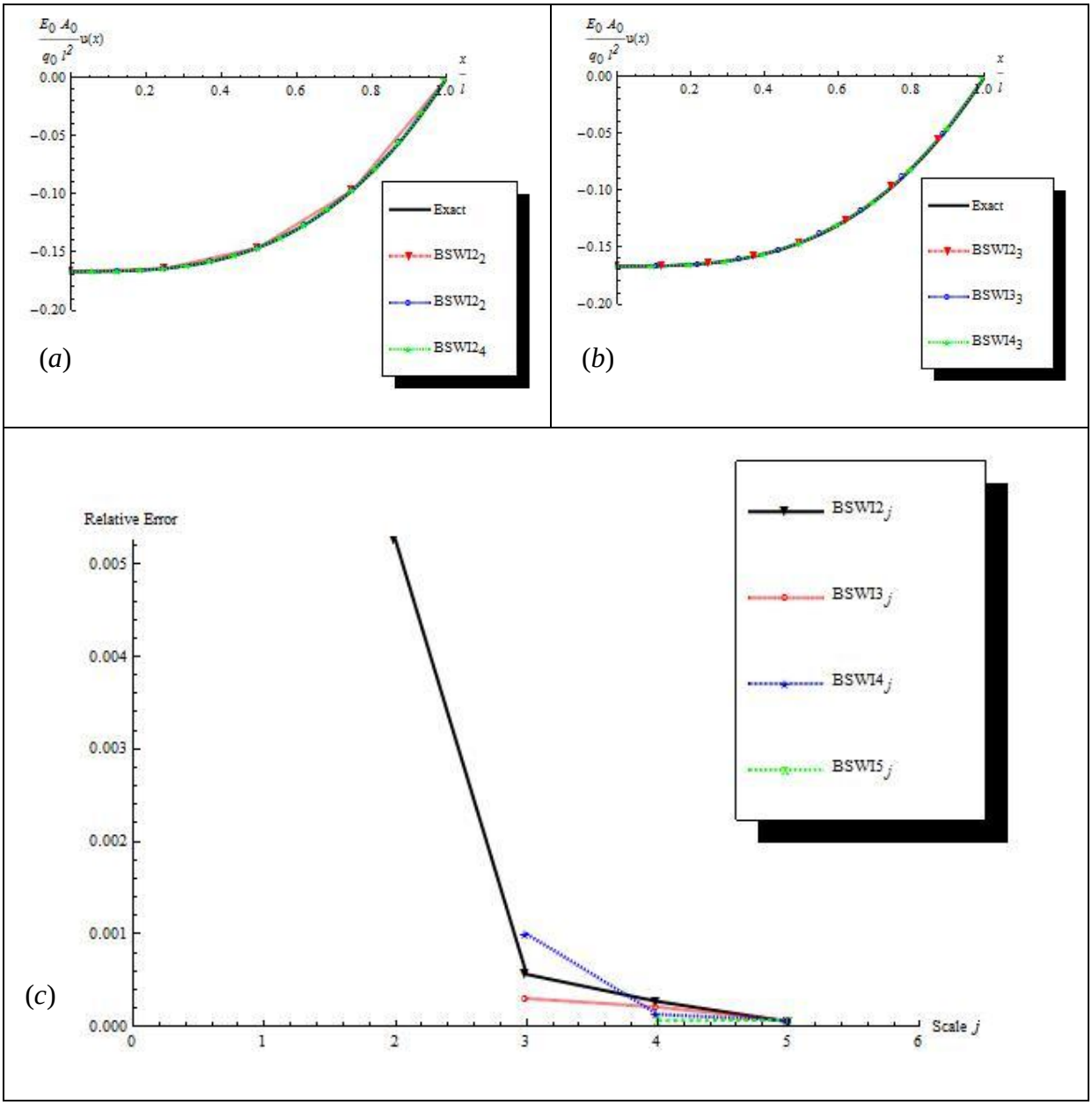

Figure 6-3: Axial deformation of a uniform cantilever rod subjected to a linear varying load $q(x)$ for BSWI WFEM. (*a*) BSWI2$_j$, (*b*) BSWIm_3. (*c*) Absolute relative error at $x = 0.1l$ for BSWI WFEM.

The convergence of the axial deformation at point $0.1l$ is compared in Figure 6-4 for the different approaches. The plot shows the absolute relative error of the axial deformation corresponding to the number of DOFs. The rates of convergence of all the methods are similar, though the WFEM approaches have a slightly improved rate. The small peak observed for the *p*-FEM formulation in the graph is attributed the fact that the location on the rod being analysed does not coincide with an elemental node point. Therefore, the approximate axial deformation at this point is obtained via interpolation.

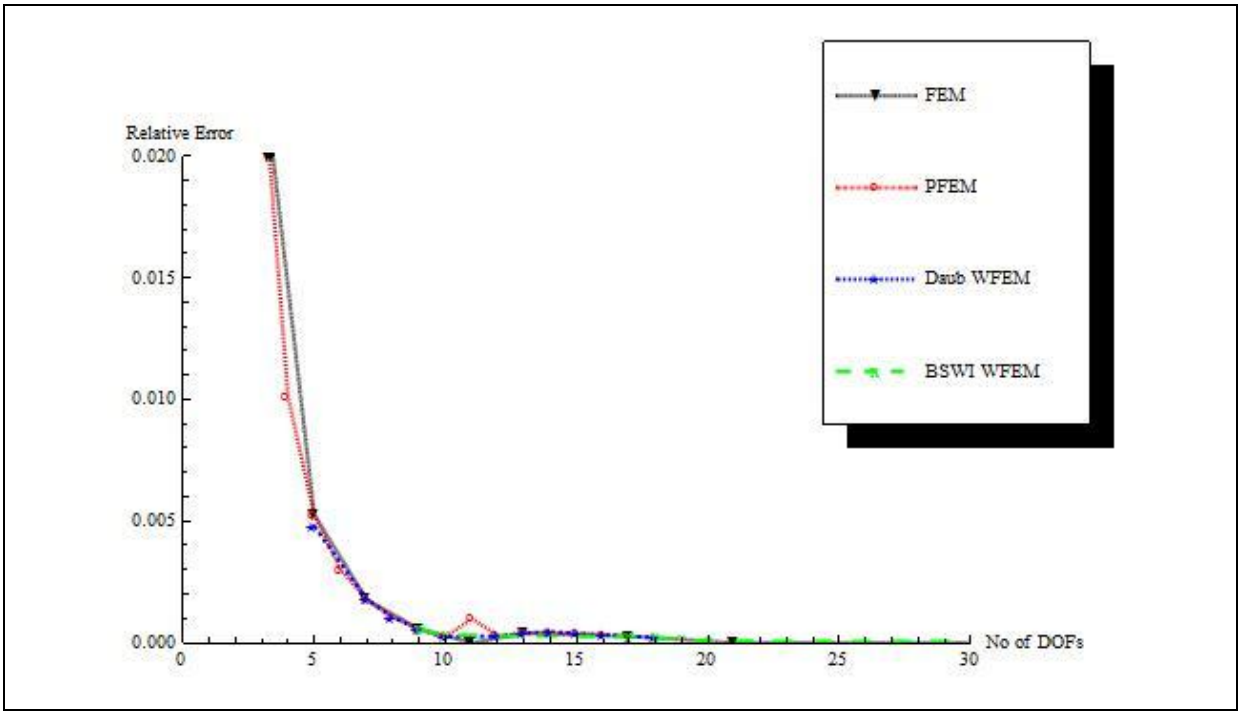

Figure 6-4: Comparison of the convergence of the axial deformation at point $x = 0.1\ l$.

The strain behaviour of the rod is similar to the stress; given that the rod has a uniform cross section and constant Young's modulus. Figure 6-5 illustrates the axial stress along the length of the rod using (*a*) the FEM approach and (*b*) higher order *p*-FEM approach. From Figure 6-5(*a*), the FEM approach with lower number of elements is not very accurate. This is due to the fact that the axial stress is evaluated from the first derivative of the axial deformation and is therefore constant within each element since the axial deformation is a linear function. Furthermore, the equilibrium across the element boundaries is not satisfied and this is evident from the discontinuities observed across the element boundaries. Therefore, so as to increase the accuracy of the axial stress approximation across the rod via the FEM solution, it is necessary to increase the number of elements.

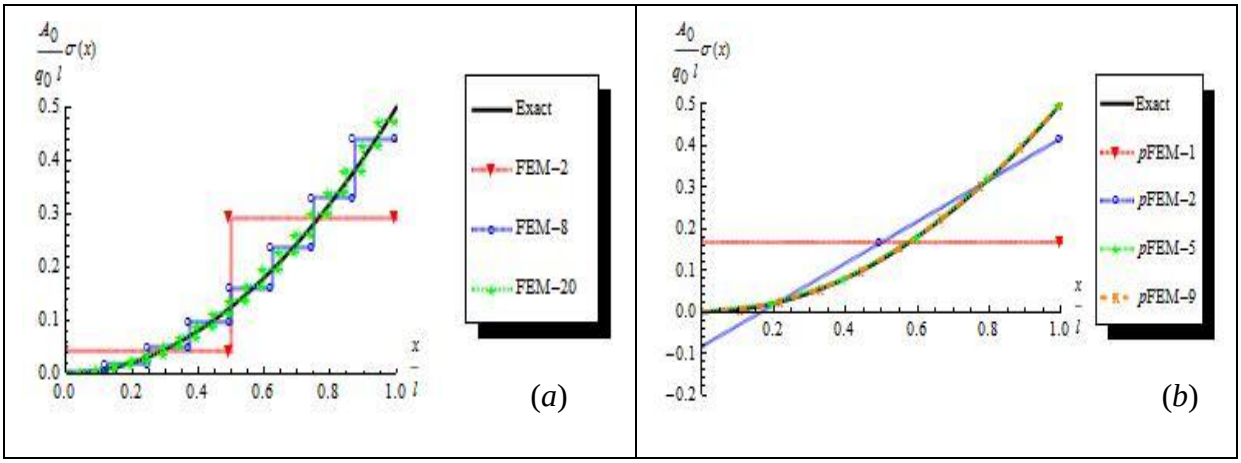

Figure 6-5: Axial stress of a uniform cantilever rod subjected to a linear varying load $q(x)$. (*a*) FEM. (*b*) *p*-FEM.

The results of the axial stress for the initial low order polynomial formulations do not exhibit high accuracy levels for the *p*-FEM, as observed in Figure 6-5(*b*). For *p*-FEM-*1*, the axial stress is constant along the entire rod element since the axial deformation is a linear function. In addition, the axial stress for *p*-FEM-*2* is linear since the axial deformation is expressed as a quadratic function. Therefore, the results converge to the exact solution as the order of the polynomial m increases. This implies that if lower order polynomial FEM formulations are used, such as $m = 1$ or 2, the results converge by increasing the number of elements.

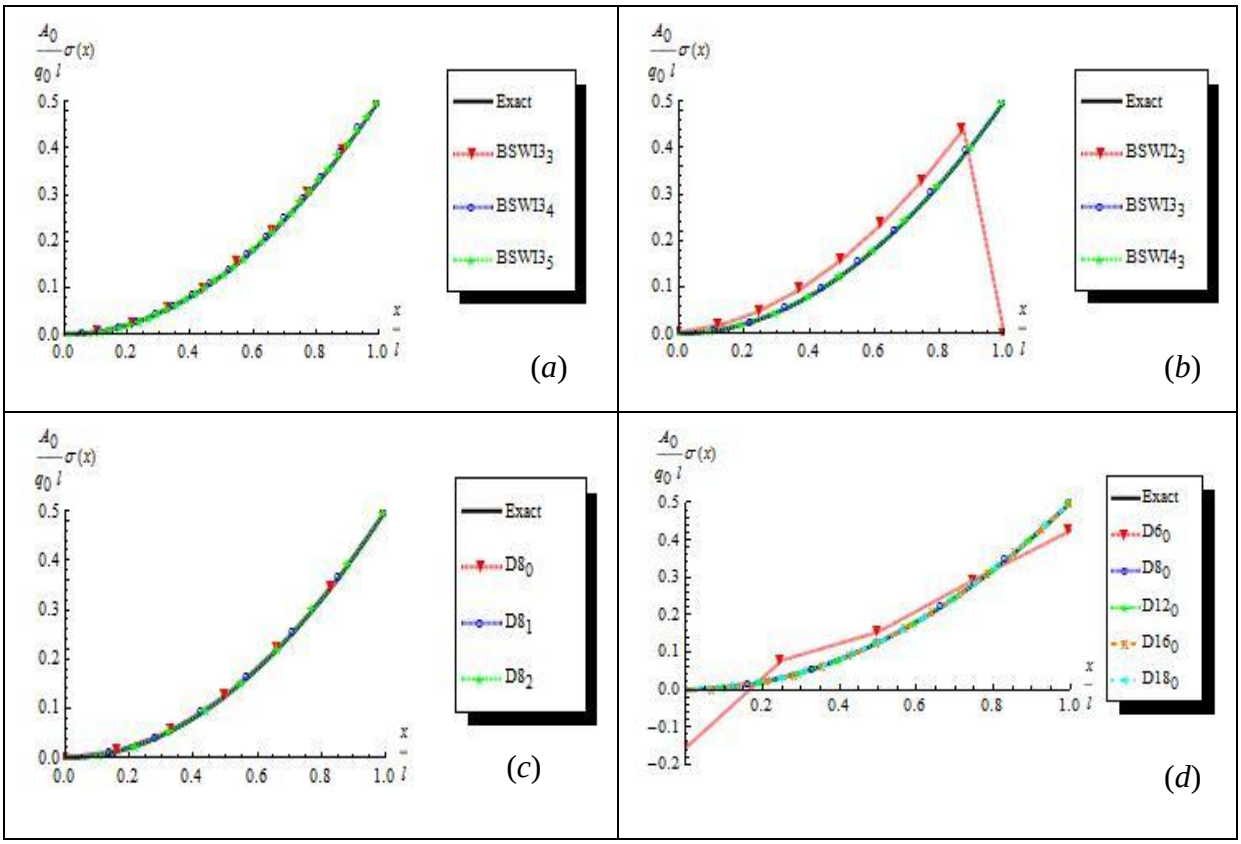

Figure 6-6: Axial stress of a uniform cantilever rod subjected to a linear varying load $q(x)$. (*a*) BSWI3$_j$. (*b*) BSWIm_3. (*c*) D8$_j$. (*d*) DL_j elements.

Figure 6-6 illustrates the variation of the axial stress across the rod element using the WFEM approaches for different orders and multiresolution scales. In Figure 6-6 (*a*), the axial stress across the rod for the BSWI3$_j$ ($3 \leq j \leq 5$) WFE solution are in very good agreement with the exact solution and better approximations are obtained by increasing the multiresolution scale j. In Figure 6-6 (*b*), the axial stress is in good agreement with the exact solution for BSWI3$_3$ and BSWI4$_3$ elements. The BSWI2$_3$ element is not as accurate, with discontinuities observed at the elemental end nodes. However, increasing the scale for BSWI2$_j$ leads to a convergence of the results as the approximation of the stresses at the inner elemental nodes increase in accuracy. The BSWI2$_j$ rod element is in C^0, therefore making it the lowest order of the BSWI that can be used to meet the completeness and continuity requirements of the field variable,

which in this case is the axial deformation. However, there are discontinuities present at the end elemental nodes, thus the stresses and strains across element boundaries are not continuous. It is therefore necessary to apply a higher order BSWI wavelet to ensure continuity of the inter element stresses and strains, as is the case for BSWIm_j for $m \geq 3$.

In the case of the Daubechies WFEM, the axial stresses across the rod for the D8_j element ($0 \leq j \leq 2$) are presented in Figure 6-6 (*c*). The results are highly accurate when compared with the exact solution. Furthermore, increasing the scale *j* leads to the convergence of the results. Similarly, increasing the order of the Daubechies wavelet based element also leads to an increase in accuracy levels as observed in Figure 6-6 (*d*). Even though continuity requirements within and between the WFEs are met, the stress variation across the rod obtained from the D6_0 element is not as precise and this is due to the highly oscillatory nature of the first derivative of the scaling functions employed to obtain axial the stresses.

Therefore, for static analysis of axial rods using the WFEMs, the axial deformation can be accurately solved using the D6_j and BSWI2_2 WFEs. However, the axial stress and stain solutions at the elemental end nodes require the higher order D8_j and BSWI3_3 WFEs. It is also important to mention that the BSWI WFEM requires that the coarsest multiresolution scale $j \geq j_0$ for the accurate formulation of the elemental matrices, which is consistent with the findings of Xiang et al. [7]. This is in contrast to the Daubechies WFE matrices which are accurately computed at multiresolution scale $j \geq 0$.

6.2. Fixed end Euler Bernoulli uniform beam subjected to a varying distributed load

An elastic Euler Bernoulli beam of uniform cross section *A*, bending stiffness EI and length 2*l*, is subjected to a varying distributed load as illustrated in Figure 6-7. The beam is fixed at both ends and the varying load $q(x) = 480q_0(\frac{x}{l} - 1)$ is subjected at the right half of the beam. The example is one that has been implemented by Ma et al. [10] and Diaz et al. [40] to carry out a static analysis of a beam using the Daubechies WFEM. However, the example is presented in this study to aid in the comparison of the Daubechies and BSWI wavelet beam solutions as well as the *h* and *p* adaptive FEM approaches. Furthermore, some aspects relating to the application of the Daubechies and BSWI WFEMs need to be further discussed for static beam analysis, such as: the effects of altering the layout of the wavelet based beam finite element and the implementation of the orders of the wavelet based elements.

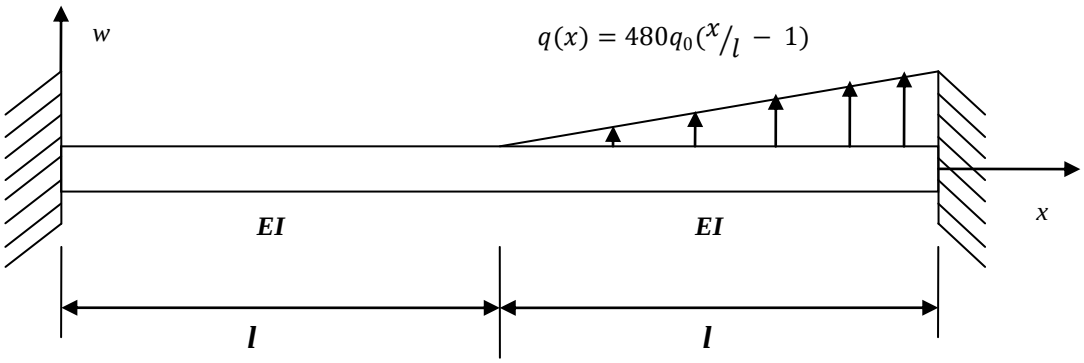

Figure 6-7: Fixed-fixed beam of uniform cross section subjected to a linear varying load on the right half of the beam.

The deflection of the beam without the implementation of boundary conditions can be obtained analytically via the double integration method and is given as:

$$w(x) = \begin{cases} \frac{1}{EI}(4\,q_0\,l\,x^3 - 7\,q_0\,l^2\,x^2 + c_1x + c_2) & \text{for } 0 \le x < l \\ \frac{1}{EI}\left(20\,q_0\,x^4 - \frac{4\,q_0\,x^5}{l} - 36q_0\,l\,x^3 + 33q_0\,l^2\,x^2 + c_3x + c_4\right) & \text{for } l \le x \le 2l \end{cases} \quad \textbf{(6.8)}$$

while the slope of the beam is

$$w'(x) = \begin{cases} \frac{1}{EI}(12\,q_0\,l\,x^2 - 14\,q_0\,l^2\,x + c_1) & \text{for } 0 \le x < l \\ \frac{1}{EI}\left(80\,q_0\,x^3 - \frac{20\,q_0\,x^4}{l} - 108q_0\,l\,x^2 + 66q_0\,l^2\,x + c_3\right) & \text{for } l \le x \le 2l \end{cases} \quad \textbf{(6.9)}$$

The integration constants c_i are obtained by imposing the boundary conditions. The beam is fixed at both ends and therefore, the rotations and displacements at both ends are zero. Thus, for this particular case, the constants are evaluated as:

$$c_1 = 0,\, c_2 = 0,\, c_3 = -20\,q_0\,l^3,\, c_3 = 4\,q_0\,l^4 \quad \textbf{(6.10)}$$

By substituting (6.10) into (6.8) and (6.9), the deflection can be evaluated as:

$$w(x) = \begin{cases} \frac{1}{EI}(4\,q_0\,l\,x^3 - 7\,q_0\,l^2\,x^2) & \text{for } 0 \le x < l \\ \frac{1}{EI}\left(20\,q_0\,x^4 - \frac{4\,q_0\,x^5}{l} - 36q_0\,l\,x^3 + 33q_0\,l^2\,x^2 - 20\,q_0\,l^3x + 4\,q_0\,l^4\right) & \text{for } l \le x \le 2l \end{cases} \quad \textbf{(6.11)}$$

and the slope function

$$w'(x) = \begin{cases} \frac{1}{EI}(12\,q_0\,l\,x^2 - 14\,q_0\,l^2\,x) & \text{for } 0 \le x < l \\ \frac{1}{EI}\left(80\,q_0\,x^3 - \frac{20\,q_0\,x^4}{l} - 108q_0\,l\,x^2 + 66q_0\,l^2\,x - 20\,q_0\,l^3\right) & \text{for } l \le x \le 2l \end{cases} \quad \textbf{(6.12)}$$

The strains and stresses can therefore be computed as:

$$\varepsilon(x) = -yu''(x) = \begin{cases} -\frac{y}{EI}\left(24\, q_0\, l\, x - 14\, q_0\, l^2\right) & \text{for } 0 \le x < l \\ -\frac{y}{EI}\left(240\, q_0\, x^2 - \frac{80\, q_0\, x^3}{l} - 216 q_0\, l\, x + 66 q_0\, l^2\right) & \text{for } l \le x \le 2l \end{cases} \quad \textbf{(6.13)}$$

$$\sigma(x) = E\varepsilon(x) = \begin{cases} -\frac{y}{I}\left(24\, q_0\, l\, x - 14\, q_0\, l^2\right) & \text{for } 0 \le x < l \\ -\frac{y}{I}\left(240\, q_0\, x^2 - \frac{80\, q_0\, x^3}{l} - 216 q_0\, l\, x + 66 q_0\, l^2\right) & \text{for } l \le x \le 2l \end{cases} \quad \textbf{(6.14)}$$

Consequently, the curvature, bending moments and shear force across the beam can be obtained by differentiating equation (6.11). The curvature of the beam is given as:

$$\frac{1}{R} = \begin{cases} \frac{1}{EI}\left(24\, q_0\, l\, x - 14\, q_0\, l^2\right) & \text{for } 0 \le x < l \\ \frac{1}{EI}\left(240\, q_0\, x^2 - \frac{80\, q_0\, x^3}{l} - 216 q_0\, l\, x + 66 q_0\, l^2\right) & \text{for } l \le x \le 2l \end{cases} \quad \textbf{(6.15)}$$

The bending moments:

$$M(x) = \frac{EI}{R} = \begin{cases} \left(24\, q_0\, l\, x - 14\, q_0\, l^2\right) & \text{for } 0 \le x < l \\ \left(240\, q_0\, x^2 - \frac{80\, q_0\, x^3}{l} - 216 q_0\, l\, x + 66 q_0\, l^2\right) & \text{for } l \le x \le 2l \end{cases} \quad \textbf{(6.16)}$$

The shear force:

$$V(x) = EI\, w'''(x) = \begin{cases} 24\, q_0\, l & \text{for } 0 \le x < l \\ \frac{1}{EI}\left(480\, q_0\, x - \frac{240\, q_0\, x^2}{l} - 216 q_0\, l\right) & \text{for } l \le x \le 2l \end{cases} \quad \textbf{(6.17)}$$

The generalised potential energy function for the Euler Bernoulli beam is [31]:

$$\Pi^b = \int_0^{2l} \frac{EI}{2}\left(\frac{d^2 v(x)}{dx^2}\right)^2 dx - \int_0^{2l} q(x) v(x) dx \quad \textbf{(6.18)}$$

Following a similar procedure as presented in Section 5.2, the equation governing the static behaviour of the system can be expressed as:

$$[\boldsymbol{K_b}]\{\boldsymbol{V_b}\} = \{\boldsymbol{F_b}\} \quad \textbf{(6.19)}$$

where $[\boldsymbol{K_b}]$ is the system global stiffness matrix, $\{\boldsymbol{V_b}\}$ is the system vector containing the global DOFs and $\{\boldsymbol{F_b}\}$ is the system global force vector.

The Daubechies and BSWI wavelet based beam finite elements derived in Section 5.2 have the vertical displacement (and corresponding force) DOFs at each elemental node and rotation (and corresponding moments) DOFs at the elemental end nodes only. However, the WFEM allows for the alteration of the elemental DOFs and corresponding number and/or position of the elemental nodes, depending on the nature of the problem and results sort after. The layout used in the formulation of the beam WFE in Section 5.2 will be referred to as layout 1 for convenience and simplicity. A second layout of the wavelet based beam finite

element, referred to as layout 2, is used to formulate a beam element for comparison and illustration purposes. The wavelet beam formulated using layout 2, as illustrated in Figure 6-8, contains the vertical displacement and rotation DOFs, and corresponding force and moment DOFs, at each elemental node. In this analysis, the Daubechies D10_1 and BSWI3_3 beam WFEs are formulated using both layouts.

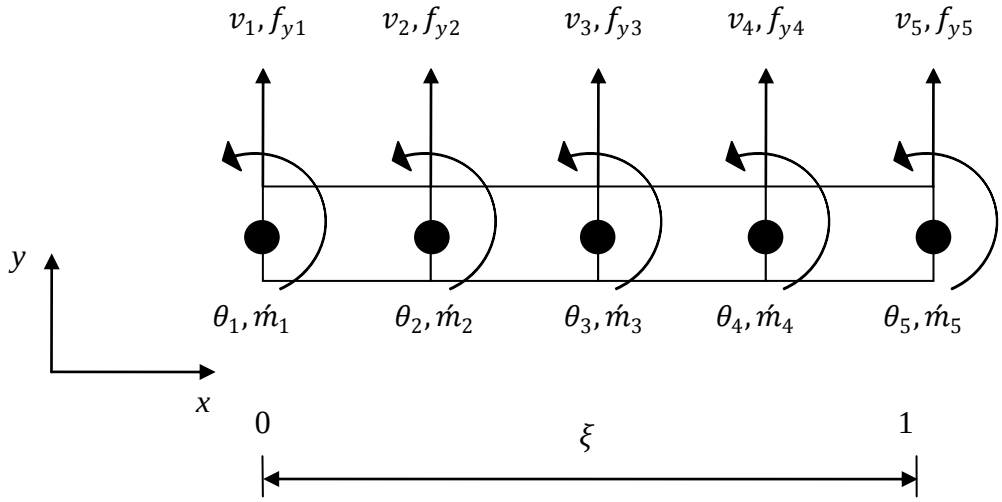

Figure 6-8: Euler Bernoulli beam wavelet finite element layout with rotation DOFs at each elemental node.

As earlier mentioned, the beam WFE total DOFs corresponding to a particular order of wavelet at scale *j* remain the same irrespective of the layout selected. The total DOFs for the Daubechies DL_j beam WFEs are obtained as $2^j + L - 2$ and $2^j + m - 1$ for the BSWIm_j beam WFEs. Thus, the total DOFs for both the D10_1 and BSWI3_3 beam WFEs are equal to 10. In order to satisfy the desired requirement of having a vertical displacement and rotation DOF at each elemental node in layout 2, the WFEs have 4 elemental segments and 5 elemental nodes. In contrast, layout 1 has 7 elemental segments and 8 corresponding elemental nodes. The vertical displacement and rotation DOFs at node *i* for the Daubechies beam D10_1 WFE are given as:

$$v_i = v(\xi_i) = \sum_{k=2-L}^{2^j-1} b_{L,k}^j \, \phi_{L,k}^j(\xi_i) = {}_{(1 \times 10)}\left\{\boldsymbol{\Phi}_{\boldsymbol{L}}^{\boldsymbol{j}}(\xi_i)\right\} \, {}_{(10 \times 1)}\{\boldsymbol{b_e}\} \qquad \textbf{(6.20)}$$

$$\theta_i = \theta(\xi_i) = \frac{1}{L_e} \sum_{k=2-L}^{2^j-1} b_{L,k}^j \, \phi'^j_{L,k}(\xi_i) = \frac{1}{L_e} \, {}_{(1 \times 10)}\left\{\boldsymbol{\Phi}'^{\boldsymbol{j}}_{\boldsymbol{L}}(\xi_i)\right\} \, {}_{(10 \times 1)}\{\boldsymbol{b_e}\} \qquad \textbf{(6.21)}$$

The D10_1 beam wavelet transformation matrices for layout 1 and layout 2 are obtained as:

$$
{}^{D10_1,1}_{(10\text{ x }10)}[\boldsymbol{T_b^w}] =
$$

$$
\begin{bmatrix}
\phi^1_{10,-8}(0) & \phi^1_{10,-7}(0) & \phi^1_{10,-6}(0) & \cdots & \phi^1_{10,-1}(0) & \phi^1_{10,0}(0) & \phi^1_{10,1}(0) \\
\frac{1}{L_e}\phi'^1_{10,-8}(0) & \frac{1}{L_e}\phi'^1_{10,-7}(0) & \frac{1}{L_e}\phi'^1_{10,-6}(0) & \cdots & \frac{1}{L_e}\phi'^1_{10,-1}(0) & \frac{1}{L_e}\phi'^1_{10,0}(0) & \frac{1}{L_e}\phi'^1_{10,1}(0) \\
\phi^1_{10,-8}\left(\frac{1}{7}\right) & \phi^1_{10,-7}\left(\frac{1}{7}\right) & \phi^1_{10,-6}\left(\frac{1}{7}\right) & \cdots & \phi^1_{10,-1}\left(\frac{1}{7}\right) & \phi^1_{10,0}\left(\frac{1}{7}\right) & \phi^1_{10,1}\left(\frac{1}{7}\right) \\
\phi^1_{10,-8}\left(\frac{2}{7}\right) & \phi^1_{10,-7}\left(\frac{2}{7}\right) & \phi^1_{10,-6}\left(\frac{2}{7}\right) & \cdots & \phi^1_{10,-1}\left(\frac{2}{7}\right) & \phi^1_{10,0}\left(\frac{2}{7}\right) & \phi^1_{10,1}\left(\frac{2}{7}\right) \\
\vdots & \vdots & \vdots & \ddots & \vdots & \vdots & \vdots \\
\phi^1_{10,-8}\left(\frac{6}{7}\right) & \phi^1_{10,-7}\left(\frac{6}{7}\right) & \phi^1_{10,-6}\left(\frac{6}{7}\right) & \cdots & \phi^1_{10,-1}\left(\frac{6}{7}\right) & \phi^1_{10,0}\left(\frac{6}{7}\right) & \phi^1_{10,1}\left(\frac{6}{7}\right) \\
\phi^1_{10,-8}(1) & \phi^1_{10,-7}(1) & \phi^1_{10,-6}(1) & \cdots & \phi^1_{10,-1}(1) & \phi^1_{10,0}(1) & \phi^1_{10,1}(1) \\
\frac{1}{L_e}\phi'^1_{10,-8}(1) & \frac{1}{L_e}\phi'^1_{10,-7}(1) & \frac{1}{L_e}\phi'^1_{10,-6}(1) & \cdots & \frac{1}{L_e}\phi'^1_{10,-1}(1) & \frac{1}{L_e}\phi'^1_{10,0}(1) & \frac{1}{L_e}\phi'^1_{10,1}(1)
\end{bmatrix}^{-1} \qquad \textbf{(6.22)}
$$

$$
{}^{D10_1,2}_{(10\text{ x }10)}[\boldsymbol{T_b^w}] =
$$

$$
\begin{bmatrix}
\phi^1_{10,-8}(0) & \phi^1_{10,-7}(0) & \phi^1_{10,-6}(0) & \cdots & \phi^1_{10,-1}(0) & \phi^1_{10,0}(0) & \phi^1_{10,1}(0) \\
\frac{1}{L_e}\phi'^1_{10,-8}(0) & \frac{1}{L_e}\phi'^1_{10,-7}(0) & \frac{1}{L_e}\phi'^1_{10,-6}(0) & \cdots & \frac{1}{L_e}\phi'^1_{10,-1}(0) & \frac{1}{L_e}\phi'^1_{10,0}(0) & \frac{1}{L_e}\phi'^1_{10,1}(0) \\
\phi^1_{10,-8}\left(\frac{1}{4}\right) & \phi^1_{10,-7}\left(\frac{1}{4}\right) & \phi^1_{10,-6}\left(\frac{1}{4}\right) & \cdots & \phi^1_{10,-1}\left(\frac{1}{4}\right) & \phi^1_{10,0}\left(\frac{1}{4}\right) & \phi^1_{10,1}\left(\frac{1}{4}\right) \\
\frac{1}{L_e}\phi'^1_{10,-8}\left(\frac{1}{4}\right) & \frac{1}{L_e}\phi'^1_{10,-7}\left(\frac{1}{4}\right) & \frac{1}{L_e}\phi'^1_{10,-6}\left(\frac{1}{4}\right) & \cdots & \frac{1}{L_e}\phi'^1_{10,-1}\left(\frac{1}{4}\right) & \frac{1}{L_e}\phi'^1_{10,0}\left(\frac{1}{4}\right) & \frac{1}{L_e}\phi'^1_{10,1}\left(\frac{1}{4}\right) \\
\vdots & \vdots & \vdots & \ddots & \vdots & \vdots & \vdots \\
\phi^1_{10,-8}\left(\frac{3}{4}\right) & \phi^1_{10,-7}\left(\frac{3}{4}\right) & \phi^1_{10,-6}\left(\frac{3}{4}\right) & \cdots & \phi^1_{10,-1}\left(\frac{3}{4}\right) & \phi^1_{10,0}\left(\frac{3}{4}\right) & \phi^1_{10,1}\left(\frac{3}{4}\right) \\
\frac{1}{L_e}\phi'^1_{10,-8}\left(\frac{3}{4}\right) & \frac{1}{L_e}\phi'^1_{10,-7}\left(\frac{3}{4}\right) & \frac{1}{L_e}\phi'^1_{10,-6}\left(\frac{3}{4}\right) & \cdots & \frac{1}{L_e}\phi'^1_{10,-1}\left(\frac{3}{4}\right) & \frac{1}{L_e}\phi'^1_{10,0}\left(\frac{3}{4}\right) & \frac{1}{L_e}\phi'^1_{10,1}\left(\frac{3}{4}\right) \\
\phi^1_{10,-8}(1) & \phi^1_{10,-7}(1) & \phi^1_{10,-6}(1) & \cdots & \phi^1_{10,-1}(1) & \phi^1_{10,0}(1) & \phi^1_{10,1}(1) \\
\frac{1}{L_e}\phi'^1_{10,-8}(1) & \frac{1}{L_e}\phi'^1_{10,-7}(1) & \frac{1}{L_e}\phi'^1_{10,-6}(1) & \cdots & \frac{1}{L_e}\phi'^1_{10,-1}(1) & \frac{1}{L_e}\phi'^1_{10,0}(1) & \frac{1}{L_e}\phi'^1_{10,1}(1)
\end{bmatrix}^{-1} \qquad \textbf{(6.23)}
$$

where ${}^{D10_1,1}[\boldsymbol{T_b^w}]$ and ${}^{D10_1,2}[\boldsymbol{T_b^w}]$ denote the D10_1 wavelet transformation matrices for layout 1 and layout 2 respectively. Similarly, the BSWI3_3 element vertical displacement and rotation DOFs are obtained as:

$$
v_i = v(\xi_i) = \sum_{k=-m+1}^{2^j-1} b^j_{m,k}\,\phi^j_{m,k}(\xi_i) = {}_{(1\text{ x }10)}\left\{\boldsymbol{\Phi^j_m}(\xi_i)\right\}_{(10\text{ x }1)}\{\boldsymbol{b_e}\} \qquad \textbf{(6.24)}
$$

$$
\theta_i = \theta(\xi_i) = \frac{1}{L_e}\sum_{k=-m+1}^{2^j-1} b^j_{m,k}\,\phi'^j_{m,k}(\xi_i) = \frac{1}{L_e}\,{}_{(1\text{ x }10)}\left\{\boldsymbol{\Phi'^j_m}(\xi_i)\right\}_{(10\text{ x }1)}\{\boldsymbol{b_e}\} \qquad \textbf{(6.25)}
$$

and the wavelet transformation matrices are

$$
{}^{BSWI3_3,1}_{(10\ x\ 10)}[\boldsymbol{T_b^w}] = \begin{bmatrix} \phi^3_{3,-2}(0) & \phi^3_{3,-1}(0) & \dots & \phi^3_{3,6}(0) & \phi^3_{3,7}(0) \\ \frac{1}{L_e}\phi'^3_{3,-2}(0) & \frac{1}{L_e}\phi'^3_{3,-1}(0) & \cdots & \frac{1}{L_e}\phi'^3_{3,6}(0) & \frac{1}{L_e}\phi'^3_{3,7}(0) \\ \phi^3_{3,-2}\left(\frac{1}{7}\right) & \phi^3_{3,-1}\left(\frac{1}{7}\right) & \cdots & \phi^3_{3,6}\left(\frac{1}{7}\right) & \phi^3_{3,7}\left(\frac{1}{7}\right) \\ \vdots & \vdots & \ddots & \vdots & \vdots \\ \phi^3_{3,-2}\left(\frac{6}{7}\right) & \phi^3_{3,-1}\left(\frac{6}{7}\right) & \dots & \phi^3_{3,6}\left(\frac{6}{7}\right) & \phi^3_{3,7}\left(\frac{6}{7}\right) \\ \phi^3_{3,-2}(1) & \phi^3_{3,-1}(1) & \cdots & \phi^3_{3,6}(1) & \phi^3_{3,7}(1) \\ \frac{1}{L_e}\phi'^3_{3,-2}(1) & \frac{1}{L_e}\phi'^3_{3,-1}(1) & \cdots & \frac{1}{L_e}\phi'^3_{3,6}(1) & \frac{1}{L_e}\phi'^3_{3,7}(1) \end{bmatrix}^{-1} \tag{6.26}
$$

$$
{}^{BSWI3_3,2}_{(10\ x\ 10)}[\boldsymbol{T_b^w}] = \begin{bmatrix} \phi^3_{3,-2}(0) & \phi^3_{3,-1}(0) & \dots & \phi^3_{3,6}(0) & \phi^3_{3,7}(0) \\ \frac{1}{L_e}\phi'^3_{3,-2}(0) & \frac{1}{L_e}\phi'^3_{3,-1}(0) & \cdots & \frac{1}{L_e}\phi'^3_{3,6}(0) & \frac{1}{L_e}\phi'^3_{3,7}(0) \\ \phi^3_{3,-2}\left(\frac{1}{4}\right) & \phi^3_{3,-1}\left(\frac{1}{4}\right) & \cdots & \phi^3_{3,6}\left(\frac{1}{4}\right) & \phi^3_{3,7}\left(\frac{1}{4}\right) \\ \frac{1}{L_e}\phi'^3_{3,-2}\left(\frac{1}{4}\right) & \frac{1}{L_e}\phi'^3_{3,-1}\left(\frac{1}{4}\right) & \cdots & \frac{1}{L_e}\phi'^3_{3,6}\left(\frac{1}{4}\right) & \frac{1}{L_e}\phi'^3_{3,7}\left(\frac{1}{4}\right) \\ \vdots & \vdots & \ddots & \vdots & \vdots \\ \phi^3_{3,-2}\left(\frac{3}{4}\right) & \phi^3_{3,-1}\left(\frac{3}{4}\right) & \dots & \phi^3_{3,6}\left(\frac{3}{4}\right) & \phi^3_{3,7}\left(\frac{3}{4}\right) \\ \frac{1}{L_e}\phi'^3_{3,-2}\left(\frac{3}{4}\right) & \frac{1}{L_e}\phi'^3_{3,-1}\left(\frac{3}{4}\right) & \cdots & \frac{1}{L_e}\phi'^3_{3,6}\left(\frac{3}{4}\right) & \frac{1}{L_e}\phi'^3_{3,7}\left(\frac{3}{4}\right) \\ \phi^3_{3,-2}(1) & \phi^3_{3,-1}(1) & \cdots & \phi^3_{3,6}(1) & \phi^3_{3,7}(1) \\ \frac{1}{L_e}\phi'^3_{3,-2}(1) & \frac{1}{L_e}\phi'^3_{3,-1}(1) & \cdots & \frac{1}{L_e}\phi'^3_{3,6}(1) & \frac{1}{L_e}\phi'^3_{3,7}(1) \end{bmatrix}^{-1} \tag{6.27}
$$

where ${}^{BSWI3_3,1}[\boldsymbol{T_b^w}]$ and ${}^{BSWI3_3,2}[\boldsymbol{T_b^w}]$ denote the BSWI3_3 beam wavelet transformation matrices corresponding to layout 1 and layout 2 respectively. The stiffness and mass matrices, as well as the loading vectors in wavelet space, for both Daubechies and BSWI based beam elements remain unchanged irrespective of which layout is selected. The D10_1 and BSWI3_3 stiffness matrices in wavelet space ${}^{D10_1}[\boldsymbol{k_{b,e}^w}]$ and ${}^{BSWI3_3}[\boldsymbol{k_{b,e}^w}]$ are obtained as:

$$
{}^{D10_1}_{(10\ x\ 10)}[\boldsymbol{k_{b,e}^w}] =
$$

$$
\begin{bmatrix} 1.48\text{E}-6 & -1.30\text{E}-5 & -6.05\text{E}-4 & 2.48E-3 & -2.99\text{E}-3 & -3.11\text{E}-6 & 3.59\text{E}-3 & -2.97\text{E}-3 & 8.21E-4 & 0 \\ 1.30E-5 & 8.18E-3 & -1.92E-2 & -1.12E-1 & 5.57E-1 & -1.01E0 & 9.38E-1 & -4.60E-1 & 9.61E-2 & 8.21E-4 \\ -6.05\text{E}-4 & -1.92E-2 & 9.23E-1 & -2.46E0 & -8.73E-1 & 1.03E1 & -1.52E1 & 9.93E0 & -2.71E0 & 9.90E-2 \\ 2.48E-3 & -1.12E-1 & -2.46E0 & 1.39E1 & -2.66E1 & 1.84E1 & 7.38E0 & -1.96E1 & 1.14E1 & -2.25E0 \\ -2.99\text{E}-3 & 5.57E-1 & -8.73E-1 & -2.66E1 & 1.25E2 & -2.32E2 & 2.21E2 & -1.06E2 & 1.71E1 & 2.43E0 \\ -3.11\text{E}-6 & -1.01E0 & 1.03E1 & 1.84E1 & -2.32E2 & 5.97E2 & -7.59E2 & 5.31E2 & -1.88E2 & 2.31E0 \\ 3.59\text{E}-3 & 9.38E-1 & -1.52E1 & 7.38E0 & 2.21E2 & -7.59E2 & 1.20E3 & -1.05E3 & 4.76E2 & -8.42E1 \\ -2.97\text{E}-3 & -4.60E-1 & 9.93E0 & -1.96E1 & -1.06E2 & 5.31E2 & -1.05E3 & 1.12E3 & -6.31E2 & 1.46E2 \\ 8.21E-4 & 9.61E-2 & -2.71E0 & 1.14E1 & 1.71E1 & -1.88E2 & 4.76E2 & -6.31E2 & 4.49E2 & -1.32E2 \\ 0 & 8.21E-4 & 9.90E-2 & -2.25E0 & 2.43E0 & 2.31E0 & -8.42E1 & 1.46E2 & -1.32E2 & 4.62E2 \end{bmatrix} \tag{6.28}
$$

$$
{}^{BSWI3_3}_{(10\ x\ 10)}[\boldsymbol{k_{b,e}^w}] =
$$

$$
\begin{bmatrix} 2.048E3 & -3.072E3 & 1.024E3 & 0 & 0 & 0 & 0 & 0 & 0 & 0 \\ -3.072E3 & 5.120E3 & -2.560E3 & 5.12E2 & 0 & 0 & 0 & 0 & 0 & 0 \\ 1.204E3 & -2.560E3 & 3.072E3 & -2.048E3 & 5.12E2 & 0 & 0 & 0 & 0 & 0 \\ 0 & 5.12E2 & -2.048E3 & 3.072E3 & -2.048E3 & 5.12E2 & 0 & 0 & 0 & 0 \\ 0 & 0 & 5.12E2 & -2.048E3 & 3.072E3 & -2.048E3 & 5.12E2 & 0 & 0 & 0 \\ 0 & 0 & 0 & 5.12E2 & -2.048E3 & 3.072E3 & -2.048E3 & 5.12E2 & 0 & 0 \\ 0 & 0 & 0 & 0 & 5.12E2 & -2.048E3 & 3.072E3 & -2.048E3 & 5.12E2 & 0 \\ 0 & 0 & 0 & 0 & 0 & 5.12E2 & -2.048E3 & 3.072E3 & -2.560E3 & 1.024E3 \\ 0 & 0 & 0 & 0 & 0 & 0 & 5.12E2 & -2.560E3 & 5.120E3 & -3.072E3 \\ 0 & 0 & 0 & 0 & 0 & 0 & 0 & 1.024E3 & -3.072E3 & 2.048E3 \end{bmatrix} \tag{6.29}
$$

The Daubechies and BSWI wavelet based stiffness matrices in physical space are then evaluated by applying the wavelet transformation matrices for each corresponding layout.

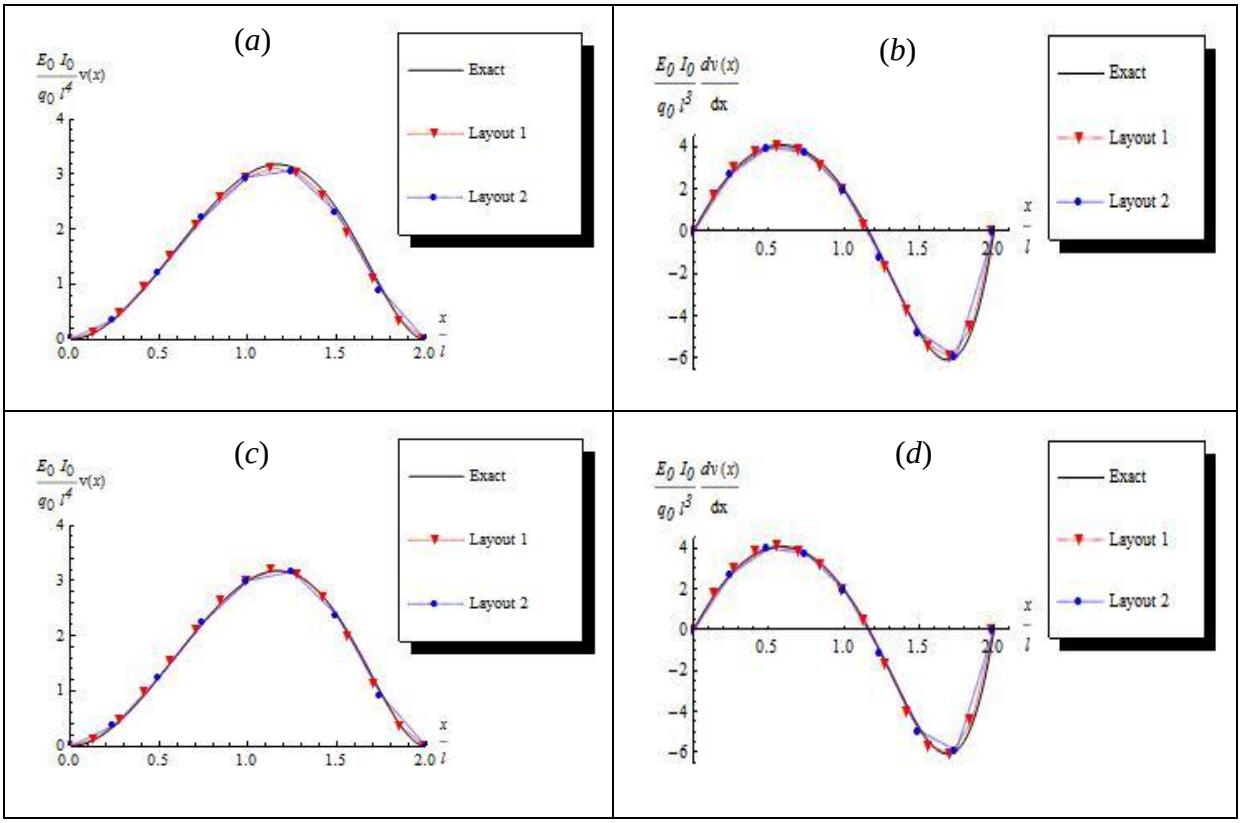

Figure 6-9: Comparison of beam wavelet based finite element layouts for BSWI3_3 WFEM (*a*) deflection and (*b*) rotation; D10_1 WFEM (*c*) deflection and (*d*) rotation of a fixed-fixed end beam of uniform cross section subjected to a varying load on the right half of the beam.

The deflections and rotations evaluated using the D10_1 and BSWI3_3 wavelet elements, formulated for both layouts, are compared with the analytical solution and presented in Figure 6-9. The approximation of the deflection in Figure 6-9 for; (*a*) BSWI3_3 and (*c*) D10_1 beam wavelet finite elements show that layout 1 leads to more accurate results in comparison to layout 2. This is expected since there are more inner elemental nodal points and consequently, vertical displacement DOFs associated with these points. Therefore, it is concluded that the number of DOFs relating to the order and multiresolution scale of a specific WFE will remain the same. However, the types and positions of the DOFs assigned to the inner elemental nodes affect the number of elemental nodes, layout of the WFEs and the accuracy of the solution. This is consistent with Xiang et al. [7] formulation of the BSWI beam WFEM, where it is stated that only the wavelet transformation matrices are modified with a change in layout of the BSWI WFE; provided the wavelet transformation matrix is non-singular. This is not restricted to the BSWI formulation of the WFEs, but also applies to the Daubechies based WFEM. Thus, the elemental matrices and loading vectors in wavelet space can be evaluated and stored so as to minimise computational costs. Furthermore, the

positions of the inner elemental nodes need not be equidistant and can be positioned such that areas with fast variations have the inner nodes closer together. The ability of the WFEM to allow for the modification of the location and number of inner elemental nodes, as well as DOFs, exhibits the versatility of the WFEM. One can manipulate the element layout in order to maximise on the efficiency and accuracy of the solutions.

If the variation of the slope along the beam is desired, it is difficult to accurate describe this variation via layout 1 by implementing the rotations obtained directly from the solutions. The rotation DOFs for both WFE approaches via layout 1 are only present at the elemental end nodes. Thus, for a case such as this where the beam is modelled using two WFEs, there are only a total of 3 rotation DOFs present, two of which are restricted by the fixed-end boundary conditions. Therefore, the 3 rotation DOFs are insufficient to accurately describe the variation of the slope across the beam.

One approach to circumvent this is to increase the number of WFEs However, this will increase the computation cost significantly. Another approach is to modify the beam WFE to include the rotation DOFs at the inner nodes, similar to layout 2. This will lead to fewer elemental nodes within the WFE, which is undesirable as it will reduce the accuracy levels and efficiency for the deflection approximation as observed earlier.

The third approach involves using the displacement solution to evaluate the rotations at each corresponding elemental node via the formulation:

$$\theta_i = \theta(\xi_i) = \frac{1}{L_e}\left\{\frac{\partial}{\partial\xi}\boldsymbol{\Phi}_{\boldsymbol{z}}^{\boldsymbol{j}}(\xi_i)\right\}[\boldsymbol{T}_{\boldsymbol{b}}^{\boldsymbol{w}}]\{\boldsymbol{v_e}\} = \frac{1}{L_e}\{\boldsymbol{N'_{b,e}}(\xi)\}\{\boldsymbol{v_e}\} \qquad \textbf{(6.30)}$$

where $\{\boldsymbol{v_e}\}$ is the vector containing the solved wavelet element DOFs in physical space. This approach is used to obtain the rotation approximations across the beam for layout 1; which is compared with the rotations obtain directly from layout 2 in Figure 6-9 for the (*b*) BSWI3_3 and (*d*) D10_1 WFEs. According to the results layout 1 provides a better approximation to layout 2 since there are more elemental nodes within the WFEs

The subsequent results in this section are obtained via layout 1. The Daubechies based WFE solutions for the variation of the deflection and rotation along the beam are presented in Figure 6-10; for different orders and multiresolution. Figure 6-10 (*a*) illustrates via the D10_j WFE that increasing the multiresolution of the wavelet element increases the accuracy of the deflection approximation. Increasing the order also improves the accuracy of the deflection since higher order Daubechies wavelets are able to exactly represent higher order

polynomials. The results for D*10*, D*12*, D*14*, D*16* and D*18* at scale $j = 0$ are in good agreement with the exact analytical solution as presented in Figure 6-10 (*b*). The results are not as precise for the D20_0 element due to the numerical instabilities that affect higher order Daubechies wavelets, which are also highlighted in [40].

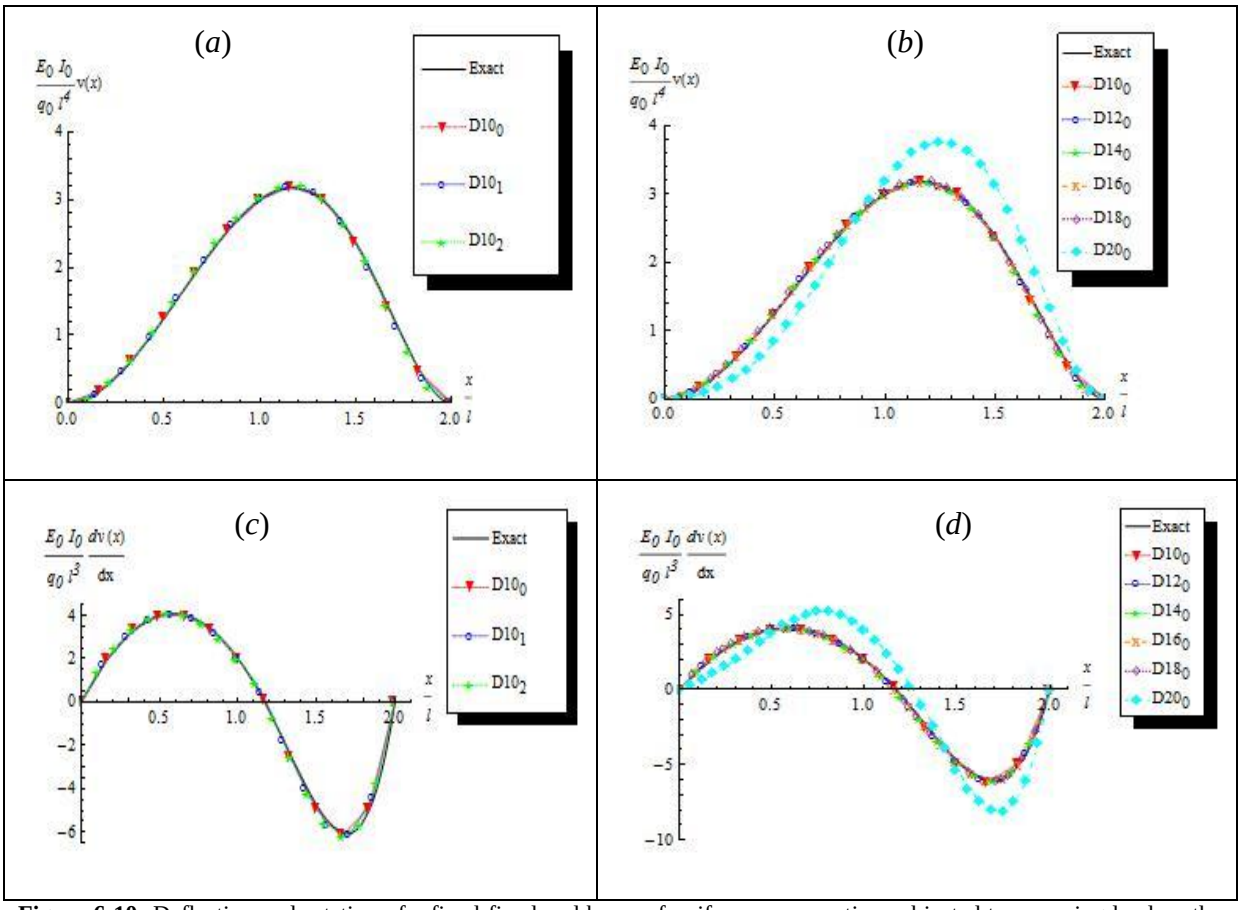

Figure 6-10: Deflection and rotation of a fixed-fixed end beam of uniform cross section subjected to a varying load on the right half of the beam for Daubechies WFEM. (*a*) Deflection D10_j. (*b*) deflection DL_j. (*c*) rotation D10_j. (*d*) rotation DL_0 elements.

The rotation of the beam for the Daubechies WFEM is illustrated in Figure 6-10 for (*c*) D10_j and (*d*) DL_0 element beams. From these graphs, the accuracy of the rotation improves as the order and/or multiresolution scale of the WFE is increased. However, since the approximation of the beam displacements is not as accurate for D20_0, the rotation across the beam is also not as accurate.

Figure 6-11 (*a*) and (*b*) show the variation of the displacement across the beam using the BSWI based WFEM for different orders and different scales *j*. The results are observed to be in very good agreement with the exact solution. Figure 6-11 (*c*) and Figure 6-11 (*d*) show that the rotation approximations across the beam obtained via the BSWI WFEM are highly accurate for the different orders and resolution scales *j*.

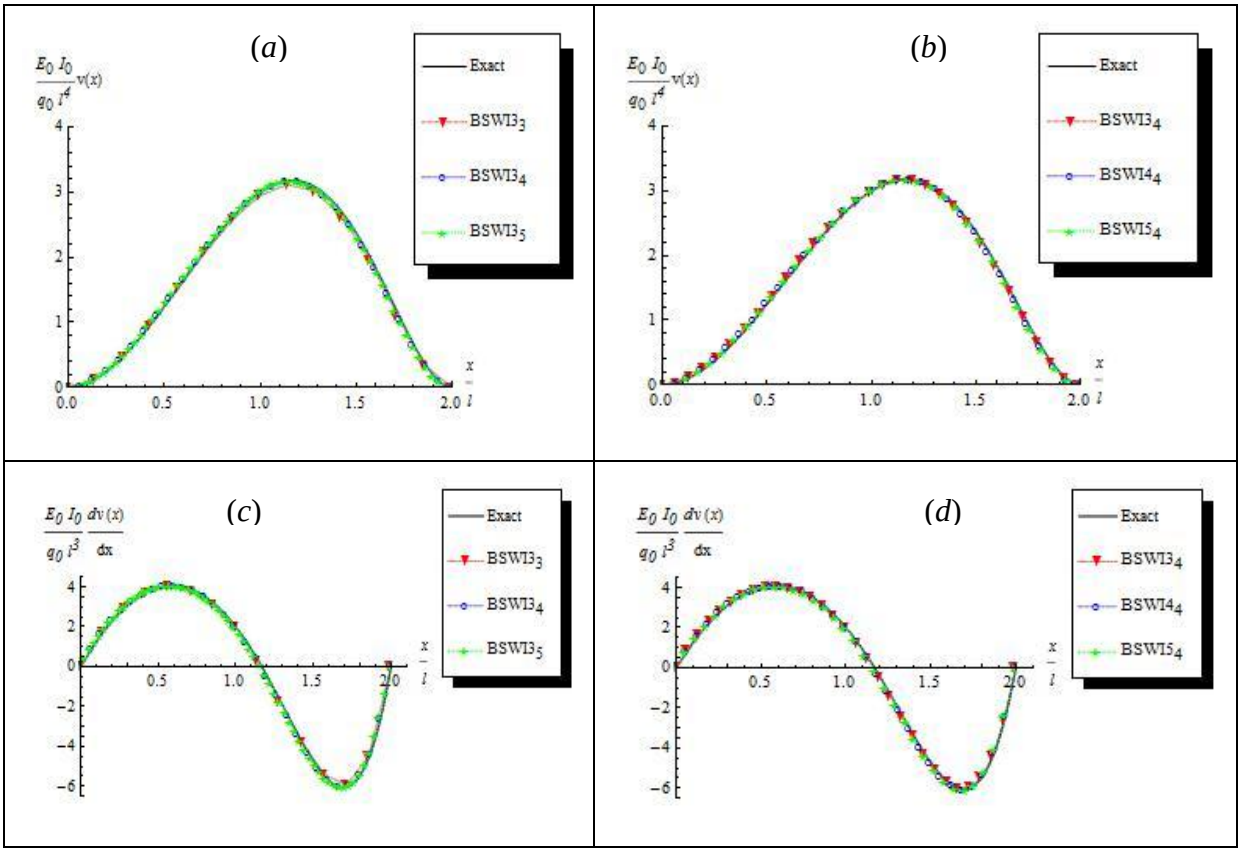

Figure 6-11: Deflection and rotation of a fixed-fixed end beam of uniform cross section subjected to a varying load on the right half of the beam for BSWI WFEM. (*a*) Deflection BSWI3_j, (*b*) deflection BSWIm_4, (*c*) rotation BSWI3_j and (*d*) rotation BSWIm_4 elements.

To expound further on the accuracy of the results of the beam displacements via the different formulations, the absolute percentage error at point 1.168 *l* is plotted in Figure 6-12 for: (*a*) FEM with varying number of elements, (*b*) *p*-FEM at different polynomial orders, (*c*) BSWI based finite element method and (*d*) Daubechies based wavelet finite element method. The approximate point 1.168 *l* is the location on the beam that the rotation is zero and is therefore the point at which maximum deflection is expected to occur.

Figure 6-12 (*a*) and Figure 6-12 (*b*) illustrates the effect of increasing the number of elements and/or order of the polynomial on the accuracy of results for FEM. Figure 6-12 (*c*) illustrates that BSWI based WFEM converges to the exact solution by either increasing the order or the scale of the BSWI wavelet element; which is consistent with the findings of Xiang et al. [7] This is also the case for Daubechies based WFEs as shown in Figure 6-12 (*d*); apart from D20_j where the effects of numerical instability for higher order Daubechies wavelets are evident and divergence of the solutions begins to occur. It is noted that for the FEM-10 (22 DOFs), *p*-FEM-11(22 DOFs), D12_1 (22 DOFs) and BSWI4_3 (19 DOFs) solutions, the errors obtained are 1.08374, 1.08374, 0.661155 and 0.766358 respectively. It is therefore evident

that the WFEM solutions lead to better approximations of the results in comparison to FEM solutions. Given the simple nature of this static problem, the computational costs for the WFE solutions as a whole are higher than the *h* and *p* FEMs. This is due to the fact that the wavelet elemental matrices and load vectors must be evaluated and transformed into physical space, particularly for Daubechies WFEM where the connection coefficients must be solved. However, fewer elements and DOFs are required to attain higher levels of accuracy with respect to WFEM and the evaluation of system equations alone is computational faster.

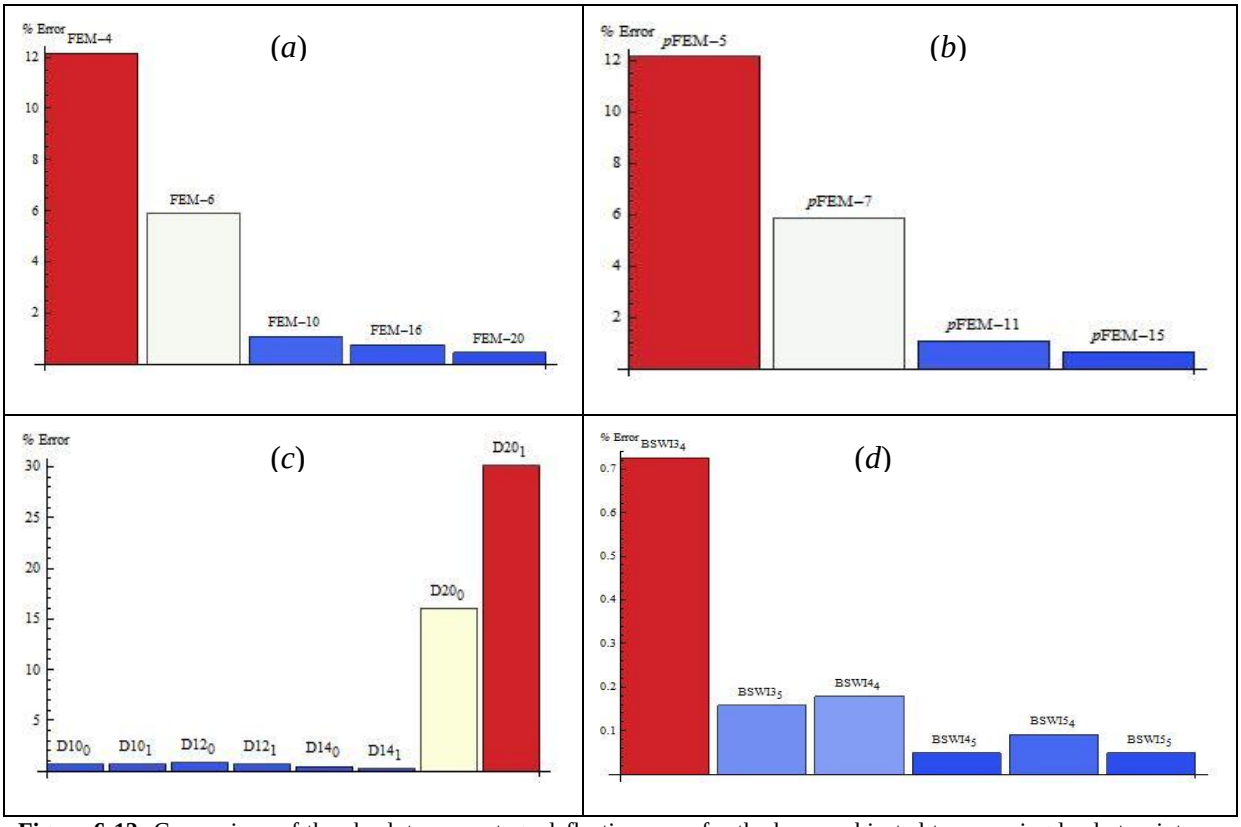

Figure 6-12: Comparison of the absolute percentage deflection error for the beam subjected to a varying load at point x = 1.168 l. (*a*) FEM. (*b*) *p*-FEM. (*c*) Daubechies WFEM and (*d*) BSWI WFEM.

Figure 6-13 contains graphs illustrating the stress variation across the beam for (*a*) FEM with different number of elements, (*b*) FEM with varying polynomial order, (*c*) BSWI4_j element for different multiresolution scales j, (*d*) BSWI$m4$ element for different orders m, (*e*) D12_j element for different multiresolution j and (*e*) DL_0 element for different orders L. The stress and strains are both evaluated from the double derivative of the vertical displacement of the beam as described in Section 5.2. The displacement function in the FEM approach is a cubic function, hence the stresses and strains vary linearly across the beam element. The elements on the left half of the beam, which are not subjected to loading, have the stresses and strains varying linearly. Therefore, the approximation of the stress variation on this half of the beam via FEM, from Figure 6-13 (*a*), is accurate for any number of elements. However, on the

right hand half of the beam that is subjected to the linear varying load, the stresses and strains vary cubically.

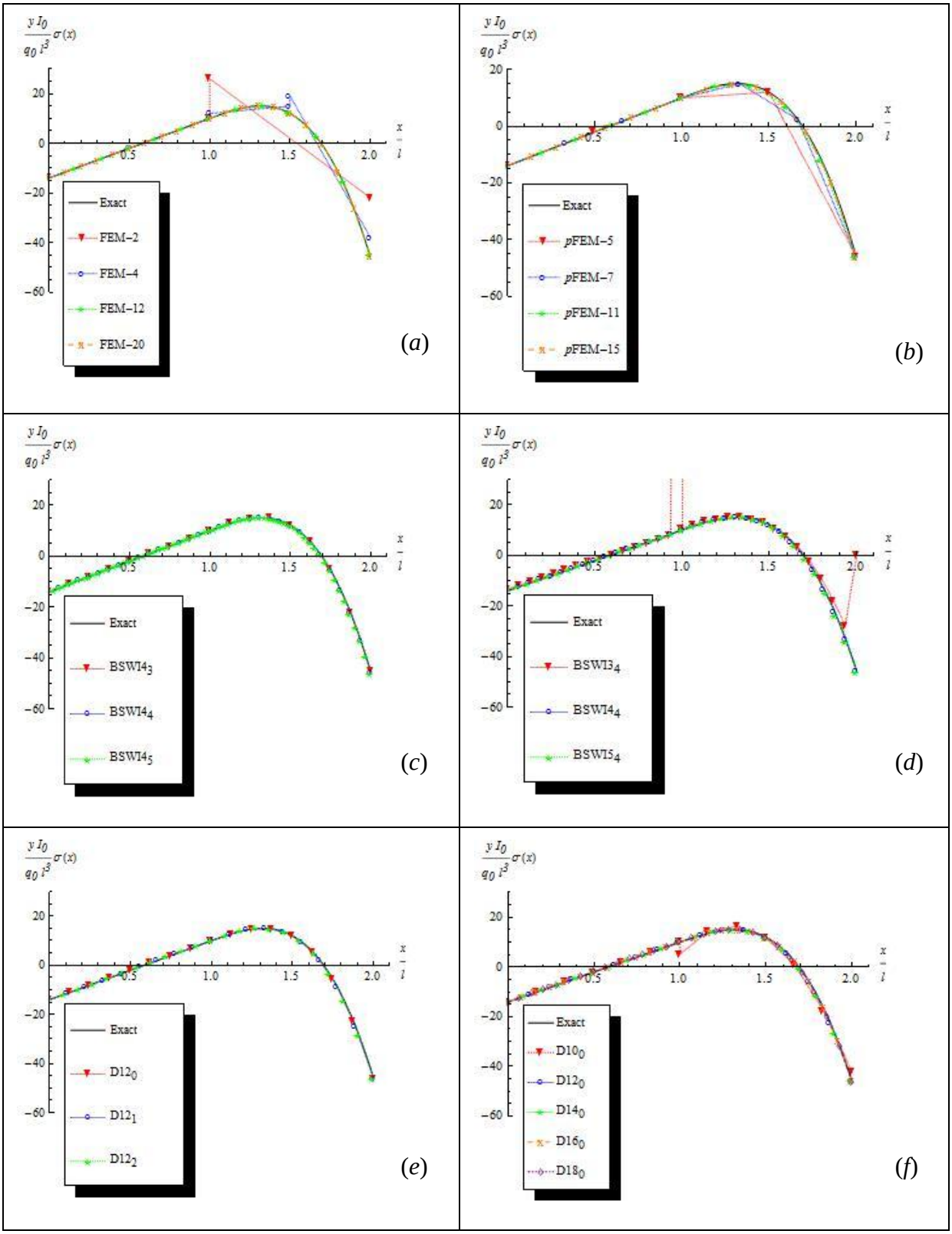

Figure 6-13: Normal stress across a fixed-fixed end beam of uniform cross section subjected to a varying load on the right end of the beam. (*a*) *h*-FEM. (*b*) *p*-FEM. (*c*) BSWI4$_j$ WFEM. (*d*) BSWIm_4 WFEM. (*e*) Daub D12$_j$ WFEM. (*f*) Daub DL_0 WFEM.

This explains the discontinuities at element boundaries and the poor approximations obtained via the FEM with lower number of elements; such as FEM-*2* and FEM-*4*. However, increasing the number of element increases the levels of accuracy with respect to the stress and strain solutions, particularly in the regions subjected to the varying load. The lower order *p*-FEM solutions, such as *p*-FEM-5 and *p*-FEM-7 modelled using only two elements, do not describe the variation of the stresses and strains on the right hand half of the beam as accurately. However, increasing the order of the approximation functions results in better accuracy as observed in Figure 6-13 (*b*).

The BSWI based wavelet finite element approach approximates the stresses and strains very accurately. Increasing the level of multiresolution leads to the convergence of the approximate solution to the exact solution, as observed in Figure 6-13 (*c*) for BSWI4_j element solutions. Increasing the order of the BSWI also leads to improved approximations of the stresses and strains across the beam as observed in Figure 6-13 (*d*). It is also noted that for BSWI3_j elements, the inner elemental nodes approximate the stresses accurately on both halves of the beam. There are discontinuities present at the boundaries of the adjacent elements. However, these discontinuities are not present for BSWI based elements of order $m \geq 4$.

It is also observed in Figure 6-13 (*e*) and Figure 6-13 (*f*) that the Daubechies based WFEM solutions for D12_j are good at both halves of the beam. The results of the stresses and strains using the Daubechies based WFEM agree very well with the exact solution for elements of order $12 \leq DL \leq 18$; subsequently, for the higher multiresolution scales for these wavelet families. However, there is a slight discontinuity present at the elemental end node boundaries coinciding with the midpoint of the beam for the D10_0 elements.

In addition to the deflection, rotation, stress and strain variations of the beam, the (*a*) bending moments (*b*) curvature and (*c*) shear force variations can be evaluated and compared for the different approaches as presented in Figure 6-14. The bending moments and curvature of the beam are obtained from the double derivative of the beam displacement function, while the shear force is obtained from the third derivative of the displacement function. The bending moment and curvature at the unloaded region of the beam vary linearly while the shear force variation is constant. However, at the right end region of the beam, the bending moments and curvature of the beam vary cubically, while the shear force varies quadratically. The variations of the bending moments (linear), curvature (linear) and shear force (constant) along the left half of the beam are in good agreement with the exact solution for all the

approaches. The main focus is the capability of the different approaches to accurately obtain the solutions for the bending moments, curvature and shear force variations along the loaded right hand segment of the beam.

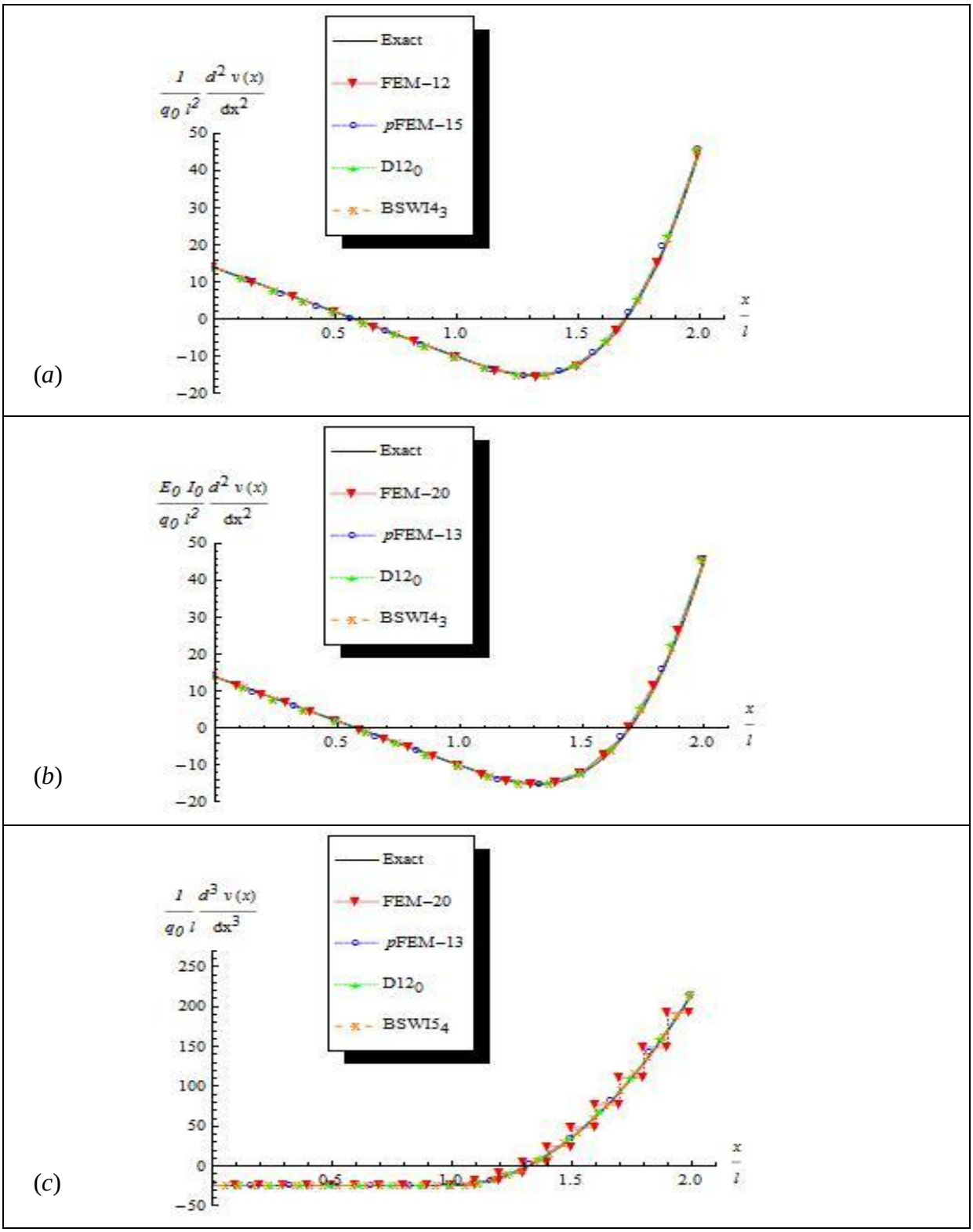

Figure 6-14: (*a*) Bending moments, (*b*) Curvature and (*c*) Shear force across a fixed-fixed end beam of uniform cross section subjected to a varying load on the right end of the beam.

The FEM approach has the variation of the bending moments and curvature in this region varying linearly rather than the actual cubic variation. Therefore, more finite elements are required for better approximations. The shear force varies constantly within the finite element rather than as a quadratic function (exact solution) in this region. Therefore, the mesh requires further refinement to improve the accuracy of the solution, as is the case in Figure 6-14 (*c*) where 20 finite elements are required. Alternatively, increasing the order of the field variable approximation improves the results.

However, for one to accurately approximate the variation of the shear force, curvature and bending moments without discontinuities at the end element nodes, for both WFEMs, higher order WFEs should be implemented. The D12_0 WFE is found to be the least order for the Daubechies WFEs that can accurately approximate the bending moments, curvature and shear force in this case. Similarly, in order to accurately approximate the variations of the bending moment and curvature, the least order for the BSWI based WFEM is BSWI4_3 and BSWI5_4 for the shear force. The results presented in Figure 6-14 show the good performance with respect to accuracy of the BSWI and Daubechies WFEMs in approximating the variation of the bending moments, curvature and shear force along the beam.

6.3. Simply supported Euler Bernoulli stepped beam with uniformly distributed load (UDL)

A simply supported two-stepped beam of length 2*l* is subjected to a uniformly distributed load $q(x) = 1$ as illustrated in Figure 6-15. The non-uniform flexural stiffness of the beam is represented by the unequal cross sections of the left and right segments; their bending stiffness is given as $E_1I_1 = E_0I_0$ and $E_2I_2 = 4\,E_0I_0$ respectively.

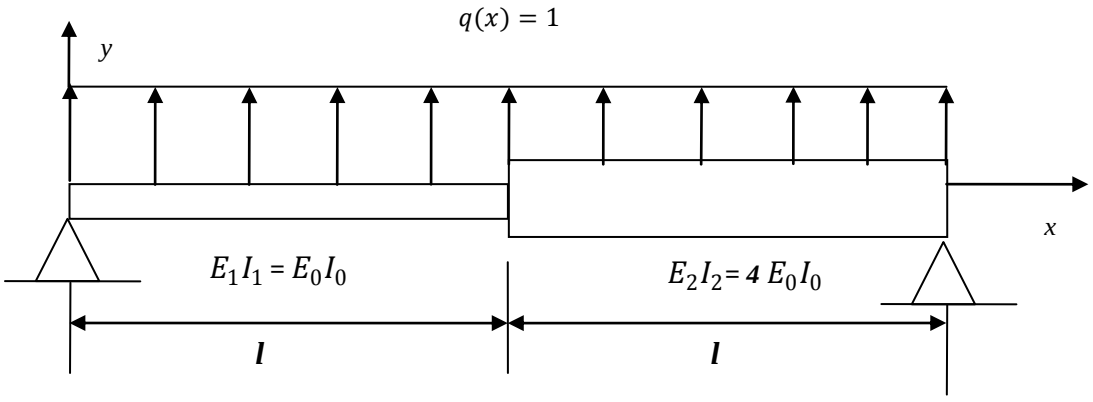

Figure 6-15: Simply supported stepped beam subjected to uniformly distributed load $q(x) = 1$.

This numerical example is carried out to have a clearer understanding of how the BSWI and Daubechies based WFEMs compare to one another, and other formulations, when a sudden flexural stiffness discontinuity is present in a beam. A similar example was carried out by Ma et al. [10] and later Diaz et al. [40], to compare the Daubechies WFEM, at scale j = 0, with the classical FEM solutions. An analytical solution for Euler-Bernoulli beams that have discontinuities in the flexural stiffness was presented by Bondi and Caddemi [105]. The flexural stiffness function is expressed as:

$$E(x)I(x) = E_0 I_0\left[1 - \gamma\, \widehat{H}(x - x_0)\right] \tag{6.31}$$

where $\gamma = 0.75$ is defined as the decrement of discontinuity intensity and satisfies the condition $0 \leq \gamma \leq 1$ to ensure positivity of the flexural stiffness [105]. $\widehat{H}(x - x_0)$ is the Heaviside function for $0 \leq x_0 \leq 2l$. The general governing equation is

$$\left\{E_0 I_0\left[1 - \gamma\, \widehat{H}(x - x_0)\right] v''(x)\right\}'' = q(x) \tag{6.32}$$

The potential energy of the beam is expressed as [27]:

$$\Pi^b = \frac{1}{2}\int_0^l E_1 I_1 \left(\frac{\partial^2 v}{\partial x^2}\right)^2 dx + \frac{1}{2}\int_l^{2l} E_2 I_2 \left(\frac{\partial^2 v}{\partial x^2}\right)^2 dx - \int_0^{2l} q\,(x) v\, dx \tag{6.33}$$

Following the principle of minimum potential energy, based on the formulations of the Euler Bernoulli beam stiffness matrix and uniformly distributed load vectors for the WFE as described in Section 5.2, the system equation is defined as:

$$[\boldsymbol{K_b}]\{\boldsymbol{V_b}\} = \{\boldsymbol{F_b}\} \tag{6.34}$$

where the vector $\{\boldsymbol{V_b}\}$ contains the displacement and rotation DOFs within the entire beam, $[\boldsymbol{K_b}]$ is the beam stiffness matrix in physical space and $\{\boldsymbol{F_b}\}$ is the equivalent load vector in physical space for the system.

Figure 6-16 describes the variation of the (*a*) deflection and (*b*) slope of the stepped beam, when subjected to a uniformly distributed load $q(x) = 1$, via the different approaches. The classical FEM solution with 8 elements (18 DOFs), *p*-FEM solution for order $m = 9$ (18 DOFs), Daubechies D10_1 WFEM solution (18 DOFs) and BSWI3_3 WFEM solution (18 DOFs) with 2 elements, are compared. The different solutions are in good agreement with the exact solution from Figure 6-16(*a*). The maximum deflection occurs on the left half of the beam since its stiffness is a quarter of the flexural stiffness of the right hand side. The slope is

also generally well approximated by all approaches. It is also observed that the slope variation significantly changes at the point of the discontinuity at $x = l$.

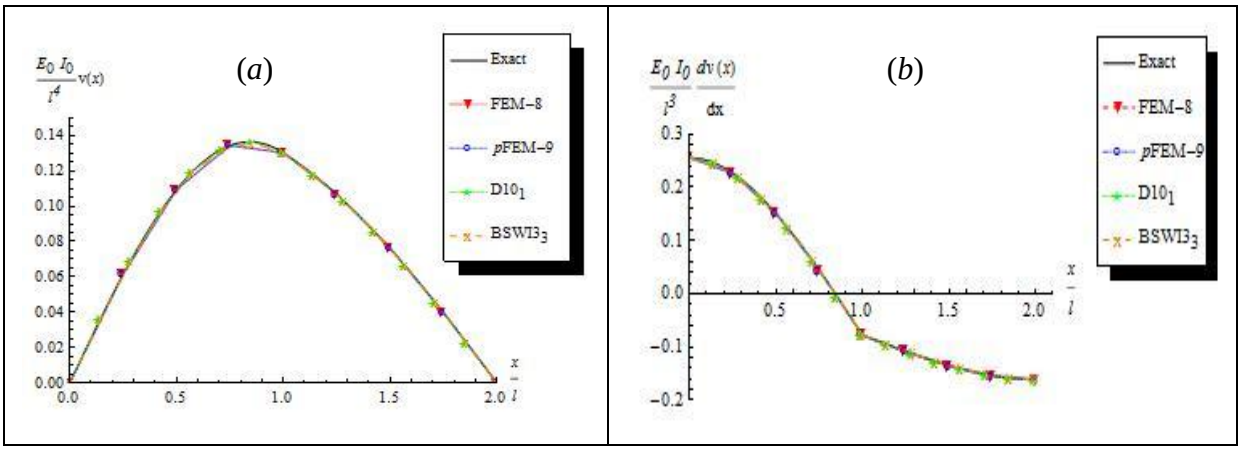

Figure 6-16: (*a*) Deflection and (*b*) rotation across a simply supported stepped beam subjected to a uniformly distributed load $q(x) = 1$.

The percentage error of the deflection across the beam using the BSWI wavelet based beam elements is presented in Figure 6-17 for different orders *m* and multiresolution scales *j*. From the results, it is observed that the BSWI3_3 element formulation has the highest error variations across the beam in comparison to the other higher order and/or multiresolution BSWI WFEs. Increasing the order to BSWI4_3 reduces the error since increasing the order of the wavelet family improves the smoothness of the scaling functions and subsequently improves the accuracy of the function approximation. Furthermore, increasing the multiresolution scale from BSWI3_3 to BSWI3_4 means that the additional detail is included in the approximation, thus increasing the levels of accuracy.

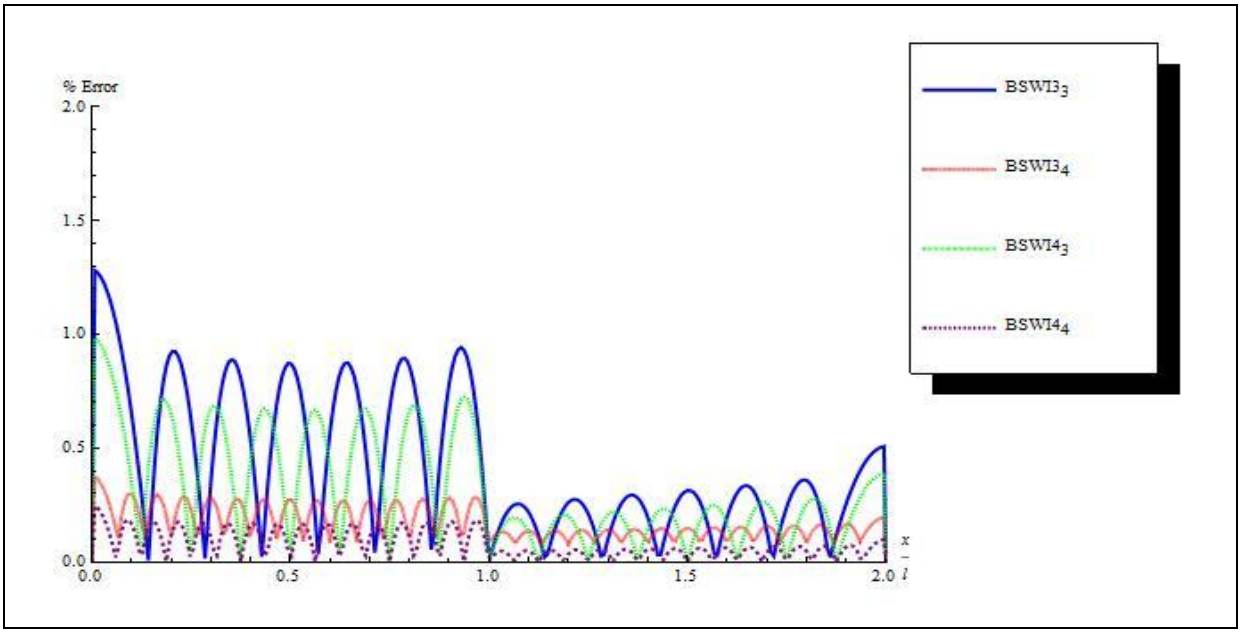

Figure 6-17: Deflection percentage error across a simply supported stepped beam subjected to a uniformly distributed load $q(x) = 1$ for the BSWI*mj* WFE.

Similarly, the percentage error of the deflection across the beam for the Daubechies WFEM is illustrated in Figure 6-18. The observations made from the results confirm that increasing the order and/or the multiresolution scale of the Daubechies WFEs increases the levels of accuracy significantly.

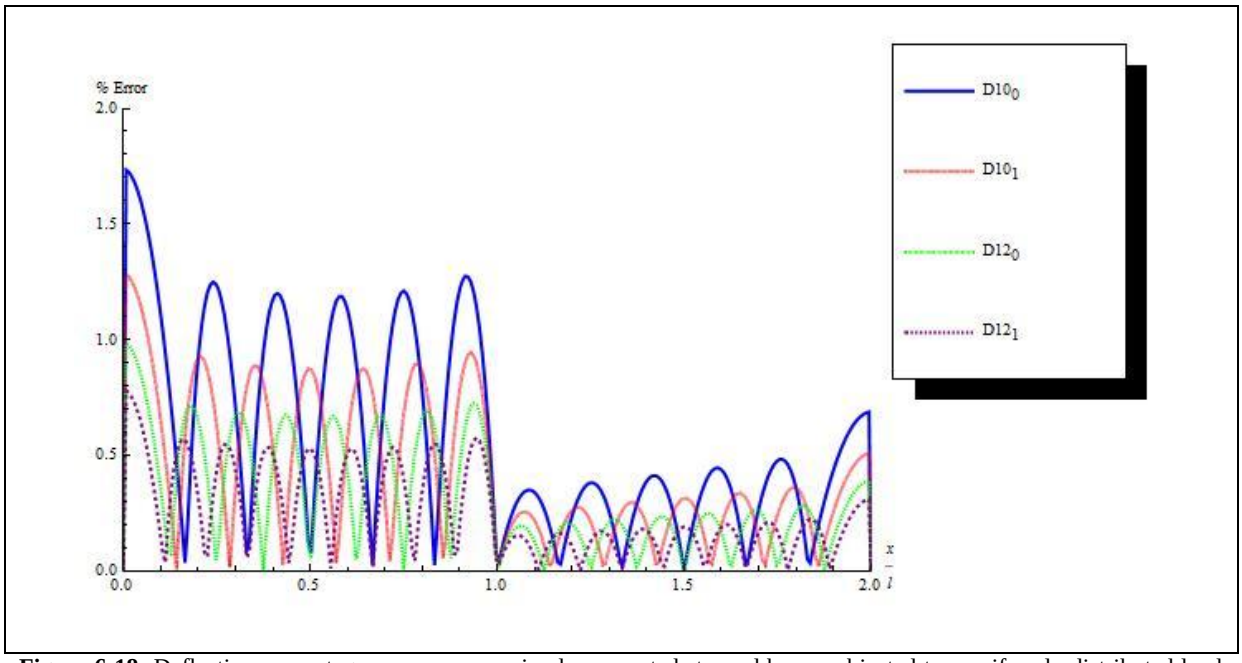

Figure 6-18: Deflection percentage error across a simply supported stepped beam subjected to a uniformly distributed load $q(x) = 1$ for the Daubechies based DL_j WFE.

A comparison of the deflection percentage errors for the different formulations is presented in Figure 6-19. All the formulations have a total number of 18 DOFs within the entire beam and this value is selected to ensure that the maximum error via any of the formulations falls below 5% at any point across the beam. This is the commonly accepted error threshold in common engineering practices. It is observed that the wavelet based elements perform very well in comparison to the FEM and *p*-FEM solutions, having maximum errors of: 1.28% (D10_1 WFEM), 1.28% (BSWI3_3 WFEM), 3.82% (FEM-8) and 3.82% (*p*FEM-9). This is implies that the results via WFEM are more accurate, with fewer elements and DOFs, than classical FEM and *p*-FEM approaches.

This is mainly attributed to the selected layout and the multiresolution property of the wavelet formulations, which improve the approximation accuracy. It is also observed that the errors are relatively higher at the more flexible left hand side of the beam since the flexural stiffness is lower than on the right hand side. This implies that for stiffer elements, lower order and/or multiresolution scale of WFEs can be selected in order to attain acceptable levels of accuracy. Correspondingly, higher orders and/or scales may be required to solve for highly flexible structures that are characterised by larger deflections.

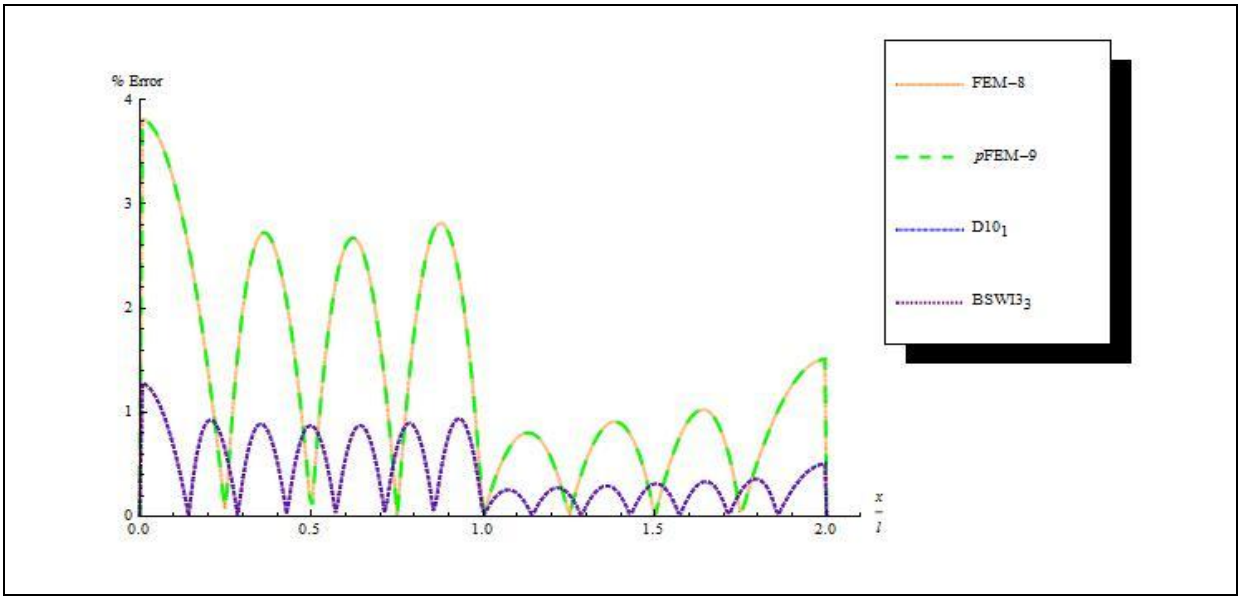

Figure 6-19: Comparison of the deflection percentage error across a simply supported stepped beam subjected to a uniformly distributed load $q(x) = 1$.

Aside from the deflection and the slope of the beam, the (*a*) normal stress, (*b*) bending moments (*c*), curvature and (*d*) shear force variations across the beam are presented in Figure 6-20.

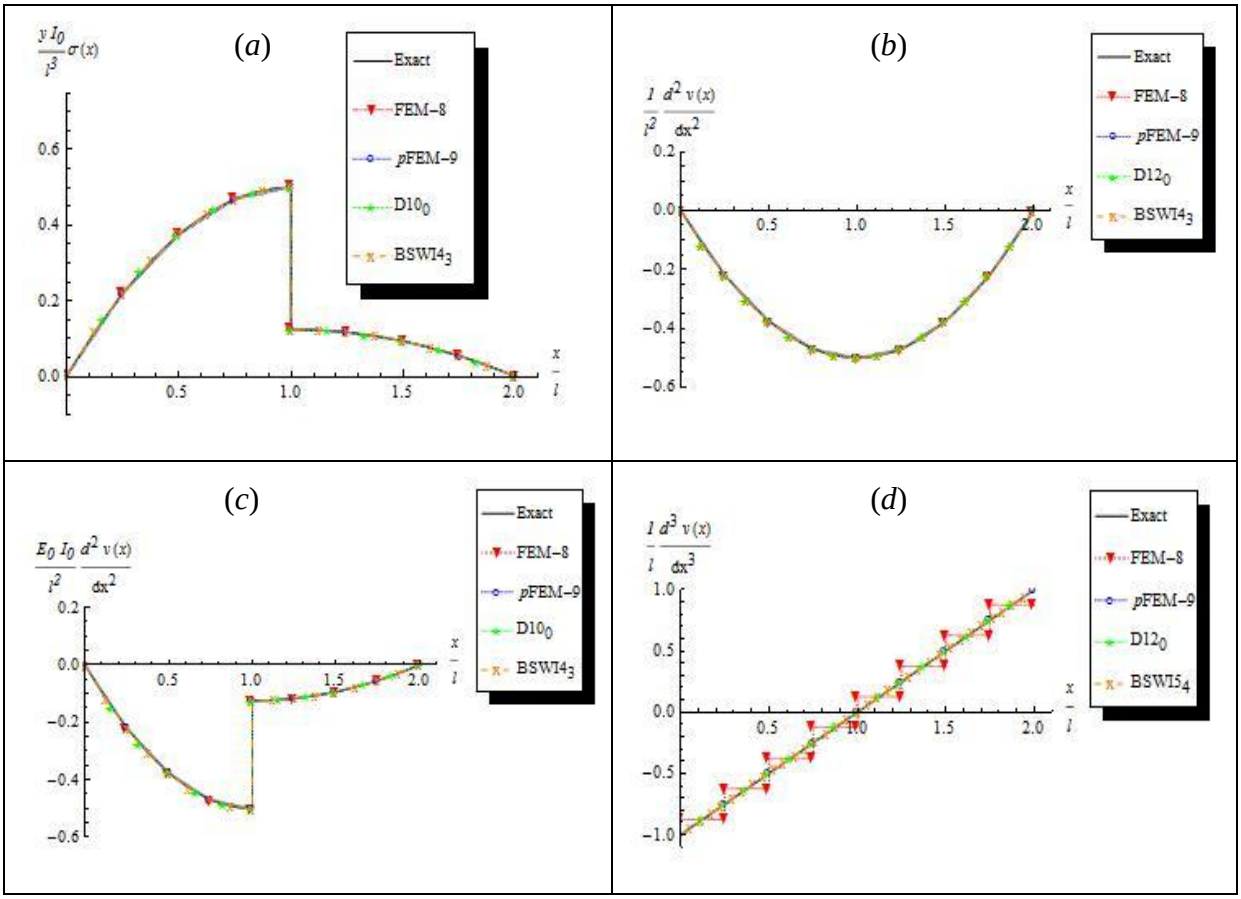

Figure 6-20: (*a*) Normal stress, (*b*) bending moments, (*c*) curvature and (*d*) shear force across a simply supported stepped beam subjected to a uniformly distributed load $q(x) = 1$.

The stress across the more flexible left side of the beam is significantly higher than the right end from Figure 6-20 (*a*). The sudden change in stress coincides to the point where the singularity in the flexural stiffness occurs within the element. All formulations are in good agreement with the analytical solution for the normal stress, accurately detect the singularity location. The bending moment variation across the beam is characterised by a smooth symmetric curve as observed in Figure 6-20 (*b*). The curvature variation from Figure 6-20 (*c*), exhibiting a discontinuity at the point $x = l$, where the flexural stiffness suddenly changes in the beam. The shear force, from Figure 6-20 (*d*), varies linearly across the beam since the uniformly distributed load is characterised by a constant variation across the beam. The *p*-FEM and both the Daubechies WFE and BSWI WFE solutions accurately approximate the shear force variation across the beam. However, the classical finite element approach has the shear force constant within each element. This is the reason for the discontinuities present at the boundaries of adjacent elements. It is therefore necessary to increase the number of elements to better approximate the shear force across the beam.

6.4. Buckling analysis of stepped planar bars under various boundary conditions

The buckling analysis of a (*a*) two-stepped and (*b*) three-stepped planar (plane) bar of length *l* and uniform Young's modulus *E*, as illustrated in Figure 6-21, is carried out in this section. For the two-stepped bar, as illustrated in Figure 6-21 (*a*), the moment of inertia for the bottom and top half of the bar are given as $I_1 = I_0$ and $I_2 = \frac{I_0}{2}$ respectively. In Figure 6-21 (*b*), the three-stepped bar is divided into three sections; according to the variation of the cross-sectional area and moment of inertia. The top segment of length $\frac{l}{4}$, middle segment of length $\frac{l}{2}$ and bottom segment of length $\frac{l}{4}$ have the moment of inertia as $I_1 = \frac{I_0}{2}$, $I_2 = I_0$ and $I_3 = \frac{I_0}{2}$ respectively. An analysis of the critical buckling load $\acute{P}$, under compressive axial loading and different boundary conditions at points *A* and *B*, is carried out via the Daubechies and BSWI based WFEMs. The buckling analysis using WFEM involves solving the system equation [27]

$$\left[[K_E] + \acute{\lambda}[K_G]\right]\{\acute{V}\} = 0 \qquad \textbf{(6.35)}$$

where $[K_E]$ and $[K_G]$ are the system elastic and geometric stiffness matrices which are obtained by assembling the corresponding element matrices derived in Section 5.3.

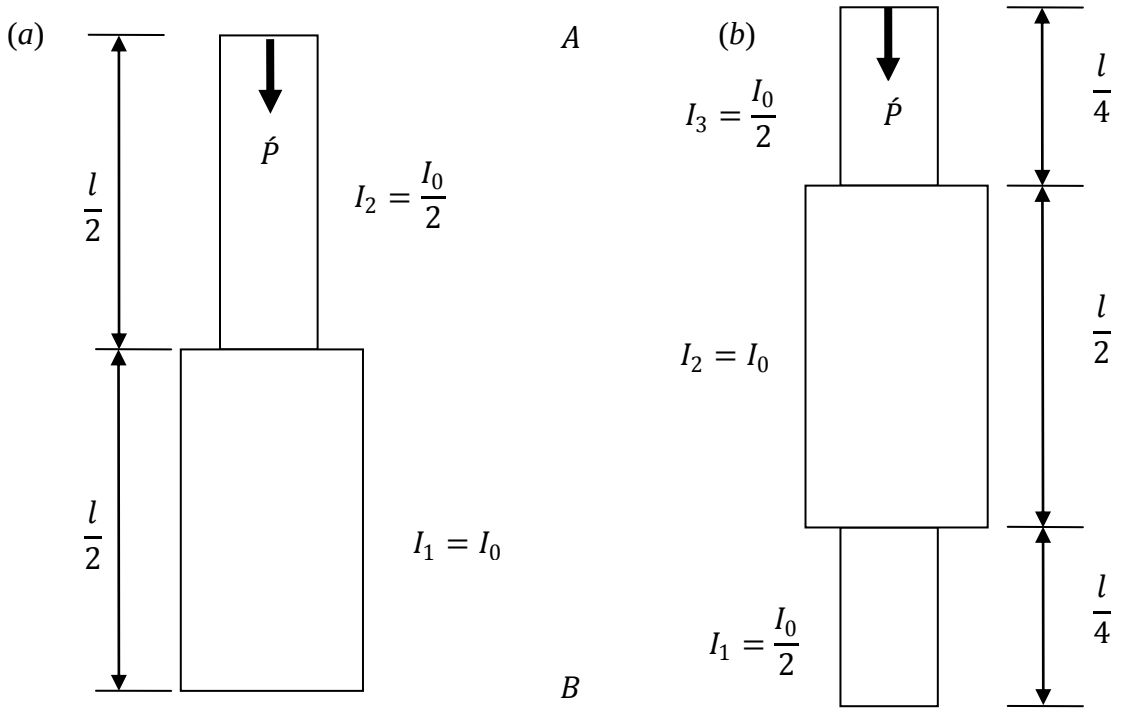

Figure 6-21: (*a*) Two-stepped and (*b*) three-stepped planar bar of length *l*.

The eigenvectors $\{\acute{V}\}$ contain the buckling modes shapes, while the eigenvalues $\acute{\lambda} = -\frac{1}{\acute{P}}$ are used to obtain the corresponding buckling loads. The critical buckling load is obtained from the first eigenvalue. The approximate solutions obtained are compared with the exact results as achieved by Wang and Li [106]. Furthermore, the first buckling mode shapes for each case are presented. The buckling analysis is carried out with various boundary conditions at *A* and *B*, with the notation *A-B* used for simplicity. In addition, the boundary conditions: free, clamped and pinned are denoted by *F*, *C* and *P* respectively. Thus, *F-C* signifies the boundary condition, free at *A* and clamped at *B*.

	Two-stepped planar bar				***Three-stepped planar bar***			
	F-C	***P-C***	***C-C***	***P-P***	***F-C***	***P-C***	***C-C***	***P-P***
Exact [106]	2.0671	12.5914	25.8120	6.4075	1.6326	14.5520	28.6765	8.2685
BSWI4$_3$ WFE	2.06723	12.5917	25.8103	6.40772	1.63264	14.5521	28.6769	8.2689
% Error	(1.06E-3)	(2.24E-3)	(1.35E-2)	(1.74E-3)	(3.46E-4)	(8.32E-4)	(3.00E-3)	(3.50E-3)
Daub D10$_0$ WFE	2.06725	12.5973	26.2083	6.40867	1.63268	14.5542	28.6856	8.26901
% Error	(1.19E-3)	(4.66E-2)	(3.15E0)	(9.26E-3)	(6.49E-4)	(1.76E-2)	(7.24E-2)	(4.08E-3)

Table 6-1: Critical buckling load of a two-stepped and three-stepped planar bar under axial compressive loading.

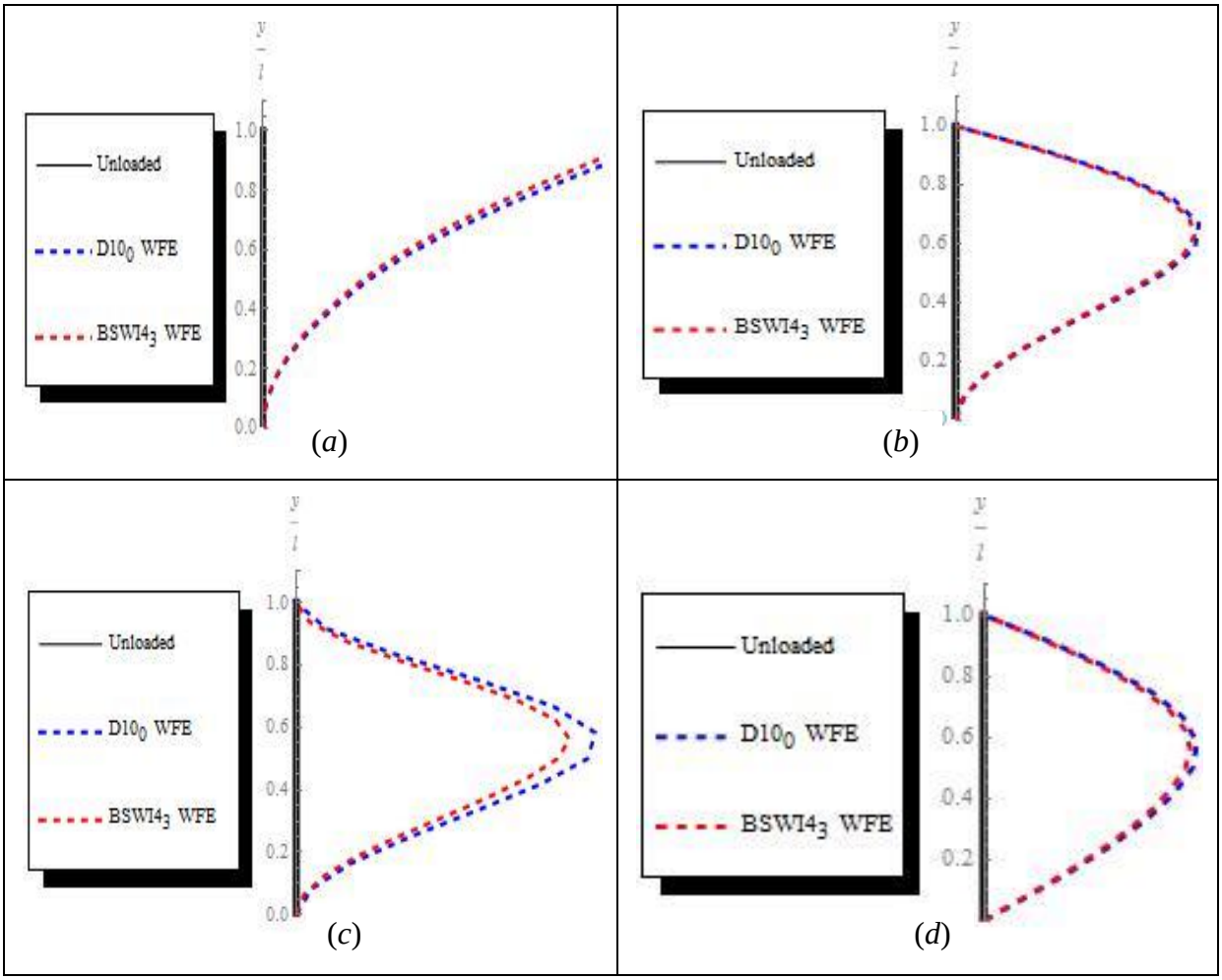

Figure 6-22: First buckling mode shapes of the two-stepped planar bar of length *l*. (*a*) *F-C* (*b*) *P-C* (*c*) *C-C* and (*d*) *P-P* boundary conditions.

Two and three planar bar WFEs are used to model the two-stepped and three-stepped planar bars respectively, for both the Daubechies and BSWI WFEMs. The Daubechies D10_0 and BSWI4_3 bar WFEs were selected in this analysis since they are the lowest order and multiresolution scale wavelet finite elements that can be applied to model the planar bar elements. The total DOFs for the two-stepped and three-stepped Daubechies WFE bars are 29 and 42 respectively, while for the BSWI4_3 bars are 37 and 54 correspondingly. The buckling critical loads for both bars under different boundary conditions are presented in Table 6-1.

It is observed both WFE approaches give highly accurate solutions for the critical buckling load of the two-stepped and three-stepped planar bar; under different boundary conditions. All results, with the exception of the Daubechies D10_0 two-stepped bar WFE *C-C* (3.15%), have a percentage error of below 0.075%. In general, the results using the BSWI4_3 WFE are slightly better than D10_0 elements since it has a higher number of DOFs.

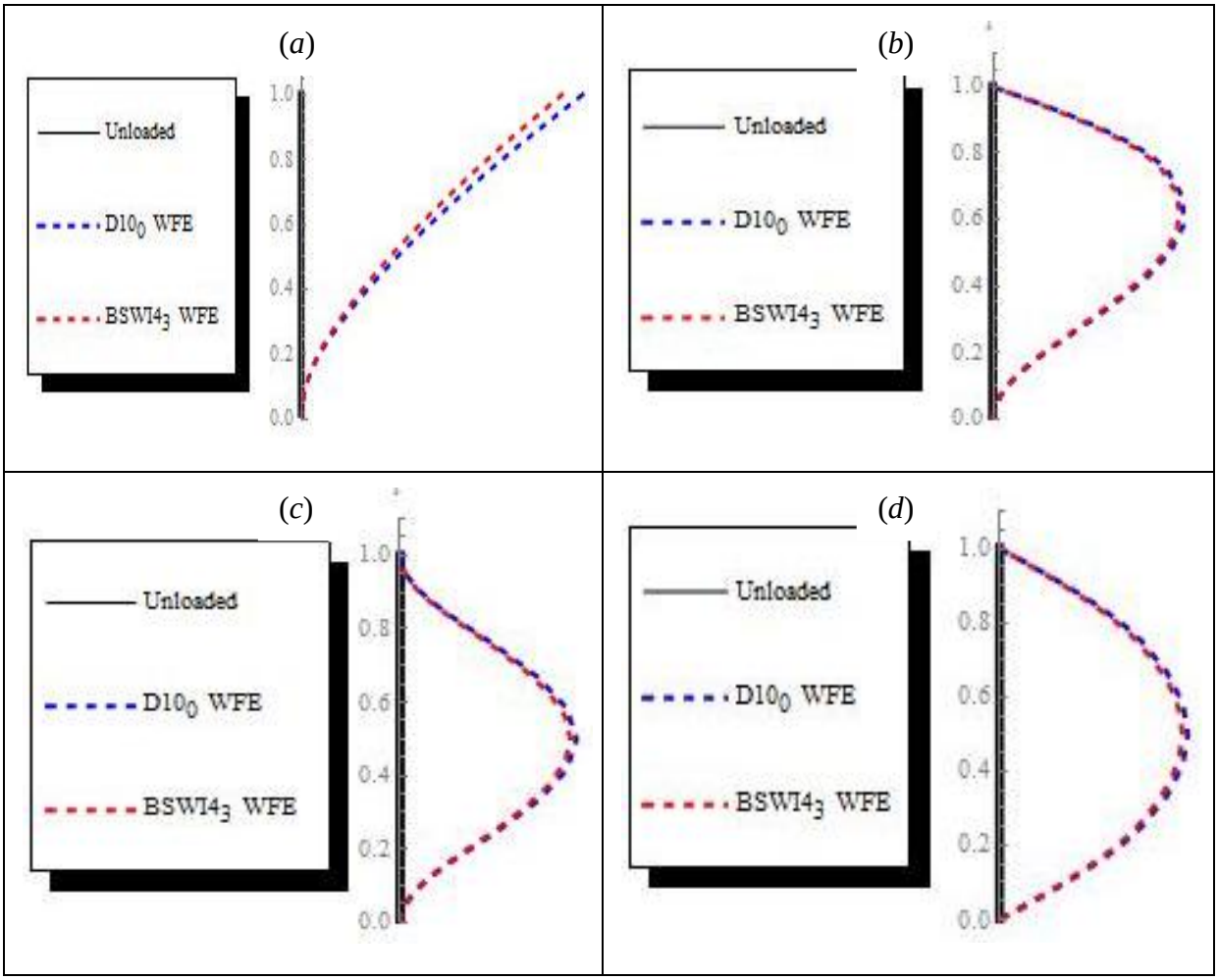

Figure 6-23: First buckling mode shapes of the three-stepped planar bar of length *l*. (*a*) *F-C* (*b*) *P-C* (*c*) *C-C* and (*d*) *P-P* boundary conditions.

The first buckling mode shapes of the two-stepped and three-stepped bar obtained via the D10_0 and BSWI4_3 are presented in Figure 6-22 and Figure 6-23 respectively; under (*a*) *F-C* (*b*) *P-C* (*c*) *C-C* and (*d*) *P-P* boundary conditions. Taking into account that the first buckling load is of importance, the first buckling mode shapes associated with the buckling load is presented for each boundary condition. The Daubechies and BSWI WFEM solutions are in relatively good agreement with each other. Increasing the order and/or multiresolution of the WFEs improves the accuracy of the solutions.

6.5. Additional remarks

The static analysis of a uniform beam subjected to a varying load and un-uniform beam subjected to a uniformly distributed load, as presented in Section 6.2 and Section 6.3 respectively, are also carried out by Ma et al. [10] and Diaz et al. [40] using the Daubechies WFEM. Ma et al. [10] indicate that different orders of the Daubechies wavelet can be applied to formulated the WFEs. However, in their study they implement the D*12* wavelet at

multiresolution scale $j = 0$. Although their analysis is also carried out using Daubechies wavelet beam finite elements at multiresolution scale $j = 0$, Diaz et al. [40] in a later study state that D*12* is the lowest applicable order of the Daubechies wavelet to achieve accuracy for the beam element formulation. However, the connection coefficients and the wavelet transformation matrices described in this thesis facilitate the use of other orders of the Daubechies wavelet family to formulate the beam WFEs. The results in chapter provide evidence that D*10* beam WFEs can be in fact implemented and attain sufficiently high levels of accuracy. The accuracy of the results can be improved further by increasing the multiresolution scale *j* without having to increase the number of WFEs.

Furthermore, in the analysis by Diaz et al. [40], it is further stated that only certain orders of the Daubechies wavelet are applicable to model a beam WFE. The layout of the beam implemented is similar to layout 1, where the rotation DOFs are only present at the element extreme nodes and displacement DOFs at each elemental node. Diaz et al. [40] suggest that Daubechies order *L* must be such that $L = 2^k + 4$, for $k \in \mathbb{Z}$, $k > 0$. This is to ensure that the location of the elemental nodes coincide exactly with the scaling functions' and their derivatives' dyadic points, $x = \frac{k}{2^i}$ for $k, i \in \mathbb{Z}$ and $i \geq 0$ for $\phi_L(x)$. Therefore, according to their findings the orders that can be implemented to model the beam WFE are restricted to *L* = 6, 8, 12, 20,....

However, from the results presented in this chapter, the Daubechies WFEM formulation allows for the implementation of the beam WFEs using the other orders D10_j, D14_j, D16_j and D18_j, while still achieving high levels of accuracy. This is made possible by selecting a value of *i* that gives an acceptable level of accuracy and then carrying out an interpolation for the approximate values of $\phi_L(x)$, $for\ x \in \mathbb{R}$, within these dyadic points to reduce the computational time. The value of *i* selected in this study to obtain the scaling functions and derivatives at dyadic points is 15. Interpolation is then carried out to obtain the real values that are not exactly situated at these dyadic points. The values are then stored to reduce computational costs. The results presented in this and subsequent chapters prove that this approach is indeed feasible and sufficient for the application of other Daubechies wavelets whose order does not meet the suggested requirement $L = 2^k + 4$ for $k \in \mathbb{Z}$, $k > 0$. This is not only restricted to the Daubechies beam WFEs and can be applied to the rod and plane bar elements as analysed in this study, irrespective of the element layout selected. Moreover, this approach also allows for the variation of the WFE layout for the different orders of the

wavelet. Thus, the DOFs at the inner nodes can be modified for different structural analysis problems.

In this chapter, the results begin to diverge for $DL \geq 20$ due to numerical instabilities and errors arising when evaluating the connection coefficients. This is consistent with the findings presented by Diaz et al. [40].

Given the simple nature of these static problems presented in this chapter, the computational costs of the WFEMs are higher than the classical FEM due to the evaluation of the element matrices and load vectors in wavelet space as well as the further transformation into physical space. However, as the complexity of problems increases, particularly for dynamic problems, the computational costs of the WFEMs are lower than the classical FEM. This is further discussed in following chapter.

6.6. Conclusion

The numerical examples presented in this chapter were carried out with the main intention of verifying, comparing and analysing the performance of the BSWI and Daubechies wavelet based finite element methods for static and buckling analysis. The wavelet based finite element approaches were highly accurate and demonstrate their capability to analyse various structural problems; with a variety of loading conditions, boundary conditions and/or geometric properties.

Furthermore, the BSWI and Daubechies based solutions attained better levels of accuracy, with fewer elements and degrees of freedom, than the classical and *p*-adaptive FEMs. This was mainly attributed to the multiresolution aspect of wavelet analysis, to which refining the scale provided additional information and subsequently reduces the level of errors of the approximate solution. Moreover, the original discretization of the system did not need modification when altering the order and/or multiresolution scale of the wavelet based functions. This was consistent with the findings presented in [6,7,10,40].

The algorithms formulated and implemented in this study allowed for the accurate formulation of the Daubechies wavelet based beam finite elements for orders D*10*, D*12*, D*14*, D*16* and D*18*, at different multiresolution scales *j*, irrespective of the layout selected. To the best of the author's knowledge, the implementation and extensive comparison of the different Daubechies wavelet finite elements formulated using these different orders, at various scales, was carried out for the first time in this study. Furthermore, the wavelet based finite elements can be formulated using different layouts, where the nodal DOFs can be varied in location.

Consequently, the location and number of elemental nodal points can be varied using the approach implemented to formulate the WFEM in this study.

The elemental matrices and load vectors in wavelet space were evaluated only once and stored to reduce computational costs since only the wavelet transformation matrix is modified when altering the wavelet based element layouts. This capability to modify the WFEs enhances the versatility of the WFEM to maximize on efficiency and increase levels of accuracy in the analysis of a wide variety of structural problems. The same also applies to the BSWI WFEM, as stated by Xiang et al. [7], and the results presented in this study were consistent with their findings.

Wavelet based finite element		***Daub WFEM***	***BSWI WFEM***
Rod element	Axial deformation	D6_0	BSWI2_2
	Axial stress/strain	D8_0	BSWI3_3
Beam element subjected to varying load	Vertical deflection	D10_0	BSWI3_3
	Rotation	D10_0	BSWI3_3
	Stress/strain, Bending moment, curvature	D12_0	BSWI4_3
	Shear force	D12_0	BSWI5_4
Beam element with flexural discontinuities	Vertical deflection	D10_0	BSWI3_3
	Rotation	D10_0	BSWI3_3
	Stress/strain, Bending moment, curvature	D12_0	BSWI4_3
	Shear force	D12_0	BSWI5_4

Table 6-2: Summary of least wavelet orders and multiresolution scales implemented for various wavelet based finite elements.

The order of the wavelet family to be used mainly depends on the problem to be analysed, the nature of required results and the necessary levels of accuracy to be achieved. It is therefore up to the analyst to decide what order and/or multiresolution scale to implement in the analysis. However, the order of the wavelet families employed must at least satisfy the necessary requirements of the approximating functions to ensure convergence i.e., compatibility and continuity within and between elements. Though it may not be

categorically stated which order and scale of the wavelet based finite elements is best suited for the analysis of various engineering structural problems, the results presented in this chapter provide the least orders and scales that may be implemented based on the field variables. Although lower order WFEs may accurately approximate the variations of these field variables within the elements, this criterion is based on the order of the field variable function to ensure inter-element compatibility; thus ensuring no inter-element discontinuities are present. Furthermore, the least value of multiresolution scale that can be implemented for the Daubechies WFEs is $j = 0$. However, for the BSWI WFEM, the requirement $j \geq j_0$ must be met. Table 6-2 presents a summary of the least order and multiresolution scale that can be implemented for various Daubechies and BSWI based wavelet finite elements. It must be mentioned that for the Daubechies WFEM, the results of the wavelet based finite elements of order > D*18* were inaccurate due to numerical instabilities. This was consistent with the findings of Diaz et al. [40].

In general, improving the accuracy of the results can be carried out by increasing the order of the wavelet family since higher order functions are better approximated due to the increased smoothness of the wavelet scaling functions. Moreover, increasing the multiresolution scale, which provides additional information, also increases accuracy. Alternatively, it is possible to increase the accuracy by refining the mesh and increasing the number of wavelet based finite elements. This was consistent with Xiang et al. [7] and Chen et al. [6] findings.

7. Wavelet Finite Element Method in Dynamic Analysis of Moving Load Problems

Summary

In this chapter, the wavelet based finite element method is implemented in the dynamic analysis of moving load problems. The results obtained via numerical examples for the Daubechies and BSWI based wavelet finite element methods are compared for different WFE orders and multiresolution scales. The numerical examples presented and discussed in this chapter include:

Example 1: The dynamic response generated by a locomotive travelling over a large-span bridge modelled as a simply supported WFE beam subjected to a harmonic moving load. This analysis is similar to an example carried out by Fryba [102] and is necessary to validate and verify the WFEM moving load formulation used in the analysis of moving load problems. The damping component within the WFE system is modelled as viscous damping. In this example the response of the beam is analysed for subcritical, critical and supercritical velocity profiles of the moving load.

Example 2: The free vibration analysis of a Vierendeel frame based on the Daubechies and BSWI WFEMs is initially carried out. The dynamic responses of the frame subjected to a moving point load, for different moving load velocities, are presented using the Daubechies and BSWI based WFEMs and compared with FEM.

Example 3: The dynamic response of a high speed locomotive travelling over a track is analysed as a long simply supported beam resting on: *a*) elastic and *b*) viscoelastic foundations, subjected to moving point load. The WFE beam is formulated based on Euler-Bernoulli beam theory and the dynamic response is analysed for subcritical, critical and supercritical velocities of the moving load. Furthermore, the analysis is carried out for subcritical, critical and supercritical viscous damping of the foundation. The BSWI and Daubechies WFEM solutions are compared with the classical FEM approach.

The effects of altering the multiresolution scales and/or orders of the Daubechies and BSWI wavelet based element formulations, on the accuracy of the response for the different moving load problems, are presented and discussed.

A comparative study is carried out for the first time based on the implementation of the Daubechies and BSWI based WFEM and the classical FEM formulations for the dynamic analysis of structural beam moving load problems.

7.1. Simply supported beam subjected to a moving harmonic load

The BSWI and Daubechies based wavelet finite element methods are used to analyse a simply supported beam subjected to a moving harmonic load, as presented in Figure 7-1. The simplified model is used to represent the dynamic effects of a steam locomotive travelling across long span bridges and this analysis is classified as vehicle-bridge interaction [107]. The wavelet based finite element solutions are compared to analytical solutions presented by Fryba [102] and the classical FEM. The example is carried out to primarily validate the WFEM moving load approach and carry out a comparative study of the different approaches implemented in this section.

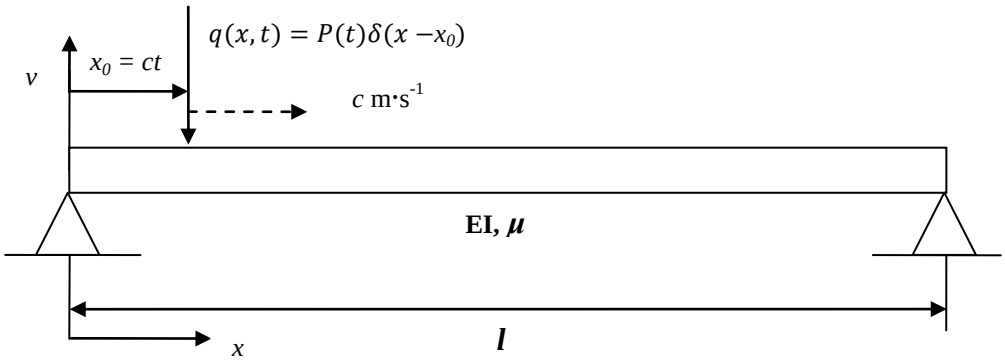

Figure 7-1: Simply supported uniform beam subjected to a harmonic moving load.

The Euler Bernoulli beam theory is used to describe the behaviour of the elastic beam with the assumptions that the beam undergoes small deformations and therefore shear deformations are neglected; the cross-sectional area and material properties are uniform across its length. Furthermore, the beam is assumed to be at rest at time $t = 0$ when the load arrives on to the bridge; thus the velocity and displacement of the beam is zero at this instant. The load is assumed to travel cross the simply supported beam from the left edge to the right edge at a constant velocity c m·s^{-1}. The analysis is carried out from the time the moving load arrives to the time it departs from the beam.

Therefore, the governing equation describing the dynamic behaviour of the damped system is given as [27]:

$$[\boldsymbol{M_b}]\{\ddot{\boldsymbol{V}}_{\boldsymbol{b}}(t)\} + [\boldsymbol{C_b}]\{\dot{\boldsymbol{V}}_{\boldsymbol{b}}(t)\} + [\boldsymbol{K_b}]\{\boldsymbol{V_b}(t)\} = \{\boldsymbol{F_b}(t)\} \quad \textbf{(7.1)}$$

where the matrices $[\boldsymbol{M_b}]$, $[\boldsymbol{C_b}]$ and $[\boldsymbol{K_b}]$ are the Euler Bernoulli beam global mass, damping and stiffness matrices respectively and $\{\boldsymbol{F_b}(t)\}$ is the time-dependent harmonic moving load vector, as formulated in Section 5.2, in physical space. The vectors $\{\boldsymbol{V_b}(t)\}$, $\{\dot{\boldsymbol{V}}_{\boldsymbol{b}}(t)\}$ and $\{\ddot{\boldsymbol{V}}_{\boldsymbol{b}}(t)\}$ contain the system global DOFs, velocities and accelerations of the beam respectively.

The beam has a bending stiffness $EI = 2.163\text{x}10^{11}$ N·m^2 and mass per unit length $\mu = 2.957\text{x}\,10^3$ kg·m^{-1}. The angular frequency of damping of the beam is given as $\omega_d = 9.62\,\text{x}\,10^{-2}$ rad·s^{-1}. The dynamics response of the beam is evaluated using the Newmark direct time integration method, as described in Section 4.6.1. The values of the Newmark parameters used in this example, and subsequently for dynamic response analysis within this study to ensure accuracy and stability are, $\acute{\delta} = 0.5$ and $\acute{\gamma} = 0.25(0.5 + \acute{\delta})^2$.

The locomotive characteristics are given by Fryba [102] in chapter 2 of his monograph. The weight of the locomotive is represented by a moving point load $R(t) = 9.7\text{x}10^5$ N as it travels across the bridge of length l = 56.56 m.

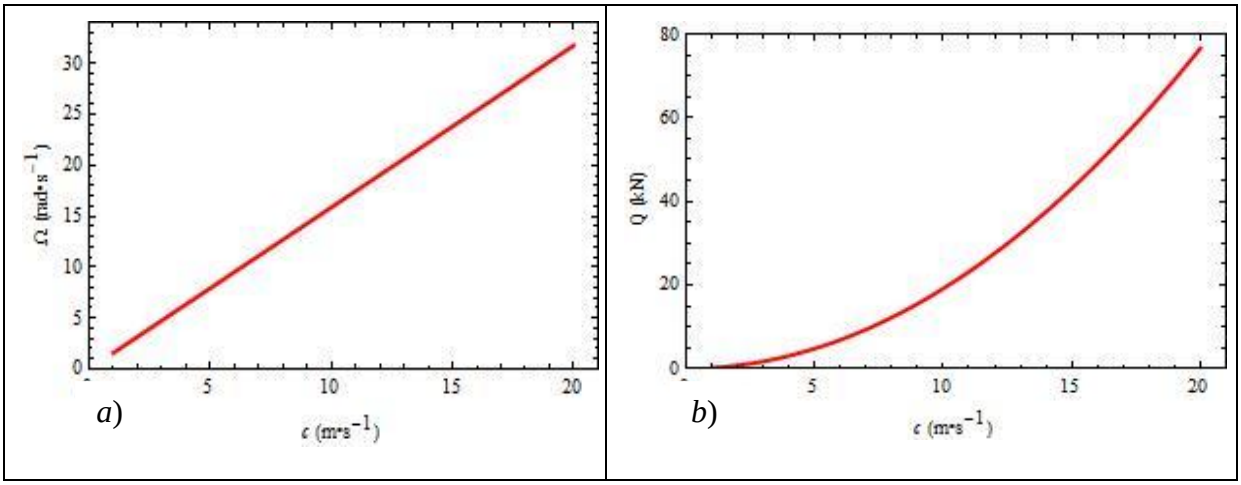

Figure 7-2: The variation of the *a*) angular frequency Ω and *b*) magnitude of the harmonic load Q with respect to the velocity of the moving load.

The locomotive produces a harmonic force when in motion due to the unbalanced counterweights of the driving wheels, which is given as Q Sin Ωt. Ω is the angular frequency of the harmonic force and Q is the amplitude of the load. The *a*) angular frequency Ω and *b*) amplitude of the harmonic load component Q vary linearly and quadratically with respect to the velocity of the locomotive respectively, as shown in Figure 7-2. They are expressed as [102]:

$$Q = \frac{1.5\,c^2}{(\pi\,r)^2}, \Omega = \frac{c}{r} \tag{7.2}$$

where the radius of the driving wheels $r = 0.63$ m. The mass per unit length of the loaded beam, $\bar{\mu} = 6.454 \text{ x } 10^3$ kg·m^{-1}, takes into account the mass effects of the locomotive and its position causes a variation of the natural frequency for the loaded beam [102]. Therefore, $\bar{\mu}$ is evaluated when the locomotive is assumed to be stationary at the mid-span of the bridge since the variation of the natural frequency at this location is relatively small. When carrying out the free vibration analysis of the beam, μ will be taken into consideration. However, when carrying out the dynamic response of the moving load problem, $\bar{\mu}$ will be used in place of μ. The beam is modelled using only 1 WFE for both Daubechies and BSWI wavelet based approaches, The results are compared with the solutions obtained using 8 classical Euler Bernoulli beam finite elements and an analytical approach from Fryba [102].

The free vibration analysis of the unloaded beam is carried out by solving the eigenvalue problem [27]

$$\left[[\boldsymbol{K_b}] - \omega^2[\boldsymbol{M_b}]\right]\{\acute{V}\} = 0 \tag{7.3}$$

The vector $\{\acute{V}\}$ represents modal displacements and ω is the corresponding natural frequencies of the system.

	Natural Frequency ω_j			
j	***Analytical***	***FEM – 8 elements***	***D18$_1$ WFEM***	***BSWI4$_4$ WFEM***
1	26.4	26.4	26.4	26.4
2	105.6	105.6	105.6	105.6
3	237.5	237.8	237.6	237.5
4	422.2	423.9	424.2	422.4
5	659.7	665.9	671.0	660.3
6	950.0	967.4	1026.9	951.7
7	1293.1	1333.4	1469.8	1297.8
8	1688.9	1874.6	1746.2	1700.5
9	2137.5	2333.9	3105.7	2163.7
10	2638.9	2979.6	4257.2	2693.8

Table 7-1: Comparison of the analytical, classical FEM, D*18$_1$* WFEM and BSWI*4$_4$* WFEM natural frequencies ω_j of a simply supported beam.

The first 10 natural frequencies of the unloaded beam obtained via the analytical, FEM (18 DOFs), Daubechies D*18$_1$* (18 DOFs) and BSWI*4$_4$* (19 DOFs) WFEM solutions are presented

in Table 7-1. The orders and scales of the WFEs are selected to aid in the comparison of the results obtained via the different approaches. According to the results presented, the lower mode natural frequencies of the simply supported beam are obtained accurately when only one element is used for both the Daubechies and BSWI based WFE solutions. The classical FEM approach approximates the first 3 natural frequencies accurately, with 8 elements employed in the analysis. This is in accordance to general FEM practice where the number of elements required to accurately approximate the natural frequencies is 3-5 times the number of the modes associated with the natural frequencies.

The Daubechies WFEM results indicate that the lower mode natural frequencies are accurately obtained, where the first 3 natural frequencies correspond to those obtained analytically. However, for the higher mode natural frequencies, the results do not perform as well as the BSWI and FEM solutions with a similar number of DOFs. This is attributed to the fact that the Daubechies scaling function and/or their derivatives have no closed form solution and the method requires the evaluation of the connection coefficients to formulate the elemental matrices. The numerical errors present in the evaluation of the connection coefficients result in a slow rate of convergence for the higher mode natural frequencies when the free vibration analysis is evaluated, particularly for lower order Daubechies based WFEM solutions. The results can however be improved by increasing the order and/or multiresolution scale of the Daubechies WFE without increasing the number of elements or subsequently altering the original model as illustrated in Figure 7-3. This verifies that the Daubechies WFEM solution converges to the exact solution by increasing the element order and/or scale.

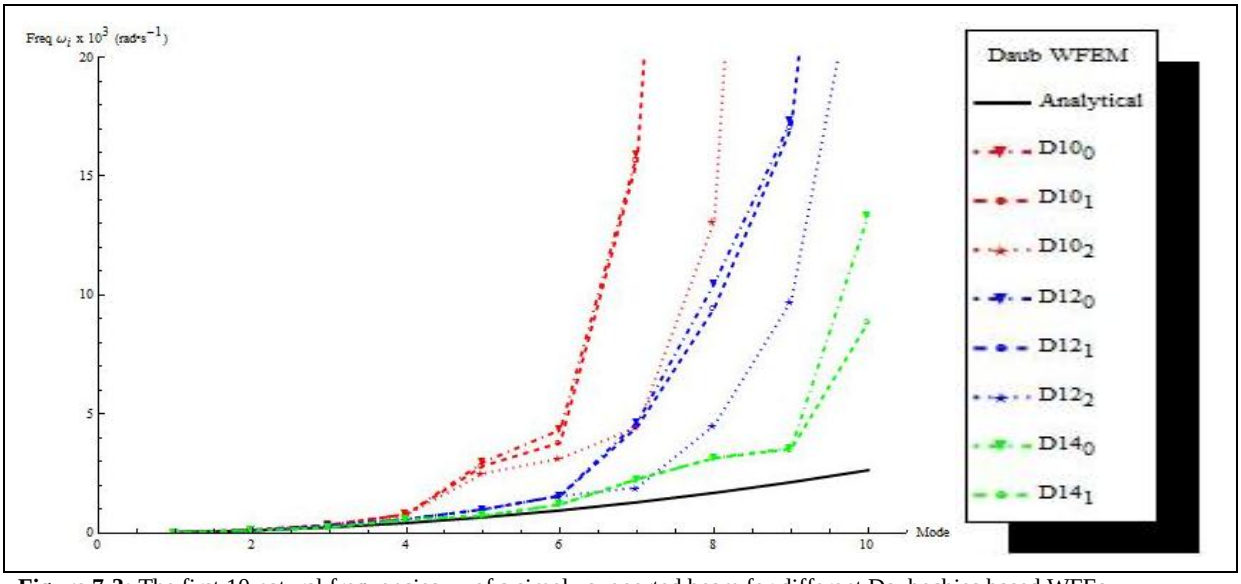

Figure 7-3: The first 10 natural frequencies ω_j of a simply supported beam for different Daubechies based WFEs.

At lower multiresolution scales, increasing the order of the Daubechies WFE improves the results more significantly than increasing the multiresolution scale. For example, from Figure 7-3, increasing the order from D10_0 to D12_0 leads to a better approximation of the natural frequencies, particularly at higher modes, than increasing the multiresolution from $j = 0$ to $j = 1$ for D10. However, for the different orders of the Daubechies WFE solutions, it is observed that as the multiresolution scale increases from $j = 1$ to $j = 2$, the improvement of the accuracy of the natural frequencies is significantly greater than altering the multiresolution from $j = 0$ to $j = 1$. This is because increasing the scale of the Daubechies wavelet based beam finite element from j to $j + 1$ increases the number of corresponding DOFs for each element by 2^j. However, increasing the order of the Daubechies WFE from L to $L + 2$, increases the DOFs per WFE by 2. Moreover, it was also noted while carrying out the analysis that the approximation of the natural frequencies diverged significantly for multiresolution scale $j \geq 3$. The inaccuracies of the approximations result from numerical instability and errors that arise when evaluating the elemental matrices in wavelet space, particularly for high values of j. Considering that increasing the order leads to a better approximation of the results, it is more effective and efficient to first increase the order of the WFE then increase the multiresolution scale so as to improve the approximation of the higher mode natural frequencies of the system.

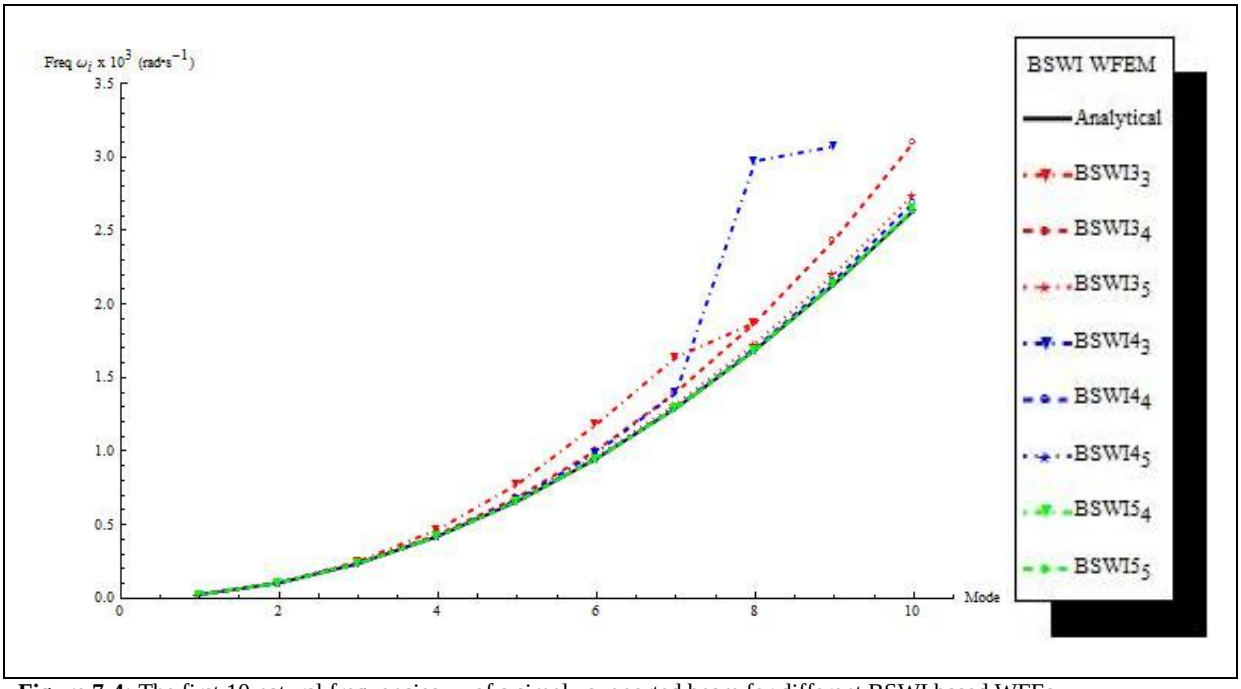

Figure 7-4: The first 10 natural frequencies ω_j of a simply supported beam for different BSWI based WFEs.

Figure 7-4 illustrates the effect of increasing the order and/or multiresolution scale on the accuracy of the first 10 natural frequencies for the BSWI based WFEM. In addition to the

observations made from the results presented in Table 7-1, the general BSWI based WFEM solutions are highly accurate for the first 10 natural frequencies in comparison to the Daubechies WFEM and classical FEM solutions, for a similar number of DOFs. Increasing the order and/or multiresolution scale leads to the convergence of the approximate solution to the exact solution as illustrated in Figure 7-4. For example, the percentage error of the 10th natural frequency via the BSWI5_5 WFE solution is 2.24×10^{-3} %; in comparison to the analytical solution.

The damping of the beam is represented by Rayleigh viscous damping and the element damping matrix in physical space $\left[\boldsymbol{c}_{b,e}^{\boldsymbol{p}}\right]$ is expressed as [100]:

$$\left[\boldsymbol{c}_{b,e}^{\boldsymbol{p}}\right] = \alpha_d \left[\boldsymbol{k}_{b,e}^{\boldsymbol{p}}\right] + \beta_d \left[\boldsymbol{m}_{b,e}^{\boldsymbol{p}}\right] \tag{7.4}$$

where the matrices $\left[\boldsymbol{m}_{b,e}^{\boldsymbol{p}}\right]$ and $\left[\boldsymbol{k}_{b,e}^{\boldsymbol{p}}\right]$ are the wavelet based mass and stiffness element matrices in physical space respectively. α_d and β_d are the damping coefficients which are obtained from solving the system of equations [100]:

$$\begin{aligned} \zeta_1 &= \alpha_d \frac{1}{2\,\omega_1} + \beta_d \frac{{\omega_1}^2}{2} \\ \zeta_2 &= \alpha_d \frac{1}{2\,\omega_2} + \beta_d \frac{{\omega_2}^2}{2} \\ &\vdots \\ \zeta_n &= \alpha_d \frac{1}{2\,\omega_n} + \beta_d \frac{{\omega_n}^2}{2} \end{aligned} \tag{7.5}$$

where ζ_i and ω_i are the i^{th} mode damping ratio and corresponding natural frequency respectively. The variation of the damping ratios with respect to the natural frequencies for the first 12 modes of vibration is presented in Figure 7-5. The variations obtained via both the Daubechies D18_1 and BSWI4_4 WFEM approaches, with one element modelling the beam, are in good agreement with the solution obtained analytically. According to the results obtained, the damping ratio decreases with an increase in the mode number due to an increase in the natural frequency of the beam. In general, the modal mass participation in a given system decreases significantly with a corresponding increase in the mode number *i*. This leads to the assumption that for the dynamic analysis of systems, although the natural frequency is increasing, only the first few modes of vibration are considered important and effectively contribute to the dynamic behaviour of the system [100]. Furthermore, for high values of *n* number of equations for large complex systems, it may be difficult to obtain solutions for the coefficients that satisfy the relations in equation (7.5) [100]. The values of the viscous

damping coefficients α_d and β_d are obtained via the different approaches as 0.192402 and 0 respectively. These values are similar for n = 3 and n = 10.

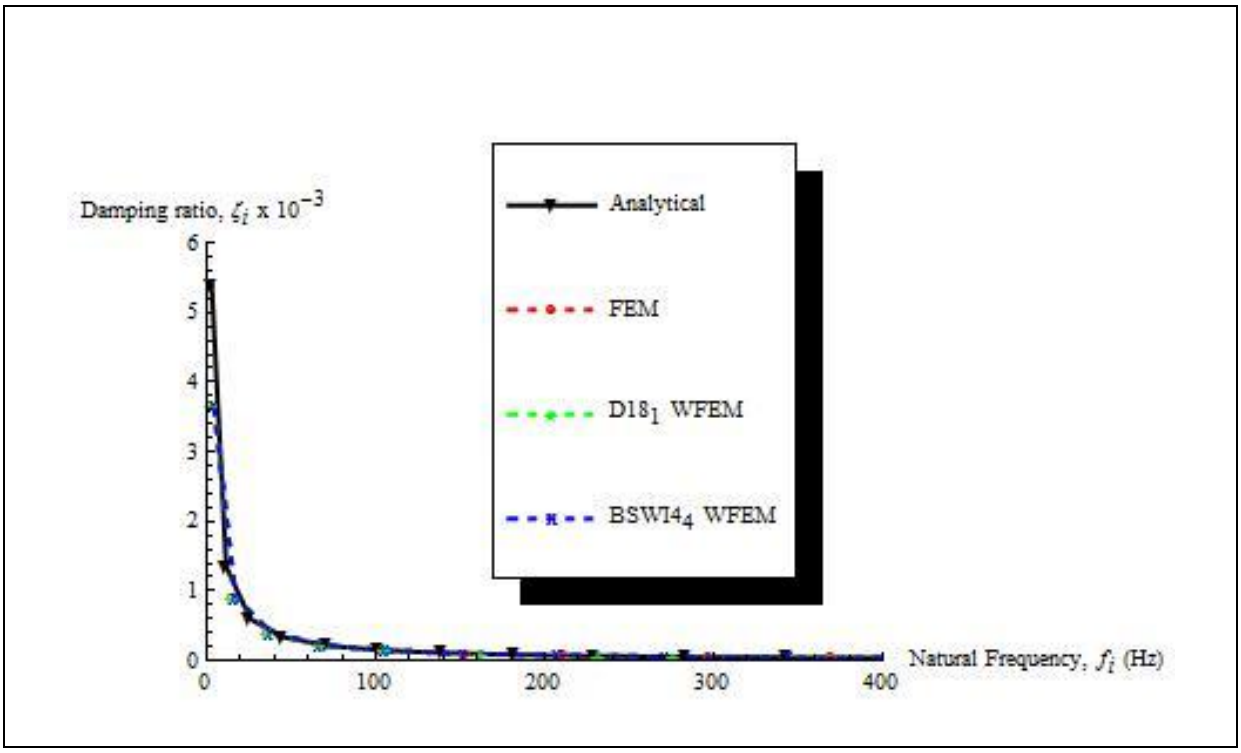

Figure 7-5: Plot of the modal damping ratio variation with respect to the corresponding natural frequency of a simply supported beam.

The static deflection mid-span of the simply supported, when subjected to a static point load *P* at the centre of the beam, is defined as [102]:

$$v_0 = \frac{Pl^3}{48EI} \tag{7.6}$$

where *EI* is the bending stiffness of the beam and *l* is the length of the beam. The point load *P* in this case represents the weight of the locomotive stationary at the centre of the beam and is assigned the value of $P = 9.7\text{x}10^5$ N. The deflection of the beam at a point *x* as the harmonic moving load travels across the beam at time *t* is denoted by $v(x,t)$. Taking into consideration that the maximum deflection occurs at the centre of the simply supported beam, the dynamic response of the beam $v(\frac{l}{2},t)$ is analysed. The normalised non-dimensional deflection, or dynamic coefficient, is defined as the ratio of the dynamic deflection to the static deflection at the centre of the beam and is expressed as $v(\frac{l}{2},t)/v_0$.

According to Fryba [102], the critical velocity of the harmonic moving load is described as the velocity of the locomotive at which its dynamic effects are maximum and is given by the simple relation $c_{cr} = 2\pi r\bar{f}_1$. The first natural frequency of the loaded beam in Hz and radius

of the driving wheels are denoted by $\bar{f}_1$ and r respectively. However, for more complicated systems it may be difficult to describe and obtain the critical velocity directly via analytical or semi-analytical formulations.

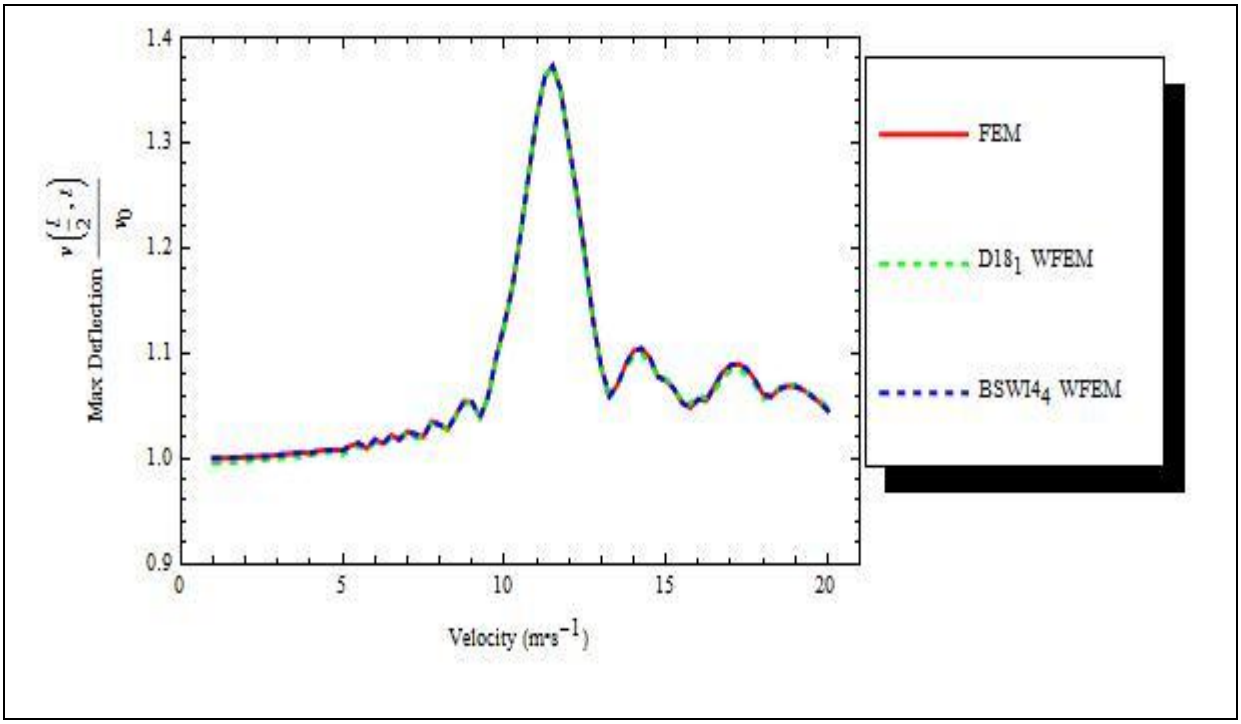

Figure 7-6: The maximum non-dimensional vertical displacement at the centre of a simply supported beam subjected to a moving harmonic load at different velocities.

Therefore, the WFEM is used to acquire the critical velocity by obtaining the maximum normalized vertical displacement at the centre of the beam, for different velocities of the moving harmonic load, as presented in Figure 7-6. The analysis is carried out for the range of velocities $1 \leq c \leq 20$ m·s^{-1} of the harmonic moving load, with increments of 0.1 m·s^{-1}. The results obtain via the BSWI4_4 and Daubechies D18_1 WFEM solutions, with only one element used to describe the entire beam, are in good agreement with the classical FEM (8 elements). The critical velocity is approximated as 11.5 m·s^{-1} via the D18_1 and BSWI4_4 WFEM solutions. The critical velocity obtained via the analytical formulation is $c_{cr} = 11.28$ m·s^{-1}. This validates the use of the WFEM to obtain the critical velocity of the moving harmonic load.

It is important to mention that, the evaluation of the critical velocity via FEM and WFEM approaches for more complicated cases requires the evaluation of the maximum deflections associated with corresponding velocities of the moving load. This implies that for each moving load velocity, the dynamic response of the system must be evaluated at each time step to identify the maximum deflection. This is computationally expensive and time

consuming, if the number of DOFs and time steps required to attain acceptable levels of accuracy is high. Given that the solutions can be approximated via the WFEM with fewer elements than the classical FEM approach, the computational and time costs are reduced significantly when carrying out the evaluation of the moving load critical velocity based on the size of the system matrices.

As mentioned earlier, the dynamic response of the beam is evaluated using the Newmark direct time integration method. The time step Δt does not need to be set at a minimum value to ensure stability for this implicit time integration scheme and is therefore selected over other explicit time integration methods. However, the accuracy of the solution may be poor if too large a time step is selected. With this in mind, as the time step decreases, the cost of computation increases since the number of time iterations also increases. It is therefore necessary to ensure when carrying out the dynamic analysis of a system via WFEM, that the time step selected leads to results that are accurate enough and efficient. It is common practice in classical FEM to initially select at time step within the range $0.1T_n \leq \Delta t \leq 0.3T_n$ [29], where $T_n = \frac{1}{f_n}$ is the period of the n^{th} mode of vibration. If the level of accuracy is not acceptable then the size of the time step can be decreased incrementally until the solution attains the desired level of accuracy. This approach is implemented for the WFEM dynamic response analysis in this example and subsequent solutions in this study. The time step employed for this analysis is $\Delta t = 3.9 \text{ x } 10^{-3}$s, which is approximately $\Delta t \approx 0.1T_3$. The time taken for the load to travel over the beam is $t_f = \frac{l}{c}$; this is used to normalise the time *t* into a non-dimensional time parameter.

The BSWI4_4 and D18_1 WFEM solutions for the non-dimensional displacement at the centre of the beam, as the harmonic moving load travels across the beam, are compared with the analytical solution from Fryba [102] and the classical FEM solution obtained with 8 beam elements; for *a*) $c = 9.64$ m·s^{-1}, *b*) $c = c_{cr} = 11.28$ m·s^{-1} and *c*) $c = 12.92$ m·s^{-1} as presented in Figure 7-7. These velocities correspond to subcritical, critical and supercritical velocity profiles respectively. The Daubechies and BSWI WFEMs accurately approximate the displacement for the 3 different velocities and are in very good agreement with the analytical solution. This validates the implementation of WFEM formulation in the analysis of moving load problems.

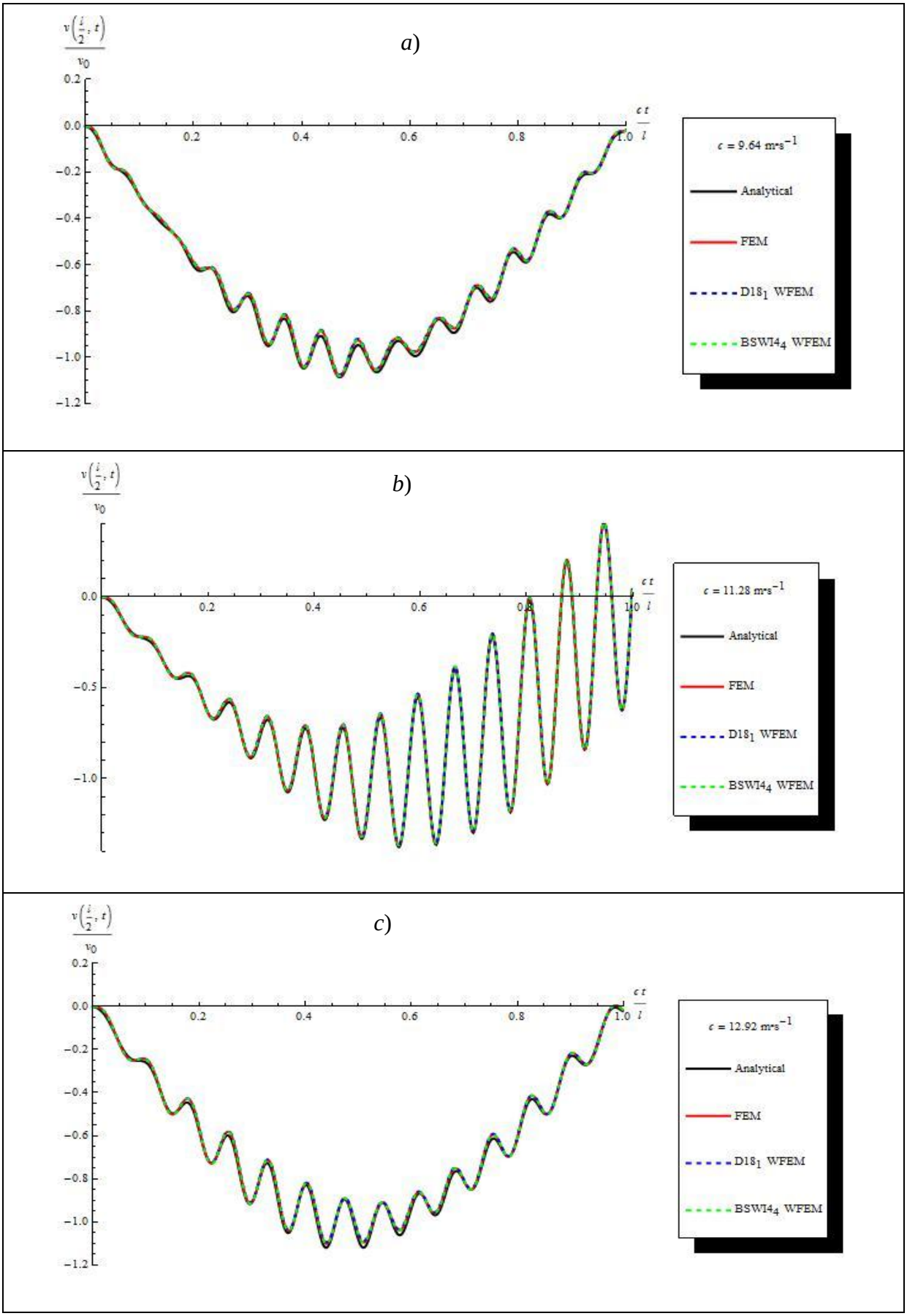

Figure 7-7: The non-dimensional vertical displacement at the centre of a simply supported beam subjected to a harmonic moving load travelling at *a*) 9.64 m·s^{-1} *b*) 11.28 m·s^{-1} and *c*) 12.92 m·s^{-1}.

Furthermore, the lateral velocity at the centre of the beam, as the harmonic moving load travels across, is analysed using the WFEMs. The BSWI4_4 and D18_1 wavelet solutions are again compared with the analytical and the classical FEM solutions and the results are presented in Figure 7-8 for the three moving load velocities. The results obtained via both the WFEMs are in very good agreement with the analytical solution, with only one WFE implemented for all velocity profiles. Similarly, the acceleration at the centre of the beam is presented in Figure 7-9 as the harmonic load travels at *a*) $c = 9.64$ m·s^{-1}, *b*) $c = c_{cr} = 11.28$ m·s^{-1} and *c*) $c = 12.92$ m·s^{-1}. The results presented illustrate that once again both WFEM solutions are in very good agreement with the analytical solution.

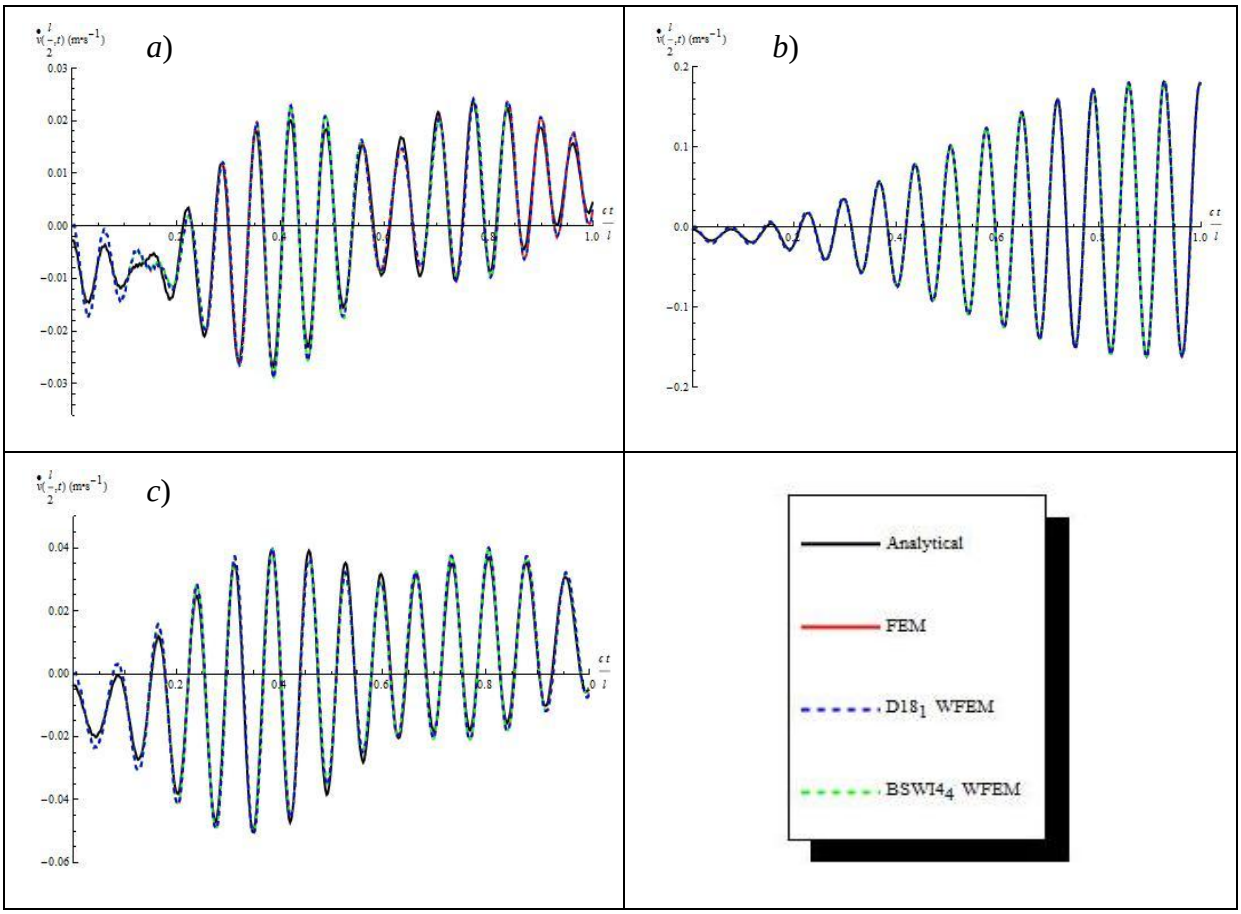

Figure 7-8: The vertical velocity at the centre of a simply supported beam subjected to a moving harmonic load travelling at *a*) 9.64 m·s^{-1} *b*) 11.28 m·s^{-1} and *c*) 12.92 m·s^{-1}.

Further analysis is carried out to investigate the effects of increasing the order and/or multiresolution scale of the WFEs on the accuracy of the solutions with respect to the displacement of the beam. The non-dimensional vertical displacement at the centre of the beam, as the harmonic moving load travels across at $c = 12.92$ m·s^{-1}, is presented in Figure 7-10; *a*) BSWI3_j and *b*) BSWIm_4 for $3 \leq j, m \leq 5$ WFEM solutions. It is observed from Figure 7-10 *a*) that the results converge to the analytical solution as the multiresolution scale

increases from BSWI3_3 (red dashed curve) to BSWI3_4 (blue dashed curve) and subsequently to BSWI3_5 (green dashed curve).

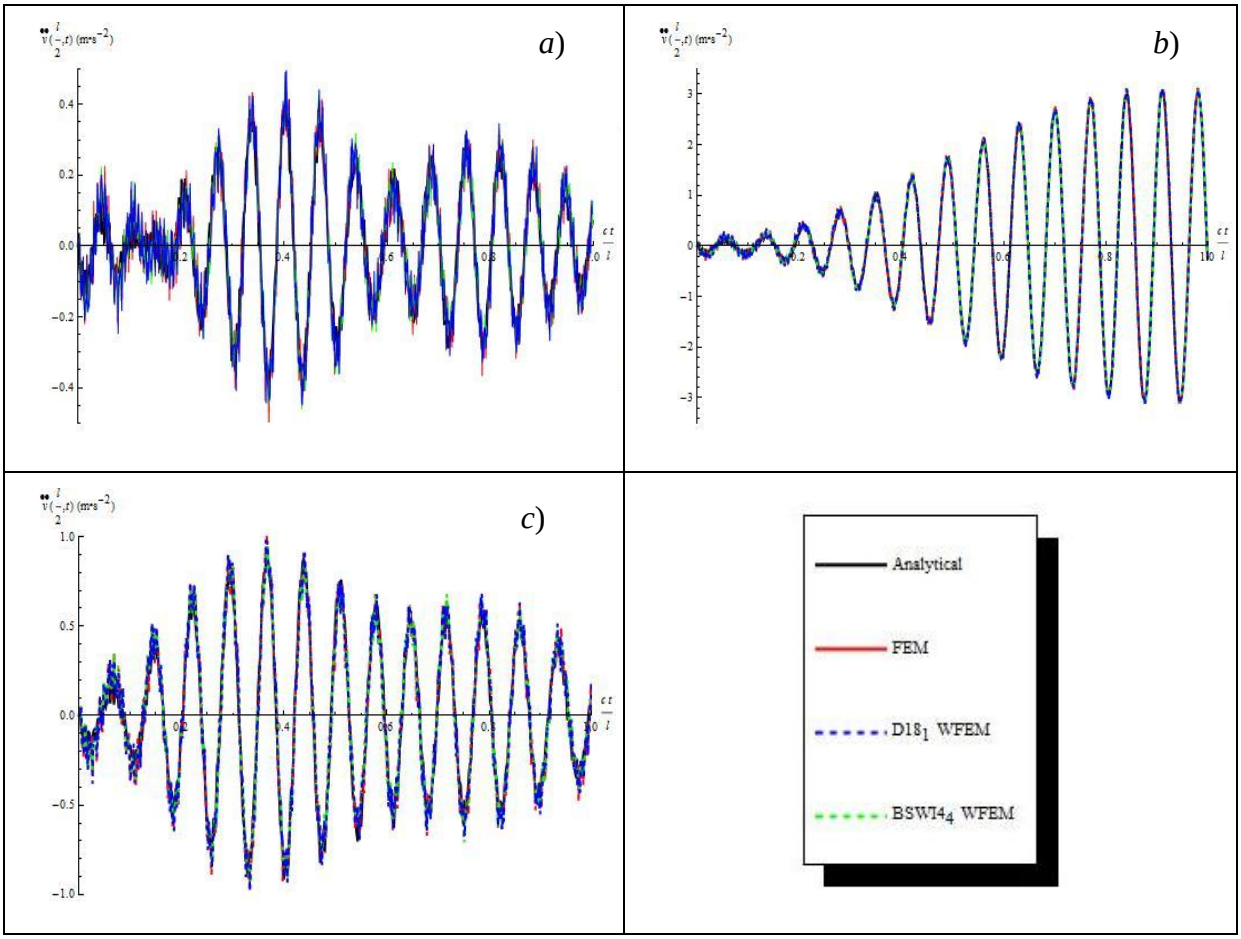

Figure 7-9: The vertical acceleration at the centre of a simply supported beam subjected to a moving harmonic load travelling at *a*) 9.64 m·s^{-1} *b*) 11.28 m·s^{-1} and *c*) 12.92 m·s^{-1}.

Likewise, the accuracy of the approximate solution improves when the order of the BSWI wavelet element is increased, as observed from Figure 7-10 *b*). The order of the BSWI based WFE is increased from $m = 3$ to $m = 5$, at multiresolution scale $j = 4$. It can therefore be concluded that increasing the multiresolution and/or order of the BSWI WFE improves the accuracy of the approximate solution and the results converge to the analytical solution.

A similar analysis is carried out for the Daubechies wavelet based finite element solution as presented in Figure 7-11. The results are obtained from the *a*) D10_j and *b*) DL_0 WFE formulations for $0 \leq j \leq 2$ and $10 \leq L \leq 18$ (L is an even integer) respectively. Observations made from Figure 7-11 *a*) indicate that increasing the multiresolution scale j improves the accuracy of the approximate solution. Although the results improve as j is increased, the D10_2 WFEM solution is not in perfect agreement with the analytical solution.

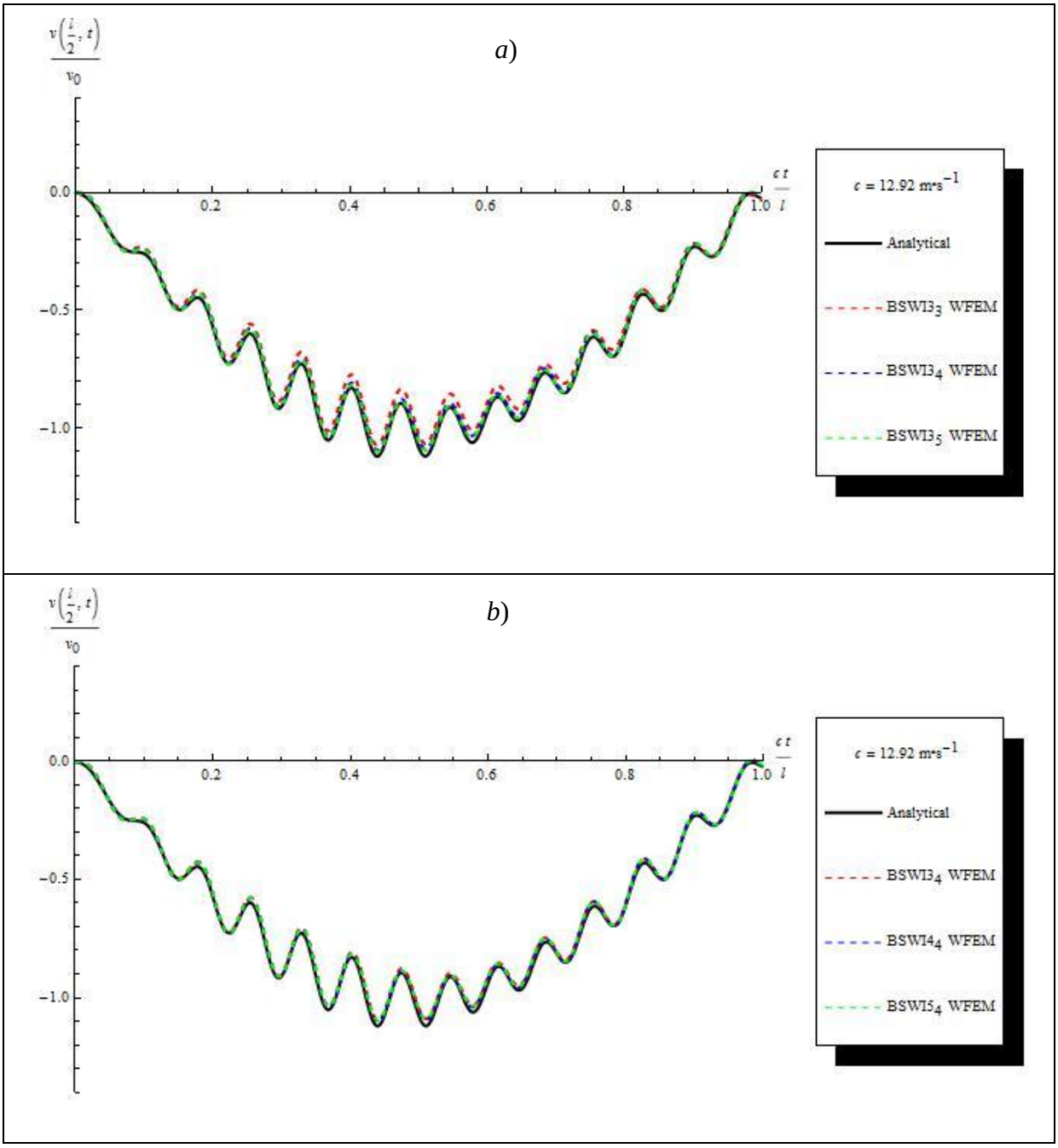

Figure 7-10: The non-dimensional vertical displacement at the centre of a simply supported beam subjected to a harmonic moving load travelling at 12.92 m·s^{-1} for *a*) BSWI3$_j$ and *b*) BSWIm_4 WFEs.

Increasing the order of the wavelet family also improves the accuracy of the solution as observed in Figure 7-11 *b*). The results obtained from the D10_0 WFE formulation are not as accurate in comparison to the other higher order Daubechies WFE solutions. However, the solution accuracy improves as the order is increased. It is therefore better to first increase the order of the WFE to improve the approximation of the dynamic response of the system. If the desired levels of accuracy are stilled not attained, the multiresolution scale can then be improved.

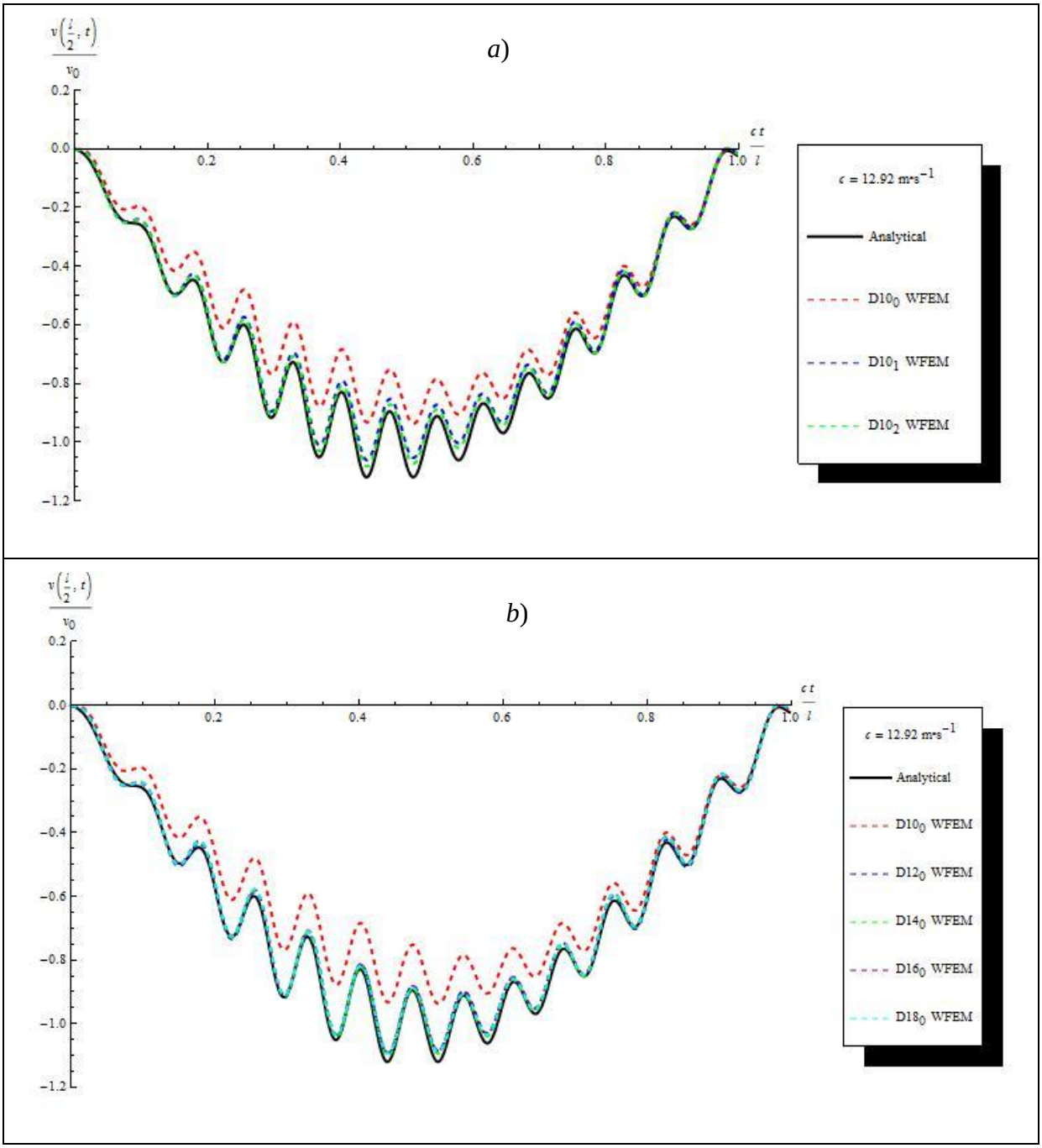

Figure 7-11: The non-dimensional vertical displacement at the centre of a simply supported beam subjected to a moving harmonic load travelling at 12.92 m·s^{-1} for *a*) D*10$_j$* and *b*) D*L$_0$* WFEs.

The implementation of the Daubechies and BSWI based WFE formulations for the free vibration and dynamic response analyses of a beam subjected to a harmonic load are validated. The convergence of the solutions via both methods, by increasing the order and/or multiresolution scale, is further verified. A single WFE is used to model the beam and the results are in perfect agreement with the analytical solutions. The comparative study demonstrates that the BSWI WFEM solutions are superior to both classical FEM and Daubechies WFEM for the analysis of free vibration and vehicle-bridge interaction.

The computational costs for carrying out this analysis are not highlighted for this relatively simple moving load problem since the comparison of the WFEMs with classical FEM is carried out for a similar number of DOFs. This is the case so as to analyse the accuracy of the different methods with similar number of DOFs. The computational costs will be compared later in this chapter.

7.2. Vierendeel frame subjected to a moving load

The dynamic response of a steel Vierendeel frame made up of 8 main uniform plane bar wavelet based finite elements is analysed when subjected to a moving point load $P = 20$ N, travelling across elements 1 – 6, as illustrated in Figure 7-12. The moving load is initiated at node 1 and departs the frame at node 7. The plane bar elements (beam with axial deformations taken into consideration) have uniform geometrical and material properties which include: Young's modulus $E = 2.07 \text{ x } 10^{11}$ N·m^{-2}, area $A = 8.06 \text{ x } 10^{-5}$ m^2, density $\rho = 7.81 \text{ x } 10^3$ kg·m^{-3}, moment inertia $I = 2.71 \text{ x } 10^{-10}$m^4 and length of each major element $l = 0.305$ m. The boundary conditions of the frame are fixed at both nodes 1 and 7, with damping neglected in the analysis. This example is carried out to present the capabilities of WFEM to solve the dynamic response of a structure comprising of elements arranged in different spatial orientations while subjected to rapidly varying loading conditions.

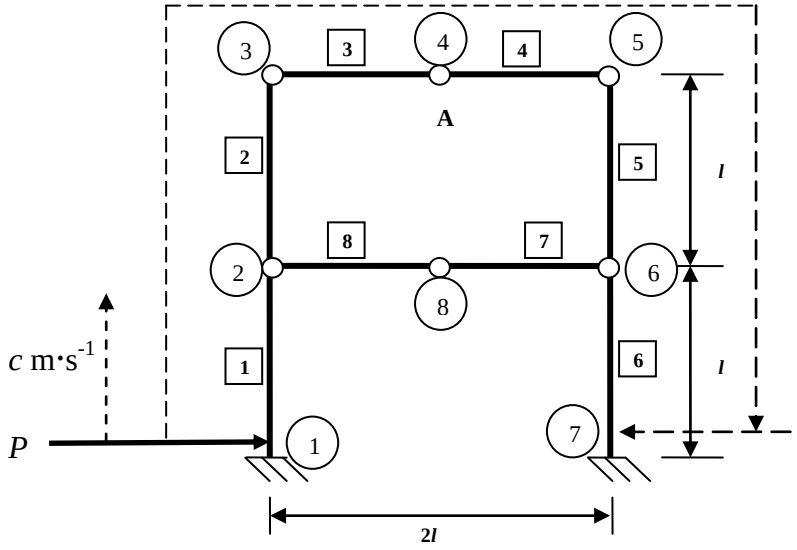

Figure 7-12: Vierendeel frame subjected to a moving load.

The free vibration analysis is carried out by solving the eigenvalue problem [**27**]

$$\left[\left[\boldsymbol{K_p}\right] - \omega^2\left[\boldsymbol{M_p}\right]\right]\{\acute{H}\} = 0 \qquad \textbf{(7.7)}$$

where the matrices $[\boldsymbol{M_p}]$ and $[\boldsymbol{K_p}]$ are the plane bar global system mass and stiffness matrices as formulated in Section 5.3. The vector $\{\acute{H}\}$ represents modal displacements and ω is the corresponding natural frequencies of the system.

	Frequency ω_i			
Mode *i*	**Ref[108]**	**FEM (48 elem)**	**D12_0 (8 elem)**	**BSWI4_3 (8 elem)**
1	107	107.101	107.101	107.101
2	377	377.122	377.121	377.121
3	397	396.903	396.9	396.9
4	476	475.313	475.308	475.309
5	1099	1098.37	1098.62	1098.33
6	1316	1315.18	1315.64	1315.1
7	1504	1502.87	1503.62	1502.75
8	1912	1910.26	1912.54	1910.03
9	2061	2060.06	2063.17	2059.76
10	2248	2445.94	2453.74	2445.53
11	2695	2693.62	2704.75	2692.97
12	2904	2902.4	2919.78	2901.59
13	4171	4170.97	4184.59	4168.7
14	4618	4619.06	4648.85	4615.97
15	4944	4945.24	5004.99	4941.47
16	5613	5616.18	5683.59	5610.87
17	5885	5890.07	5979.09	5883.82
18	6405	6411.3	6514.93	6404.13
19	6950	6959.95	7300.75	6950.2
20	7227	7239.32	7580.26	7228.48
21	9558	9256.95	11415.7	9235.98
22	9649	9681.56	11889.3	9658.45
23	10349	10393.4	12533	10364.6
24	11343	11401.7	13509.1	11365.8
25	11550	11608.5	14076	11572.8
26	11931	11974.2	15736.7	11947.2
27	12249	12313.6	15925.3	12276.6
28	12862	12895.4	17554.3	12875.1
29	13650	13755.4	18334.8	13700.8
30	14191	14267.2	19038.5	14229.9

Table 7-2: First 30 angular frequencies ω_i of the Vierendeel frame obtained via FEM, D12_0 WFEM and BSWI4_3 WFEM formulations.

The first 30 natural frequencies obtained from the Daubechies D12_0 and BSWI4_3 wavelet based element formulations, are presented in Table 7-2. The results are compared to values

obtained by Jara-Almonte and Mitchell [108] and the classical FEM solutions. To aid in the comparison of the different approaches, given that the BSWI4_3 (136 DOFs) is the lowest BSWI WFE that can be used to formulate the planar bar element, the Daubechies D12_0 (136 DOFs) WFE and 48 classical FE (144 DOFs) solutions are employed. So as to ensure uniformity during discretization of the frame, 6 classical finite elements correspond to 1 WFE. It is observed from the results that the wavelet based finite element natural frequency solutions for both Daubechies and BSWI formulations are in good agreement with solutions obtained in [108]; for the lower modes of vibration. In comparison to the classical FEM solution, the frequencies obtained via the WFEM are highly accurate, particularly for the BSWI4_3 solutions. The Daubechies D12_0 WFE solutions for the higher mode frequencies are not approximated as accurately as the other solutions.

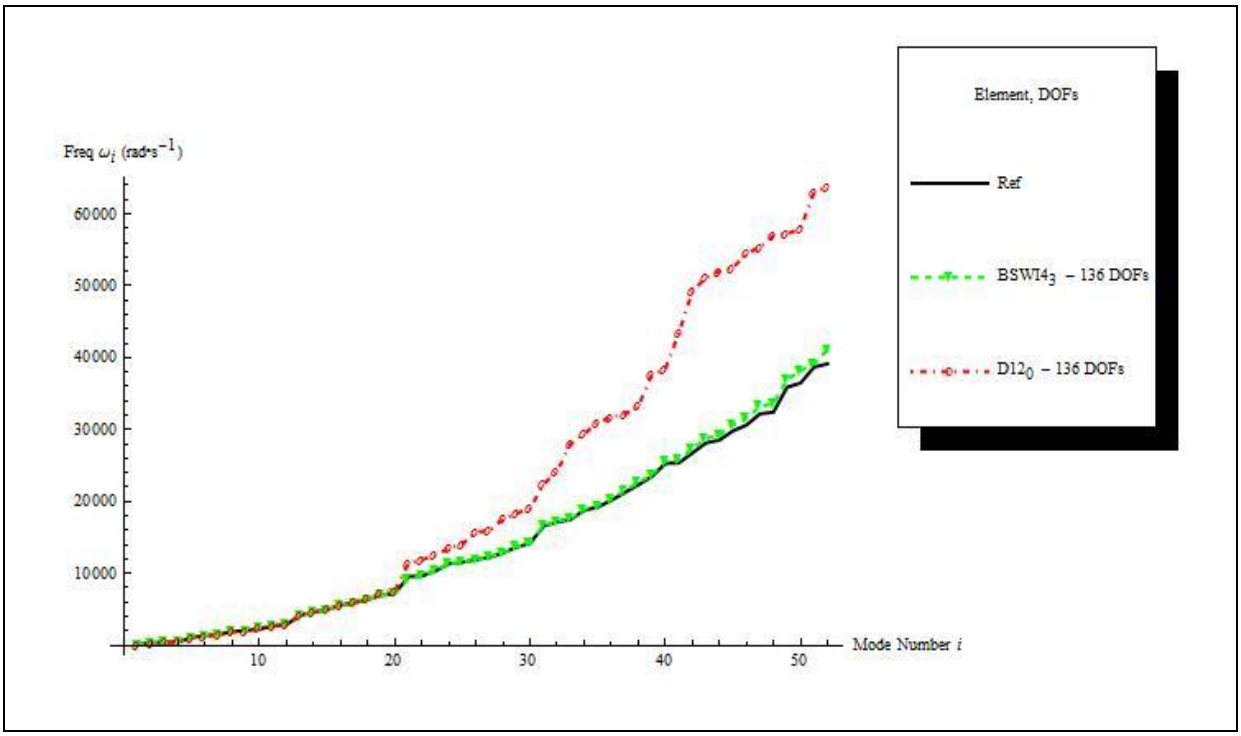

Figure 7-13: Comparison of the Vierendeel frame first 52 angular frequencies ω_i obtained via D12_0 WFEM and BSWI4_3 WFEM.

This is further evident when the D12_0 solution for the first 52 angular frequencies are compared with the BSWI4_3 solution and results obtained by Jara-Almonte and Mitchell [108]; as observed from Figure 7-13. The lower modes of vibration natural frequencies (first 20) are approximated very accurately by the D12_0 solution. However, the BSWI4_3 solution approximates all the first 52 frequencies very accurately with the same number of DOFs (136) as the D12_0 element formulation. The accuracy of the results can be improved by increasing the order and/or the multiresolution scale of the Daubechies based wavelet finite elements without increasing the number of elements, which would require an alteration in

discretization of the entire system. This is apparent from the solutions of the first 52 angular frequencies obtained via the Daubechies based WFEM for different orders D*L* and multiresolution scales *j* as presented in Figure 7-14. It is observed that increasing the order and/or the multiresolution of the Daubechies wavelet leads to better approximations of the higher mode frequencies. This confirms the convergence of the Daubechies WFEM solutions to the exact solution with respect to increasing the order and/or multiresolution scale. Furthermore, it is also seen that increasing the order of the Daubechies based elements has a more significant effect on the accuracy of the approximation than increasing the multiresolution, particularly for the higher mode frequencies.

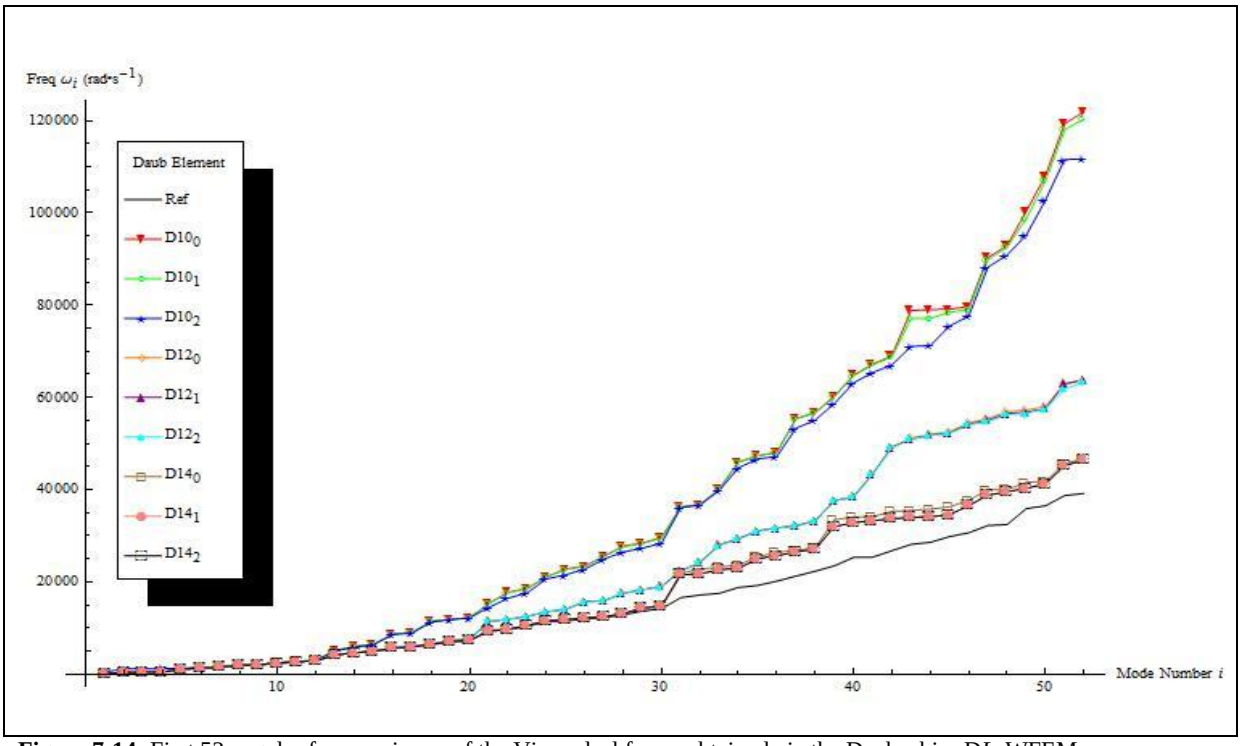

Figure 7-14: First 52 angular frequencies ω_i of the Vierendeel frame obtained via the Daubechies DL_j WFEM.

The comparison of the BSWI based WFEM solutions for the first 52 natural frequencies of the Vierendeel frame are illustrated in Figure 7-15, for the different orders and multiresolution scales. The BSWI based WFEM approximate solutions for all 52 angular frequencies are observed to be very accurate with respect to the different wavelet orders and multiresolution scales. This implies that the lower order and/or multiresolution scales of the BSWI based WFEM accurately approximate the Vierendeel frame's natural frequencies at higher modes. Furthermore, the BSWI based WFEM gives significantly better results when compared to the solutions obtained, not only via the classical FEM, but also with respect to the Daubechies based WFEM; with approximately similar number of DOFs.

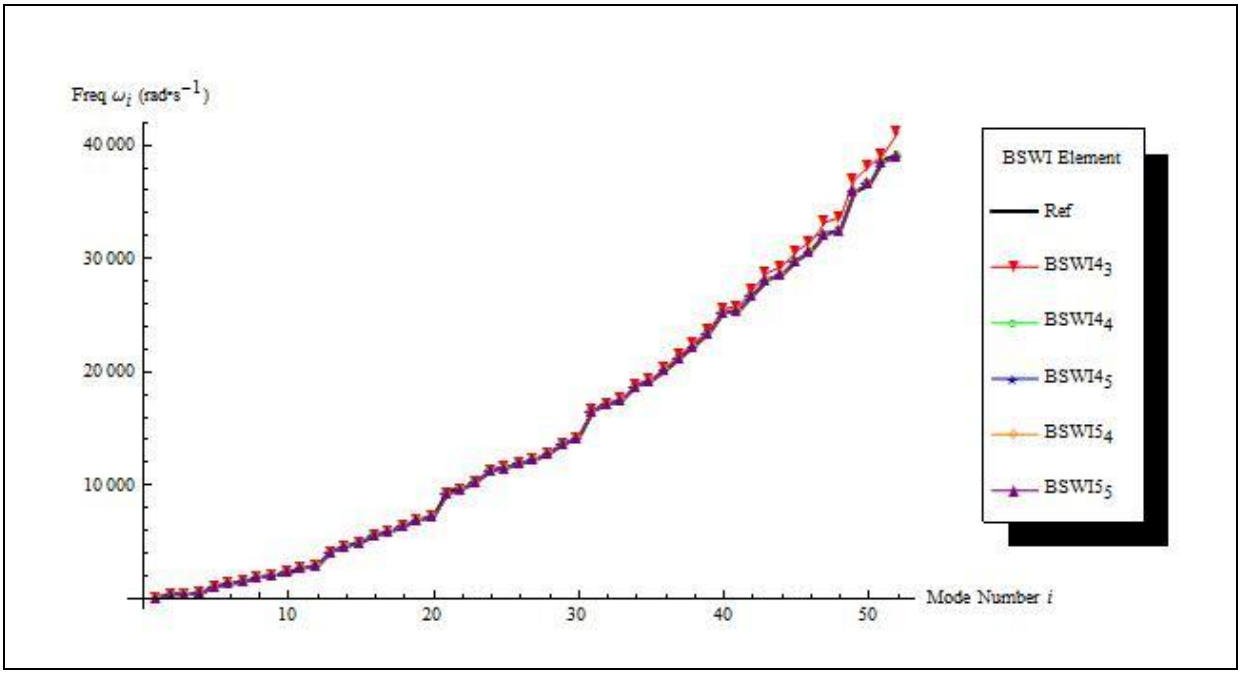

Figure 7-15: First 52 angular frequencies ω_i of the Vierendeel frame obtained via the BSWIm_j WFEM.

The governing equation describing the dynamic behaviour of the undamped system when subjected to a moving load is given as [27]:

$$[\boldsymbol{M_p}]\{\ddot{\boldsymbol{H}}_{\boldsymbol{p}}(t)\} + [\boldsymbol{K_p}]\{\boldsymbol{H_p}(t)\} = \{\boldsymbol{F_p}(t)\} \tag{7.8}$$

where the matrices $[\boldsymbol{M_p}]$ and $[\boldsymbol{K_p}]$ are the system mass and stiffness matrices in physical space as formulated in Section 5.3. $\{\boldsymbol{F_p}(t)\}$ is the time-dependent moving load vector and $\{\boldsymbol{H_p}(t)\}$ and $\{\ddot{\boldsymbol{H}}_{\boldsymbol{p}}(t)\}$ contain the system global displacement DOFs and accelerations respectively.

The maximum normalized lateral deflection at point A of the frame $\frac{\delta(x,t)}{\delta_0}$, for different moving point load velocities, is obtained via the Daubechies and BSWI WFEMs and compared with the FEM as presented in Figure 7-16. The normalizing factor δ_0 is the static lateral deflection at point A (Figure 7-12) when the frame is subjected to a point load of magnitude $P = 20$ N. The static deflection at this point is obtained by solving the governing static equation of the frame [31]

$$[\boldsymbol{K_p}]\{\boldsymbol{H_p}\} = \{\boldsymbol{F_p}\} \tag{7.9}$$

$\{\boldsymbol{F_p}\}$ is the static force vector in physical space and $\{\boldsymbol{H_p}\}$ is the vector containing the DOFs of the system.

The moving load is assumed to travel across the frame from node 1 to node 7, across elements 1 – 6, at a constant speed c m·s^{-1}. The plot presented in Figure 7-16 is for the range of speeds $0 < c \leq 200$ m·s^{-1}, at intervals of 1 m·s^{-1}, with respect to the corresponding maximum normalised lateral deflections at point A. This is carried out to give an accurate approximation of the critical speed of the frame structure since the structure is made up of elements in different spatial orientations. Simplified models such as a simply supported beam subjected to a moving load, as discussed in the previous section, may employ simple analytical or semi-analytical expressions to evaluate the critical speed of the load. In contrast, for structures of higher complexity, it may be difficult or impossible to obtain an analytical expression. It may therefore require numerical approaches, for instance the WFEM or FEM, to be used to approximate the critical speed.

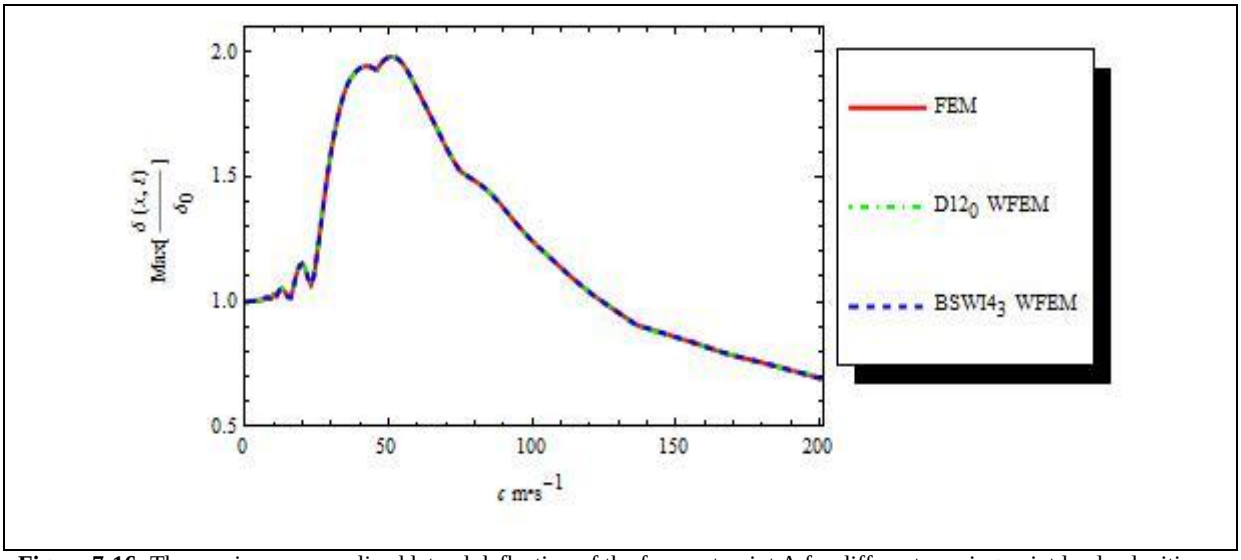

Figure 7-16: The maximum normalized lateral deflection of the frame at point A for different moving point load velocities.

The results obtained from both WFEM solutions are in good agreement with the FEM solution, accurately depicting the variation of the maximum normalised lateral deflection at point A and the critical speed. The highest value of the maximum normalised lateral deflection at point A is 1.97926 and corresponding moving load critical speed $c_{cr} = 52$ m·s^{-1}.

An analysis of the frame subjected to a moving point load is carried out for subcritical, critical and supercritical velocities. The non-dimensional moving load velocity parameter is defined as $\alpha_s = \frac{c}{c_{cr}}$. When $\alpha_s = 1$, the load is moving at a critical speed, while $\alpha_s < 1$ and $\alpha_s > 1$ correspond to subcritical and supercritical speeds respectively. The values of α_s used in this analysis to represent the subcritical, critical and supercritical speed profiles are 10^{-3}, 1 and 2 respectively.

The dynamic response of the frame is carried out via the Newmark direct time integration method with the parameters $\acute{\delta} = 0.5$ and $\acute{\gamma} = 0.25(0.5 + \acute{\delta})^2$. The time step Δt used in the analysis for both the FEM and WFEM approaches is $\Delta t = 0.1T_{15} \approx 1.27 \text{ x } 10^{-4}$ s. The time step is also small enough to ensure that the action of the moving load is subjected to each classical finite element, along its described path, at least once during the analysis for all the 3 speed profiles.

The normalised vertical displacements at point A, $\frac{\delta(t)}{\delta_0}$, for *a*) subcritical *b*) critical and *c*) supercritical speeds, are plotted in Figure 7-17 for the D10_0 WFEM, BSWI4_3 WFEM and FEM solutions. The time taken for the load to travel over the frame is $t_f = \frac{6l}{c}$ and this is used to normalise the time *t* into a non-dimensional time parameter.

The wavelet based elements presented are of the lowest order and multiresolution for the Daubechies and BSWI planar bar elements. The results obtained, when 8 of these WFEs are used to model the Vierendeel frame, are compared with the FEM (48 elements) solutions and it is observed that the wavelet solutions are in very good agreement. The higher order and/or multiresolution wavelet based element solutions are similar to the presented solutions and it is therefore not necessary to present these results.

The Daubechies D10_0 (104 DOFs) WFE solution gives a similar approximation of the dynamic response of the frame at point A as the BSWI4_3 (136 DOFs) WFE solution for the 3 different moving load speed profiles analysed. Although the higher modes of vibration natural frequencies are not accurately approximated via the Daubechies WFEM, the dynamic response is very accurately described. This is because the significant contribution to the dynamic response of the system is from the first few modes of vibration, which are accurately described via the Daubechies WFEM.

Furthermore, the Daubechies based WFEs can be formulated from the minimum multiresolution scale $j = 0$. However, with respect to the BSWI based WFEM, the condition $2^j \geq 2m - 1$, must be satisfied. Hence, the minimum multiresolution scale is dependent on order of the BSWI wavelet family. Consequently, as the order increases, the value of the minimum multiresolution scale j_0 also increases. The BSWI4_3 (20 DOFs per WFE) is the minimum WFE plane bar element that is applicable in this analysis. In contrast, the lowest order and scale corresponding to the Daubechies plane bar WFE is D10_0 (16 DOFs). This difference may not be of great consequence for one wavelet finite element. However, when a

significant number of WFEs are required, not based on accuracy but due to different spatial orientations of the WFEs within the system, the dynamic response of the system using the BSWI may be highly accurate yet inefficient.

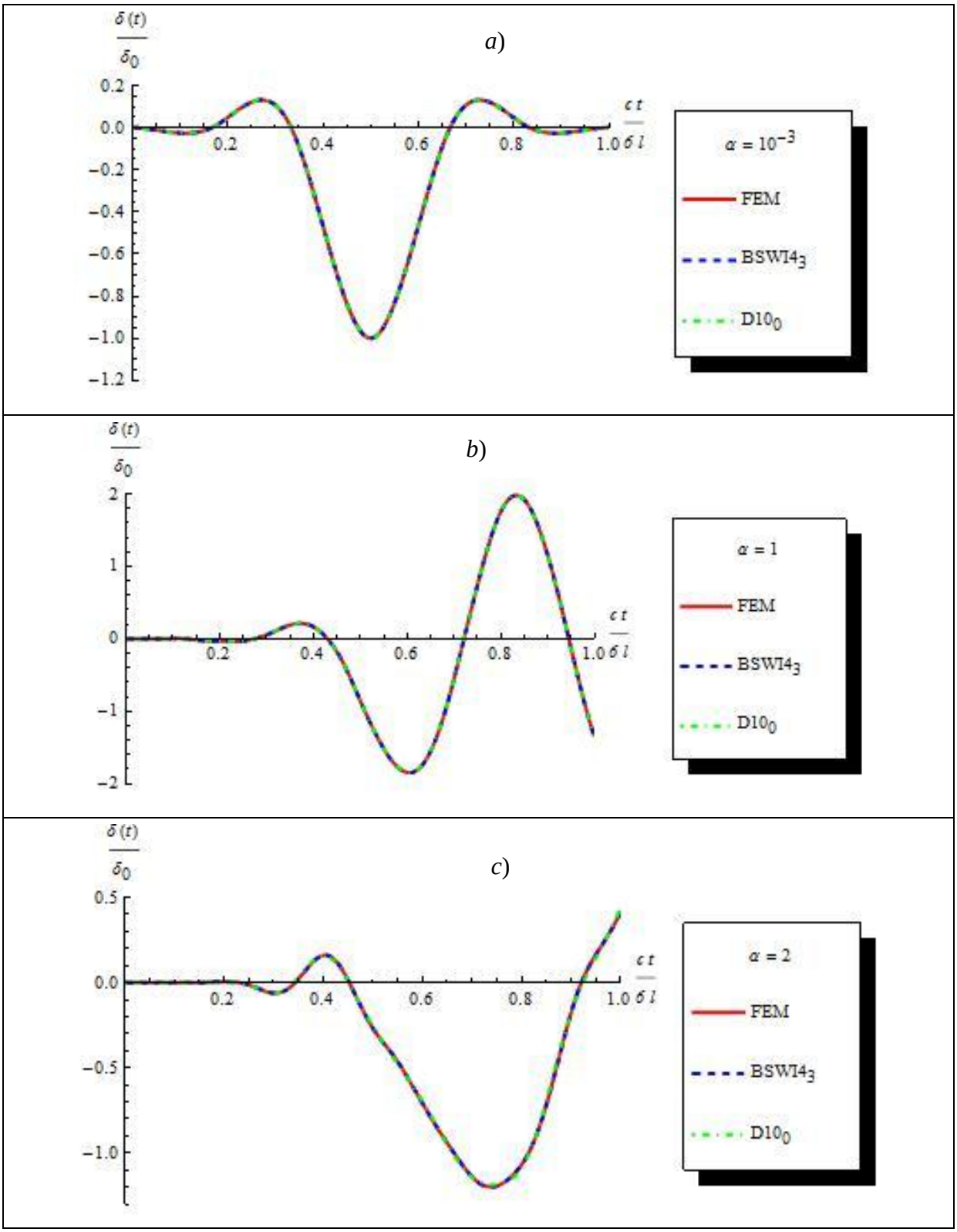

Figure 7-17: The normalized lateral displacement of the frame at point A as a moving point load travels at *a*) subcritical, *b*) critical and *c*) supercritical velocities.

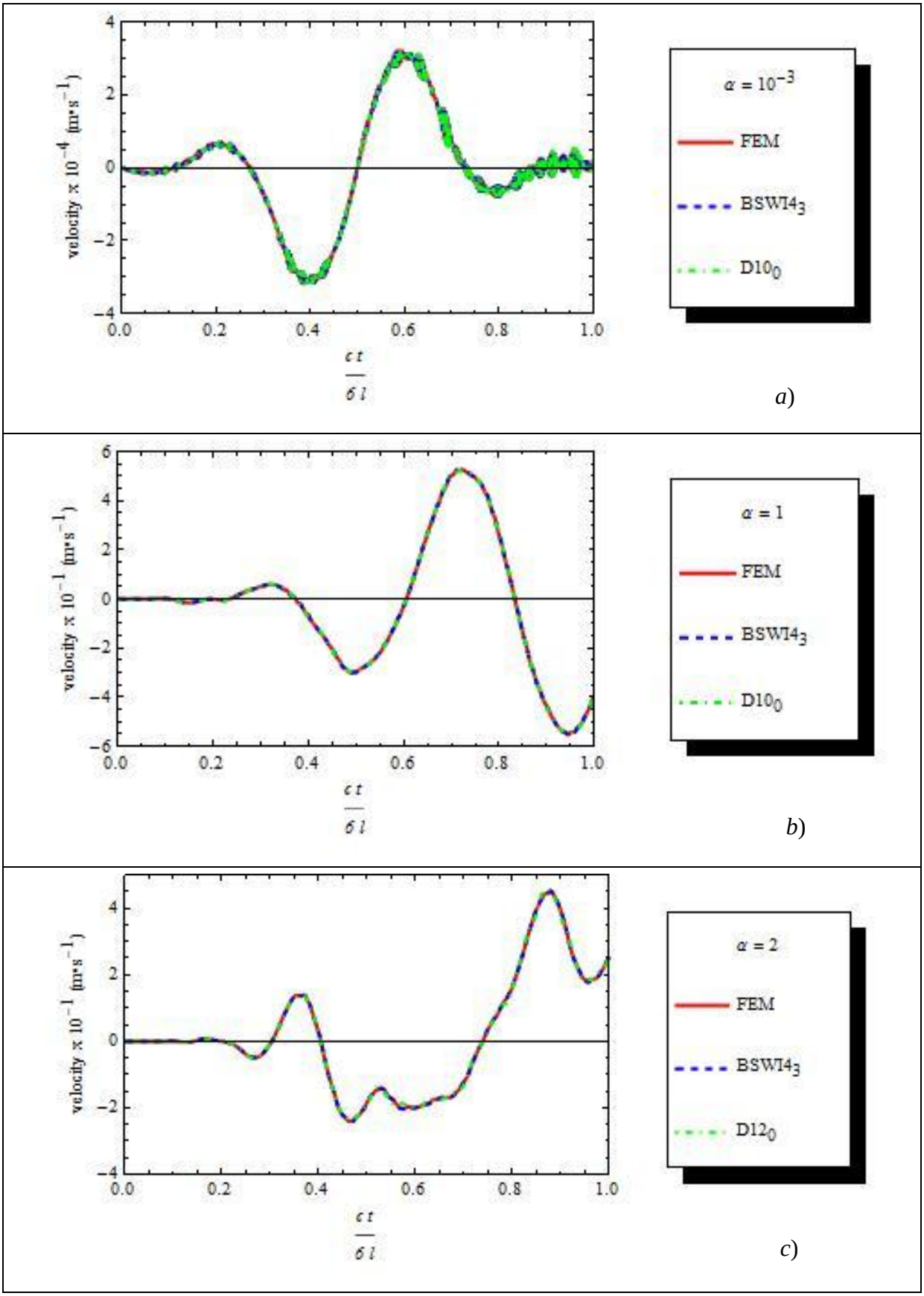

Figure 7-18: The variation of lateral velocities of the frame at point A as a moving point load travels at *a*) subcritical, *b*) critical and *c*) supercritical velocities.

According to the results presented in Figure 7-17 *a*), the maximum normalized lateral deflection at point A is 1 and occurs when the moving load is at point A. This is due to the fact that $\alpha_s \ll 1$ and the deflection is similar to that of the frame under a static load P at point A. However, when the speed of the moving point load is increased, the maximum normalized deflection occurs once the moving load has travelled past point A. When $\alpha_s = 1$, the maximum normalised lateral deflection at point A is almost double the static deflection δ_0; from Figure 7-17 *b*). When $\alpha_s = 2$, $\frac{\delta(t)}{\delta_0}$ is maximum after the moving load departs A.

The lateral velocity at point A, as the moving load moves over the frame, is presented in Figure 7-18 for the 3 speed profiles of the moving load. The WFEMs and FEM solutions approximate the velocity of the frame, for all speed profiles, very similarly. However, for the Daubechies WFEM solution, the order of the WFE is increased so as to better approximate the lateral velocity of the frame for $\alpha_s = 2$. In this case the order is increased from D10_0 (subcritical and critical speeds), to the D12_0 WFEs for the supercritical speeds.

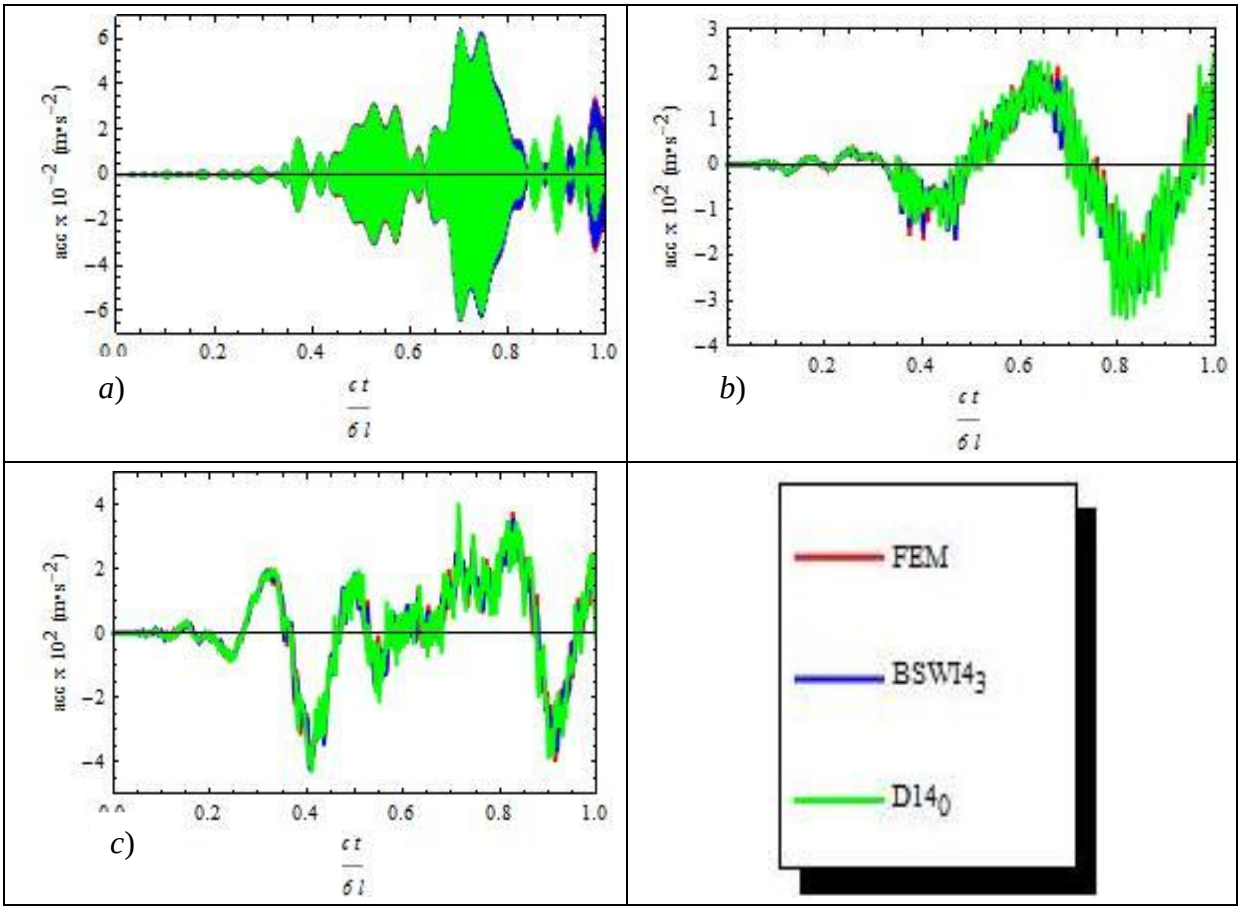

Figure 7-19: The lateral acceleration of the frame at point A as a moving point load travels on the frame at *a*) subcritical, *b*) critical and *c*) supercritical velocities.

This is also evident from Figure 7-19 where the Daubechies D14_0 WFEs are used to obtain solutions for the lateral acceleration of the frame at point A so as to improve on the accuracy

of the results. This implies that, although the deflection of a given dynamic system may be accurately approximated via a certain order of the Daubechies wavelet formulation, it may be necessary to increase the order so as to improve the approximation of the velocity and acceleration solutions.

The BSWI WFEM solution on the other hand, is in very good agreement with the classical FEM solution without alterations in scale and/or order of the wavelet based element. This implies that the BSWI wavelet based finite element formulations are better suited to the Daubechies based WFEM for the general dynamic analysis of structures.

7.3. Beam on viscoelastic foundation subjected to a moving load

The moving load problem presented in Section 7.1 involves the dynamic response analysis of a bridge as a locomotive travels across the span of the bridge, commonly referred to as vehicle-bridge interaction. Another important category of the moving load problem researched on and presented in this section is train-track interaction. This area of study is of great importance and interest for high-speed rail transportation to monitor and investigate the dynamic response of the rail system as the train/locomotive travels across the track [107,109,110]. Significant displacements, particularly in the lateral upward direction are a contributing factor in the weakening and degradation of railway track systems.

The track comprises of the rails resting on sleepers, ballast, sub-ballast, subgrade and soil. The complexity of mathematical model describing the behaviour of the system varies based on the assumptions made. Furthermore, the approach of analysis also varies based on the simplification of the system via the made assumptions and it is common to find that analytical or semi-analytical approaches are preferred in the analysis of simplified models. However, for more complicated models numerical approaches such as WFEM and FEM are preferred to accurately approximate the dynamics response of such systems when subjected to a moving load.

In this example, the track system is simplified into a beam resting on a viscoelastic foundation represented by a series of elastic springs and dashpots as illustrated in Figure 5-9. The beam represents a UIC60 standard type rail [109,110], while the viscoelastic foundation represents the sleepers, ballast, sub-ballast, subgrade and soil.

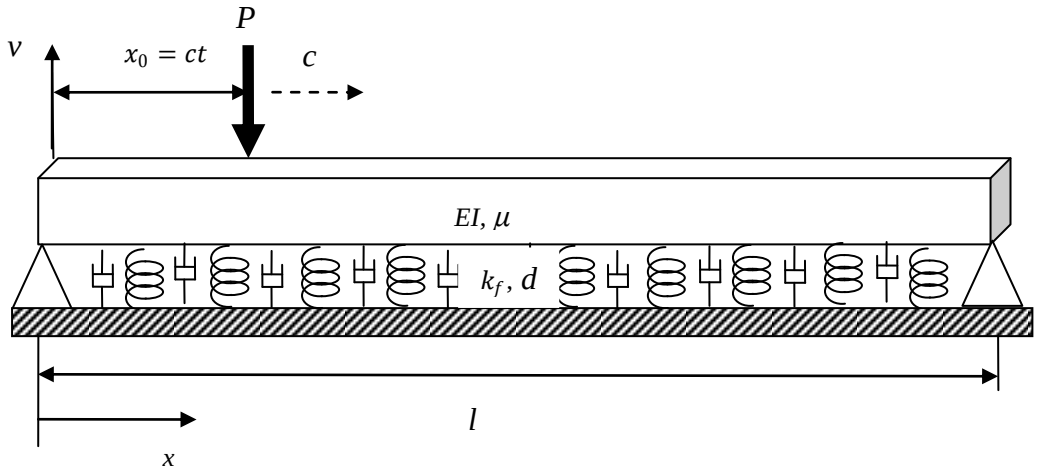

Figure 7-20: Simply supported uniform beam on a viscoelastic foundation subjected to a moving load point load.

Dimitrovova and Rodrigues **[**109**]** analysed the critical velocity of moving loads applied on beams resting on a viscoelastic foundation, comparing results obtained via a finite and a corresponding infinite beam. The results revealed that the extreme displacements increased gradually for the finite beam, in contrast to the significantly sharp increases exhibited by the infinite beam responses for a soft foundation. Furthermore, the reflections from the supports were significant and could therefore not be ignored for the finite beam case. However, for this example, the foundation is of significant stiffness and the dynamic response of the infinite beam model can be approximated using a long simply supported beam of finite length $l = 200$ m. The beam is sufficiently long enough to accurately obtain the dynamic response of the system since the effect of the moving load is localised.

The behaviour of the elastic beam is described based on the Euler-Bernoulli beam theory. The cross-sectional area, $A = 7.684 \text{ x } 10^{-3}$ m^2, is assumed to be uniform along the length of the beam. The beam has the following material properties: Young's modulus $E = 2.1 \text{ x } 10^{11}$ Pa and moment of inertia $I = 3.055 \text{ x } 10^{-5}$ m^4. The elastic stiffness of the foundation is $k_f = 3.416 \text{ x } 10^6$ N·m^{-2}.

In this analysis, the Thalys high speed train locomotive travels over the track at c m·s^{-1} and has a total axle mass of $1.7 \text{ x } 10^4$ kg. The locomotive is assumed to be of a significantly shorter span with respect to the length of the rail system and is represented by a moving point load to aid in the calculations of the system. The moving point load $P = 8.34 \text{ x } 10^4$ N acts on each of the rails with the assumption that its weight is equally supported by the two rails. The analysis is of an individual rail represented by a beam assumed to rest on the foundation. For

a beam resting on an elastic Winkler foundation, with the system undamped, the critical velocity of the moving load can be obtained analytically for an infinite beam as [102]:

$$c_{cr} = \sqrt[4]{\frac{4k_f EI}{\mu^2}} \tag{7.10}$$

where EI is the bending rigidity and μ is the mass per unit length of the beam. The non-dimensional moving load velocity parameter is defined as $\alpha_s = \frac{c}{c_{cr}}$. The critical velocity of the system can be obtained as [111]:

$$c_{cr} = \frac{l}{j_{cr}\pi}\sqrt{\left(\frac{j_{cr}\pi}{l}\right)^4 \frac{EI}{\mu} + \frac{k_f}{\mu}} \tag{7.11}$$

where $j_{cr} = \frac{l}{\pi}\sqrt[4]{\frac{k_f}{EI}}$ is the critical mode of vibration corresponding to the lowest resonant velocity and is rounded off to the nearest integer. The critical velocity of the finite beam is obtained as 395.26 m·s^{-1}, with the 54th mode of vibration being critical. The critical velocity obtained via equation (7.10) for an infinite beam is 395.24 m·s^{-1}. The critical velocity obtain via the finite beam formulation is 0.00253% higher than the infinite beam formulation. In this analysis, 3 moving load velocities are taken into consideration i.e.: 80 m·s^{-1} (subcritical), 395.26 m·s^{-1} (critical) and 500 m·s^{-1} (supercritical). It is worth mentioning that the critical and supercritical velocities are currently impractical and significantly higher than current maximum operating speeds for high-speed railway travel. These velocities are taken into account for theoretical purposes to investigate the dynamic response analysis of the presented system using WFEM.

When taking damping into consideration, it is assumed that the critical damping for the finite beam is approximated similar to an infinite beam and is expressed as [112]:

$$d_{cr} = 2\sqrt{k_f \mu} \tag{7.12}$$

The viscous damping coefficient of the foundation is evaluated as $d = \zeta d_{cr}$, with ζ being the damping ratio. The dynamic behaviour of the system is described by the governing equation [29,113]:

$$[\boldsymbol{M_b}]\{\ddot{\boldsymbol{V}}_{\boldsymbol{b}}(t)\} + [\boldsymbol{C_f}]\{\dot{\boldsymbol{V}}_{\boldsymbol{b}}(t)\} + ([\boldsymbol{K_b}] + [\boldsymbol{K_f}])\{\boldsymbol{V_b}(t)\} = \{\boldsymbol{F_b}(t)\} \tag{7.13}$$

where $[\boldsymbol{M_b}]$ is the global mass matrix of the beam, $[\boldsymbol{K_b}]$ is the global stiffness matrix of the beam, $[\boldsymbol{C_f}]$ is the damping matrix of the foundation, $[\boldsymbol{K_f}]$ is the global stiffness matrix of the foundation and the vector $\{\boldsymbol{F_b}(t)\}$ is the time-dependent load vector. The element and foundation matrices, as well as the moving load vector, are described in Section 5.2. The system DOFs, velocities and accelerations at time *t* are contained in the vectors $\{\boldsymbol{V_b}(t)\}$, $\{\dot{\boldsymbol{V}}_{\boldsymbol{b}}(t)\}$ and $\{\ddot{\boldsymbol{V}}_{\boldsymbol{b}}(t)\}$ respectively.

The dynamic response of the described system is carried and compared for 6 BSWI beam WFEs, 14 Daubechies WFEs and 150 classical finite elements used to model the beam. Furthermore, the dynamic analysis is carried out using the Newmark time integration method with the time step Δt selected in correlation with each moving load velocity i.e., 4.3 x 10^{-4} s, 8.7 x 10^{-5} s and 6.9 x 10^{-5} s for subcritical, critical and supercritical moving load velocities respectively. These values ensure that the analysis is carried out efficiently and accurately while maintaining the stability of the Newmark method for each moving load velocity. Moreover, for the FEM analysis, the time steps ensure that the effect of the moving load is subjected to each element at least once during the analysis.

The beam is simply supported at both ends and since the beam material and foundation properties are uniform across the length of the beam, the maximum deflection will occur at the centre of the beam. Hence, the analysis of the dynamic response is carried out at the location $x = \frac{l}{2}$. The vertical displacement at this location is analysed as the moving load travels across the finite beam on an elastic foundation (no damping), at subcritical, critical and supercritical velocities *a*) 80 m·s^{-1}, *b*) 395.26 m·s^{-1} and *c*) 500 m·s^{-1} respectively (Figure 7-21).

In Figure 7-21 *a*), a subcritical moving point load travels across the beam and the displacement at the centre of the beam is observed to be symmetric since there is no damping present within the system. However, when the moving load travels at a critical velocity (Figure 7-21 *b*)), the beam is excited and begins to oscillate. The dynamic response has a harmonic characteristic, and the amplitude of the deflection increases gradually in magnitude until the load just leaves the centre of the beam. When the load just departs from the centre of the beam, the upward and downward deflections are at maximum. As the moving load travels away from the mid-point of the beam, the amplitude of the oscillations begin to decrease, but the beam does not come to rest by the time the moving load departs from the system.

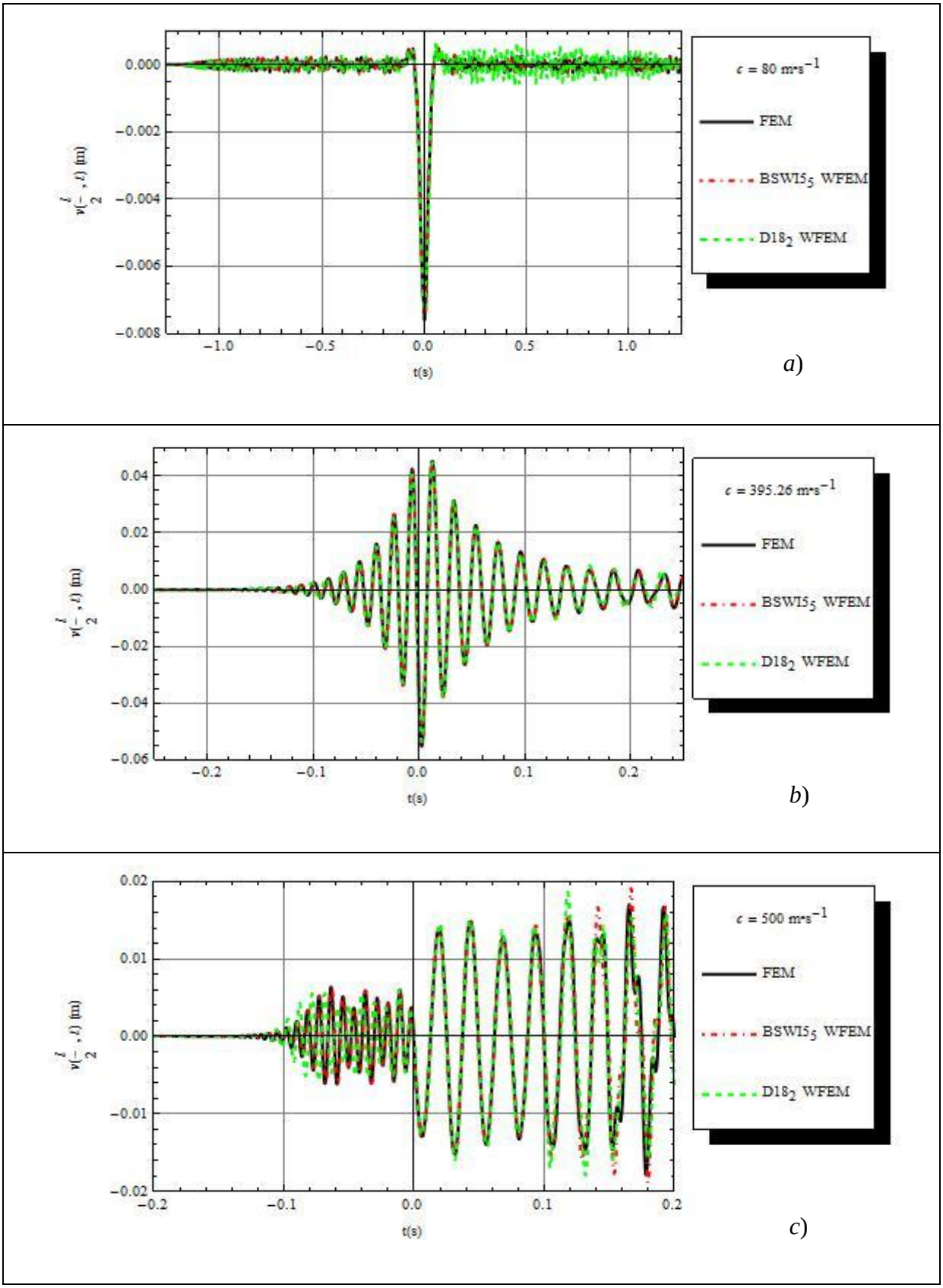

Figure 7-21: The vertical displacement at the centre of a simply supported beam on an elastic foundation (no damping) subjected to a moving point load travelling at *a*) 80 m·s^{-1} *b*) 395.26 m·s^{-1} and *c*) 500 m·s^{-1}.

In Figure 7-21 *c*), the beam is initially stationary but begins to rapidly vibrate as the moving load approaches the centre. When the moving load arrives at the centre of the beam, there is

an abrupt increase in the magnitude of the deflection amplitude. The deflection amplitude is maintained as the load leaves the centre, until it departs the beam. The maximum displacement value when the load travels at a critical velocity (55.13 mm) is significantly larger than that achieved at subcritical (7.57 mm) and supercritical (19.09 mm) velocities. The dynamic behaviour of the train-track system at critical velocities and the rapid rate of vibrations experienced at supercritical velocities are of great importance for predicting and identifying responses that may lead to the deterioration of the track system [109]. The analysis is also important to identify the nature of the response that may lead to wear, failure or in extreme cases derailment of the train.

The BSWI5_5 and D18_2 WFEM solutions are compared with the classical FEM solution. The approximations of the dynamic responses for the system are in excellent agreement with each other for the 3 different moving load velocity scenarios; as observed in Figure 7-21. Furthermore, only 6 BSWI5_5 and 14 D18_2 WFEs are implemented, in comparison to 150 classical finite elements. The WFEMs accurately approximate the maximum deflection at the mid-span as the load travels across the beam. This demonstrates that the WFEM can be implemented with significantly less number of elements in the analysis of such problems and achieve very high levels of accuracy in comparison to the classical FEM. The classical FEM would require a significant number of elements to accurately obtain the response of the system. The number of elements, and consequently the number of DOFs implemented in the analysis, is of importance in dynamic analysis, taking into account that the responses are evaluated at each time step.

The required number of time steps implemented to achieve stability and acceptable levels of accuracy may be large and this translates to high computational costs and time consumption. It is also worth mentioning that the BSWI5_5 WFEM results (206 DOFs, 6 elements) are considerably better than the D18_2 (254 DOFs, 14 elements) WFEM solution, with significantly less number of elements, and consequently DOFs. Therefore, these initial results suggest that the BSWI based WFEM is better suited to analyse train-track interaction than the Daubechies based WFEM. This is commented on further towards the end of this section.

The variations of the lateral velocity at the centre of the beam, for the 3 moving load velocity profiles, are presented in Figure 7-22. The results show the BSWI5_5 WFEM solution is in very good agreement with the FEM solution. However, the Daubechies D18_2 solution is not as highly accurate in comparison to the other solutions, particularly after the moving load departs from the centre of the beam for the subcritical case. Nevertheless, the results of the

Daubechies based WFEM for the moving load travelling at critical and supercritical velocities are approximated quite well.

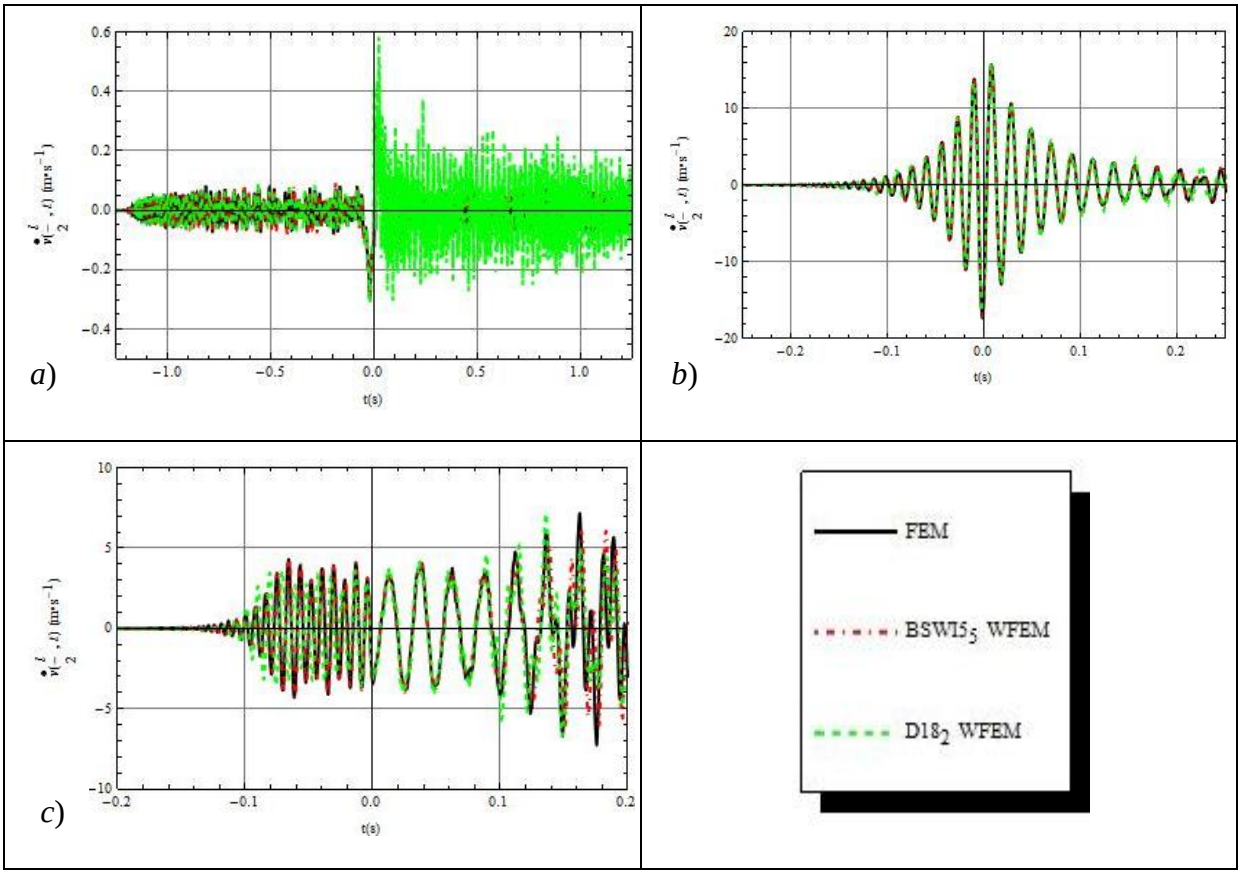

Figure 7-22: The vertical velocity at the centre of a simply supported beam on an elastic foundation (no damping) subjected to a moving point load travelling at *a*) 80 m·s^{-1} *b*) 395.26 m·s^{-1} and *c*) 500 m·s^{-1}.

The effect of increasing the *a*) order and *b*) multiresolution of the Daubechies based WFE on the solution of the vertical displacement is illustrated in Figure 7-23. The beam is resting on a viscoelastic foundation (5% damping) and the moving load is travelling at 395.26 m·s^{-1}. In Figure 7-23 *a*), it is observed that the D10_0 WFEM solution does not accurately describe the dynamic response of the beam. However, increasing the order to D14_0 improves the approximation of the solution considerably, although the response still differs from the correct solution. Increasing the order further to D18_0 leads to a very good approximation of the solution. Likewise, increasing the multiresolution scale j from 0 to 2 for the D*14* WFEM solution slightly improves the results as observed in Figure 7-23 *b*); but not as notably as increasing the order of the wavelet family.

It was also observed while carrying out the analysis that for majority of the Daubechies based wavelet finite element formulations of varying orders, the approximation of the response diverged significantly for multiresolution scale $j \geq 3$. The inaccuracies of the approximations are attributed to the numerical instability and errors that arise when evaluating the elemental

and foundation matrices in wavelet space for higher values of j. Although the Daubechies approach slightly converges for lower values of j, it is better to increase the order of the WFEs so as to improve the accuracy of the results. Increasing the order alone may not lead to the desired levels of accuracy since only the Daubechies wavelet finite elements of order D*10*, D*12*, D*14*, D*16* and D*18* at multiresolution scale $0 \leq j \leq 2$ can be implemented for dynamic analysis of beam elements. Thus, increasing the number of wavelet based elements may be necessary, as is the case in this example, where more Daubechies WFEs (14 WFEs) are required to accurately solve the dynamic response compared to the 6 BSWI WFEs.

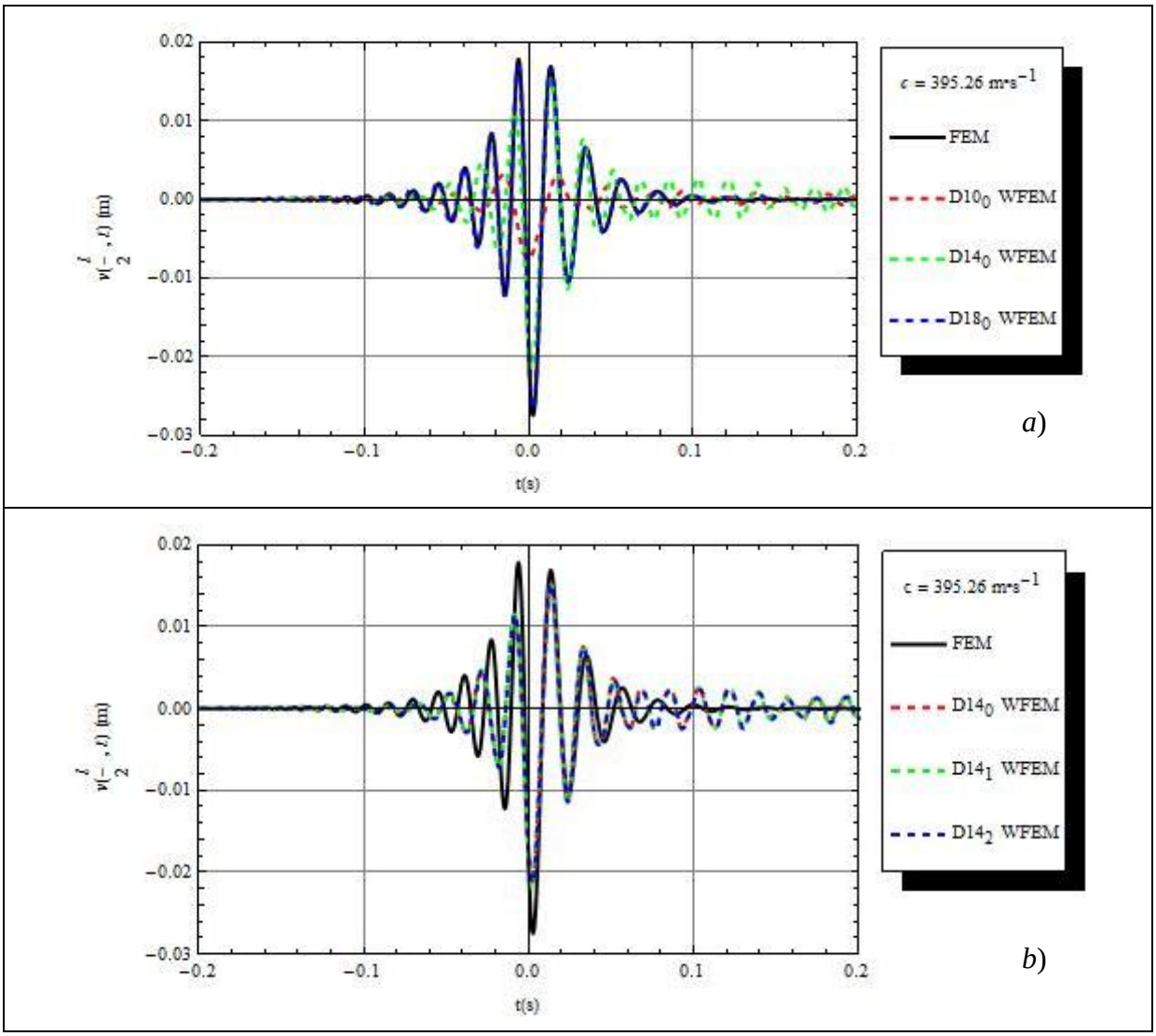

Figure 7-23: The vertical displacement at the centre of a simply supported beam on a viscoelastic (5% damping) foundation subjected to a moving point load travelling at 395.26 m·s^{-1} (Daubechies WFEM).

A similar investigation is carried out for the BSWI WFEM and the results are presented in Figure 7-24. From Figure 7-24 *a*) it is observed that the BSWI3_4 WFE solution does not accurately describe the response of the beam as the moving load travels across at critical velocity. The BSWI4_4 solution leads to a better approximation, which is further improved by

increasing the order of the WFEs to BSWI5_4. Consequently, increasing the order of the BSWI based WFEs better approximates the dynamic response of the beam; the approximate solution converges to the exact solution.

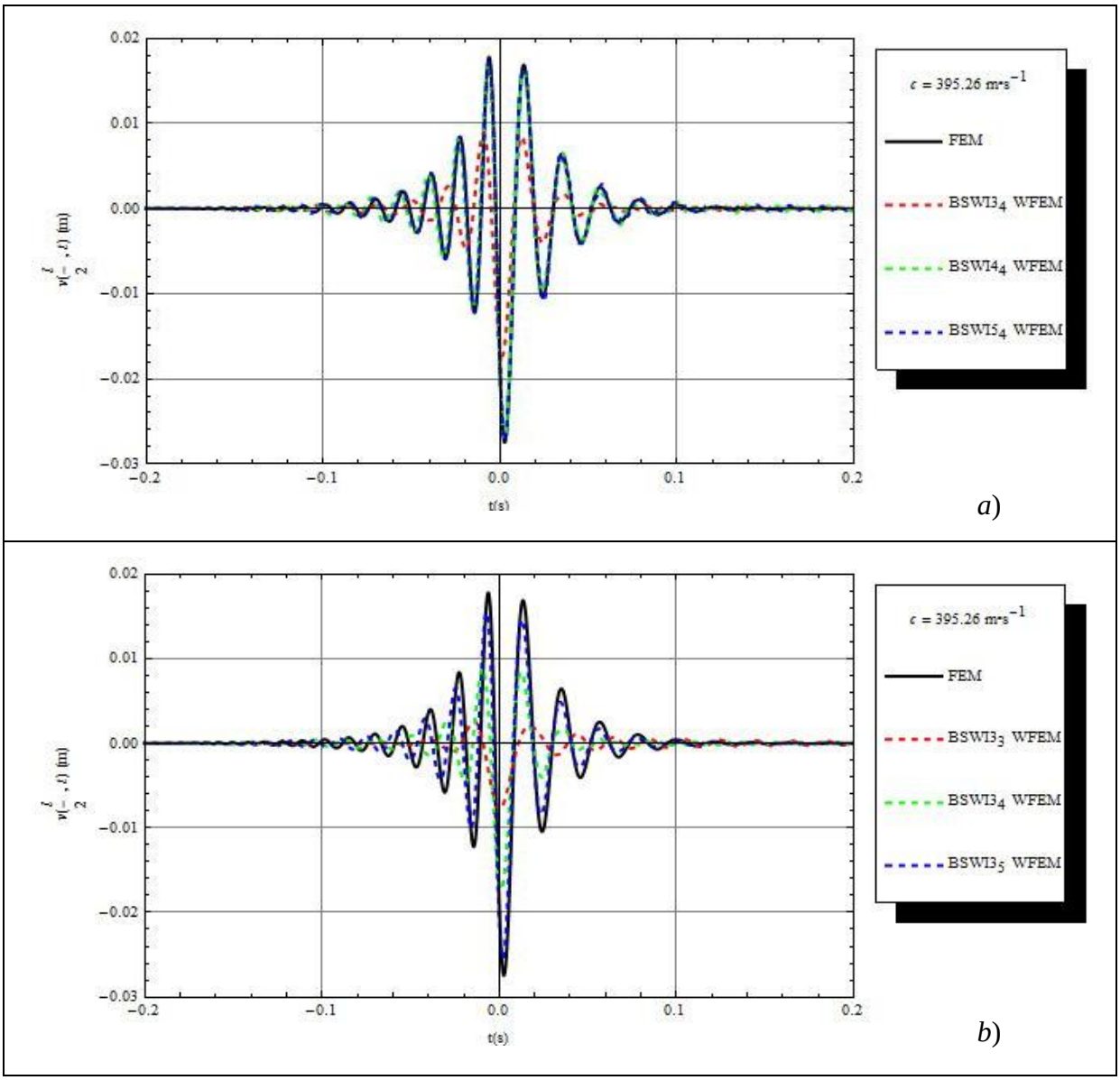

Figure 7-24: The vertical displacement at the centre of a simply supported beam on a viscoelastic foundation (5% damping) subjected to a moving point load travelling at 395.26 m·s^{-1} (BSWI WFEM).

In Figure 7-24 *b*), the multiresolution scale j $(3 \leq j \leq 5)$ is varied for the BSWI3_j WFEM formulation. It is observed that for the lower order BSWI based WFE formulations, increasing the multiresolution scales significantly improves the results. It is also noted that although the results of the BSWI3_5 WFEM formulation improve the approximation of the response, the solution is not precise. The multiresolution scale can be further increased but this leads to a considerable increase in computational costs.

In general, increasing the scale of a wavelet based beam element from j to $j+1$, for either Daubechies or BSWI WFEs, increases the number of corresponding DOFs for each element by 2^j. However, for a BSWI wavelet based beam finite element, increasing the order from m to $m+1$ only increases the number of DOFs per WFE by 1. Increasing the order of the Daubechies WFE from L to $L+2$ only increases the number of DOFs per WFE by 2. In order to effectively and efficiently improve the accuracy of the solutions for dynamic analysis, it is better to use higher order wavelet elements and then refine the solutions by increasing the multiresolution scale.

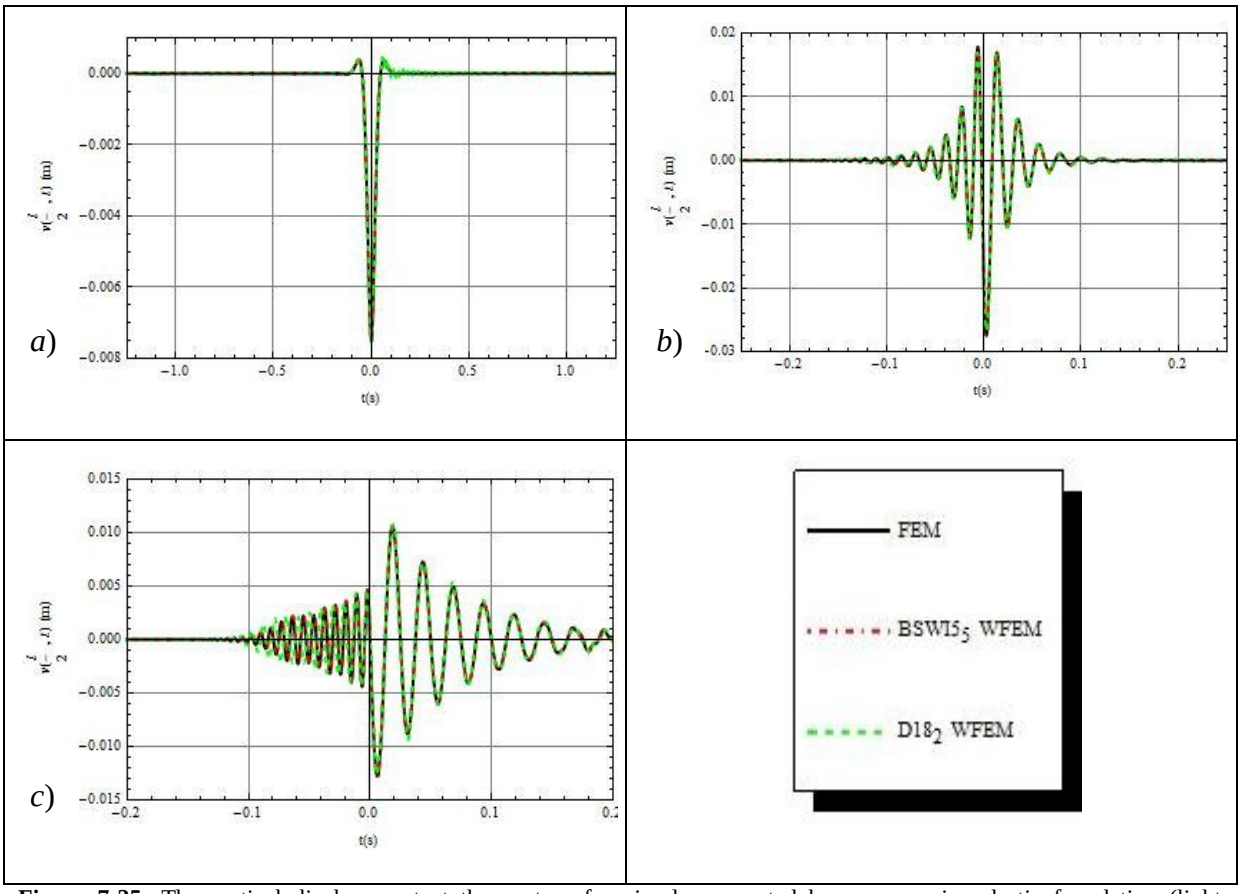

Figure 7-25: The vertical displacement at the centre of a simply supported beam on a viscoelastic foundation (light damping) subjected to a moving point load travelling at *a*) 80 m·s^{-1} *b*) 395.26 m·s^{-1} and *c*) 500 m·s^{-1}.

The variation of the deflection of the simply supported beam, resting on a viscoelastic foundation with 5% global damping, is presented in Figure 7-25. The damping value of 5% is a more practical and realistic value. It is therefore implemented in the analysis since the effects of slight damping are easily observed and it is close to the damping range of 1-3% for geomaterials [109]. The analysis of the dynamic response is extended for critical and supercritical damping values 100% and 200% respectively, for theoretical purposes.

The analysis is carried out using the BSWI5_5 WFEs, D18_2 WFEs and 150 classical FEs, for the moving load velocities *a*) 80 m·s^{-1}, *b*) 395.26 m·s^{-1} and *c*) 500 m·s^{-1}. In general, the results presented demonstrate that both WFEM solutions are in very good agreement with the FEM solution for the different velocity profiles.

In the analysis of the displacement for the subcritical moving point load (Figure 7-25 *a*)), the introduction of the light damping factor has smoothened out the low amplitude vibrations that were present in Figure 7-21 *a*) (elastic foundation). The centre of the beam virtually remains static until the moving load almost reaches the mid-span of the beam. Furthermore, the deflection curve is slightly asymmetrical with light damping and the maximum deflection at $\frac{l}{2}$ slightly decreases in comparison to the elastic foundation results.

When the moving load travels at a critical velocity as presented in Figure 7-25 *b*), the deflection at mid-span of the beam is initially negligible. The beam is excited and the amplitude of the vibration gradually increases in magnitude as the moving load advances towards the centre of the beam. The beam oscillations are fewer than in the case with no damping and rapidly decrease as the moving load departs the centre of the beam; the centre of the beam coming to a rest before the moving load departs from the beam. This is in contrast to the elastic case from Figure 7-21 *b*) where the centre of the beam is still oscillating after the moving load has departed from the beam. Moreover, the magnitude of the maximum deflection with light damping is approximately half that of the elastic foundation case (Figure 7-21 *b*)). Therefore, the light damping has a significant effect on the dynamic response of a beam when the moving load travels at critical velocities.

In Figure 7-25 *c*), the analysis of the lightly damped viscoealstic foundation is carried out at a supercritical velocity of 500m·s^{-1}. In comparison to the response of the elastic foundation at a similar moving load velocity, as presented in Figure 7-21 *c*), the beam gradually gets excited until the moving load arrives at the centre. At this time, the displacement increases abruptly, then gradually decreases in magnitude and rate of vibration as the moving load leaves the beam. The maximum deflection at the centre of the beam slightly decreases when damping is introduced. This implies that the effect of damping is more significant on the magnitude of the maximum deflection when the moving load is travelling at/or close to the critical velocity than at subcritical or supercritical velocities.

An analysis on computational cost is also carried out to investigate the performance of each approach based on the time taken to evaluate the dynamic response of the system. It must be

noted that the computer algorithms, written to carry out the simulations by the author, were not primarily focused on optimizing the efficiency of the different approaches. Furthermore, the manner in which certain sections of the algorithms were implemented varied for the different approaches. Therefore, the computational time was only analysed for sections of the algorithms that were similar for all approaches. The vital sections taken into account included: assembly of the stiffness, mass and damping matrices for the beam elements and viscoelastic foundation, evaluation of the moving load vectors at each time step, application of boundary conditions on the system matrices and load vectors and the implementation of the Newmark time integration method to obtain the dynamic response of the system. The WFE matrices were already evaluated in wavelet space, transformed into physical space and then stored. This was carried out to improve on the computational efficiency and reduce the computational costs when evaluating the system matrices. The moving load section taken into account in the analysis involved obtaining the force vectors in wavelet space at each time step and transforming them into physical space. The FEM matrices were calculated and stored; though the evaluation of the force vectors at each time step was taken into consideration.

The analysis of the computational efficiency was carried out for the case of the beam resting on the viscoelastic foundation (5% damping); subjected to a moving point load travelling at a constant velocity of 395.26 $m \cdot s^{-1}$. The time required to carry out the analysis via the FEM (302 DOFs, 150 elements), D18_2 WFEM (254 DOFs, 14 elements) and BSWI5_5 WFEM (206 DOFs, 6 elements) was 38.937 s, 30.624 s and 21.044 s respectively. The BSWI5_5 WFEM solution was obtained by taking 68.72% and 54.05% of the time taken by the Daubechies D18_2 WFEM and FEM approaches respectively. The Daubechies WFEM took 78.65% of the time it took the FEM to attain the solution. This therefore confirms that the BSWI WFEM is significantly more computationally efficient and highly accurate than the other approaches. The Daubechies WFEM also has a better performance than the FEM. The simulations were carried out using Mathematica version 7 on a Pentium (R) Dual core CPU with: 4GB RAM, 64 bit Operating System, 2.10 GHz running on Windows 8.

The deflection at the centre of the beam is analysed for the critical damped system for the 3 velocity profiles. The results are presented in Figure 7-26. The maximum deflection for the 3 moving load velocity profiles are 7.23 mm (subcritical), 4.95 mm (critical) and 4.13 mm (supercritical). It is observed from these results that when the system is critically damped, the maximum deflection at mid-span of the beam occurs for the subcritical moving load velocity and continues to decrease as the velocity of the moving load increases. From the results

presented in Figure 7-26 *a*) it is also observed that the response, for critical damping at subcritical velocity, is more asymmetric and the maximum beam deflection slightly reduces as the damping factor is increased.

When the moving load velocity is critical (395.26 m·s^{-1}), it is observed from Figure 7-26 *b*) that the effect of critical damping results in a significant decrease in maximum deflection (4.95 mm); in comparison to results obtain for no damping (55.13 mm) and light damping (27.50 mm) from Figure 7-21 *a*) and Figure 7-25 *b*) respectively.

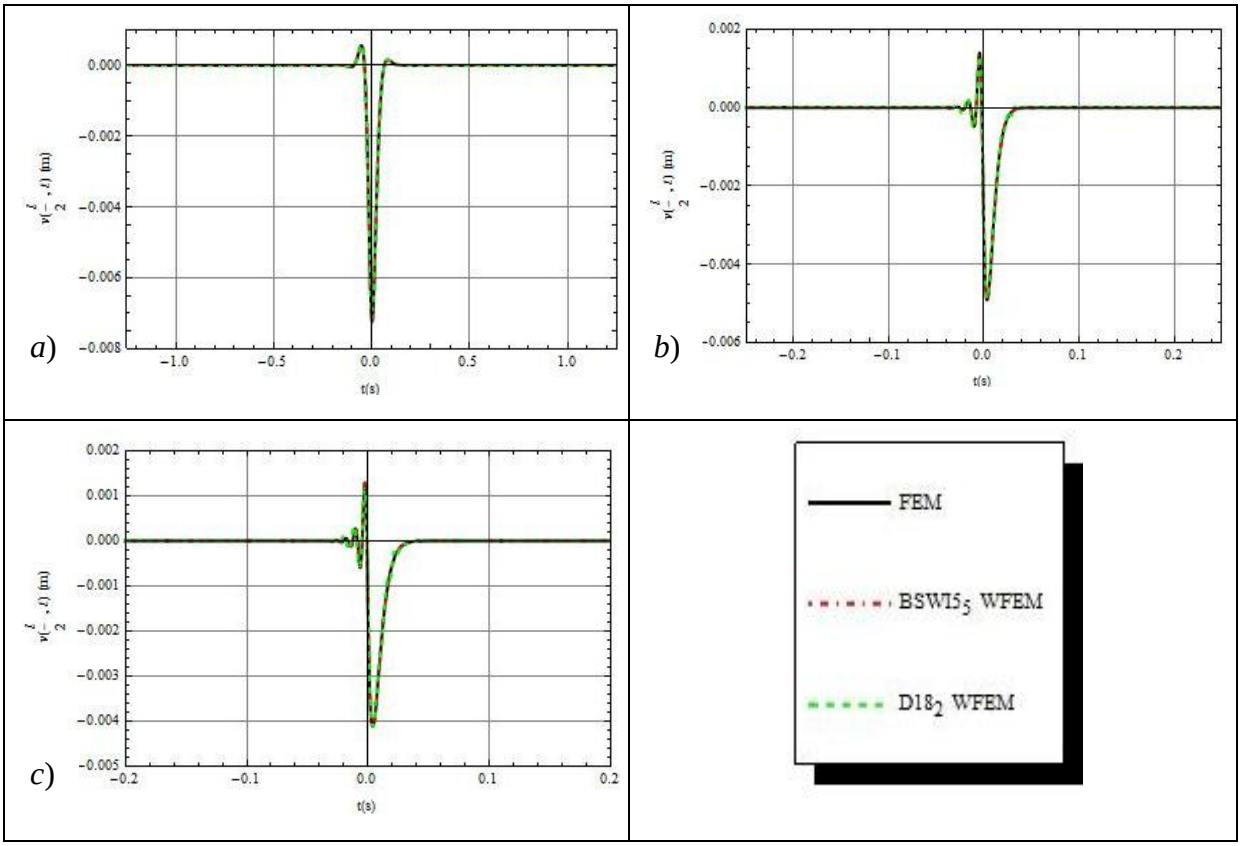

Figure 7-26: The vertical displacement at the centre of a simply supported beam on a viscoelastic foundation (critical damping) subjected to a moving point load travelling at *a*) 80 m·s^{-1} *b*) 395.26 m·s^{-1} and *c*) 500 m·s^{-1}.

The effect of the moving load on the mid-span displacement is also more localised when the damping is critical. Furthermore, there is a very small but rapid harmonic component in the deflection variation as the moving load almost arrives at the centre of the beam. The maximum deflection is observed to occur just after the moving load passes the centre of the beam. Moreover, the beam comes to rest without any harmonic component as the moving load departs. Similar observations are also noticed in the displacement variation when the moving load is travelling at supercritical velocity from Figure 7-26 *c*). The results obtained via the BSWI5_5 and D18_2 WFEs are in excellent agreement with the FEM solution and achieve high levels of accuracy.

Figure 7-27 illustrates the deflection at the centre of the beam when supercritical (200%) damping is applied for the 3 velocity profiles. It is observed that a further increase in damping reduces the maximum deflection to 6.54 mm (subcritical), 2.93mm (critical) and 2.41mm (supercritical). The maximum displacement at the centre of the beam also occurs when the moving load is travelling at subcritical velocity 80 m·s^{-1}. Furthermore, the beam takes a bit longer to come to rest once maximum displacement is achieved; just after the moving load passes the centre of the beam.

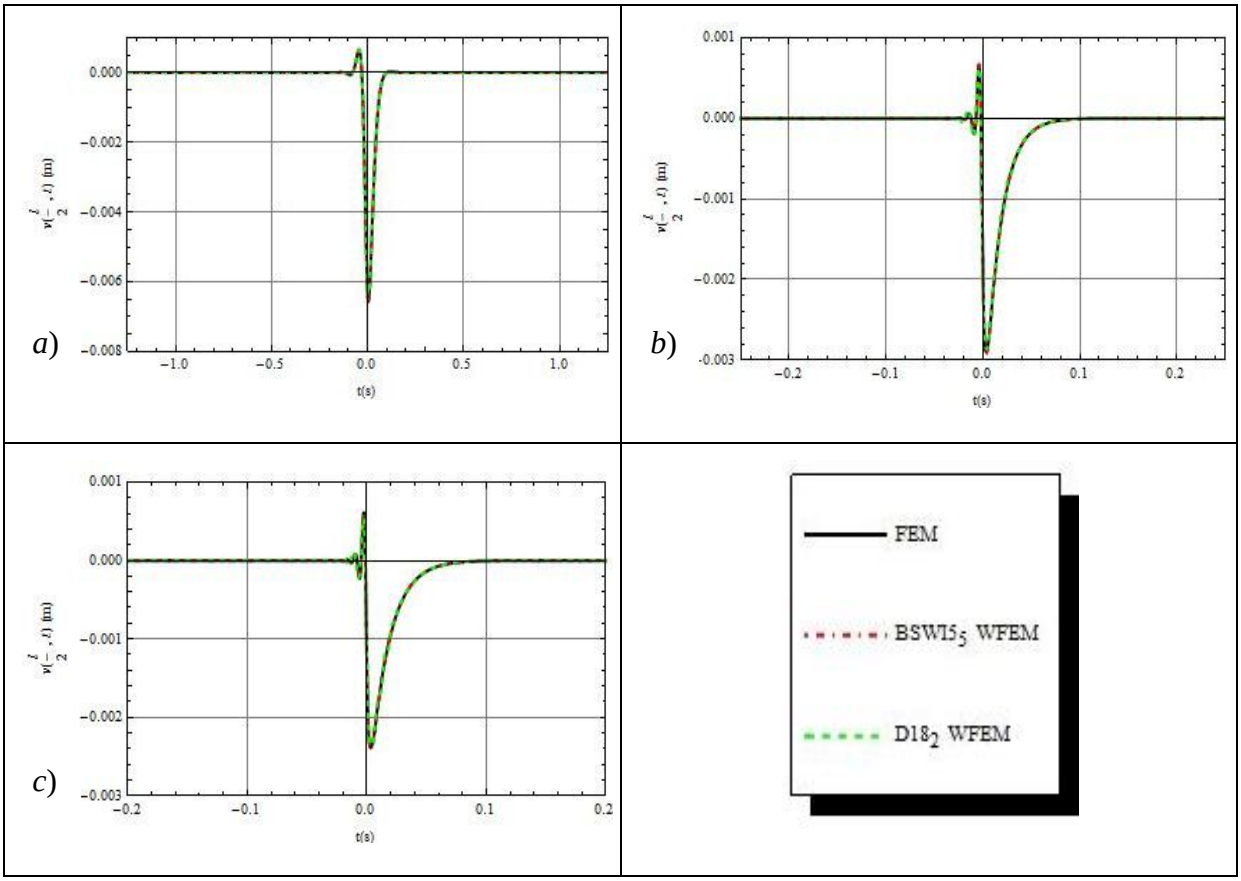

Figure 7-27: The vertical displacement at the centre of a simply supported beam on a viscoelastic foundation (supercritical damping) subjected to a moving point load travelling at *a*) 80 m·s^{-1} *b*) 395.26 m·s^{-1} and *c*) 500 m·s^{-1}.

It is evident from Figure 7-25 that the light damping of the system leads to a slight decrease in the magnitude of the maximum displacement for the 3 different moving load velocity cases. The displacement at the centre of the beam is at its maximum when the moving load is travelling at a critical velocity due to the excitation of the beam at that velocity; as is the case when the system is not damped. However, when the system is critically or supercritcally damped, the effect of damping is more significant on the maximum displacement for the critical and supercritical velocities than for the subcritical velocity, as illustrated in Figure 7-26 and Figure 7-27. Thus, the focus of the maximum deflection at mid-span of the beam shifts from the analysis of the moving load at critical and supercritical velocities to subcritical

velocities. This is because the maximum deflection is observed to be achieved when the moving load is travelling at the subcritical velocity. Furthermore, as the velocity of the moving load increases, the maximum deflection decreases for critical and supercritical damping of the system.

From the results presented in this section, the versatility and potential of both the wavelet based finite element methods is exhibited for the analysis of a finite beam on an elastic and viscoelastic foundation; for subcritical, critical and supercritical velocity and damping profiles. For moving load problems, such as the one presented in this section, the system requires large number of finite elements and time steps to accurately describe the dynamic response of the system, which is computationally demanding. However, the solutions obtained from both wavelet formulations give highly accurate results, with significantly fewer elements implemented in comparison to the classical FEM. Thus reducing the number of DOFs implemented in the analysis at each times step and decreasing the computational costs involved when implementing time integration. Furthermore, the BSWI WFEM achieves superior approximate solutions for the dynamic response in comparison to the Daubechies WFEM. This is achieved with significantly fewer elements implemented and the method is less computationally demanding. The BSWI WFEM is also not limited by numerical instabilities when higher order and/or multiresolution values are implemented since the scaling functions and their derivatives have a closed form solution. This is an added advantage of the BSWI based WFEM and it is therefore the preferred choice of wavelet based formulation to analyse train-track interaction and general structural dynamic problems.

7.4. Conclusions

The implementation of the Daubechies and BSWI based WFEMs in the analysis of moving load problems was presented in this chapter. The dynamic response analysis was carried out for three different moving load profiles via numerical examples that were of practical or theoretical importance. The accuracy and the performance of both the WFEMs for free vibration and moving load analysis were discussed and compared with the classical FEM, and in some cases, analytical solutions.

Analytical and semi-analytical solutions have been carried out and presented in literature to solve various moving load problems. However, these formulations are specific to certain systems or various assumptions are carried out to simplify the mathematical models, which

may lead to inaccurate results. The more complicated systems require numerical methods, such as FEM and WFEM, to analyse and solve for the dynamic response of the systems.

The results presented showed that the wavelet finite element methods approximated the dynamic response of systems very accurately, particularly in the analysis of moving load problems. Furthermore, the solutions obtained via the WFEMs were achieved with significantly fewer elements and consequently, less number of DOFs. The computational costs were not only related to the DOFs required to achieve the desired levels of accuracy but it was also shown in Section 7.3 that the WFEM solutions were obtained faster than the FEM solutions. This was due to the main properties of the wavelet families implemented, such as compact support, multiresolution analysis and vanishing moments, which allow for an accurate approximation of the field variables.

The impact of implementing fewer elements in the analysis was far greater in the dynamic analysis of systems rather than static cases, particularly for the identification and evaluation of the moving load critical velocities. This was because the system matrices and loading vectors were analysed at each time step to approximate the dynamic response of the system over a period of time. Larger dimensions of the elemental matrices and load vectors required additional computational and time resources to accurately describe the dynamic behaviour of the system. The results also illustrated that the accuracy of the WFEM solutions can be improved by increasing the order and/or multiresolution scale of the WFEs without altering the original system discretization.

When carrying out free vibration analysis, it was found that the BSWI WFEM natural frequency solutions were highly accurate and converged rapidly to the exact solution, particularly for higher modes of vibration as observed in Section 7.1 and Section 7.2. The BSWI WFEM solutions were also found to be of superior accuracy in comparison to both the classical FEM and Daubechies WFEM solutions, with fewer elements and DOFs applied. This was also the case in the analysis of the dynamic response for the systems presented in this chapter. The Daubechies WFEM accurately approximated the lower modes of vibration natural frequencies, but it was necessary to increase the order and/or scale to improve the accuracy of the higher mode natural frequencies.

In general, it was concluded that it is more efficient and effective to first increase the orders of the wavelet based finite elements, and then increase the multiresolution scales to improve the approximation of results when carrying out the dynamic analysis of systems via WFEM.

Increasing the order gives a better approximation of results, particularly for the Daubechies based WFEM.

The implementation of the Daubechies based WFEM is limited to the orders D*10*, D*12*, D*14*, D*16* and D*18* for the beam and planar bar WFEs as mentioned in Chapter 6. However, for the dynamic response of the systems presented, it was found that the solutions obtained when the multiresolution scale $j \geq 3$ were inaccurate and diverged from the exact solution. This was due to the numerical errors and numerical instabilities that arise when evaluating the connection coefficients of the Daubechies wavelet, particularly for higher multiresolution scales. This is a key limitation of the Daubechies WFEM.

Furthermore, it was also concluded from the results that the Daubechies WFEM may require the implementation of a higher order/and or multiresolution scale to accurately describe the velocity and acceleration responses than that used to obtain the lateral displacement of a moving load system; this was particularly observed from the results in Section 7.1 and Section 7.2.

The BSWI based WFEM does not have the limitations of numerical instability or significant numerical errors since the scaling functions and their derivatives have an explicit expression and does not require the evaluation of the connection coefficients. Furthermore, the results presented showed that the BSWI WFEM gave more accurate approximations of the natural frequencies and dynamic response descriptions, with fewer elements in comparison to the Daubechies WFEM solutions. The BSWI WFEM was also shown to be more efficient with regards to computational speed, as was discussed in Section 7.3. Therefore, it was concluded that in the evaluation of moving load problems, particularly those associated with vehicle-bridge and train-track interaction, the BSWI based WFEM is preferred to the Daubechies WFEM.

The BSWI and Daubechies WFEM solutions, for the vehicle-bridge interaction and Vierendeel frame subjected to subcritical, critical and supercritical moving load velocities, were highly accurate and fewer elements were implemented when compared with the classical FEM. Moreover, the dynamic responses for the high speed locomotive travelling over a rail track system were very accurately described for all the cases of damping introduced in the system and velocity profiles.

8. The Analysis of Functionally Graded Materials using the Wavelet Finite Element Method

Summary

In this chapter, the dynamics analysis of functionally graded beams is carried out and presented via the implementation of the wavelet finite element method. The functionally graded beam material constituents, and consequently material properties, vary continuously with respect to the spatial coordinates. This variation in material distribution is modelled based on one of the gradation laws; the power law. The power law allows the composition distribution of the FGMs to be altered continuously by changing the value of the non-negative volume fraction power law exponent, *n*. The power law and material distribution variations are briefly described and presented in this chapter. The formulation of a new modified wavelet based FG beam finite element formulation is presented. The variation of the functionally graded beam gradation is analysed in the transverse direction for two material constituents (metal and ceramic). The Daubechies and BSWI based WFEMs are implemented to carry out the analysis and compared with the solutions obtained using the classical FEM via numerical examples, which include:

- A free vibration analysis of the wavelet based functionally graded beam is carried out for different values of E_{ratio} (ratio of the Young's modulus of the constituent materials), for transverse gradation. The results obtained are compared with those presented by Simsek and Kocaturk [83] and Alshorbagy et al. [79], who carried out a similar free vibration analysis. This comparison will not only serve as a means to verify the wavelet based functionally graded beam formulations, but also evaluate their performances.
- A steel-alumina functionally graded beam free vibration analysis is carried out using the WFEM to investigate the variation of the natural frequencies with respect to variations in material distribution, slenderness ratio $\frac{l}{h}$ and boundary conditions; for transverse gradation.
- The dynamic response of a simply supported wavelet based FG steel-alumina beam when subjected to a moving point load is analysed. The beam constituents vary in the

transverse direction for different power law exponent values while subjected to different moving load velocity profiles.

- Finally, the dynamic response analysis of a functionally graded beam resting on a viscoelastic foundation, subjected to a moving point load, is carried out using the WFEMs. This is an extension of the analysis carried out in Chapter 7 for the long homogeneous steel beam resting on a viscoelastic foundation. The results presented show the effect of altering the FGM composition distribution, via the power law exponent, on the dynamic response of the functionally graded beam on the viscoelastic foundation. The analysis is carried out for subcritical, critical and supercritical moving load velocities and different viscous damping profiles.

The implementation of the Daubechies and BSWI based WFEMs in the analysis of functionally graded beams represents a novel development of this thesis. Most importantly, the dynamic response of a functionally graded beam resting on a viscoelastic foundation, while subjected to a moving load, is presented for the first time; to the best of the author's knowledge.

8.1. The FGM transverse gradation power law

By definition, the volume fractions of two phases of materials vary gradually in the gradation direction(s) of FGMs. This consequently implies that the material properties also vary along this direction(s).

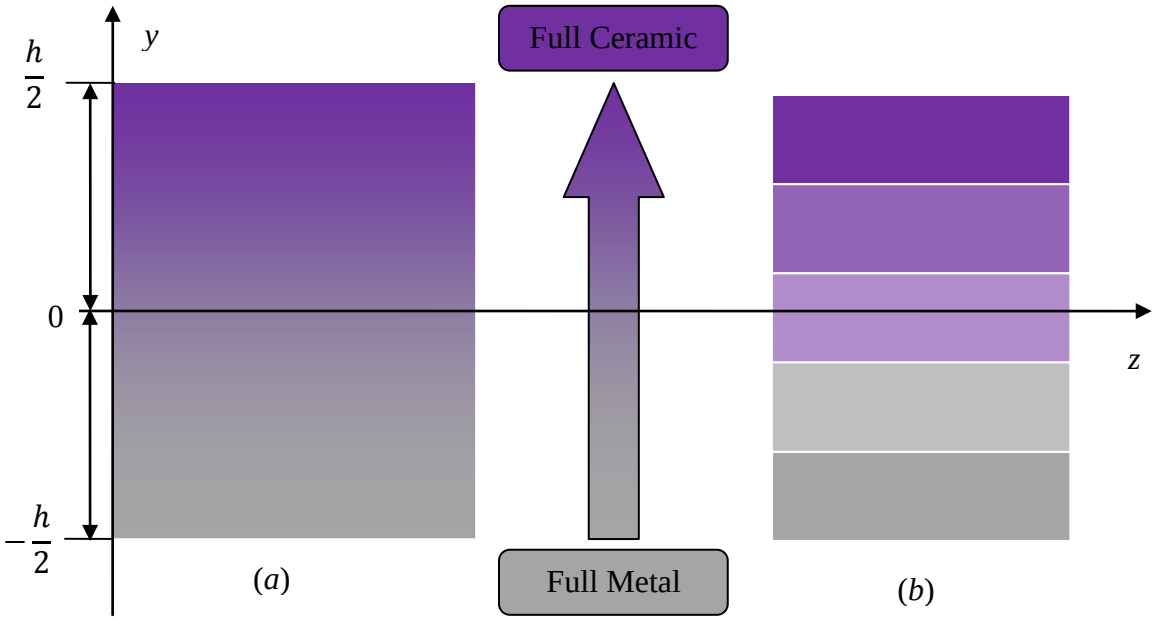

Figure 8-1: Cross-section of an FG beam composed of a metal and ceramic illustrating the transverse gradation. (*a*) Continuous variation model and (*b*) quasi-homogeneous layers model.

Consider, for example, the gradation of a functionally graded beam in the transverse direction, as illustrated in Figure 8-1. In Figure 8-1 (a) it is assumed that the volume fraction varies continuously for both materials from one surface to the other. Alternatively, a piecewise variation can be assumed, as illustrated in Figure 8-1 (b), where the volume fraction is taken to be constant in each layered region i.e., quasi-homogeneous layers [114].

It is vital for the model representing the gradation of the material constituents, and consequently the material properties, to be as accurate as possible and simple to implement in analysis. In this study, the volume fraction of the FG beam is assumed to vary continuously, allowing for a smooth transition of the material properties from one surface to another.

The power law was introduced by Wakashima et al. [115] and is an ideal approach for representing the gradation of the materials in a continuous, yet simplified manner. It is therefore selected in this study to approximate the material composition variation of the FG beam. The variation in material distributions and properties is described in this section according to Wakashima et al. [115]. The volume fractions of the upper surface V_u and lower surface V_l of the constituent materials are defined as [70]:

$$V_u(y) = (\alpha\, y + \beta)^n \tag{8.1}$$

$$V_l(y) = 1 - V_u(y) \tag{8.2}$$

where α and β are coefficients and n is the non-negative power law exponent, $0 \leq n \leq \infty$. The power law allows for the variation of the composition distribution of the FGMs by altering the volume fraction exponent n continuously. This is advantageous since the analysis of the FGM can be carried out for different variations of gradation of the materials.

The subscripts u and l denote the upper and lower material surfaces respectively. Therefore, the volume fractions of the upper and lower surface materials are:

$$\begin{aligned} V_u(y) &= \left(\frac{y}{h} + \frac{1}{2}\right)^n \\ V_l(y) &= 1 - \left(\frac{y}{h} + \frac{1}{2}\right)^n \end{aligned} \tag{8.3}$$

For simplicity and in conformity with this study based on the presented examples in this chapter, the lower surface is considered to be metallic while the upper surface ceramic. Figure 8-2 illustrates the (a) lower surface material (metal) and (b) upper surface material (ceramic) volume fraction variations of the FG beam through its thickness from equation (8.3). When n is zero, the volume fraction of the metal in the FG beam is zero and the

corresponding volume fraction of the ceramic is 1. Therefore, the effective material properties of the beam correspond to that of the ceramic. When $n = \infty$, the volume fraction of metal equals 1 and the FG beam is considered to be fully metallic. Furthermore, when $n = 1$, the variation from the metallic to ceramic phase is linear. The rate of material distribution variation also influences the effective material properties of the FG beam.

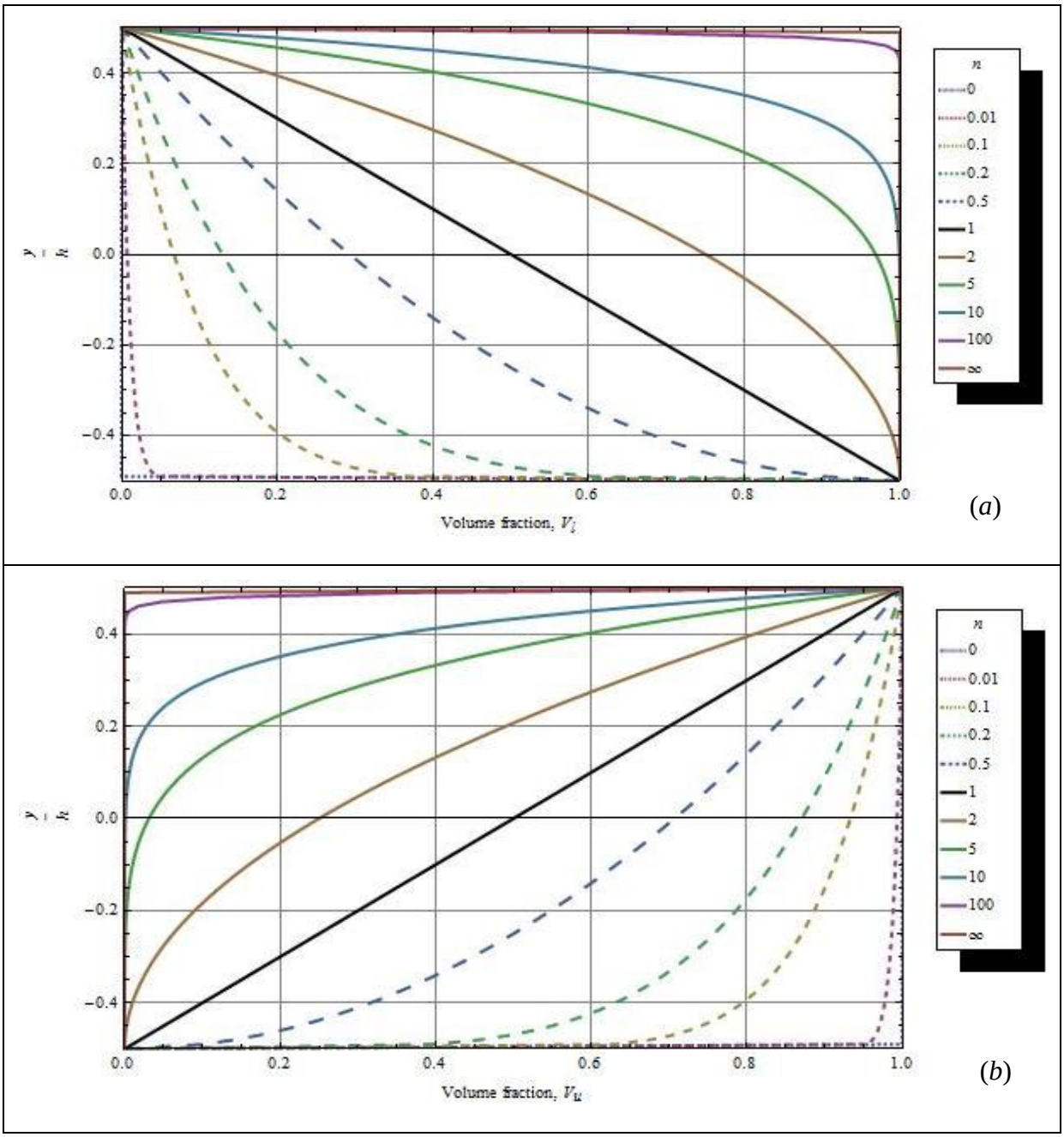

Figure 8-2: The power law variation of the volume fractions for (*a*) lower surface material (*b*) upper surface material, through the thickness of the FG beam.

The transverse variation of the material properties of the FG beam containing two constituents, according to the power gradation law, is expressed as [115]:

$$P(y) = V_u(y)[P_u - P_l] + P_l \quad \textbf{(8.4)}$$

Substituting equation (8.3) into (8.4), the expression becomes:

$$P(y) = [P_u - P_l]\left(\frac{y}{h} + \frac{1}{2}\right)^n + P_l$$

$$P(y) = P_l\left([P_{ratio} - 1]\left(\frac{y}{h} + \frac{1}{2}\right)^n + 1\right) \quad \textbf{(8.5)}$$

where P_{ratio} is the ratio of the upper and lower surface material properties, P_u and P_l respectively. The effective material properties $P(y)$ that can be described via the power law include: Young's modulus E, density ρ, Poisson's ratio υ, shear modulus G and bulk modulus K. Figure 8-3 illustrates the variation of the (*a*) effective Young's modulus $E(y)$ and (*b*) effective density $\rho(y)$ of a steel-alumina FG beam, for different values of n. The beam is fully steel ($E_l = 2.1 \times 10^{11}$ Pa, $\rho_l = 7.8 \times 10^3$ kg·m^{-3}) at the bottom surface and alumina ($E_u = 3.9 \times 10^{11}$ Pa, $\rho_u = 3.96 \times 10^3$ kg·m^{-3}) at the top surface. It is observed from Figure 8-3 (*a*) that when $n = \infty$, $E(y) = E_l$ since the volume fraction of the steel is 1 and when $n = 0$, $E(y) = E_u$. When $n < 1$ and $n \to 1$ the effective Young's modulus begins to decrease since the volume fraction of the alumina is decreasing and that of steel is increasing; given that $E_u > E_l$. When $n = 1$, the variation of the effective Young's modulus is directly proportional through the thickness of the beam. The Young's modulus at the neutral axis of the beam is the mean of E_u and E_l, given that the volume fractions of steel and alumina are equal ($V_l = V_u = 0.5$). As $n \to \infty$, the effective modulus decreases until $E(y) = E_l$, where the entire FG beam is fully steel ($n = \infty$).

The effective density at $n = 0$ corresponds to the density of alumina ($\rho(y) = \rho_u$) as illustrated in Figure 8-3 (*b*). Increase in the value of n leads to an increase in the effective density of the FG beam. When $n = \infty$, the effective density $\rho(y) = \rho_l$ since the functionally graded beam is fully steel.

In reality, it is unlikely for the variation and transition of the FGM constituents to occur in a smooth continuous manner. However, the power law can be used to approximate the variation of the FGMs by assigning the correct value of n. This is a further advantage over other FGM modelling schemes such as; the exponential law [70], Mori Tanaka scheme [116] or Hill's self-consistent method [117]. Furthermore, the material distributions of such models can also be approximated using the power law approach.

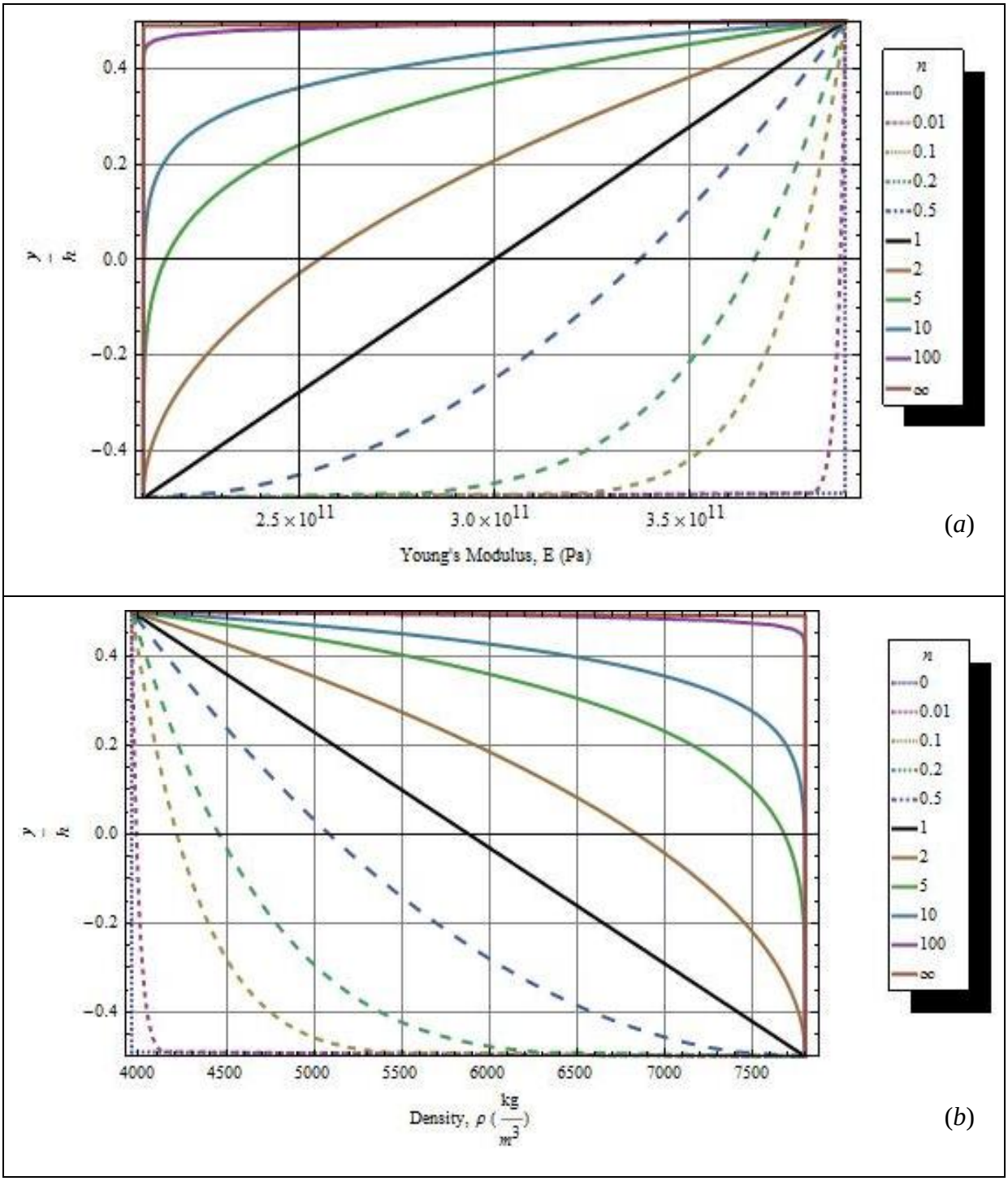

Figure 8-3: The effective (*a*) Young's modulus and (*b*) mass density, through the thickness of a steel-alumina FG beam for different power law exponents *n*.

8.2. The wavelet based functionally graded beam finite element formulation

The functionally graded beam is formulated using the wavelet finite element method based on the Euler-Bernoulli beam theory. The beam has axial and bending deformation, as well as corresponding loading effects, taken into consideration.

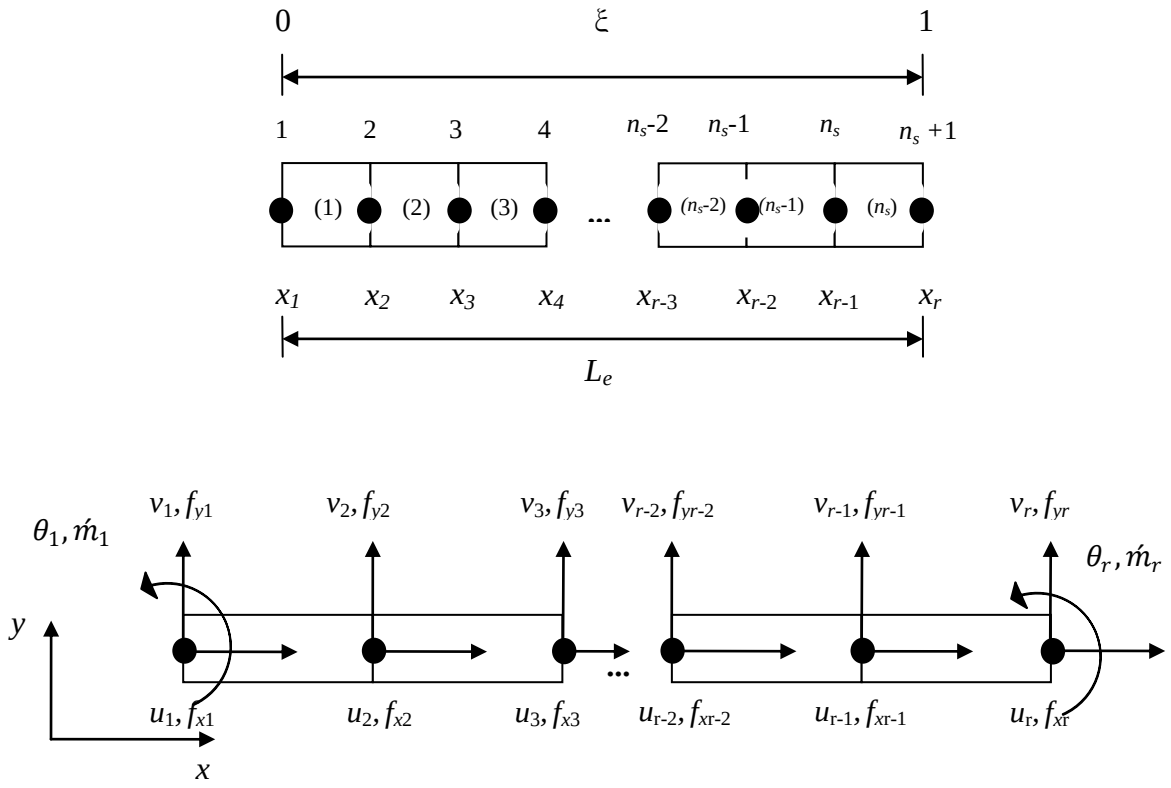

Figure 8-4 : Two dimensional FG beam wavelet finite element layout.

The variation of the material properties is analysed in the transverse direction based on the power law. The layout selected for the WFE has the axial and transverse displacement DOFs at each elemental node and the rotation DOFs only at the elemental end nodes; as presented in Figure 8-4. The total number of DOFs within each WFE is denoted by s and the total number of elemental segments is n_s.

The nodal natural coordinates within the wavelet based finite element of the FGM beam is expressed as:

$$\xi = \frac{x-x_1}{x_r-x_1} = \frac{x-x_1}{L_e} \qquad (0 \le \xi \le 1) \tag{8.6}$$

$$\xi_i = \frac{x_i-x_1}{L_e} \qquad (0 \le \xi_i \le 1,\ 1 \le i \le r) \tag{8.7}$$

The axial and transverse displacements are approximated using the wavelet scaling functions as earlier described in Section 5.1 and 5.2. For a particular multiresolution scale *j*, the axial and transverse displacements at any point, in natural coordinates, are approximated as:

$$u(\xi) = \sum_{k=h}^{2^j-1} a_{z-2,k}^{j}\, \phi_{z-2,k}^{j}(\xi)$$
$$v(\xi) = \sum_{k=i}^{2^j-1} b_{z,k}^{j}\, \phi_{z,k}^{j}(\xi) \qquad \textbf{(8.8)}$$

where *z* is the order of the wavelet scaling functions; $a_{z-2,k}^{j}$ and $b_{z,k}^{j}$ are wavelet coefficients corresponding to the elemental node axial and bending DOFs in wavelet space respectively. In general, the order of the scaling functions used to approximate the axial displacement will differ from the order approximating the transverse and rotation DOFs. The selection of the orders of the scaling functions is dependent on the element layout selected, so as to ensure that the defined DOFs are positioned at the correct elemental nodes. Thus, the order of the scaling functions selected to approximate the axial displacement, if the scaling function order approximating the transverse and rotational DOFs is z, must be $z-2$ for this layout. Furthermore, the multiresolution scale of the scaling functions representing the axial and bending deformations is *j*.

Therefore, the axial deformation, transverse displacement and rotation at any point across the wavelet based finite element, specific to the layout implemented in this formulation, are described as:

$$u(\xi) =$$

$$\left\{\phi_{z-2,h}^{j}(\xi) \quad 0 \quad 0 \quad \phi_{z-2,h+1}^{j}(\xi) \quad 0 \quad \phi_{z-2,h+2}^{j}(\xi) \quad \cdots \quad 0 \quad \phi_{z-2,2^j-2}^{j}(\xi) \quad 0 \quad \phi_{z-2,2^j-1}^{j}(\xi) \quad 0 \quad 0\right\} \begin{Bmatrix} a_{z-2,h}^{j} \\ b_{z,i}^{j} \\ b_{z,i+1}^{j} \\ a_{z-2,h+1}^{j} \\ b_{z,i+2}^{j} \\ a_{z-2,h+2}^{j} \\ \vdots \\ b_{z,2^j-4}^{j} \\ a_{z-2,2^j-2}^{j} \\ b_{z,2^j-3}^{j} \\ a_{z-2,2^j-1}^{j} \\ b_{z,2^j-2}^{j} \\ b_{z,2^j-1}^{j} \end{Bmatrix}$$

$$u(\xi) = {}^{a}_{(1 \times s)}\left\{\boldsymbol{\Phi}_{\boldsymbol{z-2}}^{\boldsymbol{j}}(\xi)\right\}_{(s \times 1)}\{\boldsymbol{c_e}\} \qquad \textbf{(8.9)}$$

$$v(\xi) =$$

$$\left\{0 \quad \phi^j_{z,i}(\xi) \quad \phi^j_{z,i+1}(\xi) \quad 0 \quad \phi^j_{z,i+2}(\xi) \quad 0 \quad \cdots \quad \phi^j_{z,2^j-4}(\xi) \quad 0 \quad \phi^j_{z,2^j-3}(\xi) \quad 0 \quad \phi^j_{z,2^j-2}(\xi) \quad \phi^j_{z,2^j-1}(\xi)\right\}\begin{Bmatrix} a^j_{z-2,h} \\ b^j_{z,i} \\ b^j_{z,i+1} \\ a^j_{z-2,h+1} \\ b^j_{z,i+2} \\ a^j_{z-2,h+2} \\ \vdots \\ b^j_{z,2^j-4} \\ a^j_{z-2,2^j-2} \\ b^j_{z,2^j-3} \\ a^j_{z-2,2^j-1} \\ b^j_{z,2^j-2} \\ b^j_{z,2^j-1} \end{Bmatrix}$$

$$v(\xi) = {}_{(1\text{ x }s)}{}^{t}\left\{\boldsymbol{\Phi}^{\boldsymbol{j}}_{\mathbf{z}}(\xi)\right\}_{(s\text{ x }1)}\{\boldsymbol{c_e}\} \qquad \textbf{(8.10)}$$

$$\theta(\xi) = \frac{\partial v(\xi)}{\partial x} = \frac{1}{L_e}\frac{\partial v(\xi)}{\partial \xi} = \frac{1}{L_e}\,{}_{(1\text{ x }s)}{}^{t}\left\{\boldsymbol{\Phi}'^{\boldsymbol{j}}_{\mathbf{z}}(\xi)\right\}_{(s\text{ x }1)}\{\boldsymbol{c_e}\} \qquad \textbf{(8.11)}$$

The vector $\{\boldsymbol{c_e}\}$ contains the coefficients corresponding to the DOFs within the wavelet based finite element in wavelet space. Furthermore, the vectors ${}^{a}\left\{\boldsymbol{\Phi}^{\boldsymbol{j}}_{\mathbf{z-2}}(\xi)\right\}$ and ${}^{t}\left\{\boldsymbol{\Phi}^{\boldsymbol{j}}_{\mathbf{z}}(\xi)\right\}$ contain the scaling functions approximating the axial deformation and transverse displacements, at the positions corresponding to the related DOFs within the element, respectively. The vector ${}^{t}\left\{\boldsymbol{\Phi}'^{\boldsymbol{j}}_{\mathbf{z}}(\xi)\right\}$ contains the first derivative of the scaling functions implemented to approximate the rotation DOFs. The relations expressed in (8.9) - (8.11) are employed to formulate the wavelet transformation matrix of the wavelet based beam element.

In physical space, the DOFs within each wavelet finite element are expressed as the vector $\{\boldsymbol{h_e}\}$:

$$\{\boldsymbol{h_e}\} = \{u_1 \quad v_1 \quad \theta_1 \quad u_2 \quad v_2 \quad u_3 \quad v_3 \quad \cdots \quad u_{r-1} \quad v_{r-1} \quad u_r \quad v_r \quad \theta_r\}^T \qquad \textbf{(8.12)}$$

Therefore, the relation between the physical space and wavelet space DOFs is formulated as:

$$\begin{Bmatrix} u_1 \\ v_1 \\ \theta_1 \\ u_2 \\ v_2 \\ u_3 \\ \vdots \\ v_{r-2} \\ u_{r-1} \\ v_{r-1} \\ u_r \\ v_r \\ \theta_r \end{Bmatrix} = \begin{bmatrix} {}^{a}\{\boldsymbol{\Phi}^{\boldsymbol{j}}_{\boldsymbol{z-2}}(\xi_1)\} \\ {}^{t}\{\boldsymbol{\Phi}^{\boldsymbol{j}}_{\mathbf{z}}(\xi_1)\} \\ \frac{1}{L_e}\ {}^{t}\{\boldsymbol{\Phi}'^{\boldsymbol{j}}_{\mathbf{z}}(\xi_1)\} \\ {}^{a}\{\boldsymbol{\Phi}^{\boldsymbol{j}}_{\boldsymbol{z-2}}(\xi_2)\} \\ {}^{t}\{\boldsymbol{\Phi}^{\boldsymbol{j}}_{\mathbf{z}}(\xi_2)\} \\ {}^{a}\{\boldsymbol{\Phi}^{\boldsymbol{j}}_{\boldsymbol{z-2}}(\xi_3)\} \\ \vdots \\ {}^{t}\{\boldsymbol{\Phi}^{\boldsymbol{j}}_{\boldsymbol{z-2}}(\xi_{r-2})\} \\ {}^{a}\{\boldsymbol{\Phi}^{\boldsymbol{j}}_{\boldsymbol{z-2}}(\xi_{r-1})\} \\ {}^{t}\{\boldsymbol{\Phi}^{\boldsymbol{j}}_{\mathbf{z}}(\xi_{r-1})\} \\ {}^{a}\{\boldsymbol{\Phi}^{\boldsymbol{j}}_{\boldsymbol{z-2}}(\xi_r)\} \\ {}^{t}\{\boldsymbol{\Phi}^{\boldsymbol{j}}_{\mathbf{z}}(\xi_r)\} \\ \frac{1}{L_e}\ {}^{t}\{\boldsymbol{\Phi}'^{\boldsymbol{j}}_{\mathbf{z}}(\xi_r)\} \end{bmatrix} \begin{Bmatrix} a^j_{z-2,h} \\ b^j_{z,i} \\ b^j_{z,i+1} \\ a^j_{z-2,h+1} \\ b^j_{z,i+2} \\ a^j_{z-2,h+2} \\ \vdots \\ b^j_{z,2^j-4} \\ a^j_{z-2,2^j-2} \\ b^j_{z,2^j-3} \\ a^j_{z-2,2^j-1} \\ b^j_{z,2^j-2} \\ b^j_{z,2^j-1} \end{Bmatrix}$$

$$_{(s\ \mathrm{x}\ 1)}\{\boldsymbol{h_e}\} = {}_{(s\ \mathrm{x}\ s)}\left[\boldsymbol{R^w_p}\right]_{(s\ \mathrm{x}\ 1)}\{\boldsymbol{c_e}\} \tag{8.13}$$

The vector $\{\boldsymbol{c^e}\}$, containing the wavelet space element DOFs, can be expressed as:

$$\{\boldsymbol{c_e}\} = \left[\boldsymbol{R^w_p}\right]^{-1}\{\boldsymbol{h_e}\} = \left[\boldsymbol{T^w_p}\right]\{\boldsymbol{h_e}\} \tag{8.14}$$

where the wavelet transformation matrix $\left[\boldsymbol{T^w_p}\right]$ is the inverse of the matrix $\left[\boldsymbol{R^w_p}\right]$. The axial deformation, transverse displacement and the rotation DOFs at any elemental node *i* can then be evaluated by substituting equation (8.14) into equations (8.9) - (8.11). Thus,

$$u(\xi_i) = {}_{(1\ \mathrm{x}\ s)}{}^{a}\left\{\boldsymbol{\Phi^j_z}(\xi_i)\right\}\ {}_{(s\ \mathrm{x}\ s)}\left[\boldsymbol{T^w_p}\right]_{(s\ \mathrm{x}\ 1)}\{\boldsymbol{h_e}\} \tag{8.15}$$

$$v(\xi_i) = {}_{(1\ \mathrm{x}\ s)}{}^{t}\left\{\boldsymbol{\Phi^j_z}(\xi_i)\right\}\ {}_{(s\ \mathrm{x}\ s)}\left[\boldsymbol{T^w_p}\right]_{(s\ \mathrm{x}\ 1)}\{\boldsymbol{h_e}\} \tag{8.16}$$

$$\theta(\xi_i) = \frac{1}{L_e}\ {}_{(1\ \mathrm{x}\ s)}{}^{t}\left\{\boldsymbol{\Phi'^j_z}(\xi)\right\}\ {}_{(s\ \mathrm{x}\ s)}\left[\boldsymbol{T^w_p}\right]_{(s\ \mathrm{x}\ 1)}\{\boldsymbol{h_e}\} \tag{8.17}$$

The relation of the transverse $v(x)$ and axial $u(x)$ displacements at any point on the mid-plane of the beam at time *t*, based on Euler Bernoulli beam theory, is defined as [83]:

$$u_0(x, y, t) = u(x, t) - y\frac{\partial v(x, t)}{\partial x} \tag{8.18}$$

$$v_0(x, y, t) = v(x, t) \tag{8.19}$$

where *x*, *y* and *t* represent the axial direction, transverse direction and time respectively. u_0 and v_0 are the axial and transverse displacements at any point of the beam. Equations (8.18) and (8.19) can also be expressed in matrix form.

$$\begin{Bmatrix} u_0 \\ v_0 \end{Bmatrix} = \begin{bmatrix} 1 & 0 & -y \\ 0 & 1 & 0 \end{bmatrix} \begin{Bmatrix} u \\ v \\ \dfrac{\partial v}{\partial x} \end{Bmatrix}$$

$$\{d\} = \begin{Bmatrix} u_0 \\ v_0 \end{Bmatrix} \tag{8.20}$$

The FG beam is assumed to undergo small deformations, thus the normal strain in the *x* direction, ε_{xx}, can be expressed in terms of the displacement.

$$\varepsilon_{xx} = \frac{\partial u_0}{\partial x} = \frac{\partial (u(x,t) - y\dfrac{\partial v(x,t)}{\partial x})}{\partial x} = \frac{\partial u(x,t)}{\partial x} - y\frac{\partial^2 v(x,t)}{\partial x^2}$$

$$\varepsilon_{xx} = [1 \quad -y] \begin{Bmatrix} \dfrac{\partial u}{\partial x} \\ \dfrac{\partial^2 v}{\partial x^2} \end{Bmatrix} \tag{8.21}$$

The FG beam is also assumed to be fully elastic; therefore obeys Hooke's law. The normal stress in the *x* direction, σ_{xx}, is defined as:

$$\sigma_{xx} = E(y)\varepsilon_{xx} = E(y)\,[1 \quad -y] \begin{Bmatrix} \dfrac{\partial u}{\partial x} \\ \dfrac{\partial^2 v}{\partial x^2} \end{Bmatrix} \tag{8.22}$$

The Young's modulus varies in the transverse direction according to the power law and the value $E(y)$ is obtained from equation (8.5), where

$$E(y) = [E_u - E_l]\left(\frac{y}{h} + \frac{1}{2}\right)^n + E_l \tag{8.23}$$

E_u and E_l denote the Young's modulus of the upper and lower material respectively. The strain energy of the beam element, U_e, is given as:

$$U_e = \frac{1}{2}\int_{vol} {\sigma_{xx}}^T \varepsilon_{xx}\, dV = \frac{1}{2}\iiint_{vol} {\sigma_{xx}}^T \varepsilon_{xx}\, dx\, dy\, dz \tag{8.24}$$

Substituting equations (8.21) and (8.22) into (8.24),

$$U_e = \frac{1}{2}\iiint_{vol} E(y)\left(\frac{\partial u(x,t)}{\partial x} - y\frac{\partial^2 v(x,t)}{\partial x^2}\right)^T \left(\frac{\partial u(x,t)}{\partial x} - y\frac{\partial^2 v(x,t)}{\partial x^2}\right) dx\, dy\, dz \tag{8.25}$$

Expressing equation (8.25) in terms of the local natural coordinates of the beam element,

$$U_e = \frac{1}{2}\int_0^b dz \int_{-\frac{h}{2}}^{\frac{h}{2}}\int_0^1 E(y)\left[\frac{1}{L_e}\left(\frac{\partial u(\xi)}{\partial \xi}\right)^T\left(\frac{\partial u(\xi)}{\partial \xi}\right) - \frac{y}{{L_e}^2}\left(\frac{\partial^2 v(\xi)}{\partial \xi^2}\right)^T\left(\frac{\partial u(\xi)}{\partial \xi}\right) - \frac{y}{{L_e}^2}\left(\frac{\partial u(\xi)}{\partial \xi}\right)^T\left(\frac{\partial^2 v(\xi)}{\partial \xi^2}\right) + \frac{y^2}{{L_e}^3}\left(\frac{\partial^2 v(\xi)}{\partial \xi^2}\right)^T\left(\frac{\partial^2 v(\xi)}{\partial \xi^2}\right)\right] d\xi\, dy \quad \textbf{(8.26)}$$

However, $\int_0^b dz = b$ is the width of the FG beam. Therefore,

$$U_e = \frac{b}{2}\int_{-\frac{h}{2}}^{\frac{h}{2}}\int_0^1 E(y)\left[\frac{1}{L_e}\left(\frac{\partial u(\xi)}{\partial \xi}\right)^T\left(\frac{\partial u(\xi)}{\partial \xi}\right) - \frac{y}{{L_e}^2}\left(\frac{\partial^2 v(\xi)}{\partial \xi^2}\right)^T\left(\frac{\partial u(\xi)}{\partial \xi}\right) - \frac{y}{{L_e}^2}\left(\frac{\partial u(\xi)}{\partial \xi}\right)^T\left(\frac{\partial^2 v(\xi)}{\partial \xi^2}\right) + \frac{y^2}{{L_e}^3}\left(\frac{\partial^2 v(\xi)}{\partial \xi^2}\right)^T\left(\frac{\partial^2 v(\xi)}{\partial \xi^2}\right)\right] d\xi\, dy \quad \textbf{(8.27)}$$

The elemental stiffness matrix for the wavelet based FG beam finite element is evaluated from equation (8.27). Let

$${}^{A}E_e = \int_{-\frac{h}{2}}^{\frac{h}{2}} E(y)dy = \int_{-\frac{h}{2}}^{\frac{h}{2}} [E_u - E_l]\left(\frac{y}{h} + \frac{1}{2}\right)^n + E_l dy \quad \textbf{(8.28)}$$

$${}^{B}E_e = \int_{-\frac{h}{2}}^{\frac{h}{2}} y\, E(y)dy = \int_{-\frac{h}{2}}^{\frac{h}{2}} y\left([E_u - E_l]\left(\frac{y}{h} + \frac{1}{2}\right)^n + E_l\right)dy \quad \textbf{(8.29)}$$

$${}^{C}E_e = \int_{-\frac{h}{2}}^{\frac{h}{2}} y^2 E(y)dy = \int_{-\frac{h}{2}}^{\frac{h}{2}} \left(y^2[E_u - E_l]\left(\frac{y}{h} + \frac{1}{2}\right)^n + E_l\right)dy \quad \textbf{(8.30)}$$

where ${}^{A}E_e$, ${}^{B}E_e$ and ${}^{C}E_e$ denote the axial, axial-bending coupling and bending stiffness of the wavelet based finite element respectively. From equation (8.27), the wavelet space axial stiffness matrix ${}^{A}[\boldsymbol{k_e^w}]$ of the WFE is evaluated by substituting equation (8.9) into (8.27)

$${}^{A}_{(s\,\mathrm{x}\,s)}[\boldsymbol{k_e^w}] = \int_0^1 {}^{a}\left\{\frac{\partial \boldsymbol{\Phi}^{\boldsymbol{j}}_{\boldsymbol{z-2}}(\xi)}{\partial \xi}\right\}^T {}^{a}\left\{\frac{\partial \boldsymbol{\Phi}^{\boldsymbol{j}}_{\boldsymbol{z-2}}(\xi)}{\partial \xi}\right\} d\xi \quad \textbf{(8.31)}$$

The axial-bending coupling stiffness matrices ${}^{B}[\boldsymbol{k_e^w}]$ and ${}^{C}[\boldsymbol{k_e^w}]$ in wavelet space are given as:

$${}^{B}_{(s\,\mathrm{x}\,s)}[\boldsymbol{k_e^w}] = \int_0^1 {}^{t}\left\{\frac{\partial^2 \boldsymbol{\Phi}^{\boldsymbol{j}}_{\boldsymbol{z}}(\xi)}{\partial \xi^2}\right\}^T {}^{a}\left\{\frac{\partial \boldsymbol{\Phi}^{\boldsymbol{j}}_{\boldsymbol{z-2}}(\xi)}{\partial \xi}\right\} d\xi \quad \textbf{(8.32)}$$

$${}^{C}_{(s\,\mathrm{x}\,s)}[\boldsymbol{k_e^w}] = \int_0^1 {}^{a}\left\{\frac{\partial \boldsymbol{\Phi}^{\boldsymbol{j}}_{\boldsymbol{z-2}}(\xi)}{\partial \xi}\right\}^T {}^{t}\left\{\frac{\partial^2 \boldsymbol{\Phi}^{\boldsymbol{j}}_{\boldsymbol{z}}(\xi)}{\partial \xi^2}\right\} d\xi \quad \textbf{(8.33)}$$

and the wavelet space bending stiffness matrix ${}^{D}[\boldsymbol{k_e^w}]$ is

$$ {}_{(s\,x\,s)}^{D}[\boldsymbol{k_e^w}] = \int_0^1 {}^{t}\left\{\frac{\partial^2 \boldsymbol{\Phi_z^j}(\xi)}{\partial \xi^2}\right\}^T \; {}^{t}\left\{\frac{\partial^2 \boldsymbol{\Phi_z^j}(\xi)}{\partial \xi^2}\right\} d\xi \tag{8.34} $$

The matrices expressed in equations (8.31) - (8.34) are transformed into the physical space via the transformation matrix $[\boldsymbol{T_p^w}]$, which is obtained from the relation in (8.14). Thus,

$$ {}_{(s\,x\,s)}^{A}[\boldsymbol{k_e^p}] = \frac{b\,{}^{A}E_e}{L_e}[\boldsymbol{T_p^w}]^T \,{}^{A}[\boldsymbol{k_e^w}][\boldsymbol{T_p^w}] \tag{8.35} $$

$$ {}_{(s\,x\,s)}^{B}[\boldsymbol{k_e^p}] = \frac{b\,{}^{B}E_e}{{L_e}^2}[\boldsymbol{T_p^w}]^T \,{}^{B}[\boldsymbol{k_e^w}][\boldsymbol{T_p^w}] \tag{8.36} $$

$$ {}_{(s\,x\,s)}^{C}[\boldsymbol{k_e^p}] = \frac{b\,{}^{B}E_e}{{L_e}^2}[\boldsymbol{T_p^w}]^T \,{}^{C}[\boldsymbol{k_e^w}][\boldsymbol{T_p^w}] \tag{8.37} $$

$$ {}_{(s\,x\,s)}^{D}[\boldsymbol{k_e^p}] = \frac{b\,{}^{C}E_e}{{L_e}^3}[\boldsymbol{T_p^w}]^T \,{}^{D}[\boldsymbol{k_e^w}][\boldsymbol{T_p^w}] \tag{8.38} $$

The elemental stiffness matrix in physical space for the wavelet based FG beam is therefore:

$$ {}_{(s\,x\,s)}[\boldsymbol{k_e^p}] = {}^{A}[\boldsymbol{k_e^p}] - {}^{B}[\boldsymbol{k_e^p}] - {}^{C}[\boldsymbol{k_e^p}] + {}^{D}[\boldsymbol{k_e^p}] \tag{8.39} $$

The kinetic energy of the wavelet based FG beam element, Λ_e, is defined as:

$$ \Lambda_e = \iiint_{vol} \rho(y)\, dx\, dy\, dz\; vel \tag{8.40} $$

vel is the velocity of the FG beam. $\rho(y)$ represents the effective density of the FG beam element, which is obtained from equation (8.5) as:

$$ \rho(y) = [\rho_u - \rho_l]\left(\frac{y}{h} + \frac{1}{2}\right)^n + \rho_u \tag{8.41} $$

The velocity components of the beam in axial and transverse directions can be expressed as:

$$ \left(\frac{\partial\, v_0(x,t)}{\partial t}\right) = \{\dot{v}(x,t)\} $$

$$ \left(\frac{\partial\, u_0(x,t)}{\partial t}\right) = \{\dot{u}_0(x,t)\} = \dot{u}(x,t) - y\frac{\partial \dot{v}(x,t)}{\partial x} \tag{8.42} $$

The velocity components can then be defined in terms of the wavelet scaling functions from equations (8.15) and (8.16).

$$ \dot{u}(\xi) = {}_{(1\,x\,s)}^{a}\left\{\boldsymbol{\Phi_z^j}(\xi)\right\}\; {}_{(s\,x\,s)}[\boldsymbol{T_p^w}]_{(s\,x\,1)}\{\dot{\boldsymbol{h}}_e\} \tag{8.43} $$

$$\dot{v}(\xi) = {}_{(1\,\mathrm{x}\,s)}{}^{t}\left\{\boldsymbol{\Phi}_{\boldsymbol{z}}^{\boldsymbol{j}}(\xi)\right\}\ {}_{(s\,\mathrm{x}\,s)}\left[\boldsymbol{T}_{\boldsymbol{p}}^{\boldsymbol{w}}\right]_{(s\,\mathrm{x}\,1)}\{\dot{\boldsymbol{h}}_{\boldsymbol{e}}\} \tag{8.44}$$

Substituting equation (8.42) into (8.40),

$$\Lambda_e = \frac{1}{2}\iiint_{vol}\rho(y)(\{\dot{u}_0(x,t)\}^T\{\dot{u}_0(x,t)\} + \{\dot{v}_0(x,t)\}^T\{\dot{v}_0(x,t)\})\,dx\,dy\,dz$$

$$\Lambda_e = \frac{1}{2}\iiint_{vol}\rho(y)\left(\left(\dot{u}(x,t) - y\frac{\partial\dot{v}(x,t)}{\partial x}\right)\left(\dot{u}(x,t) - y\frac{\partial\dot{v}(x,t)}{\partial x}\right) + (\dot{v}(x,t)\dot{v}(x,t))\right)dx\,dy\,dz \tag{8.45}$$

Equation (8.45) can be expressed in the natural coordinate system as:

$$\Lambda_e = \frac{1}{2}\int_o^b dz\int_{-\frac{h}{2}}^{\frac{h}{2}}\int_0^1 \rho(y)\left(L_e\left(\dot{u}(\xi,t)\dot{u}(\xi,t)\right) - y\left(\dot{u}(\xi,t)\frac{\partial\dot{v}(\xi,t)}{\partial x}\right) - y\left(\frac{\partial\dot{v}(\xi,t)}{\partial\xi}\dot{u}(\xi,t)\right)\right.$$
$$\left. + \frac{y^2}{L_e}\left(\frac{\partial\dot{v}(\xi,t)}{\partial x}\frac{\partial\dot{v}(\xi,t)}{\partial x}\right) + L_e(\dot{v}(\xi,t)\dot{v}(\xi,t))\right)d\xi\,dy \tag{8.46}$$

Let the inertial coefficients be denoted as:

$${}^{A}\rho_e = \int_{-\frac{h}{2}}^{\frac{h}{2}}\rho(y)dy = \int_{-\frac{h}{2}}^{\frac{h}{2}}[\rho_u - \rho_l]\left(\frac{y}{h} + \frac{1}{2}\right)^n + \rho_l dy \tag{8.47}$$

$${}^{B}\rho_e = \int_{-\frac{h}{2}}^{\frac{h}{2}} y\rho(y)dy = \int_{-\frac{h}{2}}^{\frac{h}{2}} y\left([\rho_u - \rho_l]\left(\frac{y}{h} + \frac{1}{2}\right)^n + \rho_l\right)dy \tag{8.48}$$

$${}^{C}\rho_e = \int_{-\frac{h}{2}}^{\frac{h}{2}} y^2\rho(y)dy = \int_{-\frac{h}{2}}^{\frac{h}{2}}\left(y^2[\rho_u - \rho_l]\left(\frac{y}{h} + \frac{1}{2}\right)^n + \rho_l\right)dy \tag{8.49}$$

Substituting equations (8.43) and (8.44) into (8.46), the mass matrix components in wavelet space are evaluated as follows:

$${}_{(s\,\mathrm{x}\,s)}{}^{A}[\boldsymbol{m}_{\boldsymbol{e}}^{\boldsymbol{w}}] = \int_0^1 {}^{a}\left\{\boldsymbol{\Phi}_{\boldsymbol{z-2}}^{\boldsymbol{j}}(\xi)\right\}^T\ {}^{a}\left\{\boldsymbol{\Phi}_{\boldsymbol{z-2}}^{\boldsymbol{j}}(\xi)\right\}\,d\xi \tag{8.50}$$

$${}_{(s\,\mathrm{x}\,s)}{}^{B}[\boldsymbol{m}_{\boldsymbol{e}}^{\boldsymbol{w}}] = \int_0^1 {}^{a}\left\{\boldsymbol{\Phi}_{\boldsymbol{z-2}}^{\boldsymbol{j}}(\xi)\right\}^T\ {}^{t}\left\{\frac{\partial\boldsymbol{\Phi}_{\boldsymbol{z}}^{\boldsymbol{j}}(\xi)}{\partial\xi}\right\}\,d\xi \tag{8.51}$$

$${}_{(s\,\mathrm{x}\,s)}{}^{C}[\boldsymbol{m}_{\boldsymbol{e}}^{\boldsymbol{w}}] = \int_0^1 {}^{t}\left\{\frac{\partial\boldsymbol{\Phi}_{\boldsymbol{z}}^{\boldsymbol{j}}(\xi)}{\partial\xi}\right\}^T\ {}^{a}\left\{\boldsymbol{\Phi}_{\boldsymbol{z-2}}^{\boldsymbol{j}}(\xi)\right\}\,d\xi \tag{8.52}$$

$${}_{(s\,\mathrm{x}\,s)}{}^{D}[\boldsymbol{m}_{\boldsymbol{e}}^{\boldsymbol{w}}] = \int_0^1 {}^{t}\left\{\frac{\partial\boldsymbol{\Phi}_{\boldsymbol{z}}^{\boldsymbol{j}}(\xi)}{\partial\xi}\right\}^T\ {}^{t}\left\{\frac{\partial\boldsymbol{\Phi}_{\boldsymbol{z}}^{\boldsymbol{j}}(\xi)}{\partial\xi}\right\}\,d\xi \tag{8.53}$$

$${}_{(s\,\mathrm{x}\,s)}{}^{E}[\boldsymbol{m}_{\boldsymbol{e}}^{\boldsymbol{w}}] = \int_0^1 {}^{t}\left\{\bar{\boldsymbol{\Phi}}_{\boldsymbol{z}}^{\boldsymbol{j}}(\xi)\right\}^T\ {}^{t}\left\{\bar{\boldsymbol{\Phi}}_{\boldsymbol{z}}^{\boldsymbol{j}}(\xi)\right\}\,d\xi \tag{8.54}$$

The mass matrix components are then transformed from wavelet space into physical space via the wavelet transformation matrix $\left[\boldsymbol{T_p^w}\right]$. Thus, the matrices expressed in equations (8.50) - (8.54), after transformation into physical space, are expressed as:

$$_{(s\,\mathrm{x}\,s)}^{A}[\boldsymbol{m_e^p}] = b\,{}^{A}\rho_e L_e \left[\boldsymbol{T_p^w}\right]^T {}^{A}[\boldsymbol{m_e^w}]\left[\boldsymbol{T_p^w}\right] \tag{8.55}$$

$$_{(s\,\mathrm{x}\,s)}^{B}[\boldsymbol{m_e^p}] = b\,{}^{B}\rho_e \left[\boldsymbol{T_p^w}\right]^T {}^{B}[\boldsymbol{m_e^w}]\left[\boldsymbol{T_p^w}\right] \tag{8.56}$$

$$_{(s\,\mathrm{x}\,s)}^{C}[\boldsymbol{m_e^p}] = b\,{}^{B}\rho_e \left[\boldsymbol{T_p^w}\right]^T {}^{C}[\boldsymbol{m_e^w}]\left[\boldsymbol{T_p^w}\right] \tag{8.57}$$

$$_{(s\,\mathrm{x}\,s)}^{D}[\boldsymbol{m_e^p}] = \frac{b\,{}^{C}\rho_e}{L_e}\left[\boldsymbol{T_p^w}\right]^T {}^{D}[\boldsymbol{m_e^w}]\left[\boldsymbol{T_p^w}\right] \tag{8.58}$$

$$_{(s\,\mathrm{x}\,s)}^{E}[\boldsymbol{m_e^p}] = b\,{}^{A}\rho_e L_e \left[\boldsymbol{T_p^w}\right]^T {}^{E}[\boldsymbol{m_e^w}]\left[\boldsymbol{T_p^w}\right] \tag{8.59}$$

The total element mass matrix in physical space for the wavelet based FG beam element is therefore:

$$_{(s\,\mathrm{x}\,s)}[\boldsymbol{m_e^p}] = {}^{A}[\boldsymbol{m_e^p}] - {}^{B}[\boldsymbol{m_e^p}] - {}^{C}[\boldsymbol{m_e^p}] + {}^{D}[\boldsymbol{m_e^p}] + {}^{E}[\boldsymbol{m_e^p}] \tag{8.60}$$

The FG beam stiffness and mass matrices are evaluated in the local coordinate system. The elemental matrices can then be transformed in global coordinates via the global transformation matrix $\left[\boldsymbol{T_p^G}\right]$. The relation of the local and global coordinate systems for the FG beam WFE is

$$\begin{Bmatrix} u_1 \\ v_1 \\ \theta_1 \\ u_2 \\ v_2 \\ u_3 \\ v_3 \\ \vdots \\ u_{n-1} \\ v_{n-1} \\ u_n \\ v_n \\ u_{n+1} \\ v_{n+1} \\ \theta_{n+1} \end{Bmatrix} = \begin{bmatrix} \cos\alpha & \sin\alpha & 0 & 0 & 0 & 0 & 0 & \cdots & 0 & 0 & 0 & 0 & 0 & 0 & 0 \\ -\sin\alpha & \cos\alpha & 0 & 0 & 0 & 0 & 0 & \cdots & 0 & 0 & 0 & 0 & 0 & 0 & 0 \\ 0 & 0 & 1 & 0 & 0 & 0 & 0 & \cdots & 0 & 0 & 0 & 0 & 0 & 0 & 0 \\ 0 & 0 & 0 & \cos\alpha & \sin\alpha & 0 & 0 & \cdots & 0 & 0 & 0 & 0 & 0 & 0 & 0 \\ 0 & 0 & 0 & -\sin\alpha & \cos\alpha & 0 & 0 & \cdots & 0 & 0 & 0 & 0 & 0 & 0 & 0 \\ 0 & 0 & 0 & 0 & 0 & \cos\alpha & \sin\alpha & \cdots & 0 & 0 & 0 & 0 & 0 & 0 & 0 \\ 0 & 0 & 0 & 0 & 0 & -\sin\alpha & \cos\alpha & \cdots & 0 & 0 & 0 & 0 & 0 & 0 & 0 \\ \vdots & \vdots & \vdots & \vdots & \vdots & \vdots & \vdots & \ddots & \vdots & \vdots & \vdots & \vdots & \vdots & \vdots & \vdots \\ 0 & 0 & 0 & 0 & 0 & 0 & 0 & \cdots & \cos\alpha & \sin\alpha & 0 & 0 & 0 & 0 & 0 \\ 0 & 0 & 0 & 0 & 0 & 0 & 0 & \cdots & -\sin\alpha & \cos\alpha & 0 & 0 & 0 & 0 & 0 \\ 0 & 0 & 0 & 0 & 0 & 0 & 0 & \cdots & 0 & 0 & \cos\alpha & \sin\alpha & 0 & 0 & 0 \\ 0 & 0 & 0 & 0 & 0 & 0 & 0 & \cdots & 0 & 0 & -\sin\alpha & \cos\alpha & 0 & 0 & 0 \\ 0 & 0 & 0 & 0 & 0 & 0 & 0 & \cdots & 0 & 0 & 0 & 0 & \cos\alpha & \sin\alpha & 0 \\ 0 & 0 & 0 & 0 & 0 & 0 & 0 & \cdots & 0 & 0 & 0 & 0 & -\sin\alpha & \cos\alpha & 0 \\ 0 & 0 & 0 & 0 & 0 & 0 & 0 & \cdots & 0 & 0 & 0 & 0 & 0 & 0 & 1 \end{bmatrix} \begin{Bmatrix} U_1 \\ V_1 \\ \Theta_1 \\ U_2 \\ V_2 \\ U_3 \\ V_3 \\ \vdots \\ U_{n-1} \\ V_{n-1} \\ U_n \\ V_n \\ U_{n+1} \\ V_{n+1} \\ \Theta_{n+1} \end{Bmatrix}$$

$$_{(s\times 1)}\{\boldsymbol{h_e}\} = {}_{(s\times s)}\left[\boldsymbol{T_p^G}\right]_{(s\times 1)}\{\boldsymbol{H_e}\} \tag{8.61}$$

The stiffness and mass matrices in global coordinates for the FG beam are therefore defined as:

$$_{(s\,\mathrm{x}\,s)}[\boldsymbol{K_e^p}] = {}_{(s\,\mathrm{x}\,s)}\left[\boldsymbol{T_p^G}\right]^T {}_{(s\,\mathrm{x}\,s)}[\boldsymbol{k_e^p}]_{(s\,\mathrm{x}\,s)}\left[\boldsymbol{T_p^G}\right] \tag{8.62}$$

$$_{(s\,\mathrm{x}\,s)}[\boldsymbol{M_e^p}] = {}_{(s\,\mathrm{x}\,s)}\left[\boldsymbol{T_p^G}\right]^T {}_{(s\,\mathrm{x}\,s)}[\boldsymbol{m_e^p}]_{(s\,\mathrm{x}\,s)}\left[\boldsymbol{T_p^G}\right] \tag{8.63}$$

8.3. Free vibration analysis of a transverse varying functionally graded beam

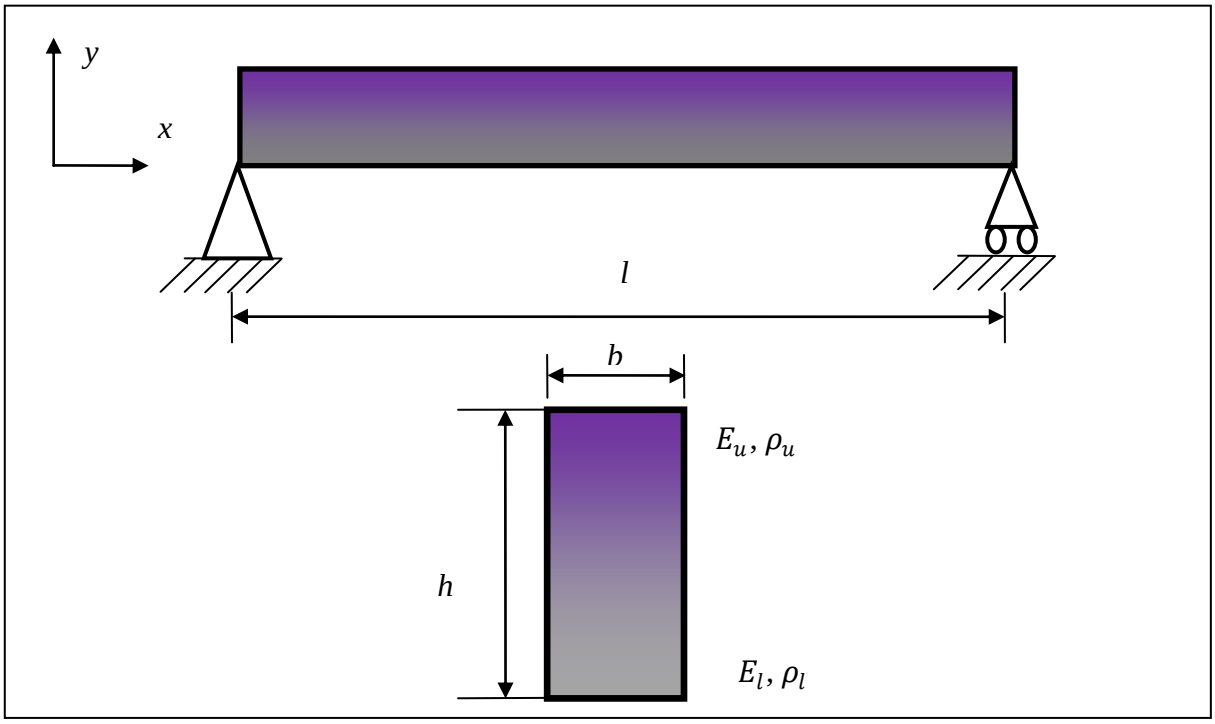

Figure 8-5: Simply supported functionally graded beam.

The free vibration analysis of a simply supported functionally graded beam is carried out using the Daubechies and BSWI based WFEMs. The functionally graded beam comprises of two constituent materials varying in the transverse direction based on the power law; as illustrated in Figure 8-5. The FG beam of length *l* and uniform cross-sectional area *A* (width *b* and height *h*), has a Young's modulus E_u, E_l and density ρ_u, ρ_l at the upper and lower surfaces respectively. The effective material properties are evaluated for the different material distributions from equation (8.5).

The free vibration analysis is carried out by solving the eigenvalue problem [27]:

$$\left[[K] - \omega^2[M]\right]\{\acute{U}\} = 0 \qquad \textbf{(8.64)}$$

where the matrices $[M]$ and $[K]$ are the mass and stiffness matrices of the system in physical space respectively. They are computed by assembling the elemental stiffness and mass matrices in equations (8.62) and (8.63) respectively, with the imposed boundary conditions applied. The vector $\{\acute{U}\}$ represents modal displacements and ω is the corresponding natural frequencies of the system.

The effect of varying E_{ratio} ($E_{\text{ratio}} = \frac{E_u}{E_l}$) on the natural frequencies of the FG beam is carried out using both the Daubechies and BSWI WFEMs. This analysis was also presented by Simsek and Kocaturk [83] using Euler-Bernoulli theory and Lagrange's equations to derive the governing equations of motion for the system. In their initial analysis, they investigate the effect of varying the Young's modulus ratio, power law exponent *n* and slenderness ratio $\frac{l}{h}$, on the non-dimensional frequencies of the FG beam. In their study, the material gradation varies in the transverse direction. Alshorbagy et al. [79] also use the classical FEM to carry out this analysis, although it is not indicated how many elements are implemented to obtain their results. Therefore, the FEM solutions presented in this chapter are evaluated based on the classical FEM formulation for FG beams presented in Appendix B.4. Alshorbagy et al. [79] also analyse the free vibration of the FG beam with axial gradation, for different boundary conditions.

In this section, the results obtained via the Daubechies and BSWI based WFEMs are compared with those presented in [83] to verify the wavelet based FG beam formulations. In this analysis, the upper surface material is alumina of Young's modulus $E_u = 390$ GPa and density $\rho_u = 3960$ kg·m^{-3}. The density ratio of the two surfaces is assumed to be equal to one i.e., $\rho_{\text{ratio}} = \frac{\rho_u}{\rho_l} = 1$. Given that $E_{\text{ratio}} = \frac{E_u}{E_l}$, the Young's modulus of the lower surface is evaluated from the relation $E_l = \frac{E_u}{E_{\text{ratio}}}$. The FG beam of length *l* is of uniform cross-sectional area *A*; height $h = 0.9$ m and width $b = 0.4$ m.

The non-dimensional frequencies λ_i of the FG beam are evaluated from the relation

$$\lambda_i{}^2 = \omega_i l^2 \left(\frac{12\,\rho_l}{E_l h^2}\right)^{\frac{1}{2}} \qquad \textbf{(8.65)}$$

where ω_i is the i^{th} mode natural frequency of the beam in radians per second.

The simply supported wavelet based functionally graded beam is modelled using 2 Daubechies D12_0 WFEs (37 DOFs), while for the BSWI WFEM, one BSWI5_4 (38 DOFs) WFE is implemented. The results are compared with the classical FEM, where 12 elements (39 DOFs) are employed. The number of elements used, order and multiresolution scale of the wavelet based elements employed allow for a comparison of the results with a similar number of DOFs within the entire FG beam. The results for the first 3 non-dimensional frequencies are obtained for different values of *n* and E_{ratio}.

Table 8-1 contains the non-dimensional fundamental frequency of the FG beam, λ_1, with slenderness ratio $\frac{l}{h} = 20$, for different values of E_{ratio} and n. The Daubechies and BSWI based WFEM solutions are in excellent agreement with the results presented in [83]; with only two and one WFEs used in the analysis respectively. Furthermore, the WFEM results are noticeably better than those obtained via the classical FEM approach.

E Ratio		***n* = 0**	***n* = 0.1**	***n* = 0.2**	***n* = 0.5**	***n* = 1**	***n* = 2**	***n* = 5**	***n* = 10**	***n* = 10^4**
0.1	Ref [83]	-	-	-	-	-	-	-	-	-
	FEM	1.76574	2.04374	2.17085	2.37367	2.53917	2.69652	2.87467	2.9776	3.13977
	Daub	1.76574	2.04338	2.17023	2.37283	2.53836	2.69594	2.87444	2.97752	3.13977
	BSWI	1.76574	2.04338	2.17023	2.37283	2.53836	2.69694	2.87444	2.97752	3.13977
0.25	Ref [83]	2.2203	2.3739	2.4606	-	2.7035	2.8053	-	3.0084	-
	FEM	2.2203	2.37469	2.46153	2.59816	2.70437	2.80598	2.93031	3.00855	3.13981
	Daub	2.2203	2.37459	2.46113	2.59773	2.7039	2.80562	2.93016	3.0085	3.1398
	BSWI	2.2203	2.37459	2.46113	2.59773	2.7039	2.80562	2.93016	3.0085	3.1398
0.5	Ref [83]	2.6403	2.7104	2.7573	-	2.8944	2.9459	-	3.0562	-
	FEM	2.6404	2.71075	2.75767	2.83636	2.89474	2.94622	3.01105	3.05632	3.13987
	Daub	2.6404	2.71073	2.75762	2.83624	2.89459	2.94609	3.01099	3.05629	3.13986
	BSWI	2.6404	2.71073	2.75762	2.83623	2.89459	2.94609	3.01198	3.05629	3.13986
1	Ref [83]	3.1399	3.1399	3.1399	-	3.1399	3.1399	-	3.1399	3.1399
	FEM	3.13998	3.13998	3.13998	3.13998	3.13998	3.13998	3.13998	3.13998	3.13998
	Daub	3.13998	3.13998	3.13998	3.13998	3.13998	3.13998	3.13998	3.13998	3.13998
	BSWI	3.13998	3.13998	3.13998	3.13998	3.13998	3.13998	3.13998	3.13998	3.13998
2	Ref [83]	3.734	3.6775	3.6301	-	3.4421	3.3765	-	3.2725	-
	FEM	3.73409	3.67727	3.62998	3.52966	3.44245	3.3769	3.31975	3.27269	3.14022
	Daub	3.73409	3.67726	3.62994	3.52955	3.44226	3.37668	3.31959	3.27262	3.14022
	BSWI	3.73409	3.67726	3.62994	3.52955	3.44226	3.37668	3.31959	3.27262	3.14022
4	Ref [83]	4.4406	4.337	4.2459	-	3.8234	3.6485	-	3.4543	-
	FEM	4.44061	4.33664	4.24558	4.03478	3.82455	3.65012	3.533	3.45511	3.14069
	Daub	4.4406	4.33661	4.2455	4.03446	3.82389	3.64923	3.5323	3.45473	3.14069
	BSWI	4.4406	4.33661	4.2455	4.03446	3.82489	3.64923	3.5323	3.45473	3.14069
10	Ref [83]	-	-	-	-	-	-	-	-	-
	FEM	5.58377	5.42438	5.28008	4.92294	4.51536	4.10325	3.8225	3.73252	3.1421
	Daub	5.58376	5.42433	5.27992	4.92228	4.51392	4.10109	3.82039	3.73103	3.1421
	BSWI	5.58376	5.42433	5.27992	4.92228	4.51392	4.10109	3.82039	3.73103	3.14209

Table 8-1: The non-dimensional fundamental frequency of a simply supported FGM beam of varying composition distributions; for different E_{ratio}.($\frac{\rho_u}{\rho_l} = \mathbf{1}, \frac{l}{h} = \mathbf{20}$).

When $E_{\text{ratio}} < 1$, it is observed that as n increases, the fundamental frequency also increases. For example, at $E_{\text{ratio}} = 0.1$, $E_l = \frac{E_u}{0.1}$ and thus the lower surface material has a higher bending rigidity than the alumina surface. When $n = 0$, the beam composition is considered fully

alumina. Therefore, as *n* increases, the effective modulus, and subsequently overall bending stiffness of the FG beam, also increases. This results in an increase of the non-dimensional fundamental frequency until *n* is infinity, where the fundamental frequency is equivalent to that of the lower material; since its volume fraction is 1.

When E_{ratio} = 1, the upper and lower surfaces have material constituents of the same stiffness; hence the beam is also fully homogenous. Therefore, variation of the power law exponent *n* does not alter the material distribution and the non-dimensional fundamental frequency remains constant for all values of *n*.

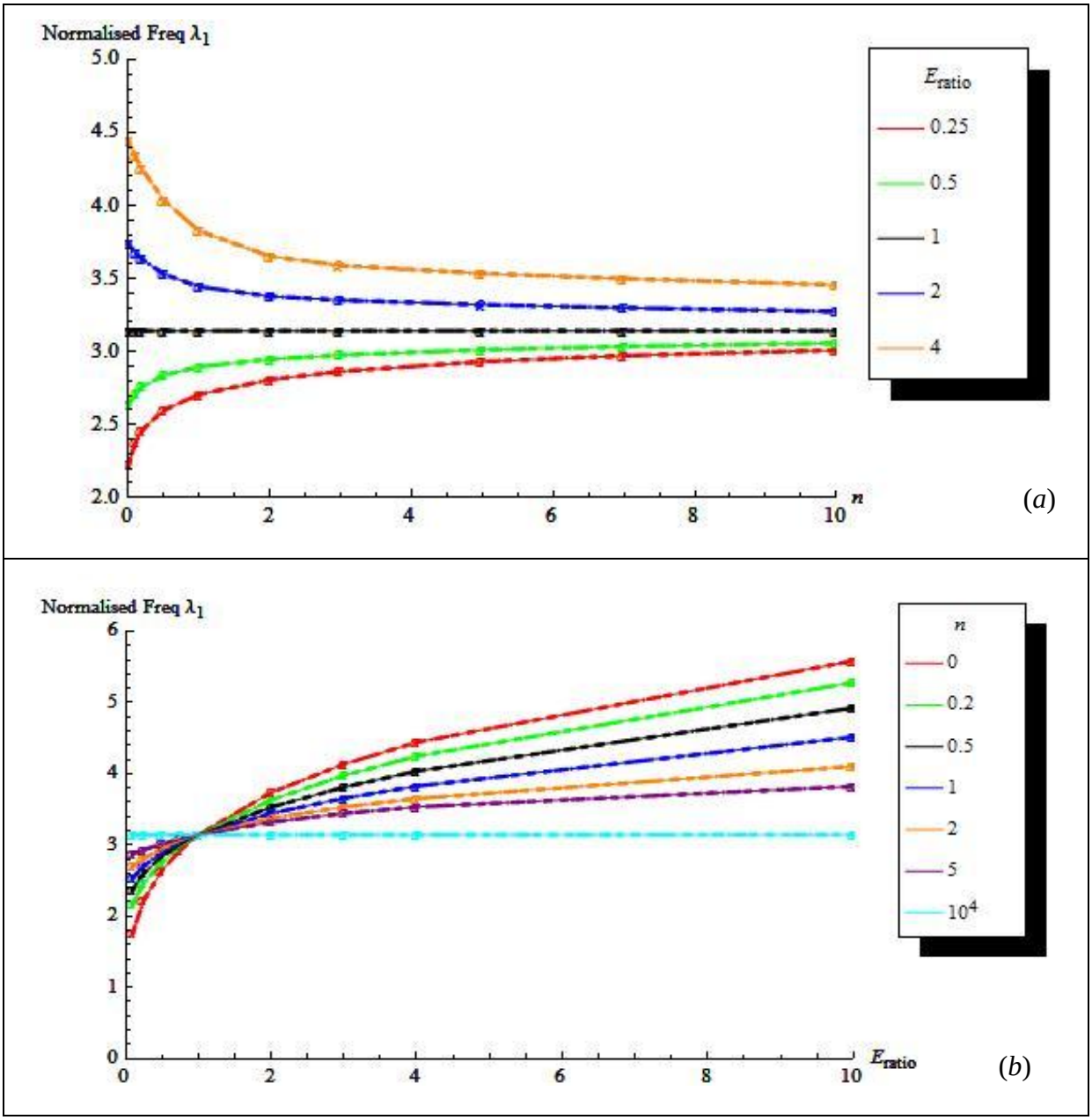

Figure 8-6: The non-dimensional fundamental frequency variation with respect to (*a*) power law exponent *n* for different E_{ratio} and (*b*) E_{ratio} for different *n*. *l*/*h* = 100. (−) FEM, (−***o*** −) D12_0 WFEM, (−**x** −) BSWI5_4 WFEM.

It is further observed from Table 8-1 that increasing n when $E_{ratio} > 1$ results in a decrease in the non-dimensional fundamental frequency until n reaches infinity; since $E_l < E_u$. These described aspects are also noticed in Figure 8-6 (a) where the non-dimensional fundamental frequency is plotted against the power law exponent n, for different values of E_{ratio}.

The non-dimensional frequency of the FG beam increases as the value of E_{ratio} increases for all values of n; with the exception of when $n = \infty$. This is because as E_{ratio} increases the FG beam has a higher bending stiffness and consequently the fundamental frequency increases. The rate of increase of the non-dimensional frequency with E_{ratio} decreases as $n \to \infty$. This is due to the fact that the normalised non-dimensional fundamental frequency λ_1 is evaluated with respect to the Young's modulus and density of the lower surface material. Increasing the value of n means the effective Young's modulus of the FG beam $E(y) \to E_l$. Therefore, at $n = \infty$, where $E(y) = E_l$, the non-dimensional frequencies will be constant (approx 3.13999) for all E_{ratio}. This is also observed from Figure 8-6 (b) where the non-dimensional fundamental frequency is plotted against E_{ratio} for different values of n.

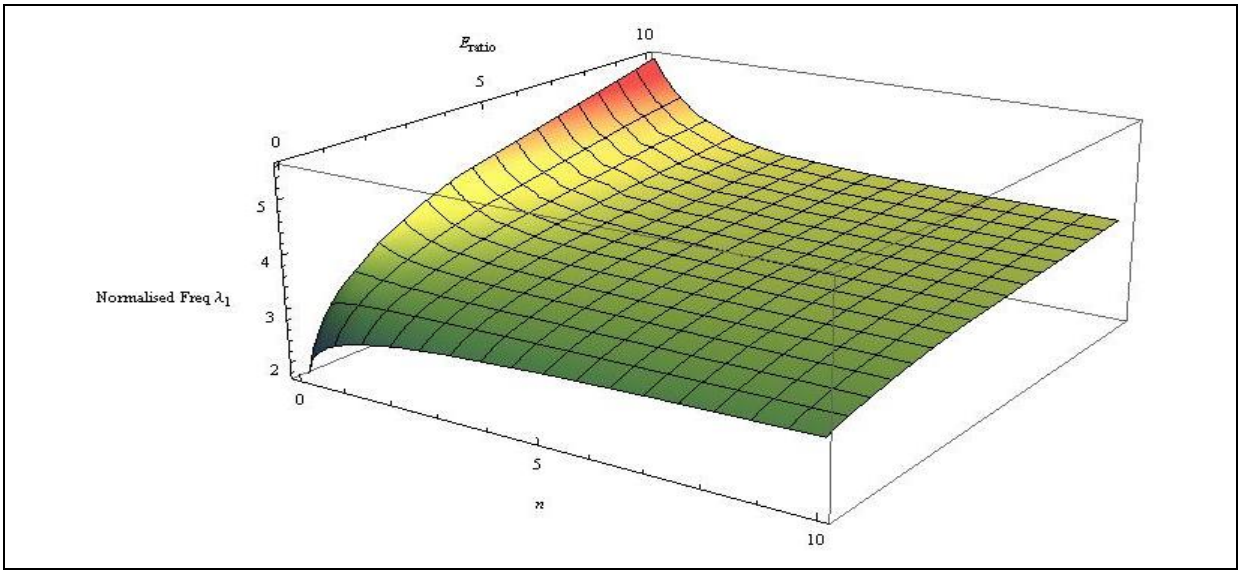

Figure 8-7: 3D plot of the non-dimensional fundamental frequency variation with respect to E_{ratio} and n for l/h = 100 using the BSWI5$_4$ WFEM.

A 3D plot representation of the non-dimensional fundamental frequency variation, with respect to E_{ratio} and n, is presented in Figure 8-7 for $\frac{l}{h} = 100$. This plot is obtained based on the results of the BSWI5$_4$ wavelet based element solution.

The plot further implies that the highest non-dimensional fundamental frequency is obtained as $n = 0$ and $E_{ratio} = 10$. However, the lowest fundamental frequency is when E_{ratio} = 0

and $n = 0$. The 3D plot for the D12_0 WFE solution is not presented since the results are similar to the BSWI5_4 WFEM solutions.

The second and third non-dimensional frequencies are presented in Table 8-2 and Table 8-3. The results obtain using both wavelet based finite element formulations are in very good agreement with those presented in [83]. However, it is observed that the non-dimensional frequencies obtained via the BSWI based WFEM are more accurate in comparison to the Daubechies based WFEM and classical FEM solutions. This difference of accuracy further increases as the modes of vibration increase.

E Ratio		***n* = 0**	***n* = 0.1**	***n* = 0.2**	***n* = 0.5**	***n* = 1**	***n* = 2**	***n* = 5**	***n* = 10**	***n* = 10^4**
0.1	Ref [83]	-	-	-	-	-	-	-	-	-
	FEM	3.52616	4.08259	4.33731	4.74328	5.0738	5.38725	5.74158	5.94654	6.27007
	Daub	3.52646	4.08008	4.33282	4.73696	5.06779	5.38309	5.74029	5.94643	6.27061
	BSWI	3.52607	4.07963	4.33233	4.73643	5.06721	5.38248	5.73965	5.94576	6.26991
0.25	Ref [83]	4.4338	4.7398	4.912	-	5.3955	5.5997	-	6.0073	-
	FEM	4.43391	4.74259	4.91646	5.19004	5.40236	5.60492	5.85238	6.00824	6.27014
	Daub	4.43429	4.7422	4.91508	5.18712	5.39913	5.60254	5.85172	6.00834	6.27068
	BSWI	4.43379	4.74167	4.91453	5.18654	5.39852	5.60192	5.85106	6.00767	6.26998
0.5	Ref [83]	5.2726	5.4124	5.5058	-	5.7789	5.882	-	6.103	-
	FEM	5.27284	5.41339	5.5072	5.6646	5.78134	5.88407	6.01324	6.10351	6.27026
	Daub	5.27329	5.41371	5.50728	5.66414	5.78061	5.88353	6.01329	6.10385	6.2708
	BSWI	5.2727	5.41311	5.50667	5.66351	5.77997	5.88287	6.01262	6.10317	6.2701
1	Ref [83]	6.2703	6.2703	6.2703	-	6.2703	6.2703	-	6.2703	-
	FEM	6.27049	6.27049	6.27049	6.27049	6.27049	6.27049	6.27049	6.27049	6.27049
	Daub	6.27103	6.27103	6.27103	6.27103	6.27103	6.27103	6.27103	6.27103	6.27103
	BSWI	6.27033	6.27033	6.27033	6.27033	6.27033	6.27033	6.27033	6.27033	6.27033
2	Ref [83]	7.4567	7.3437	7.249	-	6.8723	6.741	-	6.5346	-
	FEM	7.45692	7.34348	7.24911	7.04905	6.87521	6.74442	6.62993	6.53573	6.27096
	Daub	7.45755	7.34404	7.24951	7.04886	6.87434	6.74327	6.62942	6.5358	6.2715
	BSWI	7.45672	7.34323	7.2487	7.04808	6.87358	6.74252	6.62868	6.53507	6.2708
4	Ref [83]	8.8675	8.6607	8.4784	-	7.6304	7.2788	-	6.8946	-
	FEM	8.86782	8.66028	8.47867	8.05865	7.64009	7.29247	7.05766	6.90106	6.2719
	Daub	8.86858	8.66084	8.47876	8.05679	7.63552	7.28599	7.05272	6.89862	6.27244
	BSWI	8.86759	8.65987	8.47781	8.05589	7.63466	7.28517	7.05193	6.89785	6.27174
10	Ref [83]	-	-	-	-	-	-	-	-	-
	FEM	11.1507	10.8326	10.5448	9.8336	9.02264	8.20172	7.63969	7.45788	6.27472
	Daub	11.1516	10.8331	10.5445	9.82925	9.01194	8.18528	7.62351	7.44665	6.27525
	BSWI	11.1504	10.8319	10.5433	9.82815	9.01092	8.18435	7.62264	7.44581	6.27455

Table 8-2: The second non-dimensional frequency of a simply supported FG beam of varying composition distributions for different E_{ratio}.($\frac{\rho_u}{\rho_l} = 1, \frac{l}{h} = 20$).

The variation of the natural frequencies of the FG beam, for different values of E_{ratio} and n, are similar as those discussed for the fundamental non-dimensional frequency. Increasing E_{ratio} at lower values of n has the most significant effect on the natural frequencies than varying the values of n. Thus, the material constituents selected in FGMs are important in free vibration analysis of structures due to the differences in material and physical properties. This subsequently has a considerable effect on the dynamic response and mechanical properties of such structures.

E Ratio		$n = 0$	$n = 0.1$	$n = 0.2$	$n = 0.5$	$n = 1$	$n = 2$	$n = 5$	$n = 10$	$n = 10^4$
0.1	Ref [83]	-	-	-	-	-	-	-	-	-
	FEM	5.27639	6.11226	6.49565	7.10545	7.60005	8.0671	8.59375	8.89894	9.38226
	Daub	5.28152	6.10863	6.48569	7.08988	7.5859	8.05951	8.59615	8.9055	9.39138
	BSWI	5.2757	6.10182	4.47841	7.08187	7.57735	8.05051	8.58664	8.89569	9.38104
0.25	Ref [83]	6.6338	7.0866	7.3383	-	8.0556	8.36658	-	8.9863	-
	FEM	6.63471	7.09754	7.35887	7.77011	8.08834	8.39053	8.75872	8.99099	9.38236
	Daub	6.64115	7.10177	7.36	7.76641	8.08384	8.38916	8.76336	8.99834	9.39148
	BSWI	6.63385	7.09393	7.35185	7.75777	8.07484	8.37984	8.75368	8.98842	9.38115
0.5	Ref [83]	7.889	8.0971	8.2354	-	8.6399	8.7956	-	9.1305	-
	FEM	7.89004	8.10053	8.24119	8.47739	8.65242	8.80596	8.99853	9.13323	9.38254
	Daub	7.89771	8.10793	8.24791	8.48247	8.65674	8.81102	9.00572	9.14153	9.39166
	BSWI	7.88902	8.099	8.23882	8.47311	8.64718	8.80129	8.9958	9.13146	9.38132
1	Ref [83]	9.3816	9.3816	9.3816	-	9.3816	9.3816	-	9.3816	9.3816
	FEM	9.38289	9.38289	9.38289	9.38289	9.38289	9.38289	9.38289	9.38289	9.38289
	Daub	9.39201	9.39201	9.39201	9.39201	9.39201	9.39201	9.39201	9.39201	9.39201
	BSWI	9.38168	9.38168	9.38168	9.38168	9.38168	9.38168	9.38168	9.38168	9.38168
2	Ref [83]	11.1567	10.9872	10.8499	-	10.2747	10.0756	-	9.77344	-
	FEM	11.1582	10.9885	10.8475	10.5489	10.2895	10.0941	9.92196	9.78035	9.38359
	Daub	11.169	10.999	10.8573	10.5565	10.2947	10.0981	9.928	9.7882	9.39271
	BSWI	11.1568	10.9869	10.8454	10.5448	10.2833	10.087	9.91705	9.77742	9.38238
4	Ref [83]	13.2676	12.9571	12.6821	-	11.3924	10.8527	-	10.2862	-
	FEM	13.2694	12.9591	12.6879	12.0617	11.4386	10.9203	10.5667	10.3297	9.385
	Daub	13.2823	12.9711	12.6981	12.065	11.4323	10.9072	10.5583	10.3295	9.39412
	BSWI	13.2677	12.9568	12.6841	12.0516	11.4195	10.8949	10.5466	10.3181	9.38378
10	Ref [83]	-	-	-	-	-	-	-	-	-
	FEM	16.6854	16.2098	15.7803	14.721	13.515	12.2919	11.4476	11.1702	9.38921
	Daub	16.7016	16.2244	15.7916	14.718	13.4898	12.2466	11.4024	11.1412	9.39834
	BSWI	16.6832	16.2065	15.7742	14.7016	13.4746	12.2326	11.3893	11.1286	9.38779

Table 8-3: The third non-dimensional frequency of a simply supported FG beam of varying composition distributions for different E_{ratio}.$(\frac{\rho_u}{\rho_l} = 1, \frac{l}{h} = 20)$.

These general observations are consistent with those presented by Simsek and Kocaturk [83]. The results presented in this section show that the WFEM approaches approximate the FG

beam natural frequencies very accurately when compared with those obtained by Simsek and Kocaturk [83] and the formulations are therefore validated.

l/h = 20		n = 0	n = 0.1	n = 0.2	n = 0.5	n = 1	n = 2	n = 5	n = 10	$n = 10^4$
λ_1	BSWI5_5	4.34248	4.19217	4.07584	3.84697	3.65598	3.50318	3.36974	3.29347	3.14022
	FEM	4.34249	4.19219	4.07587	3.84706	3.65614	3.50336	3.36985	3.29352	3.14023
	D12_0	4.34248	4.19217	4.07584	3.84697	3.65598	3.50318	3.36974	3.29347	3.14022
	BSWI5_4	4.34248	4.19217	4.07584	3.84697	3.65598	3.50318	3.36974	3.29347	3.14022
λ_2	BSWI5_5	8.67165	8.37112	8.13856	7.68111	7.29967	6.99492	6.7292	6.57712	6.27081
	FEM	8.67187	8.3714	8.13898	7.68204	7.30113	6.99654	6.73023	6.57768	6.27098
	D12_0	8.67262	8.37205	8.13946	7.68197	7.30048	6.9957	6.72995	6.57786	6.27151
	BSWI5_4	8.67165	8.37112	8.13856	7.68112	7.29967	6.99492	6.7292	6.57712	6.27081
λ_3	BSWI5_5	12.9745	12.524	12.1754	11.4899	10.9191	10.4641	10.0683	9.84139	9.3824
	FEM	12.9762	12.5258	12.1777	11.4939	10.9249	10.4704	10.0726	9.84398	9.38361
	D12_0	12.9888	12.5278	12.1888	11.5026	10.9312	10.4756	10.0795	9.85225	9.38273
	BSWI5_4	12.9745	12.524	12.1754	11.49	10.9191	10.4641	10.0683	9.8414	9.3824
l/h = 50										
λ_1	BSWI5_5	4.34436	4.19403	4.07769	3.84877	3.6577	3.50478	3.37119	3.29485	3.14157
	FEM	4.34436	4.19404	4.07772	3.84886	3.65787	3.50497	3.3713	3.2949	3.14157
	D12_0	4.34436	4.19403	4.07769	3.84877	3.6577	3.50478	3.37119	3.29485	3.14157
	BSWI5_4	4.34436	4.19403	4.07769	3.84877	3.6577	3.50478	3.37119	3.29485	3.14157
λ_2	BSWI5_5	8.68657	8.38593	8.15326	7.69548	7.31343	7.00733	6.74072	6.58811	6.663
	FEM	8.68679	8.38621	8.15368	7.69638	7.31486	7.00932	6.74173	6.58866	6.66376
	D12_0	8.68754	8.38687	8.15417	7.69634	7.31425	7.00851	6.74147	6.58885	6.66374
	BSWI5_4	8.68657	8.38593	8.15326	7.69548	7.31343	7.00733	6.74072	6.58812	6.663
λ_3	BSWI5_5	13.0245	12.5736	12.2246	11.5381	10.9652	10.507	10.107	9.87823	9.99049
	FEM	13.0262	12.5754	12.2269	11.5419	10.9708	10.5131	10.1111	9.88077	9.99375
	D12_0	13.0389	12.5875	12.2381	11.5508	10.9774	10.5187	10.1181	9.88915	10.0015
	BSWI5_4	13.0245	12.5736	12.2246	11.5381	10.9652	10.507	10.107	9.87824	9.9905
l/h = 100										
λ_1	BSWI5_5	4.34462	4.1943	4.07795	3.84903	3.65795	3.50501	3.37139	3.29504	3.33251
	FEM	4.34463	4.19431	4.07798	3.84912	3.65811	3.50519	3.3715	3.2951	3.33258
	D12_0	4.34462	4.1943	4.07795	3.84903	3.65795	3.50501	3.37139	3.29504	3.33251
	BSWI5_4	4.34462	4.1943	4.07795	3.84903	3.65795	3.50501	3.37139	3.29504	3.33251
λ_2	BSWI5_5	8.68871	8.38806	8.15537	7.69754	7.31541	7.00956	6.74237	6.58969	6.66461
	FEM	8.68894	8.38834	8.15579	7.69844	7.31684	7.01115	6.74338	6.59024	6.66537
	D12_0	8.68968	8.389	8.15628	7.6984	7.31623	7.01035	6.74313	6.59043	6.66535
	BSWI5_4	8.68871	8.38806	8.15537	7.69754	7.31541	7.00957	6.74238	6.58969	6.66461
λ_3	BSWI5_5	13.0317	12.5808	12.2317	11.545	10.9719	10.5132	10.1125	9.88355	9.99591
	FEM	13.0334	12.5826	12.234	11.5489	10.9774	10.5192	10.1166	9.88608	9.99915
	D12_0	13.0461	12.5947	12.2453	11.5578	10.984	10.5249	10.1237	9.88448	10.007
	BSWI5_4	13.0317	12.5808	12.2317	11.545	10.9719	10.5132	10.1125	9.88356	9.99592

Table 8-4: The first 3 non-dimensional frequencies of a simply supported steel-alumina FG beam for different transverse varying composition distributions and slenderness ratios.

However, it must be pointed out that the assumptions made on the variations of E_{ratio} and ρ_{ratio} by Simsek and Kocaturk [83], and subsequently Alshorbagy [79], are incorrect. It is impractical to assign the value of $\rho_{\text{ratio}} = \frac{\rho_u}{\rho_l} = 1$ throughout the analysis when varying values of E_{ratio}. This assumption implies that the densities of both the top and bottom surface materials are equal and remain constant as the ratio of the Young's modulus is varying. It is noted that E_{ratio} and ρ_{ratio} cannot be assumed to have the same value since the density ratio and Young's modulus ratio will vary differently based on the constituent material properties. Thus, given that the wavelet based FGM formulation is verified, the analysis carried out in the rest of this chapter will be specific to a steel-alumina FG beam.

The Young's modulus and density of steel (bottom surface material) are $E_l = 210$ GPa and $\rho_l = 7800$ kg·m^{-3} respectively. In this section, and subsequent sections of this chapter, the effective material properties are assumed to be approximately that of steel when power law exponent $n = 10^4$. The variation of the first 3 non-dimensional frequencies with respect to n are presented in Table 8-4; for slenderness ratio $\frac{l}{h} = 20, 50, 100$. The results are obtained using two Daubechies D12_0 (37 DOFs) WFEs, one BSWI5_4 (38 DOFs) WFE and 12 classical FEs (39 DOFs). Furthermore, the solutions obtained using 2 BSWI5_5 WFEs (137 DOFs) are also presented since the solutions have converged. Thus, the results of BSWI5_5 WFEs are used as a reference for the comparison of the different solutions.

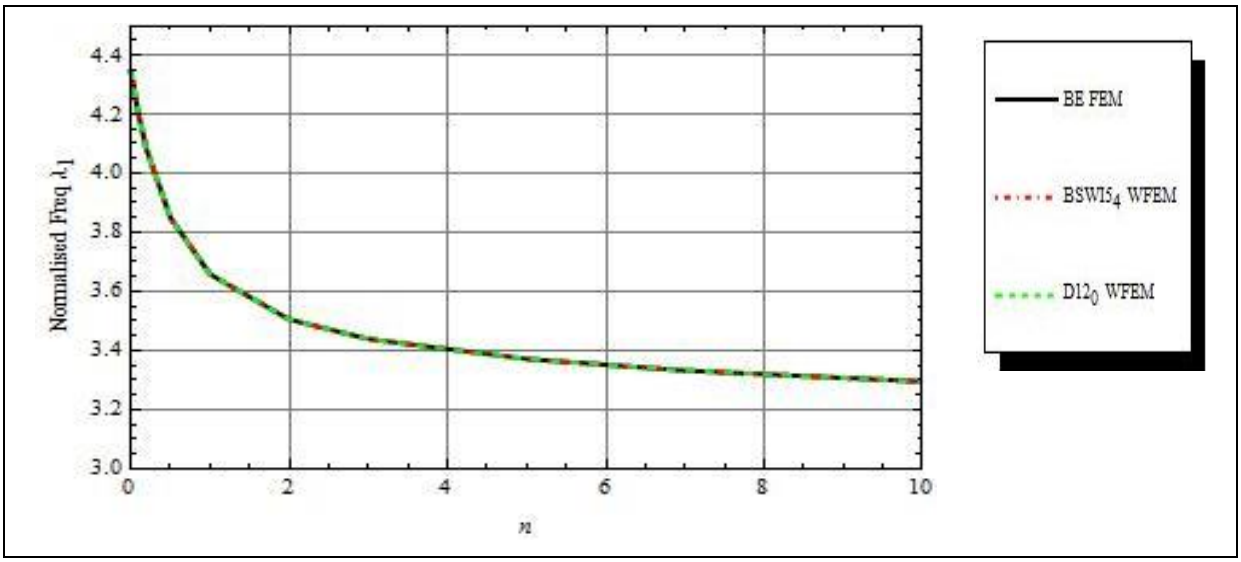

Figure 8-8: The non-dimensional fundamental frequency variation with respect to *n* for *l*/*h* = 100.

The non-dimensional frequencies of the steel-alumina beam decrease as the value of *n* increases from 0 to infinity; since the effective bending stiffness decreases. This is further evident from Figure 8-8, which illustrates the variation of the normalised fundamental frequency for different values of *n*.

Figure 8-9 shows the first 20 non-dimensional frequencies for different values of *n* via (*a*) the BSWI5_4 and (*b*) D12_0 WFEMs. The natural frequencies of the steel-alumina FG beam increase as the mode of vibration increases for the different values of *n*. The non-dimensional fundamental frequencies obtained via the D12_0 and BSWI5_4 WFEMs are in excellent agreement with the BSWI5_5 solution from Table 8-4. However, for the higher mode frequencies, the BSWI5_4 WFEM solutions are most accurate in comparison to D12_0 WFEM and classical FEM approaches. This is further evident from Figure 8-10 where the variation of the non-dimensional frequencies with respect to the first 20 modes of vibration, for $n = 5$ and $\frac{l}{h} = 100$, is presented.

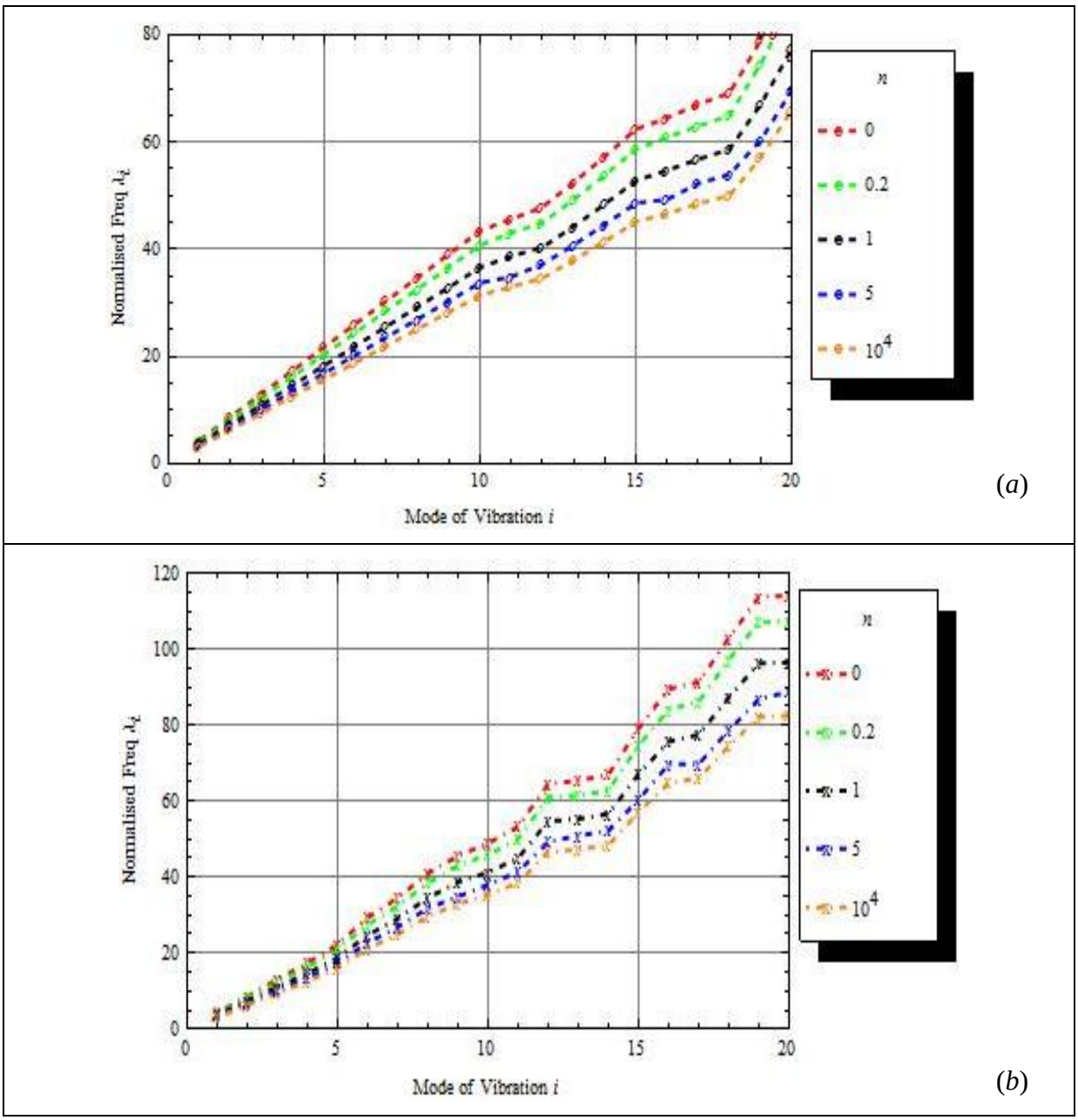

Figure 8-9: The variation of the non-dimensional frequencies for different values of *n* for *l*/*h* = 100. (*a*) BSWI5_4 and (*b*) D12_0 WFEM.

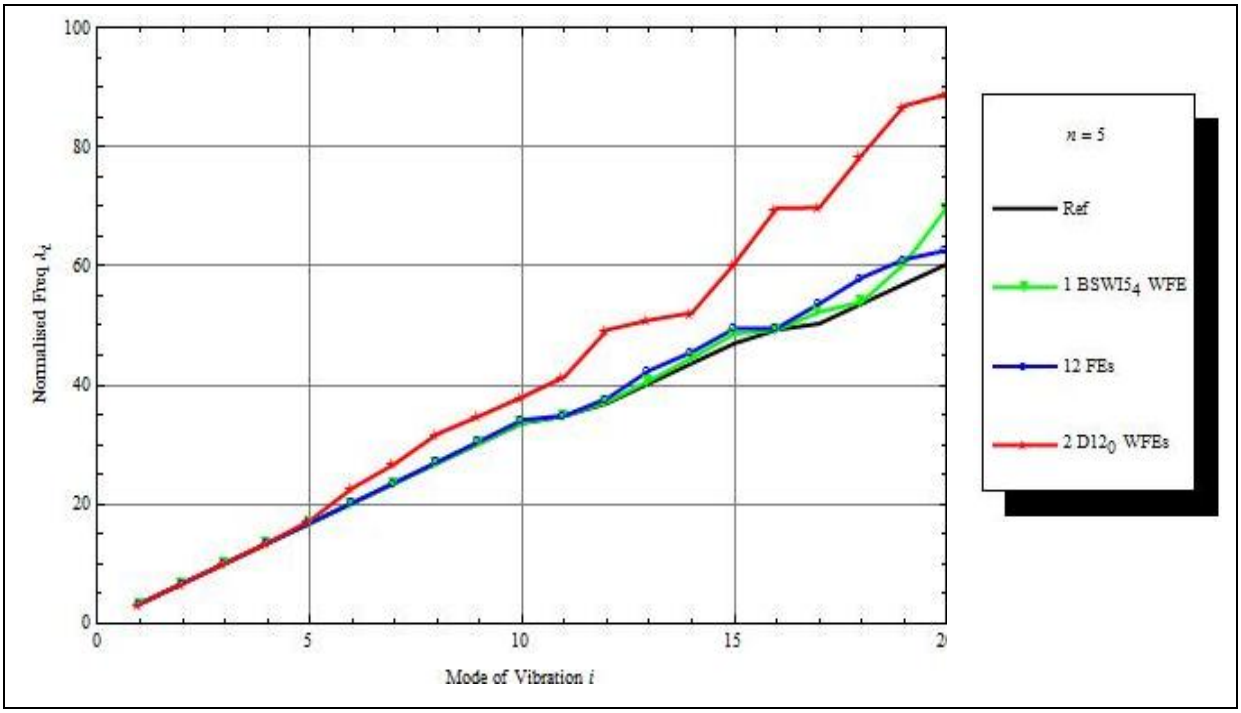

Figure 8-10: Comparison of the non-dimensional frequencies using D12_0, BSWI5_4 WFEs and 12 FEs for n = 5, l/h = 100.

It is observed that the normalised frequencies obtained via the Daubechies WFEM, for the higher modes, are not as accurate as the FEM and BSWI based WFEM solutions due to the numerical inaccuracies resulting from the evaluation of the connection coefficients. However, the results can be improved by increasing the order and/or multiresolution scale of the Daubechies based WFE; the results converge as observed in Figure 8-11. The normalised frequencies are plotted for the different orders and multiresolution scales of the Daubechies based wavelet finite elements, for $n = 5$ and $\frac{l}{h} = 100$. The black solid line indicated by "Ref" refers to the 2 element BSWI5_5 WFEM solution used for comparison. Once again it is observed that increasing the order of the Daubechies element has a more significant effect on improving the accuracy of the FG beam natural frequencies than increasing the multiresolution scale, particularly for the higher modes of vibration.

Figure 8-12 shows the non-dimensional frequencies λ_i of the FG beam analysed using different orders m and multiresolution scale j of one BSWIm_j wavelet based finite element; $n = 5$, and $\frac{l}{h} = 100$. The results demonstrate the convergence of BSWI based WFEM solution in the analysis of the functionally graded beam when the order and/or the multiresolution scale are increased. Increasing the order and/or multiresolution scale of the BSWI wavelet element leads to better approximations of the non-dimensional frequencies, particularly those associated with the higher modes of vibration. The BSWI4_3 element solution is very accurate for the first 7 non-dimensional frequencies. The frequencies are

better approximated by increasing the multiresolution scale. The BSWI4_4 solution approximates the first 17 non-dimensional frequencies very accurately. Similarly, increasing the order of the wavelet element from BSWI4_5 to BSWI5_5 improves the approximation of the non-dimensional frequencies.

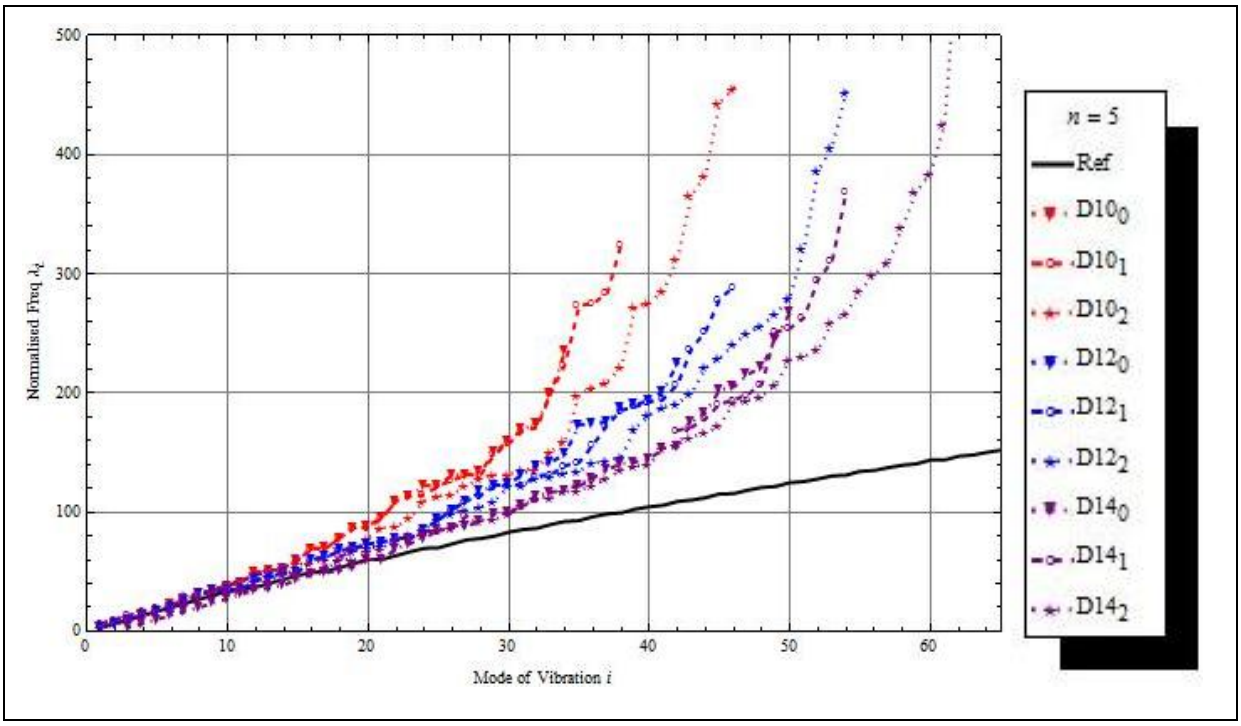

Figure 8-11: Comparison of the non-dimensional frequencies using different orders and scales of the DL_j WFE for n = 5 and l/h = 100.

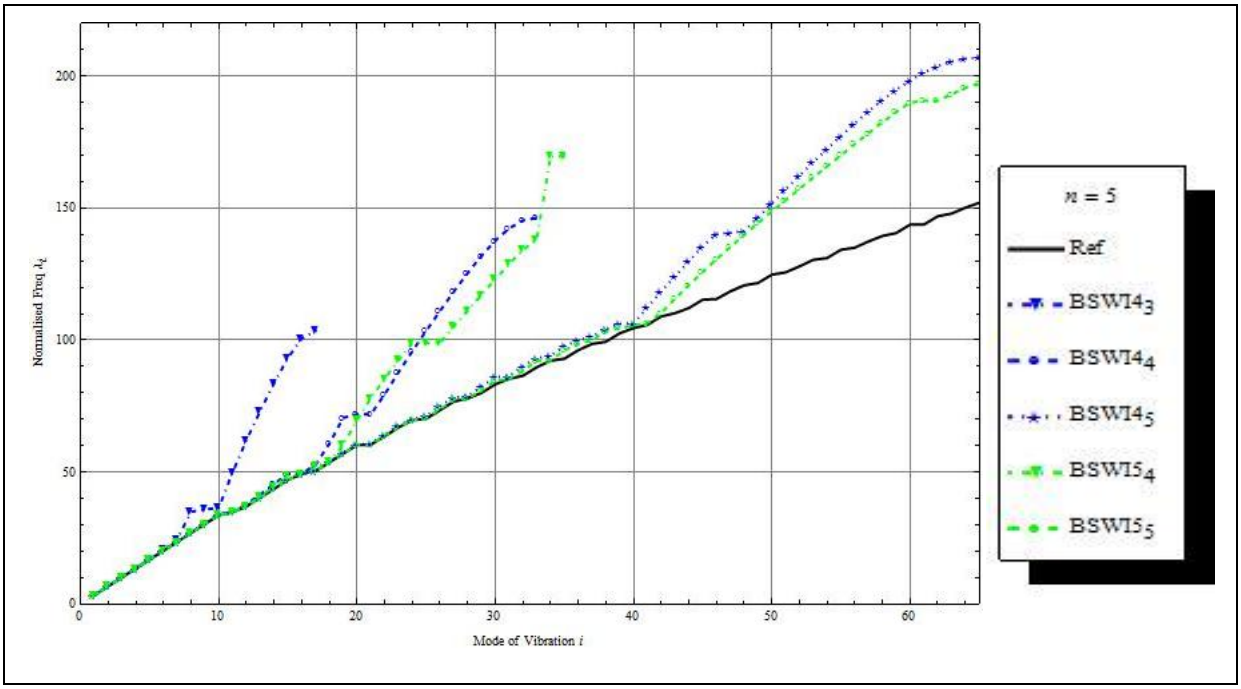

Figure 8-12: The comparison of the non-dimensional frequencies using different orders and scales of the BSWIm_j WFE for n = 5 and l/h = 100.

Figure 8-13 graphically represents the variation of λ_1 for the steel-alumina FG beam with respect to the slenderness ratio $\frac{l}{h}$ and $n = 0.5$. The classical FEM, BSWI and Daubechies based WFEM solutions are all in good agreement. The formulation of the beam elements are based on Euler-Bernoulli beam theory (the shear deformation effects are neglected). Thus, for values of $\frac{l}{h} > 20$, the variation of the fundamental frequency are small. This is also observed in Table 8-4, where for example, λ_1 when $n = 0.5$ are 3.84697, 3.84877 and 3.84903 for $\frac{l}{h} = 20, 50$ and 100 respectively (BSWI5_5 WFEM solution).

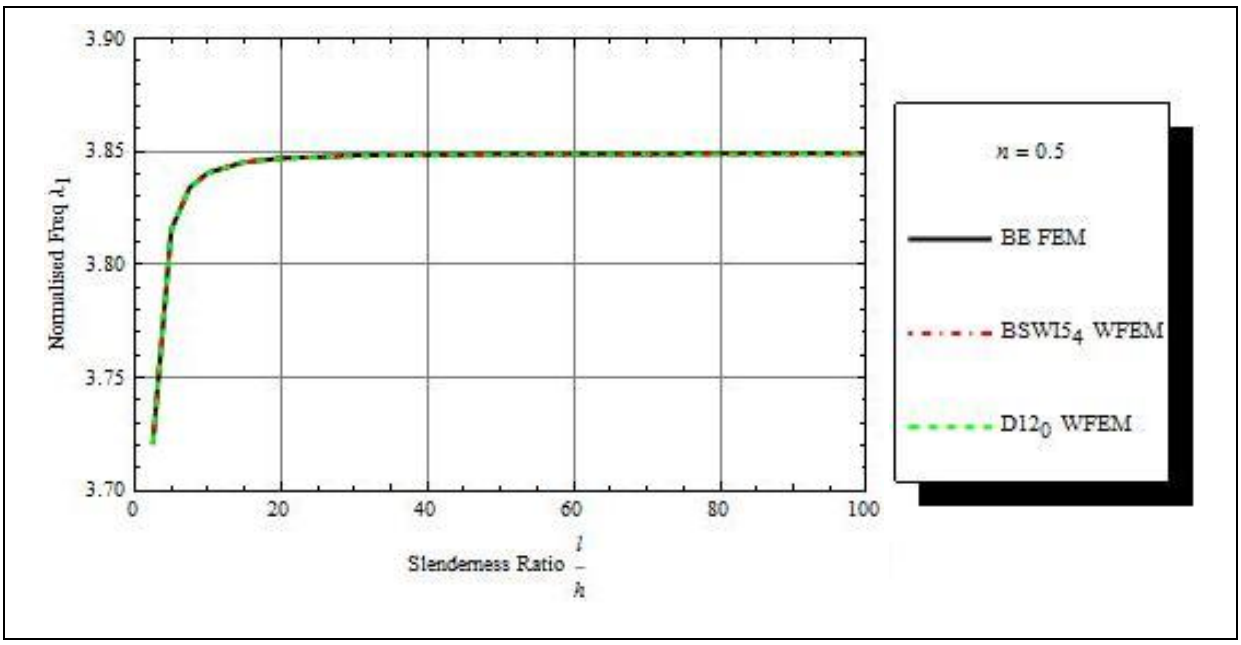

Figure 8-13: The non-dimensional fundamental frequency variation with respect to *l/h* for *n* = 0.5.

Pradhan and Chakraverty [78] analysed the impact of the slenderness ratio on the dynamic analysis of a functionally graded beam by comparing classical beam theory to Timoshenko beam theory solutions. In their analysis they conclude that for short beams ($\frac{l}{h} < 20$), the results of the non-dimensional frequencies vary considerably for the two different beam theories. However, for $\frac{l}{h} > 20$, lower mode non-dimensional frequencies are similar for both approaches. Increasing the slenderness ratio decreases the disparities between the two beam theory solutions for the higher mode frequencies. The results presented in Figure 8-13 are consistent with their findings.

The free vibration of the steel-alumina FG beam is analysed when different boundary conditions are applied, for different values of *n*. The boundary conditions are pinned-pinned (PP), pinned-clamped (PC), clamped-clamped (CC) and clamped-free (CF). Table 8-5 - Table 8-7 contain the results of the first 3 non-dimensional frequencies. The results demonstrate

that the wavelet based finite element approaches give accurate results for the different boundary conditions. In general, the different boundary restraints affect the non-dimensional frequencies of the FG beam. The highest corresponding fundamental frequencies are observed when both ends are fixed, while the least fundamental frequencies are obtained when the beam is clamped-free.

l/h = 20		***n* = 0**	***n* = 0.1**	***n* = 0.2**	***n* = 0.5**	***n* = 1**	***n* = 2**	***n* = 5**	***n* = 10**	***n* = 10^4**
PP	BSWI5_5	4.34248	4.19217	4.07584	3.84697	3.65598	3.50318	3.36974	3.29347	3.14022
	FEM	4.34249	4.19219	4.07587	3.84706	3.65614	3.50336	3.36985	3.29352	3.14023
	D12_0	4.34248	4.19217	4.07584	3.84697	3.65598	3.50318	3.36974	3.29347	3.14022
	BSWI5_4	4.34248	4.19217	4.07584	3.84697	3.65598	3.50318	3.36974	3.29347	3.14022
PC	BSWI5_5	5.4271	5.23923	5.09384	4.80779	4.56909	4.37814	4.2114	4.11608	3.92455
	FEM	5.42712	5.23928	5.09395	4.80811	4.56965	4.37877	4.21178	4.11626	3.92457
	D12_0	5.42711	5.23924	5.09384	4.80779	4.56909	4.37814	4.21141	4.11609	3.92456
	BSWI5_4	5.4271	5.23923	5.09384	4.80779	4.56909	4.37814	4.2144	4.11608	3.92455
CC	BSWI5_5	6.5373	6.31099	6.13585	5.79127	5.50374	5.27374	5.07291	4.9581	4.72738
	FEM	6.53735	6.3111	6.13609	5.79199	5.50498	5.27513	5.07375	4.95849	4.72742
	D12_0	6.5373	6.31099	6.13585	5.79127	5.50374	5.27374	5.07291	4.9581	4.72738
	BSWI5_4	6.5373	6.31099	6.13585	5.79127	5.50374	5.27374	5.07291	4.9581	4.72738
CF	BSWI5_5	2.59258	2.50286	2.43342	2.29679	2.18277	2.09152	2.01182	1.96627	1.87479
	FEM	2.59258	2.50286	2.43342	2.29682	2.18281	2.09157	2.01185	1.96628	1.87479
	D12_0	2.59258	2.50286	2.43342	2.29679	2.18277	2.09152	2.01182	1.96627	1.87479
	BSWI5_4	2.59258	2.50286	2.43342	2.29679	2.18277	2.09152	2.01182	1.96627	1.87479
l/h = 100										
PP	BSWI5_5	4.34462	4.1943	4.07795	3.84903	3.65795	3.50501	3.37139	3.29504	3.33251
	FEM	4.34463	4.19431	4.07798	3.84912	3.65811	3.50519	3.3715	3.2951	3.33258
	D12_0	4.34462	4.1943	4.07795	3.84903	3.65795	3.50501	3.37139	3.29504	3.33251
	BSWI5_4	4.34462	4.1943	4.07795	3.84903	3.65795	3.50501	3.37139	3.29504	3.33251
PC	BSWI5_5	5.43022	5.24233	5.09692	4.81079	4.57197	4.38082	4.21381	4.11838	3.92681
	FEM	5.43024	5.24238	5.09702	4.81112	4.57253	4.38144	4.21419	4.11856	3.92682
	D12_0	5.43023	5.24234	5.09692	4.8108	4.57197	4.38082	4.21382	4.11839	3.92681
	BSWI5_4	5.43022	5.24233	5.09692	4.81079	4.57197	4.38082	4.21381	4.11839	3.92681
CC	BSWI5_5	6.54131	6.31498	6.13981	5.79514	5.50745	5.27718	5.07601	4.96105	4.73028
	FEM	6.54137	6.31509	6.14005	5.79585	5.50867	5.27856	5.07685	4.96145	4.73028
	D12_0	6.54132	6.31498	6.13981	5.79514	5.50745	5.27719	5.07601	4.96106	4.73028
	BSWI5_4	6.54131	6.31498	6.13981	5.79514	5.50745	5.27718	5.07601	4.96105	4.73028
CF	BSWI5_5	2.59318	2.50345	2.43401	2.29737	2.18333	2.09204	2.01229	1.96671	1.87523
	FEM	2.59318	2.50346	2.43402	2.2974	2.18337	2.09209	2.01232	1.96673	1.87523
	D12_0	2.59318	2.50345	2.43401	2.29737	2.18333	2.09204	2.01229	1.96671	1.87523
	BSWI5_4	2.59318	2.50345	2.43401	2.29737	2.18333	2.09204	2.01229	1.96671	1.87523

Table 8-5: The non-dimensional fundamental frequency of a steel-alumina FG beam of different transverse varying distributions and boundary conditions.

l/h = 20		***n* = 0**	***n* = 0.1**	***n* = 0.2**	***n* = 0.5**	***n* = 1**	***n* = 2**	***n* = 5**	***n* = 10**	***n* = 10^4**
PP	BSWI5_5	8.67165	8.37112	8.13856	7.68111	7.29967	6.99492	6.7292	6.57712	6.27081
	FEM	8.67187	8.3714	8.13898	7.68204	7.30113	6.99654	6.73023	6.57768	6.27098
	D12_0	8.67262	8.37205	8.13946	7.68197	7.30048	6.9957	6.72995	6.57786	6.27151
	BSWI5_4	8.67165	8.37112	8.13856	7.68112	7.29967	6.99492	6.7292	6.57712	6.27081
PC	BSWI5_5	9.75388	9.4158	9.15417	8.63959	8.21052	7.8678	7.56902	7.39799	7.05342
	FEM	9.75429	9.41632	9.15498	8.64142	8.21344	7.87104	7.57106	7.39907	7.05371
	D12_0	9.75566	9.41751	9.15584	8.64117	8.21203	7.86924	7.5704	7.39934	7.0547
	BSWI5_4	9.75388	9.4158	9.15417	8.63959	8.21053	7.8678	7.56902	7.39799	7.05342
CC	BSWI5_5	10.8348	10.4592	10.1686	9.59688	9.12026	8.7396	8.40781	8.21787	7.83508
	FEM	10.8355	10.4601	10.1699	9.59999	9.12521	8.7451	8.41129	8.21971	7.83557
	D12_0	10.8388	10.4631	10.1723	9.60042	9.12363	8.74283	8.41091	8.2209	7.83796
	BSWI5_4	10.8348	10.4592	10.1686	9.59689	9.12027	8.73961	8.40782	8.21787	7.83508
CF	BSWI5_5	6.48085	6.25631	6.08254	5.74073	5.45565	5.22783	5.02912	4.91543	4.68656
	FEM	6.4809	6.2564	6.08271	5.74121	5.45647	5.22875	5.02968	4.9157	4.68659
	D12_0	6.48086	6.25632	6.08256	5.74074	5.45567	5.22784	5.02913	4.91544	4.68657
	BSWI5_4	6.48085	6.25631	6.08254	5.74073	5.45566	5.22783	5.02912	4.91543	4.68656
l/h = 100										
PP	BSWI5_5	8.68871	8.38806	8.15537	7.69754	7.31541	7.00956	6.74237	6.58969	6.66461
	FEM	8.68894	8.38834	8.15579	7.69844	7.31684	7.01115	6.74338	6.59024	6.66537
	D12_0	8.68968	8.389	8.15628	7.6984	7.31623	7.01035	6.74313	6.59043	6.66535
	BSWI5_4	8.68871	8.38806	8.15537	7.69754	7.31541	7.00957	6.74238	6.58969	6.66461
PC	BSWI5_5	9.77473	9.4365	9.17473	8.65966	8.22977	7.8857	7.58512	7.41335	7.06849
	FEM	9.77513	9.43702	9.17552	8.66145	8.23263	7.88888	7.58713	7.41442	7.06879
	D12_0	9.7765	9.43821	9.17639	8.66124	8.23127	7.88714	7.5865	7.4147	7.06977
	BSWI5_4	9.77473	9.4365	9.17473	8.65967	8.22977	7.8857	7.58512	7.41335	7.06849
CC	BSWI5_5	10.8597	10.4839	10.1931	9.62083	9.14322	8.76096	8.42702	8.23619	7.85305
	FEM	10.8604	10.4848	10.1944	9.62387	9.14808	8.76636	8.43044	8.238	7.85355
	D12_0	108636	10.4877	10.1968	9.62433	9.14655	8.76416	8.43009	8.23918	7.8559
	BSWI5_4	10.8597	10.4839	10.1931	9.62083	9.14322	8.76097	8.42702	8.23619	7.85305
CF	BSWI5_5	6.49133	6.26671	6.092287	5.75083	5.46534	5.23684	5.03722	4.92315	4.69413
	FEM	6.49138	6.2668	6.092305	5.75131	5.46615	5.23775	5.03778	4.92342	4.69417
	D12_0	6.49134	6.26673	6.092289	5.75084	5.46535	5.23686	5.03723	4.92316	4.69415
	BSWI5_4	6.49133	6.26671	6.092287	5.75083	5.46534	5.23684	5.03722	4.92315	4.69413

Table 8-6: The second non-dimensional frequency of a steel-alumina FG beam of different transverse varying distributions and boundary conditions.

Therefore, increasing the number of restrained DOFs increases the fundamental frequencies of the FG beam for the different values of *n*. This is important in the dynamic analysis of structures as higher values of the fundamental frequencies imply a reduction in vibrations when subjected to different loading conditions; such as harmonic or moving loads.

l/h = 20		***n* = 0**	***n* = 0.1**	***n* = 0.2**	***n* = 0.5**	***n* = 1**	***n* = 2**	***n* = 5**	***n* = 10**	***n* = 10^4**
PP	BSWI5_5	12.9745	12.524	12.1754	11.4899	10.9191	10.4641	10.0683	9.84139	9.3824
	FEM	12.9762	12.5258	12.1777	11.4939	10.9249	10.4704	10.0726	9.84398	9.38361
	D12_0	12.9888	12.5378	12.1888	11.5026	10.9312	10.4756	10.0795	9.85225	9.38273
	BSWI5_4	12.9745	12.524	12.1754	11.49	10.9191	10.4641	10.0683	9.8414	9.3824
PC	BSWI5_5	14.052	13.5639	13.1862	12.4437	11.8254	11.3327	10.9043	10.6586	10.1616
	FEM	14.0545	13.5667	13.1898	12.4501	11.8347	11.3428	10.911	10.6627	10.1634
	D12_0	14.079	13.59	13.2116	12.4677	11.8483	11.3546	10.9253	10.6791	10.1811
	BSWI5_4	14.0252	13.5639	13.1863	12.4438	11.8254	11.3327	10.9043	10.6587	10.1616
CC	BSWI5_5	15.1292	14.6036	14.1969	13.3974	12.7317	12.2013	11.7404	11.4759	10.9405
	FEM	15.1328	14.6077	14.2021	13.4067	12.7454	12.2163	11.7503	11.4818	10.9431
	D12_0	15.1928	14.665	14.2567	13.454	12.7855	12.253	11.7899	11.5242	10.9865
	BSWI5_4	15.1292	14.6036	14.1969	13.3975	12.7317	12.2014	11.7404	11.4759	10.9405
PC	BSWI5_5	10.8196	10.444	10.1534	9.58194	9.10587	8.72624	8.39595	8.20664	7.82405
	FEM	10.8202	10.4448	10.1545	9.5843	9.10954	8.7303	8.39856	8.20808	7.82453
	D12_0	10.8251	10.4493	10.1586	9.58684	9.11054	8.73072	8.40026	8.21084	7.82805
	BSWI5_4	10.8196	10.444	10.1534	9.58194	9.10587	8.72625	8.39596	8.20664	7.82405
l/h = 100										
PP	BSWI5_5	13.0317	12.5808	12.2317	11.545	10.9719	10.5132	10.1125	3.29504	3.33251
	FEM	13.0334	12.5826	12.234	11.5489	10.9774	10.5192	10.1166	3.2951	3.33258
	D12_0	13.0461	13.5947	12.2453	11.5578	10.984	10.5249	10.1237	3.29504	3.33251
	BSWI5_4	13.0317	12.5808	12.2317	11.545	10.9719	10.5132	10.1125	3.29504	3.33251
PC	BSWI5_5	14.1176	13.629	13.2509	12.507	11.8861	11.3892	10.9551	10.7071	10.209
	FEM	14.1201	13.6318	13.2544	12.5131	11.895	11.3989	10.9617	10.711	10.2108
	D12_0	14.1444	13.655	13.2762	12.5308	11.9088	11.411	10.9761	10.7275	10.2284
	BSWI5_4	14.1176	13.629	13.2509	12.507	11.8861	11.3892	10.9551	10.7071	10.209
CC	BSWI5_5	15.2034	14.6773	14.2701	13.4689	12.8003	12.2652	11.7977	11.5306	10.9942
	FEM	15.2071	14.6813	14.2752	13.4779	12.8135	12.2796	11.8074	11.5364	10.9968
	D12_0	15.2662	14.7379	14.329	13.5247	12.8533	12.3161	11.8466	11.5783	11.0396
	BSWI5_4	15.2034	14.6773	14.2701	13.469	12.8003	12.2652	11.7978	11.5306	10.9942
PC	BSWI5_5	10.8611	10.4853	10.1944	9.62205	9.14437	8.76209	8.42814	8.2373	7.85409
	FEM	10.8618	10.4861	10.1955	9.62437	9.14797	8.76606	8.4307	8.23872	7.85458
	D12_0	10.8667	10.4907	10.1996	9.62702	9.1491	8.76662	8.43249	8.24155	7.85814
	BSWI5_4	10.8611	10.4853	10.1944	9.62206	9.14438	8.7621	8.42815	8.2373	7.8541

Table 8-7: The third non-dimensional frequency of a steel-alumina FG beam of different transverse varying distributions and boundary conditions.

A graphical representation of these results is presented in Figure 8-14. The variation of λ_1 with respect to *n*, for the different boundary conditions, is presented. It can also be observed that λ_1 varies more rapidly for values of $n \ll 1$, as $n \to 2$, than when $n > 2$ as $n \to \infty$.

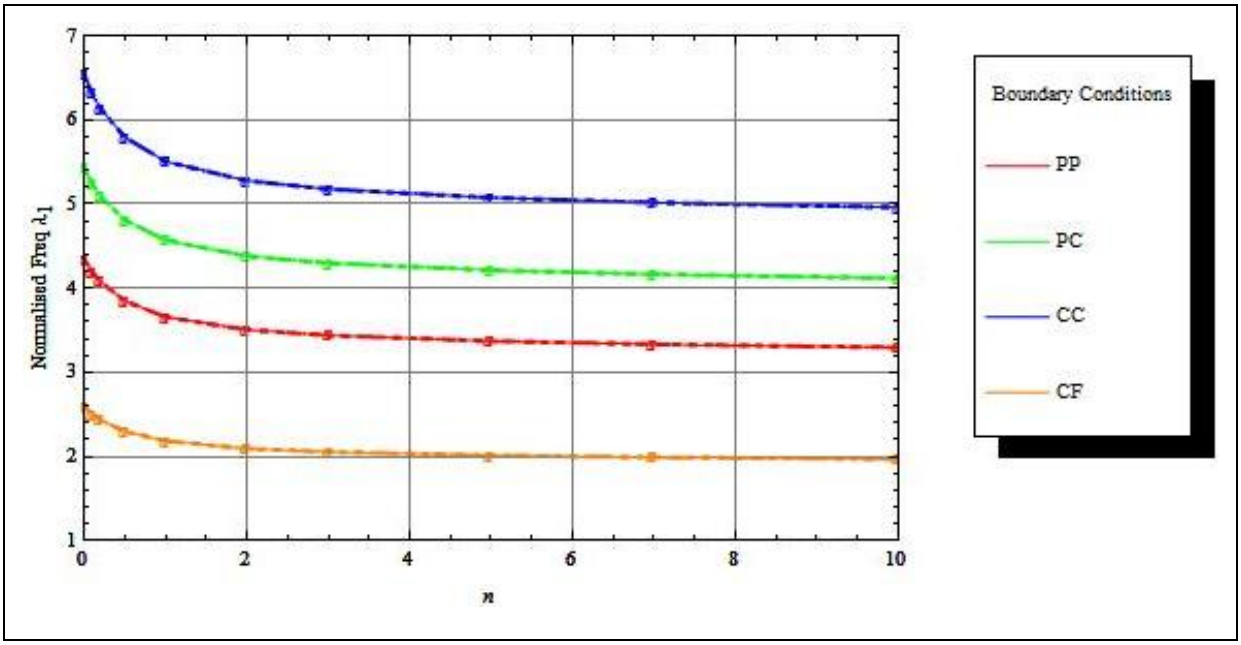

Figure 8-14: The non-dimensional fundamental frequency variation with respect to *n* for different boundary conditions. (−) FEM, (−***o*** −) D12_0 WFEM, (−**x** −) BSWI5_4 WFEM.

8.4. Simply supported functionally graded beam subjected to a moving load

A simply supported steel-alumina functionally graded beam is subjected to a moving point load of magnitude $P = 1 \text{ x } 10^5$ N, travelling across at c m·s^{-1}, as described in Figure 8-15. The FG beam, of length $l = 20$ m, has a uniform cross-sectional area $A = 0.36$ m^2 and moment of inertia $I = 2.43 \text{ x } 10^{-2}$ m^4. The upper surface is fully alumina and the lower surface fully steel, with material properties $E_u = 3.9 \text{ x } 10^{11}$ Pa, $\rho_u = 3.96 \text{ x } 10^3$ kg·m^{-3} and $E_l = 2.1 \text{ x } 10^{11}$ Pa, $\rho_l = 7.8 \text{ x } 10^3$ kg·m^{-3} respectively. E and ρ denote the Young's modulus and density respectively. The behaviour of the beam is described using Euler Bernoulli beam theory and is assumed to be undamped. The transverse gradation of the constituent materials is governed by the power law.

The governing equation describing the dynamic behaviour of the system is given by [102**]**:

$$EI\frac{\partial v^4(x,t)}{\partial x^4} + \mu\frac{\partial v^2(x,t)}{\partial t^2} + 2\mu\omega_d\frac{\partial v}{\partial t} = P\,\delta(x - x_0) \qquad \textbf{(8.66)}$$

which can also be expressed as:

$$[\boldsymbol{M}]\{\ddot{\boldsymbol{H}}(\boldsymbol{t})\} + [\boldsymbol{K}]\{\boldsymbol{H}(\boldsymbol{t})\} = \{\boldsymbol{F}(\boldsymbol{t})\} \qquad \textbf{(8.67)}$$

where the matrices $[\boldsymbol{M}]$ and $[\boldsymbol{K}]$ are the assembled functionally graded beam mass and stiffness matrices in physical space. $\{\boldsymbol{F}(\boldsymbol{t}\}$ is the time-dependent moving load vector. The

acceleration and displacement vectors of the system are denoted by $\{\ddot{\boldsymbol{H}}(\boldsymbol{t})\}$, and $\{\boldsymbol{H}(\boldsymbol{t})\}$ respectively.

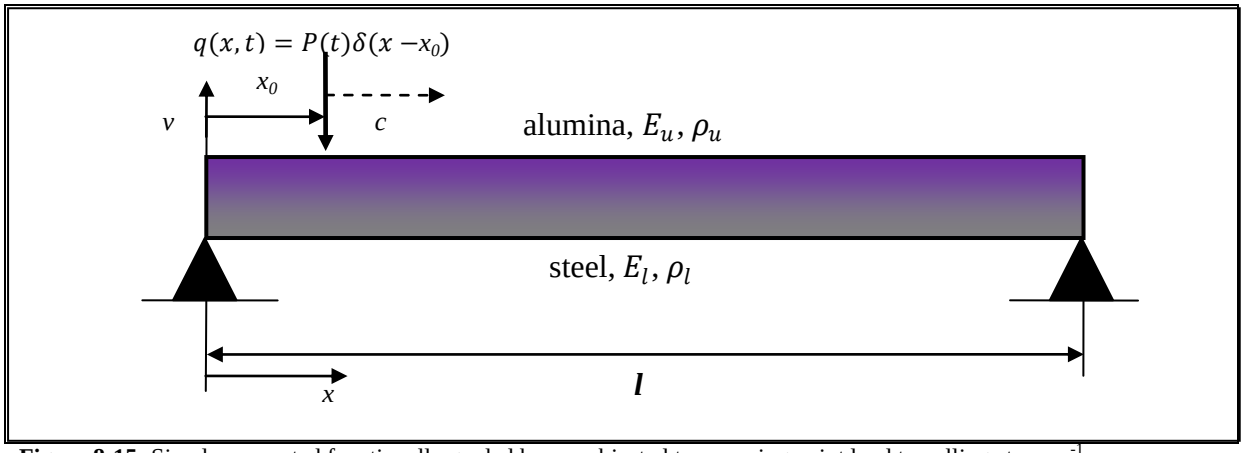

Figure 8-15: Simply supported functionally graded beam subjected to a moving point load travelling at c m·s^{-1}.

The dynamic response of the system is carried out via the Newmark time integration method with a time step of $\Delta t = 1.0 \text{ x } 10^{-5}$ s. This value ensures numerical stability and sufficient numerical accuracy for the dynamic response analysis. The deflection of the beam $v(x,t)$, as the moving load travels across, is normalised as a non dimensional parameter $v(x,t)/v_0$ where:

$$v_0 = \frac{Pl^3}{48E_l I} \tag{8.68}$$

This is the deflection at the centre of a similar simply supported steel beam when a static load of magnitude *P* is acting at the mid-span. The dynamic response of the beam is carried out at the centre of the beam, $x = \frac{l}{2}$, which corresponds to the position at which maximum deflection is expected to occur. The analysis is carried out using 2 BSWI4_3 (37 DOFs) and 2 D12_0 (37 DOFs) WFEs. The WFEM results are compared with the classical FEM solution formulated using 12 elements (39 DOFs).

Simsek and Kocaturk [83] carry out the analysis of a simply supported FG beam subjected to a moving harmonic load. The critical velocity of the moving load is initially based on the resonance of the beam due to the harmonic component of the load. In their study, they determine the velocity of the moving point load, with no harmonic component, that gives the highest maximum displacement at the centre of the beam. The focus of their study is the dynamic response when the frequency of the harmonic load corresponds with the fundamental frequency of the FG beam for a specific value of *n*. In the present study however, the moving load has no harmonic component and the analysis of the dynamic

response is carried out for subcritical, critical and supercritical velocity profiles. The term critical load velocity corresponds to the maximum displacement attained by the moving load for different values of *n*.

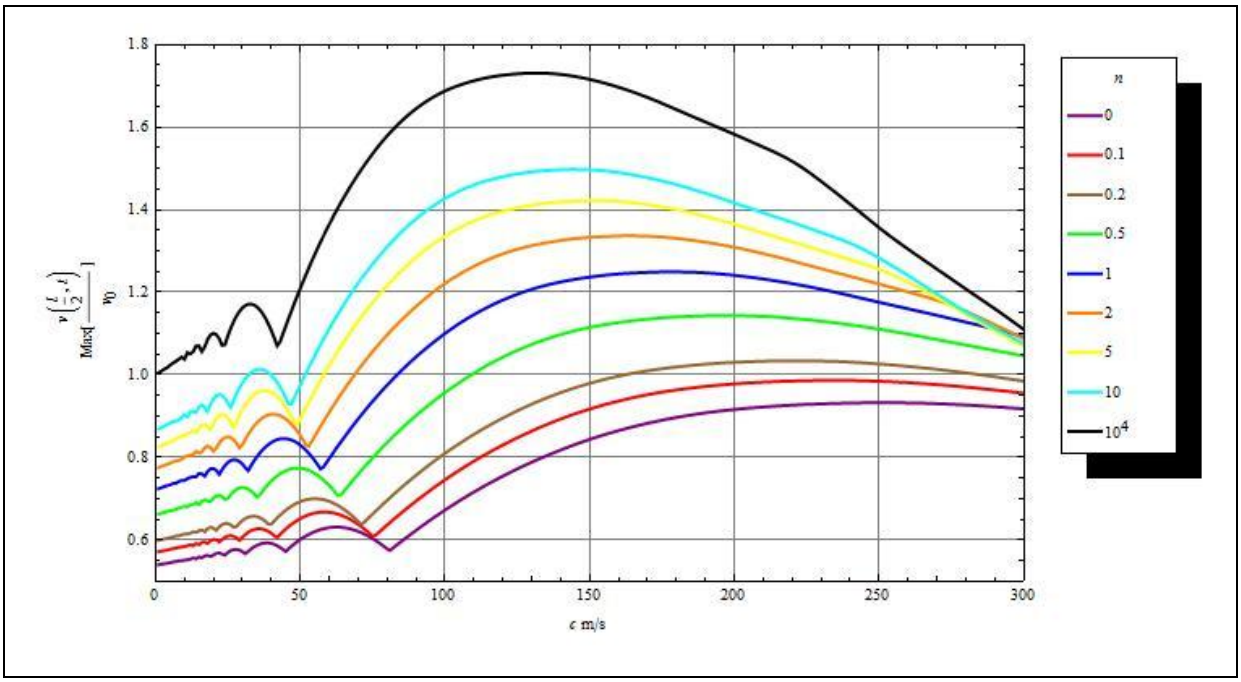

Figure 8-16: The variation of the maximum non-dimensional vertical displacement at the centre of a simply supported FG beam subjected to a moving load, with respect to the load velocities, for different *n*.

The variation of the maximum normalised deflection at mid-span, with respect to the moving load velocity, is presented in Figure 8-16 for different values of *n*. The graph is obtained for the velocity range $0 < c \leq 300$ m·s^{-1} at increments of 1 m·s^{-1}. The results presented are obtained via the BSWI4_3 WFEM solution. The results of the Daubechies D12_0 WFEM and classical FEM solutions are similar and are therefore not presented.

Initially, the maximum non-dimensional vertical displacement increases as the moving load velocity increases; for all the values of *n*. However, this maximum displacement reaches a peak value which corresponds to the critical velocity of the moving load. All the velocities below this critical velocity will be referred to as subcritical velocities in the present study. As the velocity of the moving point load further increases, the maximum deflection at the centre of the beam begins to decrease. The velocities higher than the critical velocities will be referred to as the supercritical velocities of the moving load.

The maximum normalised deflection of the FG beam also increases as $n \to \infty$. When $n = 0$, the beam is fully alumina and the effective Young's modulus $E(y) = E_u$. The maximum normalised deflection therefore increases when the value of *n* is increased since there is a decrease in stiffness. Thus, the highest values of the maximum vertical displacement are

obtained when the beam is fully steel ($n = 10^4 \cong \infty$) since $E_l < E_u$. This is consistent with the findings of Simsek and Kocaturk [83].

	Critical velocity c **m/s**				**Max**$\left[\frac{v(\frac{l}{2},t)}{v_0}\right]$			
n	**Ref** [83]	**FEM**	**D**12_0	**BSWI**4_3	**Ref** [83]	**FEM**	**D**12_0	**BSWI**5_4
0	252	252	252	252	0.9328	0.9322	0.9323	0.9322
0.1	-	235	235	235	-	0.9863	0.9864	0.9863
0.2	222	222	222	222	1.0344	1.0340	1.0340	1.0340
0.5	198	198	198	198	1.1444	1.1435	1.1437	1.1436
1	179	178	178	178	1.2503	1.2491	1.2495	1.2493
2	164	164	164	164	1.3376	1.3363	1.3368	1.3365
3	-	157	158	158	-	1.3747	1.3751	1.3748
5	-	151	151	152	-	1.4217	1.422	1.4218
7	-	148	148	148	-	1.4567	1.4570	1.4568
10	-	145	145	145	-	1.4974	1.4976	1.4974
10^4	132	132	132	132	-	1.7308	1.7309	1.7308

Table 8-8: The critical velocity and maximum normalised deflection at the centre of a steel-alumina FG beam for different values of *n*.

Table 8-8 shows the critical velocities and corresponding non-dimensional maximum deflections at the centre of the FG beam, for different values of *n*. The results presented are in relation to Figure 8-16. The solutions are obtained via the 12 classical FEs, 2 D12_0 WFEs and 2 BSWI4_3 WFEs formulations. The results are compared with the values obtained in Simsek and Kocaturk [83], and the Daubechies and BSWI WFEM solutions are found to be in very good agreement.

The variation of the maximum non-dimensional vertical displacement with respect to $n \in [0,10]$, for different moving load velocities, is presented in Figure 8-17. In Figure 8-18, the maximum deflection is plotted against the percentage content of steel within the FG beam. According to both graphs it is observed that as the value of *n* increases, for the different moving load velocities, the maximum deflection at the centre of the FG beam increases. This is because the volume fraction, and subsequently the percentage content, of steel within the FG beam increases. Since steel has a lower Young's modulus with respect to alumina, an increase in *n* results in a decrease in the effective bending stiffness. Hence, the maximum deflection of the beam increases.

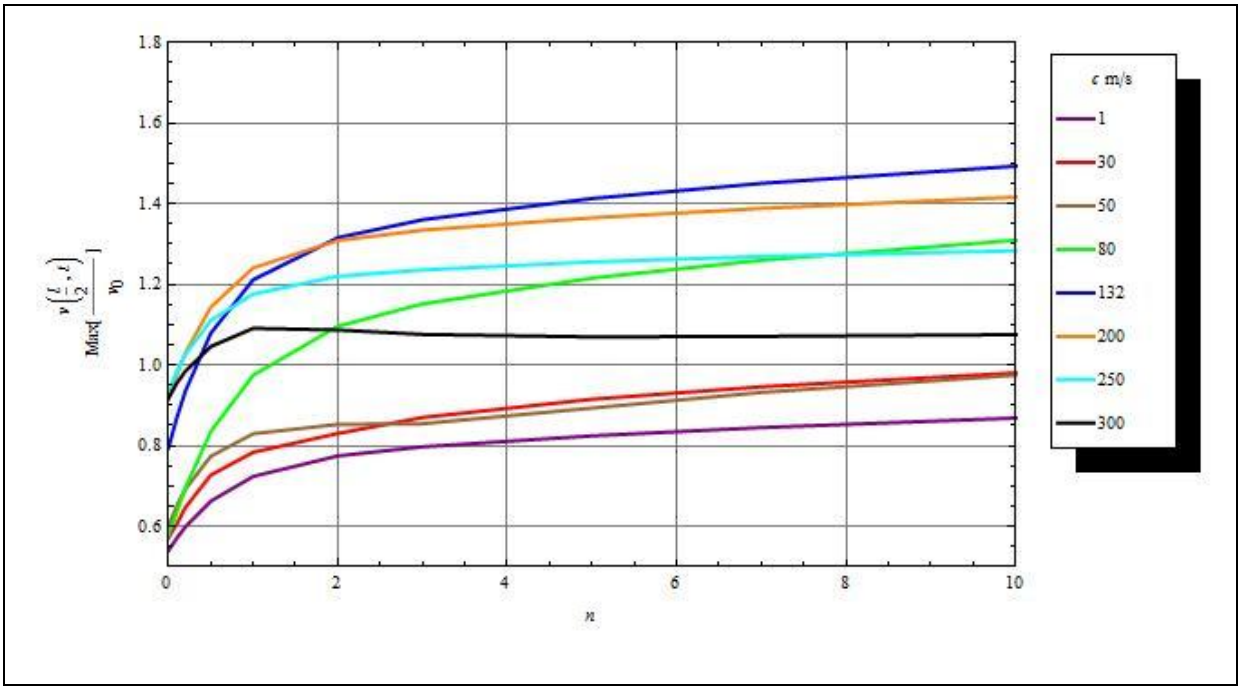

Figure 8-17: The variation of the non-dimensional maximum vertical displacement with respect to *n*, for different moving load velocities.

For the fully steel beam, as the moving load velocities increase, the maximum non-dimensional vertical displacement also increases; until 132 m·s^{-1}. The maximum displacement occurs when the velocity is $c = 132$ m·s^{-1}, which is the critical moving load velocity with respect to the fully steel beam. Increasing the velocity thereafter results in the decrease of the maximum displacement. Furthermore, the rate of increase of the maximum deflection increases as the percentage content of steel approaches 100%.

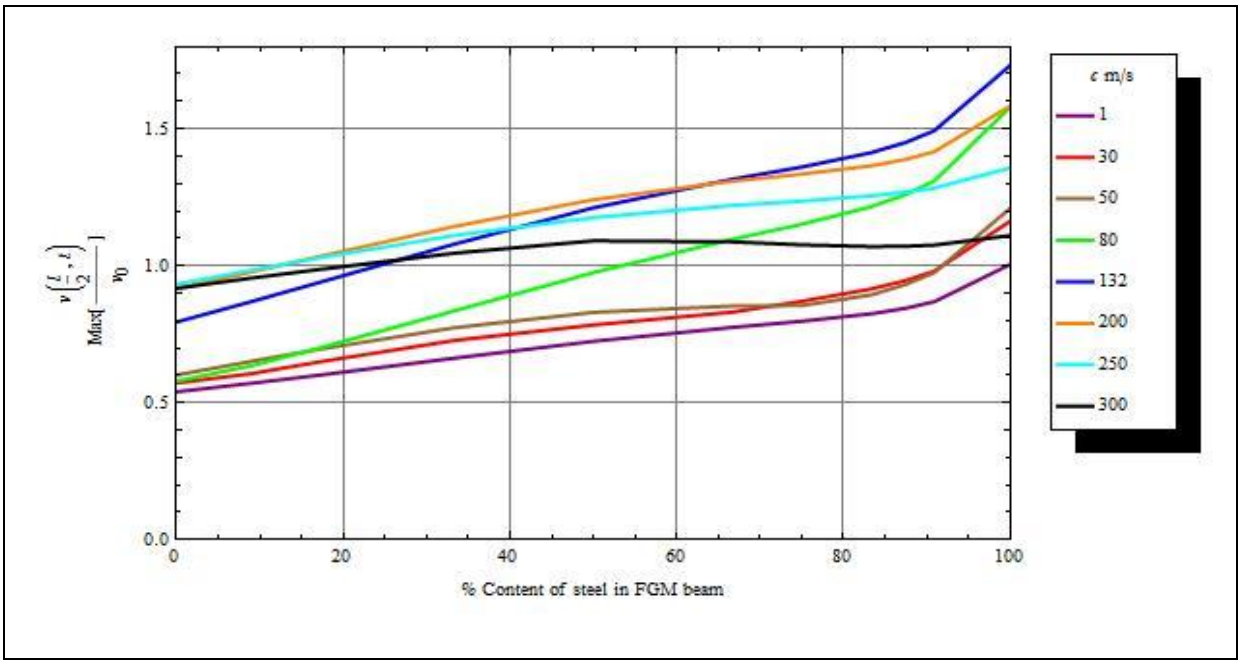

Figure 8-18: The variation of the non-dimensional maximum vertical displacement with respect to the percentage volume content of steel in the FG beam for different moving load velocities.

Figure 8-19 illustrates the non-dimensional vertical displacement variation as a moving point load travels across at $c = 250$ m·s^{-1} for $n = 0.1$. The plot shows that the results obtained via the different approaches are in excellent agreement with each other. The dynamic response of the beam obtained via the three approaches, for different velocity and power law variation profiles, are of similar accuracy. The subsequent results presented in this section will be from either of the implemented WFE approaches since the dynamic responses for different velocity profiles and power law exponents are similar. It will be stated which approach the results presented are obtained from.

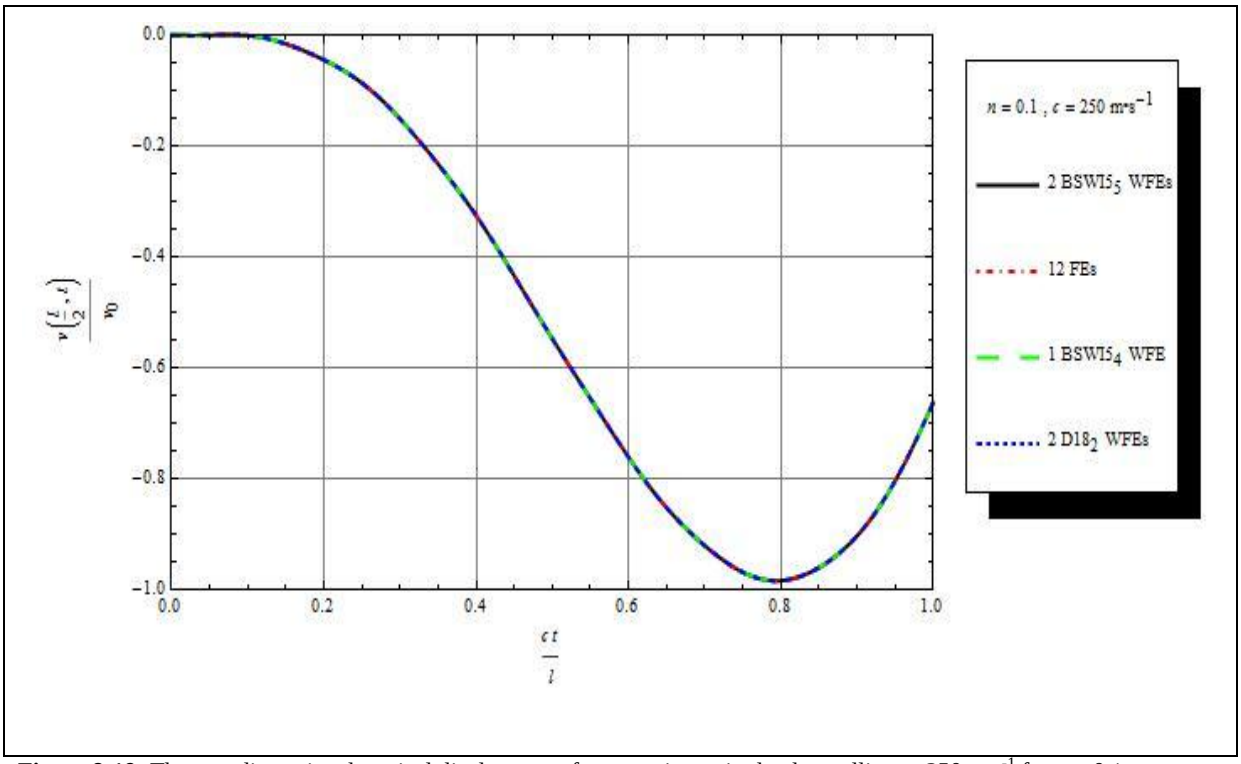

Figure 8-19: The non-dimensional vertical displacement for a moving point load travelling at 250 m.s^{-1} for n = 0.1.

Figure 8-20 illustrates the variation of the non-dimensional displacement at the centre of the steel-alumina beam. The response is analysed for different values of n as the moving point load travels across the beam at 1 m·s^{-1}. The non-dimensional time parameter is denoted by $\frac{ct}{l}$. The results presented are obtained using 2 D12_0 WFEs. The velocity of the moving load is very slow and the response is similar to that of a static point load placed at different positions of the beam over a given time span. The effect of varying the power law exponent on the dynamic response of the beam is clearly observed from this plot i.e., as n increases the deflection of the FG beam also increases as earlier discussed.

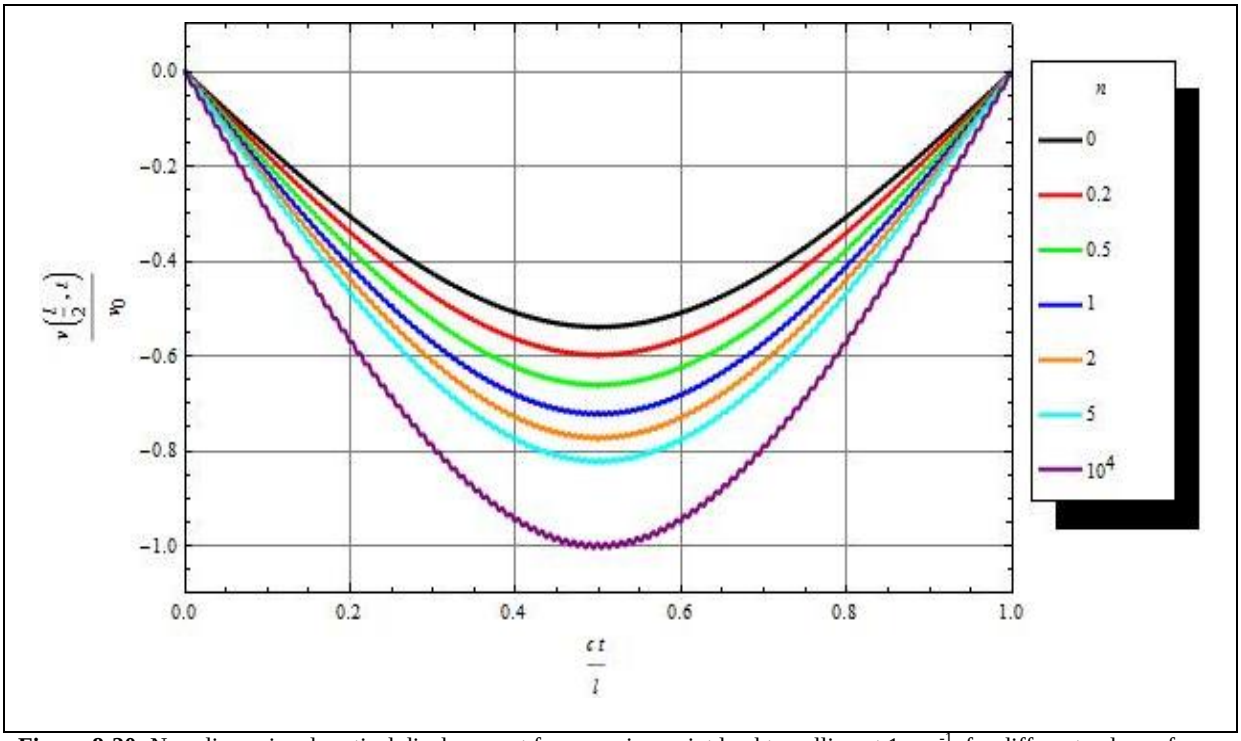

Figure 8-20: Non-dimensional vertical displacement for a moving point load travelling at 1 m·s^{-1}, for different values of *n*.

The non-dimensional deflection is also analysed for the subcritical, critical and supercritical velocity profiles. The values of *n* are varied and the dynamic responses are compared as illustrated in Figure 8-21. The velocities *a*) 50 m·s^{-1} *b*) 132 m·s^{-1} and *c*) 250 m·s^{-1} are selected to represent the 3 velocity profiles. The results presented are obtained using 2 D12_0 WFEs. It is important to note that the velocity profiles are based on a fully steel beam subjected to the moving point load, which has a critical moving load velocity of 132 m·s^{-1}. In Figure 8-21 *a*) the moving point load is travelling at a subcritical velocity for all the different material distributions. As expected, the largest deflection is observed when the beam is fully steel, which is considerably larger than the other variations of *n*. For subcritical velocities, reducing the value of *n* leads to a general decrease in deflection and this is due to the increase in effective stiffness. This decrease of the dynamic response of the FG beam is also observed in the analysis carried out for the other velocity scenarios as presented in Figure 8-21. In Figure 8-21 *b*), the applied moving load travels at 132 m·s^{-1}, which coincides with the critical velocity for the fully steel beam. In contrast, for values $n < 10^4$, this velocity of the moving load is subcritical. This can be confirmed from the critical velocities for different values of *n* presented earlier in Table 8-8. The dynamic response of the FG beam as the moving load travels across at 250 m·s^{-1} is illustrated in Figure 8-21 *c*). The moving load velocity is supercritical for all the variations of *n* analysed, with the exception of $n = 0$, to which it is very close to the critical velocity of the fully alumina beam (252 m·s^{-1}).

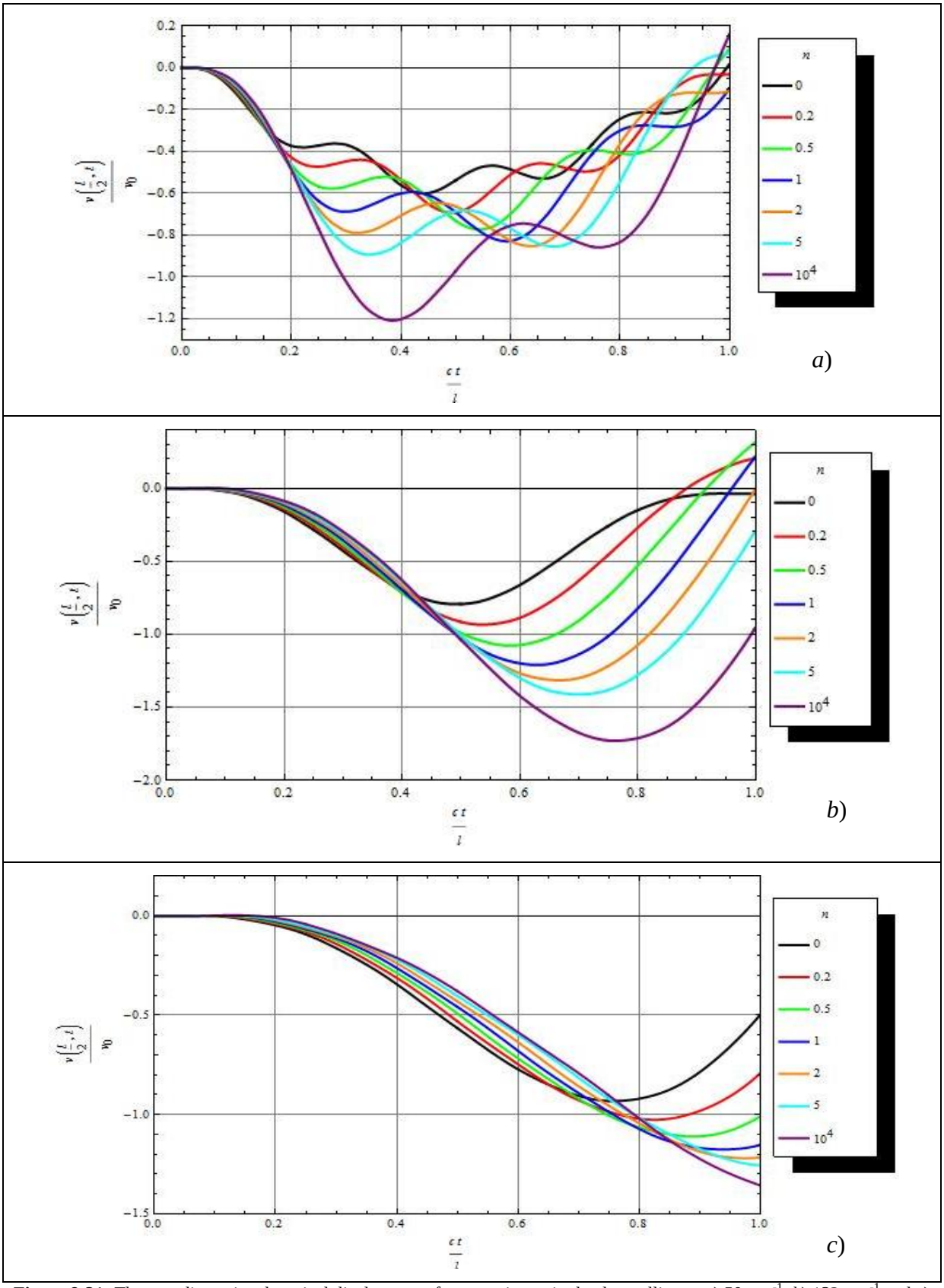

Figure 8-21: The non-dimensional vertical displacement for a moving point load travelling at *a*) 50 m·s^{-1}, *b*) 132 m·s^{-1} and *c*) 250 m·s^{-1}, for different values of *n*.

In addition to the results in Figure 8-21, the variation of the non-dimensional deflection, as the moving point load travels across at 1 m·s^{-1}, 50 ms^{-1}, 132 m·s^{-1} and 250 m·s^{-1}, is presented in Figure 8-22; for values of n: *a*) 0 *b*) 0.2 *c*) 0.5 *d*) 1 *e*) 2 *f*) 5 and *g*) 10^4.

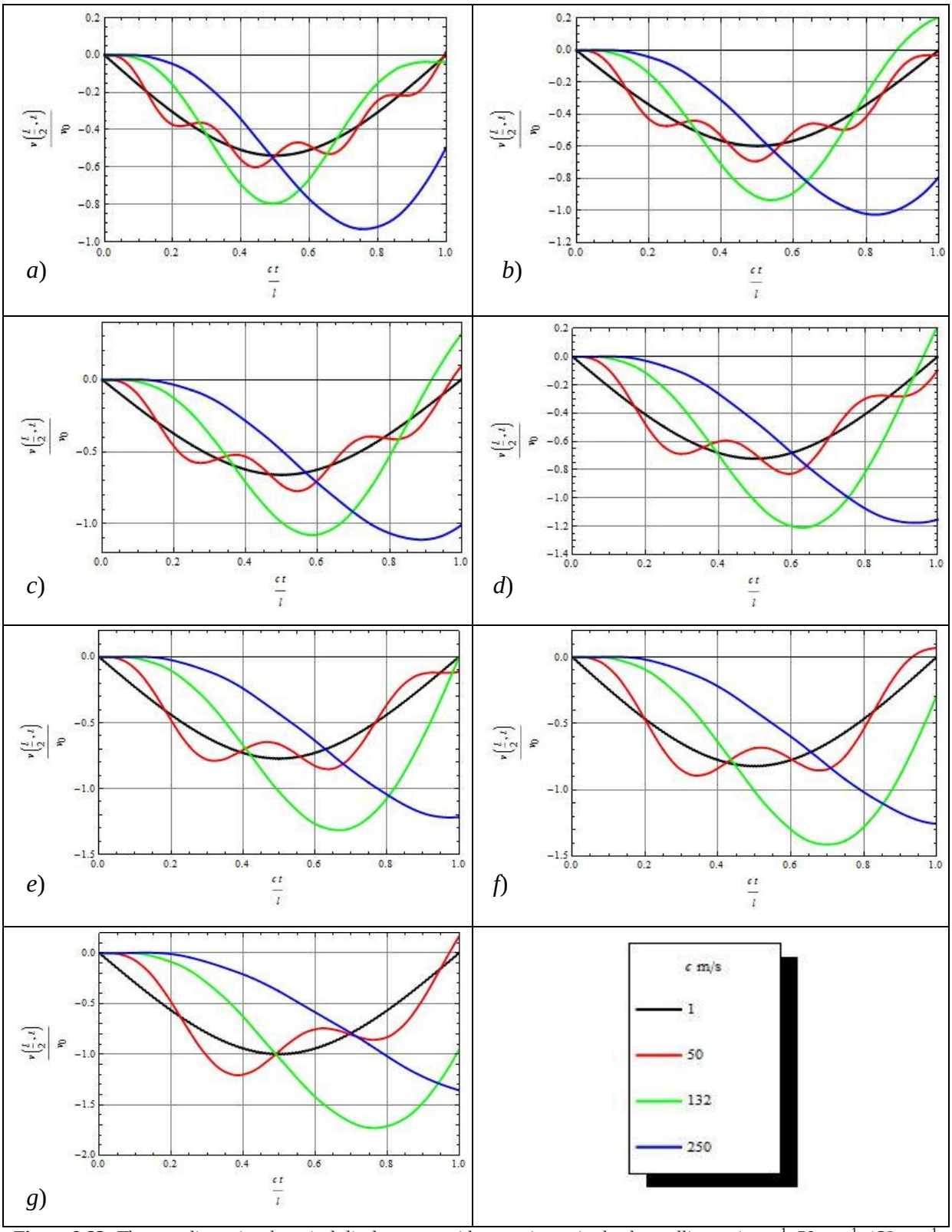

Figure 8-22: The non-dimensional vertical displacement with a moving point load travelling at 1 m·s^{-1}, 50 m·s^{-1}, 132 m·s^{-1} and 250 m·s^{-1}, for values of n: *a*) 0 *b*) 0.2 *c*) 0.5 *d*) 1 *e*) 2 *f*) 5 and *g*) 10^4.

The 2 element BSWI4_3 WFEM solution is used to obtain the results presented in Figure 8-22. It is observed that there is a general increase in vertical displacement as *n* increases; for all the applied moving load velocities. However, the responses of the beam as *n* increases, particularly for the applied velocities $c = 132$ m·s^{-1} and $c = 250$ m·s^{-1}, are of particular interest. It is observed from Figure 8-22 *a*) ($n = 0$) that the maximum deflection of the FG beam when the moving load is travelling at $c = 132$ m·s^{-1} is smaller than when the load is travelling at $c = 250$ m·s^{-1}. This is expected since the applied moving load velocity $c = 250$ m·s^{-1} is very close to the critical velocity of the FG beam associated with $n = 0$ (252 m·s^{-1}) from Table 8-8. However, as the value of *n* increases to 0.2 and 0.5, as illustrated in Figure 8-22 *b*) and Figure 8-22 *c*) respectively, it is noted that the difference between the maximum displacement when $c = 250$ m·s^{-1} and $c = 132$ m·s^{-1} is decreasing. When *n* = 1 (Figure 8-22 *d*)), the maximum displacements for both moving load velocities are similar in magnitude. However, the response characteristics of the beam are different for these two applied moving load velocities because $c = 250$ m·s^{-1} is supercritical and $c = 132$ m·s^{-1} is still subcritical with respect to *n* = 1 (critical velocity of 178 m·s^{-1}). In Figure 8-22 *e*) it is observed that the maximum vertical displacement is now achieved from the applied moving load velocity of $c = 132$ m·s^{-1} instead of $c = 250$ m·s^{-1} when *n* = 2. The difference between the maximum displacement when $c = 132$ m·s^{-1} and $c = 250$ m·s^{-1} continues to increase as *n* increases to 5 and 10^4 as observed in Figure 8-22 *f*) and Figure 8-22 *g*) respectively.

It is further observed that at 50 m·s^{-1}, the centre of the beam oscillates as the moving load travels across. When *n* = 0 the amplitude of the oscillations are small but the cycles are more frequent with shorter wavelengths. Increasing the value of *n* results in an increase in amplitude and wavelength; thus making the cycles less frequent. This is attributed to the fact that as the bending stiffness of the FG beam decreases, with increase in *n*, the magnitude of the amplitude and the wavelengths increase.

This therefore suggests that, depending on the applied moving load velocity, a variation of material distribution can lead to a significant change in the dynamic response of a system. This is not only with regards to the maximum deflection, but also the response characteristics. Furthermore, the variation of the material distribution of the FG beam can influence the velocity profile of the same applied moving load, thus impacting the dynamic response of a system. For example, in Figure 8-22 *a*) when *n* = 0, the applied moving load velocity $c = 132$ m·s^{-1} is subcritical. However, when *n* = 10^4, this same applied load velocity is now critical and the dynamic response significantly varies, as illustrated in Figure 8-22 *g*).

Moreover, the maximum deflection of the FG beam corresponding to a particular value of *n* increases at a greater rate for increasing subcritical velocities relatively closer to the critical velocity than the rate of decrease for increasing supercritical velocities.

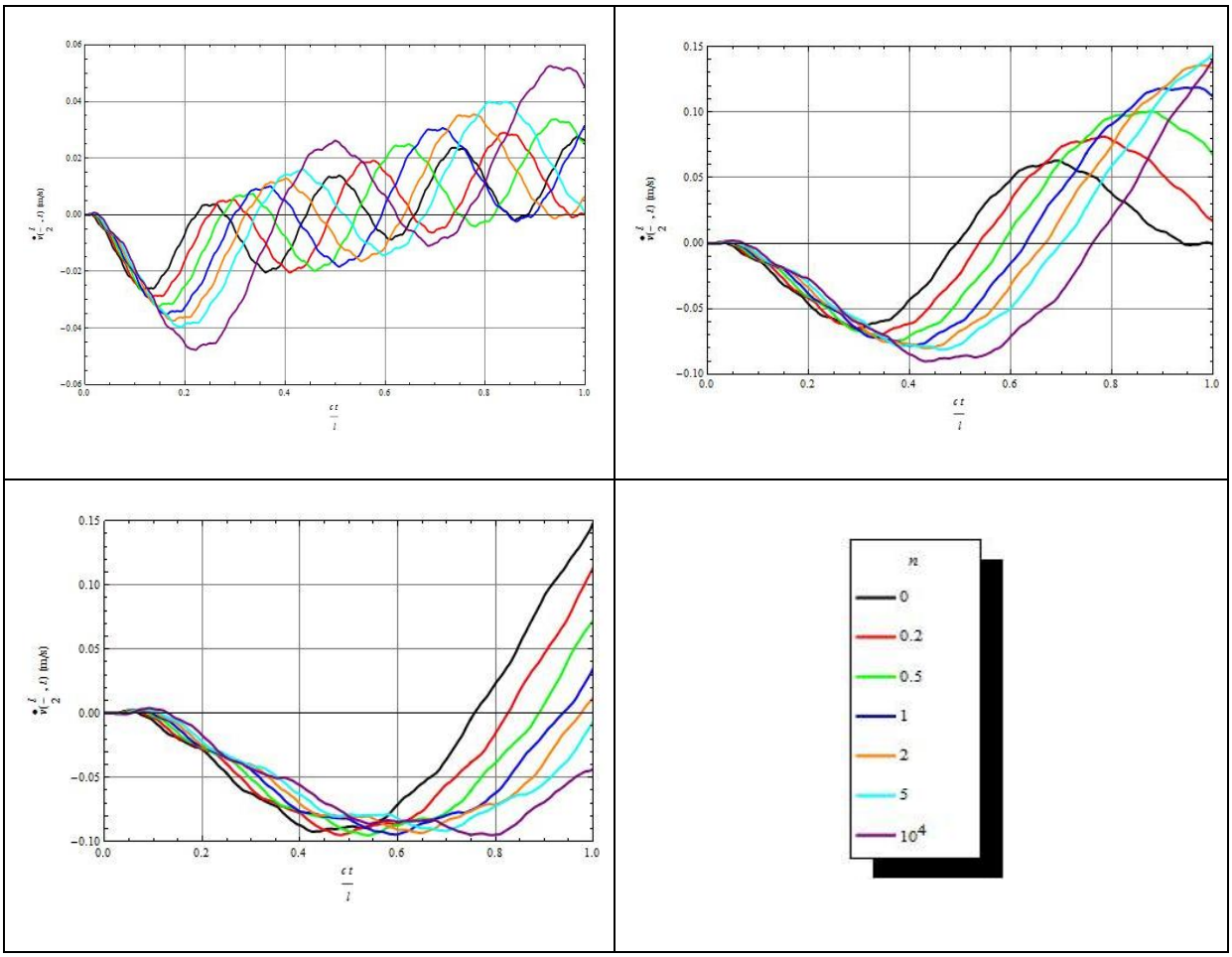

Figure 8-23: The vertical velocity at the centre of a simply supported FG beam subjected to a moving point load travelling at *a*) 50 m·s^{-1}, *b*) 132 m·s^{-1} and *c*) 250 m·s^{-1}, for different values of *n*.

Figure 8-23 illustrates the vertical velocity at the centre of the functionally graded beam for different values of *n*. The corresponding variations of the vertical acceleration of the FG beam, as the moving load travels across for the three velocity scenarios, are presented in Figure 8-24. These results are in relation to the deflection curves presented in Figure 8-21 and are obtained via two BSWI4_3 WFEs.

This is the first time the Daubechies and BSWI WFEMs are implemented to analyse the dynamic response of a functionally graded beam subjected to a moving load. According to the results presented in this section, both wavelet finite element approaches give very accurate results.

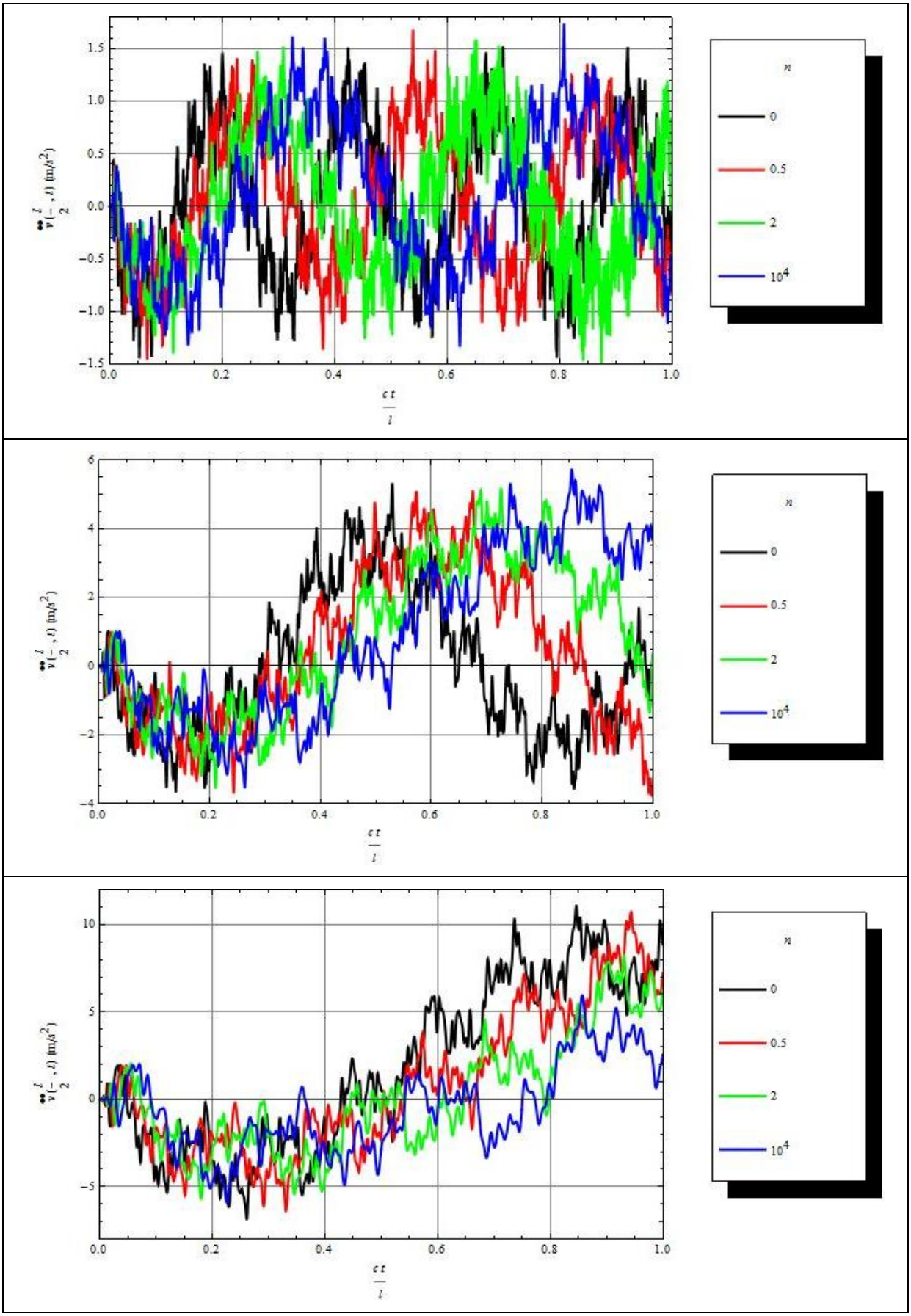

Figure 8-24: The vertical acceleration at the centre of a simply supported steel-alumina FG beam subjected to a moving point load travelling at *a*) 50 m·s^{-1}, *b*) 132 m·s^{-1} and *c*) 250 m·s^{-1} for different values of *n*.

The initial results of the moving load critical velocities are consistent with the results presented by Simsek and Kocaturk [83]; therefore the analysis is verified. The effects of varying the material distribution on the dynamics responses of the functionally graded beam, for different velocity profiles, is presented and discussed. Although the results obtained via the different approaches are of similar levels of accuracy, the BSWI solutions are marginally more accurate than the Daubechies and classical finite element methods, with similar number of DOFs implemented. In this numerical example, the wavelet family orders and multiresolution scales are selected for comparison purposes and the results are obtained with a similar number of DOFs. Furthermore, this is a relatively simple numerical example. Therefore, a comparison of the computational costs for the different approaches is not presented in this section.

8.5. Simply supported functionally graded beam on viscoelastic foundation subjected to a moving load

The dynamic response of a functionally graded beam subjected to a moving point load, while resting on a viscoelastic foundation, is analysed and presented for the first time in this section. The analysis is an extension of the numerical example presented in Section 7.3 of the previous chapter. The functionally grade beam, of length $l = 200$ m, comprises of steel at the bottom surface and alumina at the top surface. The material distribution varies in the transverse direction based on the power law.

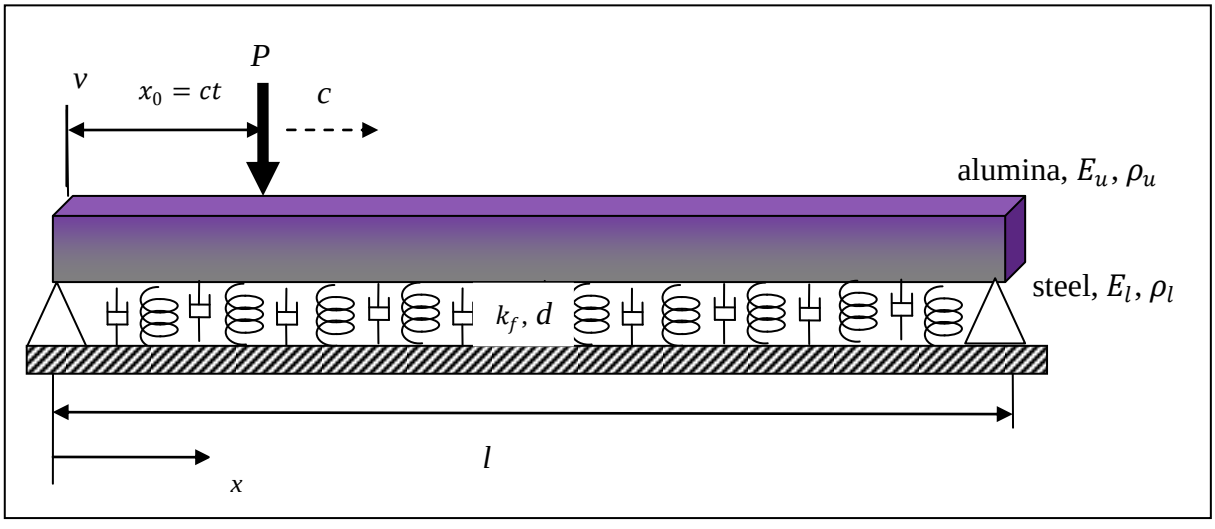

Figure 8-25: Simply supported functionally graded beam resting on a viscoelastic foundation subjected to a moving load point load.

The dynamic behaviour of the system, as illustrated in Figure 8-25, is described by the governing equation [102]:

$$EI\frac{\partial v^4(x,t)}{\partial x^4}+\mu\frac{\partial v^2(x,t)}{\partial t^2}+d\frac{\partial v(x,t)}{\partial t}+v(x,t)=P\,\delta(x-x_0) \quad \textbf{(8.69)}$$

which can also be expressed as:

$$[\boldsymbol{M}]\{\ddot{\boldsymbol{H}}(\boldsymbol{t})\}+[\boldsymbol{C_f}]\{\dot{\boldsymbol{H}}(\boldsymbol{t})\}+([\boldsymbol{K_f}]+[\boldsymbol{K}])\{\boldsymbol{H}(\boldsymbol{t})\}=\{\boldsymbol{F}(\boldsymbol{t})\} \quad \textbf{(8.70)}$$

where the matrices $[\boldsymbol{M}]$ and $[\boldsymbol{K}]$ are the assembled functionally graded beam mass and stiffness matrices in physical space. The assembled foundation damping and stiffness matrices are $[\boldsymbol{C_f}]$ and $[\boldsymbol{K_f}]$ respectively. $\{\boldsymbol{F}(\boldsymbol{t}\}$ is the time-dependent moving load vector. The acceleration, velocity and displacement vectors of the system are denoted by $\{\ddot{\boldsymbol{H}}(\boldsymbol{t})\}, \{\dot{\boldsymbol{H}}(\boldsymbol{t})\}$ and $\{\boldsymbol{H}(\boldsymbol{t})\}$ respectively.

The cross-sectional area $A = 7.684 \text{ x } 10^{-3}$ m^2 of the FG beam is assumed to be uniform through the entire length of the beam. The moment of inertia of the FG beam is $I = 3.055 \text{ x } 10^{-5}$ m^4. The material properties of the upper surface and lower surface constituent materials are: $E_u = 3.9 \text{ x } 10^{11}$ Pa, $\rho_u = 3.96 \text{ x } 10^3$ kg·m^{-3} and $E_l = 2.1 \text{ x } 10^{11}$ Pa, $\rho_l = 7.8 \text{ x } 10^3$ kg·m^{-3} respectively. E and ρ denote the Young's modulus and density correspondingly. The beam is subjected to a moving point load that travels across from left to right at c m·s^{-1}. The magnitude of the moving load is $P = 8.34 \text{ x } 10^4$ N. The dynamic response of the beam is analysed from the instant the moving load arrives on to the FG beam to the moment it departs from the beam. The beam rests on a foundation, of elastic stiffness $k_f = 3.416 \text{ x } 10^6$ N·m^{-2}, as illustrated in Figure 8-25. The viscous damping factor is denoted by d and takes into account the viscous damping of the foundation.

The dynamic response of the described system is analysed using the Daubechies and BSWI WFEMs. The results are compared with the classical FEM approach. 4 BSWI5_5 WFEs (271 DOFs), 12 Daubechies D16_2 WFEs (375 DOFs) and 130 classical finite elements (390 DOFs) are used to model the beam throughout the analysis. The dynamic analysis of the system is carried out using the Newmark time integration method. The time step Δt is selected to ensure that the analysis is accurately and efficiently carried out while maintaining the numerical stability of the analysis.

The analysis using the wavelet based FG beam element formulation is verified by comparing the displacement variation when $n = 10^4$ (fully steel) with the results obtained in Section 7.3; for a 5% undamped system. The results are in very good agreement with those presented in Section 7.3 and the approach is verified. The number of elements, order of the wavelet families and multiresolution scales are based on the results being within 3% of those obtained in Section 7.3.

The effect of the varying the power law exponent, n, on the critical velocity of the beam is first analysed. The maximum deflection at the centre of the beam, as the moving load travels across at c ms^{-1}, is presented in Figure 8-26 for different material distributions. The graph is obtained for the velocity range $0 < c \leq 800$ m·s^{-1} at increments of 1 m·s^{-1}. The results presented are those obtained using the BSWI5_5 WFEM. The Daubechies WFEM and classical FEM plots are similar and are therefore not presented.

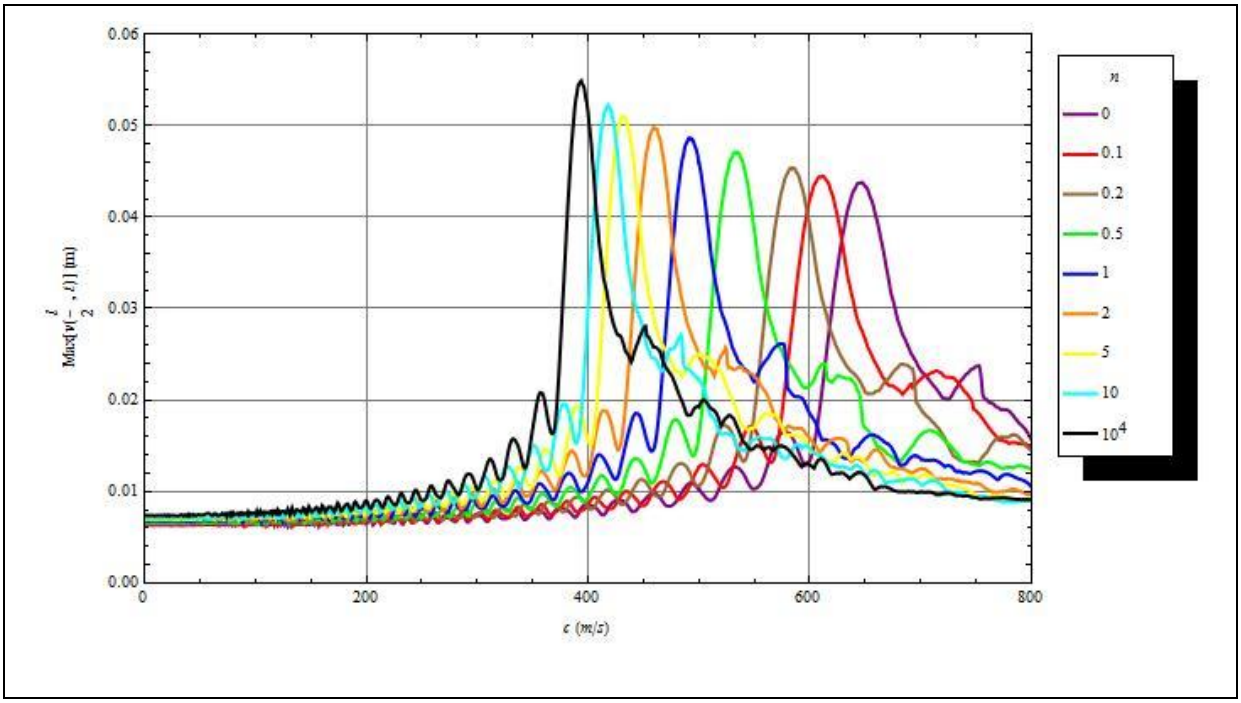

Figure 8-26: The variation of the maximum non-dimensional vertical displacement of a FG beam on elastic foundation subjected to a moving load with respect to the load velocities for different n.

From Figure 8-26, varying n has a significant effect on the magnitude of the maximum deflection and the corresponding velocity. The regions where the maximum vertical displacement is at its highest correspond to the critical velocity of the moving load. When the beam is approximately fully steel ($n = 10^4$), the maximum deflection is 0.0553879 m, with a corresponding critical velocity of 395 m·s^{-1} (BSWI5_5 WFEM solution). This is only 0.0658 % lower than the value obtained analytically in Section 7.3. This shows that wavelet based functionally graded beam solution is highly accurate. When the value of n is decreased, the highest maximum displacement decreases. The value of the moving load critical velocity is also observed to increase. This is because as $n \to 0$, $E(y) \to E_u$. Subsequently, the natural frequencies of the FG beam increase with this increase in bending stiffness. Furthermore, this increase in effective bending stiffness results in a decrease of the beam deflection. In the analysis of moving load problems, it is desirable to have the maximum deflection of the system minimised; with the critical velocity being as high as possible.

It is also observed from Figure 8-26 that the gradient of the curve is very steep before and after the critical velocity is attained when $n = 10^4$; in comparison to the other FGM material distributions. This implies that rate of increase/decrease of the maximum deflection of the beam, with respect to the moving load velocity, is greatest when the beam is fully steel. Decreasing the value of *n* reduces the rate at which the maximum deflection increases or decreases.

	Critical velocity c **m/s**			**Max[** $v(\frac{l}{2}, t)$**]**		
n	**FEM**	**D*16*$_2$**	**BSWI*5*$_5$**	**FEM**	**D*16*$_2$**	**BSWI*5*$_5$**
0	648	649	648	0.0438347	0.0420344	0.0439014
0.1	613	613	613	0.0447327	0.0428942	0.0447663
0.2	586	586	586	0.0456268	0.0436009	0.0456495
0.5	536	537	534	0.0472256	0.044732	0.0471608
1	495	496	494	0.0486466	0.0455693	0.0489605
2	462	464	462	0.0500081	0.0469853	0.0501519
3	448	449	448	0.0050398	0.047813	0.0508214
5	434	435	433	0.0510972	0.0484487	0.0513434
7	427	429	426	0.0516903	0.0487826	0.0515689
10	420	422	420	0.0521743	0.049221	0.052192
10^4	396	398	395	0.0550927	0.0523035	0.0553879

Table 8-9: The critical velocity and maximum normalised deflection of a steel-alumina FG beam on elastic foundation for different values of *n*.

To further the results in Figure 8-26, the critical velocities and corresponding maximum beam deflections, for the different material distributions, are presented in Table 8-9. The solutions obtained using 4 BSWI*5*$_5$ WFEs and 12 Daubechies D*16*$_2$ WFEs are compared with 130 classical finite elements. The results for the different approaches are in good agreement, accurately describing the critical velocity of the moving load with respect to the corresponding material distributions.

The variation of the maximum vertical displacement with respect to *n* is presented in Figure 8-27; for different moving load velocities. It is observed that for the velocities $c = 100$ m·s^{-1} and $c = 300$ m·s^{-1}, the maximum deflection is relatively lower in comparison to other applied velocities. This is because these applied moving load velocities are subcritical for the different material distributions and an increase in moving load velocity leads to an increase in the maximum beam deflection. This occurs until the critical velocity corresponding to the

material distribution is reached. Thereafter, the maximum deflection decreases as the moving load velocity increase.

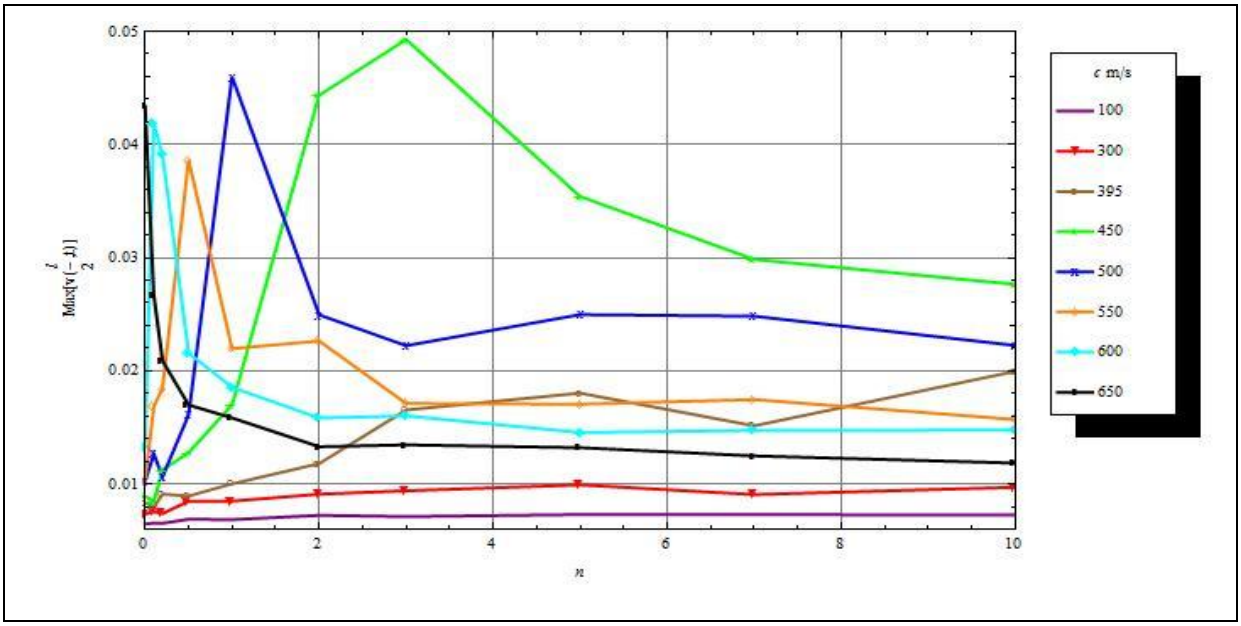

Figure 8-27: The variation of the maximum non-dimensional vertical displacement of a FG beam on elastic foundation subjected to a moving load, with respect to n for different moving load velocities.

The maximum deflection peaks when the velocity of the applied moving load velocity is close to the corresponding critical velocity. For instance, when the load is travelling at 650 m·s^{-1}, the highest maximum deflection is attained when $n = 0$. This is because the applied moving load velocity is close to the critical velocity of alumina (648 m·s^{-1}). Similarly, when the moving load is travelling at 500 ms^{-1}, the highest maximum deflection is achieved when $n = 1$.

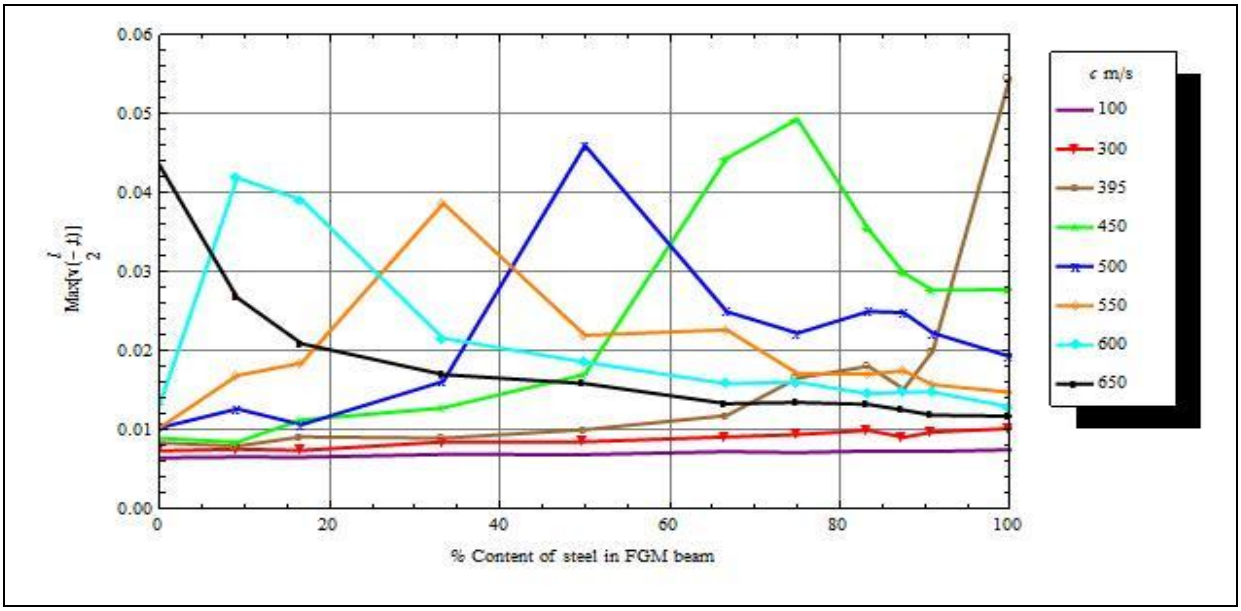

Figure 8-28: The variation of the maximum non-dimensional vertical displacement of a FG beam on elastic foundation subjected to a moving load with respect to the percentage volume content of steel for different moving load velocities.

In Figure 8-28, the maximum deflection is plotted against the percentage content of steel within the FG beam, for the different moving load velocities, to better illustrate the results presented in Figure 8-27.

The dynamics analysis of the long functionally graded beam requires a considerable number of elements to accurately describe the variation of the material distribution. Furthermore, for an accurate description of the response, the number of time steps required is significant, considering the applied load is rapidly varying. In the analysis of the moving load critical velocity, each material distribution profile is analysed at each time step for each velocity.

From the results presented, the Daubechies and the BSWI WFEM solutions accurately approximate the variation of the maximum deflection with respect to the moving load velocities with fewer elements implemented than the FEM. The BSWI5_5 WFEM solution is the most accurate for the critical velocity and corresponding maximum deflection solutions. In addition, only 4 BSWI WFEs are required to achieve this level of accuracy, in comparison to 130 classical finite elements and 12 Daubechies D16_2 WFEs. The global system of the BSWI5_5 WFE approach consists of 271 DOFs. This is approximately 30 % less number of DOFs than the classical FEM and 28% less when compared to the Daubechies WFEM. Moreover, a computational cost analysis was carried out to compare the efficiency of the three approaches. The considered analysis was for a FG beam resting on a 5% damped viscoelastic foundation subjected to a moving point load travelling at 395.26 m·s^{-1}. The viscous damping factor was evaluated based on the critical viscous damping of a homogenous steel beam resting on the foundation. This value was used in this analysis for the different material distributions. The critical damping of the system is expressed as [109]:

$$d_{cr} = 2\sqrt{k_f A \rho_l} \tag{8.71}$$

The viscous damping coefficient of the system, d, is evaluated as $d = \zeta d_{cr}$, with ζ being the damping ratio.

Furthermore, the simulation is run to obtain the dynamic responses for the different material distributions n = 0, 0.1, 0.2, 0.5, 1, 2, 3, 5, 7, 10 and 10^4. The number of time steps implemented in the Newmark algorithm is 5,800. The simulations were carried out using Mathematica Version 7 on a Pentium (R) Dual core CPU with; 4GB RAM, 64 bit Operating System, 2.10 GHz running on Windows 8. Given that the wavelet elemental matrices and wavelet transformation matrices were earlier computed and stored, the following aspects were taken into consideration: evaluation of moving load in wavelet space at each time step,

transformation of all element matrices from wavelet space into physical space, assembly of matrices and application of boundary conditions and the Newmark time integration algorithm.

The time required to carry out the stated dynamic analysis via the FEM (390 DOFs, 130 elements), D16_2 (375 DOFs, 12 elements) and BSWI5_5 WFEM (271 DOFs, 4 elements) was 574.156 s, 548.028 s and 463.59 s respectively. Subsequently, the computational resources needed to evaluate the response of the beam via the Newmark time integration for the BSWI WFEM are observed to be significantly less in comparison to the FEM and Daubechies WFEM approaches. The high levels of accuracy and efficiency demonstrate the superiority of the BSWI WFEM over the other two methods for dynamic response analysis of FG beams. The number of DOFs implemented for the Daubechies WFEM and classical FEM are also compared (Daubechies D16_2 WFEM - 375 DOFs, FEM – 390 DOFs). The effects of this difference become apparent when carrying out the dynamic analysis of the moving load critical velocity for the different material distributions, for different moving load velocities and at each time step. Therefore from this computational cost analysis, the Daubechies WFEM solution is still more efficient than the classical FEM. Moreover, the added advantage of both WFEMs over the classical finite element method is that the multiresolution and/or order of the wavelet elements can be modified to increase the levels of accuracy.

The dynamic response of the steel-alumina functionally graded beam is carried out for different moving velocity and system damping profiles and material distributions. The velocity profiles are subcritical (80 m·s^{-1}), critical (395.26 m·s^{-1}) and supercritical (500 m·s^{-1}) applied moving load velocities which correspond to that of a homogenous steel beam ($n = 10^4$). The dynamic responses of all the other material distributions of the FG beam are analysed with respect to these three velocity profiles.

The verification of the FG beam WFE, as earlier mentioned, is carried out by comparing the dynamic response when $n = 10^4$ with the results obtained in Section 7.3 (for corresponding moving loads). The compared results are presented in Figure 8-29 for *a*) subcritical, *b*) critical and *c*) supercritical moving load velocities. The curve "BSWI WFEM – Ref" is the solution obtained using 6 BSWI5_5 beam WFEs from Section 7.3. The results of the wavelet based FG beam are in excellent agreement, particularly for the subcritical and critical moving load velocities.

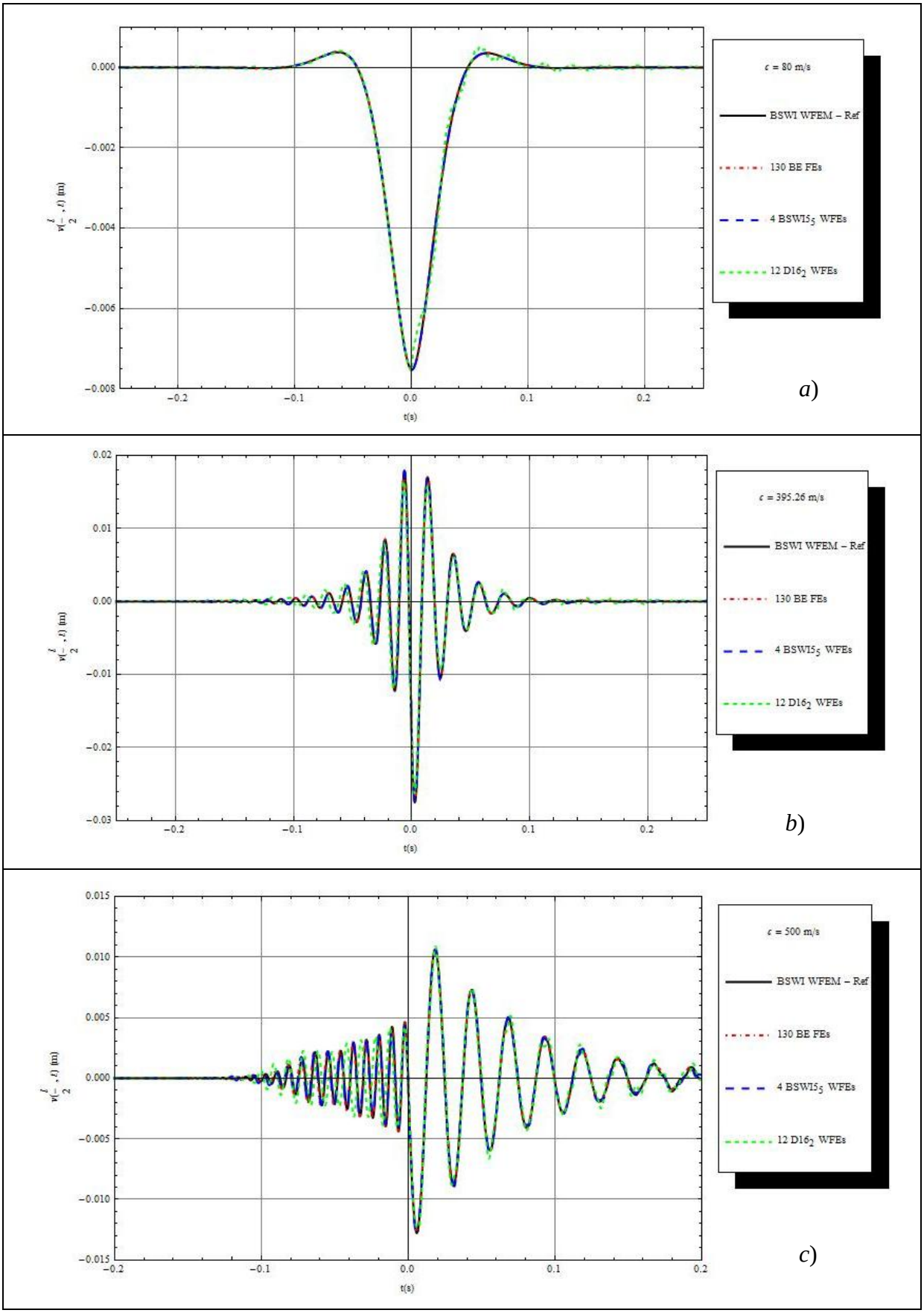

Figure 8-29: The vertical displacement of a steel-alumina FG beam on an viscoelastic foundation (5% damping) subjected to a moving point load travelling at *a*) 80 m·s^{-1} *b*) 395.26 m·s^{-1} and *c*) 500 m·s^{-1}.

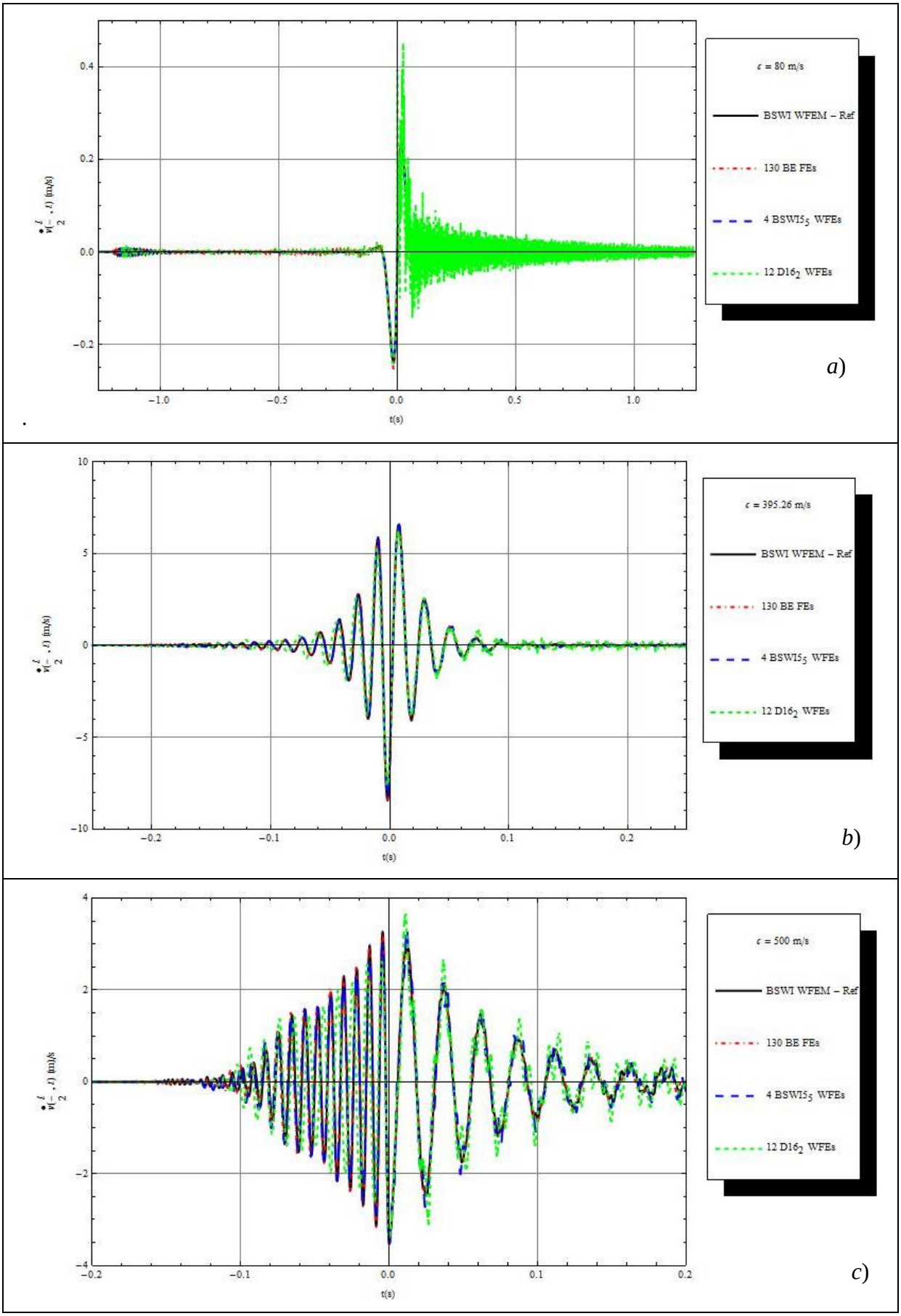

Figure 8-30: The vertical velocity of a steel-alumina FG beam on an elastic foundation (5% damping) subjected to a moving point load travelling at *a*) 80 m·s^{-1} *b*) 395.26 m·s^{-1} and *c*) 500 m·s^{-1}.

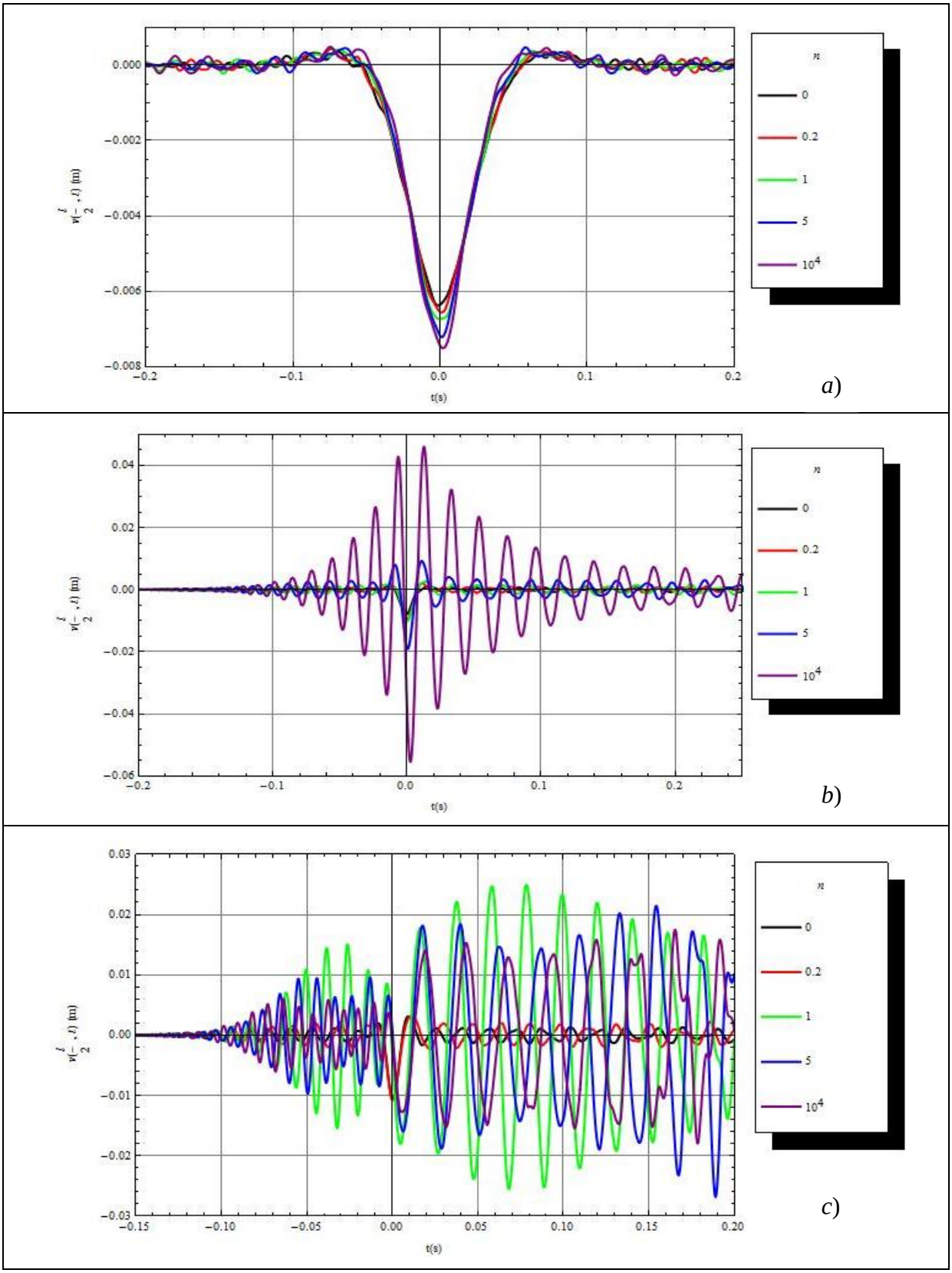

Figure 8-31: The vertical displacement at the centre of a simply supported steel-alumina FG beam on an elastic foundation (no damping) subjected to a moving point load travelling at *a*) 80 m·s^{-1} *b*) 395.26 m·s^{-1} and *c*) 500 m·s^{-1} for different values of *n*.

The vertical velocities at the centre of the FG beam are in very good agreement with the reference solution from Section 7.3 as illustrated in Figure 8-30. However, the Daubechies

WFEM solution is not as accurate when the load is travelling at subcritical velocities, but sufficiently acceptable at critical and supercritical velocities.

The variation of the deflection of the FG beam on an elastic foundation, as the moving point load travels across the beam, is presented in Figure 8-31; for the different material distributions. The results presented in this figure are obtained via the BSWI5_5 WFEM. It is observed in Figure 8-31 *a*) that when the applied moving load travels at 80 m·s^{-1}, which is subcritical for all variations of *n*, the maximum vertical displacement occurs when the moving load is at the centre of the beam. The highest maximum displacement occurs when the beam is fully steel ($n = 10^4$); and as $n \to 0$, the maximum displacement decreases in magnitude. This decrease in peak displacement, from fully steel to fully alumina, is approximately 15.06 %.

Figure 8-31 *b*) illustrates the response when the moving load is travelling at 395 m·s^{-1}. The highest maximum displacement at this moving load velocity is achieved when $n = 10^4$. Decreasing the value of *n* increases the natural frequency of the beam and thus the applied moving load velocity $c = 395$ m·s^{-1} is subcritical for the other material distributions. This explains why decreasing *n* results in a decrease of the maximum displacement of the beam as observed. The maximum vertical displacement is reduced by approximately 85.3% when *n* is varied from 10^4 to 0; which is more substantial than the subcritical case. For the different material distributions, as $n \to 0$, the amplitude of the oscillations diminishes significantly. Therefore, varying the material distribution has considerable effects on the dynamic response of the system when the applied moving load velocities are critical.

The applied moving load velocity c = 500 m·s^{-1} is subcritical for $n < 1$, supercritical for $n > 1$ and almost critical when *n* is 1. It is for this reason that the homogeneous steel beam no longer has the highest maximum displacement; even though its effective bending stiffness is lower than that of the other material distributions. The highest maximum displacement is achieved when *n* is 1, after the moving load has departed from the centre of the beam. Decreasing *n*, for $n > 1$, results in an increase in the maximum displacement of the FG beam. Conversely, decreasing *n*, for $n < 1$, results in a decrease in the maximum displacement. This is attributed to the increase in bending stiffness as well as the difference between the critical velocity corresponding to *n* and the applied moving load velocity.

The displacement variations of the system with light damping, for the different values of *n* and different velocity profiles, are presented in Figure 8-32. The introduction of the light damping smoothens out the low amplitude vibrations that are present and slightly decreases

the maximum displacement in comparison to the undamped system. This is observed from Figure 8-32 *a*) where the applied moving load velocity is 80 m·s^{-1}. The vertical displacement of the beam is highest when $n = 10^4$ and decreases as $n \to 0$, similar to the undamped case.

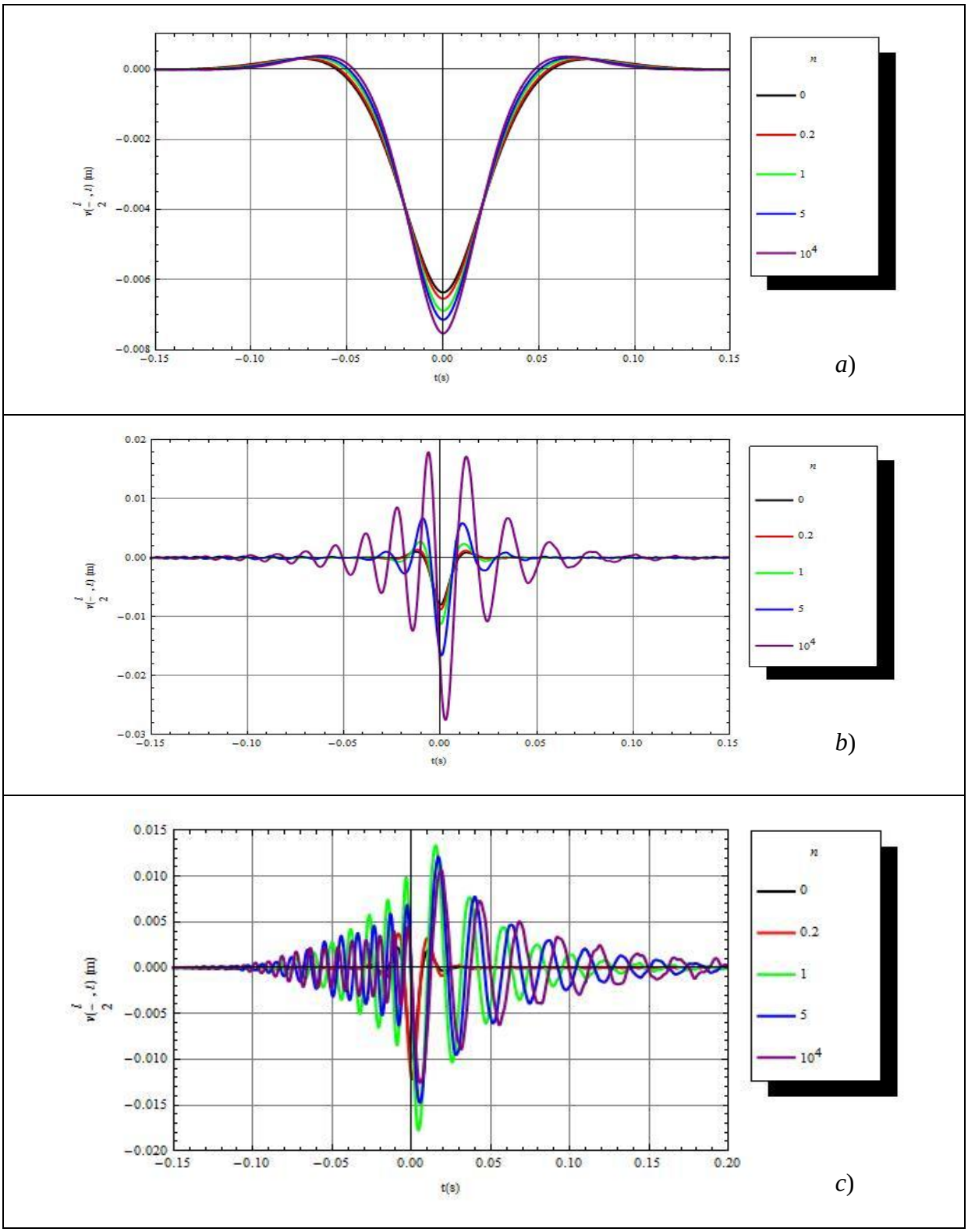

Figure 8-32: The vertical displacement of a steel-alumina FG beam on viscoelastic foundation (subcritical damping) subjected to a moving point load travelling at *a*) 80 m·s^{-1} *b*) 395.26 m·s^{-1} and *c*) 500 m·s^{-1}, for different values of *n*.

When the moving load is travelling at 395 m·s^{-1}, the maximum displacement for all the different material distributions is decreased due to damping. However, the effect of damping is greatest when n is 10^4, as observed in Figure 8-32 *b*). This is because the effect of damping is greater on the response of a beam with a moving load travelling at, or close to the critical velocity than when it is travelling at relatively slower subcritical velocities. Therefore, as n decreases, the effect of light damping on the response of the FG beam also decreases. Nevertheless, as $n \to 0$, the decrease of the maximum deflection is still significant.

When the moving load is travelling at 500 m·s^{-1}, the highest maximum displacement of the FG beam is attained when $n = 1$. The critical velocity of the functionally graded beam corresponding to this material distribution is very close to the applied moving load velocity. Furthermore, this velocity is still supercritical for values of $n > 1$ and as the value of n increases, the maximum displacement of the beam decreases. In contrast, when $n < 1$ and as n increases, the maximum displacement decreases since the velocity is subcritical for the corresponding material distributions. The introduction of the light damping results in a general decrease in the maximum displacement of all the material distributions, particularly for those whose applied moving load velocity is close to the load critical velocity.

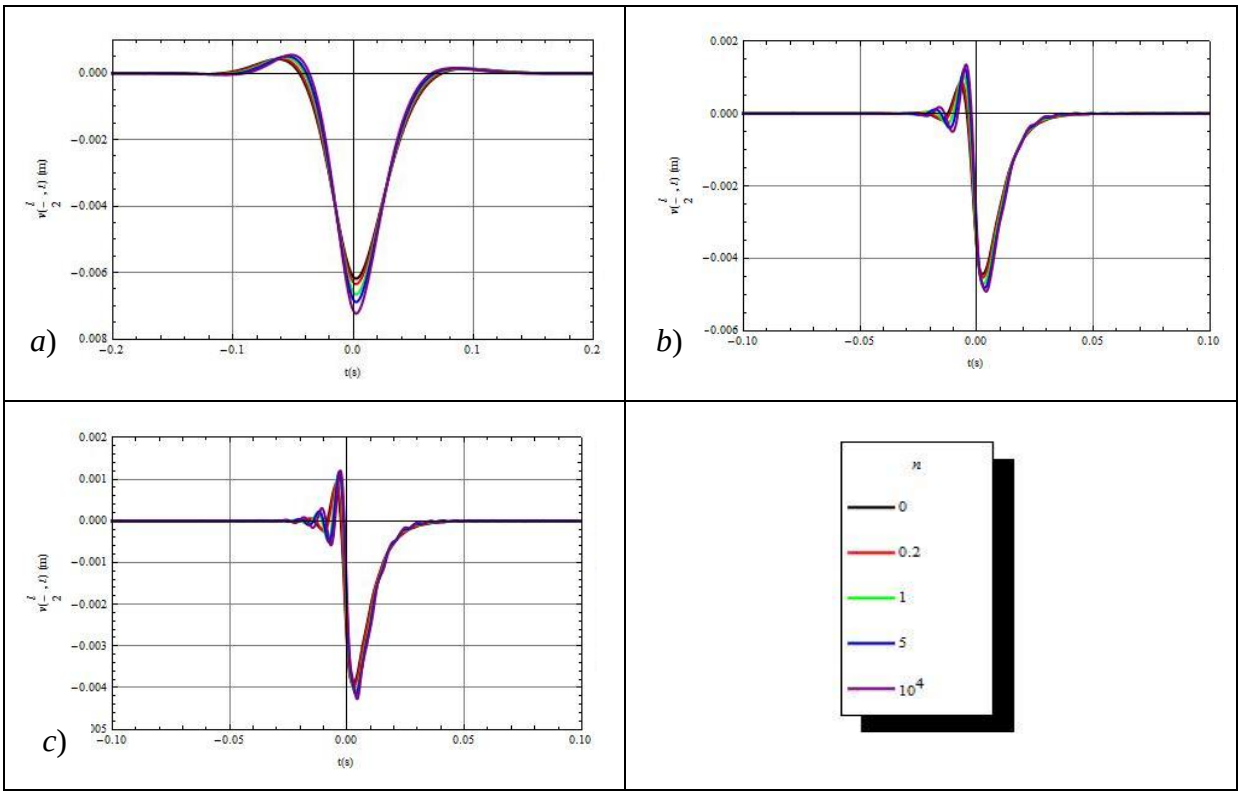

Figure 8-33: The vertical displacement of a steel-alumina FG beam on viscoelastic foundation (critical damping) subjected to a moving point load travelling at *a*) 80 m·s^{-1} *b*) 395.26 m·s^{-1} and *c*) 500 m·s^{-1} for different values of *n*.

Figure 8-33 illustrates the response of the FG beam, as the moving load travels across the beam when the damping of the system is critical ($\zeta = 1$). The effect of critical damping on

the dynamic response of the beam is very significant, particularly for moving load velocities 395 m·s^{-1} and 500 m·s^{-1}. Consequently, this also has a significant impact on the variation of the FG beam displacement for the different material distributions. The highest maximum displacement when the moving load travels at 80 m·s^{-1} is achieved when $n = 10^4$ and as $n \to 0$, the maximum displacement decreases, as presented in Figure 8-33 *a*).

When the moving load is travelling at 395 m·s^{-1} and 500 m·s^{-1}, as illustrated in Figure 8-33 *b*) and Figure 8-33 *c*) respectively, the maximum deflection of the beam decreases significantly. The FG beam can no longer be excited at these moving load velocities, for any material distribution, due to the critical viscous damping of the system. Therefore, it is observed that the highest maximum deflection of the FG beam occurs when $n = 10^4$. Furthermore, as $n \to 0$, the maximum displacement decreases. Moreover, the effect of varying the material distributions is not as significant at these moving load velocities. The maximum deflection, when the moving load travels at 395 m·s^{-1}, reduces by approximately 9.68 % as *n* varies from 10^4 to 0. Similarly, the maximum deflection at the centre of the beam reduces by approximately 8.58% for moving load velocity $c = 500$ m·s^{-1}. Thus, when the system is critically damped, the effect of varying the material distribution on the variation of the response of the FG beam is not as considerable as when the system is undamped or lightly damped.

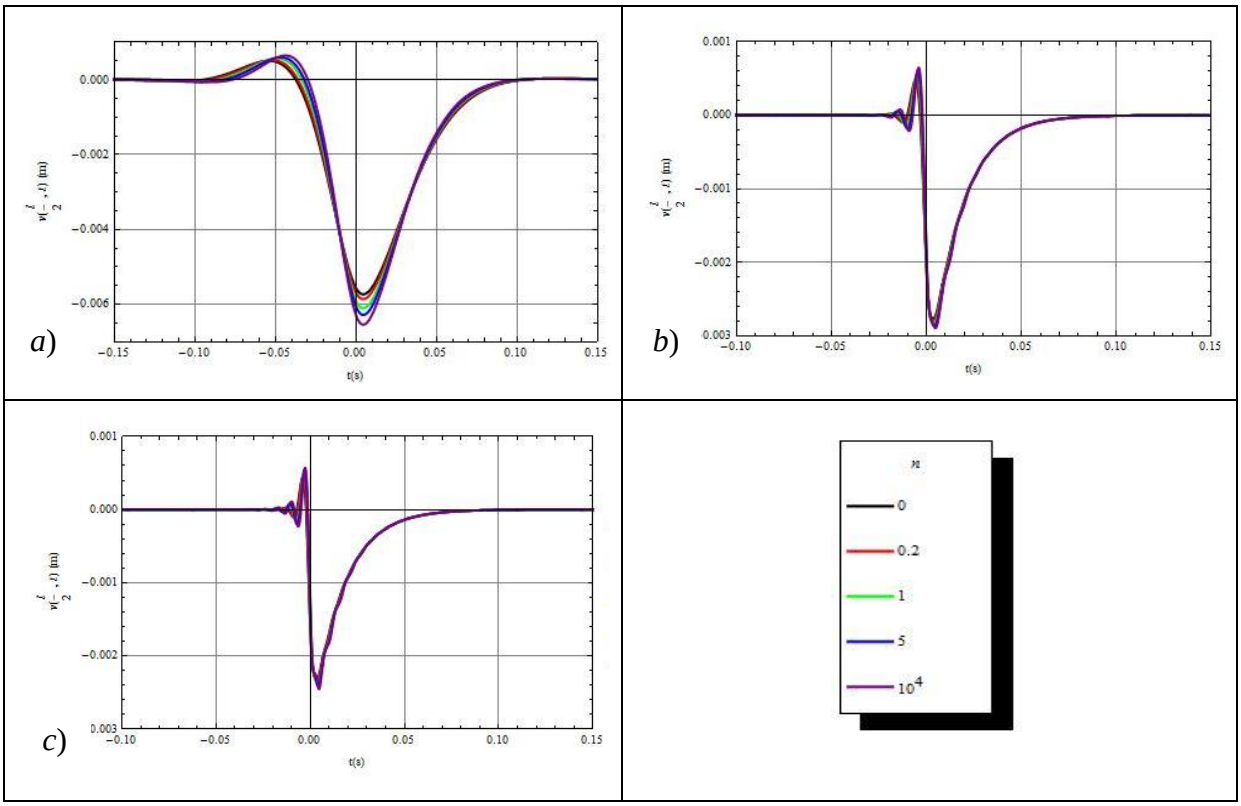

Figure 8-34: The vertical displacement of a steel-alumina FG beam on viscoelastic foundation (supercritical damping) subjected to a moving point load travelling at *a*) 80 m·s^{-1} *b*) 395.26 m·s^{-1} and *c*) 500 m·s^{-1} for different values of *n*.

The effect of varying n on the dynamic response of the beam when supercritical viscous damping ($\zeta = 2$) is introduced into the system is reduced further for the three different velocity profiles; as observed in Figure 8-34. It is therefore concluded that the effects of varying the material distribution of the FG beam on the dynamic response, decrease as the damping increases.

8.6. Conclusions

Analysis of FGMs is essential in practice to understand and predict their behaviour when subjected to various loading environments, such as mechanical, thermal or electrical, or in some cases, combinations of loading conditions. Though the materials may at times be expensive to fabricate, the functionally graded materials are often used to decrease some limitations faced by conventional composites. These include [70,73]:

- Delamination-related problems often caused by the disparity of materials in laminated composites can be eliminated. Structural and functional failure caused by the loss of structural integrity, reduction of stiffness and the destruction of load transfer mechanisms caused by the high local inter-laminar stresses, and subsequently separation of layers, is a problem commonly experienced in laminated composites.
- Reduction of in-plane and transverse through-the-thickness stresses.
- Improvement of residual stress distribution.
- Enhancement of fracture toughness.
- Reduction of stress intensity factors.
- Increase of fatigue life.

Although properties such as machinability, high toughness, high electrical conductivity from metals and high stiffness, high strength, temperature resistance and low density of ceramics are combined, the core aspect of FGMs is the continuous gradation of these materials and consequently the smooth transition of properties. Furthermore, FGMs may be used as an adhesive between different materials of structures that may be subjected simultaneously to different loading environments. This is because of the large inter-laminar stresses that are present due to the abrupt transition of the material properties that may lead to failure via plastic deformation or cracking. The applications of FGMs in various fields beyond the aerospace and automotive industries has rapidly grown e.g. medical field (dental [118] and orthopaedic implants [119]), communications industry [120] (optical fibbers,

semiconductors), energy sector [121] (thermo-generators and sensors) and building materials and structures just to name a few.

In this chapter, the WFEM was for the first time applied, to the best of the author's knowledge, for the dynamic analysis of functionally graded beams. The FG beam was formulated based on the power law of gradation given that the material distribution of the constituent materials can be altered continuously by changing the values of the power law exponent *n*. The variation of the material distribution and properties were analysed in the transverse direction. The analysis was carried out via numerical examples and compared with the classical FEM approach; and in some cases, results obtained from previous related research.

The free vibration analysis of a transverse varying steel-alumina FG beam was carried out using the Daubechies and the BSWI WFEMs. The results obtained show the effects of varying E_{ratio}, the slenderness ratio and the power law exponent *n*, on the natural frequencies of the functionally graded beam. The results were compared with Simsek and Kocaturk [83] and were found to be consistent with their findings. The results showed that increasing the value of *n* led to an increase in the natural frequencies for $E_u > E_l$. When $E_u < E_l$, increasing the value of *n* decreased the natural frequencies of the FG beam. The effects of varying the slenderness ratio on the natural frequencies of the FG beam were not significant, provided $\frac{l}{h} \geq 20$. This was consistent with findings made in Pradhan and Chakraverty [78]. However, for shorter beams where $\frac{l}{h} < 20$, the slenderness ratio affected the natural frequencies of the beam and the free vibration analysis can only be accurately approximated when the shear deformation effects are taken into consideration. When different boundary conditions were applied, increasing the number of restrained DOFs increased the fundamental frequencies of the FG beam for different values of *n*.

The dynamic response of a simply supported steel-alumina FG beam, subjected to moving loads travelling at subcritical, critical and supercritical velocities, was analysed using the Daubechies and BSWI WFEMs. The critical velocities for different material distributions and the corresponding maximum deflections at the centre of the FG beam were accurately obtained, with fewer elements and DOFs when compared with the classical FEM solution. The effects of varying the material distribution on the values of the critical velocities were consistent with Simsek and Kocaturk [83] for moving point loads. Decreasing the value of *n* decreased the maximum displacement of the simply supported functionally graded beam for all the velocity profiles presented.

A long steel-alumina FG beam resting on a viscoelastic foundation was subjected to a moving point load travelling across at subcritical, critical and supercritical velocities. The analysis was also carried out for different damping profiles. In general, the velocity of the moving load and the damping of the system influenced the effects of varying n on the dynamic response of the FG beam. Increasing damping in the system decreased the effect of varying the material distribution on the dynamic response of the beam. When the applied moving load was travelling at a velocity equal to or less than the critical velocity corresponding to the lower surface material, decreasing the value of n decreased the maximum displacement of the FG beam; for $E_u > E_l$. At supercritical velocities, the effects of varying n on the dynamic response may differ, depending on the applied moving load velocity and the critical velocity associated with the different material distributions.

The Daubechies and BSWI WFEMs approximated the transverse variation of the material properties for the functionally graded beam very accurately; with less number of elements required to achieve high levels of accuracy in comparison to the classical FEM. Furthermore, the free vibration and the dynamic response of the functionally graded beam were approximated with high levels of accuracy. This was due to the ability of the WFEMs to accurately approximate the field variables based on the main properties of the wavelet families, such as; compact support, multiresolution analysis and vanishing moments.

In general, the dynamic analysis of functionally graded beams subjected to rapidly varying loads may require a considerable number of elements to accurately describe the variation of the material distribution. Furthermore, the number of time steps required may also be significantly high to accurately describe the response of the beam for the different material distributions. The time and computational demands were reduced significantly when the WFEM was used to carry out these computations. This was evident from the efficiency analysis carried out and the system was accurately described using fewer DOFs; in comparison to the classical FEM. Moreover, the accuracy of the WFEM solutions was improved by increasing the order and/or multiresolution scale without affecting the original mesh of the system.

The BSWI WFEM is preferred to the Daubechies WFEM for the analysis of functionally grade beams. In the analysis of transverse varying functionally graded beams, the BSWI WFEM approximates the natural frequencies and dynamic response more accurately, with fewer elements and more efficiently than the Daubechies WFEM. This was mainly attributed to the fact that the Daubechies connection coefficients needed to be evaluated in the

formulation of the FGM stiffness and mass matrices for different material distributions and the numerical instabilities that were present. The BSWI based WFEM does not have these limitations of numerical instability or significant numerical errors since the scaling functions and their derivatives have an explicit expression and does not require the evaluation of the connection coefficients.

9. Conclusions and Future Work

In this study, the wavelet based finite elements are implemented in a multiresolution environment to mainly analyse static and dynamic beam problems. The Daubechies and BSWI WFEMs are selected due to the wavelet families' desirable properties, such as: multiresolution, compact support and the "two-scale" relation. It is ideal for the approaches employed in analysis of structural problems to be highly accurate while simultaneously being cost and time efficient. Research is still ongoing to discover and develop such analysis methods; of which the wavelet finite element method has recently been identified to have vast potential. Advancements are currently being made with respect to the applicability of the method to analyse different structural problems. It has been identified that its implementation for dynamic analysis is limited. Furthermore, some aspects of the Daubechies and BSWI WFEM are still unclear, with regards to implementation and performance, for dynamic analysis.

Moreover, the application of the method to analyse structures with variations in composition and material properties is currently limited. One class of structures that has recently come to the attention of researchers is the functionally graded materials. They are of practical importance as they have their material properties continuously varying spatially with respect to the constituent materials. The avenues for application and use of functionally graded materials in different disciplines are rapidly growing and therefore, different analysis tools are being developed and applied to better understand and describe their behaviour under various conditions.

In this study, the Daubechies and BSWI based WFEMs are applied to analyse the dynamic response for problems with fast variations in material properties and/or loading conditions. To the best of the author's knowledge, the implementation of the WFEM in the analysis of functionally graded beams on a viscoelastic foundation when subjected to moving loads is presented for the first time.

Based on the findings presented in this study, the WFEM is found to be a versatile, accurate and efficient numerical analysis tool which offers vast potential for structural analysis.

9.1. Conclusions

The following conclusions are made based on the findings of this extensive study.

- The BSWI and Daubechies based WFEMs generally require fewer number of elements, and consequently less number of DOFs, to accurately approximate the field variables in static and dynamic analysis of beam systems with respect to the classical FEM. This is consistent with findings from previous works. Furthermore, the variation of material properties in FG beams is accurately described and approximated with fewer DOFs. This is attributed to the desirable wavelet properties such as compact support, multiresolution analysis and vanishing moments. Therefore, the computational costs are significantly reduced, especially for the dynamic analysis of a system, where the dynamic response is evaluated at each time step.

- The layout of the WFEs can be easily modified by amending the wavelet transformation matrix. The element matrices and load vectors in wavelet space are not affected when changing the layout. They can therefore be evaluated only once and stored to reduce computational costs and improve on the efficiency of the WFE formulation. When the variation of the displacements and stresses of a system are primarily investigated in dynamic analysis, the most efficient and accurate layout for the beam wavelet finite element is to have the transverse displacement DOFs at each elemental node and the rotation DOFs only at the elemental end nodes. This is consistent with layouts presented for static analysis in previous works.

- The BSWI based WFEM is generally preferred to the Daubechies based WFEM when carrying out free vibration analysis and approximating the variation of the dynamic response of a system. This is due to the high levels of accuracy achieved with fewer elements and better computational efficiency. Furthermore, the method does not require the calculation of connection coefficients to evaluate the element matrices and load vectors. The difference in computational and time demands between the two methods becomes more apparent as the complexity of the problem analysed increases (variations in material properties or loading conditions). This is consistent with statements made in previous works and is confirmed via the comparative study of the

two WFEMs carried out in this thesis. However, the efficiency of the BSWI based WFEM for structural dynamic analysis may be impeded by the minimum applicable multiresolution scale condition $2^j \geq 2m - 1$. The Daubechies WFEM may be a more effective and efficient approach where a considerable number of wavelet finite elements are required, primarily due to variations in spatial orientation of the WFEs.

- The Daubechies based WFEM can be accurately applied for the static and dynamic analysis of beam structures for different orders of the WFE. The results converge more rapidly to the exact solution when the order of the Daubechies WFE is increased in comparison to the multiresolution. This is evident when improving the accuracy of the natural frequencies and dynamic response of a system. This is also the case for the BSWI based WFEM when the multiresolution scale j is relatively low. However, when the multiresolution scale is high, the results are better approximated but the computational costs are significantly increased due to the increase in the number of DOFs in each WFE. It is therefore more efficient and effective to first increase the orders of the wavelet based finite elements, then increase the multiresolution scales.

- The results for the free vibration analysis of a transversely varying functionally graded beam indicate that as the power law exponent $n \to 0$, the natural frequency of the FG beam reduces for $E_u > E_l$. The effects of varying the slenderness ratio on the natural frequencies of the FG beam are not significant provided $\frac{l}{h} \geq 20$. However, for shorter beams where $\frac{l}{h} < 20$, the slenderness ratio affects the natural frequencies of the beam and the free vibration analysis can only be accurately carried out when the shear deformation effects are taken into consideration. This is consistent with results presented using other approaches.

- The material distribution of a transversely varying functionally graded beam resting on a viscoelastic foundation subjected to a moving point load influences the dynamic response of the system. When the moving load is travelling at a velocity equal to or less than the critical velocity of the lower surface material, decreasing the value of n decreases the maximum displacement of the FG beam, for $E_u > E_l$. At supercritical velocities, the variation of n should be carried out in a manner that ensures the

corresponding critical velocity is as distant as possible from the applied moving load velocity; thus, the maximum displacement of the beam is kept to a minimum. Increasing damping of the system decreases the effect of varying the material distribution of the FG beam on the dynamic response of the beam.

9.2. Recommendations for future work

The versatility and effectiveness of the wavelet finite element method, particularly in the analysis of dynamic structural problems with fast variations in loading conditions and/or material properties, offers vast potential. Therefore, the following are recommendations for future work:

- Implement the WFEM in the formulation and dynamic analysis of functionally graded plates and shells.
- Apply WFEM to analyse functionally graded materials, for different material distributions, when temperature effects are taken into consideration.
- Formulate 3D wavelet based finite element for the analysis of functionally graded materials with variations of material distributions occurring in all the three axis directions.
- Carry out analysis of impact and wave propagation problems based on the wavelet finite element method.

Appendix

A. Wavelet theory

The key principles, theories and formulations of wavelet analysis related to the work presented in this study, specifically Chapter 3, are highlighted and expounded in this section based on previous literature [15,16,19,20,87].

A.1. Multiresolution analysis

The decomposition and reconstruction formulations explaining how multiresolution is achieved in wavelets are presented in this section as previously discussed in Section 3.1. Let us define the projections of a function $f \in L^2(\mathbb{R})$ at scale j in the subspaces V_j and W_j as $P_j f$ and $Q_j f$ respectively. Furthermore [19],

$$P_j f = \sum_k a_k^j \phi_k^j(x) \tag{A.1}$$

$$Q_j f = \sum_k b_k^j \psi_k^j(x) \tag{A.2}$$

where a_k^j and b_k^j are coefficients in the subspaces V_j and W_j respectively. At scale j = 1, the corresponding projection of f, $P_1 f$, can be decomposed into the projections of f in V_0 and W_0 since $V_1 = V_0 \oplus W_0$ [20].

$$P_1 f = P_0 f + Q_0 f \tag{A.3}$$

$$\sum_k a_k^1 \phi_k^1(x) = \sum_k a_k^0 \phi_k^0(x) + \sum_k b_k^0 \psi_k^0(x) \tag{A.4}$$

$$2^{\frac{1}{2}} \sum_k a_k^1 \phi(2x-k) = \sum_k a_k^0 \phi(x-k) + \sum_k b_k^0 \psi(x-k) \tag{A.5}$$

The coefficient a_k^1 is a refined version of a_k^0 while b_k^0 contains the difference in "information". This is a similar concept for the subspaces, where the additional information to get from V_0 to V_1, is in the subspace W_0. Given that $\phi_k^1(x)$ is the orthonormal basis of V_1, then from equation (A.3) the coefficients a_k^0 can be evaluated as [19]:

$$a_k^0 = \langle \phi_k^0(x), P_0 f \rangle = \langle \phi_k^0(x), P_1 f \rangle \tag{A.6}$$

Substituting (A.1), for j = 1, into (A.6),

$$a_k^0 = \langle \phi_k^0(x), P_1 f \rangle = \langle \phi_k^0(x), \sum_i a_i^1 \phi_i^1(x) \rangle \quad \textbf{(A.7)}$$

Substituting equation (3.9) into (A.7)

$$a_k^0 = 2^{\frac{1}{2}} \sum_i a_i^1 \langle \phi(x-k), \phi(2x-i) \rangle = \sum_i h(i-2k) a_i^1 \quad \textbf{(A.8)}$$

where

$$h(k) = 2^{\frac{1}{2}} \int_{-\infty}^{\infty} \phi(x) \phi(2x-k) dx \quad \textbf{(A.9)}$$

Similarly, the coefficients b_k^0 can be stated as:

$$b_k^0 = \sum_i g(i-2k) a_i^1(x) \quad \textbf{(A.10)}$$

$$g(k) = 2^{\frac{1}{2}} \int_{-\infty}^{\infty} \psi(x) \phi(2x-k) dx \quad \textbf{(A.11)}$$

The coefficient $a_i^1(x)$ decomposes into the coefficients a_k^0 and b_k^0 from equations (A.8) and (A.10). Furthermore, the coefficient $a_i^1(x)$ can be reconstructed from the coefficients a_k^0 and b_k^0, i.e.,

$$a_k^1 = \sum_i h(2k-i) a_i^0 + \sum_i g(2k-i) b_i^0 \quad \textbf{(A.12)}$$

In general, at any scale *j* [20]

$$P_{j+1} f(x) = P_j f(x) + Q_j f(x) \quad \textbf{(A.13)}$$

$$\sum_k a_k^{j+1} \phi_k^{j+1}(x) = \sum_k a_k^j \phi_k^j(x) + \sum_k b_k^j \psi_k^j(x) \quad \textbf{(A.14)}$$

$$a_k^j = \sum_i h(i-2k) a_i^{j+1}, a^j = \boldsymbol{H} a^{j+1} \quad \textbf{(A.15)}$$

$$b_k^j = \sum_i g(i-2k) a_i^{j+1}, b^j = \boldsymbol{G} a^{j+1} \quad \textbf{(A.16)}$$

$$a_k^{j+1} = \sum_i h(2k-i) a_i^j + \sum_i g(2k-i) b_i^j$$
$$a^{j+1} = \boldsymbol{H^T} a^j + \boldsymbol{G^T} b^j \quad \textbf{(A.17)}$$

This give rise to what is commonly referred to as the refinement and wavelet equations, which are expressed as:

$$\phi(x) = \sum_k c(k)\phi(2x-k) \tag{A.18}$$

$$\psi(x) = \sum_k (-1)^n c(k+1)\phi(2x+k) \tag{A.19}$$

where c denotes the general scaling function filter coefficients. Figure A-1 illustrates the (a) decomposition and (b) reconstruction algorithms of the coefficients in the subspaces at different scales.

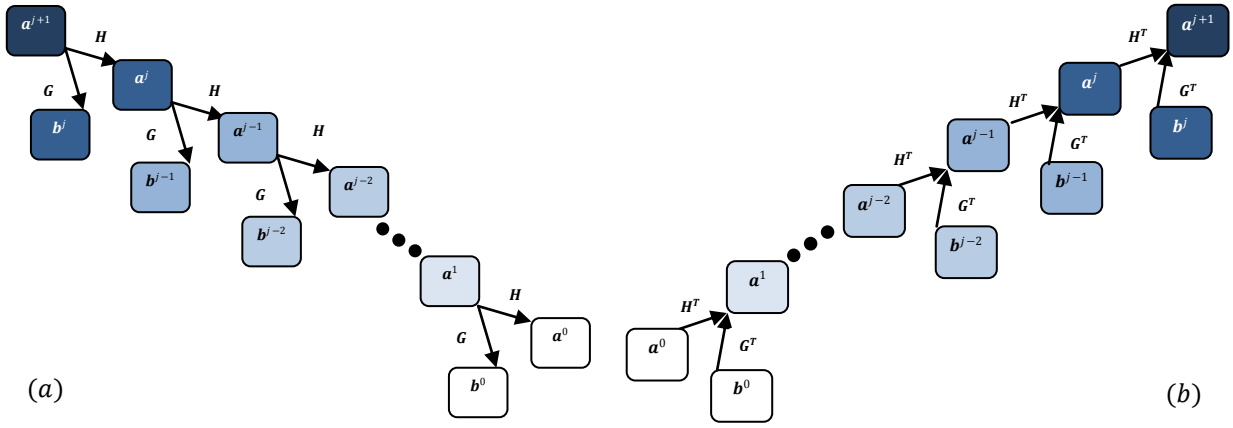

Figure A-1: Wavelet (a) decomposition and (b) reconstruction.

A.2. The Daubechies wavelet

This section contains a more detailed mathematical description of the Daubechies filter coefficients, moments and connection coefficients as discussed in Chapter 3 of this thesis.

A.2.1. The Daubechies filter coefficients

In this section, the Daubechies filter coefficients discussed in Section 3.2.1, are derived in detail based on theory and formulations described by Daubechies [15,20] and subsequent publications by Strang and Nguyen [16] and Hong et al. [88].

We define the 2π-periodic function

$$m_0(\omega) = \frac{1}{\sqrt{2}} \sum_k h(k) e^{-ik\omega} \tag{A.20}$$

where the filter coefficients $h(k)$ satisfy the conditions (3.30) and (3.32). Therefore, for an orthonormal scaling function $\phi_k^0(x)$,

$$|m_0(\omega)|^2 + |m_0(\omega+\pi)|^2 = 1 \tag{A.21}$$

Given that the moment condition holds, then m_0 factorizes in the form [15]

$$m_0(\omega) = \left[\frac{1+e^{i\omega}}{2}\right]^M q(\omega) \tag{A.22}$$

where $q(\omega)$ is also a trigonometric function and $M \geq 1$. Let the polynomial M_0 be given as:

$$M_0(\omega) = |m_0(\omega)|^2 = m_0\left(e^{i\omega}\right)m_0\left(e^{-i\omega}\right) \tag{A.23}$$

Therefore,

$$M_0(\omega) = \left[\frac{1+e^{-i\omega}}{2}\right]^M \left[\frac{1+e^{i\omega}}{2}\right]^M q(e^{-i\omega})q(e^{i\omega}) = \left(\cos^2\left(\frac{\omega}{2}\right)\right)^M q(e^{-i\omega})q(e^{i\omega}) \tag{A.24}$$

For convenience, we define

$$B(y) = q(e^{-i\omega})q(e^{i\omega}) \tag{A.25}$$

Furthermore, given the trigonometric relations

$$\begin{gathered}\sin^2\theta + \cos^2\theta = 1 \\ \cos^2\theta = 1 - \sin^2\theta \\ \cos 2\theta = 1 - 2\sin^2\theta\end{gathered} \tag{A.26}$$

$$\begin{gathered}y = \sin^2\theta \\ \cos^2\theta = 1 - y \\ \cos 2\theta = 1 - 2y\end{gathered} \tag{A.27}$$

Equation (A.24) can be expressed in terms of $B(y)$ as

$$M_0(\omega) = M_0\left(e^{-i\omega}\right) = [1-y]^M B(y) \tag{A.28}$$

and subsequently

$$M_0(\omega+\pi) = M_0\left(-e^{-i\omega}\right) = y^M B(1-y) \tag{A.29}$$

The condition expressed in equation (A.21) can be expressed in terms of equations (A.28) and (A.29) as

$$[1-y]^M B(y) + y^M B(1-y) = 1 \tag{A.30}$$

This holds for all $y \in [0,1]$ and thus, for all $y \in \mathbb{R}$. Daubechies [20] in her earlier work solved equation (A.30) via two combinatorial lemmas and later used Bezout's theorem which states that:

> "If p_1 and p_2 are two polynomials of degree n_1 and n_2 respectively, with no common zeros, then there exists unique polynomials q_1 and q_2 of degree n_2 - 1, n_1 - 1 respectively so that." [15]

$$p_1(x)q_1(x) + p_2(x)q_2(x) = 1 \tag{A.31}$$

Thus, $B(y)$ from equation (A.30) is expressed as

$$B(y) = [1-y]^{-M}[1 - y^M B(1-y)] \tag{A.32}$$

By applying Taylor expansion for the first M terms of $[1-y]^{-M}$,

$$B(y) = \sum_{k=0}^{M-1} \binom{M+k-1}{k} y^k + O(y^M) \tag{A.33}$$

where $O(y^M)$ is the general power series. However, for $B(y)$ of degree $\geq M$

$$[1-y]^M (B(y) - B_M(y)) + y^M (B(1-y) - B_M(1-y)) = 0 \tag{A.34}$$

where $B_M(y)$ is the unique lowest solution

$$B_L(y) = \sum_{k=0}^{M-1} \binom{M+k-1}{k} y^k \tag{A.35}$$

Substituting the values of y from equation (A.27) i.e.,

$$\begin{aligned} y &= \left[\frac{1-e^{-i\omega}}{2}\right]\left[\frac{1-e^{i\omega}}{2}\right] \\ 1-y &= \left[\frac{1+e^{-i\omega}}{2}\right]\left[\frac{1+e^{i\omega}}{2}\right] \end{aligned} \tag{A.36}$$

and from equation (A.28), we obtain

$$M_0(\omega) = \left[\frac{1+e^{-i\omega}}{2}\right]^M \left[\frac{1+e^{i\omega}}{2}\right]^M \sum_{k=0}^{M-1} \binom{M+k-1}{k} \left[\frac{1-e^{-i\omega}}{2}\right]^k \left[\frac{1-e^{i\omega}}{2}\right]^k \tag{A.37}$$

Shifting from the frequency domain into the z-domain for convenience, where $z = e^{i\omega}$, let the polynomial $P_L(\omega) = M_0(\omega)$ and $P_L(z) = |m_L(z)|^2 = m_L(z)m_L\left(1/z\right)$. In the case of the Daubechies family of wavelets, the order $M = \frac{L}{2}$.

$$P_L(z) = \left[\frac{1+z}{2}\right]^{\frac{L}{2}} \left[\frac{1+z^{-1}}{2}\right]^{\frac{L}{2}} \sum_{k=0}^{\frac{L}{2}-1} \left(\frac{L}{2}+k-1\right) \left[\frac{1-z}{2}\right]^k \left[\frac{1-z^{-1}}{2}\right]^k \tag{A.38}$$

$$P_L(z) = \left[\frac{1+z}{2}\right]^{\frac{L}{2}} \left[\frac{1+z^{-1}}{2}\right]^{\frac{L}{2}} M_L(z) \tag{A.39}$$

where $M_L(z)$ is a Laurent polynomial

$$\widehat{M}_L(z) = \sum_{k=0}^{\frac{L}{2}-1} \left(\frac{L}{2}+k-1\right) \left[\frac{1-z}{2}\right]^k \left[\frac{1-z^{-1}}{2}\right]^k \tag{A.40}$$

Table A-1 gives the values of $\widehat{M}_L(z)$ for $2 \leq L \leq 20$ as evaluated from an algorithm developed by the author using Mathematica version 7.

L	$\widehat{M}_L(z)$
2	1
4	$2-\frac{1}{2z}-\frac{z}{2}$
6	$\frac{19}{4}+\frac{3}{8z^2}-\frac{9}{4z}-\frac{9z}{4}+\frac{3z^2}{8}$
8	$13-\frac{5}{16z^3}+\frac{5}{2z^2}-\frac{131}{16z}-\frac{131z}{16}+\frac{5z^2}{2}-\frac{5z^3}{16}$
10	$\frac{2509}{64}+\frac{35}{128z^4}-\frac{175}{64z^3}+\frac{95}{8z^2}-\frac{1825}{64z}-\frac{1825z}{64}+\frac{95z^2}{8}-\frac{175z^3}{64}+\frac{35z^4}{128}$
12	$\frac{4027}{32}-\frac{63}{256z^5}+\frac{189}{64z^4}-\frac{4067}{256z^3}+\frac{399}{8z^2}-\frac{12687}{128z}-\frac{12687z}{128}+\frac{399z^2}{8}-\frac{4067z^3}{256}+\frac{189z^4}{64}-\frac{63z^5}{256}$
14	$\frac{107727}{256}+\frac{231}{1024z^6}-\frac{1617}{512z^5}+\frac{10353}{512z^4}-\frac{39837}{512z^3}+\frac{203161}{1024z^2}-\frac{89033}{256z}-\frac{89033z}{256}+\frac{203161z^2}{1024}-\frac{39837z^3}{512}+\frac{10353z^4}{512}-\frac{1617z^5}{512}+\frac{231z^6}{1024}$
16	$\frac{46309}{32}-\frac{429}{2048z^7}+\frac{429}{128z^6}-\frac{50919}{2048z^5}+\frac{7227}{64z^4}-\frac{714429}{2048z^3}+\frac{98451}{128z^2}-\frac{2528431}{2048z}-\frac{2528431z}{2048}+\frac{98451z^2}{128}-\frac{714429z^3}{2048}+\frac{7227z^4}{64}-\frac{50919z^5}{2048}+\frac{429z^6}{128}-\frac{429z^7}{2048}$
18	$\frac{83211409}{16384}+\frac{6435}{32768z^8}-\frac{57915}{16384z^7}+\frac{244101}{8192z^6}-\frac{2552121}{16384z^5}+\frac{4614291}{8192z^4}-\frac{24360435}{16384z^3}+\frac{24126075}{8192z^2}-\frac{72599193}{16384z}-\frac{72599193z}{16384}+\frac{24126075z^2}{8192}-\frac{24360435z^3}{16384}+\frac{4614291z^4}{8192}-\frac{2552121z^5}{16384}+\frac{244101z^6}{8192}-\frac{57915z^7}{16384}+\frac{6435z^8}{32768}$
20	$\frac{148279949}{8192}-\frac{12155}{65536z^9}+\frac{60775}{16384z^8}-\frac{2294435}{65536z^7}+\frac{847275}{4096z^6}-\frac{14015287}{16384z^5}+\frac{10737155}{4096z^4}-\frac{100677555}{16384z^3}+\frac{45926485}{4096z^2}-\frac{526213405}{32768z}-\frac{526213405z}{32768}+\frac{45926485z^2}{4096}-\frac{100677555z^3}{16384}+\frac{10737155z^4}{4096}-\frac{14015287z^5}{16384}+\frac{847275z^6}{4096}-\frac{2294435z^7}{65536}+\frac{60775z^8}{16384}-\frac{12155z^9}{65536}$

Table A-1: Laurent polynomial $M_L(z)$ for $2 \leq L \leq 20$.

In order to solve for the filter coefficients, it is vital to solve for $m_0(\omega)$ from equation (A.22) to which we express in the z domain as:

$$m_L(z) = \left[\frac{1+z}{2}\right]^{\frac{L}{2}} \hat{q}_L(z) \qquad \textbf{(A.41)}$$

The subscript L denotes the order of the Daubechies wavelet and $\widehat{M}_L(z) = \left|\widehat{q}_L(z)\right|^2$. In order to obtain $m_0(\omega)$, it is important to obtain the square root from the non-negative trigonometric polynomial $\widehat{M}_L(z)$ via spectral factorization [16].

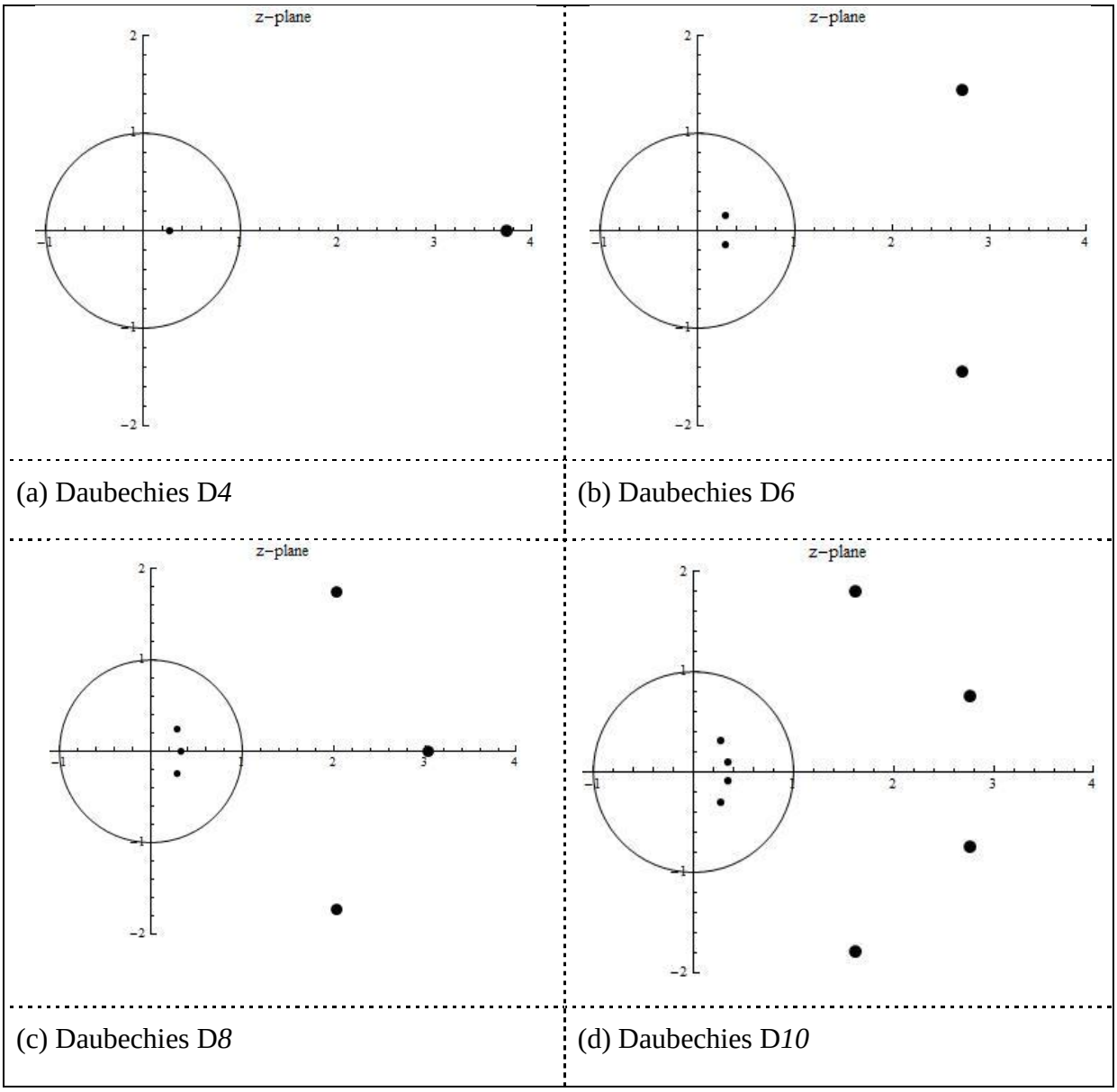

(a) Daubechies D*4* (b) Daubechies D*6*

(c) Daubechies D*8* (d) Daubechies D*10*

Figure A-2: Roots for the different orders of the Daubechies wavelet family.

According to Riesz Lemma, given that a real Laurent polynomial $R(z) > 0$ that has symmetric coefficients and thus satisfies the condition $R(z) = R(z^{-1})$, then [88]:

$$R(z) = c(z)c(z^{-1}) \tag{A.42}$$

where $c(z)$ is a real polynomial. The real roots r_k and $\frac{1}{r_k}$, the complex roots z_i and its conjugate $\bar{z}_i$ inside the unit circle, as well as $\frac{1}{z_i}$ and corresponding conjugate $\frac{1}{\bar{z}_i}$ outside the unit circle and/or the complex conjugate roots e^{iw_j} and e^{-iw_j}, are obtained from the

polynomial $\widehat{M}_L(z)$. The diagram above is an illustration of the roots for Daubechies D*4* to D*10* as evaluated using a Mathematica version 7 code developed by the author.

Daubechies D*4* has a pair of real roots as illustrated in Figure A-2 (a), while D*6* has a quadruplet of complex roots z_i, $\bar{z}_i$, $\frac{1}{z_i}$ and $\frac{1}{\bar{z}_i}$. On the other hand, D*8* has both a pair of the real roots and the four complex roots. Therefore, as the order of the Daubechies wavelet increases, so does the number of roots which correspond to $L-2$. However, only one of the roots is required from each pair so as to solve for the filter coefficients.

Therefore, the polynomial $R(z)$ is written as:

$$R(z) = \sum_{-N}^{N} b(k) z^k \tag{A.43}$$

Due to even multiplicity conditions we now have

$$\begin{aligned} z^N R(z) = b(N) \prod_{i=1}^{M} (z - z_i)(z - \bar{z}_i) \left(z - \frac{1}{z_i}\right) \Big(z \\ - \frac{1}{\bar{z}_i}\Big) \prod_{j=1}^{J} (z - e^{iw_j})^2 (z - e^{-iw_j})^2 \prod_{k}^{K} (z - r_k)(z - r_k{}^{-1}) \end{aligned} \tag{A.44}$$

and furthermore,

$$\begin{aligned} \left|(z - z_i)(z - \frac{1}{\bar{z}_i})\right| = |z_i|^{-1} |z - z_i|^2 \\ |(z - r_k)(z - r_k{}^{-1})| = |r_k|^{-1} |z - r_k|^2 \end{aligned} \tag{A.45}$$

Substituting these values and taking z^N to the right hand side of the equation, we obtain

$$\begin{aligned} R(z) = b(N) z^{-N} \prod_{i=1}^{M} |z_i|^{-1} |z - z_i|^2 |z_i|^{-1} |z - \bar{z}_i|^2 \prod_{j=1}^{J} (z - z_j)^2 (z \\ - \bar{z}_j)^2 \prod_{k}^{K} |r_k|^{-1} |z - r_k|^2 \end{aligned} \tag{A.46}$$

Let $b(N) z^{-N} = a_N$, which is a coefficient of $b(N)$. Therefore,

$$\begin{aligned} R(z) = 2a_N \prod_{i=1}^{M} |z_i|^{-2} \prod_{k=1}^{K} |r_k|^{-1} \prod_{i=1}^{M} |(z - z_i)(z \\ - \bar{z}_i)|^2 \prod_{j=1}^{J} \left|\left(z - z_j\right)(z - \bar{z}_j)\right|^2 \prod_{k}^{K} |z - r_k|^2 \end{aligned} \tag{A.47}$$

k	$p_L(k)$			
	D*4*	**D*6***	**D*8***	**D*10***
0	0.683012701892	0.470467207784	0.325803428051	0.226418982584
1	1.183012701892	1.141116915831	1.010945715092	0.853943542705
2	0.316987298108	0.650365000526	0.892200138247	1.024326944259
3	-0.183012701892	-0.190934415568	-0.039575026236	0.195766961348
4	-	-0.120832208310	-0.264507167369	-0.342656715383
5	-	0.049817499737	0.043616300474	-0.045601131884
6	-	-	0.046503601071	0.109702658642
7	-	-	-0.014986989330	-0.008826800108
8	-	-	-	-0.017791870102
9	-	-	-	0.004717427939
	D*12*	**D*14***	**D*16***	**D*18***
0	0.157742432003	0.110099430746	0.076955622109	0.053850349589
1	0.699503814075	0.560791283626	0.442467247152	0.344834303814
2	1.062263759882	1.031148491636	0.955486150428	0.855349064359
3	0.445831322930	0.664372482211	0.827816532422	0.929545714366
4	-0.319986598892	-0.203513822463	-0.022385735334	0.188369549506
5	-0.183518064060	-0.316835011281	-0.401658632781	-0.414751761802
6	0.137888092975	0.100846465009	0.000668194092	-0.136953549025
7	0.038923209708	0.114003445160	0.182076356847	0.210068342279
8	-0.044663748330	-0.053782452590	-0.024563901046	0.043452675461
9	0.000783251152	-0.023439941564	-0.062350206650	-0.095647264120
10	0.006756062363	0.017749792379	0.019772159297	0.000354892813
11	-0.001523533806	0.000607514995	0.012368844820	0.031624165853
12	-	-0.002547904718	-0.006887719257	-0.006679620226
13	-	0.000500226853	-0.000554004549	-0.006054960575
14	-	-	0.000955229711	0.002612967280
15	-	-	-0.000166137261	0.000325814671
16	-	-	-	-0.000356329759
17	-	-	-	0.000055645514

Table A-2: Table of Daubechies filter coefficients $p_L(k)$ for Daubechies wavelets D*4* – D*18*.

Let us define a constant T where

$$T^2 = 2a_N \prod_{i=1}^{M} |z_i|^{-2} \prod_{k=1}^{K} |r_k|^{-1} \qquad \textbf{(A.48)}$$

Then,

$$R(z) = T^2 \left| \prod_{i=1}^{M} (z - z_i)(z - \bar{z}_i) \right|^2 \left| \prod_{j=1}^{J} (z - z_j)(z - \bar{z}_j) \right|^2 \left| \prod_{k}^{K} (z - r_k) \right|^2 \quad \textbf{(A.49)}$$

It is therefore possible to evaluate for $q_L(z)$ from (A.49) as,

$$q_L(z) = T \prod_{i=1}^{M} (z - z_i)(z - \bar{z}_i) \prod_{j=1}^{J} (z - z_j)(z - \bar{z}_j) \prod_{k}^{K} (z - r_k) \quad \textbf{(A.50)}$$

and consequently solve for $m_L(z)$ in equation (A.41). The values of the coefficients in this polynomial are the values of the filter coefficients $h_L(k)$ and can now be used in the dilation equation to obtain the scaling functions and the wavelets functions. Table A-2 contains the filter coefficients normalized $\sum_k p_L(k) = 2$ for D*4* to D*16* as computed via a code written by the author using Mathematica version 7.

A.2.2. Daubechies moments M_k^m

Latto et al. [36] outlined an efficient and quick technique to calculate the moments of the Daubechies wavelet scaling function $\phi_L(x)$ and its translates of the form

$$M_k^m = \langle x^m, \phi_L(x - k) \rangle = \int_{-\infty}^{\infty} x^m \phi_L(x - k) dx \quad \textbf{(A.51)}$$

The scaling relation from the dilation equation in equation (3.18) is used to derive a sufficient number of linear conditions to determine the moments uniquely. Furthermore, from the property of vanishing moments in equation (3.24), the linear combination of the Daubechies scaling function and its translates of order *L* can exactly represent low order polynomials of order up to and not greater than $\frac{L}{2} - 1$ [36]. Therefore, a given function $f(x) = x^m$ can be represented as:

$$x^m = \sum_k M_k^m \phi_L(x - k) \quad \textbf{(A.52)}$$

The moments for the translates of the scaling function are expressed as

$$M_k^m = \langle x^m, \phi_L(x - k) \rangle = \int_{-\infty}^{\infty} x^m \phi_L(x - k) dx \quad \textbf{(A.53)}$$

By definition, from the properties of the Daubechies wavelets highlighted in Section 3.2, we know that the scaling function is normalised as follows:

$$\int_{-\infty}^{\infty} \phi_L(x)dx \ = 1 \tag{A.54}$$

Therefore, if in equation (A.53), $m = 0$ and $k = 0$, then

$$M_0^0 = \int_{-\infty}^{\infty} \phi_L(x)dx \ = 1 \tag{A.55}$$

and similarly,

$$M_k^0 = \int_{-\infty}^{\infty} \phi_L(x-k)dx \ = 1 \tag{A.56}$$

When $k = 0$, the m^{th} moment of the Daubechies scaling function is denoted as

$$M_0^m = \langle x^m, \phi_L(x) \rangle = \int_{-\infty}^{\infty} x^m \phi_L(x)dx \tag{A.57}$$

Applying the refinement equation, (A.57) can be rewritten as

$$M_0^m = \sum_{i=0}^{L-1} p(i) \int_{-\infty}^{\infty} x^m \phi_L(2x-i)dx \tag{A.58}$$

Multiplying equation (A.58) by 2^m and expressing $dx = \frac{d(2x)}{2}$

$$2^m M_0^m = \sum_{i=0}^{L-1} p(i) \int_{-\infty}^{\infty} (2x)^m \phi_L(2x-i) \frac{d(2x)}{2}$$

$$M_0^m = \frac{1}{2^{m+1}} \sum_{i=0}^{L-1} p(i) \int_{-\infty}^{\infty} (2x)^m \phi_L(2x-i)d(2x) \tag{A.59}$$

However,

$$\int_{-\infty}^{\infty} (2x)^m \phi_L(2x-i)d(2x) \ = M_i^m \tag{A.60}$$

Therefore, equation (A.59) can be expressed as:

$$M_0^m = \frac{1}{2^{m+1}} \sum_{i=0}^{L-1} p(i) M_i^m \tag{A.61}$$

In order to reduce the number of unknowns, it is vital to remove the moments M_i^m for $i \neq 0$. Let $u = (2x - i)$. Equation (A.60) becomes

$$M_i^m = \int_{-\infty}^{\infty} (u+i)^m \phi_L(u)d(u) \tag{A.62}$$

Expanding the term $(u+i)^m$ via binomial expansion

$$(u+i)^m = \frac{u^m}{0!} + \frac{mu^{m-1}i}{1!} + \frac{m(m-1)u^{m-2}i^2}{2!} + \cdots + \frac{i^m}{0!}$$

$$(u+i)^m = \binom{m}{2}u^m i^0 + \binom{m}{1}u^{m-1}i^1 + \binom{m}{2}u^{m-2}i^2 + \cdots + \binom{m}{m}u^0 i^m$$

$$(u+i)^m = \sum_{l=0}^{m}\binom{m}{l}u^l i^{m-l} \quad \textbf{(A.63)}$$

Substituting equation (A.63) into equation (A.62),

$$M_i^m = \sum_{l=0}^{m}\binom{m}{l} i^{m-l}\int_{-\infty}^{\infty} u^l \ \phi_L(u)d(u) = \sum_{l=0}^{m}\binom{m}{l} i^{m-l}\, M_0^l \quad \textbf{(A.64)}$$

We can now substitute equation (A.64) into equation (A.61)

$$M_0^m = \frac{1}{2^{m+1}}\sum_{i=0}^{L-1} p(i)\sum_{l=0}^{m}\binom{m}{l} i^{m-l}\, M_0^l \quad \textbf{(A.65)}$$

$$M_0^m = \frac{1}{2^{m+1}}\sum_{l=0}^{m-1}\binom{m}{l} M_0^l\left[\sum_{i=0}^{L-1} p(i)\, i^{m-l}\right] + \frac{1}{2^{m+1}}\sum_{i=0}^{L-1} p(i)\, M_0^m \quad \textbf{(A.66)}$$

However, from the normalization property of the filter coefficients expressed in equation (3.30), equation (A.66) can be rewritten as

$$M_0^m = \frac{1}{2^{m+1}}\sum_{l=0}^{m-1}\binom{m}{l} M_0^l\left[\sum_{i=0}^{L-1} p(i)\, i^{m-l}\right] + \frac{2}{2^{m+1}} M_0^m$$

$$M_0^m = \frac{1}{2(2^m-1)}\sum_{l=0}^{m-1}\binom{m}{l} M_0^l \sum_{i=0}^{L-1} p(i)\, i^{m-l} \quad \textbf{(A.67)}$$

This is the m^{th} moment M_0^m, for the scaling function $\phi_L(x)$. We can now compute the moments M_k^m by substituting equation (A.67) into equation (A.64). These are the moments expressed in equation (3.46) at multiresolution scale $j = 0$. However, it is crucial to evaluate the moments at multiresolution scale $j > 0$ for the purpose of implementing the multiresolution aspect in the formulation of the Daubechies WFEs. The moments at scale j for the scaling function translates are defined as [6]:

$$M_k^{j,m} = \langle x^m, \phi_{L,k}^j(x)\rangle = 2^{\frac{j}{2}}\int_{-\infty}^{\infty} x^m \phi_L\left(2^j x - k\right)dx \quad \textbf{(A.68)}$$

The moments of the scaling function translates at scale $j = 0$ is represented in equation (A.64)

$$M_k^{0,m} = M_k^m = \sum_{l=0}^{m} \binom{m}{l} k^{m-l} M_0^l \quad \textbf{(A.69)}$$

And subsequently the m^{th} moment of the scaling function at j = 0 is defined in equation (A.67) as:

$$M_0^{0,m} = M_0^m = \frac{1}{2(2^m - 1)} \sum_{l=0}^{m-1} \binom{m}{l} M_0^{0,l} \sum_{i=0}^{L-1} p(i)\, i^{m-l} \quad \textbf{(A.70)}$$

Having obtained the moments of the scaling function at scale j = 0, the moments at scale $j > 0$ are evaluated by solving equation (A.68), which can be rewritten as:

$$M_k^{j,m} = \frac{2^{\frac{j}{2}}}{2^{j\,(m+1)}} \int_{-\infty}^{\infty} \left(2^j x\right)^m \phi_L(2^j x - k) d(2^j x) \quad \textbf{(A.71)}$$

Let $2^j x = u$,

$$M_k^{j,m} = \frac{2^{\frac{j}{2}}}{2^{j\,(m+1)}} \int_{-\infty}^{\infty} (u + k)^m \phi_L(u) d(u) \quad \textbf{(A.72)}$$

from equation (A.63), equation (A.72) becomes

$$M_k^{j,m} = \frac{1}{2^{j\,(m+\frac{1}{2})}} \sum_{l=0}^{m} \binom{m}{l} k^{m-l} M_0^{0,l} \quad \textbf{(A.73)}$$

where the moment $M_0^{0,l}$ is evaluated from equation (A.70).

A.3. The B-splines and B-wavelet

Cardinal B-splines, general B-splines and the B-wavelet, which are related to the the BSWI wavelet described in Section 3.3, are formulated and discussed in this section.

A.3.1. The cardinal B-splines

Defining the cardinal B-splines of order $m \geq 2$ as:

$$N_m(x) = N_{m-1}(x) * N_1(x) = \int_0^1 N_{m-1}(x - t) dt \quad \textbf{(A.74)}$$

where for $m = 1$, $N_1(x)$ is the characteristic function of interval [0,1)

$$N_1(x) = \begin{cases} 1 & 0 \leq x < 1 \\ 0 & otherwise \end{cases} \quad \textbf{(A.75)}$$

The properties of the cardinal B-splines at multiresolution scale j = 0, for every $f(x) \in C$ and $g^m(x) \in C^m$, include [19]:

$$\int_{-\infty}^{\infty} f(x) N_m(x) dx = \int_0^1 \cdots \int_0^1 f(x_1 + x_2 + \cdots + x_{m-1} + x_m) dx_1\, dx_2 \cdots dx_{m-1} dx_m \quad \textbf{(A.76)}$$

$$\int_{-\infty}^{\infty} g^m(x) N_m(x) dx = \sum_{k=0}^{m} (-1)^{m-k} \binom{m}{k} g(k) \quad \textbf{(A.77)}$$

$$_{supp}\, N_m(x) = [0, m] \quad \textbf{(A.78)}$$

$$N_m(x) > 0 \quad for\ 0 < x < m \quad \textbf{(A.79)}$$

$$\sum_{k=-\infty}^{\infty} N_m(x - k) = 1 \quad \textbf{(A.80)}$$

$$N'_m(x) = \Delta N_{m-1}(x) = N_{m-1}(x) - N_{m-1}(x - 1) \quad \textbf{(A.81)}$$

$$N_m(x) = \frac{x}{m-1} N_{m-1}(x) + \frac{m - x}{m-1} N_{m-1}(x - 1) \quad \textbf{(A.82)}$$

$$N_m\left(\frac{m}{2} + x\right) = N_m\left(\frac{m}{2} - x\right) \quad \textbf{(A.83)}$$

The properties highlighted in equations (A.76) and (A.77) are proved in [19]. The support of the cardinal splines of order m is finite from 0 to m, therefore $N_m(x)$ disappears for $0 < x$ and $x > m$ as seen in (A.78). This property of compact support is an attractive wavelet feature as less scaling functions are necessary in the approximation of functions; thus reducing computational costs. Furthermore, the cardinal splines have positive values for all $x \in (0, m)$ from (A.79). The sum of the translates $N_m(x - k)$ provide the normalizing condition highlighted in equation (A.80). From equation (A.81), the derivative of the cardinal splines of order m, can be expressed in terms of the difference of cardinal spline of order m – 1 and its translate. Equation (A.83) implies that the cardinal splines have symmetry from the centre of its support.

Let the nested subspaces of the cardinal splines of $L^2(\mathbb{R})$ be expressed as:

$$\cdots V_{-2}^m \subset V_{-1}^m \subset V_0^m \subset V_1^m \subset V_2^m \subset \cdots \quad \textbf{(A.84)}$$

which via the multiresolution conditions satisfy the relation

$$\overline{\bigcup_{j \in \mathbb{Z}} V_j^m} = L^2(\mathbb{R}) \quad \textbf{(A.85)}$$

$$\bigcap_{j\in\mathbb{Z}} V_j^m = \{0\} \tag{A.86}$$

Therefore, for each $N_m(2^j x) \in V_j^m$, and from the nested relation given in equation (A.84), the cardinal splines have the property [19]

$$N_m\left(2^j x\right) = \sum_{k=-\infty}^{\infty} p_m(k)\, N_m\left(2^{j+1}x - k\right) \tag{A.87}$$

where $p_m(k)$, for $k \in \mathbb{Z}$, is a sequence in the space l^2.

$$p_m(k) = 2^{-m+1} \sum_{k=0}^{m} \binom{m}{k} \tag{A.88}$$

The cardinal splines can therefore be expressed in terms of the two-scale relation

$$N_m(x) = 2^{-m+1} \sum_{k=0}^{m} \binom{m}{k} N_m(2x - k) \tag{A.89}$$

Figure A-3 below illustrates the cardinal splines *a*) $N_1(x)$, *b*) $N_2(x)$, *c*) $N_3(x)$ and *b*) $N_4(x)$. It is observed that as the order *m* increase, the cardinal spline function becomes smoother; which is an ideal property of the cardinal splines.

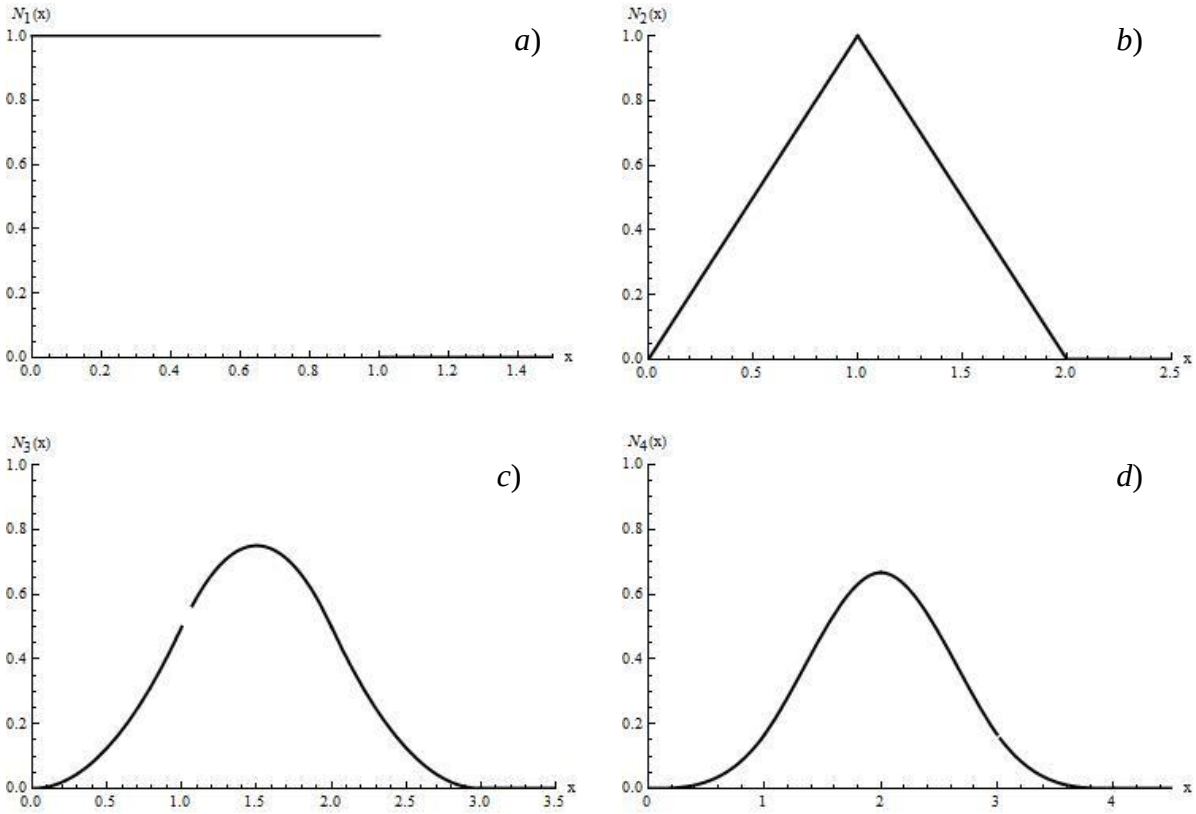

Figure A-3: Cardinal splines a) $N_1(x)$, b) $N_2(x)$, c) $N_3(x)$ and d) $N_4(x)$.

Furthermore, the Riesz basis of subspace V_j^m is defined as

$$B_{m,k}^j(x) = 2^{\frac{j}{2}} N_m\left(2^j x - k\right) \tag{A.90}$$

A.3.2. General B-splines

In this study, the general B-splines are constructed using a knot sequence. In the formulation of B-splines in this thesis, the approach of using knots sequences, similar to one presented by Boor [93] and Schumaker [94], will be used. The key property of B-spline knots emanates from the fact that the values contained within the knot sequence must be non-decreasing i.e., the knot value must be greater than or equal to the preceding knot value. Thus,

$$t_k \leq t_{k+1} \tag{A.91}$$

The knot values determine the point value of *t* at which the "pieces of the curve" join. The cardinal B-splines are classified as uniform B-splines, therefore, the knot values of uniform splines have the property

$$t_{k+1} - t_k = constant \tag{A.92}$$

where the knots are equally spaced. Open uniform knots have *i* equal knot values at each end and uniform inner knots. Thus,

$$\begin{aligned} t_k &= t_i && k \leq i \\ t_{k+1} - t_k &= \text{constant} && i \leq k < n+2 \\ t_k &= t_{k+i+1} && k \geq n+2 \end{aligned} \tag{A.93}$$

where the control points are $n + 1$. Non-uniform knots are only constrained by the condition in equation (A.91). A knot has multiplicity *i* if it appears *i* times in the knot sequence. Given the knots $t = (t_k, \dots, t_{k+m})$, the B-spline of order *m* (degree $m - 1$) is therefore given as:

$$B_{m,k}(x) = (t_{k+m} - t_k)[t_k, \dots, t_{k+m}]_f (. - x)_+^{m-1} \tag{A.94}$$

$[t_k, \dots, t_{k+m}]_f$ is the m^{th} divided difference of $(. - x)_+^{m-1}$ with respect to the variable *t*. Hence, $(. - x)_+^{m-1}$ can be written as $(t - x)_+^{m-1}$. Using the truncated power function

$$y_+^n = \begin{cases} y^n & y \geq 0 \\ 0 & y < 0 \end{cases} \tag{A.95}$$

one obtains

$$(t - x)_+^{m-1} = \begin{cases} (t - x)_+^{m-1} & (t - x) \geq 0 \\ 0 & (t - x) < 0 \end{cases} \tag{A.96}$$

The compact support of the B-splines is specified in terms of the knots.

$$_{supp}\, B_{m,k} = [t_k, t_{k+m}] \tag{A.97}$$

If f is a polynomial of degree $\leq m - 1$, then $[t_k, \dots, t_{k+m}]_f$ is constant as a function of $t_k, \dots, t_{k+m}$ and $[t_k, \dots, t_{k+m-1}]_f = 0$ for all $f \in \mathbb{P}_{m-1}$(space with a point at infinity). Taking into consideration equation (A.94), if x is not within the support interval, $B_{m,k}(x) = 0$ and $g(t) := (t - x)_+^{m-1}$ is a polynomial of degree < m on $[t_k, t_{k+m}]$. Hence,

$$[t_k, \dots, t_{k+m}]_g = 0 \tag{A.98}$$

For the order m B-splines with knot sequence t, there are only m B-splines that may be non-zero within the interval $[t_k, t_{k+m}]$. The normalization chosen for $B_{m,k}$ is the m^{th} divided difference at $t_k, \dots, t_{k+m}$ multiplied by $(t_{k+m} - t_k)$. For a situation with i multiple knots, i.e.,

$$t_k = t_{k+i} \Rightarrow\ t_k = t_{k+1} = t_{k+2} = \cdots = t_{k+i-1} = t_{k+i} \tag{A.99}$$

when computing for $[t_k, \dots, t_{k+i}]_g$, given that (A.99) applies, one obtains

$$[t_k, \dots, t_{k+i}]_g = \frac{g^{(i)}(t_k)}{k\,!} \tag{A.100}$$

However, if equation (A.99) does not apply then

$$[t_k, \dots, t_{k+i}]_g = \frac{[t_{k+1}, \dots, t_{k+i}]_g - [t_k, \dots, t_{k+i-1}]_g}{(t_{k+i} - t_k)} \tag{A.101}$$

Equations (A.100) and (A.101), with the assumption that the knots are non-uniform and $i = m$, allow equation (A.94) to be expressed as

$$B_{m,k}(x)$$
$$= \frac{(t_{k+m} - t_k)\{[t_{k+1}, \dots, t_{k+m}](. - x)_+^{m-1} - [t_k, \dots, t_{k+m-1}](. - x)_+^{m-1}\}}{(t_{k+m} - t_k)}$$
$$B_{m,k}(x) = [t_{k+1}, \dots, t_{k+m}](. - x)_+^{m-1} - [t_k, \dots, t_{k+m-1}](. - x)_+^{m-1} \tag{A.102}$$

In general, equations (A.100) and (A.101) may be expressed as:

$$[t_k, \dots, t_{k+m}]_f := \begin{cases} \dfrac{[t_{k+1}, \dots, t_{k+m}]_f - [t_k, \dots, t_{k+m-1}]_f}{(t_{k+m} - t_k)} & t_k < t_{k+m} \\ \dfrac{f^{(m+k)}(t_k)}{(m+k)\,!} & t_k = t_{k+m} \end{cases} \tag{A.103}$$

From equation (A.94)

$$\frac{B_{m,k}(x)}{(t_{k+m}-t_k)} = [t_k, \dots, t_{k+m}](.-x)_+^{m-1} \quad \textbf{(A.104)}$$

$$(x-t_k)[t_{k+1}, \dots, t_{k+m-1}](.-x)_+^{m-2} = (x-t_k)\frac{B_{m-1,k}(x)}{(t_{k+m-1}-t_k)} \quad \textbf{(A.105)}$$

$$(t_{k+m}-x)[t_{k+1}, \dots, t_{k+m}](.-x)_+^{m-2} = (t_{k+m}-x)\frac{B_{m-1,k+1}(x)}{(t_{k+m}-t_{k+1})} \quad \textbf{(A.106)}$$

Thus,

$$\frac{B_{m,k}(x)}{(t_{k+m}-t_k)} = \frac{(x-t_k)}{(t_{k+m}-t_k)}\frac{B_{m-1,k}(x)}{(t_{k+m-1}-t_k)} + \frac{(t_{k+m}-x)}{(t_{k+m}-t_k)}\frac{B_{m-1,k+1}(x)}{(t_{k+m}-t_{k+1})} \quad \textbf{(A.107)}$$

Multiplying both sides of equation (A.107) by $(t_{k+m}-t_k)$

$$B_{m,k}(x) = \frac{x-t_k}{t_{k+m-1}-t_k}B_{m-1,k}(x) + \frac{t_{k+m}-x}{t_{k+m}-t_{k+1}}B_{m-1,k+1}(x) \quad \textbf{(A.108)}$$

This is the general formulation for computing B-splines using knot sequences. The initial condition for the B-spline of order m = 1, is evaluated from equation (A.108) as

$$B_{1,k}(x) = \frac{x-t_k}{t_k-t_k}B_{0,k}(x) + \frac{t_k-x}{t_k-t_{k+1}}B_{0,k+1}(x)$$

$$B_{1,k}(x) = \begin{cases} 1 & t_k \le x \le t_{k+1} \\ 0 & otherwise \end{cases} \quad \textbf{(A.109)}$$

In the case of cardinal B-splines that have uniform knots, equation (A.92) applies and thus $B_{m,k}(x) = N_{m,k}(x)$. From equation (A.97), the support for m^{th} order B-splines is [0,m], thus the difference of the knots is $t_{k+1} - t_k = 1$. Taking this into consideration $t_k = k$, equation (A.109) therefore becomes

$$N_{1,k}(x) = \begin{cases} 1 & k \le x \le k+1 \\ 0 & otherwise \end{cases} \quad \textbf{(A.110)}$$

Subsequently, equation (A.108) for uniform splines is

$$N_{m,k}(x) = \frac{x-k}{k+m-1-k}N_{m-1,k}(x) + \frac{k+m-x}{k+m-k-1}N_{m-1,k+1}(x)$$

$$N_{m,k}(x) = \frac{x-k}{m-1}N_{m-1,k}(x) + \frac{k+m-x}{m-1}N_{m-1,k+1}(x) \quad \textbf{(A.111)}$$

A.3.3. B-spline Wavelet (B-wavelet)

The B-spline wavelet function, commonly referred to as the B-wavelet [19] or Chui-Wang B-wavelet [95], was presented by Chui and Quak [54] The wavelet functions are derived based on the cardinal B-splines. The discussion carried out on the formulation and properties of these wavelet functions are based on the theory presented by Chui [19].

Having defined the m^{th} order cardinal B-spline generated multiresolution subspace V_j^m in equation (A.85), there also exists the orthogonal complementary subspace W_j^m for $j \in \mathbb{Z}$ which obeys the multiresolution property in equation (3.2), i.e.,

$$V_{j+1}^m = V_j^m \oplus W_j^m \tag{A.112}$$

Let the m^{th} order fundamental cardinal spline be defined as

$$L_m(x) = \sum_{k=-\infty}^{\infty} c_k^{(m)} N_m\left(x + \frac{m}{2} - k\right) \tag{A.113}$$

with the interpolation property

$$L_m(i) = \delta_{i,0} \tag{A.114}$$

from

$$\sum_{k=-\infty}^{\infty} c_k^{(m)} N_m\left(\frac{m}{2} + i - k\right) = \delta_{i,0} \tag{A.115}$$

for $i \in \mathbb{Z}$. Unlike the cardinal B-splines N_m, the fundamental cardinal spline L_m does not vanish identically outside any compact set since the coefficient sequence $\left\{c_k^{(m)}\right\}$ is not finite for $m \geq 3$ [19]. However, $L_m(x)$ decays to zero linearly as $x \to \pm\infty$ since $\left\{c_k^{(m)}\right\}$ decays to zero exponentially as $k \to \pm\infty$. Therefore, let the wavelet function corresponding to wavelet subspace W_j^m be defined as

$$\psi_m(x) = L_{2m}^{(m)}(2x - 1) \tag{A.116}$$

with the properties

$$\int_{-\infty}^{\infty} N_m(x - k)\, \psi_m(x) dx = 0 \tag{A.117}$$

$$_{supp}\, \psi_m(x)[0, 2m - 1] \tag{A.118}$$

The B-wavelet can be expressed in terms of the cardinal B-spline via the two scale relation:

$$\psi_m(x) = \sum_{k=-\infty}^{\infty} q_k N_m(2x - k) \tag{A.119}$$

From equation (A.113),

$$L_{2m}(x) = \sum_{k=-\infty}^{\infty} c_k^{(2m)} N_{2m}(x + m - k) \tag{A.120}$$

Substituting equation (A.120) into (A.119)

$$\psi_m(x) = \sum_{k=-\infty}^{\infty} c_k^{(2m)} \sum_{l=0}^{m} (-1)^l \binom{m}{l} N_m(2x - 1 + m - k - l) \tag{A.121}$$

Therefore,

$$q(k) = \sum_{l=0}^{m} (-1)^l \binom{m}{l} c_{m+k-1-l}^{(2m)} = \frac{(-1)^k}{2^{m-1}} \sum_{l=0}^{m} \binom{m}{l} N_{2m}(k+1-l) \quad \textbf{(A.122)}$$

The B-wavelet of order m is expressed as

$$\psi_m(x) = \frac{1}{2^{m-1}} \sum_{l=0}^{2m-2} (-1)^l N_{2m}(l+1) N_{2m}^{(m)}(2x-l) \quad \textbf{(A.123)}$$

It can therefore be shown via the decomposition relation (A.13) and (A.14)

$$N_m(2x-k) = \sum_{n\in\mathbb{Z}} a_{k-2n} N_m(x-n) + \sum_{n\in\mathbb{Z}} b_{k-2n} \psi_m(x-n) \quad \textbf{(A.124)}$$

where the two sequences in space l^2, $\{a_n\}$ and $\{b_n\}$, ensure $\psi_m(x)$ generates all of the wavelet subspace W_0.

B. The Finite Element Matrices and Load Vectors

In this section, the finite element matrices and load vectors are briefly derived based on general finite element theory and contains mathematical concepts as presented in [27,29-31,97,98]. The axial rod, Euler Bernoulli beam and planar bar elements are formulated and used to solve the various numerical examples discussed in previous chapters of this thesis. The functionally graded beam finite element is as also described based on the formulations presented by Alshorbagy et al. [79].

B.1. Axial rod finite element

An axial rod is discretized into n_e number of elements of length L_e, with axial deformations u_1 and u_2 at the elemental nodes 1 and 2 respectively; as shown in Figure B-1. The rod has a uniform cross-sectional are *A* and Young's modulus *E*. The axial rod is subjected to surface forces $\acute{f}_s$, body forces $\acute{f}_b$ and point nodal loads f_i at node *i*.

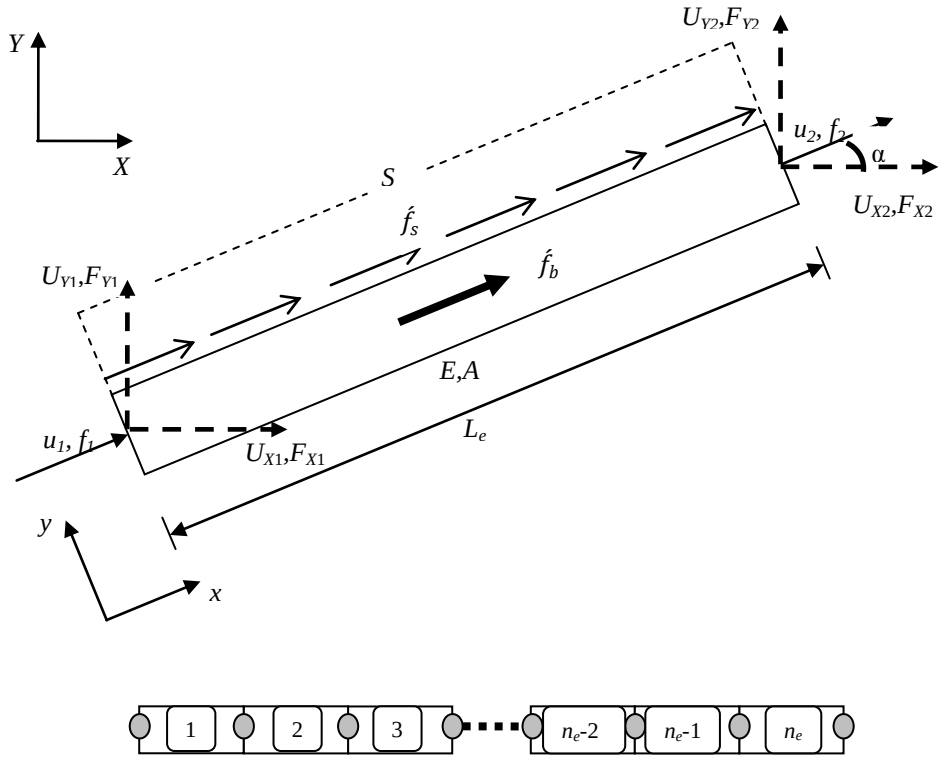

Figure B-1 : Axial rod finite element subjected to external forces.

The approximation of the axial displacement at point *x* within the rod is given by the binomial

$$u(x) = \beta_0 + \beta_1 x = \{1 \quad x\}\begin{Bmatrix}\beta_0\\ \beta_1\end{Bmatrix} = \{\acute{\mathbf{p}}\}^T\{\boldsymbol{\beta}\}$$

$$u(x) = \{N_1(x) \quad N_2(x)\}\begin{Bmatrix} u_1 \\ u_2 \end{Bmatrix} = \{\boldsymbol{N}_a(x)\}\{\boldsymbol{u_e}\} \tag{B.1}$$

where the vector $\{\boldsymbol{\beta}\}$ contains the unknown constants and $\{\dot{\mathbf{p}}\}$ contains the polynomial basis functions. The vector $\{N_a(x)\}$ contains the shape functions N_i for the axial rod element corresponding to the degrees of freedom (DOFs) within the element, where

$$\begin{aligned} N_1(x) &= 1 - \frac{x}{L_e} \\ N_2(x) &= \frac{x}{L_e} \end{aligned} \tag{B.2}$$

Having selected the order of the polynomials to formulate the shape functions of the rod element, the axial rod elemental stiffness and mass matrices can be obtained from the strain and kinetic energy of the rod. The FEM axial shape function $N_1(\xi)$ and $N_2(\xi)$, where $\xi = \frac{x}{L_e}$, are presented in Figure B-2.

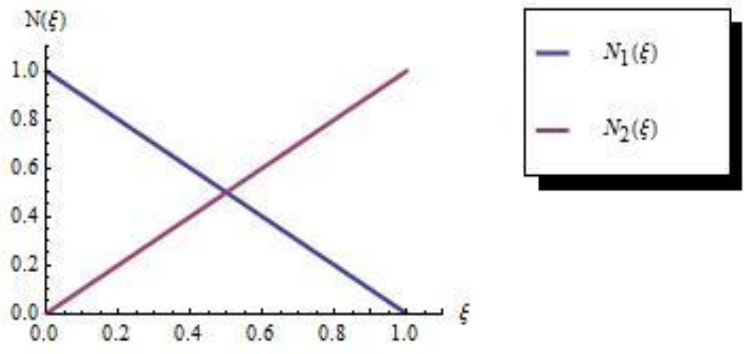

Figure B-2 : Axial rod linear shape functions.

The axial rod FEM stiffness and mass matrices are obtained from the strain and kinetic energy relations are given as [31]:

$$[\boldsymbol{k}_{r,e}] = \frac{EA}{L_e}\begin{bmatrix} 1 & -1 \\ -1 & 1 \end{bmatrix} \tag{B.3}$$

$$[\boldsymbol{m}_{r,e}] = \rho A L_e \begin{bmatrix} 2 & 1 \\ 1 & 2 \end{bmatrix} \tag{B.4}$$

The load vector of external forces $\{\boldsymbol{f_{r,e}}\}$ acting on the axial rod element *e* is given by

$$\{\boldsymbol{f_{r,e}}\} = \begin{Bmatrix} f_{x1} \\ f_{x2} \end{Bmatrix}_e = \{\boldsymbol{f^p_{r,e}}\} + \{\boldsymbol{f^s_{r,e}}\} + \{\boldsymbol{f^b_{r,e}}\} \tag{B.5}$$

where the vectors $\{\boldsymbol{f^p_{r,e}}\}$, $\{\boldsymbol{f^s_{r,e}}\}$ and $\{\boldsymbol{f^b_{r,e}}\}$ are the nodal point forces, nodal surface load equivalents and nodal body load equivalents within the axial rod element respectively and are given by

$$\{\boldsymbol{f^p_{r,e}}\} = \begin{Bmatrix} f_1 \\ f_2 \end{Bmatrix}_e \tag{B.6}$$

$$\{\boldsymbol{f}^{\boldsymbol{s}}_{\boldsymbol{r,e}}\} = \begin{Bmatrix} f^{s}_{x1} \\ f^{s}_{x2} \end{Bmatrix}_e = bL_e \int_0^1 \acute{f}_s(\xi) \begin{Bmatrix} 1-\xi \\ \xi \end{Bmatrix} d\xi \quad \textbf{(B.7)}$$

$$\{\boldsymbol{f}^{\boldsymbol{b}}_{\boldsymbol{r,e}}\} = \begin{Bmatrix} f^{b}_{x1} \\ f^{b}_{x2} \end{Bmatrix}_e = AL_e \int_0^1 \acute{f}_b(\xi) \begin{Bmatrix} 1-\xi \\ \xi \end{Bmatrix} d\xi \quad \textbf{(B.8)}$$

f_i is the axial point loads acting at node *i*.

B.2. Euler Bernoulli beam finite element

Figure B-3 below illustrates a two node Euler Bernoulli beam element of length L_e and uniform cross-section *A* in local coordinates *x*-*y*. The DOFs at node *i* of the beam element consist of the vertical deflection v_i and rotation θ_i with corresponding node forces f_i and bending moments $\acute{m}_1$ respectively.

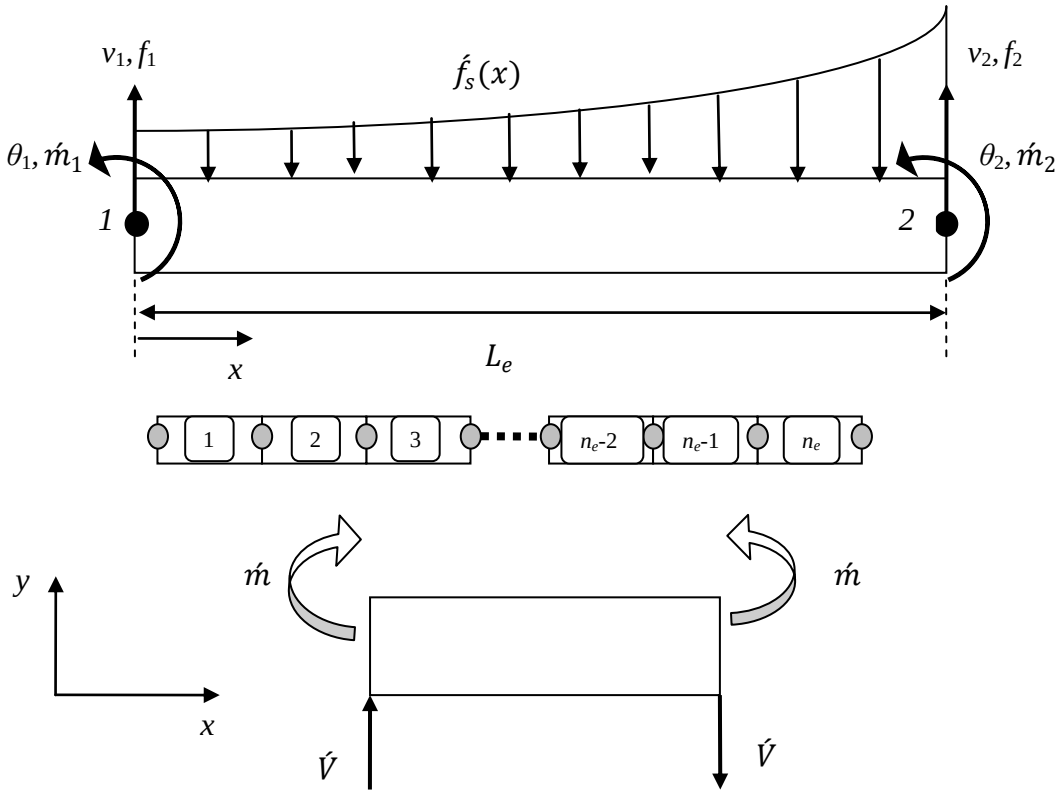

Figure B-3 : Euler-Bernoulli beam finite element subjected to external forces.

The beam is also subjected to a distributed load $\acute{f}_s(x)$ along the entire element. It is assumed that the axial effects are neglected. The vertical displacement, corresponding nodal forces and distributed loads are positive in the *y* direction while the rotation and corresponding moments are positive in the anticlockwise direction. The sign conventions for the shear forces $\acute{V}$ and bending moments for the beam elements $\acute{m}$ are also illustrated below. The beam element has four DOFs, hence the order of the polynomial selected must have the same number of

constants that correspond to these DOFs. Therefore, a polynomial of order 3 with four unknown constants α_0-α_3 is selected to approximate the displacement at any point *x* within the element. Thus,

$$v(x) = \alpha_0 + \alpha_1 x + \alpha_2 x^2 + \alpha_3 x^3 = \{1 \quad x \quad x^2 \quad x^3\}\begin{Bmatrix}\alpha_0\\ \alpha_1\\ \alpha_2\\ \alpha_3\end{Bmatrix} = \{\acute{\mathbf{p}}\}^T\{\acute{\boldsymbol{\alpha}}\} \tag{B.9}$$

$$v(x) = \{\boldsymbol{N}_b(x)\}\begin{Bmatrix}v_1\\ \theta_1\\ v_2\\ \theta_2\end{Bmatrix} = \{\boldsymbol{N}_b(x)\}\{v_e\} \tag{B.10}$$

and the rotation DOFs at any point within the beam element are given by

$$\theta(x) = \frac{\partial v(x)}{\partial x} = 0 + \alpha_1 + 2\alpha_2 x + 3\alpha_3 x^2 = \{0 \quad 1 \quad 2x \quad 3x^2\}\begin{Bmatrix}\alpha_0\\ \alpha_1\\ \alpha_2\\ \alpha_3\end{Bmatrix} \tag{B.11}$$

$$\theta(x) = \{\boldsymbol{N'}_b(x)\}\begin{Bmatrix}v_1\\ \theta_1\\ v_2\\ \theta_2\end{Bmatrix} = \{\boldsymbol{N'}_b(x)\}\{v_e\} \tag{B.12}$$

where the vector $\{\acute{\alpha}\}$ contains the unknown constants and $\{\acute{\mathbf{p}}\}$ the polynomial basis functions. The vector $\{N_b(x)\}$ contains the four shape functions ($\{N_1(x) \quad N_2(x) \quad N_3(x) \quad N_4(x)\}$) for the beam element corresponding to the degrees of freedom within the element:

$$\begin{aligned} N_1(x) &= 1 - 3(\frac{x}{L_e})^2 + 2(\frac{x}{L_e})^3 \\ N_2(x) &= x - 2\frac{x^2}{L_e} + \frac{x^3}{{L_e}^2} \\ N_3(x) &= 3(\frac{x}{L_e})^2 - 2(\frac{x}{L_e})^3 \\ N_4(x) &= \frac{x^3}{{L_e}^2} - \frac{x^2}{L_e} \end{aligned} \tag{B.13}$$

The shape functions in equation (B.13) are presented graphically in Figure B-4 below

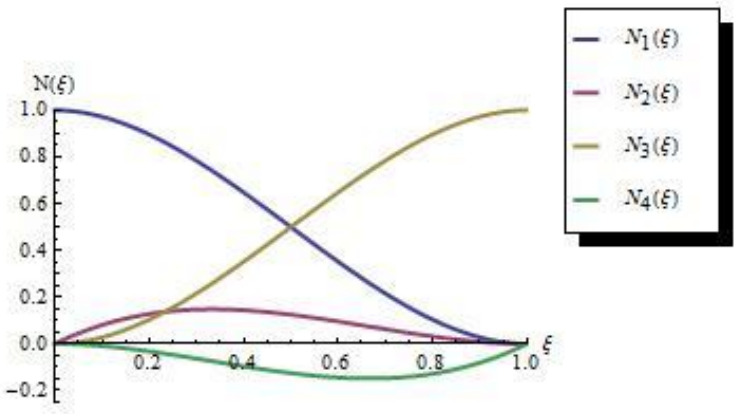

Figure B-4 : Euler Bernoulli beam shape functions.

The FEM beam element stiffness $[\boldsymbol{k}_{b,e}]$ and mass $[\boldsymbol{m}_{b,e}]$ matrices are evaluated from the bending strain energy and kinetic energy respectively as [30]:

$$[\boldsymbol{k}_{b,e}] = \frac{E\,I}{{L_e}^3}\begin{bmatrix} 12 & 6L_e & -12 & 6L_e \\ 6L_e & 4{L_e}^2 & -6L_e & 2{L_e}^2 \\ -12 & -6L_e & 12 & -6L_e \\ 6L_e & 2{L_e}^2 & -6L_e & 4{L_e}^2 \end{bmatrix} \tag{B.14}$$

$$[\boldsymbol{m}_{b,e}] = \frac{\rho A L_e}{420}\begin{bmatrix} 156 & 22L_e & 54 & -13L_e \\ 22L_e & 4{L_e}^2 & 13L_e & -3{L_e}^2 \\ 54 & 13L_e & 156 & -22L_e \\ -13L_e & -3{L_e}^2 & -22L_e & 4{L_e}^2 \end{bmatrix} \tag{B.15}$$

The total of the loads acting on the beam element is a sum of the nodal point loads $\{\boldsymbol{f}^{\boldsymbol{p}}_{\boldsymbol{b,e}}\}$, the concentrated moments $\{\boldsymbol{f}^{\boldsymbol{m}}_{\boldsymbol{b,e}}\}$ and the distributed load $\{\boldsymbol{f}^{\boldsymbol{s}}_{\boldsymbol{b,e}}\}$ acting across the element, i.e.,

$$\{\boldsymbol{f}_{\boldsymbol{b,e}}\} = \begin{Bmatrix} f_{y1} \\ m_1 \\ f_{y2} \\ m_2 \end{Bmatrix}_e = \{\boldsymbol{f}^{\boldsymbol{p}}_{\boldsymbol{b,e}}\} + \{\boldsymbol{f}^{\boldsymbol{m}}_{\boldsymbol{b,e}}\} + \{\boldsymbol{f}^{\boldsymbol{s}}_{\boldsymbol{b,e}}\} \tag{B.16}$$

where

$$\{\boldsymbol{f}^{\boldsymbol{p}}_{\boldsymbol{b,e}}\} = \begin{Bmatrix} f_1 \\ 0 \\ f_2 \\ 0 \end{Bmatrix}_e \tag{B.17}$$

$$\{\boldsymbol{f}^{\boldsymbol{m}}_{\boldsymbol{b,e}}\} = \begin{Bmatrix} 0 \\ \acute{m}_1 \\ 0 \\ \acute{m}_2 \end{Bmatrix}_e \tag{B.18}$$

$$\{\boldsymbol{f}^{\boldsymbol{s}}_{\boldsymbol{b,e}}\} = \begin{Bmatrix} f^s_{y1} \\ m^s_1 \\ f^s_{y2} \\ m^s_2 \end{Bmatrix}_e = bL_e \int_0^1 \acute{f}_s(\xi) \begin{Bmatrix} 1-3\xi^2+2\xi^3 \\ L_e(\xi-2\xi^2+\xi^3) \\ 3\xi^2-2\xi^3 \\ L_e(\xi^3-\xi^2) \end{Bmatrix} d\xi \tag{B.19}$$

B.3. Two dimensional planar bar finite element

A two dimensional planar bar, frame or generalized beam element, as illustrated in Figure B-5, is assumed to undergo both axial and transverse deformation. Furthermore, the bar element of length L_e may be subjected to axial loading, transverse loading and bending moments. Let the axial deformation, transverse displacement and rotation of the element at node *i*, in local coordinates, be described by u_i, v_i and θ_i respectively. Therefore, for a two node element, as described below, the total number of DOFs is 6. The bar element is therefore a combination of both the axial rod and Euler Bernoulli beam elements from the description given.

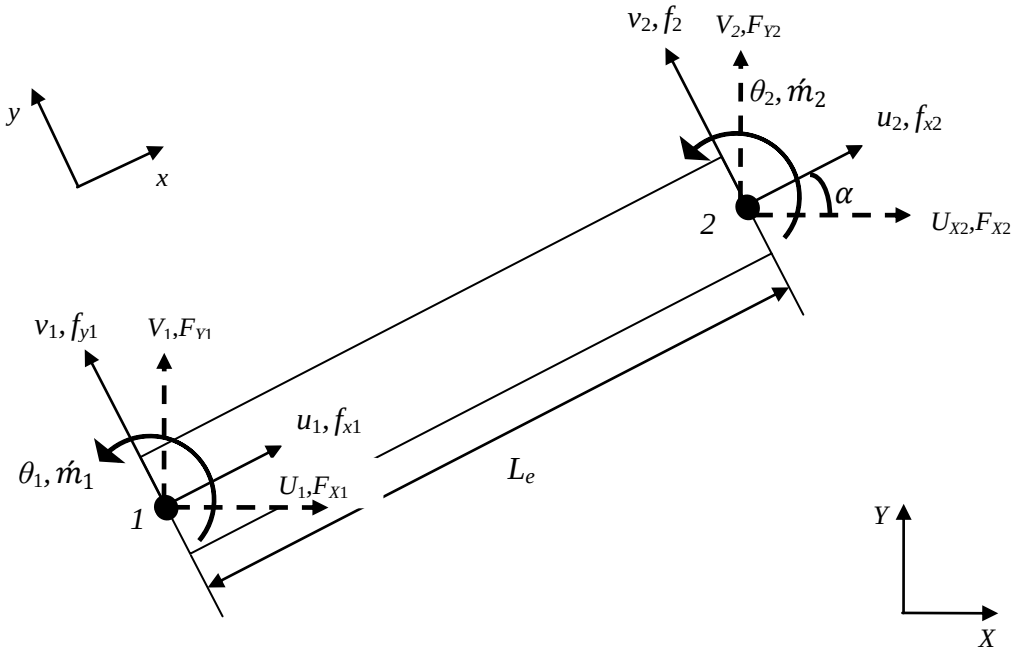

Figure B-5: Plane bar finite element.

Let the vector containing the planar bar element DOFs be denoted by

$$\{h_e\} = \begin{Bmatrix} u_1 \\ v_1 \\ \theta_1 \\ u_2 \\ v_2 \\ \theta_2 \end{Bmatrix} \tag{B.20}$$

The set of polynomials selected to approximate the axial and transverse deformations are as described in equations (B.1) and (B.9) respectively. There are 6 shape functions, which correspond to the number of DOFs within each element. They are obtained from equations (B.1), (B.10) and (B.12), where the axial and transverse deformations are given as:

$$\begin{Bmatrix} u(x) \\ v(x) \end{Bmatrix} = \begin{Bmatrix} N_1(x) & 0 & 0 & N_4(x) & 0 & 0 \\ 0 & N_2(x) & N_3(x) & 0 & N_5(x) & N_6(x) \end{Bmatrix}$$

$$\begin{Bmatrix} u(x) \\ v(x) \end{Bmatrix} = \{\boldsymbol{N}_p(x)\} \begin{Bmatrix} u_1 \\ v_1 \\ \theta_1 \\ u_2 \\ v_2 \\ \theta_2 \end{Bmatrix} \tag{B.21}$$

The shape functions are graphically represented in Figure B-6 below.

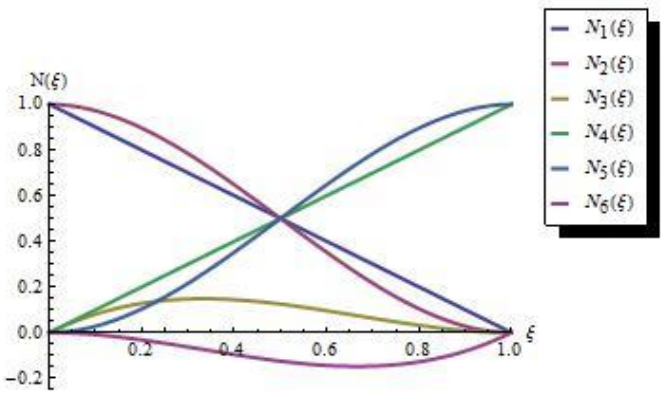

Figure B-6 : Planar bar element shape functions.

Taking into consideration that the planar bar is a combination of the axial rod and beam finite elements, the simplest and most straightforward way to evaluate the stiffness and mass element matrices, in local coordinates, is via superimposing the respective matrices for the rod and beam elements. In the case of the stiffness matrix, the rod and beam stiffness matrix is expanded to include the all the element DOFs. The entries of the additional DOFs are set at zero as shown in equations (B.22) and (B.23).

$$[\boldsymbol{k}_{r,e}] = \begin{bmatrix} \frac{EA}{L_e} & 0 & 0 & -\frac{EA}{L_e} & 0 & 0 \\ 0 & 0 & 0 & 0 & 0 & 0 \\ 0 & 0 & 0 & 0 & 0 & 0 \\ -\frac{EA}{L_e} & 0 & 0 & \frac{EA}{L_e} & 0 & 0 \\ 0 & 0 & 0 & 0 & 0 & 0 \\ 0 & 0 & 0 & 0 & 0 & 0 \end{bmatrix} \tag{B.22}$$

$$[\boldsymbol{k}_{b,e}] = \begin{bmatrix} 0 & 0 & 0 & 0 & 0 & 0 \\ 0 & \frac{12EI}{{L_e}^3} & \frac{6EI}{{L_e}^2} & 0 & -\frac{12EI}{{L_e}^3} & \frac{6EI}{{L_e}^2} \\ 0 & \frac{6EI}{{L_e}^2} & \frac{4EI}{L_e} & 0 & -\frac{6EI}{{L_e}^2} & \frac{2EI}{L_e} \\ 0 & 0 & 0 & 0 & 0 & 0 \\ 0 & -\frac{12EI}{{L_e}^3} & -\frac{6EI}{{L_e}^2} & 0 & \frac{12EI}{{L_e}^3} & -\frac{6EI}{{L_e}^2} \\ 0 & \frac{6EI}{{L_e}^2} & \frac{2EI}{L_e} & 0 & -\frac{6EI}{{L_e}^2} & \frac{4EI}{L_e} \end{bmatrix} \tag{B.23}$$

These two matrices are then superimposed so that the axial and transverse entries correspond to the associated DOFs in order to obtain the planar bar stiffness matrix in equation (B.24)

$$[\boldsymbol{k}_{p,e}] = [\boldsymbol{k}_{r,e}] + [\boldsymbol{k}_{b,e}]$$

$$[\boldsymbol{k}_{p,e}] = \begin{bmatrix} \frac{EA}{L_e} & 0 & 0 & -\frac{EA}{L_e} & 0 & 0 \\ 0 & \frac{12E\,I}{{L_e}^3} & \frac{6E\,I}{{L_e}^2} & 0 & -\frac{12E\,I}{{L_e}^3} & \frac{6E\,I}{{L_e}^2} \\ 0 & \frac{6E\,I}{{L_e}^2} & \frac{4E\,I}{L_e} & 0 & -\frac{6E\,I}{{L_e}^2} & \frac{2E\,I}{L_e} \\ -\frac{EA}{L_e} & 0 & 0 & \frac{EA}{L_e} & 0 & 0 \\ 0 & -\frac{12E\,I}{{L_e}^3} & -\frac{6E\,I}{{L_e}^2} & 0 & \frac{12E\,I}{{L_e}^3} & -\frac{6E\,I}{{L_e}^2} \\ 0 & \frac{6E\,I}{{L_e}^2} & \frac{2E\,I}{L_e} & 0 & -\frac{6E\,I}{{L_e}^2} & \frac{4E\,I}{L_e} \end{bmatrix} \quad \textbf{(B.24)}$$

The same applies for the mass matrix

$$[\boldsymbol{m}_{p,e}] = [\boldsymbol{m}_{r,e}] + [\boldsymbol{m}_{b,e}]$$

$$[\boldsymbol{m}_{p,e}] = \frac{\rho A L_e}{420}\begin{bmatrix} 140 & 0 & 0 & 70 & 0 & 0 \\ 0 & 156 & 22L_e & 0 & 54 & -13L_e \\ 0 & 22L_e & {4L_e}^2 & 0 & 13L_e & -3{L_e}^2 \\ 70 & 0 & 0 & 140 & 0 & 0 \\ 0 & 54 & 13L_e & 0 & 156 & -22L_e \\ 0 & -13L_e & -3{L_e}^2 & 0 & -22L_e & {4L_e}^2 \end{bmatrix} \quad \textbf{(B.25)}$$

The planar bar element is assumed to be capable of carrying various axial and transverse loads and bending moments. The total load vector is also obtained as a superposition of the expanded total axial loads of equation (B.5) and total transverse loads of equation (B.16), i.e.,

$$\{\boldsymbol{f}_{p,e}\} = \{\boldsymbol{f}_{r,e}\} + \{\boldsymbol{f}_{b,e}\}$$

$$\{\boldsymbol{f}_{p,e}\} = \begin{Bmatrix} f_{x1} \\ 0 \\ 0 \\ f_{x2} \\ 0 \\ 0 \end{Bmatrix}_e + \begin{Bmatrix} 0 \\ f_{y1} \\ m_1 \\ 0 \\ f_{y2} \\ m_2 \end{Bmatrix}_e = \begin{Bmatrix} f_{x1} \\ f_{y1} \\ m_1 \\ f_{x2} \\ f_{y2} \\ m_2 \end{Bmatrix}_e \quad \textbf{(B.26)}$$

B.4. The finite element method for the analysis of functionally graded materials

An approach taken by Alshorbagy et al. [74] analyses the free vibration of a FG beam derived from Euler Bernoulli beam theory and virtual work principle using FEM. Via the power law, the material properties of the FG beam vary through the thickness and also in the longitudinal direction. The shape functions used in this approach are those used to formulate a conventional FEM beam element with two nodes and three degrees of freedom (DOFs) at each node i.e. axial displacement, transverse displacement and rotation. The shape functions

are then employed to formulate the stiffness and mass matrices of the FG beam element. The variation of the FGM material properties is taken into account during the formulation of these matrices. Outlined below is the approach taken to formulate the FG Euler Bernoulli beam finite element.

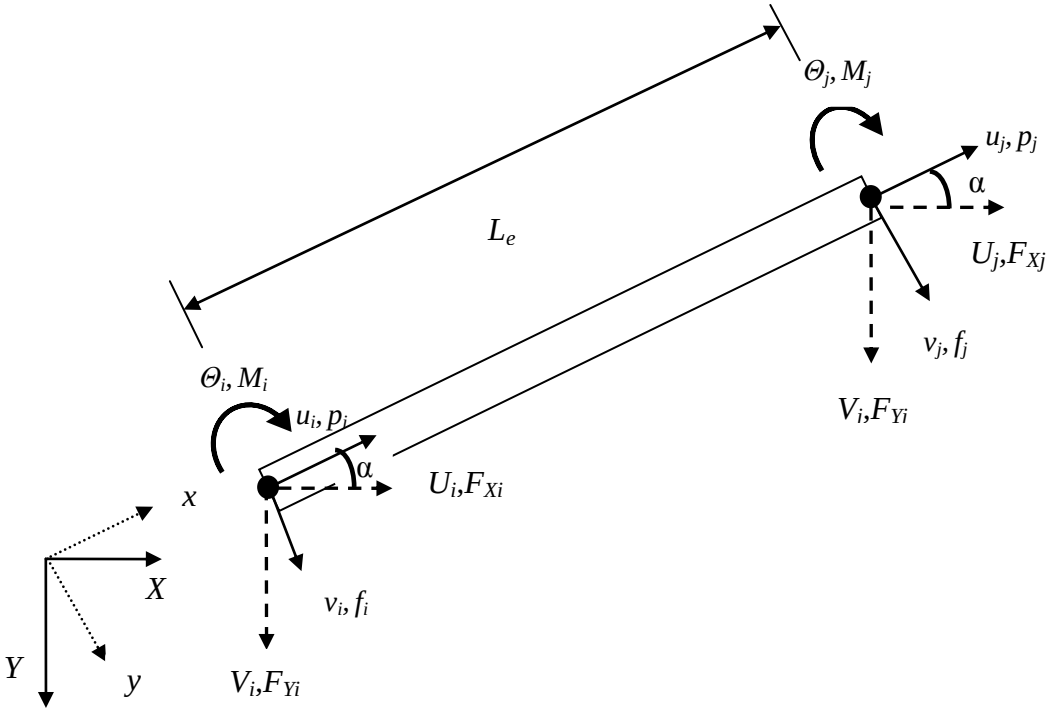

Figure B-7: Euler Bernoulli FG beam element.

The following formulation is carried out based on the Euler Bernoulli beam theory. It is assumed that at any point the axial and transverse displacements, denoted by u and v respectively, are given by:

$$u(x,z,t) = u_0(x,t) - y\frac{\partial v_0(x,t)}{\partial x}$$
$$v(x,z,t) = v_0(x,t) \qquad \textbf{(B.27)}$$

where u_0 is the axial displacement and w_0 is the transverse displacement at any point on the mid-plane. Furthermore, x, z and t represent the axial direction, transverse direction and time respectively. Equation (B.27) can be represented in matrix form as

$$\begin{Bmatrix} u \\ v \end{Bmatrix} = \begin{bmatrix} 1 & 0 & -y \\ 0 & 1 & 0 \end{bmatrix} \begin{Bmatrix} u_0 \\ v_0 \\ \dfrac{\partial v_0}{\partial x} \end{Bmatrix}$$

$$\{d\} = \begin{Bmatrix} u \\ v \end{Bmatrix} \tag{B.28}$$

where d is the displacement vector. Given that the beam will undergo small deformations, the normal strain ε_{xx} can be expressed in terms of the displacement as:

$$\varepsilon_{xx} = \frac{\partial u}{\partial x} = \frac{\partial (u_0(x,t) - y\frac{\partial v_{0(x,t)}}{\partial x})}{\partial x}$$

$$\varepsilon_{xx} = \frac{\partial u_0(x,t)}{\partial x} - y\frac{\partial^2 v_0(x,t)}{\partial x^2}$$

$$\varepsilon_{xx} = [1 \quad -y] \begin{Bmatrix} \frac{\partial u_0}{\partial x} \\ \frac{\partial^2 v_0}{\partial x^2} \end{Bmatrix} \tag{B.29}$$

The FG beam is also assumed to obey Hooke's law, thus the normal stress is given as:

$$\sigma_{xx} = E(y)\varepsilon_{xx} = E(y)\,[1 \quad -y] \begin{Bmatrix} \frac{\partial u_0}{\partial x} \\ \frac{\partial^2 v_0}{\partial x^2} \end{Bmatrix} \tag{B.30}$$

if the gradation variation of the Young's modulus is in the transverse direction. The natural coordinate of the beam, ξ, is defined as:

$$\xi = \frac{x}{L_e} \qquad\qquad \xi \in [0,1] \tag{B.31}$$

The axial and transverse displacements can be represented as polynomial functions, i.e.,

$$u_0(\xi) = \alpha_0 + \alpha_1\xi \tag{B.32}$$

$$v_0(\xi) = \beta_0 + \beta_1\xi + \beta_2\xi^2 + \beta_3\xi^3 \tag{B.33}$$

where α_i and β_i are coefficients. The slope of the beam is given as:

$$\theta(\xi) = \frac{\partial v_0(\xi)}{\partial x} = \frac{\partial v_0(\xi)}{\partial \xi}\frac{\partial \xi}{\partial x} = \frac{1}{L_e}\frac{\partial v_0(\xi)}{\partial \xi}$$

$$\theta(\xi) = \frac{1}{L_e}\frac{\partial(\beta_0 + \beta_1\xi + \beta_2\xi^2 + \beta_3\xi^3)}{\partial x} = \frac{1}{L_e}\beta_1 + 2\beta_2\xi + 3\beta_3\xi^2 \tag{B.34}$$

Equations (B.32), (B.33) and (B.34) can be rewritten as:

$$u_0(\xi) = \{1 \quad \xi\}\begin{Bmatrix} \alpha_0 \\ \alpha_1 \end{Bmatrix} \tag{B.35}$$

$$v_0(\xi) = \{1 \quad \xi \quad \xi^2 \quad \xi^3\}\begin{Bmatrix} \beta_0 \\ \beta_1 \\ \beta_2 \\ \beta_3 \end{Bmatrix} \tag{B.36}$$

$$\theta(\xi) = \frac{1}{L_e}\{0 \quad 1 \quad 2\xi \quad 3\xi^2\}\begin{Bmatrix} \beta_0 \\ \beta_1 \\ \beta_2 \\ \beta_3 \end{Bmatrix} \tag{B.37}$$

The next step is to evaluate the DOFs at the nodes of the FG beam element. Therefore, when $x = 0,\ \xi = 0$

$$u_0(0) = u_i = \{1 \quad 0\}\begin{Bmatrix}\alpha_0\\ \alpha_1\end{Bmatrix}$$
$$v_0(0) = v_i = \{1 \quad 0 \quad 0 \quad 0\}\begin{Bmatrix}\beta_0\\ \beta_1\\ \beta_2\\ \beta_3\end{Bmatrix} \tag{B.38}$$
$$\theta(0) = \theta_i = \frac{1}{L_e}\{0 \quad 1 \quad 0 \quad 0\}\begin{Bmatrix}\beta_0\\ \beta_1\\ \beta_2\\ \beta_3\end{Bmatrix}$$

When $x = L_e$, $\xi = 1$. Thus,

$$u_0(1) = u_j = \{1 \quad 1\}\begin{Bmatrix}\alpha_0\\ \alpha_1\end{Bmatrix}$$
$$v_0(1) = v_j = \{1 \quad 1 \quad 1 \quad 1\}\begin{Bmatrix}\beta_0\\ \beta_1\\ \beta_2\\ \beta_3\end{Bmatrix} \tag{B.39}$$
$$\theta(1) = \theta_j = \frac{1}{L_e}\{0 \quad 1 \quad 2 \quad 3\}\begin{Bmatrix}\beta_0\\ \beta_1\\ \beta_2\\ \beta_3\end{Bmatrix}$$

Equations (B.38) and (B.39) can be combined and expressed as:

$$\begin{Bmatrix}u_i\\ u_j\end{Bmatrix} = \begin{bmatrix}1 & 0\\ 1 & 1\end{bmatrix}\begin{Bmatrix}\alpha_0\\ \alpha_1\end{Bmatrix} \tag{B.40}$$

$$\begin{Bmatrix}v_i\\ \theta_i\\ v_j\\ \theta_j\end{Bmatrix} = \begin{bmatrix}1 & 0 & 0 & 0\\ 0 & \frac{1}{L_e} & 0 & 0\\ 1 & 1 & 1 & 1\\ 0 & \frac{1}{L_e} & \frac{2}{L_e} & \frac{3}{L_e}\end{bmatrix}\begin{Bmatrix}\beta_0\\ \beta_1\\ \beta_2\\ \beta_3\end{Bmatrix} \tag{B.41}$$

The coefficients in (B.40) and (B.41) can be made the subject of the formulations and substituted into equations (B.32), (B.33) and (B.34).

$$\begin{Bmatrix}\alpha_0\\ \alpha_1\end{Bmatrix} = \begin{bmatrix}1 & 0\\ 1 & 1\end{bmatrix}^{-1}\begin{Bmatrix}u_i\\ u_j\end{Bmatrix} \tag{B.42}$$

$$\begin{Bmatrix}\beta_0\\ \beta_1\\ \beta_2\\ \beta_3\end{Bmatrix} = \begin{bmatrix}1 & 0 & 0 & 0\\ 0 & \frac{1}{L_e} & 0 & 0\\ 1 & 1 & 1 & 1\\ 0 & \frac{1}{L_e} & \frac{2}{L_e} & \frac{3}{L_e}\end{bmatrix}^{-1}\begin{Bmatrix}v_i\\ \theta_i\\ v_j\\ \theta_j\end{Bmatrix} \tag{B.43}$$

Therefore,

$$u_0(\xi) = \{1 \quad \xi\}\begin{bmatrix} 1 & 0 \\ -1 & 1 \end{bmatrix}\begin{Bmatrix} u_i \\ u_j \end{Bmatrix} = \{1-\xi \quad \xi\}\begin{Bmatrix} u_i \\ u_j \end{Bmatrix} \tag{B.44}$$

$$v_0(\xi) = \{1 \quad \xi \quad \xi^2 \quad \xi^3\}\begin{bmatrix} 1 & 0 & 0 & 0 \\ 0 & L_e & 0 & 0 \\ -3 & -2L_e & 3 & -L_e \\ 2 & L_e & -2 & L_e \end{bmatrix}\begin{Bmatrix} v_i \\ \theta_i \\ v_j \\ \theta_j \end{Bmatrix}$$

$$v_0(\xi) = \{1-3\xi^2+2\xi^3 \quad L_e\xi - 2L_e\xi^2 + L_e\xi^3 \quad 3\xi^2 - 2\xi^3 \quad -L_e\xi^2 + L_e\xi^3\}\begin{Bmatrix} v_i \\ \theta_i \\ v_j \\ \theta_j \end{Bmatrix} \tag{B.45}$$

The strain energy within the given beam element is

$$\Pi_p = \frac{1}{2}\int_{vol} {\sigma_{xx}}^T \varepsilon_{xx}\, dV = \frac{1}{2}\iiint_{vol} {\sigma_{xx}}^T \varepsilon_{xx}\, dx\, dy\, dz \tag{B.46}$$

Substituting equations (B.29) and (B.30) into (B.46)

$$\Pi_p = \frac{1}{2}\iiint_{vol} E(y)\left(\frac{\partial u(x,t)}{\partial x} - y\frac{\partial^2 v(x,t)}{\partial x^2}\right)^T\left(\frac{\partial u(x,t)}{\partial x} - y\frac{\partial^2 v(x,t)}{\partial x^2}\right) dx\, dy\, dz \tag{B.47}$$

Expressing equation (B.47) in terms of the local coordinates of the beam element,

$$\Pi_p = \frac{1}{2}\iiint_{vol} E(y)\left(\frac{\partial \xi}{\partial x}\frac{\partial u(\xi,t)}{\partial \xi} - y\frac{\partial^2 \xi}{\partial x^2}\frac{\partial^2 v(\xi,t)}{\partial \xi^2}\right)^T\left(\frac{\partial \xi}{\partial x}\frac{\partial u(\xi,t)}{\partial \xi} - y\frac{\partial^2 \xi}{\partial x^2}\frac{\partial^2 v(\xi,t)}{\partial \xi^2}\right) dx\, dy\, dz$$

$$\Pi_p = \frac{L_e}{2}\iint_{dA}\int_0^1 E(y)\left(\frac{1}{L_e}\frac{\partial u(\xi)}{\partial \xi} - y\frac{1}{{L_e}^2}\frac{\partial^2 v(\xi)}{\partial \xi^2}\right)^T\left(\frac{1}{L_e}\frac{\partial u(\xi)}{\partial \xi} - y\frac{1}{{L_e}^2}\frac{\partial^2 v(\xi)}{\partial \xi^2}\right) d\xi\, dy\, dz$$

$$\Pi_p = \frac{L_e}{2}\iint_{dA}\int_0^1 E(y)\left[\frac{1}{{L_e}^2}\left(\frac{\partial u(\xi)}{\partial \xi}\right)^T\left(\frac{\partial u(\xi)}{\partial \xi}\right) - y\frac{1}{{L_e}^3}\left(\frac{\partial^2 v(\xi)}{\partial \xi^2}\right)^T\left(\frac{\partial u(\xi)}{\partial \xi}\right) - y\frac{1}{{L_e}^3}\left(\frac{\partial^2 v(\xi)}{\partial \xi^2}\right)^T\left(\frac{\partial u(\xi)}{\partial \xi}\right) + \frac{1}{{L_e}^4}y^2\left(\frac{\partial^2 v(\xi)}{\partial \xi^2}\right)^T\left(\frac{\partial^2 v(\xi)}{\partial \xi^2}\right)\right] d\xi\, dy\, dz \tag{B.48}$$

From equations (B.44) and (B.45), the derivative and second derivatives can be evaluated as:

$$\frac{\partial u(\xi)}{\partial \xi} = \{-1 \quad 1\}\begin{Bmatrix} u_i \\ u_j \end{Bmatrix} \tag{B.49}$$

$$\frac{\partial u(\xi)}{\partial \xi} = \{-1 \quad 0 \quad 0 \quad 1 \quad 0 \quad 0\} \begin{Bmatrix} u_i \\ v_i \\ \theta_i \\ u_i \\ v_j \\ \theta_j \end{Bmatrix}$$

$$\frac{\partial^2 v(\xi)}{\partial \xi^2} = \{-6+12\xi \quad -4L_e+6L_e\xi \quad 6-12\xi \quad -2L_e+6L_e\xi\} \begin{Bmatrix} v_i \\ \theta_i \\ v_j \\ \theta_j \end{Bmatrix}$$

$$\frac{\partial^2 v(\xi)}{\partial \xi^2} = \{0 \quad -6+12\xi \quad -4L_e+6L_e\xi \quad 0 \quad 6-12\xi \quad -2L_e+6L_e\xi\} \begin{Bmatrix} u_i \\ v_i \\ \theta_i \\ u_i \\ v_j \\ \theta_j \end{Bmatrix} \qquad \textbf{(B.50)}$$

Substituting equations (B.49) and (B.50) into (B.48)

$$\frac{1}{{L_e}^2}\int_z \int_{-\frac{h}{2}}^{\frac{h}{2}}\int_0^1 E(y)\left(\frac{\partial u(\xi)}{\partial \xi}\right)^T\left(\frac{\partial u(\xi)}{\partial \xi}\right) d\xi\, dy\, dz$$

$$= \frac{1}{{L_e}^2}\int_z \int_{-\frac{h}{2}}^{\frac{h}{2}}\int_0^1 E(y)\left(\{-1 \quad 0 \quad 0 \quad 1 \quad 0 \quad 0\}\begin{Bmatrix} u_i \\ v_i \\ \theta_i \\ u_i \\ v_j \\ \theta_j \end{Bmatrix}\right)^T\left(\{-1 \quad 0 \quad 0 \quad 1 \quad 0 \quad 0\}\begin{Bmatrix} u_i \\ v_i \\ \theta_i \\ u_i \\ v_j \\ \theta_j \end{Bmatrix}\right) d\xi\, dy\, dz$$

$$= \frac{1}{{L_e}^2}\int_z \int_{-\frac{h}{2}}^{\frac{h}{2}}\int_0^1 E(y)\begin{bmatrix} 1 & 0 & 0 & -1 & 0 & 0 \\ 0 & 0 & 0 & 0 & 0 & 0 \\ 0 & 0 & 0 & 0 & 0 & 0 \\ -1 & 0 & 0 & 1 & 0 & 0 \\ 0 & 0 & 0 & 0 & 0 & 0 \\ 0 & 0 & 0 & 0 & 0 & 0 \end{bmatrix}\left(\begin{Bmatrix} u_i \\ v_i \\ \theta_i \\ u_i \\ v_j \\ \theta_j \end{Bmatrix}^T\begin{Bmatrix} u_i \\ v_i \\ \theta_i \\ u_i \\ v_j \\ \theta_j \end{Bmatrix}\right) d\xi\, dy\, dz \qquad \textbf{(B.51)}$$

However, from equation (8.5)

$$E(y) = [E_c - E_m]\left(\frac{y}{h}+\frac{1}{2}\right)^n + E_m \qquad \textbf{(B.52)}$$

Substituting equation (B.52) into (B.51)

$$\frac{1}{{L_e}^2}\int_0^b \int_{-\frac{h}{2}}^{\frac{h}{2}}\int_0^1 E(y)\begin{bmatrix} 1 & 0 & 0 & -1 & 0 & 0 \\ 0 & 0 & 0 & 0 & 0 & 0 \\ 0 & 0 & 0 & 0 & 0 & 0 \\ -1 & 0 & 0 & 1 & 0 & 0 \\ 0 & 0 & 0 & 0 & 0 & 0 \\ 0 & 0 & 0 & 0 & 0 & 0 \end{bmatrix}\left(\begin{Bmatrix} u_i \\ v_i \\ \theta_i \\ u_i \\ v_j \\ \theta_j \end{Bmatrix}^T\begin{Bmatrix} u_i \\ v_i \\ \theta_i \\ u_i \\ v_j \\ \theta_j \end{Bmatrix}\right) d\xi\, dy\, dz$$

$$= \frac{b}{{L_e}^2}\left(\int_{-\frac{h}{2}}^{\frac{h}{2}}[E_c - E_m]\left(\frac{y}{h}+\frac{1}{2}\right)^n + E_m\, dy\right)\begin{bmatrix} 1 & 0 & 0 & -1 & 0 & 0 \\ 0 & 0 & 0 & 0 & 0 & 0 \\ 0 & 0 & 0 & 0 & 0 & 0 \\ -1 & 0 & 0 & 1 & 0 & 0 \\ 0 & 0 & 0 & 0 & 0 & 0 \\ 0 & 0 & 0 & 0 & 0 & 0 \end{bmatrix}\left(\begin{Bmatrix} u_i \\ v_i \\ \theta_i \\ u_i \\ v_j \\ \theta_j \end{Bmatrix}^T\begin{Bmatrix} u_i \\ v_i \\ \theta_i \\ u_i \\ v_j \\ \theta_j \end{Bmatrix}\right) \qquad \textbf{(B.53)}$$

where *b* is the width of the beam.

$$\int_z \int_{-\frac{h}{2}}^{\frac{h}{2}}\int_0^1 E(y)\frac{y}{{L_e}^3}\left(\frac{\partial u(\xi)}{\partial \xi}\right)^T\left(\frac{\partial^2 v(\xi)}{\partial \xi^2}\right) d\xi\, dy\, dz$$

$$= \int_z \int_{-\frac{h}{2}}^{\frac{h}{2}}\int_0^1 E(y)\frac{y}{{L_e}^3}\left(\{-1 \quad 0 \quad 0 \quad 1 \quad 0 \quad 0\}\begin{Bmatrix} u_i \\ v_i \\ \theta_i \\ u_i \\ v_j \\ \theta_j \end{Bmatrix}\right)^T\left(\{0 \quad -6+12\xi \quad -4L_e+6L_e\xi \quad 0 \quad 6-12\xi \quad -2L_e+6L_e\xi\}\begin{Bmatrix} u_i \\ v_i \\ \theta_i \\ u_i \\ v_j \\ \theta_j \end{Bmatrix}\right) d\xi\, dy\, dz$$

$$= \int_0^b \int_{-\frac{h}{2}}^{\frac{h}{2}} \int_0^1 E(y) \frac{y}{{L_e}^3} \begin{bmatrix} 0 & 6-12\xi & 4L_e-6L_e\xi & 0 & -6+12\xi & 2L_e-6L_e\xi \\ 0 & 0 & 0 & 0 & 0 & 0 \\ 0 & 0 & 0 & 0 & 0 & 0 \\ 0 & -6+12\xi & -4L_e+6L_e\xi & 0 & 6-12\xi & -2L_e+6L_e\xi \\ 0 & 0 & 0 & 0 & 0 & 0 \\ 0 & 0 & 0 & 0 & 0 & 0 \end{bmatrix} \left(\begin{Bmatrix} u_i \\ v_i \\ \theta_i \\ u_i \\ v_j \\ \theta_j \end{Bmatrix}^T \begin{Bmatrix} u_i \\ v_i \\ \theta_i \\ u_i \\ v_j \\ \theta_j \end{Bmatrix} \right) d\xi \, dy \, dz$$

$$= \frac{b}{{L_e}^3} \left(\int_{-\frac{h}{2}}^{\frac{h}{2}} \left(y[E_c - E_m] \left(\frac{y}{h} + \frac{1}{2} \right)^n + E_m \right) dy \right) \begin{bmatrix} 0 & 0 & L_e & 0 & 0 & -L_e \\ 0 & 0 & 0 & 0 & 0 & 0 \\ 0 & 0 & 0 & 0 & 0 & 0 \\ 0 & 0 & -L_e & 0 & 0 & L_e \\ 0 & 0 & 0 & 0 & 0 & 0 \\ 0 & 0 & 0 & 0 & 0 & 0 \end{bmatrix} \left(\begin{Bmatrix} u_i \\ v_i \\ \theta_i \\ u_i \\ v_j \\ \theta_j \end{Bmatrix}^T \begin{Bmatrix} u_i \\ v_i \\ \theta_i \\ u_i \\ v_j \\ \theta_j \end{Bmatrix} \right) \quad \textbf{(B.54)}$$

Furthermore,

$$\int_z \int_{-\frac{h}{2}}^{\frac{h}{2}} \int_0^1 E(y) \frac{y}{{L_e}^3} \left(\frac{\partial^2 v(\xi)}{\partial \xi^2} \right)^T \left(\frac{\partial u(\xi)}{\partial \xi} \right) d\xi \, dy \, dz$$

$$= \int_z \int_{-\frac{h}{2}}^{\frac{h}{2}} \int_0^1 E(y) \frac{y}{{L_e}^3} \left(\{0 \quad -6+12\xi \quad -4L_e+6L_e\xi \quad 0 \quad 6-12\xi \quad -2L_e+6L_e\xi\} \begin{Bmatrix} u_i \\ v_i \\ \theta_i \\ u_i \\ v_j \\ \theta_j \end{Bmatrix} \right)^T \left(\{-1 \quad 0 \quad 0 \quad 1 \quad 0 \quad 0\} \begin{Bmatrix} u_i \\ v_i \\ \theta_i \\ u_i \\ v_j \\ \theta_j \end{Bmatrix} \right) d\xi \, dy \, dz$$

$$= \int_0^b \int_{-\frac{h}{2}}^{\frac{h}{2}} \int_0^1 E(y) \frac{y}{{L_e}^3} \begin{bmatrix} 0 & 0 & 0 & 0 & 0 & 0 \\ 6-12\xi & 0 & 0 & -6+12\xi & 0 & 0 \\ 4L_e-6L_e\xi & 0 & 0 & -4L_e+6L_e\xi & 0 & 0 \\ 0 & 0 & 0 & 0 & 0 & 0 \\ -6+12\xi & 0 & 0 & 6-12\xi & 0 & 0 \\ 2L_e-6L_e\xi & 0 & 0 & -2L_e+6L_e\xi & 0 & 0 \end{bmatrix} \left(\begin{Bmatrix} u_i \\ v_i \\ \theta_i \\ u_i \\ v_j \\ \theta_j \end{Bmatrix}^T \begin{Bmatrix} u_i \\ v_i \\ \theta_i \\ u_i \\ v_j \\ \theta_j \end{Bmatrix} \right) d\xi \, dy \, dz$$

$$= \frac{b}{{L_e}^3} \left(\int_{-\frac{h}{2}}^{\frac{h}{2}} \left(y[E_c - E_m] \left(\frac{y}{h} + \frac{1}{2} \right)^n + E_m \right) dy \right) \begin{bmatrix} 0 & 0 & 0 & 0 & 0 & 0 \\ 0 & 0 & 0 & 0 & 0 & 0 \\ L_e & 0 & 0 & -L_e & 0 & 0 \\ 0 & 0 & 0 & 0 & 0 & 0 \\ 0 & 0 & 0 & 0 & 0 & 0 \\ -L_e & 0 & 00 & L_e & 0 & 0 \end{bmatrix} \left(\begin{Bmatrix} u_i \\ v_i \\ \theta_i \\ u_i \\ v_j \\ \theta_j \end{Bmatrix}^T \begin{Bmatrix} u_i \\ v_i \\ \theta_i \\ u_i \\ v_j \\ \theta_j \end{Bmatrix} \right) \quad \textbf{(B.55)}$$

Finally,

$$\int_z \int_{-\frac{h}{2}}^{\frac{h}{2}} \int_0^1 E(y) \frac{1}{{L_e}^4} y^2 \left(\frac{\partial^2 v(\xi)}{\partial \xi^2} \right)^T \left(\frac{\partial^2 v(\xi)}{\partial \xi^2} \right) d\xi \, dy \, dz$$

$$= \int_z \int_{-\frac{h}{2}}^{\frac{h}{2}} \int_0^1 E(y) \frac{y^2}{{L_e}^4} \left(\{0 \quad -6+12\xi \quad -4L_e+6L_e\xi \quad 0 \quad 6-12\xi \quad -2L_e+6L_e\xi\} \begin{Bmatrix} u_i \\ v_i \\ \theta_i \\ u_i \\ v_j \\ \theta_j \end{Bmatrix} \right)^T \left(\{0 \quad -6+12\xi \quad -4L_e+6L_e\xi \quad 0 \quad 6-12\xi \quad -2L_e+6L_e\xi\} \begin{Bmatrix} u_i \\ v_i \\ \theta_i \\ u_i \\ v_j \\ \theta_j \end{Bmatrix} \right) d\xi \, dy \, dz$$

$$= \int_0^b \int_{-\frac{h}{2}}^{\frac{h}{2}} \int_0^1 E(y) \frac{y^2}{{L_e}^4} \begin{bmatrix} 0 & 0 & 0 & 0 & 0 & 0 \\ 0 & 36-144\xi+144\xi^2 & 24L_e-84L_e\xi+72L_e\xi^2 & 0 & -36+144\xi-144\xi^2 & 12L_e-60L_e\xi+72L_e\xi^2 \\ 0 & 24L_e-84L_e\xi+72L_e\xi^2 & {16L_e}^2-48{L_e}^2\xi+36{L_e}^2\xi^2 & 0 & -24L_e+84L_e\xi-72L_e\xi^2 & 8{L_e}^2-36{L_e}^2\xi+36{L_e}^2\xi^2 \\ 0 & 0 & 0 & 0 & 0 & 0 \\ 0 & -36+144\xi-144\xi^2 & -24L_e+84L_e\xi-72L_e\xi^2 & 0 & 36-144\xi+144\xi^2 & -12L_e+60L_e\xi-72L_e\xi^2 \\ 0 & 12L_e-60L_e\xi+72L_e\xi^2 & 8{L_e}^2-36{L_e}^2\xi+36{L_e}^2\xi^2 & 0 & -12L_e+60L_e\xi-72L_e\xi^2 & 4{L_e}^2-24\xi+36{L_e}^2\xi^2 \end{bmatrix} \left(\begin{Bmatrix} u_i \\ v_i \\ \theta_i \\ u_i \\ v_j \\ \theta_j \end{Bmatrix}^T \begin{Bmatrix} u_i \\ v_i \\ \theta_i \\ u_i \\ v_j \\ \theta_j \end{Bmatrix} \right) d\xi \, dy \, dz$$

$$= \frac{b}{{L_e}^4} \left(\int_{-\frac{h}{2}}^{\frac{h}{2}} \left(y^2[E_c - E_m] \left(\frac{y}{h} + \frac{1}{2} \right)^n + E_m \right) dy \right) \begin{bmatrix} 0 & 0 & 0 & 0 & 0 & 0 \\ 0 & 12 & 6L_e & 0 & -12 & 6L_e \\ 0 & 6L_e & 4{L_e}^2 & 0 & -6L_e & 2{L_e}^2 \\ 0 & 0 & 0 & 0 & 0 & 0 \\ 0 & -12 & -6L_e & 0 & 12 & -6L_e \\ 0 & 6L_e & 2{L_e}^2 & 0 & -6L_e & 4{L_e}^2 \end{bmatrix} \left(\begin{Bmatrix} u_i \\ v_i \\ \theta_i \\ u_i \\ v_j \\ \theta_j \end{Bmatrix}^T \begin{Bmatrix} u_i \\ v_i \\ \theta_i \\ u_i \\ v_j \\ \theta_j \end{Bmatrix} \right) \quad \textbf{(B.56)}$$

The stiffness matrix of the FG beam can be obtained from equations (B.53), (B.54), (B.55) and (B.56) as follows

$$[k_e^a] = \frac{b}{L_e} \left(\int_{-\frac{h}{2}}^{\frac{h}{2}} \left([E_c - E_m] \left(\frac{y}{h} + \frac{1}{2} \right)^n + E_m \right) dy \right) \begin{bmatrix} 1 & 0 & 0 & -1 & 0 & 0 \\ 0 & 0 & 0 & 0 & 0 & 0 \\ 0 & 0 & 0 & 0 & 0 & 0 \\ -1 & 0 & 0 & 1 & 0 & 0 \\ 0 & 0 & 0 & 0 & 0 & 0 \\ 0 & 0 & 0 & 0 & 0 & 0 \end{bmatrix} \quad \textbf{(B.57)}$$

$$[k_e^b] = \frac{b}{{L_e}^2}\left(\int_{-\frac{h}{2}}^{\frac{h}{2}}\left(y[E_c - E_m]\left(\frac{y}{h}+\frac{1}{2}\right)^n + E_m\right)dy\right)\begin{bmatrix}0 & 0 & L_e & 0 & 0 & -L_e\\ 0 & 0 & 0 & 0 & 0 & 0\\ 0 & 0 & 0 & 0 & 0 & 0\\ 0 & 0 & -L_e & 0 & 0 & L_e\\ 0 & 0 & 0 & 0 & 0 & 0\\ 0 & 0 & 0 & 0 & 0 & 0\end{bmatrix} \quad \textbf{(B.58)}$$

$$[k_e^c] = \frac{b}{{L_e}^2}\left(\int_{-\frac{h}{2}}^{\frac{h}{2}}\left(y[E_c - E_m]\left(\frac{y}{h}+\frac{1}{2}\right)^n + E_m\right)dy\right)\begin{bmatrix}0 & 0 & 0 & 0 & 0 & 0\\ 0 & 0 & 0 & 0 & 0 & 0\\ L_e & 0 & 0 & -L_e & 0 & 0\\ 0 & 0 & 0 & 0 & 0 & 0\\ 0 & 0 & 0 & 0 & 0 & 0\\ -L_e & 0 & 0 & L_e & 0 & 0\end{bmatrix} \quad \textbf{(B.59)}$$

$$[k_e^d] = \frac{b}{{L_e}^3}\left(\int_{-\frac{h}{2}}^{\frac{h}{2}}\left(y^2[E_c - E_m]\left(\frac{y}{h}+\frac{1}{2}\right)^n + E_m\right)dy\right)\begin{bmatrix}0 & 0 & 0 & 0 & 0 & 0\\ 0 & 12 & 6L_e & 0 & -12 & 6L_e\\ 0 & 6L_e & 4{L_e}^2 & 0 & -6L_e & 2{L_e}^2\\ 0 & 0 & 0 & 0 & 0 & 0\\ 0 & -12 & -6L_e & 0 & 12 & -6L_e\\ 0 & 6L_e & 2{L_e}^2 & 0 & -6L_e & 4{L_e}^2\end{bmatrix} \quad \textbf{(B.60)}$$

Therefore, the stiffness FG beam element matrix is

$$[k_e] = [k_e^a] - [k_e^b] - [k_e^c] + [k_e^d] \quad \textbf{(B.61)}$$

The kinetic energy Λ, is given by

$$\Lambda = \frac{1}{2} mass\ vel^2 \quad \textbf{(B.62)}$$

mass and *vel* are the mass and velocity of the beam respectively. However, the mass can be expressed as

$$mass = \rho\int_{vol} dV = \iiint_{vol} \rho(y)\, dx\, dy\, dz \quad \textbf{(B.63)}$$

$\rho(y)$ represents the varying density of the FG beam element obtained from equation (8.5)

$$\rho(y) = [\rho_c - \rho_m]\left(\frac{y}{h}+\frac{1}{2}\right)^n + \rho_m \quad \textbf{(B.64)}$$

The velocity components of the beam in axial and transverse directions can be expressed as:

$$\begin{gathered}\left(\frac{\partial\, u_0(x,t)}{\partial t}\right) = \{\dot{u}_0(x,t)\}\\ \left(\frac{\partial\, v_0(x,t)}{\partial t}\right) = \{\dot{v}_0(x,t)\}\\ \left(\frac{\partial\, u(x,t)}{\partial t}\right) = \{\dot{u}(x,t)\} = \dot{u}_0(x,t) - y\frac{\partial \dot{v}_0(x,t)}{\partial x}\end{gathered} \quad \textbf{(B.65)}$$

The kinetic energy of the beam from equation (B.63) is

$$\Lambda = \frac{1}{2}\iiint_{vol} \rho(y)(\{\dot{u}(x,t)\}^T\{\dot{u}(x,t)\} + \{\dot{v}_0(x,t)\}^T\{\dot{v}_0(x,t)\})\, dx\, dy\, dz$$

$$\Lambda = \frac{1}{2}\iiint_{vol} \rho(y)\left(\left(\dot{u}_0(x,t) - y\frac{\partial \dot{v}_0(x,t)}{\partial x}\right)\left(\dot{u}_0(x,t) - y\frac{\partial \dot{v}_0(x,t)}{\partial x}\right) + (\dot{v}_0(x,t)\dot{v}_0(x,t))\right) dx\, dy\, dz$$

$$\Lambda = \frac{L_e}{2}\iint_A \int_0^1 \rho(y)\Bigg(\left(\dot{u}_0(\xi,t)\dot{u}_0(\xi,t)\right) - \frac{y}{L_e}\left(\dot{u}_0(\xi,t)\frac{\partial \dot{v}_0(\xi,t)}{\partial x}\right) - \frac{y}{L_e}\left(\frac{\partial \dot{v}_0(\xi,t)}{\partial \xi}\dot{u}_0(\xi,t)\right) + \frac{y^2}{{L_e}^2}\left(\frac{\partial \dot{v}_0(\xi,t)}{\partial x}\frac{\partial \dot{v}_0(\xi,t)}{\partial x}\right) + \left(\dot{v}_0(\xi,t)\dot{v}_0(\xi,t)\right)\Bigg)\, d\xi\, dy\, dz \quad \textbf{(B.66)}$$

From equations (B.44) and (B.45)

$$\dot{u}_0(\xi) = \{1-\xi \quad 0 \quad 0 \quad \xi \quad 0 \quad 0\}\begin{Bmatrix}\dot{u}_i\\ \dot{v}_i\\ \dot{\theta}_i\\ \dot{u}_i\\ \dot{v}_j\\ \dot{\theta}_j\end{Bmatrix} \quad \textbf{(B.67)}$$

$$\dot{v}_0(\xi) = \{0 \quad 1-3\xi^2+2\xi^3 \quad L_e\xi - 2L_e\xi^2 + L_e\xi^3 \quad 0 \quad 3\xi^2-2\xi^3 \quad -L_e\xi^2 + L_e\xi^3\}\begin{Bmatrix}\dot{u}_i\\ \dot{v}_i\\ \dot{\theta}_i\\ \dot{u}_i\\ \dot{v}_j\\ \dot{\theta}_j\end{Bmatrix} \quad \textbf{(B.68)}$$

Solving the individual parts of equation (B.66)

$$\iint_A \int_0^1 L_e\rho(y)\left(\dot{u}_0(\xi,t)\dot{u}_0(\xi,t)\right) d\xi\, dy\, dz = b\, L_e \int_{-\frac{h}{2}}^{\frac{h}{2}}\int_0^1 \rho(y)\left(\dot{u}_0(\xi,t)\dot{u}_0(\xi,t)\right) d\xi\, dy \quad \textbf{(B.69)}$$

Substituting equation (B.67) into (B.69)

$$\iint_A \int_0^1 L_e\rho(y)\left(\dot{u}_0(\xi,t)\dot{u}_0(\xi,t)\right) d\xi\, dy\, dz$$

$$= b\, L_e \int_{-\frac{h}{2}}^{\frac{h}{2}}\int_0^1 \rho(y)\left(\{1-\xi \quad 0 \quad 0 \quad \xi \quad 0 \quad 0\}\begin{Bmatrix}\dot{u}_i\\ \dot{v}_i\\ \dot{\theta}_i\\ \dot{u}_i\\ \dot{v}_j\\ \dot{\theta}_j\end{Bmatrix}\right)^T\left(\{1-\xi \quad 0 \quad 0 \quad \xi \quad 0 \quad 0\}\begin{Bmatrix}\dot{u}_i\\ \dot{v}_i\\ \dot{\theta}_i\\ \dot{u}_i\\ \dot{v}_j\\ \dot{\theta}_j\end{Bmatrix}\right) d\xi\, dy$$

$$= b\, L_e \int_{-\frac{h}{2}}^{\frac{h}{2}}\int_0^1 \rho(y)\begin{bmatrix}1-2\xi+\xi^2 & 0 & 0 & \xi-\xi^2 & 0 & 0\\ 0 & 0 & 0 & 0 & 0 & 0\\ 0 & 0 & 0 & 0 & 0 & 0\\ \xi-\xi^2 & 0 & 0 & \xi^2 & 0 & 0\\ 0 & 0 & 0 & 0 & 0 & 0\\ 0 & 0 & 0 & 0 & 0 & 0\end{bmatrix} d\xi\, dy \begin{Bmatrix}\dot{u}_i\\ \dot{v}_i\\ \dot{\theta}_i\\ \dot{u}_i\\ \dot{v}_j\\ \dot{\theta}_j\end{Bmatrix}^T\begin{Bmatrix}\dot{u}_i\\ \dot{v}_i\\ \dot{\theta}_i\\ \dot{u}_i\\ \dot{v}_j\\ \dot{\theta}_j\end{Bmatrix}$$

$$= b\, L_e \int_{-\frac{h}{2}}^{\frac{h}{2}} \rho(y)\, dy \begin{Bmatrix}\dot{u}_i\\ \dot{v}_i\\ \dot{\theta}_i\\ \dot{u}_i\\ \dot{v}_j\\ \dot{\theta}_j\end{Bmatrix}^T\begin{bmatrix}\frac{1}{3} & 0 & 0 & \frac{1}{6} & 0 & 0\\ 0 & 0 & 0 & 0 & 0 & 0\\ 0 & 0 & 0 & 0 & 0 & 0\\ \frac{1}{6} & 0 & 0 & \frac{1}{3} & 0 & 0\\ 0 & 0 & 0 & 0 & 0 & 0\\ 0 & 0 & 0 & 0 & 0 & 0\end{bmatrix}\begin{Bmatrix}\dot{u}_i\\ \dot{v}_i\\ \dot{\theta}_i\\ \dot{u}_i\\ \dot{v}_j\\ \dot{\theta}_j\end{Bmatrix} \quad \textbf{(B.70)}$$

The second part

$$\iint_A \int_0^1 L_e\frac{y}{L_e}\left(\dot{u}_0(\xi,t)\frac{\partial \dot{v}_0(\xi,t)}{\partial x}\right) d\xi\, dy\, dz$$

$$= b\, L_e \int_{-\frac{h}{2}}^{\frac{h}{2}}\int_0^1 \rho(y)\left(\{0 \quad 1-3\xi^2+2\xi^3 \quad L_e\xi - 2L_e\xi^2 + L_e\xi^3 \quad 0 \quad 3\xi^2-2\xi^3 \quad -L_e\xi^2 + L_e\xi^3\}\begin{Bmatrix}\dot{u}_i\\ \dot{v}_i\\ \dot{\theta}_i\\ \dot{u}_i\\ \dot{v}_j\\ \dot{\theta}_j\end{Bmatrix}\right)^T\left(\{1-\xi \quad 0 \quad 0 \quad \xi \quad 0 \quad 0\}\begin{Bmatrix}\dot{u}_i\\ \dot{v}_i\\ \dot{\theta}_i\\ \dot{u}_i\\ \dot{v}_j\\ \dot{\theta}_j\end{Bmatrix}\right) d\xi\, dy$$

$$= b\,L_e \int_{-\frac{h}{2}}^{\frac{h}{2}} \int_0^1 \rho(y) \begin{bmatrix} 0 & -6\xi + 12\xi^2 - 6\xi^3 & L_e - 5\xi L_e + 7\xi^2 L_e - 3\xi^3 L_e & 0 & 6\xi - 12\xi^2 + 6\xi^3 & -2\xi L_e + 5\xi^2 L_e - 3\xi^3 L_e \\ 0 & 0 & 0 & 0 & 0 & 0 \\ 0 & 0 & 0 & 0 & 0 & 0 \\ 0 & -6\xi^2 + 6\xi^3 & \xi L_e - 4\xi^2 L_e + 3\xi^3 L_e & 0 & 6\xi^2 - 6\xi^3 & -2\xi^2 L_e + 3\xi^3 L_e \\ 0 & 0 & 0 & 0 & 0 & 0 \\ 0 & 0 & 0 & 0 & 0 & 0 \end{bmatrix} d\xi\, dy \begin{Bmatrix} \dot{u}_i \\ \dot{v}_i \\ \dot{\theta}_i \\ \dot{u}_i \\ \dot{v}_j \\ \dot{\theta}_j \end{Bmatrix}^T \begin{Bmatrix} \dot{u}_i \\ \dot{v}_i \\ \dot{\theta}_i \\ \dot{u}_i \\ \dot{v}_j \\ \dot{\theta}_j \end{Bmatrix}$$

$$= b\,L_e \int_{-\frac{h}{2}}^{\frac{h}{2}} \rho(y)\, dy \begin{Bmatrix} \dot{u}_i \\ \dot{v}_i \\ \dot{\theta}_i \\ \dot{u}_i \\ \dot{v}_j \\ \dot{\theta}_j \end{Bmatrix}^T \begin{bmatrix} 0 & -\frac{1}{2} & \frac{L_e}{12} & 0 & \frac{1}{2} & -\frac{L_e}{12} \\ 0 & 0 & 0 & 0 & 0 & 0 \\ 0 & 0 & 0 & 0 & 0 & 0 \\ 0 & -\frac{1}{2} & -\frac{L_e}{12} & 0 & \frac{1}{2} & \frac{L_e}{12} \\ 0 & 0 & 0 & 0 & 0 & 0 \\ 0 & 0 & 0 & 0 & 0 & 0 \end{bmatrix} \begin{Bmatrix} \dot{u}_i \\ \dot{v}_i \\ \dot{\theta}_i \\ \dot{u}_i \\ \dot{v}_j \\ \dot{\theta}_j \end{Bmatrix} \quad \textbf{(B.71)}$$

The third part

$$\iint_A \int_0^1 L_e \frac{y}{L_e} \left(\frac{\partial \dot{v}_0(\xi,t)}{\partial x} \dot{u}_0(\xi,t) \right) d\xi\, dy\, dz$$

$$= b\,L_e \int_{-\frac{h}{2}}^{\frac{h}{2}} \int_0^1 \rho(y) \left(\{0 \quad 1-3\xi^2+2\xi^3 \quad L_e\xi - 2L_e\xi^2 + L_e\xi^3 \quad 0 \quad 3\xi^2 - 2\xi^3 \quad -L_e\xi^2 + L_e\xi^3\} \begin{Bmatrix} \dot{u}_i \\ \dot{v}_i \\ \dot{\theta}_i \\ \dot{u}_i \\ \dot{v}_j \\ \dot{\theta}_j \end{Bmatrix} \right)^T \left(\{1-\xi \quad 0 \quad 0 \quad \xi \quad 0 \quad 0\} \begin{Bmatrix} \dot{u}_i \\ \dot{v}_i \\ \dot{\theta}_i \\ \dot{u}_i \\ \dot{v}_j \\ \dot{\theta}_j \end{Bmatrix} \right) d\xi\, dy$$

$$= b\,L_e \int_{-\frac{h}{2}}^{\frac{h}{2}} \int_0^1 \rho(y) \begin{bmatrix} 0 & 0 & 0 & 0 & 0 & 0 \\ -6\xi + 12\xi^2 - 6\xi^3 & 0 & 0 & -6\xi^2 + 6\xi^3 & 0 & 0 \\ L_e - 5\xi L_e + 7\xi^2 L_e - 3\xi^3 L_e & 0 & 0 & \xi L_e - 4\xi^2 L_e + 3\xi^3 L_e & 0 & 0 \\ 0 & 0 & 0 & 0 & 0 & 0 \\ 6\xi - 12\xi^2 + 6\xi^3 & 0 & 0 & 6\xi^2 - 6\xi^3 & 0 & 0 \\ -2\xi L_e + 5\xi^2 L_e - 3\xi^3 L_e & 0 & 0 & -2\xi^2 L_e + 3\xi^3 L_e & 0 & 0 \end{bmatrix} d\xi\, dy \begin{Bmatrix} \dot{u}_i \\ \dot{v}_i \\ \dot{\theta}_i \\ \dot{u}_i \\ \dot{v}_j \\ \dot{\theta}_j \end{Bmatrix}^T \begin{Bmatrix} \dot{u}_i \\ \dot{v}_i \\ \dot{\theta}_i \\ \dot{u}_i \\ \dot{v}_j \\ \dot{\theta}_j \end{Bmatrix}$$

$$= b\,L_e \int_{-\frac{h}{2}}^{\frac{h}{2}} \rho(y)\, dy \begin{Bmatrix} \dot{u}_i \\ \dot{v}_i \\ \dot{\theta}_i \\ \dot{u}_i \\ \dot{v}_j \\ \dot{\theta}_j \end{Bmatrix}^T \begin{bmatrix} 0 & 0 & 0 & 0 & 0 & 0 \\ -\frac{1}{2} & 0 & 0 & -\frac{1}{2} & 0 & 0 \\ \frac{L_e}{12} & 0 & 0 & -\frac{L_e}{12} & 0 & 0 \\ 0 & 0 & 0 & 0 & 0 & 0 \\ \frac{1}{2} & 0 & 0 & \frac{1}{2} & 0 & 0 \\ -\frac{L_e}{12} & 0 & 0 & \frac{L_e}{12} & 0 & 0 \end{bmatrix} \begin{Bmatrix} \dot{u}_i \\ \dot{v}_i \\ \dot{\theta}_i \\ \dot{u}_i \\ \dot{v}_j \\ \dot{\theta}_j \end{Bmatrix} \quad \textbf{(B.72)}$$

The forth part

$$\iint_A \int_0^1 L_e \frac{y}{L_e} \left(\frac{\partial \dot{v}_0(\xi,t)}{\partial x} \frac{\partial \dot{v}_0(\xi,t)}{\partial x} \right) d\xi\, dy\, dz$$

$$= b\,L_e \int_{-\frac{h}{2}}^{\frac{h}{2}} \int_0^1 \rho(y) \left(\{0 \quad 1-3\xi^2+2\xi^3 \quad L_e\xi - 2L_e\xi^2 + L_e\xi^3 \quad 0 \quad 3\xi^2 - 2\xi^3 \quad -L_e\xi^2 + L_e\xi^3\} \begin{Bmatrix} \dot{u}_i \\ \dot{v}_i \\ \dot{\theta}_i \\ \dot{u}_i \\ \dot{v}_j \\ \dot{\theta}_j \end{Bmatrix} \right)^T \left(\{0 \quad 1-3\xi^2+2\xi^3 \quad L_e\xi - 2L_e\xi^2 + L_e\xi^3 \quad 0 \quad 3\xi^2 - 2\xi^3 \quad -L_e\xi^2 + L_e\xi^3\} \begin{Bmatrix} \dot{u}_i \\ \dot{v}_i \\ \dot{\theta}_i \\ \dot{u}_i \\ \dot{v}_j \\ \dot{\theta}_j \end{Bmatrix} \right) d\xi\, dy$$

$$= b\,L_e \int_{-\frac{h}{2}}^{\frac{h}{2}} \int_0^1 \rho(y) \begin{bmatrix} 0 & 0 & 0 & 0 & 0 & 0 \\ 0 & 36\xi^2 - 72\xi^3 + 36\xi^4 & -6\xi L_e + 30\xi^2 L_e - 42\xi^3 L_e + 18\xi^4 L_e & 0 & -36\xi^2 + 72\xi^3 - 36\xi^4 & 12\xi^2 L_e - 30\xi^3 L_e + 18\xi^4 L_e \\ 0 & -6\xi L_e + 30\xi^2 L_e - 42\xi^3 L_e + 18\xi^4 L_e & L_e^2 - 8\xi L_e^2 + 22\xi^2 L_e^2 - 24\xi^3 L_e^2 + 9\xi^4 L_e^2 & 0 & 6\xi L_e - 30\xi^2 L_e + 42\xi^3 L_e - 18\xi^4 L_e & -2\xi L_e^2 + 11\xi^2 L_e^2 - 18\xi^3 L_e^2 + 9\xi^4 L_e^2 \\ 0 & 0 & 0 & 0 & 0 & 0 \\ 0 & -36\xi^2 + 72\xi^3 - 36\xi^4 & 6\xi L_e - 30\xi^2 L_e + 42\xi^3 L_e - 18\xi^4 L_e & 0 & 36\xi^2 - 72\xi^3 + 36\xi^4 & -12\xi^2 L_e + 30\xi^3 L_e - 18\xi^4 L_e \\ 0 & 12\xi^2 L_e - 30\xi^3 L_e + 18\xi^4 L_e & -2\xi L_e^2 + 11\xi^2 L_e^2 - 18\xi^3 L_e^2 + 9\xi^4 L_e^2 & 0 & -12\xi^2 L_e + 30\xi^3 L_e - 18\xi^4 L_e & 4\xi^2 L_e^2 - 12\xi^3 L_e^2 + 9\xi^4 L_e^2 \end{bmatrix} d\xi\, dy \begin{Bmatrix} \dot{u}_i \\ \dot{v}_i \\ \dot{\theta}_i \\ \dot{u}_i \\ \dot{v}_j \\ \dot{\theta}_j \end{Bmatrix}^T \begin{Bmatrix} \dot{u}_i \\ \dot{v}_i \\ \dot{\theta}_i \\ \dot{u}_i \\ \dot{v}_j \\ \dot{\theta}_j \end{Bmatrix}$$

$$= b\,L_e \int_{-\frac{h}{2}}^{\frac{h}{2}} \rho(y)\, dy \begin{Bmatrix} \dot{u}_i \\ \dot{v}_i \\ \dot{\theta}_i \\ \dot{u}_i \\ \dot{v}_j \\ \dot{\theta}_j \end{Bmatrix}^T \begin{bmatrix} 0 & 0 & 0 & 0 & 0 & 0 \\ 0 & \frac{6}{5} & \frac{L_e}{10} & 0 & -\frac{6}{5} & \frac{L_e}{10} \\ 0 & \frac{L_e}{10} & \frac{2L_e^2}{15} & 0 & -\frac{L_e}{10} & -\frac{L_e^2}{30} \\ 0 & 0 & 0 & 0 & 0 & 0 \\ 0 & -\frac{6}{5} & -\frac{L_e}{10} & 0 & \frac{6}{5} & -\frac{L_e}{10} \\ 0 & \frac{L_e}{10} & -\frac{L_e^2}{30} & 0 & -\frac{L_e}{10} & \frac{2L_e^2}{15} \end{bmatrix} \begin{Bmatrix} \dot{u}_i \\ \dot{v}_i \\ \dot{\theta}_i \\ \dot{u}_i \\ \dot{v}_j \\ \dot{\theta}_j \end{Bmatrix} \quad \textbf{(B.73)}$$

The fifth part

$$\iint_A \int_0^1 L_e \frac{y}{L_e} (\dot{v}_0(\xi,t) \dot{v}_0(\xi,t))\, d\xi\, dy\, dz$$

$$= b\,L_e \int_{-\frac{h}{2}}^{\frac{h}{2}} \int_0^1 \rho(y) \left(\{0 \quad 1-3\xi^2+2\xi^3 \quad L_e\xi - 2L_e\xi^2 + L_e\xi^3 \quad 0 \quad 3\xi^2 - 2\xi^3 \quad -L_e\xi^2 + L_e\xi^3\} \begin{Bmatrix} \dot{u}_i \\ \dot{v}_i \\ \dot{\theta}_i \\ \dot{u}_i \\ \dot{v}_j \\ \dot{\theta}_j \end{Bmatrix} \right)^T \left(\{0 \quad 1-3\xi^2+2\xi^3 \quad L_e\xi - 2L_e\xi^2 + L_e\xi^3 \quad 0 \quad 3\xi^2 - 2\xi^3 \quad -L_e\xi^2 + L_e\xi^3\} \begin{Bmatrix} \dot{u}_i \\ \dot{v}_i \\ \dot{\theta}_i \\ \dot{u}_i \\ \dot{v}_j \\ \dot{\theta}_j \end{Bmatrix} \right) d\xi\, dy$$

$$= b\,L_e \int_{-\frac{h}{2}}^{\frac{h}{2}}\int_0^1 \rho(y) \begin{bmatrix} 0 & 0 & 0 & 0 & 0 & 0 \\ 0 & 1-6\xi^2+4\xi^3+9\xi^4-12\xi^5+4\xi^6 & \xi L_e-2\xi^2L_e-2\xi^3L_e+8\xi^4L_e-7\xi^5L_e+2\xi^6L_e & 0 & 3\xi^2-2\xi^3-9\xi^4+12\xi^5-4\xi^6 & -\xi^2L_e+\xi^3L_e+3\xi^4L_e-5\xi^5L_e+2\xi^6L_e \\ 0 & \xi L_e-2\xi^2L_e-2\xi^3L_e+8\xi^4L_e-7\xi^5L_e+2\xi^6L_e & \xi^2L_e^2-4\xi^3L_e^2+6\xi^4L_e^2-4\xi^5L_e^2+\xi^6L_e^2 & 0 & 3\xi^3L_e-8\xi^4L_e+7\xi^5L_e-2\xi^6L_e & -\xi^3L_e^2+3\xi^4L_e^2-3\xi^5L_e^2+\xi^6L_e^2 \\ 0 & 0 & 0 & 0 & 0 & 0 \\ 0 & 3\xi^2-2\xi^3-9\xi^4+12\xi^5-4\xi^6 & 3\xi^3L_e-8\xi^4L_e+7\xi^5L_e-2\xi^6L_e & 0 & 9\xi^4-12\xi^5+4\xi^6 & -3\xi^4L_e+5\xi^5L_e-2\xi^6L_e \\ 0 & -\xi^2L_e+\xi^3L_e+3\xi^4L_e-5\xi^5L_e+2\xi^6L_e & -\xi^3L_e^2+3\xi^4L_e^2-3\xi^5L_e^2+\xi^6L_e^2 & 0 & -3\xi^4L_e+5\xi^5L_e-2\xi^6L_e & \xi^4L_e^2-2\xi^5L_e^2+\xi^6L_e^2 \end{bmatrix} d\xi\,dy \begin{Bmatrix} \dot{u}_i \\ \dot{v}_i \\ \dot{\theta}_i \\ \dot{u}_j \\ \dot{v}_j \\ \dot{\theta}_j \end{Bmatrix}^T \begin{Bmatrix} \dot{u}_i \\ \dot{v}_i \\ \dot{\theta}_i \\ \dot{u}_j \\ \dot{v}_j \\ \dot{\theta}_j \end{Bmatrix}$$

$$= b\,L_e \int_{-\frac{h}{2}}^{\frac{h}{2}} \rho(y)\,dy \begin{Bmatrix} \dot{u}_i \\ \dot{v}_i \\ \dot{\theta}_i \\ \dot{u}_i \\ \dot{v}_j \\ \dot{\theta}_j \end{Bmatrix}^T \begin{bmatrix} 0 & 0 & 0 & 0 & 0 & 0 \\ 0 & \frac{13}{35} & \frac{11L_e}{210} & 0 & \frac{9}{70} & -\frac{13L_e}{420} \\ 0 & \frac{11L_e}{210} & \frac{L_e^2}{105} & 0 & \frac{13L_e}{420} & -\frac{L_e^2}{140} \\ 0 & 0 & 0 & 0 & 0 & 0 \\ 0 & \frac{9}{70} & \frac{13L_e}{420} & 0 & \frac{13}{35} & -\frac{11L_e}{210} \\ 0 & -\frac{13L_e}{420} & -\frac{L_e^2}{140} & 0 & -\frac{11L_e}{210} & \frac{L_e^2}{105} \end{bmatrix} \begin{Bmatrix} \dot{u}_i \\ \dot{v}_i \\ \dot{\theta}_i \\ \dot{u}_i \\ \dot{v}_j \\ \dot{\theta}_j \end{Bmatrix} \quad \textbf{(B.74)}$$

From equations (B.28), (B.44) and (B.45), the velocity vector $\{\dot{d}\}$ maybe rewritten as:

$$\{\dot{d}\} = \begin{Bmatrix} \dot{u} \\ \dot{v} \end{Bmatrix} = \begin{bmatrix} 1 & 0 & -y \\ 0 & 1 & 0 \end{bmatrix} \begin{Bmatrix} \dot{u}(\xi) \\ \dot{v}(\xi) \\ \dot{\theta}(\xi) \end{Bmatrix}$$

$$\begin{Bmatrix} \dot{u}(\xi) \\ \dot{v}(\xi) \\ \dot{\theta}(\xi) \end{Bmatrix} = \begin{bmatrix} 1-\xi & 0 & 0 & \xi & 0 & 0 \\ 0 & 1-3\xi^2+2\xi^3 & L_e\xi-2L_e\xi^2+L_e\xi^3 & 0 & 3\xi^2-2\xi^3 & -L_e\xi^2+L_e\xi^3 \\ 0 & -6\xi+6\xi^2 & L_e-4L_e\xi+3L_e\xi^2 & 0 & 6\xi-6\xi^2 & -2L_e\xi+3L_e\xi^2 \end{bmatrix} \begin{Bmatrix} u_i \\ v_i \\ \theta_i \\ u_j \\ v_j \\ \theta_j \end{Bmatrix}$$

$$\{\dot{d}\} = \begin{bmatrix} 1 & 0 & -y \\ 0 & 1 & 0 \end{bmatrix} \begin{bmatrix} 1-\xi & 0 & 0 & \xi & 0 & 0 \\ 0 & 1-3\xi^2+2\xi^3 & L_e\xi-2L_e\xi^2+L_e\xi^3 & 0 & 3\xi^2-2\xi^3 & -L_e\xi^2+L_e\xi^3 \\ 0 & -6\xi+6\xi^2 & L_e-4L_e\xi+3L_e\xi^2 & 0 & 6\xi-6\xi^2 & -2L_e\xi+3L_e\xi^2 \end{bmatrix} \begin{Bmatrix} u_i \\ v_i \\ \theta_i \\ u_j \\ v_j \\ \theta_j \end{Bmatrix} \quad \textbf{(B.75)}$$

Substituting equations (B.64) and (B.75) into (B.63)

$$\Lambda = \frac{1}{2}\iiint_{vol} \rho(y)(\{\dot{u}(x,t)\}^T\{\dot{u}(x,t)\} + \{\dot{w}_0(x,t)\}^T\{\dot{w}_0(x,t)\})\,dx\,dy\,dz$$

$$\rho(y) \begin{bmatrix} 1 & 0 & -y \\ 0 & 1 & 0 \end{bmatrix}^T \begin{bmatrix} 1 & 0 & -y \\ 0 & 1 & 0 \end{bmatrix}$$

$$\begin{bmatrix} 1-\xi & 0 & 0 & \xi & 0 & 0 \\ 0 & 1-3\xi^2+2\xi^3 & L_e\xi-2L_e\xi^2+L_e\xi^3 & 0 & 3\xi^2-2\xi^3 & -L_e\xi^2+L_e\xi^3 \\ 0 & \frac{-6\xi+6\xi^2}{L_e} & 1-4\xi+3\xi^2 & 0 & \frac{6\xi-6\xi^2}{L_e} & -2\xi+3\xi^2 \end{bmatrix}^T$$

$$\Lambda = \frac{1}{2}\iiint_{vol} \begin{bmatrix} 1-\xi & 0 & 0 & \xi & 0 & 0 \\ 0 & 1-3\xi^2+2\xi^3 & L_e\xi-2L_e\xi^2+L_e\xi^3 & 0 & 3\xi^2-2\xi^3 & -L_e\xi^2+L_e\xi^3 \\ 0 & \frac{-6\xi+6\xi^2}{L_e} & 1-4\xi+3\xi^2 & 0 & \frac{6\xi-6\xi^2}{L_e} & -2\xi+3\xi^2 \end{bmatrix}$$

$$\begin{Bmatrix} u_i \\ v_i \\ \theta_i \\ u_j \\ v_j \\ \theta_j \end{Bmatrix}^T \begin{Bmatrix} u_i \\ v_i \\ \theta_i \\ u_j \\ v_j \\ \theta_j \end{Bmatrix} dx\,dy\,dz$$

$$\Lambda = \frac{1}{2}\int_z \int_{-\frac{h}{2}}^{\frac{h}{2}}\int_0^1 \rho(y) \begin{bmatrix} 1-\xi & 0 & 0 & \xi & 0 & 0 \\ 0 & 1-3\xi^2+2\xi^3 & L_e\xi-2L_e\xi^2+L_e\xi^3 & 0 & 3\xi^2-2\xi^3 & -L_e\xi^2+L_e\xi^3 \\ 0 & \frac{-6\xi+6\xi^2}{L_e} & 1-4\xi+3\xi^2 & 0 & \frac{6\xi-6\xi^2}{L_e} & -2\xi+3\xi^2 \end{bmatrix}^T \begin{bmatrix} 1 & 0 & -y \\ 0 & 1 & 0 \\ -y & 1 & y^2 \end{bmatrix}$$

$$\begin{bmatrix} 1-\xi & 0 & 0 & \xi & 0 & 0 \\ 0 & 1-3\xi^2+2\xi^3 & L_e\xi-2L_e\xi^2+L_e\xi^3 & 0 & 3\xi^2-2\xi^3 & -L_e\xi^2+L_e\xi^3 \\ 0 & \frac{-6\xi+6\xi^2}{L_e} & 1-4\xi+3\xi^2 & 0 & \frac{6\xi-6\xi^2}{L_e} & -2\xi+3\xi^2 \end{bmatrix} \begin{Bmatrix} u_i \\ v_i \\ \theta_i \\ u_j \\ v_j \\ \theta_j \end{Bmatrix}^T \begin{Bmatrix} u_i \\ v_i \\ \theta_i \\ u_j \\ v_j \\ \theta_j \end{Bmatrix} d\xi\,dy\,dz \quad \textbf{(B.76)}$$

The mass matrix of the FG beam is obtained from equation (B.76) as

$$[m_e] = b\int_{-\frac{h}{2}}^{\frac{h}{2}}\left([\rho_c - \rho_m]\left(\frac{y}{h}+\frac{1}{2}\right)^n \rho_m\right)\begin{bmatrix} 1-\xi & 0 & 0 & \xi & 0 & 0 \\ 0 & 1-3\xi^2+2\xi^3 & L_e\xi - 2L_e\xi^2 + L_e\xi^3 & 0 & 3\xi^2-2\xi^3 & -L_e\xi^2 + L_e\xi^3 \\ 0 & \frac{-6\xi+6\xi^2}{L_e} & 1-4\xi+3\xi^2 & 0 & \frac{6\xi-6\xi^2}{L_e} & -2\xi+3\xi^2 \end{bmatrix}^T \begin{bmatrix} 1 & 0 & -y \\ 0 & 1 & 0 \\ -y & 1 & y^2 \end{bmatrix} \begin{bmatrix} 1-\xi & 0 & 0 & \xi & 0 & 0 \\ 0 & 1-3\xi^2+2\xi^3 & L_e\xi - 2L_e\xi^2 + L_e\xi^3 & 0 & 3\xi^2-2\xi^3 & -L_e\xi^2 + L_e\xi^3 \\ 0 & \frac{-6\xi+6\xi^2}{L_e} & 1-4\xi+3\xi^2 & 0 & \frac{6\xi-6\xi^2}{L_e} & -2\xi+3\xi^2 \end{bmatrix} dy \quad \textbf{(B.77)}$$

Bibliography

[1] S. S. Rao, *The Finite Element Method in Engineering*, 3rd ed. Massachusetts: Butterworth-Heinemann, 1999.

[2] J. Ko, A. J. Kurdila, and M. S. Pilant, "A Class of Wavelet-Based Finite Element Methods for Computational Mechanics," in *Proceedings of the 35th Structures, Structural Dynamics and Materials Conference*, South Carolina, 1994, pp. 665-675.

[3] W. .-H. Chen and C. .-W. Wu, "A Spline Wavelets Element Method for Frame Structures Vibration," *Computational Mechanics*, vol. 16, no. 1, pp. 11-21, 1995.

[4] A. Grossmann and J. Morlet, "Decomposition of Hardy Functions into Square Integrable Wavelets of Constant Shape," *SIAM Journal of Mathematical Analysis*, vol. 15, no. 4, pp. 723-736, 1984.

[5] G. Strang, "Wavelet and Dilation Equations: A Brief Introduction," *Society for Industrial and Applied Mathematics Review*, vol. 31, no. 4, pp. 614-627, 1989.

[6] X. Chen, Z. He, J. Xiang, and B. Li, "A Dynamic Multiscale Lifting Computation Method using Daubechies Wavelet," *Journal of Computational and Applied Mathematics*, vol. 188, no. 2, pp. 228-245, 2006.

[7] J. W. Xiang, X. F. Chen, Z. J. He, and H. B. Dong, "The Construction of 1D Wavelet Finite Elements for Structural Analysis," *Computational Mechanics*, vol. 40, no. 2, pp. 325-339, 2007.

[8] X. Chen, S. Yang, J. Ma, and Z. He, "The Construction of Wavelet Finite Element and its Applications," *Finite Elements in Analysis and Design*, vol. 40, no. 5-6, pp. 541-554, 2004.

[9] J. Ko, J. Kurdila, and M. S. Pilant, "A Class of Finite Element Methods Based on Orthonormal, Compactly Supported Wavelets," *Computational Mechanics*, vol. 16, no. 4, pp. 235-244, 1995.

[10] J. Ma, J. Xue, S. Yang, and Z. He, "A Study of the Construction and Application of a Daubechies Wavelet-Based Beam Element," *Finite Elements in Analysis and Design*, vol. 39, no. 10, pp. 965-975, 2003.

[11] J. Xiang, X. Chen, Y. He, and Z. He, "The Construction of Plane Elastomechanics and Mindlin Plate Elements of B-spline Wavelet on the Interval," *Finite Elements in Analysis and Design*, vol. 42, no. 14-15, pp. 1269-1280, 2006.

[12] J. Xiang, X. Chen, Y. He, and Z. He, "Static and Vibration Analysis of Thin Plates by using Finite Element Method of B-spline Wavelet on the Interval," *Structural Engineering and Mechanics*, vol. 25, no. 5, pp. 613-629, 2007.

[13] W. .-Y. He and W. .-X. Ren, "Finite Element Analysis of Beam Structures Based on Trigonometric Wavelet," *Finite Elements in Analysis and Design*, vol. 51, pp. 59-66, 2012.

[14] W. .-Y. He and W. .-X. Ren, "Trigonometric Wavelet-Based Method for Elastic Thin Plate Analysis," *Applied Mathematical Modelling*, vol. 37, no. 4, pp. 1607-1617, Feb. 2013.

[15] I. Daubechies, *Ten Lectures on Wavelets*. Philadelphia: Society for Industrial and Applied Mathematics, 1992.

[16] G. Strang and T. Nguyen, *Wavelets and Filter Banks*. Massachusetts: Wellesley-Cambridge Press, 1996.

[17] A. Graps, "An Introduction to Wavelets," *IEEE Journal of Computation Science and Engineering*, vol. 2, no. 2, pp. 1-17, 1995.

[18] S. G. Mallat, "Multiresolution Approximations and Wavelet Orthonormal Bases of L2(R)," *Transactions of the American Mathematical Society*, vol. 315, no. 1, pp. 69-87, 1989.

[19] C. K. Chui, *An Introduction to Wavelets*, 1st ed. London, United Kingdom: Academic Press Limited, 1992.

[20] I. Daubechies, "Orthonormal Bases of Compactly Supported Wavelets," *Communications on Pure and Applied Mathematics*, vol. 41, no. 7, pp. 909-996, 1988.

[21] M. D. Harpen, "An Introduction to Wavelet Theory and Application for the Radiological Physicist," *Medical Physics*, vol. 25, no. 10, pp. 1985-1993, 1998.

[22] H. Rabbani, R. Nezafat, and S. Gazor, "Wavelet-Domain Medical Image Denoising using Bivariate Laplacian Mixture Model," *IEEE Transactions on Biomedical Engineering*, vol. 56, no. 12, pp. 2826-2837, 2009.

[23] J. B. Ramsey, "The Contribution of Wavelets to the Analysis of Economics and Financial Data," *Philosophical Transactions of The Royal Society*, vol. 357, no. 1760, pp. 2593-2606, 1999.

[24] P. Kumar and E. Foufoula-Georgiou, "Wavelet Analysis for Geophysical Applications," *Reviews in Geophysics*, vol. 35, no. 4, pp. 385-412, 1997.

[25] J. .-L. Starck and J. Bobin, "Astronomical Data Analysis and Sparity: From Wavelets to Compressed Sensing," *Proceedings of the IEEE*, vol. 98, no. 6, pp. 1021-1030, 2010.

[26] J. Song, H. .-Y. Fan, and H. .-C. Yuan, "Wavelet Transform of Quantum Chemical States," *International Journal of Quantum Chemistry*, vol. 112, no. 11, pp. 2343-2347, 2012.

[27] K. J. Bathe, *Finite Element Procedures*, 1st ed. New Jersey, United States of America: Prentice Hall, 1996.

[28] T. G. Huebner, D. L. Dewhirst, D. E. Smith, and T. G. Byrom, *The Finite Element Method for Engineers*, 4th ed. New York, USA: John Wiley and Sons Inc, 2001.

[29] R. D. Cook, D. S. Malkus, M. E. Plesha, and R. J. Witt, *Concepts and Applications of Finite Element Analysis*, 4th ed. New Jersey: John Wiley and Sons Inc, 2001.

[30] G. R. Liu and S. S. Quek, *The Finite Element Method: A Practical Course*. Oxford: Elsevier Science Ltd., 2003.

[31] D. L. Logan, *A First Course in the Finite Element Method*, 4th ed. Toronto, Canada: Nelson, 2006.

[32] Y. El-Kurdi, D. Gainnacopoulos, and W. J. Gross, "Hardware Acceleration for Finite-Element Electromagnetics: Efficient Sparse Matrix Floating-Point Computations with FPGAs," *IEEE Transactions on Magnetics*, vol. 43, no. 4, pp. 1525-1528, 2007.

[33] P. K. Basu, A. B. Jorge, S. Badri, and J. Lin, "Higher-order Modeling of Continua by Finite Element, Boundary Element, Meshless and Wavelet Methods," *Computers and Mathematics with Applications*, vol. 46, no. 1, pp. 15-33, 2003.

[34] G. Beylkin, "On the Representation of Operators in Bases of Compactly Supported Wavelets," *SIAM Journal on Numerical Analysis*, vol. 6, no. 6, pp. 1716-1740, 1992.

[35] W. Dahmen and C. A. Micchelli, "Using the Refinement Equation for Evaluating Integrals of Wavelets," *SIAM Journal of Numerical Analysis*, vol. 30, no. 2, pp. 507-537, 1993.

[36] A. Latto, H. L. Resnikoff, and E. Tenenbaum, "The Evaluation of Connection Coefficients of Compactly Supported Wavelets," in *Proceedings of the French-USA Workshop on Wavelets and Turbulence*, New York, 1991.

[37] J. Ko, A. J. Kurdila, and M. S. Pilant, "Triangular Wavelet Based Finite Elements Via Multivalued Scaling Equations," *Computer Methods in Applied Mechanics and Engineering*, vol. 146, no. 1-2, pp. 1-17, 1997.

[38] Y. Zhou, J. Wang, and X. Zheng, "Applications of Wavelet Galerkin FEM to Bending of Beams and Plate Structures," *Applied Mathematics and Mechanics*, vol. 19, no. 8, pp. 745-755, 1998.

[39] M. .-Q. Chen, C. Hwang, and Y. .-P. Shih, "The Computation of Wavelet-Galerkin Approximation on a Bounded Interval," *Journal for Numerical Methods in Engineering*, vol. 39, no. 17, pp. 2921-2944, 1996.

[40] L. A. Diaz, M. T. Martin, and V. Vampa, "Daubechies Wavelet Beam and Plate Finite Elements," *Finite Elements in Analysis and Design*, vol. 45, no. 3, pp. 200-209, 2009.

[41] L. A. Diaz, V. Vampa, and M. T. Martin, "The Construction of Plate Finite Elements using Wavelet Basis Functions," *Revista Investigacion Operacional*, vol. 30, no. 3, pp. 193-204, 2009.

[42] X. .-M. Zhang, K. A. Liu, and J. .-Q. Liu, "A Wavelet Finite Element Method for 2-D Wave Equation in the Fluid-Saturated Porous Media," *Chinese Journal of Geophysics*, vol. 48, no. 5, pp. 1234-1246, 2005.

[43] Y. M. Wang, X. F. Chen, and Z. J. He, "Daubechies Wavelet Finite Element Method and Genetic Algorithm for Detection of Pipe Crack," *Nondestructive Testing and Evaluation*, vol. 26, no. 1, pp. 87-99, 2011.

[44] B. Zhao and K. Wang, "The Application of the Wavelet Finite Element Method on the Temperature Field and Thermal Stress Analysis of the Petroleum Tank," *Journal of Information and Computational Science*, vol. 8, no. 7, pp. 1103-1111, 2011.

[45] B. Zhao, "Study on Temperature-Pressure Gas-Liquid Coupled Field of LPG Tank under Fire Based on Wavelet Finite Element Method," *Journal of Computers*, vol. 24, no. 2, pp. 10-19, 2013.

[46] B. Zhao, "Identification of Multi-Cracks in the Gate Rotor Shaft Based on the Wavelet Finite Element Method," *American Journal of Engineering and Applied Sciences*, vol. 6, no. 3, pp. 309-319, 2013.

[47] Y. .-H. Zhou and J. Zhou, "A Modified Wavelet Approximation of Deflections for solving PDEs of Beams and Square Thin Plates," *Finite Elements in Analysis and Design*, vol. 44, no. 12-13, pp. 773-783, 2008.

[48] M. Mitra and S. Gopalakrishnan, "Spectral Formulated Wavelet Finite Element For Wave Propagation and Impact Force Identification in Connected 1D Waveguides," *International Journal of Solids and Structures*, vol. 42, no. 16-17, pp. 4695-4721, 2005.

[49] M. Mitra and S. Gopalakrishnan, "Extraction of Wave Characteristics from Wavelet-Based Spectral Finite Element Formulation," *Mechanical Systems and Signal*

Processing, vol. 20, no. 8, pp. 2046-2079, 2006.

[50] M. Mitra and S. Gopalakrishnan, "Wavelet Based Spectral Finite Element for Analysis of Coupled Wave Propagation in Higher Order Composite Beams," *Composite Structures*, vol. 73, no. 3, pp. 263-277, 2006.

[51] S. Pengcheng and H. Peixiang, "Bending Analysis of Plates and Spherical Shells by Multivariable Spline Element Method Based on Generalized Variational Principle," *Computers and Structures*, vol. 55, no. 1, pp. 151-157, 1995.

[52] S. Pengcheng and H. Peixiang, "Bending Analysis of Rectangular Moderately Thick Plates using Spline Element Method," *Computers and Structures*, vol. 54, no. 6, pp. 1023-1029, 1995.

[53] S. Pengcheng and H. Peixiang, "Analysis of Bending, Vibration and Stability for Thin Plate on Elastic Foundation by Multivariable Spline Element Method," *Applied Mathematics and Mechanics*, vol. 18, no. 8, pp. 779-787, 1997.

[54] C. K. Chui and E. Quak, "Wavelets on a Bound Interval," *Numerical Methods of Approximation Theory*, vol. 9, pp. 53-57, 1992.

[55] J. Xiang, Z. He, and X. Chen, "The Construction of Wavelet-Based Truncated Conical Shell Element using B-spline Wavelet on the Interval," *Acta Mechanica Solida Sinica*, vol. 19, no. 4, pp. 316-326, 2006.

[56] J. Xiang, X. Chen, Z. He, and Y. Zhang, "A New Wavelet-Based Thin Plate Element using B-spline Wavelet on the Interval," *Computational Mechanics*, vol. 41, no. 2, pp. 243-255, 2008.

[57] J. Xiang, D. Chen, X. Chen, and Z. He, "A Novel Wavelet-based Finite Element Method for the Analysis of Rotor-Bearing Systems," *Finite Element in Analysis and Design*, vol. 45, no. 12, pp. 908-916, 2009.

[58] X. Zhang, X. Chen, X. Wang, and Z. He, "Multivariable Finite Elements based on B-Spline Wavelet on the Interval for Thin Plate Static and Vibration Analysis," *Finite Elements in Analysis and Design*, vol. 46, no. 5, pp. 416-427, 2010.

[59] Z. Yang, et al., "Wave Motion Analysis in Arch Structures via Wavelet Finite Element Method," *Journal of Sound and Vibration*, vol. 333, no. 2, pp. 446-469, 2014.

[60] Z. Yang, X. Chen, Y. He, Z. He, and J. Zhang, "The Analysis of Curved Beam Using B-Spline Wavelet on Interval Finite Element Method," *Shock and Vibration*, vol. 2014, no. Article ID: 738162, p. 9Pages, 2014.

[61] J. W. Xiang, J. Q. Long, and Z. S. Jiang, "A Numerical Study using Hermitian Cubic

Spline Wavelets for the Analysis of Shafts," *Journal of Mechanical Engineering Science*, vol. 224, no. 9, pp. 1843-1851, 2010.

[62] J. W. Xiang and M. Liang, "Multiple Damage Detection Method for Beams Based on Multi-scale Elements using Hermite Cubic Spline Wavelet," *Computer Modeling in Engineering and Sciences*, vol. 73, no. 3, pp. 267-298, 2011.

[63] J. W. Xiang, Y. X. Wang, Z. S. Jiang, J. Q. Long, and G. Ma, "Numerical Simulation of Plane Crack using Hermite Cubic Spline Wavelet," *Computer Modelling in Engineering and Sciences*, vol. 88, no. 1, pp. 1-16, 2012.

[64] L. M. S. Castro, "Polynomial Wavelets in Hybrid-Mixed Stress Finite Element Models," *International Journal for Numerical Methods in Biomedical Engineering*, vol. 26, no. 10, pp. 1293-1312, 2010.

[65] R. T. Mario and L. M. S. Castro, "Structural Dynamic Analysis using Hybrid and Mixed Finite Element Models," *Finite Elements in Analysis and Design*, vol. 57, pp. 43-54, 2012.

[66] Y. M. Wang, X. F. Chen, and Z. J. He, "An Adaptive Inverse Iteration Algorithm using Interpolating Multiwavelets for Structural Eigenvalue Problems," *Mechanical Systems and Signal Processing*, vol. 25, no. 2, pp. 591-600, 2011.

[67] S. M. Quraishi and K. Sandeep, "A Second Generation Wavelet Based Finite Elements on Triangulations," *Computational Mechanics*, vol. 48, no. 2, pp. 163-174, 2011.

[68] B. Li and X. Chen, "Wavelet-Based Numerical Analysis: A Review and Classification," *Finite Elements in Analysis and Design*, vol. 81, pp. 14-31, 2014.

[69] A. Chakraborty, S. Gopalakrishnan, and J. N. Reddy, "A New Beam Finite Element for the Analysis of Functionally Graded Materials," *International Journal of Mechanical Sciences*, vol. 45, no. 3, pp. 519-539, 2003.

[70] E. Carrera, G. Giunta, and M. Petrolo. (2011, Sep.) Beam Structures: Classical and Advanced Theories. Electronic Book. [Online]. http://www.myilibrary.com?ID=320455

[71] H. .-S. Shen, *Functionally Graded Materials: Nonlinear Analysis of Plates and Shells*, 1st ed. Boca Raton, FL, USA: CRC Press, Taylor & Francis Group, 2009.

[72] M. Koizumi, "FGM Activities in Japan," *Composites Part B: Engineering*, vol. 28, no. 1-2, pp. 1-4, 1997.

[73] D. K. Jha, T. Kant, and R. K. Singh, "A Critical Review of Recent Research on Functionally Graded Plates," *Composite Structures*, vol. 96, pp. 833-849, 2013.

[74] M. Aydogdu and V. Taskin, "Free Vibration Analysis of Functionally Graded Beams with Simply Supported Edges," *Materials and Design*, vol. 28, no. 5, pp. 1651-1656, 2007.

[75] R. Kadoli, K. Akhtar, and N. Ganesan, "Static Analysis of Functionally Graded Beams using Higher Order Shear Deformation Theory," *Applied Mathematical Modelling*, vol. 32, no. 12, pp. 2509-2525, 2008.

[76] S. A. Sina, H. M. Navazi, and H. Haddadpour, "An Analytical Method for Free Vibration Analysis of Functionally Graded Beams," *Materials and Design*, vol. 30, no. 3, pp. 741-747, 2009.

[77] H. .-T. Thai and T. P. Vo, "Bending and Free Vibration of Functionally Graded Beams using Various Higher-Order Shear Deformation Beam Theories," *International Journal of Mechanical Science*, vol. 62, no. 1, pp. 57-66, 2012.

[78] K. K. Pradhan and S. Chakraverty, "Free Vibration of Euler and Timoshenko Functionally Graded Beams by Rayeigh-Ritz Method," *Composites: Part B*, vol. 51, pp. 175-184, 2013.

[79] A. E. Alshorbagy, M. A. Eltaher, and F. F. Mahmoud, "Free Vibration Characteristics of a Functionally Graded Beam by Finite Element Method," *Applied Mathematical Modelling*, vol. 35, no. 1, pp. 412-425, 2011.

[80] Y. Huang and X. .-F. Li, "A New Approach for Free Vibration of Axially Functionally Graded Beams with Non-Uniform Cross-Section," *Journal of Sound and Vibration*, vol. 329, no. 11, pp. 2291-2303, 2010.

[81] A. Shahba and S. Rajasekaran, "Free Vibration and Stability of Tapered Euler-Bernoulli Beams Made of Axially Functionally Graded Materials," *Applied Mathematical Modelling*, vol. 36, no. 7, pp. 3094-3111, 2012.

[82] J. Yang, Y. Chen, Y. Xiang, and X. L. Jia, "Free and Forced Vibration of Cracked Inhomogeneous Beams Under an Axial Force and a Moving Load," *Journal of Sound and Vibration*, vol. 312, no. 1-2, pp. 166-181, 2008.

[83] M. Simsek and T. Kocaturk, "Free and Forced Vibration of a Functionally Graded Beam Subjected to a Concentrated Moving Harmonic Load," *Composite Structures*, vol. 90, no. 4, pp. 465-473, 2009.

[84] M. Simsek, "Vibration Analysis of a Functionally Graded Beam Under a Moving Mass by Using Different Beam Theories," *Composite Structures*, vol. 92, no. 4, pp. 904-917, 2010.

[85] M. Simsek, "Non-linear Vibration Analysis of a Functionally Graded Timoshenko

Beam Under Action of a Moving Harmonic Load," *Composite Structures*, vol. 92, no. 10, pp. 2532-2546, 2010.

[86] S. M. R. Khalili, A. A. Jafari, and S. A. Eftekhari, "A Mixed Ritz-DQ Method for Forced Vibration of Functionally Graded Beams Carrying Moving Loads," *Composite Structures*, vol. 92, no. 10, pp. 2497-2511, 2010.

[87] S. G. Mallat, "A Theory for Multiresolution Signal Decomposition: The Wavelet Representation," *IEEE Transactions on Pattern Analysis and Machine Intelligence*, vol. 11, no. 7, pp. 674-693, 1989.

[88] D. Hong, J. Wang, and R. Gardner, *Real Analysis with an Introduction to Wavelets and Applications*. Burlington, Massachusetts: Elsevier Academic Press, 2005.

[89] M. .-Q. Chen, C. Hwang, and Y. .-P. Shih, "A Wavelet-Galerkin Method for Solving Population Balance Equations," *Computers and Chemical Engineering*, vol. 20, no. 2, pp. 131-145, 1996.

[90] T. Zhang, Y. .-C. Tian, M. O. Tade, and J. Utomo, "Comments on "The Computation of Wavelet-Galerkin Approximation on a Bounded Interval"," *International Journal for Numerical Methods in Engineering*, vol. 72, no. 2, pp. 244-251, 2007.

[91] C. H. Romine and B. W. Peyton, "Computing Connection Coefficients of Compactly Supported Wavelets on Bounded Intervals," 1997.

[92] E. B. Lin and X. Zhou, "Connection Coefficients on an Interval and Wavelet Solutions of Burgers Equation," *Journal of Computational and Applied Mathematics*, vol. 135, no. 1, pp. 63-78, 2001.

[93] C. d. Boor, *A Practical Guide to Splines*, Revised ed. New York: Springer-Verlag, 2001.

[94] L. L. Schumaker, *Spline Functions: Basic Theory*. New York: Wiley, 1981.

[95] E. Quak and N. Weyrich, "Decomposition and Reconstruction Algorithms for Spline Wavelets on a Bounded Interval," *Applied and Computational Harmonic Analysis*, vol. 1, no. 3, pp. 217-231, 1994.

[96] J. C. Goswami, A. K. Chan, and C. K. Chui, "On Solving First-Kind Integral Equations using Wavelets on a Bounded Interval," *IEEE Transactions on Antennas and Propagation*, vol. 43, no. 6, pp. 614-622, 1995.

[97] G. L. Narasaiah, *Finite Element Analysis*. Hyderabad: BS Publications, 2008.

[98] O. C. Zienkiewicz and R. L. Taylor, *The Finite Element Method Volume 2: Solid*

Mechanics, 5th ed. Oxford: Butterworth-Heinenmann, 2000, vol. 3.

[99] S. C. Chapra and R. P. Canale, *Numerical Methods for Engineers: With Software and Programming Applications*, 4th ed. McGraw-Hill Higher Education, 2001.

[100] I. Chowdhury and S. P. Dasgupta, "Computation of Rayleigh Damping Coefficients for Large Systems," *The Electronic Journal of Geotechnical Engineering*, vol. 8, no. C, 2003.

[101] K. A. Stroud, *Further Enginnering Mathematics*, 3rd ed. London, U.K.: Macmillan Press Ltd., 1996.

[102] L. Fryba, *Vibration of Solids and Structures Under Moving Loads*, 3rd ed., E. Stott, Ed. London, United Kingom: Thomas Telford Ltd., 1999.

[103] G. Jones, *Analysis of Beams on Elastic Foundations*, 1st ed. London, United Kingdom: Thomas Telford Publishing, 1997.

[104] J. E. Akin, *Finite Elements for Analysis and Design*, 1st ed. London, United Kingdom: Academic Press Limited, 1994.

[105] B. Bondi and S. Caddemi, "Closed Form Solutions of Euler-Bernoulli Beams with Singularities," *International Journal of Solids and Structures*, vol. 42, no. 9-10, pp. 3027-3044, 2005.

[106] K.-s. Wang and Y.-d. Li, "Calculation of Stability for Elastic Compression Bar using Block-Pulse Functions," *Machinery Design and Manufacture*, vol. 3, pp. 5-7, 2004.

[107] H. Ouyang, "Moving-Load Dynamic Problems: A Tutorial (With a Brief Overview)," *Mechanical Systems and Signal Processing*, vol. 25, no. 6, pp. 2039-2060, 2011.

[108] J. Jara-Almonte and L. D. Mitchell, "A Hybrid Eigenproblem Formulation Using the Finite Element Method; Part II Examples," *International Journal of Analytical and Experimental Modal Analysis*, vol. 6, pp. 117-130, 1991.

[109] Z. Dimitrovova and A. F. S. Rodrigues, "Critical Velocity of a Uniformly Moving Load," *Advanced Engineering Software*, vol. 50, pp. 44-56, 2012.

[110] Z. Dimitrovova and J. N. Varandas, "Critical Velocities of a Load Moving on a Beam with a Sudden Change of Foundation Stiffness: Applications to High-Speed Trains," *Computers and Structures*, vol. 87, no. 19-20, pp. 1224-1232, Oct. 2009.

[111] Y.-H. Chen and Y.-H. Huang, "Dynamic Characteristics of Infinite and Finite Railways to Moving Loads," *ASCE Journal of Engineering Mechanics*, vol. 129, no. 9, pp. 987-995, 2003.

[112] A. D. Senalp, A. Arikoglu, I. Ozkol, and V. Z. Dogan, "Dynamic Response of a Finite Length Euler-Bernoulli Beam on Linear and Nonlinear Viscoelastic Foundations to a Concentrated Moving Force," *Journal of Mechanical Science and Technoogy*, vol. 24, no. 10, pp. 1957-1961, 2010.

[113] J. R. Rieker, Y. .-H. Lin, and M. W. Trethewey, "Discretization Considerations in Moving Load Finite Element Beam Models," *Finite Element Analysis and Design*, vol. 21, no. 3, pp. 129-144, 1996.

[114] H. .-S. Shen, *Functionally Graded Materials: Nonlinear Analysis of Plates and Shells*. Boca Raton, FL, USA: CRC Press, 2009.

[115] K. Wakashima, T. Hirano, and M. Niino, "Space Applications of Advanced Structural Materials," in *European Space Agency: Proceedings of an International Symposium*, Paris, France, 1990, pp. 303-397.

[116] T. Mori and K. Tanaka, "Average Stress in Matrix and Average Elastic Energy of Materials with Misfiting Inclusions," *Acta Metallurgica*, vol. 21, pp. 571-574, 1973.

[117] R. Hill, "A Self-Consistent Mechanics of Composite Materials," *Journal of the Mechanics and Physics of Solids*, vol. 13, no. 4, pp. 213-222, 1965.

[118] F. Watari, A. Yokoyama, F. Saso, M. Uo, and T. Kawasaki, "Fabrication and Properties of Functionally Graded Dental Implants," *Composites Part B: Engineering*, vol. 28, no. 1-2, pp. 5-11, 1997.

[119] S. A. Khanoki and D. Pasini, "Multiscale Design and Multiobjective Optimization of Orthopedic Hip Implants with Functionally Graded Cellular Material," *Journal of Biomedical Engineering*, vol. 134, no. 4, pp. 031004-1-031004-10, 2012.

[120] I. Bharti, N. Gupta, and K. M. Gupta, "Novel Applications of Functionally Graded Nano, Optoelectronic and Thermoelectric Materials," *International Journal of Materials, Mechanics and Manufacturing*, vol. 1, no. 3, pp. 221-224, 2013.

[121] G. Udupal, S. S. Rao, and K. V. Gangadharan, "Future Applications of Carbon Nanotube Reinforced Functionally Graded Composite Materials," in *Proceedings of the IEEE International Conference on Advances in Engineering, Science and Management (ICAESM)* , Nagapattinam, Tamil Nadu, 2012, pp. 399-404.